Transactions of the ASME

Journal of Fluids Engineering

Published Quarterly by The American Society of Mechanical Engineers

VOLUME 114 • NUMBER 4 • DECEMBER 1992

(Contents continued on page 592)

FLUIDS ENGINEERING DIVISION
Technical Editor
DEMETRI P. TELIONIS (1995)
Executive Secretary
PAT WHITE (1995)
Technical Editor's Office
SAAD A. RAGAB
Calendar Editor
M. F. ACKERSON

Associate Technical Editors
R. K. AGARWAL (1994)
O. BAYSAL (1995)
MICHAEL L. BILLET (1992)
DENNIS M. BUSHNELL (1993)
N. A. CUMPSTY (1995)
FRANKLIN T. DODGE (1992)
CHIH-MING HO (1993)
THOMAS T. HUANG (1993)
J. A. C. HUMPHREY (1994)
O. C. JONES (1995)
E. E. MICHAELIDES (1992)
R. L. PANTON (1995)
ANDREA PROSPERETTI (1993)
M. W. REEKS (1995)

BOARD ON COMMUNICATIONS
Chairman and Vice-President
R. D. ROCKE

Members-at-Large
T. BARLOW, W. BEGELL, T. F. CONRY,
T. DEAR, J. KITTO, R. MATES, W. MORGAN,
E. M. PATTON, S. PATULSKI, R. E. REDER,
A. VAN DER SLUYS, F. M. WHITE,

President, **J. A. FALCON**
Exec. Dir.
D. L. BELDEN
Treasurer,
ROBERT A. BENNETT

PUBLISHING STAFF
Mng. Dir., Publ.,
CHARLES W. BEARDSLEY
Managing Editor,
CORNELIA MONAHAN
Production Asstistant, **MARISOL ANDINO**

Transactions of the ASME, Journal of Fluids Engineering (ISSN 0098-2202) is published quarterly (Mar., June, Sept., Dec.) for $130.00 per year by The American Society of Mechanical Engineers, 345 East 47th Street, New York, NY 10017. Second class postage paid at New York, NY and additional mailing offices. POSTMASTER: Send address changes to Transactions of the ASME, Journal of Fluids Engineering, c/o THE AMERICAN SOCIETY OF MECHANICAL ENGINEERS, 22 Law Drive, Box 2300, Fairfield, NJ 07007-2300. **CHANGES OF ADDRESS** must be received at Society headquarters seven weeks before they are to be effective. Please send old label and new address. **PRICES:** To members, $40.00, annually: to nonmembers, $130.00. Add $24.00 for postage to countries outside the United States and Canada.

STATEMENT from By-Laws. The Society shall not be responsible for statements or opinions advanced in papers or . . . printed in its publications (B7.1, Par. 3). **COPYRIGHT** © **1992** by The American Society of Mechanical Engineers. Authorization to photocopy material for internal or personal use under circumstances not falling within the fair use provisions of the Copyright Act is granted by ASME to libraries and other users registered with the Copyright Clearance Center (CCC) Transactional Reporting Service provided that the base fee of $3.00 per article plus $.30 per page is paid directly to CCC, 27 Congress St., Salem, MA 01970. Request for special permission or bulk copying should be addressed to Reprints/Permission Department.

INDEXED by Applied Mechanics Reviews and Engineering Information, Inc.
Canadian Goods & Services Tax Registration #126148048

Downloaded 03 Jun 2010 to 171.66.16.159. Redistribution subject to ASME license or copyright; see http://www.asme.org/terms/Terms_Use.cfm

Contents (continued)

Technical Briefs

Announcements and Special Notices

Journal of Fluids Engineering

Editorial

With our editorial of March, 1992, we announced that we were working on establishing an electronic data bank for our Journal. In the present issue are included four papers which are accompanied by more extensive data deposited to the Journal Data Bank. These articles are identified by a note following the title. Each article contains a short description of the type of material included in the electronic file. Directions on how one would link with the Journal Data Bank and transfer a file are included in the last page of each issue.

The need for establishing a data bank arose naturally with the flood of experimental data that modern experimental methods can produce. Authors are often forced to select an example of their more representative data to include in the figures of their paper. This is often adequate to convey the basic message of their findings. However, researchers working on the same topic, experimentalist or numerical analysts may need the entire set of data to compare with their own results. There is also a significant practical aspect of considerable importance. It is more convenient and more accurate to have the exact digital data in a file rather than trying to obtain such information manually from a scaled-down figure.

Many organizations have already established electronic data banks. However, such activities were focused on a specific theme, as for example aircraft aerodynamics, or turbulent boundary layers. Moreover, such data were available only to selected scientists. The JFE data bank was organized in the spirit of an archival scientific journal. In fact, it was designed as a natural extension of scientific archiving. Data accompanying a paper must be reviewed and deemed significant to the engineering community. These data are then archived and remain in the bank for posterity in a standard form. This information is contributed to open literature and is therefore available to all readers.

This process is still in the experimental stage. It is anticipated that the submission of data, the reviewing and the organization of the files will be standardized over the years. For the time being, the Scholarly Communications Project and the Library Automation Program of Virginia Polytechnic Institute and State University is contributing this service to the Journal. It is anticipated that with the growth of the deposits, larger storage facilities may be necessary.

In this issue we also publish our first Perspective. This new genre was described in our editorial of June, 1992. Authors of Perspectives are invited to provide their own interpretation of advances in understanding of physical phenomena or gains in experimental or analytical methods of investigation. The Perspective appearing in the following pages falls in the category of "evaluative research." The proliferation of scientific material that appears in the pages of archival journals and conference proceedings has resulted in a flood of scientific information which is very difficult to evaluate. This journal will actively seek to publish in the form of Perspectives, articles which collect such information, examine it critically and present a clear opinion on its value. It is of course preferable that such information be accompanied by data deposited in the Journal Data Bank.

Finally, the readers may have noticed the establishment of a "Technical Forum." The first contribution to our Forum appeared in our September issue. In this space we will publish technical information of interest to our readers. Unanswered questions in fluid mechanics will be included in the Forum. This effort was initiated by Dr. Lloyd Trefethen in association with Dr. Ronald Panton and Dr. Joseph A. C. Humphrey who over the past few years have organized very successfully forums on this theme at ASME meetings. The first few articles will be contributed by Dr. Trefethen but subsequent columns will be solicited and edited by Drs. Panton and Humphrey who are in fact members of our Editorial Board. The Technical Forum will also include in this and the next few issues a series of contributions derived from the 1991 Panel on U.S. Technological Competitiveness.

The Editor

Journal of Fluids Engineering Technical Forum

Questions in Fluid Mechanics—II

by Lloyd M. Trefethen[1]

This is the second in a series of columns about questions in fluid mechanics, questions that appear to be of current interest and are on the boundary of what we know.

Two areas of emerging, and perhaps unconventional interest in fluid mechanics are small-scale fluid motions and motions in low gravity. They have newness in common. They also overlap.

Small-scale fluid mechanics is suddenly receiving increased attention, largely because of the information industry. But this is a case where, if ever we needed a guide to the future, she is here. Nature, well ahead of us in micro-scale engineering, has evolved mechanisms with length scales as small as a few nanometers in. Some of these questions reflect Nature's achievement:

> *Are the assumptions of fluid mechanics valid on a scale of 10 nanometers?*
> (Note: the helical filaments that rotate and propel E-coli bacteria are about 10 nm in diameter, driven by rotary motors about 20 nm in diameter.)
>
> *When a muscle fiber shortens, what is the flow field of the liquid within the bounding membrane, and how does this flow change as the thick and thin filaments slide past one another?*
> (Note: muscle filaments are about 10 nm in diameter.)
>
> *Does Brownian motion or viscous damping play any role in the filament motions?*
>
> *How can flow occur at a moving triple line where liquid, solid, and gas meet?*
>
> *What explains the long-known fact that, when a glass plate is withdrawn through a water surface that is covered by an insoluble monolayer, all water molecules can be expelled between the glass and the deposited monolayer?*
>
> *What phenomena typically ignored at large scales become important at small scales?*
>
> *Is transition to turbulence affected by small size of channels in ways not yet understood?*
>
> *What is the thickness of a shock wave in a liquid?*

We are so used to gravity in our everyday experiences that fluid motions in micro-gravity can seem strange, particularly under circumstances where surface tension or electrical forces dominate. The technological move into space has made such quaint phenomena important. Questions representative of current interest include:

> *Are the Young-Laplace condition and the contact angle sufficient to predict the possible static, free-surface configurations for liquids in fuel-tank geometries?*
>
> *When a non-soluble gas is slowly bubbled into a liquid in micro-gravity, what then happens? Do bubbles coalesce, and if so what is the time scale—days?*
>
> *How do bubbles and droplets interact in a liquid in which there is a temperature gradient?*
>
> *How can Marangoni motions be minimized during processing of materials in space?*
>
> *When and under what conditions will suction dip, distortion of the free surface, lead to blow through of gas while fuel is being drawn from a fuel tank?*
>
> *What are the flow patterns and shear distributions in multiphase flows in micro-gravity?*

There is a practical reason for looking to common features of these two classes of questions. Experiments can be difficult to perform at small scale, and experiments are certainly difficult to arrange at low g. Yet there are occasions where understanding can be obtained from the more easily performed experiment, whether micro-gravity or micro-scale. There has been to date little examination of such trade offs.

The preceding discussion is posed in large part as questions, which is not typical. Questions hardly ever appear in our fluid mechanics literature. This is unfortunate because they are efficient definers of what we know and don't know. Their absence appears to be partly psychological, partly custom. Whatever the reasons, we should change our attitudes towards asking questions.

A new feature in our world is electronic communication. It certainly will change how we cooperate, how we find answers to our questions. A vivid, possible view of our future is drawn in the article, "Surfing the Sea of Stories: Riding the Information Revolution," by Meyers, Wilson and Lienhard in the October 1992 issue of *Mechanical Engineering*.

Electronic communication will lead to more spontaneous,

---

[1] Mechanical Engineering Department, Tufts University, Medford MA 02155. Fellow ASME.

ephemeral exchanges than have existed in the past. An important task for all of us will be finding ways optimally to exploit such exchange. Sharing Questions is one such direction, about which we would very much like to hear your suggestions (or requests for background about any of the above questions) to qbank@pearl.tufts.edu.

The Journal welcomes submission of drafts for future question columns.

U.S. Technological Competitiveness: A Fluids Engineers' Viewpoint

by Jules L. Dussourd[2]

Column 1—Gridlock Among Fluids Engineers?

In the previous column, the thesis was advanced that we, in the US, have become deadlocked over conflicting social and economic imperatives so strongly entrenched that compromises are quite unlikely, creating a permanent state of gridlock. This is quite apart from the governmental gridlock so often mentioned by our presidential candidates in the recent election campaign.

Figure 1 serves to illustrate the condition. The three main imperatives are: greater economic well being, still more human freedoms and a pristine environment. These are really mutually incompatible in spite of political claims to the contrary. These imperatives are represented by the three main sectors of the chart.

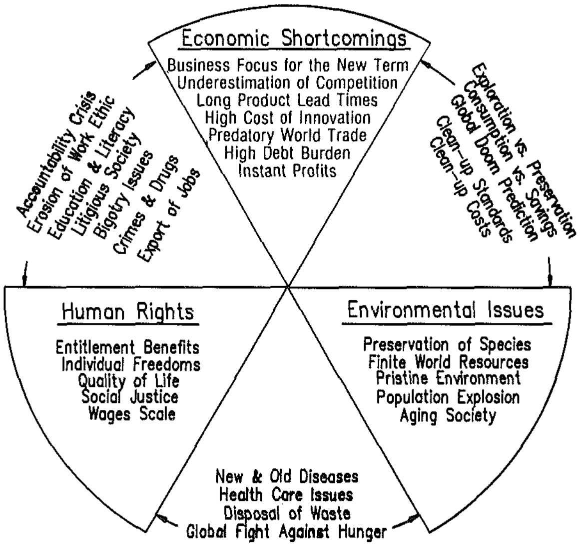

Between the sectors are some of the more visible side effects, as consequences of their incompatibilities. These side effects, often lightly dismissed as merely "signs of the times" are really consciously provoked by divergent or unrealistic expectations that have come to be exaggerated and have polarized major segments of our society. Under these conditions, the main imperatives, well intended as they may be, now work at cross purposes to the detriment of the common good. A society in such a state cannot develop the needed synergism for rapid progress. It becomes mired in a state of gridlock in which issues can only be resolved through lengthy, costly and acrimonious litigation. Experience tells us that a team in such a frame of mind cannot win.

A similar predicament can be seen to have emerged within the community of fluids engineers and for that matter other categories of engineers as well. Imperatives, also originally well intended, have become hardened and exclusionary, and as such can become counterproductive. For example, if mathematical sophistication is made an overriding goal, the output product may well be unintelligible to the great majority of would-be users. As a result of such, the proficiencies of the practitioning sectors of Fluids Engineering, industry, academia and government, can all be severely weakened.

This condition can also be represented by the three accented sectors on the pie chart of Fig. 2. Between them are some of the side effects. In time and in the absence of vigorous interchanges of people and ideas, a similar state of gridlock can be expected. The effective transfer of knowledge between the sectors is stymied and a technology assimilation gap is created. Some of the underlying forces that may be responsible can be seen as follows.

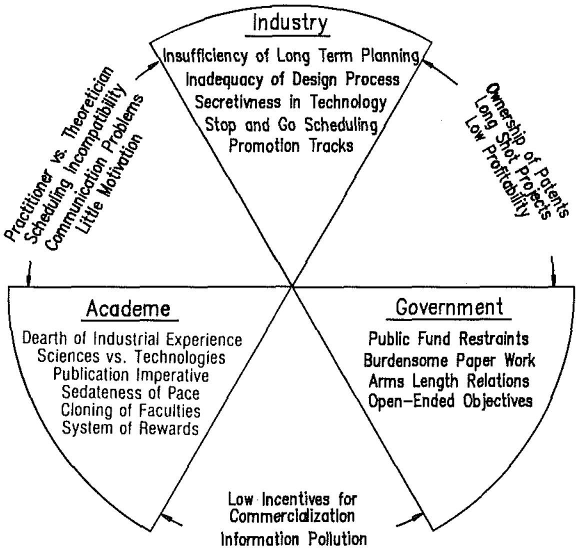

Fluids engineers working in product development in industry are expected by their management to deliver their goods promptly, (preferably tomorrow) and at a minimum cost. The goods to be delivered are forecasts, solutions, but more often designs which must meet or come close to meeting the target the first time tested, matching or exceeding the competitor's

---

[2] Fluids Engineering Associates. Princeton, N.J. 08540.

ephemeral exchanges than have existed in the past. An important task for all of us will be finding ways optimally to exploit such exchange. Sharing Questions is one such direction, about which we would very much like to hear your suggestions (or requests for background about any of the above questions) to qbank@pearl.tufts.edu.

The Journal welcomes submission of drafts for future question columns.

U.S. Technological Competitiveness: A Fluids Engineers' Viewpoint

by Jules L. Dussourd[2]

Column 1—Gridlock Among Fluids Engineers?

In the previous column, the thesis was advanced that we, in the US, have become deadlocked over conflicting social and economic imperatives so strongly entrenched that compromises are quite unlikely, creating a permanent state of gridlock. This is quite apart from the governmental gridlock so often mentioned by our presidential candidates in the recent election campaign.

Figure 1 serves to illustrate the condition. The three main imperatives are: greater economic well being, still more human freedoms and a pristine environment. These are really mutually incompatible in spite of political claims to the contrary. These imperatives are represented by the three main sectors of the chart.

Between the sectors are some of the more visible side effects, as consequences of their incompatibilities. These side effects, often lightly dismissed as merely "signs of the times" are really consciously provoked by divergent or unrealistic expectations that have come to be exaggerated and have polarized major segments of our society. Under these conditions, the main imperatives, well intended as they may be, now work at cross purposes to the detriment of the common good. A society in such a state cannot develop the needed synergism for rapid progress. It becomes mired in a state of gridlock in which issues can only be resolved through lengthy, costly and acrimonious litigation. Experience tells us that a team in such a frame of mind cannot win.

A similar predicament can be seen to have emerged within the community of fluids engineers and for that matter other categories of engineers as well. Imperatives, also originally well intended, have become hardened and exclusionary, and as such can become counterproductive. For example, if mathematical sophistication is made an overriding goal, the output product may well be unintelligible to the great majority of would-be users. As a result of such, the proficiencies of the practitioning sectors of Fluids Engineering, industry, academia and government, can all be severely weakened.

This condition can also be represented by the three accented sectors on the pie chart of Fig. 2. Between them are some of the side effects. In time and in the absence of vigorous interchanges of people and ideas, a similar state of gridlock can be expected. The effective transfer of knowledge between the sectors is stymied and a technology assimilation gap is created. Some of the underlying forces that may be responsible can be seen as follows.

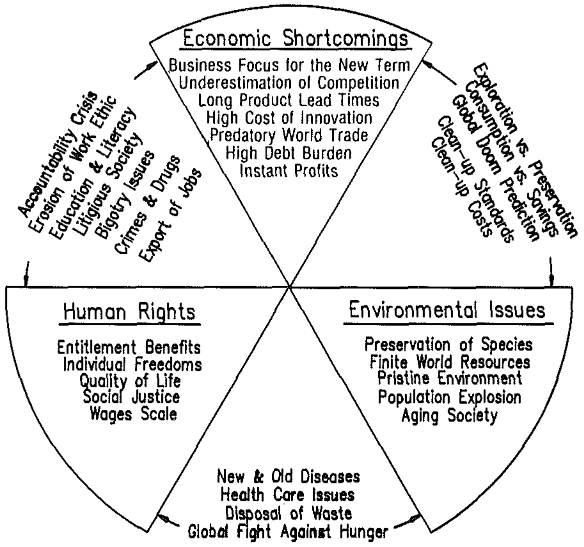

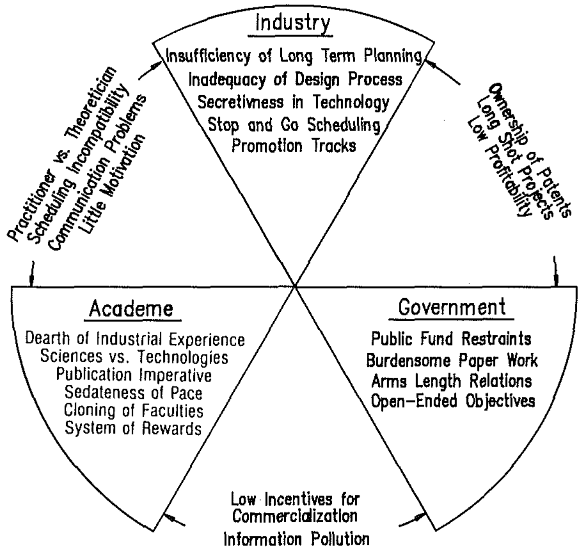

Fluids engineers working in product development in industry are expected by their management to deliver their goods promptly, (preferably tomorrow) and at a minimum cost. The goods to be delivered are forecasts, solutions, but more often designs which must meet or come close to meeting the target the first time tested, matching or exceeding the competitor's

---

[2] Fluids Engineering Associates. Princeton, N.J. 08540.

and with a lower manufacturing cost. Prompt, low cost, accurate predictability of fluid flow phenomena then constitute a first imperative.

To succeed in this race, the fluids engineer needs the best techniques, the best design tools, accurate, yet readily exercised. He must become more than just familiar with them, understand or trust them; he must identify himself with them. In brief, he needs accurate quantitative physical models to supplement his qualitative knowledge which is based on experience.

The culture surrounding him for the most part is not always disposed to supply him with all the desired conveniences for the implementation of this laborious process. Development customarily is done under some sales orders, inevitably pressured by time and cost imperatives of their own. And if outside design help should be required, it must be supplied "instantly," by someone with the answers.

The practicality of this latter option however conflicts with new imperatives. There are company proprietary and confidentiality issues which demand secretiveness. And there are also issues of self-respect and human sensitivities on the part of those needing the help. These considerations more often than not discourage the involvement of outsiders and compel the home team to work behind closed doors.

In the extreme, the entire effort can even become infected by a sales mentality in which the vision of quick sales and profits overrides the need for quality and high performance. In such a climate, the fluids engineer can be driven to irrational compromises, to do second guessing and to resort to quick but unproven procedures. Design excellence and design optimization are no longer possible and unfortunately, neither is designer self-esteem. All too often the project becomes an exercise in arm waving, double talk and over-reaching; credibility quickly goes out of the window.

Now let us look at the imperatives guiding the fluids engineer in academia. His future is geared to his publications as an end in themselves. The more prestigious the journal and the greater the global dissemination, the greater his reputation. There are no incentives and little motivation to address industrial problems which are perceived as intellectually unchallenging and professionally unrewarding. In this world, a different culture evolves; one that is inbred and impervious to the realities from outside. Intellectuality, academic freedom, the absence of constraints and the pressure to publish become the overriding imperatives which in the present context must be evaluated in terms of how they may contribute to competitiveness.

University policy makers assiduously seek to win grant awards, from which flow fame and financial benefits. Grant monies come much more easily from the government than from industry and there are fewer strings attached. There is greater security behind a reciprocal relationship with a funding agency than from a stop and go association with a private company. And this security is reinforced if the output products are highly sophisticated and prized by peer groups, notwithstanding they being impervious to adoption or implementation by others.

Such a culture offers much for the good, because it generates an abundance of knowledge, but *when carried to extremes* it fails to meet the criteria of serving the common good. It purports to serve the world but fails to provide the needed support at home to those in industry, the very ouput of whom is a measure of the competitiveness of the society which generates the resources for its funding.

Separate and independent cultures can thus be created, inbred in the sense that faculty cloning becomes one way of life in academia and a systematic exclusion of alien contributions a way of life in industry. The vigorous cross exchanges of personnel, ideas and technologies are impeded. Our society's humanistic and practical philosophies are out of synchronism.

Our capitalistic democratic society is subject to imperatives that place restrictions on the level of influence government can exert in harmonizing the activities of its citizens. And when public funding is involved, the notion that corporate profits may be directly generated from the application of such funding remains a taboo, notwithstanding the passage of some more recent pieces of legislation.

Among the questions which have been raised in this context are the following. Who should ultimately own title to the inventions that are so made? Is government support more freely given to those who are not in for profit? And if commercialization is a stated objective, but the government is not the buyer of the product so developed, how can real motivation to develop marketable products be instilled in the partnership? In brief, can a focused team approach on the part of all sectors, rather than arms length approaches, be achieved, given the legal and ethical considerations and the lack of incentives? In a global economic race, can our current unstructured approach compete against the coordinated practices of some of our competitors?

In the light of all these divergent imperatives, is it a surprise really that the stream of technologies between the sectors of Fig. 2 seems to flow slowly and its translation into commercial products is equally slow? Knowledge, truths and technologies are being generated, but they are not being used. Can subtle human behavior, though rightfully motivated by ethical or professional imperatives, yet inadvertantly impede this process to the point where our economy suffers from progressive suffocation through gridlock? And while much has been said politically about the causes for the current recession, the state of gridlock may well be one main reason for the slowness of the recovery.

To reverse this trend should certain practices and sacred cows be reexamined? Should the product divisions of industry and the fluids engineers therein be more receptive to partnerships with others? Should academic specialists be given greater incentives to participate in cooperative efforts with industry? Should there be a greater exchange of personnel between academe and industry, beyond sabbaticals, stages or residencies? Should the engineering teaching qualifications be reasessed? In a world flooded with products of increasingly complex technologies, does secretiveness really afford protection in lieu of impressive engineering talent? Certainly, the promise of achieving technical successes in shorter time spans should reinvigorate the defunct long range development plans. But would all this stimulate industry enough to consider creating new markets, instead of keeping its eye glued to current markets only, which can only perpetuate a state of catchup in the world game? Does the purity of certain policies from our government lead to miscarriages rather than real successes in the development of new products?

These considerations were being expressed as challenges to the participants in the 1991 panel on the subject of U.S. Competitiveness. The panelists have undertaken the task to voice the problems in their own light and make recommendations on how these should be addressed. Their findings will appear in this column in the next issues of the *Journal of Fluids Engineering*.

M. S. Ölçmen
Research Associate.

R. L. Simpson
Jack E. Cowling Professor.
Fellow ASME

Department of Aerospace
and Ocean Engineering,
Virginia Polytechnic Institute and
State University,
Blacksburg, VA 24061

Perspective: On the Near Wall Similarity of Three-Dimensional Turbulent Boundary Layers

(Data Bank Contribution*)

The possible existence of a "law-of-the-wall" similarity velocity profile for 3-D boundary layers was investigated using nine different proposed relations with the data from nine experiments carried out in 3-D turbulent boundary layers. Both for pressure driven and shear-driven flows, the "law-of-the-wall" relation of Johnston for the local freestream velocity direction component best applies. Although not well described by any relation, the crosswise velocity component of pressure-driven flows and shear-driven flows is best represented by Mager's relation and Chandrashekhar and Swamy equation, respectively.

Introduction

The term "near wall similarity" represents the "likeliness" of the near wall velocity profiles when presented in an appropriate nondimensionalized coordinate system. The existence of the similarity "law-of-the-wall" velocity profile in the form of $U/q^* = f(yq^*/\nu)$ for two-dimensional turbulent boundary layers has been well established (Coles and Hirst, 1968). The existence of such a similarity law of the wall either for the two-dimensional or for the three-dimensional boundary layer flows reduces the computation time by reducing the required near wall spatial resolution and gives the necessary information between the mean velocity profile and the wall shear stress. Since the inner layer is represented with a law of the wall and therefore fine grid calculations need not be made at points near the wall where the law of the wall is valid. Existence of such a law of the wall in three-dimensional boundary layers was investigated by several authors (Coles, 1956; Johnston, 1960; Hornung and Joubert, 1963; Perry and Joubert, 1965; Pierce and Krommenhoek, 1968; East and Hoxey, 1969; White, Lessmann and Christoph, 1975; Van den Berg, 1975a; Pierce et al., 1982).

Nine existing law-of-the-wall similarity profiles are compared here with nine different sets of 3-D turbulent boundary layer data in order to further investigate if such a law exists for three-dimensional flow. Some conclusions are made about a three-dimensional "law of the wall." The relations chosen include the Coles, Johnston, Hornung and Joubert (HJ), Pierce and Krommenhoek (PK), Chandrashekhar and Swamy (1975) (CS), East and Hoxey (EH), Perry and Joubert (PJ), White, Lessmann and Christoph (WLC), and van den Berg relations.

The pressure-driven experimental data were of Anderson and Eaton (1987a, 1987b), Dechow and Felsch (1977a, 1977b), Müller (1982), Fernholz and Vagt (1981), Elsenaar and Boelsma (1972, 1974), and Ölçmen (1990). The shear driven data were taken from Bissonnette and Mellor (1974), and Lohmann (1976). Schematic figures of these flows are given in Figs. 1(*a*) to 1(*h*).

These sets were chosen since they include all six components of the Reynolds stress tensor, the mean velocity, the pressure distribution, and the skin friction on the wall. Station locations used in this study are given in same notation as originating authors. A summary of the data sets used and some conclusions from those studies are presented in Table 1. All these data sets were obtained in air. Except in the case of Van den Berg's relation, all the relations were expressed in local free-stream coordinates and the data used were calculated in local free-stream coordinates before used. Figure 2 shows the local free-stream coordinates.

Experimental Data for the Ölçmen Flow (1990)

The data for the Ölçmen (1990) flow will be briefly discussed here since they have not previously been published. A three-dimensional, pressure driven turbulent boundary layer created by a wing-body junction flow was experimentally studied. The wing used was 3:2, semi-elliptical nosed NACA 0020 tailed symmetric profile which has a chord length of 30.5 cm (12 in.), maximum thickness of 7.17 cm (2.824 in.), and height of 22.9 cm (9.016 in.). The wing was mounted on the centerline of the flat plate wind tunnel floor. The nominal reference velocity of the flow was 27 m/s and the Reynolds number based on the momentum thickness at 0.75 chord upstream of the wing on the centerline of the tunnel and wing was ≈ 5936.

The data included the mean velocity and all Reynolds stresses at several (x, z) stations on a line determined by translating in the direction of the mean velocity vector component parallel to the wall in the layer where the $\overline{u^2}$ normal stress is maximum. Data were obtained both with hot-wire (HW, at 24 stations) and laser Doppler-velocimeter (LDV, at 8 stations) techniques. The incoming boundary layer was measured at 15 different stations located at 0.75 chord upstream of the wing across the

---

*Data have been deposited to the JFE Data Bank. To access the file for this paper, see instructions on p. 705 of this issue.

Contributed by the Fluids Engineering Division for publication in the JOURNAL OF FLUIDS ENGINEERING. Manuscript received by the Fluids Engineering Division July 27, 1992. Associate Technical Editor: D. Telionis.

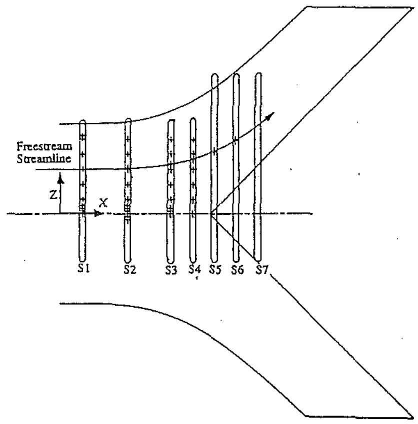

Fig. 1(a) Schematic figure of Anderson-Eaton flow. Data taken along the free-stream streamline (from Anderson and Eaton, 1987a).

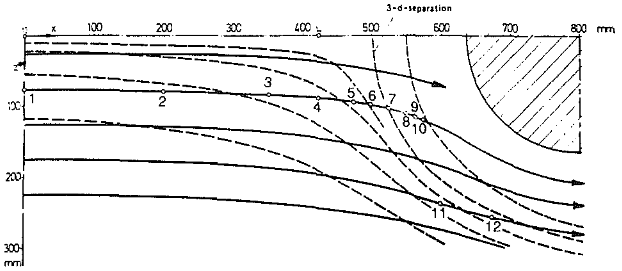

Fig. 1(b) Schematic plan view of boundary layer approaching circular-nosed cylinder on a flat plate. Dechow-Felsch flow (from Dechow and Felsch, 1977a).

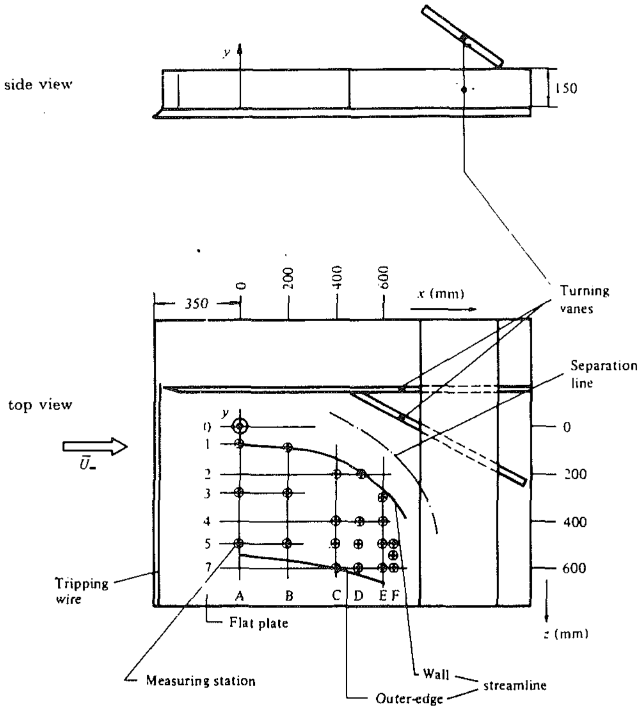

Fig. 1(c) Schematic views of Müller's flow (from Müller, 1982)

half of the tunnel test section. The LDV measurements were taken twice due to the differences observed between the HW and the LDV data. The uncertainties on the mean velocity and the stresses were examined extensively.

Nomenclature

A = $-\delta_2/\delta_1$
A_0, B_0 = constants
a_1 = $\sqrt{\overline{uv}^2+\overline{vw}^2}/(\overline{u^2}+\overline{v^2}+\overline{w^2})$ structural parameter
H = $\int_0^{y^*}[1+(dw/du)^2]^{1/2}*du$ = arc length on Johnston's polar plot
h_1 = metric coefficient
N = $(-(\overline{vw})/(\partial W/\partial y))/(-(\overline{uv})/(\partial U \partial y))$ ratio of streamwise eddy viscosity to cross stream eddy viscosity
Q^+ = common term used for the dependent variable of law-of-the-wall relations
q = magnitude of velocity vector, $\sqrt{U^2+W^2}$ (m/s)
q^* = skin friction velocity = $\sqrt{\tau_w/\rho}$ (m/s)
U = streamwise velocity component (m/s)
U_0 = working section reference velocity
U_∞ = free-stream velocity
W = cross-wise velocity component (m/s)
W_0 = surface velocity for rotating cylinder in shear-driven flows
$\overline{u^2}, \overline{v^2}, \overline{w^2}$ = kinematic normal stress components in local freestream coordinates: streamwise, normal to wall, and spanwise directions, respectively
$-\overline{uv}, -\overline{vw}, -\overline{uw}$ = kinematic shear stress components in local free-stream coordinates: streamwise, normal to wall, and spanwise directions, respectively
x, y, z = tunnel coordinates: streamwise, normal to wall, and spanwise directions, respectively
y^+ = q^*y/ν wall law variable
α = $((\partial p/\partial x)^2+(\partial p/\partial z)^2)^{1/2}$ = pressure gradient magnitude
α_g = flow gradient angle, arctan $((\partial W/\partial y)/(\partial U/\partial y))$
α_s = shear stress angle, arctan $(-(\overline{vw})/-(\overline{uv}))$
β = flow angle with respect to the local freestream direction at boundary-layer edge
β_0 = $\arcsin[(\sin\gamma/(Kq^*/U_0))]-\gamma$
β_w = wall flow angle and wall shear stress vector angle with respect to the local free-stream direction at the boundary-layer edge
γ = arctan (A)
δ_1 = $\int_0^{\delta}(1-U/U_\infty)dy$
δ_2 = $\int_0^{\delta}-(W/U_\infty)dy$
κ = Von Karman constant (0.41)
ρ = density
τ_w = skin-friction at the wall
ν = kinematic viscosity

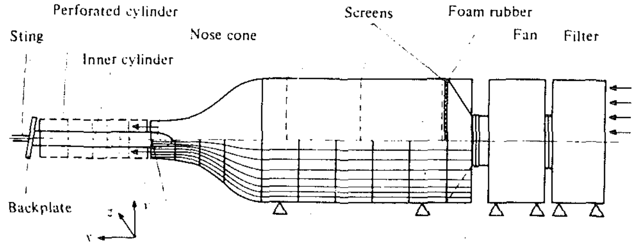

Fig. 1(*d*) Schematic figure of Fernholz-Vagt asymmetric flow over a circular cylinder (from Fernholz and Vagt, 1981)

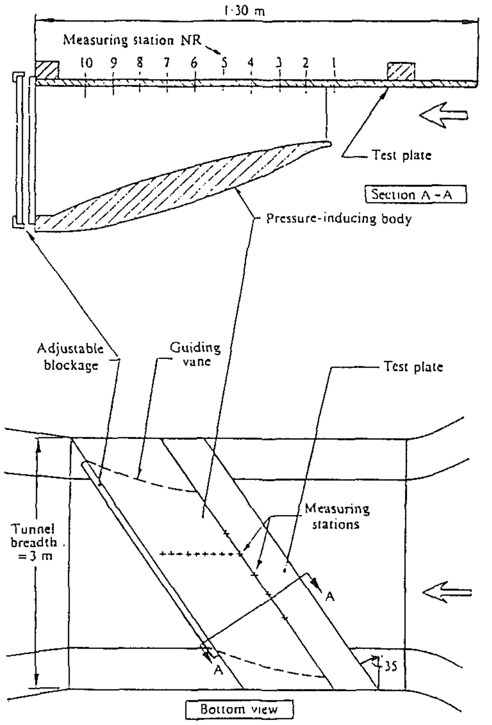

Fig. 1(*e*) Schematic views of "infinite" wing Elsenaar-Boelsma flow (from Van den Berg et al., 1975b)

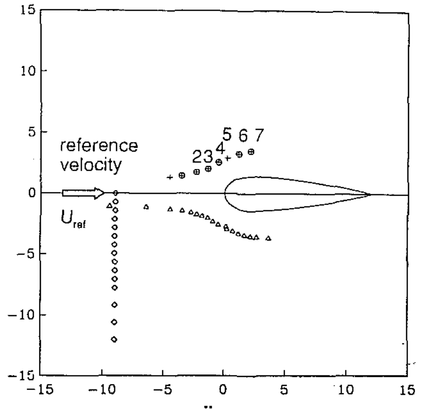

Fig. 1(*f*) Schematic plan view of Ölçmen flow. The scale of the plot is in inches. △ Left-hand side hot-wire locations, ○ right-hand side hot-wire locations, ◇ 0.75 chord upstream hot-wire locations, + Laser-Doppler-Velocimeter locations.

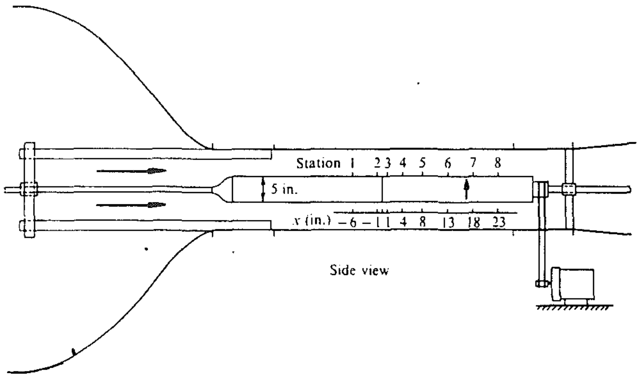

Fig. 1(*g*) Schematic side view of Bissonnette-Mellor flow (from Bissonnette and Mellor, 1974)

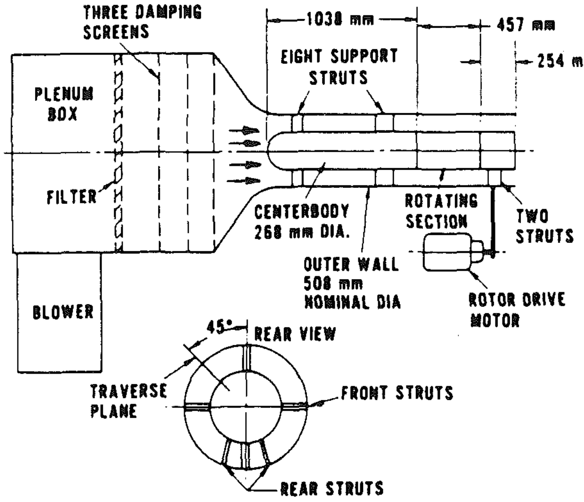

Fig. 1(*h*) Schematic figure of Lohmann's experimental setup (from Lohmann, 1976)

Table 1 Summary of experimental data sets

Authors	Flow studied, U_r/ν of the flow, stations included in the study	Measurement method for mean velocity and Reynolds shear stress tensor	Method for skin friction measurements	Comments
Anderson-Eaton (1987a, 1987b)	Flow towards a 90° wedge. $1.023 \cdot 10^6$/m, stations S1, S2, S3, S4, S5. (Fig. 1a)	X-array hot-wire probe, three-hold yaw probe, static pressure probe	Surface fence	N changes -1.0 to 0.5. a_1 is not a constant, changes ≈0.14 to ≈0.04 proceeding downstream. α_s lags α_g
Dechow-Felsch (1977a, 1977b)	3-D flow induced by a cylinder standing on a flat plate. $1.451 \cdot 10^6$/m, stations 1, 2, 3, 4, 5, 6, 7. (Fig. 1b)	Conrad tube, boundary layer type single wire, X wire	Preston tube	Flow is anisotropic, N changes ≈-2 to ≈0.5, a_1 is not a constant, changes ≈0.14 to ≈0.06 proceeding downstream. α_s lags α_g
Müller (1982)	3-D flow created by transverse and lateral pressure gradients with use of turning vanes on a flat plate, $1.95 \cdot 10^6$/m, stations A1, B1, C2, D2, E3, F5. (Fig. 1c)	X wire	Preston tubes	N above y^+=100 scattered around ≈1.5, a_1 is scattered around ≈ 0.14, α_s leads α_g at some stations, velocity skewed down to the wall
Fernholz-Vagt (1981)	3-D flow created by a downstream back plate on a cylinder with an elliptical nose, $1.23 \cdot 10^6$/m, stations 0102, 0202, 0302, 0402, 0502, 0602, 0702, 0802. (Fig. 1d)	X wire, slanted or single normal wires, Cobra probes	Surface fence and Preston tube	Velocity skewed down to the wall, α_s leads α_g; a_1 not a constant
Elsenaar-Boelsma (1974, 1972)	Incompressible turbulent boundary layer under infinite swept conditions in a adverse pressure gradient, $2.42 \cdot 10^6$/m, stations 1, 4, 5, 6, 7, 8, 9, 10/ (Fig. 1e)	X wire, slanted wire, single straight wire, cobra probe	Stanton type surface pressure probes, Clauser plots	N changes ≈-0.5 to 0.75. a_1 is not a constant, changes ≈0.15 to ≈0.08 proceeding downstream, below y^+=1000. Flow is anisotropic, α_s lags α_g.
Ölçmen (1990)	3-D flow induced by 3:2 elliptical nosed NACA 0020 tailed body protruding from a flat plate, $1.726 \cdot 10^6$/m, stations 2, 3, 4, 5, 6, 7. (Fig. 1f)	Laser-Doppler-velocimeter, single hot wire	Skin-friction interferometer	N changes from ≈-0.5 to ≈1.5. Flow is not isotropic, α_s lags α_g, a_1 is not a constant.
Bissonnette-Mellor (1974)	3-D turbulent boundary layer on an axially rotating cylinder, $U_{ref} \cdot D/2\nu = 4.14 \cdot 10^4$ and $7.95 \cdot 10^4$. D=5 inches. Stations 5, 6, 7, 8 for both flows (Fig. 1g)	Straight and slanted wires	Obtained by extrapolating the data to the wall	N changes ≈0.3 to 1.0 for low Re and ≈0.7 for high Re; flow is collateral near the wall in a rotating frame of reference., a_1 is not a constant, varies from ≈0.06 to ≈0.18, and ≈0.15 between y^+=70 to y^+=300. α_s lags α_g.
Lohmann (1976)	3-D turbulent boundary layer formed on an axially rotating cylinder, $U_{ref} \cdot D/2\nu = 2.9 \cdot 10^5$. D=10 inches. Stations 1, 2, 3, 4, 7, 9. (Fig. 1h)	Slanted wire, single wire	Obtained from Clauser plots	N varies ≈0.7 to ≈1.7 below y^+ less than 500. a_1 is not a constant, varies from ≈0.01 to ≈0.14. Near wall flow was collateral, α_s leads α_g.

Also, time-mean static pressure as well as the skin friction magnitude and direction on the wall (at LDV locations) were measured. Skin friction vectors at several locations on the wall were measured independently in another study by Ailinger (1990) using oil-flow laser interferometry, which employs no assumptions or relationships with the mean velocity profile.

These data showed that the eddy viscosity of the flow was not isotropic (i.e., $N \neq 1$). However, the ratio of eddy viscosities perpendicular and parallel to the direction of the mean velocity vector component parallel to the wall at the point in the layer where $\overline{u^2}$ is maximum was close to unity. The shear-stress vector direction α_s in the flow lagged behind the velocity gradient vector direction α_g. Townsend's structural parameter a_1, was not a constant of 0.15, but was consistently lower near the wall and was close to it or higher in the outer layer. The

Table 2 "Law-of-the-wall" relation review

Authors, assumptions	
Coles (1956) assumed that (i) the velocity vector throughout the layer could be written as a sum of near surface and wake vectors and (ii) the magnitude of the wake vector near the wall should be small so that the direction of the near surface velocity vector should have the direction as the shear stress vector on the wall.	$\frac{q\cos(\beta_w-\beta)}{q^*}=A\ln(\frac{yq^*}{\nu})+B$ (1)
Johnston (1960) used his "triangular model" $(\frac{U}{q})$ vs. $(\frac{W}{q})$ which points to the existence of a collateral region near the wall and the fact that the direction of the velocity vector at this region is coincident with the shear stress vector. Furthermore, he assumed that the fictitious velocity component in the direction of the shear stress direction defined as $\frac{U}{\cos\beta_w}$ obeyed the 2-D law of the wall of Clauser.	$\frac{U}{q^*\cos(\beta_w)}=A_1\ln(\frac{yq^*}{\nu})+B_1$ (2)
Hornung-Joubert (HJ) (1963) applied Clauser's law of the wall for 2-D turbulent boundary layers to 3-D turbulent boundary layers.	$\frac{q}{q^*}=A_2\ln(\frac{yq^*}{\nu})+B_2$ **(3)**
Pierce-Krommenhoek and Chandrashekhar-Swamy (PK and CS) (1968) assumed the validity of the 2-D law of the wall with the nondimensionalizing skin-friction velocity derived from the shear stress vector component in the local freestream direction. Very near wall velocity vector direction is not assumed to be coincident with the wall shear stress vector direction. Cross-flow component is given by the latter relation.	$\frac{U}{q^*(\cos\beta_w)^{1/2}}=A_3\ln(\frac{yq^*(\cos\beta_w)^{1/2}}{\nu})+B_3$ **(4)** $\frac{W}{q^*(\sin\beta_w)^{1/2}}=A_4\ln(\frac{yq^*(\sin\beta_w)^{1/2}}{\nu})+B_4$ **(5)**
East and Hoxey (EH) (1969) *assumed that since* U^+ *in 2-D flows was a function of* y^+*, the same* relation in 3-D flows would hold, taking into account the vectorial nature of the local velocity. Modified Johnston's relation.	$\frac{U}{\cos(\beta_o)q^*}=A_5\ln(y^*)+B_5$ **(6)**
Perry-Joubert (PJ) (1965) take into account the effect of the pressure gradient near the wall region. *They assumed that the near wall region could be treated as an equilibrium layer* and that mixing length theory was valid. They further assumed that the maximum shear stress acts in the same direction as the maximum rate of strain, which in turn assumes that the turbulence is isotropic.	$\frac{H}{q^*}=\int_0^{y^*}[1+(\frac{dw}{du})^2]^{1/2}\frac{du}{q^*}=A_6\ln(y^*)+B_6$ $\approx\frac{1}{\kappa}\int_0^{y^*}\frac{1}{y^*}(1-2\cos\theta(\frac{\alpha\nu}{q^3})y^*+(\frac{\alpha\nu}{q^{*3}})^2y^{*2})^{(1/4)}dy^*+constant$ **(7)** θ =angle between the pressure gradient vector and the wall shear stress vector.
White-Lessmann-Christoph (WLC) (1975) take into account the effect of the pressure gradient on the streamwise velocity component. It was part of an integral method for the analysis of 3-D incompressible turbulent boundary layers. The key assumption in the development of the relation is that the shear stress component in the local free-stream direction could be written as a sum of the shear stress component at the wall in the local free-stream direction and the pressure force in the direction of the local free-stream direction ($\tau_x\approx\tau_{xw}+\frac{1}{h_1}\frac{\partial p}{\partial x}y\approx\rho\kappa^2y^2\vert\frac{\partial U}{\partial y}\vert\frac{\partial U}{\partial y}$). The relation between *the shear stress and velocity was established by the mixing length theory. The law of the wall for* the cross-flow component belongs to Mager (1951).	$q^*\cos^{1/2}(\beta_w)=(\frac{\tau_w\cos(\beta_w)}{\rho})^{1/2}$ $U^+=\frac{U}{q^*(\cos\beta_w)^{1/2}}=\frac{1}{\kappa}[2(S-S_o)+\ln(\frac{(S-1)}{(S+1)}\frac{(S_o+1)}{(S_o-1)})]$ **(8)** $S=(1+\alpha y^+)^{1/2}$, $S_o=(1+0.1108\alpha)^{1/2}$, $\alpha=\frac{\nu}{\rho(q^*\cos^{1/2}(\beta_w))^3h_1}\frac{\partial p}{\partial x}$ S_0 was chosen such that in the zero pressure gradient limit $U^+=\frac{1}{\kappa}\ln(y^+)+5.5$ would be obtained. Unilateral hodograph proposed by Mager 1951 $W^+=\frac{W}{q^*(\cos\beta_w)^{1/2}}=U^+\zeta(1-y^+/\delta^+)^2$ **(9)** ζ = tan(θ) ; θ =angle between the resultant surface shear τ_w direction with the streamwise direction.
Van den Berg (1975a) takes into account both pressure gradient and inertial force effects. The relation was developed as a part of a calculation method for 3-D turbulent boundary layers. The relation assumes that mixing length theory holds outside the viscous sublayer and the shear stress *direction coincides with the direction of the maximum rate of deformation in the region where the* law of the wall is supposed to hold. The correction of the logarithmic law of the wall for the shear stress variation due to inertial effects was done using the log-law form in the equations of motion for thin layers. Van den Berg preferred to formulate his equations in a right-handed coordinate system in which x lies in the direction of the wall shear stress, z is perpendicular to this direction lying on the floor plane, and y is perpendicular to both directions.	$U_x^*=\frac{q\cos(\beta_w-\beta)}{q^*}=\frac{1}{\kappa}[\ln y^*+\frac{1}{2}\alpha_x y^*+\frac{1}{2}\beta_x\frac{(\ln y^*)^2y^*}{\kappa^2}]+B_7$ **(10)** $U_z^*=\frac{q\sin(\beta_w-\beta)}{q^*}=\frac{1}{\kappa}[\alpha_z(y+)+\beta_z\frac{(\ln y^*)^2y^*}{\kappa^2}]+B_8$ **(11)** $\alpha_x=\frac{\nu}{\rho q^{*3}}\frac{\partial p}{\partial x}$; $\alpha_z=\frac{\nu}{\rho q^{*3}}\frac{\partial p}{\partial z}$; $U_x^*=\frac{q\cos(\beta_w-\beta)}{q^*}$ $\beta_x=\frac{\nu}{q^{*3}}\frac{\partial q^*_x}{\partial x}$; $\beta_z=\frac{\nu}{q^{*3}}\frac{\partial q^*_z}{\partial x}$; $U_z^*=\frac{q\sin(\beta_w-\beta)}{q^*}$ $\phi=[\alpha_z(y^*+\kappa B_8/\alpha_z)+\beta_z(\ln y^*)^2y^*/\kappa^2]/[\ln y^*+\kappa B_7]$

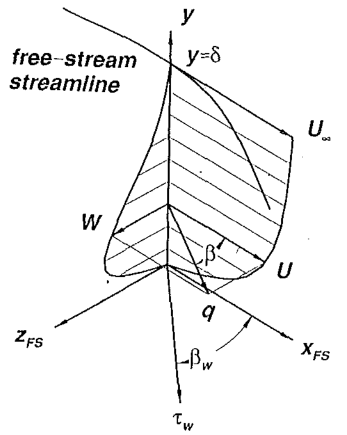

Fig. 2 Local free-stream coordinates

Table 3 Summary of y^+ range of semi-logarithmic regions for "law-of-the-wall" relations

Flows / Relations studied	Coles	Johnston	Hornung-Joubert	Pierce-Krommenhoek	Chandrashekhar-Swamy	East-Hoxey
Elsenaar-Boelsma	45-400	60-250	30-450	35-250	35-250	45-200
Müller	30-250	30-200	30-250	20-200	20-200	20-100
Fernholz-Vagt	15-150	15-100	15-100	15-100	15-100	20-100
Dechow-Felsch	20-200	20-150	20-150	20-150	20-150	10-100
Anderson-Eaton	60-200	60-200	60-200	60-200	60-200	60-200
Ölçmen	40-500	40-200	40-400	40-250	40-250	40-400
Bissonnette-Mellor Low Re	20-200	45-250	30-200	20-200	20-200	20-200
Bissonnette-Mellor High Re	-	20-250	-	25-250	25-250	20-250
Lohmann	-	60-250	-	40-150	40-150	70-300

production of the turbulent kinetic energy and the production of the shear stresses were higher nearer the wall than in the logarithmic regions of the U velocity component profiles. The skin friction velocity was not the scale of the turbulence in such a flow.

Law-of-the-Wall Similarity Relations

A summary of the relations used and the assumptions made by the individual authors may be found in Table 2. From the equations of the proposed relations, it can be observed that the left-hand side of the U component (Eq. (8)) of WLC and U component of the CS and PK relations (Eq. (4)) are equivalent. The WLC law of the wall was investigated only for the pressure-driven data since in the limit of zero pressure gradient it degenerates to the 2-D law of the wall. The right-hand side of the PJ relation (Eq. (7)) also takes into account the effect of the pressure gradient. For all the data sets the left-hand side of the relation (Eq. (7)) could be tested separately. Van den Berg chose the velocity component in the direction of the wall shear stress and the component perpendicular to it in the x-z plane to be non-dimensionalized with the q^*. This equation in the shear stress direction is the same as Coles' law of the wall. The comparison for the computed values versus the variables U_x^+ and U_z^+ (Eqs. (10) and (11)) was done for $\beta_x = \beta_z = 0$ since the extraction of these terms from the data necessitated either more information or the neglect of some terms whose order of magnitude could not be determined. For the Fernholz and Vagt data β_x and β_z were computed by neglecting the terms mentioned above, with little effect on the computed U_x^+ and U_z^+.

Results and Discussion

The analysis of the data sets was done by the present authors independently, in a uniform manner. Data taken from the nine data sets were plotted in the nondimensional coordinates of the nine selected law-of-the-wall relations in order to investigate the applicability and the range of validity of these relations. The ranges of y^+ parameter obtained from the plots, where the profiles are semi-logarithmic are given in Table 3. Figure 3 shows the difference of maximum and minimum values for each relation for the different data sets at $y^+ = 70$, which was a point well out of the viscous sublayer and presumably within any semi-logarithmic region. Thicker lines show the difference when the least fitting profiles were excluded. Figure 4 shows the ranges at $y^+ = 40$ and 100 starting from the Q^+ corresponding to each relation. This figure also shows the computed ranges of the right-hand sides of relations.

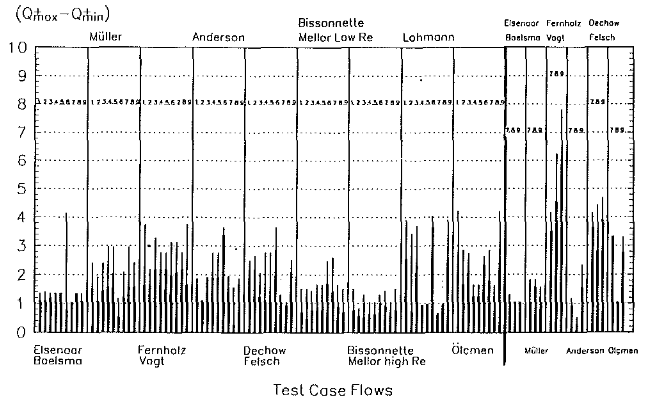

Fig. 3 Deviation of experimental data when plotted in given wall law coordinates at $y^+ = 70$ for the streamwise component. Various wall law relations denoted by numbers 1 = Coles; 2 = Johnston; 3 = Hornung-Joubert; 4 = Pierce-Krommenhoek; 5 = Chandrashekhar-Swamy; 6 = East-Hoxey; 7 = Perry-Joubert; 8 = White-Lessman-Christoph; 9 = Van den Berg. Thin lines show the ranges when all the profiles are included, thick lines show the ranges when the least fitting profile is omitted. Second ranges shown to the right for relations 7, 8, 9 are obtained using right hand side of the equations in particular relations.

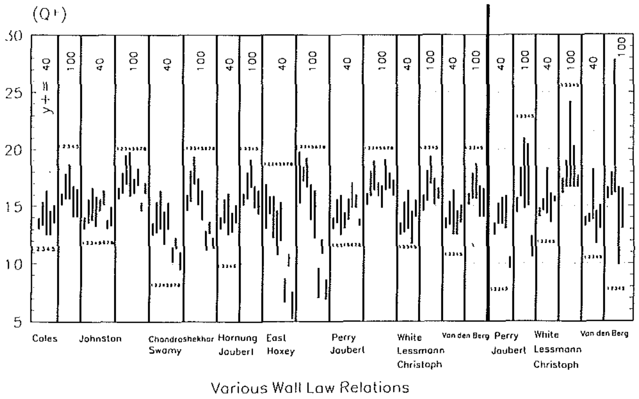

Fig. 4 Q^+ range obtained at $y^+ = 40$ and $y^+ = 100$ for various similarity relations using various data sets. 1 = Elsenaar-Boelsma; 2 = Müller; 3 = Fernholz-Vagt; 4 = Dechow-Felsch; 5 = Anderson; 6 = Bissonnette-Mellor low Re; 7 = Bissonnette-Mellor high Re; 8 = Lohmann. Second ranges shown to the right for data sets 1, 2, 3, 4, 5 are obtained with the right-hand side of the equations.

All of the examined relations are seen to be equally applicable for the Elsenaar-Boelsma flow. The semi-logarithmic region was well defined for all relations. Based on the scatter of the data at $y^+ = 70$, Johnston's relation was seen to be slightly better than the rest with $A_1 = 2.48$ and $B_1 = 4.1$. Figures 5(a) and 5(b) show the pressure-driven and shear-driven data in the nondimensional coordinates of Johnston's wall law. Van den Berg and Elsenaar (1972) had plotted their data in Clauser's 2-D law-of-the-wall coordinates with the velocity magnitude and had found good agreement. The y^+ range of the Johnston's relation extends up to $y^+ = 300$.

For Müller's data it was not easy to see the existence of a logarithmic region in the CS, WLC, and PK relations at stations D2, E3 and F5. Scatter of the Q^+ at different y^+ values for Coles and HJ relations was around 4.9 percent of the Q^+ plot range (i.e., 0-50) of their relations. The East and Hoxey relation was seen to be the most promising for this flow for $20 \le y^+ \le 200$. None of the relations except Coles' and Van

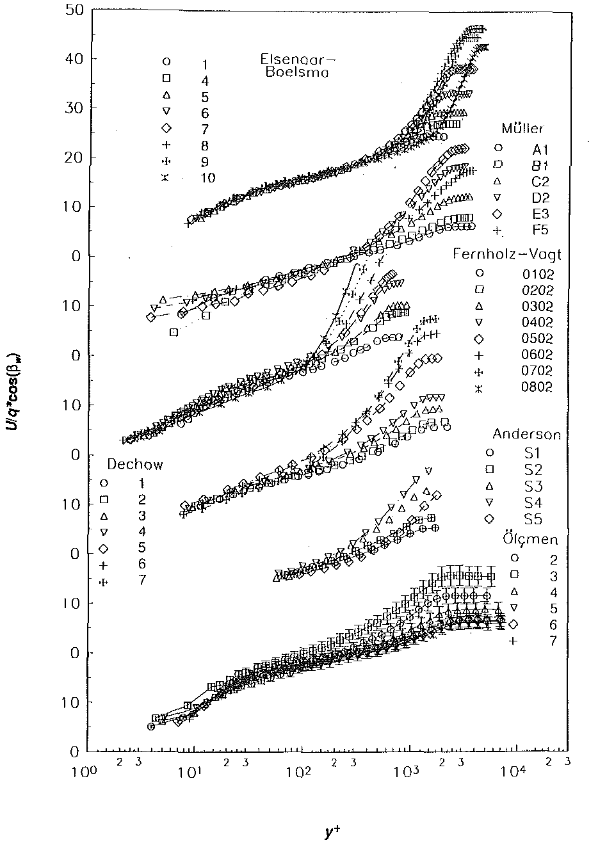

Fig. 5(*a*) Pressure-driven data in the similarity relation coordinate system of Johnston. Station location given in same notation as originating authors.

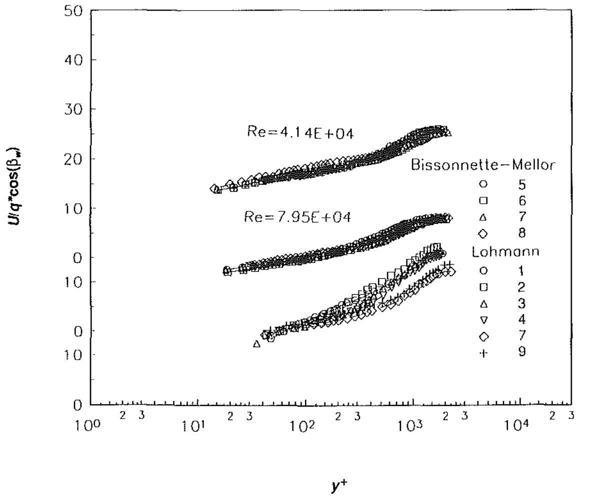

Fig. 5(*b*) Shear-driven data in the similarity relation coordinate system of Johnston. Station location given in same notation as originating authors.

den Berg's relations was able to predict a logarithmic region for station E3. Excluding this station, the Johnston relation (Fig. 5(*a*)) may be approximately fit with $A_1 = 2.922$ and $B_1 = 4.557$ and East and Hoxey with $A_5 = 2.71$, $B_5 = 3.57$. Müller 1982), plotted his data using the q^* that he computed using Spalding's formula with Coles' law of the wall constants. The computed τ_w was within 10% of that he measured with Preston tubes.

In most of the stations of the Fernholz and Vagt flow the turning angle of the flow was less than 15 deg. Since the distinction between the proposed relations depended on treatment of this angle, all of the relations perform equally well within 7.5 percent scatter among the profiles within each nondimensional coordinate. The distinction was clear at station 0802 where the maximum β was about 22.5 deg. For this station, Johnston's relation was able to include this station within 4.6 percent scatter for $15 \le y^+ \le 60$ with $A_1 = 3.514$ and $B_1 = 1.367$. Fernholz and Vagt (1981), discussed the possibility of a law of the wall with four different relations including U/q^* versus y^+, $U/q^*\cos(\beta)$ versus $y^+\cos\beta$, HJ, and Van den Berg's law of the wall. They concluded that the Hornung-Joubert relation was in much better agreement with the data than the others. They also favored the validity of use of the law of the wall for 2-D boundary layers in 3-D boundary layers.

For the Dechow-Felsch data, the flow skewed up to 50 deg, which resulted in a good test case for the relations. Even though the Coles, Van den Berg and Johnston relations predict logarithmic regions, the profiles diverge from each other (Fig. 5(*a*)) starting from $y^+ = 20$, with 5 percent scatter for Coles and Van den Berg and 6.4 percent for Johnston of the overall range of these plots. The PK and CS relations as well as the WLC relation predict a law of the wall for this flow except at St 7. When this station is excluded these relations show a good semi-logarithmic fit within 2.3 percent of their overall range. The HJ relation shows a semi-logarithmic fit within 4.3 percent over all of the range including station 7, in contrast to 5.6 percent scatter of the CS and PK relations. Excluding station 7 the latter relations produce a fit with $A_3 = 3.025$ and $B_3 = 3.06$. The HJ relation including station 7 fits the data with $A_2 = 2.502$ and $B_2 = 4.167 \le 5.21$. For this flow the PJ relation was seen to be the best relation since the scatter of the data at $y^+ = 70$ was the least with and without including the station 7. Within the range of $20 < y^+ < 200$ left-hand side of Eq. (7) in Table 2 produce a fit with a slope of $A_6 = 2.48$ and a constant $B_6 = 3.93$ in $A_6\ln(y^+) + B_6$ form.

Due to the measurement technique, the Anderson-Eaton flow did not have any data at less than $y^+ = 55$ which made it hard to investigate the range and applicability of the proposed relations. The flow had turning angles up to 45 deg. For this flow Coles, Van den Berg, HJ, PK and CS, and WLC relations showed 3.8, 3.8, 4, 5.6, 5.6, and 5.6 percent scatter of the data, respectively, up to $y^+ = 150$. For the last station S5, Coles' relation had almost zero slope as did Van den Berg's relation. In this severe test case, Johnston's relation with $A_1 = 2.91$ and $B_1 = 3.357$ seemed to be the only one to work up to $y^+ = 250$ with scatter of 12.5 percent. Up to $y^+ = 150$ the scatter was 5.7 percent (Fig. 5(*a*)).

The law-of-the-wall plots of Ölçmen's data include the uncertainties. For this data set, the CS and PK relations work better than the others if all the profiles are included. To compare the law-of-the-wall relations, the computed quantities (Q^+), at y^+ coordinates of 40, 70, 100, and 250 of each relation at each station, were plotted separately (Fig. 6). The uncertainties of the quantities are shown with bars. Since S in (Eq. (8)) was imaginary at several locations, as discussed below, the WLC relation is not included into this plot. The Van den Berg relation was also excluded, since it was the same as the Coles relation for the left-hand side of the U component (Eq. (10)). From this plot (Fig. 6) it is seen that, the PK relation is superior to the others (Fig. 7). The constants are $A_3 = 1.514$, $B_3 = 8.98$ (Eq. (4)). Even though the PJ relation applies as well as the previous relations, the uncertainty band is bigger; and the Johnston relation needed station 3 data to be excluded. The logarithmic region within $y^+ = 40$ to 300 was clearly observable. The second best fit belongs to the Johnston relation. This was observed with $A_1 = 1.93$, $B_1 = 8.33$ when the least fitting third station profile was omitted. The free-stream direction component for the other relations was seen to be less satisfactory.

For the Bissonnette-Mellor low Reynolds number data, Coles, Van den Berg and HJ relations did not work since the slopes of Coles' and Van den Berg relations were negative and HJ relations was on the average equal to zero. Among the

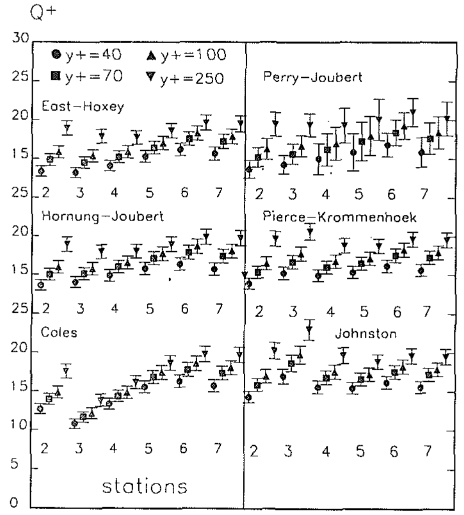

Fig. 6 Computed values for various similarity relations for Ölçmen's data at $y^+=40$ •, 70 ■, 100 ▲, 250 ▼, at different stations, with the uncertainty bands. Best similarity relation is indicated when Q^+ same at all stations for given y^+.

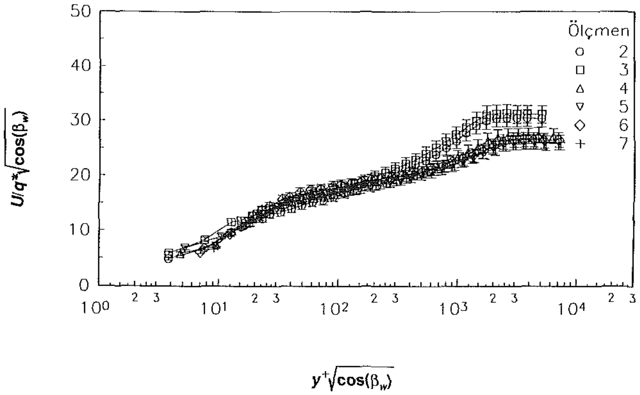

Fig. 7 Ölçmen's data in the coordinate system of Pierce-Krommenhoek and Chandrashekhar-Swamy similarity relation. Bars show the uncertainty bands.

other six proposed relations, Johnston's relation was superior. Plots of the data in CS, WLC and PK relation coordinates had scatter of 3.5 percent, in contrast to 2.6 percent scatter of Johnston's relation (percent of the ordinate range i.e., 0–50) (Fig. 5(*b*)). The scatter for the PJ relation was 10 percent. Within a y^+ range of $45 \le y^+ \le 250$ Johnston's relation could be approximated with $A_1=1.78$ and $B_1=9.378$.

For the high Reynolds number data of Bissonnette and Mellor, the Coles and Van den Berg relations showed approximately zero slope. The HJ relation was able to capture the semi-logarithmic region with a reasonable slope. The scatter of data was least in Johnston's relation coordinates, 1.85 percent of the ordinate range (Fig. 5(*b*)), with $A_1=1.741$ and $B_1=7.554$. The scatter in the PK, CS, WLC, and HJ and PJ relations was 2.2, 2.2, 2.2, 2.75, and 2.85 percent, respectively. Bissonnette and Mellor (1974), discussed the possibility of a law of the wall in a coordinate system of $\sqrt{U^2+(W_0+W)^2}/q^*$ versus yq^*/ν in order to test the applicability of Clauser's proposition for such a flow. Even though Clauser's law of the wall did not fit the data, they still had shown existence of a law of the wall in such a coordinate system.

Surprisingly, none of the relations seemed to collapse Lohmann's data. The HJ relation had approximately zero slope and scatter in Coles' and Van den Berg's relations' coordinates was 9.5 percent. Even though the remaining six relations merged the data into a law of the wall, the slopes of the individual profiles were different. If stations 1 and 2 were excluded, Johnston's relation was able to collapse the data within 1.7 percent of the overall range of the data within $60 \le y^+ \le 250$. If station 2 data were included, the range was between $60 \le y^+ \le 150$ (Fig. 5(*b*)) and $A_1=2.182$ and $B_1=6.213$. For this flow the PJ relation has scatter of only 0.65 percent at $y^+=70$, however the scatter goes up to a value of 5.55 percent at $y^+=100$. Lohmann (1976), plotted his velocity data relative to the moving wall W_0, divided by friction velocity q^* versus y^+ and found good agreement except at stations 1 and 2, where data followed at the law of the wall for the $40 \le y^+ \le 80$ range only.

The summary of the overlapping regions for the left-hand side and right-hand side of equations for the streamwise velocity component of the last three relations which take into account the effect of the pressure gradients are given in Table 4.

The computed values for the streamwise velocity component from the derived W-L-C Eq. (8) and the measured Q^+ seemed to overlap each other reasonably well but only in a short y^+ range for the Dechow, Anderson-Eaton, and Elsenaar-Boelsma flows. For the profiles in which αy^+ was below (-1), it was not possible to compute the square root terms in Eq. (8). These kind of profiles were observed for Anderson's S4 and S5 stations, Dechow's 6th and 7th stations, and in all stations except at station 2 for Ölçmen's data and were excluded from the comparison. For Müller's data, computed values could not resemble the wide range of Q^+ observed and for the Fernholz and Vagt data the resemblance was in a very short range of y^+ (Table 4). Within the available points for Ölçmen's data, only station 2 was observed to match within the uncertainty bands the left and right-hand sides of (Eq. (8)) until $y^+=2000$.

For the PJ relation (Eq. (7)) the computed values with the use of θ, α, q^*, and y^+ were compared with the $Q^+=H/q^*$ values discussed above. In a limited y^+ range, a match of Q^+ with the computed values were observed (Table 4). For Ölçmen's data, the match of the left-hand side and right-hand side of (Eq. (7)) was within a short range of y^+, from 20 to 70. The integration constant was approximately 8.5 for the data sets used.

For the Van den Berg relation, it was observed from these comparisons that computed and measured values overlapped within a limited y^+ range for all data sets. For the Fernholz and Vagt data, the y^+ range of agreement between computed and measured was very short (Table 4). For Ölçmen's data the left-hand side and the right-hand side of the same equation did not overlap, except for station 7. For this station, an overlap region within $y^+=40$ to 700 with $B_7=8.57$, was observed. The constants for this relation were observed to be close to $B_7=4.7$ and $B_8=0.15$ including all the data sets.

The W component of velocity could not be represented with any of the laws of the wall presented. The computed W^+ values from data and Mager's formulation (Mager, 1951) for defining the same quantity in terms of U^+ did not match. Mager's method presented in the WLC scheme consistently estimated higher values than the data (Fig. 8(*a*) and Fig. 8(*b*)), with up to 100 percent difference for the pressure driven data. For the shear-driven data the profiles did not resemble each other. The Van den Berg relation resulted in much different values than the data for $y^+>30$, except for the Elsenaar-Boelsma's data in which the prediction was good up to $y^+=200$. Also, near the wall measured values of U_z^+ were small, by definition, which made it hard to judge the agreement with this relation. The law of the wall proposed by CS for the W velocity component did not work for the pressure-driven data and seemed to collapse only the Bissonnette and Mellor data for the shear driven data. For the low-Reynolds-number case, scatter was 1.2 percent of the ordinate range (i.e., 0–25) and for the high-Reynolds-number case, scatter was 1.7 percent (Fig. 9). If there has to be a choice made among these three methods, Mager's

Table 4 Overlap y^+ ranges for the left-hand side and the right-hand side of the proposed relations for pressure-driven data sets for the axial component

Flows / Models Studied	Perry-Joubert	White-Lessmann-Christoph	van Den Berg
Elsenaar-Boelsma	40-500	30-200	30-200
Muller	6-150	4-60	4-40
Fernholz-Vagt	10-100	15-30	15-30
Dechow-Felsch	7-20	7-60	7-20
Anderson-Eaton	60-100	60-100	60-80
Ölçmen	20-100	20-40	30-40

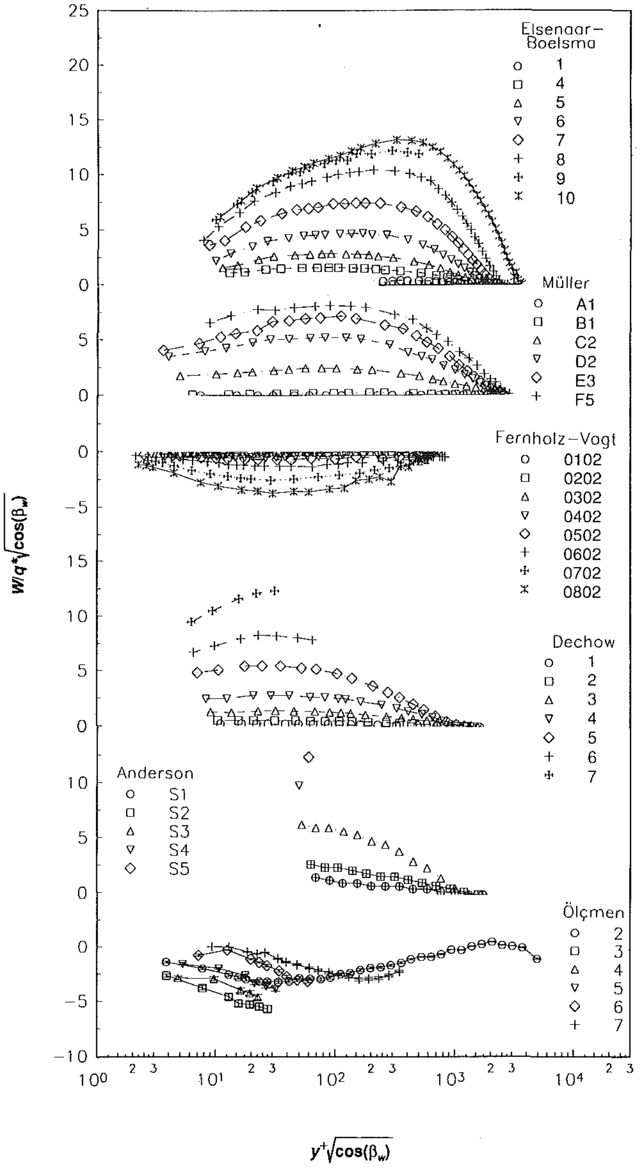

Fig. 8(*a*) Pressure-driven data in the coordinate system of White-Lessman-Christoph crosswise velocity component similarity relation. Left-hand side of Eq. (9). Station location given in same notation as originating authors.

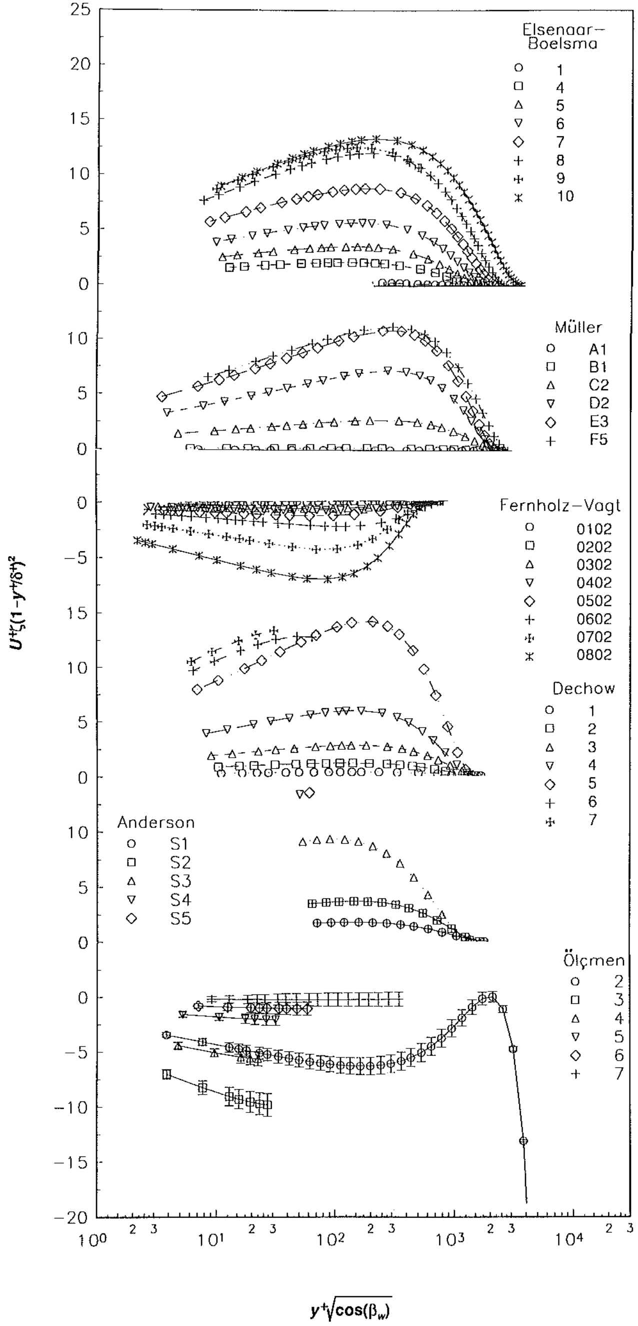

Fig. 8(*b*) Pressure-driven data in the coordinate system of White-Lessman-Christoph crosswise velocity component similarity relation. Right-hand side of Eq. (9). Station location given in same notation as originating authors.

method for the pressure-driven flows and CS relation for the shear-driven data might be suggested.

Conclusions

These data show that there is not strong evidence for a three-dimensional turbulent boundary layer law-of-the-wall similarity profile. Johnston, Coles, HJ, EH, and PK-CS models are variations for extending the well established two-dimensional law of the wall to three-dimensional turbulent boundary-layer flows. It is not clear why the fictitious velocity $U/\cos(\beta_w)$ used by Johnston works better than the other velocity expressions used by the other models. Although all the velocity expressions used seem to be close to each other very near the wall, Johnston's fictitious velocity has higher values in the other regions. Even though different wall similarity relations fit some of the cases better than Johnston's relation, the Johnston law of the

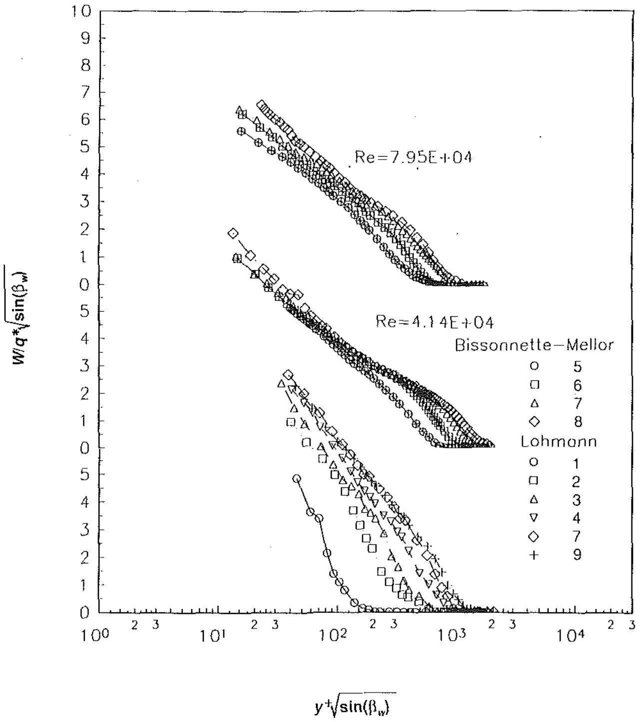

Fig. 9 Shear-driven data in the coordinate system of Chandrashekhar-Swamy similarity relation for the crosswise velocity component. Station location given in same notation as originating authors.

wall seems to fit all of the examined cases within reasonable uncertainty and therefore it should be preferred.

The functions which took into account the pressure gradient effect in the WLC, PJ, and Van den Berg law-of-the-wall relations were seen to perform well for some profiles up to $y^+ = 1000$, but overall the predictions agreed with data only over short ranges of y^+. The reason for this is believed to be due to the assumptions contained in the development of these models: validity of the mixing length concept, isotropic eddy viscosity, and equilibrium flow conditions in three-dimensional turbulent boundary layers. In three-dimensional flows the assumption of $N = 1$ is an exception rather than the rule. Furthermore, including the pressure gradient in the functional form of the law of the wall does not improve three-dimensional similarity. This lack of functional dependence on the pressure gradient is not different than what is observed in two-dimensional boundary layers where the law of the wall applies for all pressure gradients up to separation (Simpson et al., 1981). Among these latter relations the PJ relation performs best.

For the W component none of the proposed relations work well. If there has to be a choice made among these three methods, Mager's method for the pressure driven flows and the CS relation for the shear driven data are suggested.

JFE Data Bank Contributions

The experimental data sets obtained from the authors which are used in the calculations for this paper are being added to the *Journal of Fluids Engineering* data bank. The data sets include flow conditions, pressure distributions, skin friction, and the mean velocity and Reynolds' stress profiles in different coordinate systems. To access the file for this paper see instructions on p. 705 of this issue.

Acknowledgment

This work was partially supported by the Office of Naval Research and the Defense Advanced Research Projects Agency.

References

Ailinger, K., 1990, "Measurements of Surface Shear Stresses under a Three-Dimensional Turbulent Boundary Layer Using Oil-Film Laser Interferometry," M.S. thesis, Virginia Tech, Aerospace and Ocean Engineering Department.

Anderson, S. D., and Eaton, J. K., 1987a, "Experimental Study of a Pressure-Driven Three-D, Turbulent Boundary Layer," *AIAA Journal*, Vol. 25, No. 8, Aug., pp. 1086-1092.

Anderson, S. D., and Eaton, J. K., 1987b, "An Experimental Investigation of Pressure-Driven Three-Dimensional Turbulent Boundary Layers," Report MD-49, Thermoscience Division, Department of Mechanical Engineering, Stanford University, Stanford, CA 96305, June.

Bissonnette, L. R., and Mellor, G. L., 1974, "Experiments on the Behavior of an Axisymmetric Turbulent Boundary Layer with a Sudden Circumferential Strain," *Journal of Fluid Mechanics*, Vol. 63, Part 2, pp. 369-413.

Chandrashekhar, N., and Swamy, N. V. C., 1975, "Wall Shear Stress Inference for Three-Dimensional Turbulent Boundary Layer Velocity Profiles," ASME JOURNAL OF FLUIDS ENGINEERING, Vol. 97, pp. 550-557.

Coles, D., 1956, "The Law of the Wake in the Turbulent Boundary Layers," *Journal of Fluid Mechanics*, Vol. 1, Part 2, pp. 191-226.

Coles, D., and Hirst, E. A., 1968, "Computation of Turbulent Boundary Layers," AFOSR-IFP-Stanford Conference, Stanford University Press, Stanford, Calif.

Dechow, R., and Felsch, K. O., 1977a, "Measurements of the Mean Velocity and of the Reynolds Stress Tensor in a Three-Dimensional Turbulent Boundary Layer Induced by a Cylinder Standing on a Flat Wall," *Symposium on Turbulent Shear Flows*, Apr. 18-20, University Park, PA, pp. 9.11-9.20.

Dechow, R., 1977b, "Mittlere Geschwindigkeit and Reynoldsscher Spannungstensor in der dreidimensionalen turbulenten Wandgrenzschicht von einen Stehenden Zylinder," Stromungsmechanik and Strömungsmoschinen Mitteilungen des Instituts fur Strömungsmechanik and Strömungsmoschinen, Universitat (TH) Karlsruhe, Heft 21 Marz.

East, L. F., and Hoxey, R. P., 1969, "Low Speed Three-Dimensional Turbulent Boundary Layer Data," Parts 1 and 2 Aeronautical Research Council R&M 3653.

Elsenaar, A., and Boelsma, S. H., 1974, "Measurements of the Reynolds Stress Tensor in a Three-Dimensional Turbulent Boundary Layer Under Infinite Swept Wing Condition," NLR TR 74095 21.

Fernholz, H. H., and Vagt, J. D, 1981, "Turbulence Measurements in an Adverse Pressure-Gradient Three-Dimensional Turbulent Boundary Layer Along a Circular Cylinder," *Journal of Fluid Mechanics*, Vol. 111, pp.233-269.

Hornung, H. G., and Joubert, P. N., 1963, "The Mean Velocity Profile in Three-Dimensional Turbulent Boundary Layers," *Journal of Fluid Mechanics*, Vol. 15, Part 3, pp. 368-384.

Johnston, J. P., 1960, "On the Three-Dimensional Turbulent Boundary Layer Generated by Secondary Flow," ASME *Journal of Basic Engineering*, pp. 233-248.

Lohmann, R. P., 1976, "The Response of a Developed Turbulent Boundary Layer to Local Transverse Surface Motion," ASME JOURNAL OF FLUIDS ENGINEERING, Vol. 98, pp. 354-363.

Mager, A., 1951, "Generalization of Boundary Layer Momentum Integral Equations to Three-Dimensional Flows, Including Those of a Rotating Disk," NACA Technical Note No. 2310.

Müller, U. R., 1982, "Measurement of Reynolds Stresses and the Mean-Flow Field in a Three-Dimensional Pressure-Driven Boundary Layer," *Journal of Fluid Mechanics*, Vol. 119, pp. 121-153.

Ölçmen, M. S., 1990, "An Experimental Study of a Three-Dimensional Pressure-Driven Turbulent Boundary Layer," Ph.D. dissertation, Virginia Tech, Aerospace and Ocean Engineering Deparment.

Perry, A. E., and Joubert, P. N., 1965, "A Three-Dimensional Turbulent Boundary Layer," *Journal of Fluid Mechanics*, Vol. 22, Part 2, pp. 285-304.

Pierce, F. J., McAllister, J. E., and Tennant, M. H., 1982, "Near-Wall Similarity in Three-Dimensional Turbulent Boundary Layers, Part I: Model Review, Part II: Pressure-Driven Flow Results," *Three Dimensional Turbulent Shear Flows, Proceedings AIAA/ASME Joint Fluids Conference*, June 7-11, pp. 85-103, ASME publication.

Pierce, F. J., and Krommenhoek, D. H., 1968, "Wall Shear Stress Diagnostics in 3-D Turbulent Boundary Layers," Interim Technical Report No. 2, ARO-D Project 6858E, Virginia Polytechnic Institute and State University.

Simpson, R. L., Chew, Y. T., and Shivaprasad, B. G, 1981, "The Structure of a Separating Turbulent Boundary Layer. Part 1. Mean Flow and Reynolds Stresses," *Journal of Fluid Mechanics*, Vol. 113, pp. 23-51.

Van den Berg, B., 1975a, "A Three-Dimensional Law of the Wall for Turbulent Shear Flows," *Journal of Fluid Mechanics*, Vol. 70, Part 1, pp. 149-160.

Van den Berg, B., Elsenaar, A., Lindhout, J. P. F., and Wesseling, P., 1975b, "Measurements in an Incompressible Three-Dimensional Turbulent Boundary Layer, Under Infinite Swept-Wing Conditions, and Comparison with Theory," *Journal of Fluid Mechanics*, Vol. 70, Part 1, pp. 127-148.

Van den Berg, B., and Elsenaar, A., 1972, "Measurements in a Three-Dimensional Incompressible Turbulent Boundary Layer in an Adverse Pressure Gradient Under Infinite Swept Wing Conditions," NLR TR 72092 21.

White, F. M., Lessmann, R. C., and Christoph, G. H., 1975, "A Three-Dimensional Integral Method for Calculating Incompressible Skin Friction," ASME JOURNAL OF FLUIDS ENGINEERING, Vol. 97, pp. 550-557.

S. Majumdar[1]

W. Rodi

J. Zhu

Institute for Hydromechanics,
University of Karlsruhe,
D-7500 Karlsruhe 1,
Federal Republic of Germany

Three-Dimensional Finite-Volume Method for Incompressible Flows With Complex Boundaries

A finite-volume method is presented for calculating incompressible 3-D flows with curved irregular boundaries. The method employs structured nonorthogonal grids, cell-centered variable arrangement, and Cartesian velocity components. A special interpolation procedure for evaluating the mass fluxes at the cell-faces is used to avoid the nonphysical oscillation of flow variables usually encountered with the cell-centered arrangement. The SIMPLE algorithm is used to handle the pressure-velocity coupling. A recently proposed low diffusive and bounded scheme is introduced to approximate the convection terms in the transport equations. The computer code and the relevant data structure are so organized that most of the code except the implicit linear solver used is fully vectorizable so as to exploit the potential of modern vector computers. The capabilities of the numerical procedure are demonstrated by application to a few internal and external three-dimensional laminar flows. In all cases the CPU-time on a grid with typically 28,000 grid nodes was below half a minute.

1 Introduction

Incompressible fluid-flow phenomena encountered in engineering practice are mostly three-dimensional, involve curved, irregular boundaries and are subject to viscous and turbulence effects. Numerical prediction of such complicated flow situations with the available computer resources demands an efficient and accurate algorithm for the solution of the strongly coupled linear differential equations governing the flow. In recent years, finite-volume methods have become rather popular for carrying out such calculations. In these methods, the solution domain is subdivided into discrete volumes through a computational grid, and approximations are introduced to replace each differential equation by a set of linearized algebraic equations written in terms of discrete, nodal values of the dependent variables. These algebraic equations representing the balances of fluxes of various flow variables across the finite control-volume faces are then solved to calculate the flow field. Finite-volume methods have been widely applied to problems with regular geometries where the boundaries happen to coincide with the coordinate lines of an analytic orthogonal coordinate system. But this approach is quite unsatisfactory for many problems of practical interest involving complex irregular boundaries since prescription of conditions at boundaries not conforming to the coordinate lines is problematic and near-wall regions with steep gradients are difficult to resolve accurately. Further, most commonly used solution algorithms converge rather slowly, which poses limitations on grid refinement, particularly for three-dimensional situations.

This paper presents an efficient finite-volume method for calculating incompressible flows in complex three-dimensional situations. The method can accept boundary-conforming nonorthogonal but structured grids and was programmed so as to make optimal use of the vector capabilities of modern computers. The numerical accuracy was improved by incorporating a recently proposed composite differencing scheme for the convection terms (Zhu and Rodi, 1991) which is capable of yielding bounded and low diffusive solutions. The strategy of the method development is outlined in Section 2.1 and the resulting finite-volume method is discussed in Section 2.4. Application examples are presented and discussed in Section 3. With the main emphasis of this paper being on the numerical solution procedure, we restrict attention to the calculation of three-dimensional laminar flows. The application examples include the flow in a curved pipe, in an S-shaped diffuser, over a surface-mounted hemisphere and around a circular cylinder placed in a channel. The calculation examples demonstrate the performance of the method with respect to numerical accuracy, computational efficiency and flexibility in handling complex geometries.

2 Numerical Calculation Procedure

2.1 Choice of Basic Method. A number of different ways can be taken for the development of a general and efficient finite-volume method. Hence, a choice has to be made on the method for generating appropriate curvilinear grids and on the type of finite-volume method suited for their use, with the aim of satisfying the following requirements: (i) the method

---

[1] Present address: CTFD Division, National Aeronautical Laboratory, Bangalore 560017, India.

Contributed by the Fluids Engineering Division for publication in the JOURNAL OF FLUIDS ENGINEERING. Manuscript received by the Fluids Division February 18, 1991. Associate Technical Editor: R. K. Agarwal.

can be applied to general flow situations involving complex boundaries, (ii) the solution of the differential equations is sufficiently accurate for practical purposes and in particular numerical diffusion is sufficiently small, (iii) storage and computing time requirements are of acceptable level, which requires an efficient solution algorithm with good convergence characteristics, (iv) the method is able to use without difficulty an advanced turbulence model, like the k-ϵ model, and (v) the code is user-friendly and has good stability behavior. A discussion on the various possibilities and on the strategies for the development of general, accurate and efficient finite-volume methods for solving the incompressible flow equations has been given by Rodi et al. (1989). Following these strategies, methods have been chosen for the grid generation and the flow solver, and the present section describes these choices in brief and gives justifications for them.

Simple rectangular geometries can be handled by Cartesian coordinates for which the derivation of finite difference equations is simple and noncontroversial since nonorthogonal and curvature terms do not arise. But when the boundaries are curved and irregular, an obvious choice is the use of curvilinear boundary-conforming coordinates which may be either orthogonal or nonorthogonal. Nonorthogonal curvilinear coordinates are chosen in the present method since orthogonal grids are more difficult and sometimes even impossible to generate for complex three-dimensional configurations.

The choice of axes along which the velocity vector is resolved decides how the divergence and curl of the velocity vector in the tensor form of the equations of motion are transformed to velocity gradients in the partial differential equations for the individual velocity components. The transport equations may be formulated using either Cartesian velocity components or grid-oriented velocity components. Cartesian velocity components are chosen because, in contrast to grid-aligned components, no grid-sensitive curvature terms appear in the momentum equations. Such terms depending on the second-derivative of grid coordinates are difficult to discretize in a conservative manner and may lead to severe inaccuracies unless the grid is very smooth. The convergence and stability of a numerical procedure for solving the incompressible flow equations depend largely on how the gradients of pressure and velocities are evaluated in the discretized form of the momentum and continuity equations. An adequate formulation of the pressure-velocity coupling can be obtained either via a staggered or a non-staggered arrangement of the variables. For the present method, the latter arrangement is chosen since it involves one and only one control volume per grid point for every dependent variable. This is much more transparent and easier to handle in three-dimensional problems, specially in connection with the use of the multigrid method, than several staggered control volumes for each grid point. The transport equations are solved in a decoupled way in order to keep the storage requirement low and to facilitate the solution of additional transport equations. With the discretization schemes employed, the resulting coefficient matrix of the linear system of equations to be solved has a sparse-band structure. In preliminary investigations several iterative linear solvers were tested with respect to convergence rate, vectorization capability, and smoothing property which is important for multigrid methods. The strongly implicit procedure of Stone (1968) was chosen which has both good convergence rate and smoothing properties, but is very difficult to be fully vectorized.

2.2 Governing Equations. The equations for steady, three-dimensional flows in nonorthogonal coordinates using Cartesian velocity components may be written in a generalized form as follows:

$$\frac{\partial}{\partial x_i}\,(C_i\phi + D_{i\phi}) = JS_\phi, \quad i=1,2,3 \tag{1}$$

where, for different variables ϕ, the terms C_i related to convection and $D_{i\phi}$ related to diffusion, the source terms S_ϕ and the definition of the Jacobian J are given in Table 1. The coordinate directions x_i are shown in Fig. 1.

Table 1 Form of terms in the individual equations

ϕ	$D_{i\phi}$	S_ϕ
1	0	0
V_1	$-\frac{\mu}{J}\left(B_j^i\frac{\partial V_1}{\partial x_j}+\beta_j^i\omega_1^j\right)$	$-\frac{1}{J}\frac{\partial}{\partial x_j}\,(\beta_1^j p)$
V_2	$-\frac{\mu}{J}\left(B_j^i\frac{\partial V_2}{\partial x_j}+\beta_j^i\omega_2^j\right)$	$-\frac{1}{J}\frac{\partial}{\partial x_j}\,(\beta_2^j p)$
V_3	$-\frac{\mu}{J}\left(B_j^i\frac{\partial V_3}{\partial x_j}+\beta_j^i\omega_3^j\right)$	$-\frac{1}{J}\frac{\partial}{\partial x_j}\,(\beta_3^j p)$

$$C_i=\rho\beta_j^iV_j, \quad \omega_j^i=\beta_j^n\frac{\partial V_i}{\partial x_n},$$

$$\beta_j^i=\text{cofactor of }\partial y_j/\partial x_i\text{ in }J,\quad J=\begin{vmatrix}\frac{\partial y_1}{\partial x_1} & \frac{\partial y_2}{\partial x_1} & \frac{\partial y_3}{\partial x_1}\\ \frac{\partial y_1}{\partial x_2} & \frac{\partial y_2}{\partial x_2} & \frac{\partial y_3}{\partial x_2}\\ \frac{\partial y_1}{\partial x_3} & \frac{\partial y_2}{\partial x_3} & \frac{\partial y_3}{\partial x_3}\end{vmatrix}$$

$$B_j^i=\beta_n^i\beta_n^j,$$

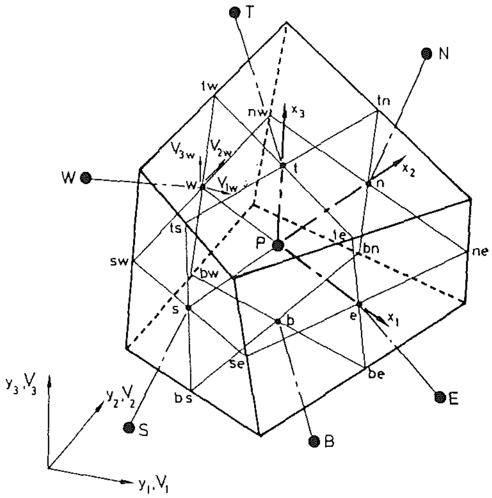

Fig. 1 Three-dimensional control volume

2.3 Grid Generation. For use in connection with the finite-volume method described, algebraic as well as differential grid generation methods for two- and three-dimensional problems have been developed and are described in Zhu et al. (1988, 1989) and Naar and Schönung (1986), respectively. The algebraic method is based on the concept of transfinite mapping, with blending functions being calculated from cubic splines. Any number of constraint curves can be used to apply a control on the grid, and the grid remains smooth over the entire computational field. The procedure of Naar and Schönung (1986) is based on the method of Sorenson (1980). It involves the solution of Poisson-type partial differential equations. During the solution process, the source terms are calculated iteratively in such a way that certain prescribed boundary conditions are satisfied. Specifically, the distribution of grid points along boundaries, the grid intersection angles at the boundary and the mesh size normal to the boundary can be specified. For three-dimensional problems, the surface grids are generated with the algebraic method and the grids in the interior of the solution domain are generated via a recently developed hybrid method (Zhu et al., 1989). The latter is based on a two-step

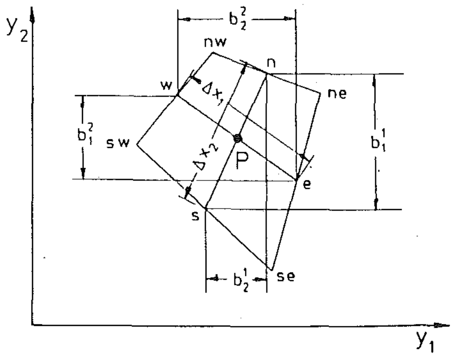

Fig. 2 Projection areas for 2-D control volume

procedure. First, the constraint curves in the interior are calculated with a three-dimensional extension of Sorenson's differential method. A fine grid with desired concentration of grid lines is then obtained by fitting tricubic spline functions on the coarse grid. A primary feature of the method is that the mesh spacing can be quickly and explicitly changed while retaining the smoothness over the entire field and the boundary-orthogonality.

2.4 Finite-Volume Method

Control Volume and Variable Arrangement. Figure 1 shows the kind of control volume and the variable arrangement used in the present method. The grid generation procedure calculates the coordinates of the control volume vertices which are simply joined by linear segments to form the same. All the variables are stored at the geometric center P of the control volume. The six neighboring control volume centers are indicated by N, S, E, W, T, and B for the north, south, east, west, top and bottom neighbors. The face center points n, s, e, w, t, and b are located at the intersection of the lines joining the midpoint of the opposite edge, e.g., te, be, ne, se are the middle points of the edges forming the east face with e at its center. These points specified on faces and edges are used for locating the variables and their gradients on the control volume faces. The Cartesian velocity V_{iw} etc. indicated in Fig. 1 for the west face of the control volume, are calculated for consideration of cellwise continuity. However what needs to be stored at each face of the control volume are not these velocity components but the total convective mass fluxes.

Flux Balance Equations. The difference equations representing the flux balance are derived by integrating the governing differential equations over the control volumes with the aid of the Gauss theorem. Thus, the volume integral of the terms under the differential operator on the left hand side of the transport Eq. (1) may be converted to surface integrals (fluxes) over the six different faces of the control volume. The resulting balance equation for each control volume and variable ϕ may then be expressed as follows:

$$I_e - I_w + I_n - I_s + I_t - I_b = \int_{\Delta V} S_\phi dV \tag{2}$$

where, I_e, for example, represents the total flux of ϕ across the face e. Each of the surface fluxes I_e, I_w etc. is made of three distinct parts, namely a convective contribution I^C, a normal diffusive contribution I^{DN}, and a cross-derivative diffusive part I^{DC}. Equation (2) involves no approximation and represents the finite volume analogue of the differential Eq. (1). The numerical evaluation of the different terms in Eq. (2) requires the calculation of geometric factors for nonorthogonal control volumes and the introduction of a discretization scheme for interpolating quantities at the cell faces from their nodal values.

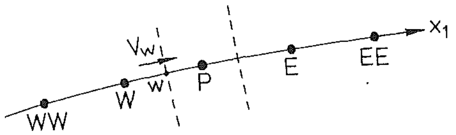

Fig. 3 Nodes required by SOUCUP scheme in x_1-direction

Geometric Factors. The most important geometrical parameters required in the present formulation are the factors β_j^i which may be expressed in terms of the projection area of the control volume faces as follows:

$$\beta_j^i = b_j^i \Delta x_i / (\Delta x_1 \Delta x_2 \Delta x_3) \tag{3}$$

where the projection areas b_j^i for the control volume around P are shown in Fig. 2 for a two-dimensional situation on the $y_1 - y_2$ plane. The volume of the control cell is calculated from the cell corner coordinates assuming that the cell corners are joined by linear segments to form the six cell faces and employing the method suggested by Kordulla and Vinokur (1983). The other geometrical quantities of interest are the normal distance of a near-boundary node from the boundary surface, the Cartesian components of a unit vector normal to the boundary faces of a control volume and the boundary face areas. The calculation of these quantities, however, involves only some simple arithmetic operations, using vector algebraic formulas connecting the known coordinates of the cell vertices.

Difference Equations. The expression for convective and diffusive fluxes of ϕ through the cell face w, for example, can be written as:

$$I_w^C = \rho_w b_j^1 V_j \phi_w = c_w \phi_w \tag{4}$$

$$\begin{aligned} I_w^{DN} &= -(\mu/\Delta V)_w D_{1w}^1 (\phi_P - \phi_W) \\ I_w^{DC} &= -(\mu/\Delta V)_w D_{2w}^1 (\phi_{nw} - \phi_{sw}) \end{aligned} \tag{5}$$

where

$$D_j^i = b_k^i b_k^j$$

The normal derivative diffusion flux, I^{DN}, is coupled with the convective flux, I^C, to calculate the main coefficients of the difference equations, while the cross-derivative diffusion flux, I^{DC}, is treated explicitly as a pseudo-source term to avoid the possibility of producing negative coefficients in an implicit treatment. The cell face value ϕ_w appearing in the convective flux I_w^C is evaluated by the SOUCUP scheme which combines three simple discretization schemes, namely, second-order upwind, central, and first-order upwind differencing. A detailed discussion of the scheme would go beyond the scope of this paper; the reader is referred to Zhu and Rodi (1991) for details so that it may suffice here to give a brief description of the salient features of the scheme.

The derivation of the SOUCUP scheme is based on the variable normalization proposed by Leonard (1987, 1988) and the convection boundedness criterion (CBC) by Gaskell and Lau (1988). Consider the "w" face of the control volume shown in Fig. 3 and assume, without loss of generality, that $V_w > 0$ (V_w is the normal velocity at the w-face). The variable normalization is defined by

$$\hat{\phi} = \frac{\phi - \phi_{WW}}{\phi_P - \phi_{WW}} \tag{6}$$

In case that the normalized face value $\hat{\phi}_w$ is only a continuous increasing function of the normalized upstream nodal value $\hat{\phi}_W$, that is, $\hat{\phi}_w = f(\hat{\phi}_W)$, the CBC is that a numerical approximation to ϕ_w is bounded if: (i) for $0 \le \hat{\phi}_W \le 1$, f is bounded below by the function $\hat{\phi}_w = \hat{\phi}_W$ and above by unity and passes through the points (0, 0) and (1, 1); (ii) for $\hat{\phi}_W < 0$ or $\hat{\phi}_W > 1$, f is equal to $\hat{\phi}_W$. The CBC can be clearly illustrated in Fig. 4 where the line $\hat{\phi}_w = \hat{\phi}_W$ and the shaded area are the region

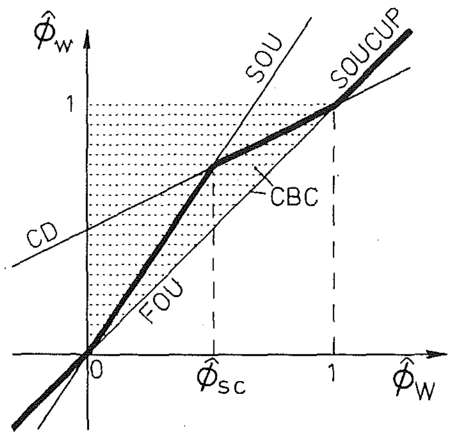

Fig. 4 Normalized-variable diagram

over which the CBC is valid. It is easy to show that in the normalized form, the face values of ϕ evaluated by the first-order upwind (FOU), second-order upwind (SOU) and central differencing (CD) schemes are all the linear functions of the upstream adjacent nodal value (Fig. 4), and the last two higher-order schemes satisfy the CBC only in the monotonic range of $0 \leq \hat{\phi}_W \leq 1$. As a result, the SOUCUP scheme approximates the face value $\hat{\phi}_w$ by a continuous piecewise-linear function consisting of the above three schemes (see bold-faced line in Fig. 4).

The contribution of a source in the discretized equation may be expressed as follows:

$$\int_{\Delta V} J S_\phi dx_1 dx_2 dx_3 = S_U + S_P \phi_P \tag{7}$$

Replacing the respective expressions for convective and diffusive face fluxes and the corresponding source terms, the difference equations can always be cast into the following linearized form:

$$\begin{aligned} A_P \phi_P &= \sum_i A_i \phi_i + S_U \\ A_p &= \sum_i A_i - S_P, \quad i = \text{E, W, N, S, T, B} \end{aligned} \tag{8}$$

where the main coefficients A's represent the combined effect of convection and normal derivative diffusion.

Momentum Interpolation for Calculation of Pressure Field. In incompressible flows, the momentum equations link the velocities to the respective pressure gradients whereas the continuity equation, apparently having no link to the pressure, is just an additional constraint on the velocity field. Due to such weak linkage, the convergence and stability of a numerical solution of the momentum and continuity equations depend largely on how the gradients of pressure and velocity are evaluated in these equations. Storing the variables at the geometrical center of the control volume coupled with the use of linear interpolation for internodal variation usually leads to non-physical oscillation or the so-called red-black checkerboard splitting of the pressure field and the associated difficulties in obtaining a converged solution. The first solution to this problem, proposed by Harlow and Welch (1965) was to use a staggered variable arrangement. But this arrangement has its own disadvantages, one being that the calculation of coefficients and geometrical interpolation factors is time-consuming when different kinds of control volumes are used for different variables. The other alternative to avoid checkerboard splitting for cell-centered arrangement is to use a special interpolation, termed as momentum interpolation in this paper, to evaluate cell face variables from the cell centered quantities. The concept of momentum interpolation, first proposed by Rhie and Chow (1983), has been explained in detail with practical application and assessment of relative performance compared to that of staggered arrangement by Majumdar (1986, 1988). The present method uses this momentum interpolation technique for calculation of the pressure field from the continuity and momentum equations.

The basic idea of the SIMPLE algorithm (Patankar and Spalding, 1972) is to (i) assume an artificial link between the cell-centered pressure and the cell-face velocities from the discretized momentum equations, (ii) to frame a system of linear equations for pressure correction that satisfy continuity and (iii) finally to correct the pressure and velocities accordingly. A similar strategy is followed in the present procedure too with the only difference that, unlike in the classical staggered arrangement, the velocities at cell-face locations, not being available there, are to be calculated from the adjacent cell-centered quantities using the momentum interpolation.

For 3D flows, the discretized momentum equations for cell-centered velocities V_{iP} using underrelaxation parameter α_v are as follows:

$$\begin{aligned} V_{iP} = \alpha_v[H^i_P + D^i_1(p_w - p_e) + D^i_2(p_s - p_n) \\ + D^i_3(p_b - p_t)] + (1-\alpha_v) V^0_{iP} \end{aligned} \tag{9}$$

$$H^i_P = \left(\sum A^i_{nb} V_{inb} + S_U \right) / A^i_P \tag{10}$$

where A^i_{nb} represents the coefficients for neighboring nodes; V^0_{iP} is the old value of the variable V_{iP} at the previous iteration and A^i_P is the value of A_P for V_i at the node P. The D^i_j may be defined as follows:

$$D^i_j = b^i_j / A^i_P \tag{11}$$

Now similar to the basic concept of staggering, the momentum interpolation also assumes that the velocities at any control volume face are, in principle, driven by the pressure difference between two adjacent nodes lying on either side of the face in question. The discretized momentum equations for the cell centered velocities show that each velocity component at the cell center consists of two contributions, namely the convective and diffusive transport from neighboring control volumes and the pressure difference. Now the momentum interpolation procedure assumes a linear variation for the first contribution whereas no interpolation is needed for pressure which is available right at the nodes (at P and W for example for the face w in Fig. 1) where its value is required. Accordingly the west face velocities V_{1w} or V_{2w} with proper underrelaxation may be expressed as:

$$\begin{aligned} V_{iw} = \alpha_v[\overline{H^i_P + D^i_2(p_s - p_n) + D^i_3(p_b - p_t)} \\ + \overline{D^i_1}(p_W - p_P)] + (1+\alpha_v) V^0_{iw} \end{aligned} \tag{12}$$

where the expressions with overbars represent the linear average of the same quantities evaluated at the cell-centers P and W adjacent to the face w; V^0_{1w} is the value of V_{iw} at the previous iteration level.

In order to link the pressure and velocity via the continuity equation, the SIMPLE algorithm assumes that the velocity at any node is changed due to the change of pressure at the same node or at any of the six neighboring nodes. One further assumption in the present nonorthogonal formulation is that the change in face velocities (V_{iw} for example) is predominantly due to a change in pressure gradient along the main direction (along W-P for face w), whereas the changes due to the cross-direction gradients (along nw-sw and tw-bw for face w) are negligible. Using these assumptions, one may express the pressure-velocity correction relationship for the cell-center as:

$$V'_{iP} = \alpha_v[D^i_1(p'_w - p'_e) + D^i_2(p'_s - p'_n) + D^i_3(p'_b - p'_t)] \tag{13}$$

The corresponding relationship for the pressure-velocity linkage at the cell-face for V_{iw} is for example:

$$V'_{iw} = \alpha_v \overline{D_1^i}(p'_W - p'_P) \tag{14}$$

The continuity equation may now be expressed as follows:

$$C_e - C_w + C_n - C_s + C_t - C_b = 0 \tag{15}$$

where the mass-flux C_w for the west face, for example, may be written as:

$$C_w = \rho_w b^1_{iw}(V_{iw} + V'_{iw}) \tag{16}$$

Substitution of the face velocities V_{iw} etc. from equations similar to Eq. (12) and the corrections V'_{iw} etc. from equations similar to Eq. (14) leads to a system of linear equations for p', expressible in the form of the general equation (Eq. (8)). Cell-center pressures are then corrected by the amount $\alpha_p p'$ and corrections are applied to the three cell-centered velocities according to Eq. (13) and to all the eighteen cell-face velocity components on the six cell faces according to correction equation similar to Eq. (14).

Boundary Conditions. The most frequently encountered boundary conditions are (i) inlet, (ii) outlet, (iii) symmetry axes or planes, and (iv) rigid walls. At the inlet, usually the known boundary values are prescribed. For all the other kinds of boundaries, the links to the adjacent control volumes are disconnected by setting the convective fluxes, the normal as well as the cross-derivative fluxes to zero. At the outlet, symmetry planes or axes or at boundaries with specified flux, the boundary values need to be updated using the interior field values so that the required gradient condition is fulfilled. At the wall all the three velocity components are set to zero and further for the near-wall control volumes the wall shear stress vector is expressed as a function of the nodal velocity component parallel to the wall. The wall shear stress is again decomposed in the Cartesian components along V_1, V_2, and V_3, respectively, to be used as source terms in the corresponding momentum equations. The pressure on the boundary nodes is evaluated by linear extrapolation from its value at interior nodes.

Solution Algorithm. The strongly implicit procedure of Stone (1968) is used for solving the system of linear equations for each variable. For velocities and scalars where strong convective coefficients are present, one iterative sweep is sufficient to bring down the corresponding residue to a reasonably low level. On the other hand for pressure correction, the Poisson equation is of diffusion type for which the coefficient matrix is symmetric but without any convective fluxes in it so that convergence is relatively slow. Since good mass conservation is crucial at every outer iteration for an efficient and reliable solution using a segregated (uncoupled) approach, a given percentage of the initial residuum is prescribed as termination of the pressure correction sweep in each iteration cycle as recommended by Van Doormal and Raithby (1984). A combination of underrelaxation factor of 0.8 for momentum equations with a reduction to 10 percent of the initial residuum for continuity and the partial cancellation parameter of 0.9 for Stone's method have been found to work reasonably well for all the test problems.

3 Application Examples

The calculation procedure described in the foregoing sections was applied to four different three-dimensional laminar flows; the results are discussed in this section. Grid-dependence tests were performed for two of the flows, one without and one with separation. All calculations were carried out on the Siemens S600/20 vector computer of the University of Karlsruhe, and the computer program was vectorized to a major extent. The most important part not fully vectorized is the strongly implicit algorithm of Stone which consumed more than 50 percent of CPU-time in each of the calculations. Nevertheless, the total computational efficiency is very high, as can be seen from the computing times quoted for each example. The normalized residua are defined for the continuity equation as:

$$R_0 = \left[\sum_{ii} (C_e - C_w + C_n - C_s + C_t - C_b)^2_{ii} \right]^{1/2} / F_0 \tag{17}$$

and for the momentum equations for $\phi = V_i (i = 1, 2, 3)$ as:

$$R_i = \left[\sum_{ii} \left(\sum_{nb} A_{nb}\phi_{nb} + S_U - A_P\phi_P \right)^2_{ii} \right]^{1/2} / F_i,$$

$$(nb = E, W, N, S, T, B) \tag{18}$$

where ii runs over all the computational nodes and $F_i (i = 0, 1, 2, 3)$ is the corresponding mass or momentum flux at the inlet. The calculation results were declared converged when

$$\mathrm{MAX}(R_0, R_1, R_2, R_3) < 10^{-5} \tag{19}$$

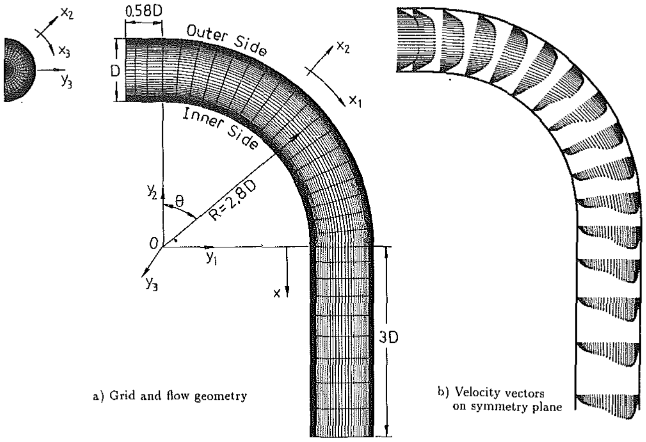

a) Grid and flow geometry

b) Velocity vectors on symmetry plane

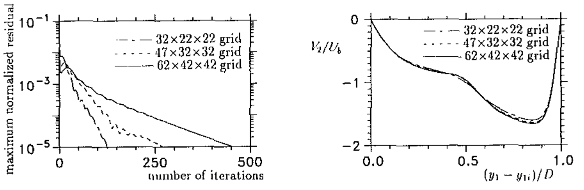

c) Convergence history

d) Streamwise velocity at x/D=1

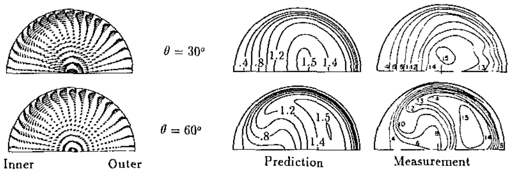

e) Calculated secondary flow velocity vectors

f) Comparison of streamwise velocity contours

Fig. 5 Laminar flow in a 90 deg bend of circular cross-section (Re = 1093)

3.1 Flow in a 90 deg Bend of Circular Cross Section. This is a strongly three-dimensional flow where the main flow in the streamwise direction along the pipe is associated with strong secondary currents in the pipe cross section, arising from the centrifugal forces due to the bend curvature. Figure 5(*a*) shows a grid on two different sections (the planes $x_3 = 0$ and $x_1 =$ constant) for the experimental situation studied by Enayet et al. (1982). The flow is at Reynolds number Re $= \rho U_b D/\mu = 1093$, where U_b is the bulk velocity. For symmetry reasons, the computation domain has been limited to the top half of the pipe only. Three grids with $32 \times 22 \times 22$ points (grid 1), $47 \times 32 \times 32$ points (grid 2) and $62 \times 42 \times 42$ points (grid 3) were used to test the grid-dependency of the solution. The CPU-times in minutes required were 0.24/1.4/4.9 for grid 1/grid 2/grid 3. Figure 5(*c*) shows the convergence history and Fig. 5(*d*) the profiles of streamwise velocity at $x/D = 1$. It can

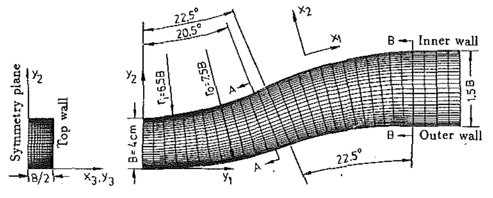

a) Grid and flow geometry

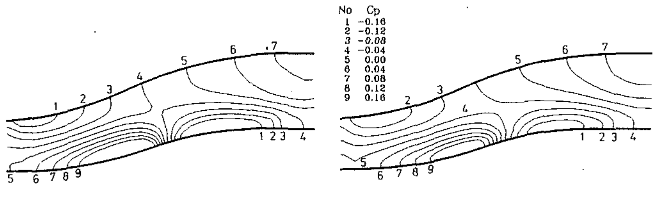

b) Isobars on the symmetry plane

c) Isobars on the top wall

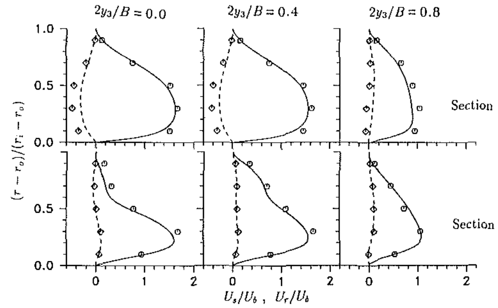

d) Streamwise and radial velocity profiles.
———: Calculated U_s/U_b, ○: Measured U_s/U_b,
- - - - -: Calculated U_r/U_b, ◇: Measured U_r/U_b.

Fig. 6 Laminar flow in an S-shaped diffuser (Re = 790)

be seen that the results on grid 2 and grid 3 are almost the same, and the velocity peak is only slightly underpredicted on grid 1. The results shown in Figs. 5(*b*), (*e*) and (*f*) were obtained on grid 3 and are virtually grid-independent. Figure 5(*b*) shows the calculated velocity vectors in the plane of symmetry. Along the bend, at each cross section, the velocity peak is observed to be shifted from the pipe axis toward the outer side of the bend. This shift may be explained by the fluid movement on a cross-plane from the inner to the outer side of the bend, caused by the lateral pressure difference arising from the bend-curvature effect. The development of the secondary flow pattern is demonstrated more clearly in Fig. 5(*e*), where the calculated flow vectors are shown at two different cross-planes. Figure 5(*f*) compares the present prediction with the measurements of Enayet et al. (1982) for the streamwise velocity contours, and a reasonably good agreement can be seen.

3.2 Flow in an S-Shaped Diffuser. Flow in an S-shaped diffuser with rectangular cross section was studied experimentally by Rojas et al. (1983) in a water model. The velocity field was measured by means of laser Doppler velocimetry. Cross-flow pressure gradients are produced in this flow due to the curvature of the duct which eventually lead to strong secondary motions. Figure 6(*a*) shows the diffuser geometry along with the 32×30×14 grid employed. The top and bottom walls are parallel whereas the side walls have S-shape and the cross section increases from 4cm×4cm at the inlet to 6cm×4cm at the outlet. For symmetry reasons, the calculation domain was restricted to only one (upper) half of the diffuser. The values of the streamwise and radial velocity components at the diffuser inlet were obtained by interpolation from experimental data. According to the experiment, the spanwise velocity component (in x_3 direction) was small at the inlet and was hence set to zero in the calculation. The flow Reynolds number based on the mean velocity U_b and hydraulic diameter at the inlet is 790. The calculation took 95 iterations and 0.16 minutes of CPU time. Figures 6(*b*) and 6(*c*) show the predicted isobars at the horizontal symmetry plane and at the top wall. In the first bend, the isobars exhibit clearly the expected pressure rise from the inner toward the outer side of the bend. In the second bend, the curvature changes direction and the isobars show the opposite behavior. A comparison of the isobars in Figs. 6(*b*) and 6(*c*) indicates that the nature of the pressure fields near the top wall and at the plane of symmetry are quite similar; but the pressure level is lower near the top wall. No separation was observed anywhere in the diffuser, neither in the experiments nor in the calculation. Fig. 6(*d*) compares predicted transverse profiles of streamwise and radial velocity with the measurements at three different spanwise stations (along y_3) for two different cross sections, viz., one at the transition from the first to the second bend and another at the end of the second bend. The agreement is good for the streamwise velocity; but the radial velocity is underpredicted by 25–30 percent in the transition region between first and second bend. This discrepancy may be due to the uncertainty and errors of interpolation in prescribing the inlet conditions from measured values at limited points only.

3.3 Flow Over a Surface-Mounted Hemisphere. This example was chosen mainly to demonstrate the capability of the method to calculate three-dimensional external flows. Figure 7(*a*) shows the computational domain and the H-O type 58×26×18 boundary-orthogonal grid used. The calculation was restricted to one half of the flow field due to symmetry. The oncoming flow was assumed uniform and parallel to the wall, and the surrounding free-surface boundary was placed at R = 7D where the flow condition was set to that of the oncoming flow. Since no information on this kind of flow was available to the authors, neither from experiments nor from previous calculations, a calculation was first carried out for the axisymmetric flow around a sphere, simply replacing the wall by a symmetry plane at $y_2 = 0$. The predicted drag coefficient of the sphere is shown and compared with the experimental data taken from Batchelor (1967) in Fig. 7(*b*) for a range of Reynolds numbers Re = $\rho U_\infty D/\mu$ at which flow separation occurs. The agreement between predictions and experiments can be seen to be good. The calculation was then carried out for the flow around a surface-mounted hemisphere at a Reynolds number Re = 100. Figure 7(*c*) shows the predicted velocity vectors at two different x_3 planes, one at the symmetry plane ($\theta = 0°$) and the other near the wall (θ = 84 deg). The predicted flow pattern seems to be physically realistic, but in the absence of any experimental information the calculation confirms only in a qualitative sense the correctness of the solution. 125 iterations and 0.3 minutes of CPU-time were required for this calculation.

3.4 Flow Around a Circular Cylinder in a Channel. The flow around a cylinder between channel walls is of great practical importance, e.g., in plate-fin heat exchangers with cross flow around rows of cylindrical obstructions placed between top and bottom plates. Figure 8(*a*) shows the grid and flow geometry used for this case which was studied numerically also by Kiehm et al. (1986). The calculations of Kiehm et al. covering a wider parameter range have shown that no periodicity or vortex shedding occurs in this kind of flow at a Reynolds number of 67, a channel-width-to-cylinder-diameter ratio of 3 and a channel ratio of 0.36. The computation domain is limited to one quarter of the total flow domain assuming a horizontal symmetry plane at half height of the cylinder and a vertical symmetry plane passing through the diametral plane of the cylinder. A fully-developed parabolic velocity profile is

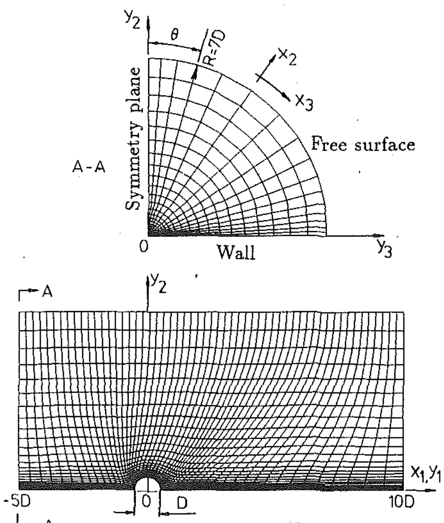

a) Grid and flow geometry

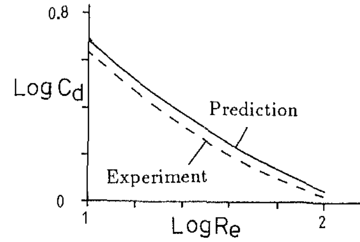

b) Comparison of drag coefficient on a sphere

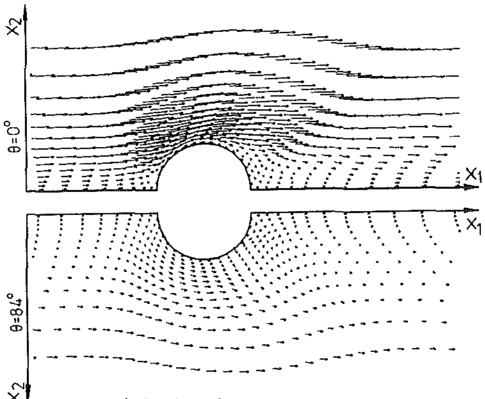

c) Predicted velocity vectors

Fig. 7 Laminar flow over a surface-mounted hemisphere (Re = 100)

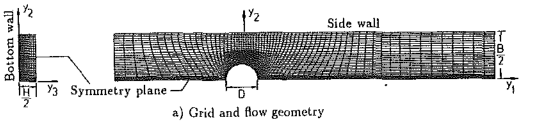

a) Grid and flow geometry

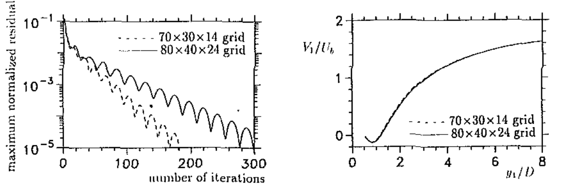

b) Convergence history

c) Centerline velocity behind the cylinder

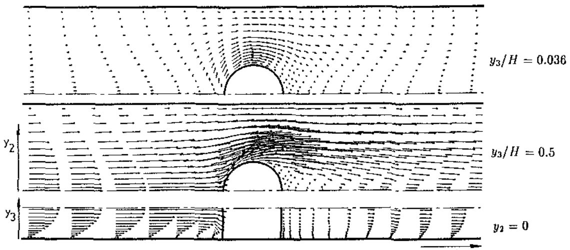

d) Calculated velocity vectors on three planes

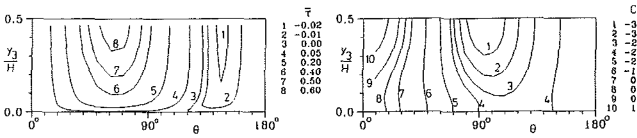

e) Calculated contours of horizontal wall shear stress component ($\bar{\tau} = \tau_{wall}/\rho U_b^2$) on cylinder surface

f) Calculated isobars ($C_p = (p - p_\infty)/\rho U_b^2$) on cylinder surface

Fig. 8 Laminar flow around a circular cylinder in a channel (Re = 67)

prescribed at the channel inlet (4D upstream of the cylinder). The grid dependence of the solution was examined by using two grids with 70×30×14 points (grid 1) and 80×40×24 points (grid 2). The CPU-times required for grid 1 and grid 2 were 0.5 and 1.7 minutes, respectively. Figure 8(*b*) shows the convergence history. The periodic convergence behavior indicates a tendency to unsteadiness of the solution, but such low residuals are reached that the final solution is virtually steady at this Reynolds number. Figure 8(*c*) shows the centerline velocity behind the cylinder and it can be seen that the results on both grids are nearly the same. In the following, the results obtained on grid 1 are presented. Figure 8(*d*) shows the calculated velocity vectors on three planes. Close to the bottom floor ($y_3/H = 0.036$) the velocity vectors near the front stagnation point clearly indicate separation of the oncoming floor boundary layer. This separation gives rise to the horse-shoe vortex. Further, the flow separates at $\theta = 132$ deg, and behind the cylinder a vertical vortex is formed which extends to about 0.7D from the rear stagnation point. At the top symmetry plane ($y_3/H = 0.5$), the length of the recirculation region behind the cylinder is 0.72D, which is about the same as in Kiehm et al.'s calculation. The formation of a horse-shoe vortex near the front stagnation point is quite clear from the figure. In the wake region behind the cylinder the velocity vectors show an upward motion from the bottom wall toward the symmetry plane. A similar phenomenon was also observed by Kiehm et al. in their calculations and was designated as "screw-like helical motion" inside the separation region bringing in low-energy fluid from bottom to top. The contours of constant wall shear stress (horizontal component) on the cylinder surface are shown in Fig. 8(*e*). The contours indicate a maximum positive wall shear stress near $\theta = 65$ deg all along the height whose value depends on the inflow velocity at the height considered. $\bar{\tau} = 0$ indicates separation and the figure shows that the initiation of separation is almost independent of the cylinder height (at $\theta = 132$ deg) except in a small region near the bottom wall where separation starts further upstream ($\theta = 120$ deg) due to the presence of the horse-shoe vortex. Figure 8(*f*) shows the contours of constant pressure, nondimensionalized by the dynamic head ρU_b^2, where U_b = average flow velocity at inlet. The pressure field always has a positive peak at the front stagnation point. The maximum value varies however from 1.4 near the top to 0.4 near the bottom, where the separation of the oncoming boundary layer causes flow reversal and a consequent reduction in local pressure. Similar to 2-D free flow around a circular cylinder, the negative peak of pressure occurs at $\theta = 95$ deg for the top symmetry plane. The separated region ($120° < \theta < 180$ deg) at any height has however little variation of pressure, as indicated by the magnitude and spacing of the isobars. The calculation shows that the present procedure is able to capture all the gross features of this complex three-dimensional flow. Further validation for accuracy, however, needs the comparison with reliable experimental results.

4 Conclusions

A general finite-volume method has been described for calculating incompressible 3-D flows with complex boundaries. The application examples have shown that the method allows an efficient calculation of a wide range of flows with CPU-times on a fast vector computer below half a minute on a grid with typically 28000 grid points. The method can also be used to calculate turbulent flows when equipped with a suitable turbulence model. With only a slight extension, the method can be modified to allow the calculation of unsteady flow, and work in this area is under way. Although the computing times have been reduced already considerably through vectorizing the computer program, it is expected that further reduction can be achieved by incorporating the multigrid method, especially when finer grids are used. This method has been implemented already in the three-dimensional code and the multigrid version of the code was tested extensively for 2-D flows and also for a few 3-D flows (Orth, 1991). Work is in progress on further testing of the implemented multigrid method for three-dimensional complex problems, including calculations for turbulent flows with the k-ϵ turbulence model.

Acknowledgments

The work described in the paper was sponsored by the Deutsche Forschungsgemeinschaft and by the Volkswagen Foundation. The authors are grateful to Dr. Y. Kawahara for his suggestions on the partial vectorization of the Stone solver.

References

Batchelor, G. K., 1967, *An Introduction to Fluid Dynamics*, Cambridge University Press, p. 234.

Enayet, M., Gibson, M., Taylor, A., and Yianneskis, M., 1982, "Laser Doppler Measurements of Laminar and Turbulent Flow in a Pipe Bend," *International Journal of Heat and Fluid Flow*, Vol. 3, pp. 213-220.

Gaskell, P. H., and Lau, A. K. C., 1988, "Curvature-Compensated Convective Transport: SMART, A New Boundedness-Preserving Transport Algorithm," *International Journal for Numerical Methods in Fluids*, Vol. 8, pp. 617-641.

Harlow, F. H., and Welch, J. E., 1965, "Numerical Calculation of Time Dependent Viscous Incompressible Flow of Fluid with Free Surface," *The Physics of Fluids*, Vol. 8, pp. 2182-2189.

Kiehm, P., Mitra, N. K., and Fiebig, M., 1986, "Numerical Investigation of Two- and Three-dimensional Confined Wakes Behind a Circular Cylinder in Channel," AIAA Paper 86-0035.

Kordulla, W., and Vinokur, M., 1983, "Efficient Computation of Volume in Flow Predictions," *AIAA Journal*, Vol. 21, pp. 917-918.

Leonard, B. P., 1987, "Locally Modified QUICK Scheme for Highly Convective 2-D and 3-D Flows," *Proceedings, 5th International Conference on Numerical Methods in Laminar and Turbulent Flow*, Montreal, pp. 35-47.

Leonard, B. P., 1988, "Simple High-Accuracy Resolution Program for Convective Modelling of Discontinuities," *International Journal for Numerical Methods in Fluids*, Vol. 8, pp 1291-1318.

Majumdar, S., 1986, "Development of a Finite-Volume Procedure for Prediction of Fluid Flow Problems with Complex Irregular Boundaries," Report SFB 210/T/29, University of Karlsruhe.

Majumdar, S., 1988, "Role of Underrelaxation in Employing Momentum Interpolation Practice for Calculation of Flow with Non-Staggered Grids," *Numerical Heat Transfer*, Vol. 13, pp. 125-132.

Naar, M., and Schönung, B., 1986, "Numerische Gittererzeugung bei Vorgabe von Randwinkeln und Randmaschenweiten," Report No. 644, Institute for Hydrodynamics, University of Karlsruhe.

Orth, A., 1991, "Mehrgittermethode zur Berechnung inkompressliber, stationärer Strömungen mit krummlinigen Berandungen," Doctoral dissertation, University of Karlsruhe.

Patankar, S. V., and Spalding, D. B., 1972, "A Calculation Procedure for Heat, Mass and Momentum Transfer in Three-Dimensional Parabolic Flows," *International Journal of Heat and Mass Transfer*, Vol. 15, pp. 1778-1806.

Rhie, C. M., and Chow, W. L., 1983, "A Numerical Study of the Turbulent Flow Past an Isolated Airfoil with Trailing Edge Separation," *AIAA Journal*, Vol. 21, pp. 1525-1532.

Rodi, W., Majumdar, S., and Schönung, B., 1989, "Finite-Volume Method for Two-Dimensional Incompressible Flows With Complex Boundaries," *Computer Methods in Applied Mechanics and Engineering*, Vol. 75, pp. 369-392.

Rojas, J., Whitelaw, J. H., and Yianneskis, M., 1983, "Developing Flow in S-Shaped Diffuser," Report FS/83/12, Department of Mechanical Engineering, Imperial College of Science and Technology, London.

Sorenson, R. L., 1980, "A Computer Program to Generate Two-Dimensional Grids About Airfoils and Other Shapes by the Use of Poisson Equations," NASA TN81198.

Stone, H. L., 1968, "Iterative Solution of Implicit Approximations of Multidimensional Partial Differential Equations," *SIAM Journal on Numerical Analysis*, Vol. 5, pp. 530-558.

Van Doorman, J. P., and Raithby, G. D., 1984, "Enhancements of the SIMPLE Method for Predicting Incompressible Fluid Flows," *Numerical Heat Transfer*, Vol. 7, pp. 147-163.

Zhu, J., Rodi, W., and Schönung, B., 1988, "Algebraic Generation of Smooth Grids," *Proceedings, 2nd International Conference on Numerical Grid Generation in Computational Fluid Dynamics*, S. Sengupta et al., eds., Pineridge Press, pp. 217-226.

Zhu, J., Rodi, W., and Schönung, B., 1989, "A Fast Method for Generating Smooth Grids," *Proceedings, 6th International Conference on Numerical Methods in Laminar and Turbulent Flow*, Swansea, pp. 1639-1649.

Zhu, J., and Rodi, W., 1991, "A Low Dispersion and Bounded Convection Scheme," *Computer Methods in Applied Mechanics and Engineering*, Vol. 92, pp. 87-96.

J. A. Schetz
W. Martin Johnson Professor and
Department Head,
Department of Aerospace and
Ocean Engineering,
Fellow ASME

E. Hytopoulos
Graduate Student,
Aerospace and Ocean
Engineering Department.

M. Gunzburger
Professor,
Department of Mathematics.

Virginia Polytechnic Institute and
State University,
Blacksburg, VA 24061

Numerical Solution of the Incompressible Boundary-Layer Equations Using the Finite Element Method

A new approach to the solution of the two-dimensional, incompressible, boundary-layer equations based on the Finite Element Method in both directions is investigated. Earlier Finite Element Method treatments of parabolic boundary-layer problems used finite differences in the streamwise direction, thus sacrificing some of the possible advantages of the Finite Element Method. The accuracy and computational efficiency of different interpolation functions for the velocity field are evaluated. A new element especially designed for boundary layer flows is introduced. The effect that the treatment of the continuity equation has on the stability and accuracy of the numerical results is also discussed. The parabolic nature of the equations is exploited in order to reduce the memory requirements. The solution is obtained for one line at a time, thus only two levels are required to be stored at any time. Efficient solvers for tridiagonal and pentadiagonal forms are used for solving the resulting matrix problem. Numerical predictions are compared to analytical and experimental results for laminar and turbulent flows, with and without pressure gradients. The comparisons show very good agreement. Although most of the cases were tested on a mainframe, the low requirements in CPU time and memory storage allows the implementation of the method on a conventional PC.

Introduction

The present paper is concerned with the application of the Finite Element Method (FEM) to the formulation and solution of the boundary layer equations governing the flow of incompressible fluids in two dimensions. Traditionally, numerical solutions for this set of equations have been obtained using the Finite Difference Method (FDM) and integral methods (Schetz, 1984). In the finite difference approach, the continuous problem domain is "discretized" so that dependent variables are considered to exist only at discrete points. The derivatives are approximated by difference quotients resulting in an algebraic representation of the partial differential equations. For the flowfields solved by a FDM method, the accuracy of the solution depends to a large extent on the grid resolution, and a high number of nodes can be required to accurately describe regions of large gradients. Integral methods require prescribed velocity profiles and empirical relations in addition to the basic conservation laws.

In FEM, the region is subdivided into a number of small regions called finite elements. The dependent variables are interpolated within each element by functions of compatible order. Using these approximations in the field equations, we introduce residuals or errors. The general method seeks to reduce these errors to zero in a weighted sense, thus the partial differential equations describing the problem in the region as a whole are replaced by algebraic equations in each element. A description of the basic FEM approach can be found in Fletcher (1984).

The earliest attempts to treat the boundary layer equations with what might be broadly called Finite Element Methods date back almost 30 years (Schetz, 1963 and 1966 and Schetz and Jannone, 1965). With the limited computer power available at that time, it was necessary to use very large "elements" of the order of one-half the boundary-layer thickness. To achieve acceptable accuracy with such large elements, one needs to use very good basis or trial functions. The functions chosen were developed from solutions of the linearized version of the boundary layer equations for the problem of interest. These functions were then distorted by adding factors to the argument of the solutions. The values of these stretching factors were found by enforcing the simplest type of variational constraint, namely Collocation (i.e., using a Dirac Delta function as the weight function). The final "numerical" solution obtained had very good qualitative behavior and acceptable quantitative accuracy, e.g., about 5 percent on skin friction.

In more recent times, the application of FEM to viscous flow problems has concentrated on the Navier-Stokes equa-

---

Contributed by the Fluids Engineering Division for publication in the JOURNAL OF FLUIDS ENGINEERING. Manuscript received by the Fluids Engineering Division February 20, 1992. Associate Technical Editor: D. M. Bushnell.

tions (Oden and Wellford, 1972). Of course, small element sizes are now workable, and this means that simpler and more general basis functions (often simply linear or quadratic) can be used. Also, more powerful variational constraints than Collocation (or more general weight functions) can be applied. The elliptic character of the Navier-Stokes problem requires the resulting system of equations to be solved simultaneously for the velocities and the pressure. The continuity equation is treated as a constraint.

Baker and Manhardt (1978) have applied FEM to the 2-D boundary-layer equations in one direction and 2-D parabolized Navier-Stokes equations, transforming the system of partial differential equations to a first-order, ordinary differential equation system. Solution of this system is obtained using a finite difference numerical integration algorithm. This sacrifices some of the advantages of the FEM. Dorodnitsyn (1960) developed a method for the boundary layer equations transformed such that the usual dependent variables (U, V) are replaced by essentially the local shear as a function of (x, U). This required the use of special interpolation functions. The resulting system of ordinary differential equations was solved by a Crank-Nicolson FDM. Fletcher and Fleet (1982) have also applied this method. In this paper, a full FEM treatment is considered for approximating solutions of the boundary-layer equations. The dependent variables are interpolated within each element, and the Galerkin method is applied in order to reduce the interpolation error to zero in a weighted sense. This procedure transforms the governing equations to a set of algebraic equations in each element. The parabolic nature of the problem allows the solution of the algebraic system for one column of elements at a time. This leads to tridiagonal or pentadiagonal systems of linear equations, the solution of which can be obtained using very efficient algorithms. This solves one of the biggest problems in using FEM in general, the simultaneous solution of a large number of equations, which is generally associated with high computational cost. The continuity equation cannot be treated as a constraint anymore. It is now an ordinary differential equation, numerical integration of which yields the required solution at the nodes. Also, the pressure is not an unknown as in FEM treatment of the Navier-Stokes equations.

The FEM was chosen for three main reasons. First, this method has been successfully applied before to the full Navier-Stokes equations. It is efficient and robust. Second, the purely "local" approximations of the phenomena under consideration effectively frees the analyst from traditional difficulties associated with irregular geometries, multi-connected domains, and mixed boundary conditions. Third, applications are firmly rooted in the physics of the problem, and for a given accuracy, the resulting equations are better conditioned than those obtained by finite difference approximations of the governing differential equations (Oden and Wellford, 1972).

The new method is applied to a number of classical problems of laminar and turbulent boundary layer flows. The accuracy of the method as compared to theoretical and experimental results is investigated. Results concerning the effect of aspect ratio of the elements, the type of interpolation functions and the different rules used for the numerical integration of the continuity equation on the accuracy of the solution are presented. The efficiency of the method in terms of CPU time and storage requirements is also discussed.

Equations of Motion

For high Reynolds number, attached flow, the boundary layer assumptions lead to the following expressions for the two momentum equations and the continuity Eq. (1):

$$U\frac{\partial U}{\partial x}+V\frac{\partial U}{\partial y}=-\frac{1}{\rho}\frac{dP}{dx}+\nu\frac{\partial^2 U}{\partial y^2}-\frac{\partial(\overline{uv})}{\partial y} \tag{1}$$

$$\frac{\partial P}{\partial y}\approx 0 \tag{2}$$

$$\frac{\partial U}{\partial x}+\frac{\partial V}{\partial y}=0 \tag{3}$$

Turbulence Modeling

In the case of a turbulent flow, the set of equations is not adequate for solving the problem, since the last term in Eq. (1) is an additional unknown. It was decided that simple algebraic models were adequate for this paper, since the main thrust is on numerical methods. Thus, an eddy viscosity and a mixing length model have been used. In the first case, the turbulent stress is expressed as:

$$\tau_T=\mu_T\frac{\partial U}{\partial y} \tag{4}$$

where:

$$\mu_T=\kappa\rho\nu\left[y^+-y_a^+\tanh\left(\frac{y^+}{y_a^+}\right)\right] \tag{5}$$

for the inner region. In the second case, the turbulent for the inner region stress is equal to

$$\tau_T=\rho l_m^2\left|\frac{\partial U}{\partial y}\right|\frac{\partial U}{\partial y} \tag{6}$$

where l_m is equal to $l_m = \kappa y$ for the logarithmic region and given from the van Driest model for the region near the wall. For the outer region, the Clauser model has been used with both approaches. The turbulent viscosity is calculated as:

$$\mu_T=\min(\mu_T^{\text{inner}},\ \mu_T^{\text{outer}}) \tag{7}$$

Finite Element Method

The object of the FEM is to reduce the continuous problem of the governing equations to a discrete problem described by a system of algebraic equations. We subdivide the continuous region of interest into a number of simply shaped regions called elements. Within each element, the dependent variables, here the components of velocity (U, V), are interpolated by functions of compatible order in terms of values to be determined at a set of nodal points. Specifically, let $U(x, y)$ and $V(x, y)$ denote the approximations of the two components of velocity over an element, u_i, v_i the values of velocity components at node i of the element, and ϕ_i the interpolation function corresponding to that node over an element. Then, the finite approximations over the element can be written in the following form:

$$U(x, y)=\sum_{i=1}^{N}u_i\phi_i(x, y) \tag{8}$$

$$V(x, y)=\sum_{i=1}^{N}v_i\phi_i(x, y) \tag{9}$$

Introducing these approximations in the momentum equation, one gets a set of equations:

$$f_1(\phi, u_i)=R \tag{9}$$

where R is a residual resulting from the use of the approximations.

The Galerkin Method of Weighted Residuals seeks to reduce these errors to zero, in a weighted sense, by making the residuals orthogonal to the interpolation functions of the flow domain. The Galerkin method, when applied to the momentum equation, leads to the following matrix problem:

$$[K][u]=[F] \tag{10}$$

where the stiffness matrix, K, and the force vector, F, over each element are:

$$K_{ij}^{e}=\int_{\Omega e}\left.\tilde{U}\,\frac{\partial\phi_j}{\partial x}\,\phi_i+\tilde{V}\,\frac{\partial\phi_j}{\partial y}\,\phi_i+(\nu+\nu_T)\,\frac{\partial\phi_j}{\partial y}\,\frac{\partial\phi_i}{\partial y}\right)dxdy \qquad (11)$$

$$F_i^{e}=-\int_{\Omega_e}\frac{1}{\rho}\,\frac{dP}{dx}\,\phi_i dxdy+\int_{\Gamma_e}(\nu+\nu_T)\,\frac{\partial U}{\partial y}\,\phi_i\eta_y ds \qquad (12)$$

and $\tilde{U}$ and $\tilde{V}$ are evaluated using the most recent nodal values. The last term in Eqs. (11) and (12) is the result of the application of the Divergence Theorem on the viscous term. Normally, two iterations are sufficient to determine converged values for U and V.

The general FEM method would require the continuity equation to be integrated using weight functions that are one degree lower than the interpolation functions. When linear polynomials are used as interpolation functions, a constant function should be used as the weight function. This approach leads to the discrete integral form of the continuity equation. The use of this approach, leads to V components that change sign from one x location to the next. A von Neumann analysis of the discrete continuity equation leads to an amplification factor equal to -1, which explains the numerical behavior. The problem lies in the treatment of the continuity equation. The character of this equation is now changed with the boundary layer assumptions from that of a constraint as with the Navier-Stokes equations to that of an initial value problem. Thus, the continuity equation should be integrated along the vertical direction, starting from the known value for the V-component on the lower boundary after the x-momentum equation is solved for the U-nodal values. The choice of the integration rule used for the continuity equation depends on the accuracy of the elements used.

Two elements have been used in this work. The first one is the 4 node quadrilateral element, with bilinear interpolation of the velocity (see Fig. 1). The second element attempts to exploit the physics of the problem. Since in a boundary layer the gradients in the y-direction are much higher compared to those in the x-direction, the new element incorporates quadratic interpolation functions in the y-direction and linear functions in the x-direction. The 2-D shape functions associated with each node are given as the tensor product of the one-dimensional linear and quadratic interpolation functions. The new element, which will be called QLBL consists of 6 nodes and is also shown in Fig. 1. Some details of these two elements are given in the Appendix.

The numerical evaluation of the integrals in Eqs. (11) and (12) is performed using a quadrature rule compatible with the order of the elements used. For the linear element, a 2 × 2 quadrature integrates the expressions exactly. In the case of the QLBL element, a 2 × 3 quadrature is used. The K-matrix for each element has dimensions 4 × 4 for the linear element and 6 × 6 for the QLBL element. The F-vector has 4 and 6 elements, respectively. The values of the nodal unknowns 1 and 4 for the linear element and 1, 5 and 6 for the QLBL element (see Fig. 1) are known from the solution of the previous column, and they can be applied as boundary conditions at the element level. Modification of the element matrix leads to a 2 × 2 matrix for the linear element and a 3 × 3 matrix for the QLBL element. Solution for the column of elements requires the assembly of the element stiffness matrix into a global matrix and assembly of the element force vector into a global force vector. The assembly procedure leads to a tridiagonal system of equations for the nodes on the downstream side of the column in the case of the linear elements, and to a pentadiagonal system in the case of the QLBL elements. The Thomas algorithm is used for the solution of the tridiagonal system. The pentadiagonal system is reduced to upper diagonal form by Gaussian Elimination and the solved by back substation.

An initial profile for the U and V components of the velocity is required at the first station. On the lower boundary of the domain, the no-slip, no-penetration condition is applied. For the upper boundary, the formulation allows the application of either natural (stresses) or essential (velocities) boundary conditions. Since the solution of the boundary layer equations should be matched with the inviscid solution, $U_e(x)$ is used on the top boundary. The pressure gradient is also imposed from the inviscid solution and is considered constant across the boundary layer. The term appearing on the righthand side of Eq. (12) is thus known and is treated as a simple forcing function.

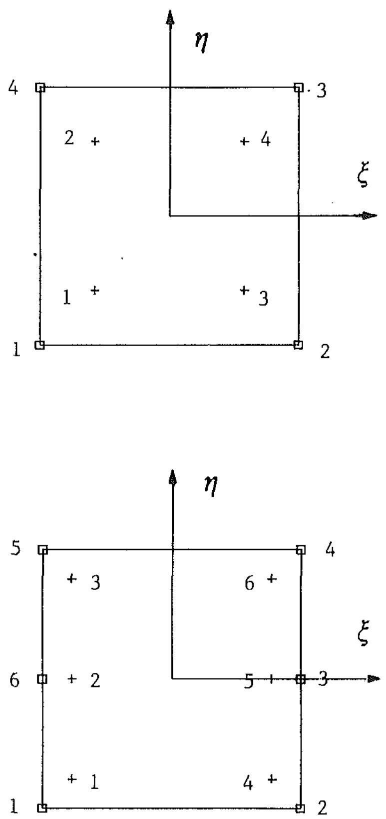

Fig. 1 Linear and QLBL master elements. Numbering conventions for the nodal and quadrature points.

Test Cases and Discussion

To validate the approach presented in this paper, four benchmark problems have been solved. These are: (*a*) the laminar flow over a flat plate with zero pressure gradient (Blasius problem), (*b*) laminar flow with adverse pressure gradient (Howarth's problem, 1938), (*c*) the turbulent flow over a flat plate with zero pressure gradient, and (*d*) the turbulent flow over a flat plate with increasing adverse pressure gradient (Samuel and Joubert Flow, 1974). The behavior of the method will be discussed separately for each case.

Laminar Flow Over a Flat Plate. The Blasius profile at $x/L = 0.0625$ with $\delta/L = 0.02$ was used as an initial condition. The results are shown in Figs. 2–4, for linear elements. Similar results have been obtained for the QLBL elements. Figures 2 and 3 show a comparison between the initial and final nondimensional velocity profiles for the U and V components. Since the solution is self-similar, we expect no changes in the nondimensional profiles. Figure 4 shows the skin friction coefficient. The agreement is excellent.

This problem is also an ideal case for checking the convergence characteristics of the method, since an "exact" numerical solution exists. The error is measured in the L^2 norm, which is defined as:

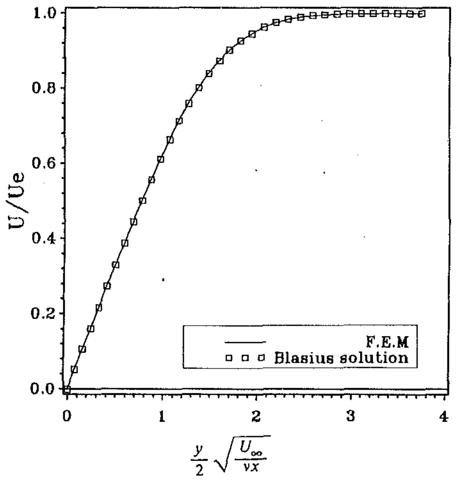

Fig. 2 U-profiles for laminar flow over a flat plate

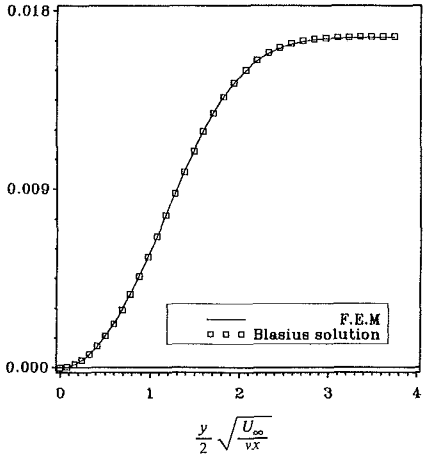

Fig. 3 V-profiles for laminar flow over a flat plate

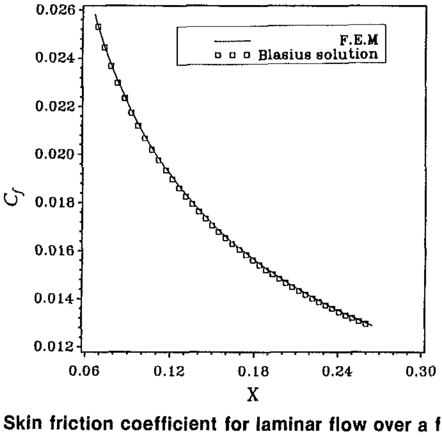

Fig. 4 Skin friction coefficient for laminar flow over a flat plate

$$\| U_{\text{ex}} - U_{\text{num}} \| = \left[\int_{\Omega} (U_{\text{ex}} - U_{\text{num}})^2 d\Omega \right]^{1/2} \tag{13}$$

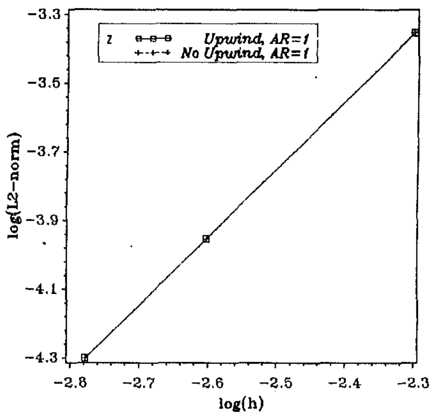

Fig. 5 L-2 norm versus characteristic dimension of element. Uniform grid, linear element for Blasius problem.

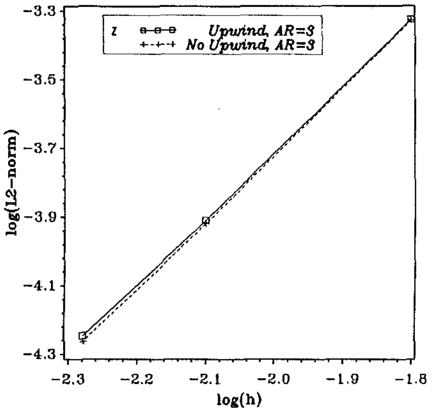

Fig. 6 L-2 norm versus characteristic dimension of element. Linear elements, AR = 3 for Blasius problem.

Figure 5 shows the convergence rate for the case of linear elements of aspect ratio (dx/dy) equal to 1. Two approaches have been used for evaluating $\tilde{U}$ in Eq. (11), and they are compared to each other. The first uses all the nodal values; the second is equivalent to upwinding, since only nodes 1 and 4 (for the linear element) and 1, 5, 6 (for the QLBL element) are used for interpolating $\tilde{U}$ within each element. The advantage of the latter approach is that there is no need for iterative solution; $\tilde{U}$ is evaluated using known values from the last station, and thus the solution time is greatly reduced. Without upwinding, two or three iterations are required at each station to obtain a convergent solution. The results are almost identical. Since it is known that upwinding reduces the accuracy of FDM schemes, it should be assumed that this result occurs mainly due to the small gradients in the streamwise direction. The convergence rate agrees with the theoretical result; the global error behaves like h^2. Figure 6 shows the same comparison for an aspect ratio of 3. Again, the results are very close. The CPU time per node was $\approx 2.3 \times 10^{-4}$ s on an IBM 3090.

Convergence rate data for the QLBL element is given in Fig. 7. For aspect ratio equal to 1, the convergence rate is ≈ 2.95 for no upwinding. This result approaches the theoretical result for quadratic elements. Thus, this element taking advantage of the physics governing the problem is able to produce a high convergence rate. Upwinding hurts the accuracy of the method for this element. Also, the aspect ratio affects the accuracy, and it is expected that for high aspect ratio, the convergence will be quadratic instead of cubic.

The CPU time per node was $\approx 3.35 \times 10^{-4}$. But, the QLBL element was found to be on average, 11 to 13 times faster than the linear element for the same level of accuracy.

Laminar Flow With Adverse Pressure Gradient. The solution to the problem of the flow with external velocity U_e/U_∞ = 1-0.125 (x/L) has been given by Howarth (1938), in the form of a series. The flow separates somewhere near x/L = 0.96. Unfortunately, the series converges slowly in the neigh-

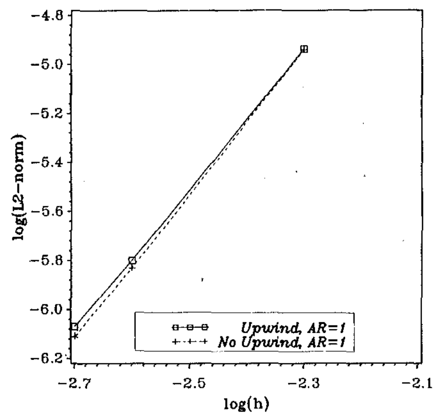

Fig. 7 **L-2 norm versus characteristic dimension of element. Uniform grid, QLBL elements for Blasius problem.**

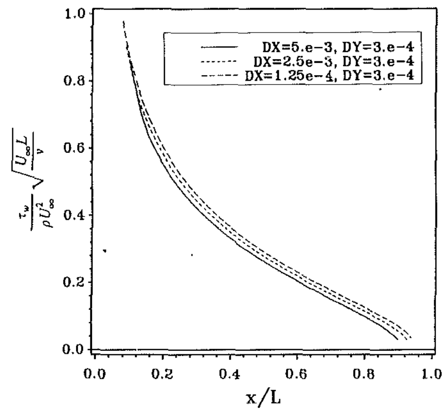

Fig. 10 **Effect of the aspect ratio.** ***dx*** **= varying,** ***dy*** **= constant for the Howarth problem.**

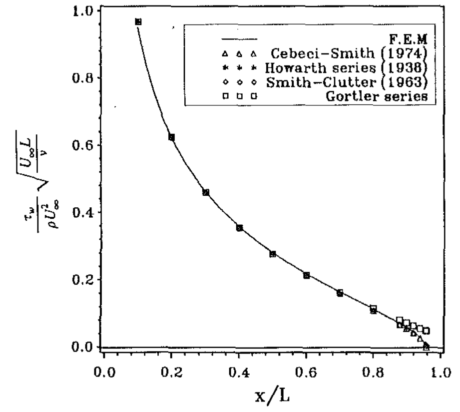

Fig. 8 Nondimensional wall stress for the Howarth problem

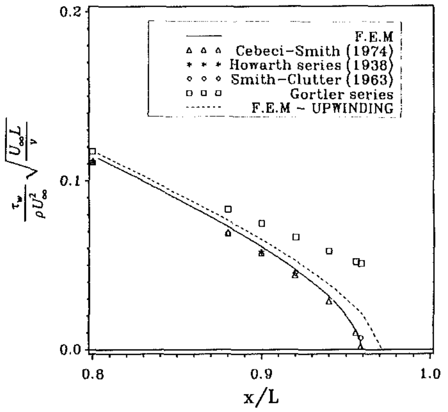

Fig. 11 Nondimensional wall stress for the Hoarth problem. Upwinding versus *non-upwinding.*

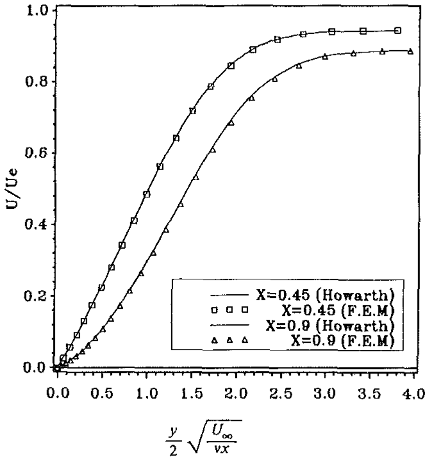

Fig. 9 U-velocity profile for the Howarth problem

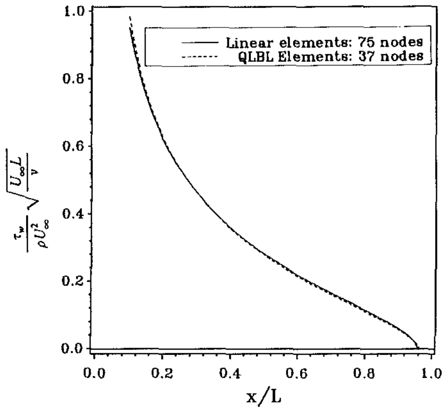

Fig. 12 Nondimensional wall stress for the Howarth problem. Linear versus QLBL elements.

borhood of separation, and sufficient terms have not been obtained to give the point of separation with great accuracy. For our purposes here, the "exact" solution is given by the first 9 terms as in the original paper by Howarth. This problem has also been treated with modern FDM methods by Smith and Clutter (1963) and Cebeci and Smith (1974) and others.

The initial profile was taken as constant velocity, equal to 1.0. The results obtained using linear elements are presented in Figs. 8-12. Figure 8 shows a comparison between the analytic and numerical solution for the non-dimensional wall stress. The comparison is good, and a difference exists only near the separation point, which might be expected since the location is not well established analytically. Numerical values for the current FEM results are compared with the Howarth values, two sets of FDM results and a solution using Görtler Series in Table 1. Our results compare favorably with other published results for the problem, even though our solution was obtained in the (U, V), (x, y) plane with no special treatment of the leading edge singularity. The uncertainty in the results from all the methods increases near separation. Figure 9 compares the velocity profiles for (x/L) = equal to 0.45 and 0.90. The agreement is again good. Figure 10 shows the effect of the aspect ratio of the elements, when dy is kept constant and only

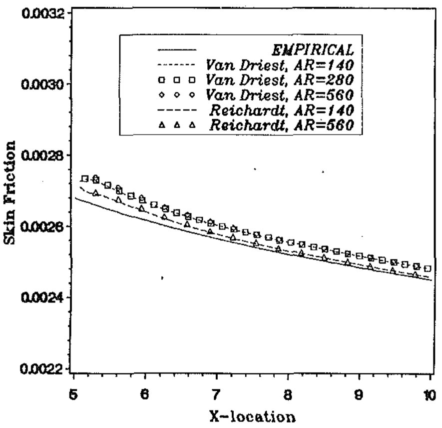

Fig. 13 Skin friction for turbulent flow with zero pressure gradient

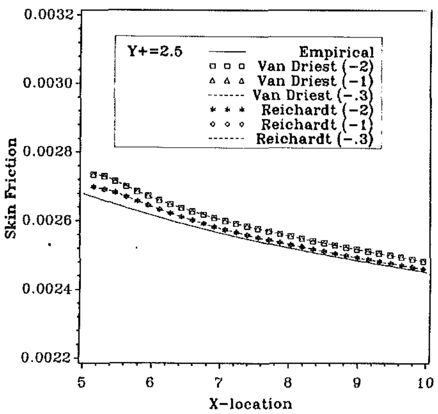

Fig. 15 Influence of the maximum allowable relative error on the global accuracy of the solution

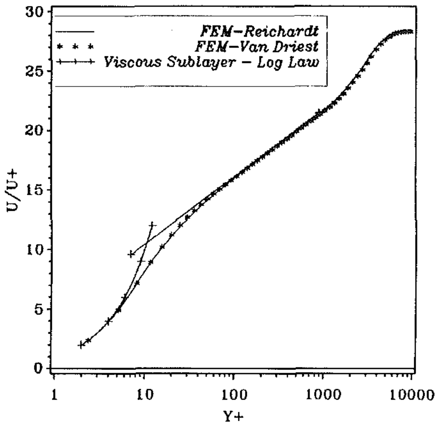

Fig. 14 Comparison between the final U-velocity profiles for turbulent flow with zero pressure gradient and the log-law of the wall

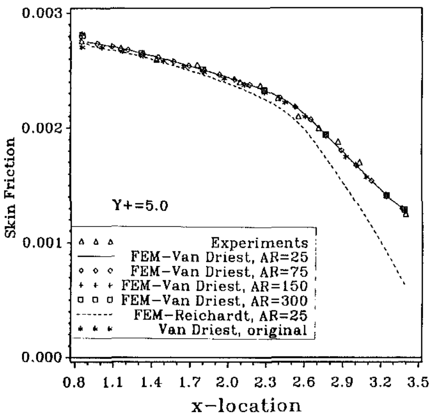

Fig. 16 Skin friction coefficient for turbulent flow with adverse pressure gradient. Numerical versus experimental data from Samuel and Joubert.

dx is allowed to vary. The prediction deteriorates as the aspect ratio increases.

The effect of upwinding is shown in Fig. 11. The solution obtained using upwinding predicts separation later than the solution without upwinding. The consensus of all the previous workers is $x/L \approx 0.96$ as the point of separation. This prediction is closer to the result obtained using the method with no upwinding.

A comparison between linear and QLBL elements is shown in Fig. 12. The comparison indicates that the use of the QLBL element reduces the number of points required across the boundary layer by more than half to obtain equivalent accuracy. The CPU time required for the solution, keeping the number of stations the same in both cases, is reduced by 35 percent.

Turbulent Flow Over a Flat Plate. The first case concerning turbulent flows, was the flow over a flat plate with zero pressure gradient. The initial profile was constructed using Cole's Law of the Wake. The results for the variation of the skin friction coefficient in the streamwise direction are given in Fig. 13. The difference observed between the empirical/integral method and numerical prediction is misleading. The actual percentage error is between 0.5 and 2.5 percent, for the case where the first node is located at y^+ equal to 2.5. The same figure indicates that the Reichardt model gives predictions which are closer to those of the integral method. The aspect ratio of the elements is seen to have a very small effect on the accuracy of the method. This is a desirable feature, since it reduces the CPU time required for obtaining accurate results. The velocity profile predicted at the last station ($x = 10.0$) is compared to the universal profiles for the viscous sublayer and the log region in Fig. 14. The agreement is very good. The difference observed in the outer part of the log region can be attributed to the small difference in the prediction of the skin friction. The solution has been obtained using a total of 60 points in the direction normal to the wall, and the initial profile is described by 40 points.

The maximum relative error allowed at each location affects the number of iterations required and thus the solution time. Figure 15 shows the effect of this parameter on the accuracy. The numbers in parentheses represent the log of the maximum allowable error. The figure shows that when the solution at the previous x-station is used as a first guess, a very low criterion for convergence is adequate for high overall accuracy.

Turbulent Flow With Adverse Pressure Gradient. The final test case was the flow studied experimentally by Samuel and Joubert (1974). The flow is 2-D and has an increasing adverse pressure gradient. The solution was started at the first station, $x = 0.855$, and both the van Driest and Reichardt models were used for the inner region while the Clauser model was used for the outer region. The results are presented in terms of skin friction coefficient and displacement thickness (δ^*). Figure 16 shows the predictions for the skin friction coefficient using the two models. The two models seem to behave in the same way up to $x \sim 2.2$. This is in the neighborhood where the change in the pressure gradient is steepest. Then, Reichardt model underestimates the skin friction coefficient, while the van Driest model gives very good agreement with the experimental data even for high aspect ratio elements. It should be noted that

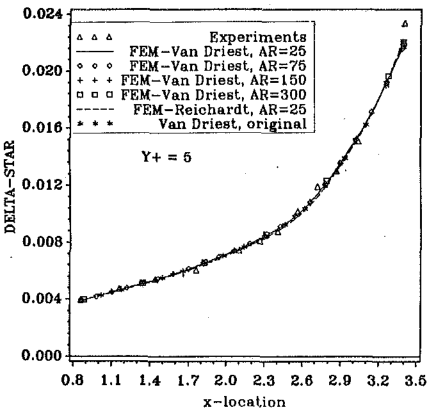

Fig. 17 Turbulent flow with adverse pressure gradient numerical versus experimental data from Samuel and Joubert for δ^*

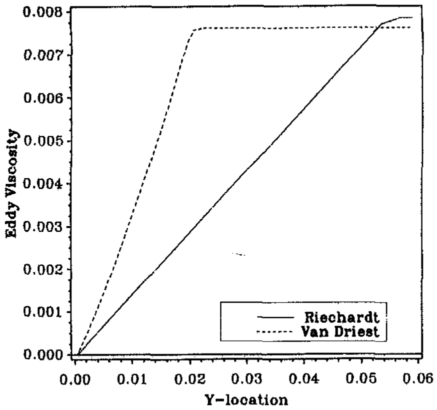

Fig. 18 Eddy viscosity predictions at the last station. Samuel and Joubert case.

the skin friction results given in Samuel and Joubert (1974) are based on a log profile with $k = 0.4$ and $A = 5.1$. The van Driest model is derived so that it reproduces a log law with constants $k = 0.4$ and $A = 5.24$. Thus, the constant A^+ should be modified in order to agree with the experimental values. Such a procedure leads to a value of $A^+ = 25.3$. Both this "modified" model and the "original" models have been used, and the results for the skin friction are indistinguishable. Figure 17 indicates that both methods give predictions that compare well with experiments for the displacement thickness. This is a strong indication that the difference in the results comes from the different model used for the inner region. Figure 18 confirms this assumption. The eddy viscosity differs only 3 percent in the outer region, but the predictions for the inner region are completely different. The CPU time for both models was almost the same and on the order of 5.2×10^{-4} s per node.

Conclusions

A new approach using the Finite Element Method is presented for the two-dimensional, incompressible, boundary-layer equations. The parabolic differential equations are transformed to a system of algebraic equations, whose solution can be obtained with a number of fast solvers. Two different elements were used in the numerical simulations, and the theoretical accuracy of the method was achieved in the case of the new QLBL element. The effect of the aspect ratio of the elements is more important for the QLBL element. It was found that the use of this element dramatically reduces the number of nodes required across the boundary layer to achieve a given level of accuracy. An upwinding approach was also tested and shown to decrease the convergence rate for the QLBL element but not for the linear element, at least for the simple flow over a flat plate with no pressure gradient. The general method gives excellent agreement compared to analytical and experimental results both for laminar and turbulent flow. For turbulent flows, the method showed better behavior when the van Driest eddy viscosity model was used for the inner region.

The method has been proven to be robust and efficient for all the test cases. The test cases treated here did not require anything but quadrilateral elements, so one advantage of the FEM compared to FEM is not apparent. These cases were chosen, since prior solutions were available for comparison. For other problems with more complex geometry, the true power of FEM will show through. Future applications will include three-dimensional and compressible flows.

Table 1 Accuracy of various methods for Howarth's flow: dimensionless wall shear values, $[\tau_w/\rho U_\infty^2]\,(U_\infty L/\nu)^{1/2}$

x/L	Current Work (FEM)	Cebeci-Smith (FDM) (1974)	Howarth series (1938)	Smith-Clutter (FDM) (1963)	Görtler series
0.1	0.948312	0.968524	0.968382	—	0.968781
0.2	0.621218	0.626392	0.626496	0.626249	0.626567
0.3	0.461754	0.462645	0.462801	—	0.462815
0.4	0.358186	0.357197	0.357442	0.357301	0.357427
0.5	0.281123	0.279150	0.279307	—	0.279611
0.6	0.218613	0.216119	0.216728	—	0.217221
0.7	0.164328	0.161602	0.162281	—	0.164296
0.8	0.113563	0.110918	0.111369	0.111546	0.117472
0.88	0.071128	0.068963	—	0.068942	0.082980
0.9	0.059194	0.057228	0.057629	—	0.074667
0.92	0.045898	0.044295	—	0.045254	0.066458
0.94	0.029653	0.028807	—	—	0.058344
0.956	0.008934	0.009863	—	—	0.051917
0.9588	0.001716	0.001602	—	0.006717	0.050798

Acknowledgments

This work was supported in part by the Cornell Theory Center, including the Cornell National Supercomputer Facility. The work of M. Gunzburger was supported by the Air Force Office of Sci. Res.

References

Baker, A. J., and Manhardt, P. D., 1978, "Numerical Prediction of Mean and Fluctuating Velocities for Jet-Flap Flows," *AIAA Journal*, Vol. 16, No. 8, pp. 807-814.

Cebeci, T., and Smith, A. M. O., 1974, *Analysis of Turbulent Boundary Layers*, Academic Press, New York.

Dorodnitsyn, A. A., 1960, *Advances in Aeronautical Sciences*, Vol. 3, Pergamon Press, New York.

Fletcher, C. A. J., 1984, *Computational Galerkin Methods*, Springer-Verlag, New York.

Fletcher, C. A. J., and Fleet, R. W., 1982, "A Dorodnitsyn Finite Element Boundary Layer Formulation," *8th International Conference on Numerical Methods in Fluid Dynamics*, Aachen.

Howarth, L., 1938, "On the Solution of the Laminar Boundary Layer Equations," *Proceedings of the Royal Society*, London, Vol. 164, p. 547.

Oden, T. J., and Wellford, L. C., 1972, "Analysis of Flow of Viscous Fluids by the Finite-Element Method," *AIAA Journal*, Vol. 10, No. 12, pp. 1590-1599.

Samuel, A. E., and Joubert, P. N., 1974, "A Boundary Layer Developing in an Increasingly Adverse Pressure Gradient," *Journal of Fluid Mechanics*, Vol. 66, Part 3, pp. 481-505.

Schetz, J. A., 1963, "On the Approximate Solution of Viscous Flow Problems," ASME *Journal of Applied Mechanics*, Vol. 30, No. 2, pp. 263-268.

Schetz, J. A., 1966, "Analytic Approximations of Boundary Layer Problems," ASME *Journal of Applied Mechanics*, Vol. 33, No. 2, pp. 425-428.

Schetz, J. A., 1984, *Foundations of Boundary-Layer Theory for Momentum, Heat, and Mass Transfer*, Prentice-Hall, Englewood Cliffs.

Schetz, J. A., and Jannone, J., 1965, "A Study of Linearized Approximations to the Boundary Layer Equations," ASME *Journal of Applied Mechanics*, Vol. 32, No. 4, pp. 757-764.

Smith, A. M. O., and Clutter, D. W., 1963, "Solution of the Incompressible Laminar Boundary-Layers Equations," *AIAA Journal*, No. 1, pp. 2062-2071.

APPENDIX

The interpolation functions used for the Finite Element Method, written in the local coordinate system with the origin created at the centroid of the element, are:

(*a*) Bilinear element (see Fig. 1(*a*))

Location of nodal point in the local system

1	(−1, −1)
2	(1, −1)
3	(1, 1)
4	(−1, 1)

$$\phi_1=\frac{1}{4}(1-\xi)(1-\eta)$$

$$\phi_2=\frac{1}{4}(1+\xi)(1-\eta)$$

$$\phi_3=\frac{1}{4}(1+\xi)(1+\eta)$$

$$\phi_4=\frac{1}{4}(1-\xi)(1+\eta)$$

(*b*) Quadratic element (see Fig. 1(*b*))

Location of nodal point in the local system

1	(−1, −1)
2	(1, −1)
3	(1, 0)
4	(1, 1)
5	(−1, 1)
6	(−1, 0)

$$\phi_1=-\frac{1}{4}(1-\xi)(1-\eta)\eta$$

$$\phi_2=-\frac{1}{4}(1+\xi)(1-\eta)\eta$$

$$\phi_3=\frac{1}{2}(1+\xi)(1-\eta^2)$$

$$\phi_4=+\frac{1}{4}(1+\xi)(1+\eta)\eta$$

$$\phi_5=\frac{1}{4}(1-\xi)(1+\eta)\eta$$

$$\phi_6=\frac{1}{2}(1-\xi)(1-\eta^2)$$

The interpolation functions are given over the square master element, since evaluation of the integrals of Eqs. (11) and (12) are easily performed over the element. The mapping corresponds each point (x, y) of each element of the general FEM mesh to a unique point of the master element. The mapping can be written as

$$x=\sum x_i\phi_i$$
$$y=\sum y_i\phi_i$$

where x_i and y_i are the coordinates of the nodal points.

Details about the numerical evaluation of the integrals can be found in any general book on the Finite Element Method (Fletcher, 1984).

Vortex Shedding From a Circular Cylinder of Finite Length Placed on a Ground Plane

Shiki Okamoto
Department of Mechanical Engineering,
Shibaura Institute of Technology,
Tokyo, Japan

Yukisada Sunabashiri
Nissan Motor Co., Ltd.,
Tokyo, Japan

This paper describes a study of changes in the vortex formation and the turbulent wake from a circular cylinder with a finite aspect ratio, placed on a ground plane. The experiment was carried out in an N.P.L. blow down type wind-tunnel, with a working section of 500 mm × 500 mm × 2,000 mm, and between the Reynolds number 2.5×10^4 and 4.7×10^4. The surface-pressure distributions on the circular cylinder were measured and the drag coefficient was determined from these measurements. Vortices of two kinds generated in the flow-field around the cylinder were observed. The power spectrum, auto-correlation, space-correlation, velocity defects, and turbulent intensities in the turbulent wake behind a circular cylinder were also measured. It was found that the flow pattern changed rapidly above aspect ratio $H/D = 4$, with vortex shedding changing from symmetric "arch" type to antisymmetric "Karman" type.

1 Introduction

A number of investigations of the flow past circular cylinders placed on a ground plane have recently been performed with air flow past structures, such as stacks, gas tanks, and cooling towers, for the purpose of collecting data concerned with the design of structures and the prevention of air pollution. The majority of these recent investigations (Etzold and Fiedler, 1976; Farivar, 1981) have been done in order to study the flow around circular cylinders with large aspect ratios (height/diameter ratio), such as stacks, and especially the effect of the free end of the cylinder on the air flow around the structure (Okamoto and Yagita, 1973, Slaouti and Gerrard, 1981).

Other studies concerned cases of circular cylinders with small aspect ratios such as gas tanks (Taniguchi et al., 1980). A recent study (Okamoto, 1982) was concerned with vortex formation from a circular cylinder of $H/D = 1$, which showed that the periodically shed vortices were arch vortices of the symmetric row type, rather than antisymmetric Karman vortices. It was concluded that vortices change from symmetric to antisymmetric as the aspect ratio increased. One might suppose that surface pressure distribution and turbulent wake must accompany different characteristics with the transformation of vortex shedding mode. Other studies (Okamoto and Yagita, 1973; Etzold and Fiedler, 1976) investigated surface pressure distributions, drag, and velocity profiles in the turbulent wake of circular cylinders, as a function of aspect ratio. However, there are few studies which have investigated changes in vortex shedding mode from circular cylinders (Taniguchi et al., 1980, excepted). This paper presents an experimental study of the process of changing from shedding of symmetric to antisymmetric vortices, and the accompanying changes in the surface pressure and turbulent wake, as a function of the aspect ratio of a circular cylinder.

2 Apparatus and Procedure of Measurement

The experiment was carried out in a wind-tunnel of N.P.L. blow down type, with a 500 mm × 500 mm working section of 2000 mm length and a free-stream turbulence level of 0.4 percent. The ground plate was set with a spacing of 25 mm from the lower wall of the tunnel exit in order to avoid the boundary layer on the tunnel wall (as shown in Fig. 1). The cylinder was placed at a downstream distance of 500 mm from the leading edge of the ground plate. The thickness of the boundary layer at the model position was about 4 mm. There was little effect of the boundary layer on the shear flow behind the cylinder, because the ratio of the boundary-layer thickness to the height of the cylinder was less than 0.11. The aspect ratios, namely the ratio of diameter to height of the circular cylinder used in this experiment, used were $H/D = 0.5$, 1, 2,

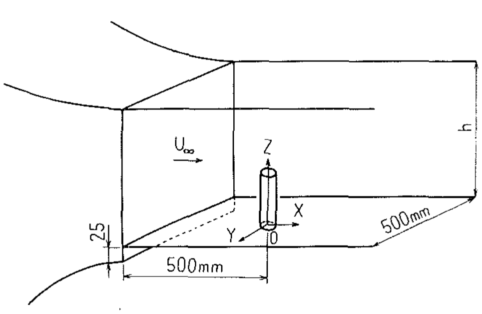

Fig. 1 Schema of apparatus and nomenclature

Contributed by the Fluids Engineering Division for publication in the JOURNAL OF FLUIDS ENGINEERING. Manuscript received by the Fluids Engineering Division March 27, 1991. Associate Technical Editor: Chih-Ming Ho.

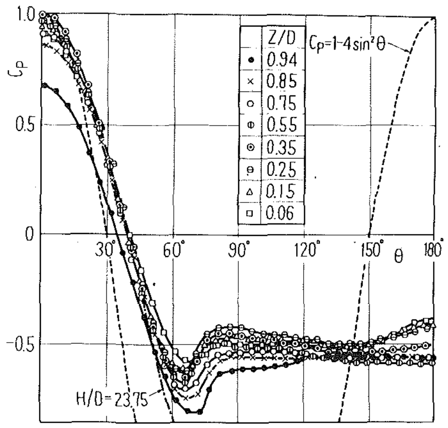

Fig. 2 Surface pressure distribution (H/D = 1) (Uncertainty in Cp = 0.0848)

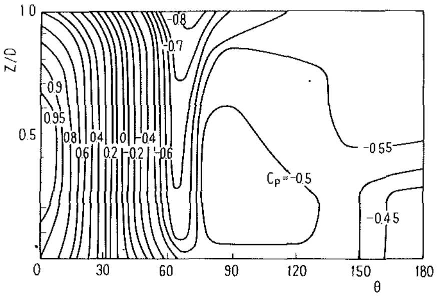

Fig. 3(a) H/D = 1

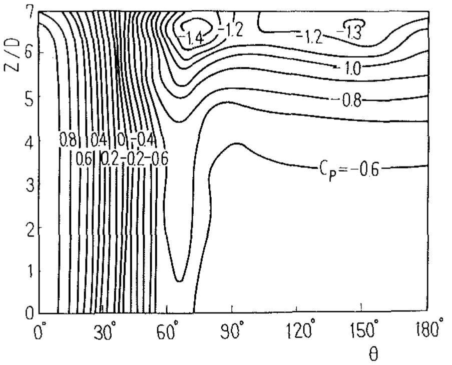

Fig. 3(b) H/D = 7 (Uncertainty in Cp = 0.0848)

Fig. 3 Isobars

4, 7, and 23.75 and the diameters of the cylinders used for the surface-pressure measurements were D = 70 mm for cases of H/D = 0.5 and 1, D = 40 mm for H/D = 2 and 4, and D = 30 mm for H/D = 7, but the diameter used for the wake measurement was kept at D = 20 mm for H/D = 0.5 to 7 and 23.75. It was supposed that there was no blockage effect in this experiment because the blockage ratio 0.021 for even the largest cylinder of 70 mm diameter was less than the limiting value 0.05 obtained by Farell et al. (1977).

Measurement of the surface-pressure on the cylinder was done through pressure holes of 0.5 mm ϕ bored along the generating line of the cylinder. The pressure distribution on the whole surface was measured by rotating the cylinder about its axis. Furthermore, flow separation and vortex formation were observed by flow visualization in a water channel at Re = 1.06×10^3. The water channel used is an open-circuit type having a 300 mm × 400 mm working section of 1000 mm length. A Pitot-tube and a constant temperature hot wire anemometer type with the function of measurement of time-mean velocity and turbulence were used. The U and u' components of velocity were measured by a single wire. The v' and w' fluctuating velocities were measured by an X-wire with calibration routines supplied by the manufacturing (Kanomax, Osaka, Japan). The turbulence quantities, auto-correlation, power spectrum, and space-correlation were obtained from the data processing system and an F.F.T. Analyzer connected to the hot-wire anemometer. No velocity measurements were reported for the near-wake region, because of the limitations of hot-wire anemometers in the region of high turbulence intensity. Since it is well known that the flow around a circular cylinder is almost independent of Reynolds number so long as Re = $10^3 \sim 10^5$ (Hoerner, 1958), the experiment was performed at a wind velocity of $U_\infty = 10.2 \sim 19$ m/s, corresponding to Re = $U_\infty D/\nu = 2.5 \times 10^4 \sim 4.7 \times 10^4$.

3 Experimental Results and Discussion

3.1 Surface-Pressure and Drag. Figure 2 shows surface-pressure distribution along the circumference of a cylinder of H/D = 1. The broken line in Fig. 2 represents the theoretical value $Cp = 1 - 4\sin^2\theta$ based on the potential-flow theory. The surface pressure distributions varied little in a range of $0 \leqq \theta \leqq 60$ deg except in the vicinity of the free end, or Z/D

Nomenclature

C_D = drag coefficient
C_p = pressure coefficient = $(P-P_\infty)/(\rho U_\infty^2/2)$
D = diameter of circular cylinder
Eu = power spectrum function for fluctuating velocity u'
H = height of a circular cylinder
n = frequency of vortex shedding (Hz)
P = static pressure
P_∞ = static pressure in free stream
Re = Reynolds number = DU_∞/ν
Ru = auto-correlation coefficient of fluctuating velocity u'
$Ruuy$ = space-correlation coefficient of fluctuating velocity u' in the transverse direction
St = Strouhal number = Dn/U_∞
U = time-mean velocity
U_∞ = free stream velocity
u', v', w' = X, Y, and Z instantaneous components of fluctuating velocity
X, Y, Z = coordinate axes with origin at the bottom center of a circular cylinder, X, Y, Z axes being taken in the streamwise, lateral, and vertical directions, respectively (Fig. 1)
Xr = length of recirculation region
y = distance between two hot wires in the transverse direction for the measurement of space correlation
θ = circular angle measured from the forward stagnation point
τ = time delay (ms)
ν = kinematic viscosity of air
ρ = density of air

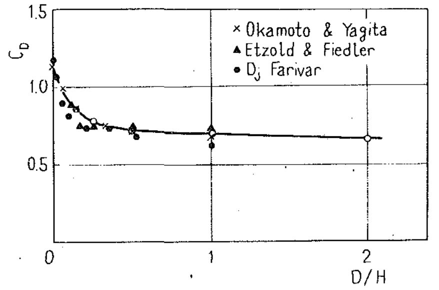

Fig. 4 Drag coefficient: open circles are present work (Uncertainty in C_D = 0.125 and in D/H = 0.035)

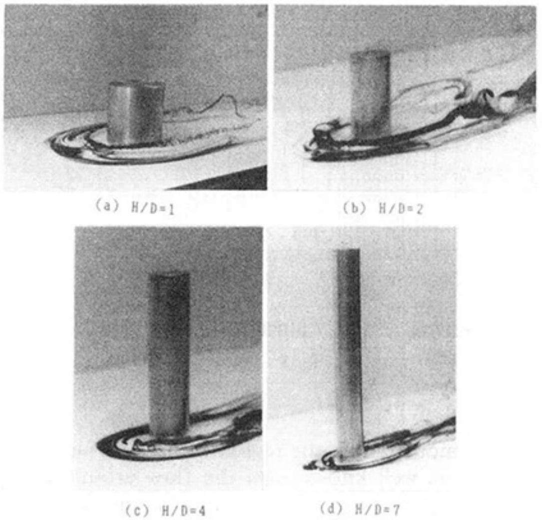
(a) H/D=1 (b) H/D=2
(c) H/D=4 (d) H/D=7

Fig. 5 Horse-shoe vortices
(*a*) $H/D = 1$, (*b*) $H/D = 2$, (*c*) $H/D = 4$, (*d*) $H/D = 7$

≧ 0.94, as seen from this figure. The pressure coefficient in a range of 60 deg $\leqq \theta \leqq$ 180 deg varied with the value of Z/D for the case of $H/D \leqq 5$, because the effect of the free end of the circular cylinder on the surface pressure extends to the base of the cylinder (Okamoto and Yagita, 1973). Figure 3 shows isobars on the surface obtained from surface-pressure distributions for $H/D = 1$ and 7, respectively. The effect of the free end on the surface pressure is especially remarkable on the rear face. Since the constant pressure lines on the rear face extend to the base of the cylinder, the end effect reaches to the base of the cylinder, in the case of $H/D = 1$. The lowest pressure area, that is, a depression of pressure, clearly appears near $Z/D = 0.95$ and $\theta = 70$ deg for the case of $H/D = 1$. On the other hand, for the case of $H/D = 7$ (shown in Fig. 3(*b*)), the end effect is confined to the vicinity of the free end of the cylinder, and the contours of constant pressure seen in the range of $Z/D \leqq 3$ are caused by the appearance of a nearly two-dimensional portion. Furthermore, another depression appears near $Z/D = 6.5$ and $\theta = 140$ deg in addition to the one at $Z/D = 6.5$ and $\theta = 70$ deg. Okamoto and Yagita (1973) reported that the depression of pressure near $\theta = 140$ deg occurs at one end of the vortex filament separated from the side face of the cylinder. Therefore, the disappearance of this depression near $\theta = 140$ deg, as in the case of $H/D = 1$, means that vortices shedding from the cylinder are not anti-symmetric vortices (i.e., Karman vortices). Observation of the isobars showed that the type of vortices shed from a circular cylinder of $H/D = 1$ was different from those of $H/D = 7$.

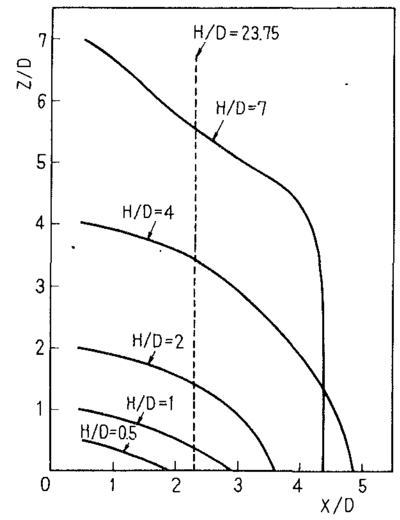

Fig. 6 Recirculation region (Uncertainty in Z/D = 0.035 and in X/D = 0.10)

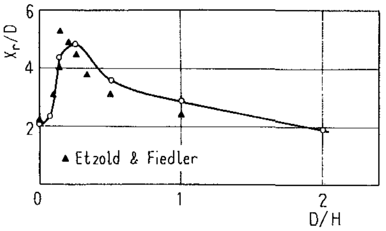

Fig. 7 Length of recirculation region; open circles are present work. (Uncertainty in Xr/D = 0.10 and in D/H = 0.035)

The drag coefficient of the circular cylinder was determined from integrating the surface pressure as follows:

$$C_D=\frac{D}{H}\int_0^{H/D}\int_0^{\pi} C_p(\theta, Z/D)\cos\theta d\theta d(Z/D).$$

Figure 4 shows the drag coefficient of the circular cylinder, together with results of Etzold and Fiedler (1976, Re = 3×10^4), Farivar (1981, Re = 7×10^4) and Okamoto and Yagita (1973, Re = 1.33×10^4) for comparison. The drag coefficient varies rapidly at $H/D \geqq 4$. This rapid variation is due to the increase of the local drag due to the two depressions of pressure in the vicinity of the free end of the cylinder. The drag coefficient decreases gradually in the range of $H/D \leqq 4$ and tends to have a smaller value than that for $H/D \geqq 4$. The decrease of drag is caused by the recovery of pressure on the rear face due to the strong downwash from the free end of the cylinder. From the variation of drag coefficient, it can be confirmed that the mean drag coefficient of a circular cylinder of $H/D = 23.75$ attains the maximum value, since the rear pressure is recovered slowly without downwash from the free end.

3.2 Vortex Formation. It is well known that two kinds of vortices exist in the flow-field around a circular cylinder placed on a ground plane:

(1) horseshoe vortices generated at the corner between the frontal face of the circular cylinder and the ground plate;

(2) vortices generated in the lee of circular cylinder.

Horseshoe vortices formed inside the separation line in the neighborhood of the circular cylinder on the ground plane, are shed downstream with the axes of the vortices in the streamwise direction, passing around both sides of the circular cylinder. The horseshoe vortices were observed in the flow

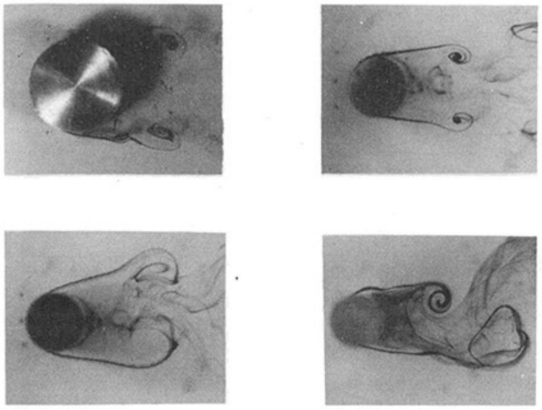

(*c*) ***H/D* = 4,** (*d*) ***H/D* = 7**

Fig. 8 Symmetrically and antisymmetrically shed vortices. Dye released at mid-span location.

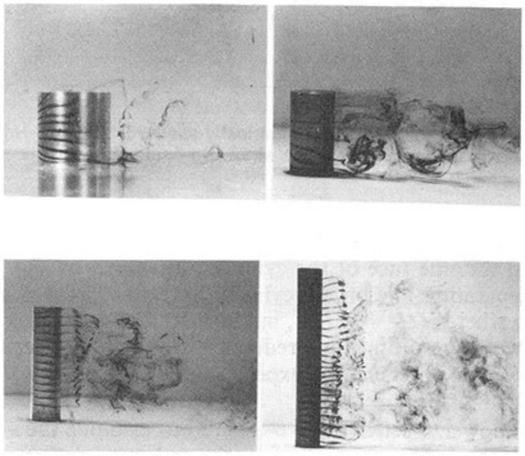

(*c*) ***H/D* = 4,** (*d*) ***H/D* = 7**

Fig. 9 Symmetrically- and antisymmetrically-shed vortices

visualization by using the ink shedding method in the water channel as shown in Fig. 5. There was an upwash outside the horseshoe vortices and a downwash inside them, which augmented the downwash from the free end of the cylinder in cases where H/D was low. Figure 6 shows that the size of the horseshoe vortices, relative to the height of the cylinder, decreases as the height of cylinder increases. The effect of the downwash from the free end of the circular cylinder weakens as aspect ratios increases.

The streamline over the top of a circular cylinder with a small aspect ratio reattaches to the ground plate downstream, forming a recirculation region behind the cylinder. To find the size of this recirculation region, the line of zero dynamic pressure, (zero velocity) was determined in the section of $Y/D = 0$ by using the Pitot tube. Figure 6 shows the locus of zero velocity, demonstrating how the recirculation region enlarges with an increase in H/D, so long as $H/D \leqq 4$. But the recirculation region decreases in the case of $H/D = 7$, because the end effect is limited to the portion near the free end, and the downwash from the top stops near the base of cylinder. The case of $H/D = 23.75$ is also shown by the broken line in Fig. 6. The length ($Xr/D = 2.25$) of the recirculation region for $H/D = 23.75$ is consistent with the results reported by Etzold and Fiedler (1976). The length of the recirculation region on the ground plane seems to correspond to the distance of the reattachment point of the streamline over the top for the case of $H/D = 1$. The reattachment point on the ground plane, namely the point of maximum pressure, $X/D = 2.92$, in the isobars on the ground plate, is consistent with the junction line of zero velocity with the ground plane. Figure 7 shows the variation of the length of the recirculation region on the ground plane using data from Fig. 6. Moreover, Fig. 7 also shows the results of Etzold and Fiedler (1976), who used smoke rather than a Pitot tube. Figure 7 also shows that the length of the recirculation region was maximum at $D/H = 0.25$ (namely $H/D = 4$) and was longer than Etzold and Fiedler's (1976) measurements beyond $D/H = 0.25$.

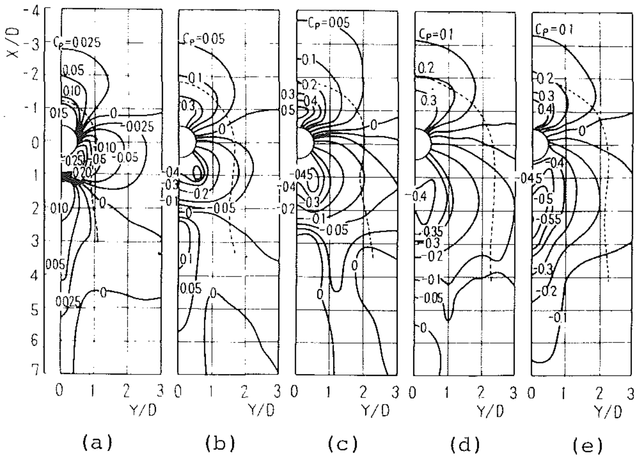

Fig. 10 Surface pressure distribution on ground plane. Dashed line represents the separation locus.
(*a*) *H/D* = 0.5, (*b*) *H/D* = 1, (*c*) *H/D* = 2, (*d*) *H/D* = 4, (*e*) *H/D* = 7 (Uncertainty in *Cp* = 0.0848, in *X/D* = 0.10 and in *Y/D* = 0.025)

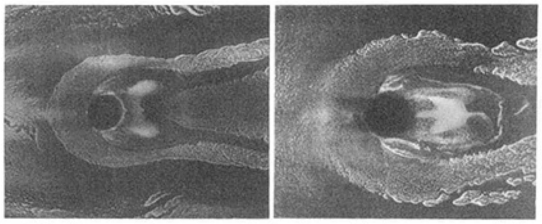

Fig. 11 Flow pattern around circular cylinder on ground plane
(*a*) *H/D* = 1, (*b*) *H/D* = 7

Figure 8 shows photographs of the plan view of vortex shedding from both sides of the cylinder of $H/D = 1 \sim 7$. The dye was released at the mid-span of the cylinder "contrast this with Fig. 13 below." Symmetric vortices, which separated from both sides and shed periodically downstream, appear when $H/D = 1$ to 2. The formation of antisymmetric vortices were seen when the value of H/D increased from $H/D = 4$ to 7. Figure 9 shows side view photographs, of both vortices. It can be seen that the symmetric vortices generated for $H/D = 1$ and 2 are increasing, inclined in the downstream direction due to the strong downwash. They are shed downstream in a similar manner to the vortices shed from a hemisphere placed on a ground plane (Savory and Toy, 1986).

Antisymmetric vortices are shed downstream with the axes parallel to the cylinder for $H/D = 7$. The movement of these vortices can be surmised from the isobars on the ground plane shown in Fig. 10, which was drawn from data derived from a few hundred pressure tappings (the number of tappings depending on the cylinder diameter). There are two areas of low pressure behind the cylinder for $H/D = 0.5 \sim 2$, which coincide with the attachment points of the base of the symmetrically-shed vortices on the ground plate. In order to confirm this, the flow pattern was visualized by coating the ground plate with a solution of tooth powder (Fig. 11). It can be seen from Fig. 11(a) that the vortices are attached to the ground

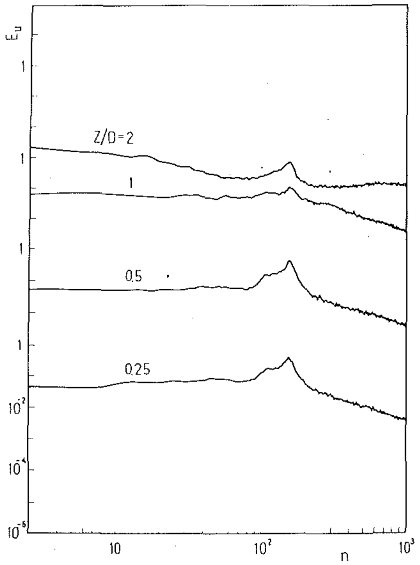

Fig. 12(*a*) ***H/D* = 2**

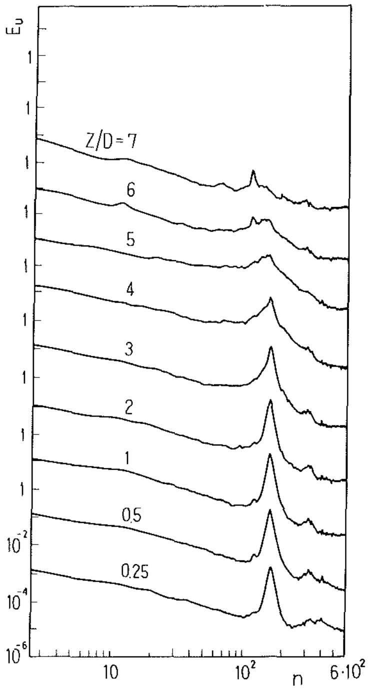

Fig. 12(*b*) ***H/D* = 7 (Uncertainty in *Eu* = 0.03 and in *n* = 12.75 Hz)**

Fig. 12 Power spectrum

plate behind the cylinder at $H/D = 1$. The location of these attachment point is consistent with that of the two areas of minimum pressure behind a circular cylinder shown by the isobars in Fig. 10. The symmetric vortices shed downstream, incline about these attachment points under the action of strong downwash from the free end. These vortices were the same type of vortices generated behind spheres and hemisphere-cylinders placed on a ground plane (Okamoto, 1982). In the case of $H/D = 7$, (shown in Fig. 11(*b*)) there is an area corresponding to the bases of antisymmetrically shed vortices behind the circular cylinder, which is different from the case of $H/D = 1$. This area is almost the same as the area of minimum pressure on the ground plane shown in Fig. 10.

The vortices near the free end of the cylinder are a symmetric row, as shown in the flow visualized by Shimizu (1988). The upper ends of the antisymmetrically-shed vortices are located at the position of 0.5D below the free end, and $\theta = \pm 140$ deg on the side face of the cylinder, as shown by Fig. 3(*b*). The separation line on the cylinder surface is located at $\theta < 90$ deg where $H/D = 1 \sim 4$, but it shifts to $\theta = 140$ deg where $H/D > 4$, resulting in a reduction of the wake region, as shown in the water channel experiment by Okamoto and Yagita (1973).

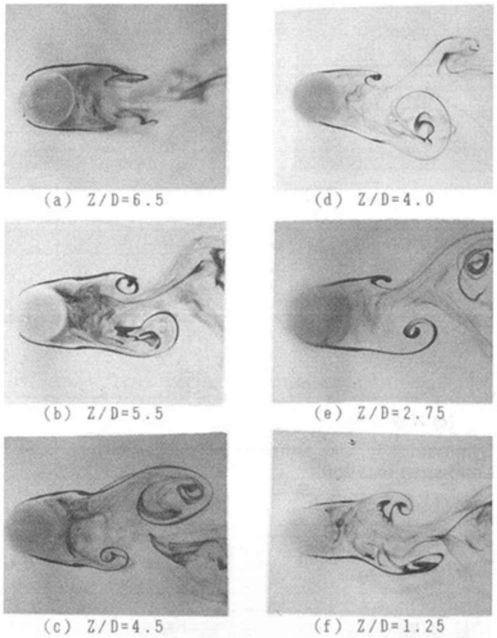
(a) Z/D=6.5
(d) Z/D=4.0
(b) Z/D=5.5
(e) Z/D=2.75
(c) Z/D=4.5
(f) Z/D=1.25

Fig. 13 Formation of antisymmetrically-shed vortices for *H/D* = 7. Spanwise location of dye release shown in figure captions.

The power spectrum was measured to examine the vortices shed from the circular cylinder using a hot-wire anemometer and an F.F.T. Analyzer. Figure 12 shows the power spectrum in the lengthwise direction at $X/D = 1.65$ and $Y/D = 0.85$ for $H/D = 2$ and $X/D = 1.5$ and $Y/D = 2$ for $H/D = 7$. The power spectrum had a steep peak at a frequency which corresponds to that of the vortex shedding. The frequency is almost constant in the lengthwise direction where $H/D = 2$. However, the magnitude of the peak at $Z/D = 2$, namely in the vicinity of the free end, is small compared with the energies at lower frequencies. Symmetric vortices near the free end are affected by a strong downwash from the top. However, the predominant frequency is almost constant in the range of $Z/D = 0.25$ to 5 where $H/D = 7$, while it shifts to a lower frequency at $Z/D = 6$ and 7 near the free end. The peak becomes weaker between $Z/D = 4$ and 7 near the free end. Hence, the antisymmetric vortices are shed at $Z/D \leqq 3$ for the circular cylinder of $H/D = 7$ and, it may be supposed, that symmetric vortices are generated at $Z/D \geqq 4$ due to the downwash from the free end.

The variation of the antisymmetric vortices in the lengthwise direction was examined by flow visualization in a water channel. Figure 13 shows the pictures of vortices shed from a circular cylinder of $H/D = 7$. The spanwise location of the dye release is indicated in the caption of Fig. 13. The antisymmetric vortices disappear and symmetric row vortices appear at $Z/D = 6.5$ in Fig. 13(*a*), but Fig. 13(*b*) ~ (*f*) show the formation of antisymmetric vortices at $Z/D \leqq 5.5$, which is in agreement with the results of the power spectrum measurement.

The Strouhal number of vortex shedding was obtained from the predominant frequency near $Z/H \fallingdotseq 0.5$, which is shown in Fig. 14. The results reported by Farivar (1981) and Okamoto and Yagita (1973) are shown in this figure for comparison.

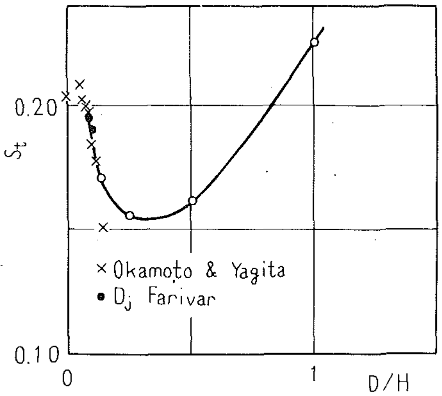

Fig. 14 Strouhal number: open circles are present work (Uncertainty in St = 0.127 and in *D/H* = 0.035)

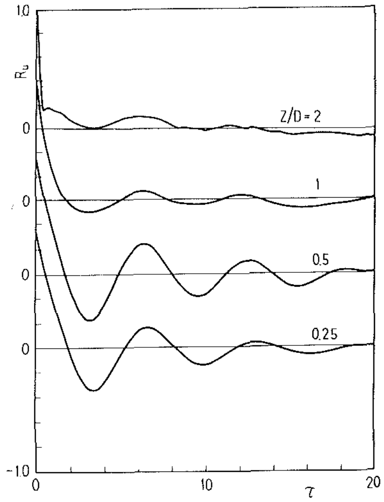

Fig. 15(*a*) *H/D* = 2

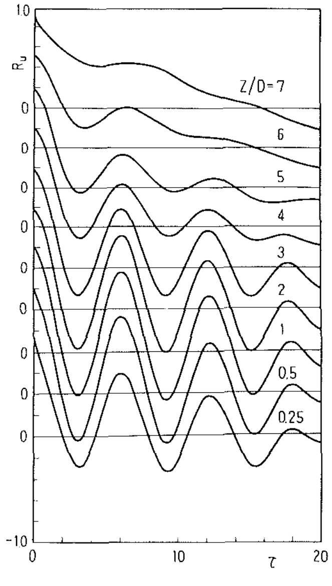

Fig. 15(*b*) *H/D* = 7 (Uncertainty in Ru = 0.156)

Fig. 15 Auto-correlation; units of τ are ms.

The Strouhal number decreases in the region of symmetric vortex shedding, that is, in the range of $H/D < 4$, and attains the minimum value near $H/D = 3 \sim 4$. However, it increases most evident in the region of antisymmetric vortex shedding, that is, in the range of $H/D \geqq 4$.

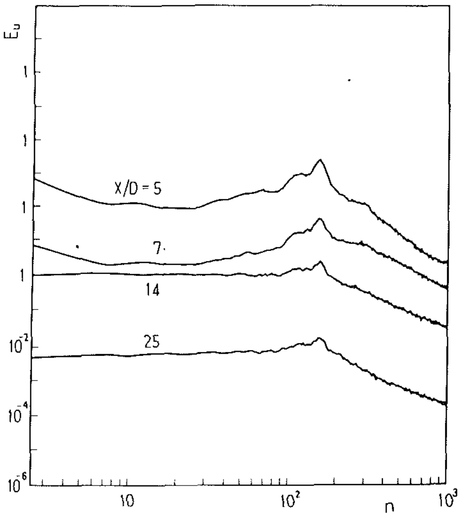

Fig. 16(*a*) *H/D* = 2

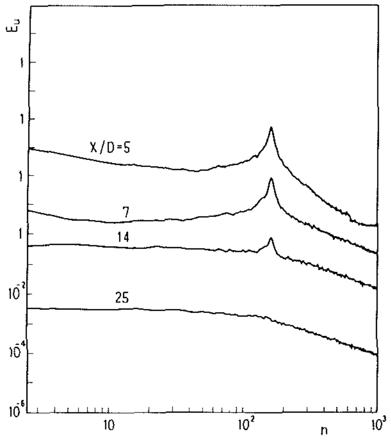

Fig. 16(*b*) *H/D* = 7

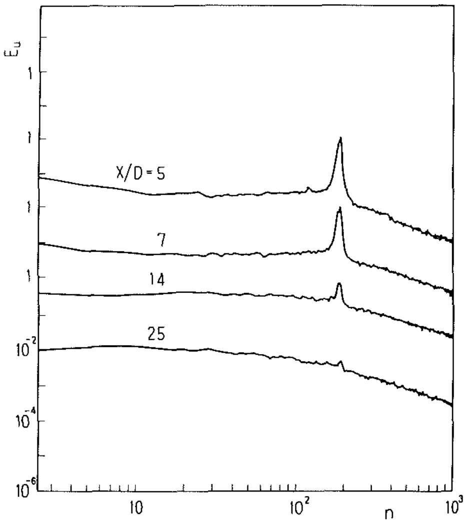

Fig. 16(*c*) *H/D* = 23.75 (Uncertainty in Eu = 0.03 and in *n* = 12.75 Hz)

Fig. 16 Power spectrum at *Y/D* = 2.55 and *Z/H* = 0.5; units of *n* are Hz.

In order to investigate the feature of the turbulent eddies, the auto-correlation of the X-component of fluctuation velocity was measured. Figure 15 shows the auto-correlation coefficient $Ru(\tau)$ of the X-component of the fluctuation velocity in the lengthwise direction, where the auto-correlation coefficient for u' is defined as:

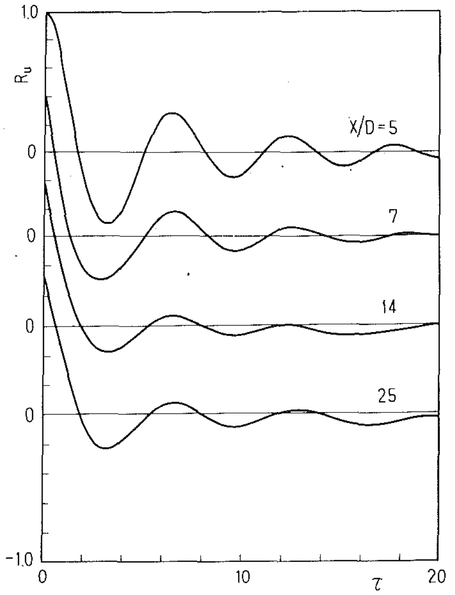

Fig. 17(*a*) *H/D* = 2

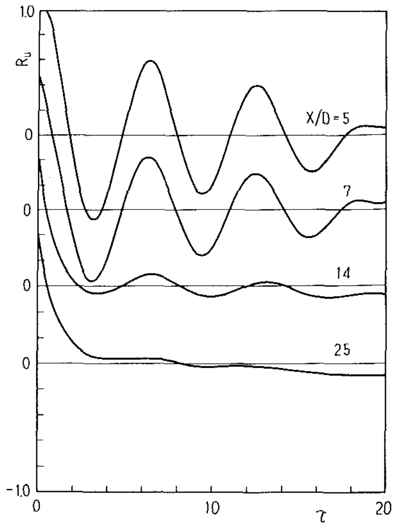

Fig. 17(*b*) *H/D* = 7

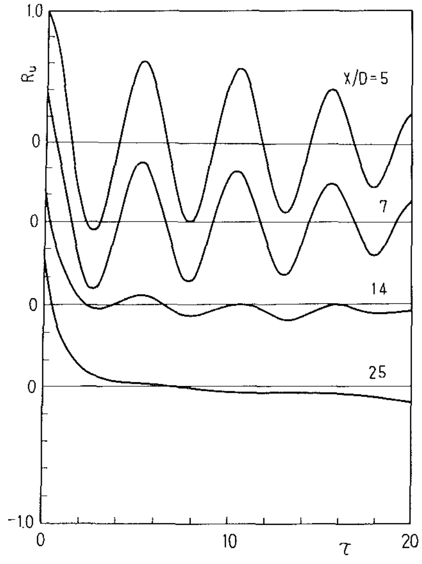

Fig. (*c*) *H/D* = 23.75 (Uncertainty in Ru = 0.156)

Fig. 17 Auto-correlation at *Y/D* = 2.55 and *Z/H* = 0.5

$$Ru(\tau)=\frac{\overline{u'(t)u'(t+\tau)}}{\overline{u'^2}}$$

The auto-correlation coefficient was measured at $X/D = 1.65$, $Y/D = 0.85$ for $H/D = 2$ and $X/D = 1.5$, $Y/D = 2$ for $H/D = 7$. Figure 15 also shows periodicity in the correlation, which arises from periodical vortex shedding.

The time-delay of first zero correlation represents the rate of decay of the eddies dependent on the average scale of the eddies. The time-delay to the first zero correlation is almost constant between $Z/D = 0.25$ and 1 where $H/D = 2$, but it is longer at $Z/D = 2$ than the others. This means that the rate of decay of the turbulent eddies is constant in the lengthwise direction in the range of $Z/D = 0.25 \sim 1$, and slows at $Z/D = 2$ near the free end, as opposed to other points, because the downwash from the top causes enlargement in the scale of the eddies.

The time delay to the zero correlation is almost constant at $Z/D \leqq 5$ for $H/D = 7$ and equal to that for $H/D = 2$. The rate of decay of eddies is constant at $Z/D \leqq 5$ for $H/D = 7$ and equal to that for $H/D = 2$. Furthermore, beyond $Z/D = 6$, the time delay to the zero correlation becomes longer with increasing Z/D. Hence, the rate of decay of the turbulent eddies is faster in the region of antisymmetric vortex shedding, but slower near the free end where $H/D = 7$ and in the same manner as the rate of decay of the turbulent eddies where $H/D = 2$.

3.3 Power Spectrum, Auto-Correlation, and Space-Correlation in Turbulent Near Wake. The structure of the turbulent near wake behind a circular cylinder of finite length was observed and compared to the observations made for a circular cylinder of $H/D = 23.75$. The shedding of symmetric and antisymmetric vortices from a circular cylinder of $H/D = 2$ and 7 have already been observed in the water channel experiment as shown in Figs. 8 and 9. The power spectrum was measured to examine the decay of vortices shed from a circular cylinder in the turbulent near wake. Figure 16 shows the power spectrum at $Y/D = 2.55$, $Z/H = 0.5$, and $X/D = 5 \sim 25$ for the cases of $H/D = 2$, 7 and $H/D = 23.75$. The particular value of Y/D was chosen to give strong frequency peaks. A steep peak appears in the spectra for $X/D \leqq 14$ independently of the value of H/D, and so the existence of periodic vortex shedding was confirmed. The peak gradually vanishes, however, as X/D approaches 25 for cylinders with $H/D = 7$ and $H/D = 23.75$. This indicates that the periodic vortices have decayed, while a small peak still remains at $X/D = 25$ for $H/D = 2$. Consequently, the symmetric and asymmetric vortices shed from a circular cylinder of $H/D = 2$, 7 and 23.75. These vortices exist in the region of $X/D \leqq 14$, and the symmetric vortices are still present at $X/D = 25$, though the antisymmetric vortices have vanished. The rate of decay of the symmetric vortices is slower than that of the antisymmetric vortices. This fact can be observed in the auto-correlation, Fig. 17, which shows the auto-correlation at $Y/D = 2.55$, $Z/H = 0.5$ and $X/D = 5 \sim 25$ for the cases of $H/D = 2$, 7 and 23.75. A steep peak in the power spectrum and a large negative correlation due to the shedding of the periodic vortices exist at $X/D = 5 \sim 25$ where $H/D = 2$. On the other hand, there is no large negative correlation at $X/D = 25$ for the cases of $H/D = 7$ and 23.75, while a large negative correlation appears at $X/D = 5 \sim 14$. Therefore, antisymmetric vortices are shed from a circular cylinder of $H/D = 7$ and 23.75. The antisymmetric vortices decay rapidly in the downstream direction as compared with symmetric vortices for the case of $H/D = 2$, which matches the measurement for the power spectrum.

The time-delay to zero correlation is almost constant at X/

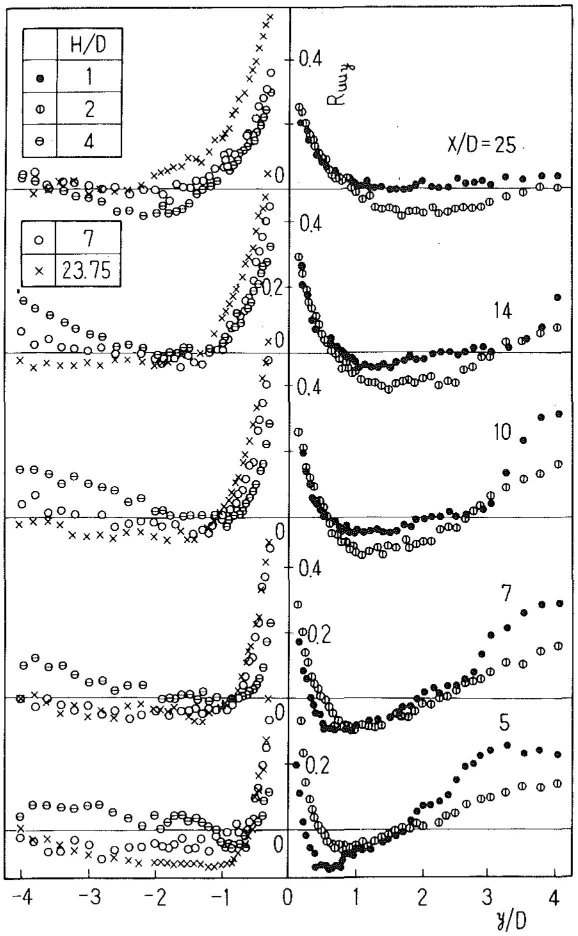

Fig. 18 Space-correlation at $Z/H = 0.5$ (Uncertainty in Ruuy = 0.156 and in $Y/D = 0.025$)

$D \leqq 14$ for all values of H/D. The time-delay to the first zero-correlation is discussed in order to investigate the rate of decay of the turbulent eddies. This means that the rate of decay of the turbulent eddies is almost unchanged in this region, independent of H/D. Accordingly, the time-delay to zero correlation increases at $X/D = 25$ as compared with that at $X/D \leqq 14$ for all values of H/D. Therefore, at $X/D = 25$ the rate of decay of the turbulent eddies is slow, and the average scale of large eddies increases as compared with those at the upstream position. Consequently, the average scale of the eddies was found to be small and constant in the region of periodic vortex shedding, but this scale increases in the region of the decaying periodic vortices. The time delay to zero correlation at $X/D = 25$ is larger for $H/D = 7$ and 23.75 than for $H/D = 2$. This means that the progress of the mixing of the turbulent eddies with the decaying antisymmetric vortices is rapid for $H/D = 7$ and 23.75 as compared with the case of $H/D = 2$. The average scale of large eddies becomes bigger for $H/D = 7$ and 23.75 than for $H/D = 2$. This can be explained from the variation of spatial correlation.

Figure 18 shows the spatial correlation coefficient Ruuy defined as

$$Ruuy(X, Y, Z) = \frac{\overline{u'(X, Y, Z, t)u'(X, Y-y, Z, t)}}{\overline{u'^2(X, Y, Z)}}$$

in the horizontal center section ($Z/H = 0.5$). The spatial correlation coefficient was measured by two hot wires in such a way that hot wire ① was fixed at $Y/D = 0$, $Z/H = 0.5$ and hot wire ② was moved in the transverse direction. The correlation spreads transversely with an increase in the downstream distance. Therefore, the average scale of the eddies enlarges transversely with an increase in the downstream distance. Furthermore, the correlation spreads transversely with an increase in the value of H/D, implying that the scale of the eddies in the near wake enlarges with an increase in the value of H/D.

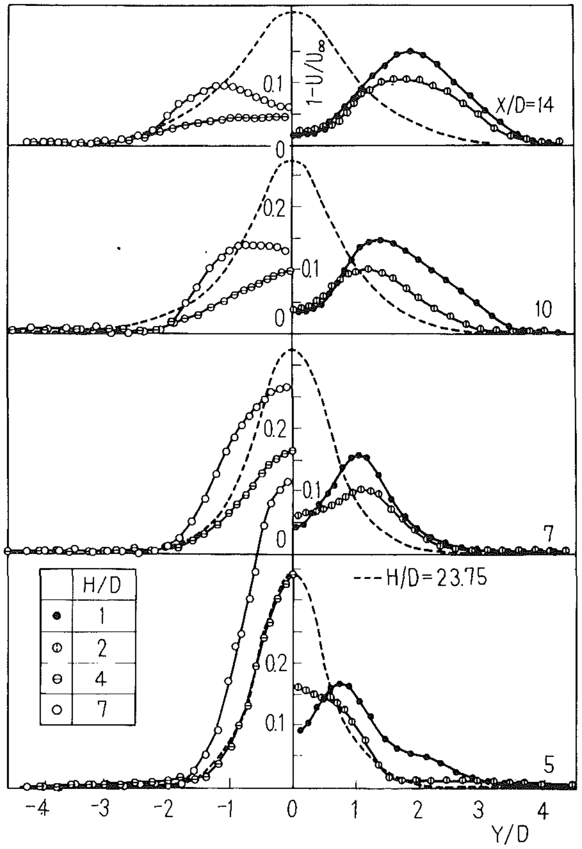

Fig. 19 Velocity defect profile ($Z/H = 0.5$) (Uncertainty in $(1 - U/U_\infty = 0.0901$ and in $Y/D = 0.025$)

3.4 Distributions of Velocity and Turbulent Intensities in Turbulent Wake. The turbulent wake behind a cylinder of finite length is significant because of its relation to the problems of air pollution, and the influence of downwash from the top of stacks on the behavior of the plume. Figures 19 and 20 show the profiles of the mean velocity defect, and X-, Y-, and Z-components of turbulence intensity, in the horizontal center section ($Z/H = 0.5$). The broken line denotes the result from $H/D = 23.75$. Furthermore, Figs. 19 and 20 show that one peak appears at $Y/D = 0$ for $H/D = 23.75$, and this peak or maximum velocity defect decreases as the downstream distance increases. It follows that the turbulent wake spreads transversely with increasing downstream distance. The profile of velocity defect for a circular cylinder of $H/D = 1$ has two peaks for the positions of $X/D = 5 \sim 14$, while one peak appears at $X/D = 5$ and two peaks appear at $X/D \geqq 7$ in the case of $H/D = 2$. Furthermore, in the case of $H/D = 4$, one peak appears at $Y/D = 0$ for the positions of $X/D = 5 \sim 14$, while the profile of velocity defect for the case of $H/D = 7$ has one peak at $X/D \leqq 7$ and two peaks at $X/D \geqq 10$.

The appearance of two peaks in the profile of velocity defect in the Y-direction, was supposed to be due to the downwash from the free end of the circular cylinder. This phenomenon is a feature of circular cylinder of finite length. Since the velocity profile is expressed as the velocity defect against the

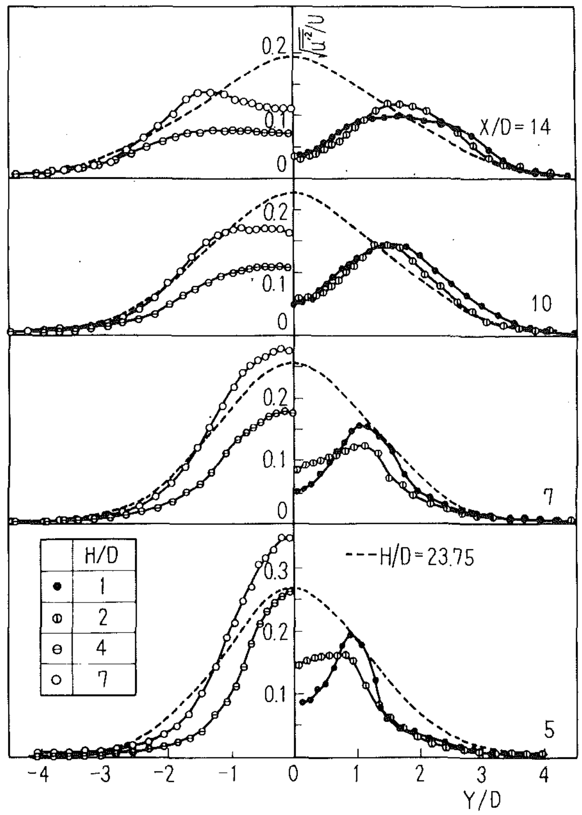

Fig. 20(*a*) *X*-component

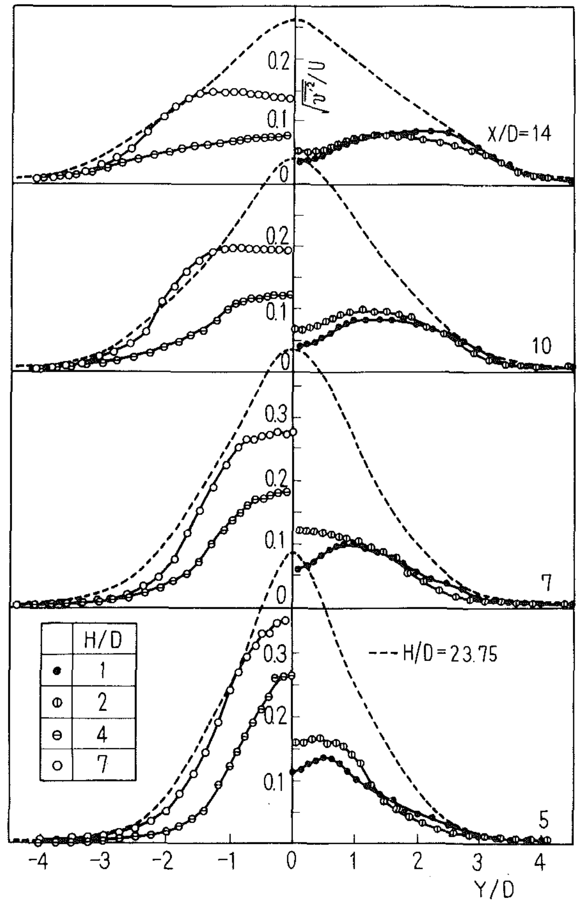

Fig. 20(*b*) *Y*-component

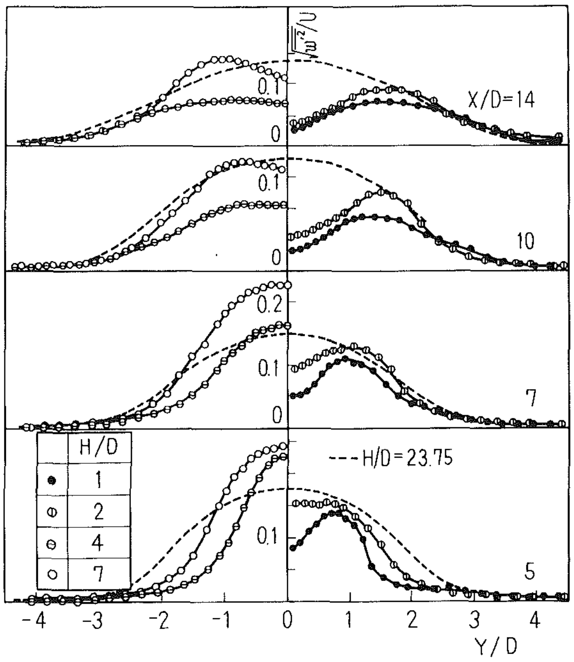

Fig. 20(*c*) *Z*-component (Uncertainty in $\sqrt{u'^2}/U$ = 0.028, in $\sqrt{v'^2}/U$ = 0.039, in $\sqrt{w'^2}/U$ = 0.039 and Y/D = 0.025)

Fig. 20 Turbulent intensities (Z/H = 0.5)

free stream velocity, the value at the midpoint between the two peaks represents the velocity excess due to the downwash. Therefore, the downwash from the free end reaches the center section ($Z/H = 0.5$) at $X/D = 5$ for a circular cylinder of $H/D = 1$. Furthermore, in the case of $H/D = 2$, the effect of the downwash from the free end does not appear at $X/D = 5$, while one peak appears in the profile. The downwash effect from the free end appears at $X/D \geqq 7$ and the profile of velocity defect has two peaks. On the other hand, in the case of $H/D = 4$, the downwash effect does not appear even at $X/D = 14$, resulting in one peak of the velocity defect profile. In the case of $H/D = 7$, the downwash effect appears at $X/D \geqq 10$, and thus two peaks exist in the profile of the velocity defect. As a whole, the profile of velocity defect shown in Fig. 19 is divided mainly into two different groups: $H/D = 1, 2$; and $H/D = 4.7$. This division seems to be closely related to the variation of the recirculation region in Fig. 7. Therefore, the turbulent wakes behind a circular cylinder are divided into two groups: (i) the wake in which the effect of the downwash from the free end is predominant in the case of $H/D < 4$; and (ii) the wake in which the downwash effect disappears in the case of $H/D \geqq 4$.

Figure 20 shows the downstream development of three components of turbulence intensities, which indicates, as a whole, similar variations as the velocity defect. Comparing the X- and Y-components of turbulence intensity, the Y-component is larger than the X-component near $Y/D = 0$ for the case of $H/D = 1$ and 2, and where the effect of the downwash from the free end appears and two peaks exist in the profiles. The X- and Y- components become almost the same for $H/D = 4$, while the Y-component is larger than the X-component in the wake for the case of $H/D = 7$. The wake has a relatively strong tendency to spread transversely with an increase in X/D in the cases of $H/D = 7$ and 23.75, but this tendency is weak for the case of $H/D = 1$ and 2. The Z-component of turbulence intensity almost equals the X-component near $Y/D = 0$ at $X/D = 5$ and 7, in the cases of $H/D = 1, 2$, while it is remarkably smaller than the X-component for the cases of $H/D = 4$ and 7. As a result, it may be concluded that, since the Z-component of the turbulence intensity is relatively larger than the X-component near $Y/D = 0$, for the case of $H/D = 1$ and 2, the wake has a strong tendency to descend along the ground plane. Comparatively the tendency of transverse spreading is relatively weak at $H/D = 4$ and 7.

4 Conclusion

The results of the present study can be summarized as follows:

(1) The drag coefficient increases as the value of H/D increases. This rapid increase is especially true for a circular cylinder equal to approximately $H/D = 4$, where depression of pressure appears near $\theta = 140°$, in addition to one that appears at $\theta = 70°$, and 0.5D below the free end of the circular cylinder.

(2) The relative size of the horseshoe vortices to the height of the cylinder decreases as the height of cylinder increases. The effect of the downwash from the free end of the circular cylinder weakens with an increase in H/D.

(3) The recirculation region behind the circular cylinder enlarges with an increase in H/D. But the length of the recirculation region near the ground plane increases in the downstream direction and reaches its maximum near $H/D = 4$. After that, the length of the recirculation region decreases as the value of H/D increases.

(4) The vortices from both sides of a circular cylinder are shed symmetrically for $H/D = 1$ and 2, and changed into antisymmetrically shed vortices at $H/D = 4 \sim 7$. The Strouhal number decreases as the value of H/D increases in the region of symmetrical vortex shedding, and reaches a minimum value at $H/D = 3 \sim 4$, and furthermore it increases with an increase in H/D in the region of the antisymmetric vortex shedding.

(5) The rate of decay of the turbulent eddies slows near the free end of the cylinder and the average scale of eddies enlarges for a circular cylinder of $H/D = 2$ as compared with those in other positions. On the other hand, antisymmetric vortex disappear and symmetric row vortices are generated near the free end for a circular cylinder of $H/D = 7$.

Furthermore, the rate of decay of the turbulent eddies is rapid in the region of antisymmetric vortex shedding, but slow near the free end. Therefore, the average scale of the eddies tends to enlarge near the free end in the lengthwise direction.

(6) Antisymmetric vortices decay rapidly in the turbulent near wake as compared with symmetric vortices.

(7) The average scale of the turbulent eddies is small and constant in the region of periodic vortex shedding, but it becomes larger and the rate of decay of turbulent eddies is slower in the region of the decay of periodic vortices. The average scale of the turbulent eddies enlarges as the downstream distance and the value of H/D increase.

(8) The effect of the downwash from the free end on the velocity defect and turbulence intensities of the wake flow is predominant for the cases of $H/D = 1$ and 2. The Z-component of turbulence intensity becomes larger than the X-component. Therefore, the wake descends and spreads transversely with an increase in the downstream distance. However, for the case of $H/D = 4$ and 7, the effect of the downwash is weak, and the Y-component of turbulence intensity becomes large in the whole region of the wake. It follows that the tendency of the wake to spread transversely is stronger than the tendency of the wake to descend along the ground plane.

References

Etzold, F., and Fiedler, S., 1976, "The Near-Wake Structure of a Cantilevered Cylinder in a Cross Flow," *Zeitshrift für Flugwiss Weltraum-forsch*, Vol. 24, pp. 77–82.

Farell, C., Carrasquel, S., Güben, O., and Patel, V. C., 1977, "Effect of Wind Tunnel Walls on the Flow Past Circular Cylinders and Cooling Towers Models," ASME JOURNAL OF FLUIDS ENGINEERING, Vol. 99, pp. 470–479.

Farivar, Dj, 1981, "Turbulent Uniform Flow Around Cylinders of Finite Length," *AIAA Journal*, Vol. 19, pp. 275–281.

Hoerner, S. F., 1958, "Fluid-Dynamic Drag," pp. 3.8–3.9.

Okamoto, S., 1982, "Turbulent Shear Flow Behind Hemisphere-Cylinder Placed on Ground Plane," *Turbulent Shear Flows*, Vol. 3, Springer-Verlag, Berlin, Heidelberg, New York, pp. 171–185.

Okamoto, T., and Yagita, M., 1973, "The Experimental Investigation on the Flow Past a Circular Cylinder of Finite Length," *Bulletin of Japan Society of Mechanical Engineers*, Vol. 16, pp. 805–814.

Savory, E., and Toy, N., 1986, "The Flow Regime in the Turbulent Near Wake of a Hemisphere," *Experiments in Fluids*, Vol. 4, pp. 181–188.

Slaouti, A., and Gerrard, J. H., 1981, "An Experimental Investigation of the End Effects on the Wake of a Circular Cylinder Towed through Water at Low Reynolds Numbers," *Journal of Fluid Mechanics*, Vol. 112, pp. 297–314.

Taniguchi, S., et al., 1980, "Flow Around a Circular Cylinder of Finite Height Placed Vertically in Turbulent Boundary Layer," *Transactions of Japan Society of Mechanical Engineers*, (in Japanese), Vol. 46, 405B, pp. 802–811.

Shimizu, M., 1988, *Visualized Flow*, Edited Japan Society of Mechanical Engineers, Pergamon Press, pp. 54–55.

Redeveloping Turbulent Boundary Layer in the Backward-Facing Step Flow

Jung Yul Yoo
Professor,
Department of Mechanical Engineering,
College of Engineering,
Seoul National University,
Seoul 151-742, Korea.
Mem. ASME

Se Jin Baik
Senior Researcher,
Korea Atomic Energy Research Institute,
Taejon 305-353, Korea

An experimental study has been performed to investigate the redeveloping turbulent boundary layer beyond separation-reattachment for a transitional separated flow. By considering the distribution of the intermittency, it has been confirmed that the turbulent structure changes gradually from a mixing layer to a turbulent boundary layer downstream of reattachment. The balances of the respective terms in the turbulent kinetic energy transport equation are evaluated from the energy dissipation rate obtained through numerical integration of the second moment of the energy spectrum. These terms together with those in the shear stress transport equation indicate the recovery process of the redeveloping boundary layer from nonequilibrium to equilibrium.

Introduction

Flow fields containing turbulent separation and reattachment regions are very important in engineering applications. Such flows can be observed in diffusers, combustors, turbomachinery, and around wings or buildings. In particular, the flow over a backward-facing step is associated with a simple geometry, where the separation line is nearly straight and the separation point is fixed at the step corner. However, the flow structure is fairly complicated, especially the redeveloped boundary layer.

In general, the separation-reattachment turbulent flow can be divided into the boundary-layer flow before separation, the separated shear layer, a reattachment region, and the redeveloping boundary-layer flow (see Bradshaw and Wong, 1972). In the downstream region after reattachment the mean velocity distribution slowly recovers the form of an equilibrium boundary layer. During this process the flow in the inner region near the wall reaches equilibrium rapidly, while the flow in the outer region experiences a much slower change. In other words, the regular logarithmic region grows in the inner region of the boundary layer, whereas a "dip" below the "universal logarithmic law" is seen in the outer region which slowly disappears as we move downstream (see Kim et al. 1980; Chandrsuda and Bradshaw, 1981; and Pronchick and Kline, 1983).

Until recently, most experimental studies were confined to the recirculating flow and the reattachment flow with less attention being paid to the redeveloping boundary layer. The primary objective of the present paper is to investigate the structure of the redeveloping turbulent boundary layer and its change from nonequilibrium to equilibrium flow structure. In a sense, the present study may be regarded as a supplement to those of Bradshaw and Wong (1972), and Chandrsuda and Bradshaw (1981). The former investigated the relaxation of the redeveloping boundary layer up to 52 step heights, mainly with mean velocity measurements (including only a few turbulence measurements) while the latter studied the turbulence structure of a reattaching mixing layer up to 12 step heights downstream of the step.

Experimental Apparatus and Methods

The wind tunnel used in the experiment was a closed circulation Göttingen type made of steel, with test section dimensions of 900 mm X 900 mm X 3600 mm. The mean velocity was 20 m/s, with discrepancy from uniformity of 0.3 percent and turbulence level order of 0.2 percent throughout the test section. The two-dimensional model used for generating the flow over a backward-facing step was assembled by attaching half of a 4:1 elliptical body with 100 mm long radius and 25 mm short radius to the leading edge of a flat plate with 10 mm thickness and 1100 mm length, as shown schematically in Fig. 1. The location of the step from the model leading edge was 100 mm. The width of this model was 860 mm and thus the aspect ratio of the step height to width was 1:43. This model was carefully and firmly fixed in the mid-section of the wind tunnel with the leading edge located at 1800 mm downstream of the test section inlet so that the static pressure distributions on the top and bottom surfaces of the left and right sides of the plate were coincident. Half of this symmetric model is similar to the model Bradshaw and Wong (1972) used in their backward-facing step study. In the present work the height of the contraction exit over the step was the order of 42.5 cm, compared to the step height of 2 cm. This experimental arrangement reduced the tunnel roof effect to better simulate infinite-stream conditions. For comparison, a step of 2.5 cm and a contraction exit of 10 cm height was used by Bradshaw and Wong (1972), while a step of 5.1 cm with a contraction exit of 7.6 cm was utilized by Chandrsuda and Bradshaw (1981).

Contributed by the Fluids Engineering Division for publication in the JOURNAL OF FLUIDS ENGINEERING. Manuscript received by the Fluids Engineering Division June 5, 1991. Associate Technical Editor: D. M. Bushnell.

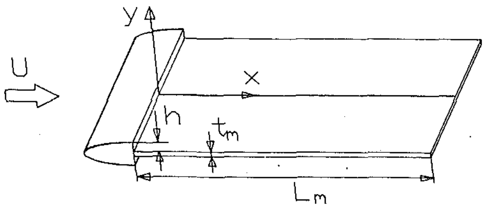

Fig. 1 Experimental configuration

The static pressure distributions were measured by using a Scanivalve (Model J) and YEW digital pressure gage connected to 24 pressure holes of 1 mm diameter on each side of the plate along the flow direction at a distance of 200 mm from the center plane of the model.

The oil dot flow visualization method was used to confirm the location of the reattachment point and the two-dimensionality of the flow. The oil dots were made of a mixture composed of oleic acid, paraffin oil and carbon powder and placed on the plate in a regular array. Two-dimensionality of the flow was observed over the central 56 cm part of the plate. As would be expected, three dimensional flows were detected very near the sides of the plate adjacent to the tunnel wall. In the present study velocity measurements were made on the center plane of the test model. A stagnation-static Pitot tube (United Sensors) of 1.8 mm outside diameter was used to measure the mean velocity at different locations downstream of the step. A Pitot tube of 0.6 mm outside diameter was used near the plate. Measurements were made at x/h = 0, 1, 2, 3, 4, 5, 6, 7, 8, 9, 10, 11, 12, 13, 14, 15, 17, 19, 21, 23, 25, 30, 35, 40, 45, and 50. In addition, the mean velocities U and V, and the fluctuation velocities u and v were measured at the same locations using DISA 55P63 cross wire probes, two channel Kanomax 1010 constant temperature anemometers, Kanomax 1013 linearizers and an analog adder/subtracter. Turbulent stresses $\overline{u^2}$, $\overline{v^2}$ and $\overline{uv}$ were obtained from a Kanomax 1075 rms meter and an analong multiplier equipped with a Kanomax 1019 signal processor. To obtain the third order moments $\overline{u^3}$, $\overline{u^2v}$, $\overline{uv^2}$ and $\overline{v^3}$, the signals of u and v were first changed into digital signals simultaneously by using a two channel A/D converter with 12 bit and 1 μs conversion time (Iwatsu SM-2100 signal analyzer) and then stored for numerical calculations. To obtain intermittency data, signals of uv from the analog multiplier were changed into digital signals by using an A/D converter and then stored for numerical calculations. The one-dimensional turbulent energy spectrum of u was also obtained from the signal analyzer. The reverse flows were not measured because the hot-wire probes would affect the flow resulting in uncertain measurements.

Data were taken over a 40 minute time period at a fixed streamwise location. The corresponding temperature rise in the wind tunnel was only about 0.5°C and therefore temperature compensation of the hot-wire anemometer was not considered. The maximum ratio of rms u-component intensity to mean velocity in the present experiment, excluding the recirculating region, was approximately 0.25. Chandrsuda and Bradshaw (1981) argue that hot-wire measurements are likely to be reliable only if the ratio of rms u-component intensity to mean velocity is less than about 0.3. Therefore, compensation with respect to turbulent intensity was also not considered. Calibrations of the hot-wire anemometers were made at each fixed streamwise location.

Intermittency can be determined via two methods, utilizing either temperature fluctuations or velocity fluctuations. The present study utilized the latter method, in particular the instantaneous product uv. This method was utilized by Castro (1973), verified in detail by Muck (1980) and Murlis et al. (1982), and adopted also by Chandrsuda and Bradshaw (1981). According to this method, the intermittency was determined by classifying turbulence or non-turbulence to the extent that the instantaneous values of $\partial uv/\partial t$ and $\partial^2 uv/\partial t^2$ were larger or smaller than respective threshold values. More specifically, the threshold value for $\partial uv/\partial t$ was set as 0.24 times the rms value of $\partial uv/\partial t$ (th1), and that for $\partial^2 uv/\partial t^2$ was set as 0.28 times the rms value of $\partial^2 uv/\partial t^2$ (th2). The signals of uv were sampled 1000 times at intervals of 24 μs. For each interval the state was classified into turbulent or non-turbulent, and then the isolated states not lasting more than 96 μs were simply neglected under the assumption that these were electrical noises.

The lower limit of the integral for the one-dimensional energy spectrum was determined by the signal analyzer to be approximately 5 ~ 6 Hz. This value is irrelevant to $\overline{u^2}$, $\overline{v^2}$ and $\overline{uv}$ because they were measured with the analog signal in the multimeter. Below this lower limit F_{11} (n) was assumed to be

Nomenclature

C_f = coefficient of skin friction
C_p = pressure coefficient
F_{11} (n), F_{11} (k) = one-dimensional energy spectrum of u
G = Clauser parameter
H = shape factor
h = step height
IR = retail intermittency
IW = wholesale intermittency
k = turbulent kinetic energy
k_1 = the wave number in x-direction
n = frequency
P, p = mean and fluctuation pressures, respectively
U, u = x-components of mean and fluctuation velocities, respectively
U_0 = reference velocity
U_i, u_i = components of mean and fluctuation velocities, respectively
u_τ = friction velocity
u^+ = U/u_τ = dimensionless mean velocity based on u_τ
V, v = y-components of mean and fluctuation velocities, respectively
x, x_1 = streamwise coordinate
x_R = reattachment length
y = transverse coordinate
y^+ = $(yu_\tau)/\nu$ = dimensionless transverse coordinate
γ = intermittency
δ = boundary layer thickness at which U/U_0 equals to 0.995
δ_1 = displacement thickness
δ_r = equilibrium boundary layer thickness corresponding to the same momentum thickness as in the present experiment
ϵ = dissipation rate of the turbulent kinetic energy
ν = kinematic viscosity
θ = momentum thickness
ρ = density
τ = shear stress

constant by considering the general trend of the one-dimensional energy spectrum. Although the energy level in the low frequency region is high, the band width from 0 to this lower limit is narrow. The upper limit of the integral for the one-dimensional energy spectrum was taken to be 10 kHz. Thus, the selection interval bounded by both limits and the assumption on the value of $F_{11}(n)$ below the lower limit were judged to be appropriate because the difference between the value of $\overline{u^2}$ measured by the rms meter and that obtained by taking the following integral

$$\overline{u^2}=\int_0^{\infty} F_{11}\ (n)dn \approx \int_0^{10\ kHz} F_{11}\ (n)dn \tag{1}$$

was less than 3 percent. Based on Taylor's hypothesis, the conversion from frequency n to wave number k_1 was made through the relation $k_1 = \frac{2\pi n}{U_1}$. Therefore, the definition of the one-dimensional energy spectrum was given by

$$F_{11}(k_1)=\frac{U_1}{2\pi}F_{11}(n) \tag{2}$$

Assuming locally isotropic turbulence, the energy dissipation rate ϵ can be written as follows (see Hinze, 1975):

$$\epsilon = 15\ \nu\ \overline{\left(\frac{\partial u_1}{\partial x_1}\right)^2} \tag{3}$$

Therefore, ϵ can now be obtained by the second moment of the energy spectrum (see Champagne, 1978):

$$\epsilon = 15\nu \int_0^{\infty} k_1^2 F_{11}\ (k_1)dk_1 \tag{4}$$

In the present study, the energy spectrum $F_{11}\ (k_1)$ was obtained by the signal analyzer using the FFT algorithm and the energy dissipation rate was obtained through numerical integration.

Measurements of the third order moments $\overline{u^3}$, $\overline{u^2v}$, $\overline{uv}$, and $\overline{v^3}$ were made by sampling the fluctuation signals of u and v 1000 times at intervals of 24 μs, taking triple products and averaging over them, and then repeating this procedure 5 times and taking a final overall average. The deviation in the distribution of these third order moment data was about 50 percent near the wall and in the outer region where the magnitudes were comparably small, while it was about 20 percent in the intermediate region of the boundary layer where the magnitudes were large. In the outer region of the redeveloping boundary layer where the characteristics of the mixing layer still persist, the turbulence level may be low but large eddies of very low frequency may be relatively dominant. Thus, the large deviation in the outer region may have been caused by the insufficient sampling period of 24 ms for very low frequency components, which can lead to a substantial error. However, the present sampling technique is thought to be tolerable, since the low frequency components are not dominant through the boundary layer except for a part of the outer region. The selection time of 24 μs and the duration of 24 ms were determined by considering the entire region of the boundary layer and the memory capacity of the experimental apparatus.

The estimated uncertainties of the measured quantities are shown in Table 1.

Experimental Results and Discussions

All measurements in this experimental study were made at the mean tunnel velocity of 20 m/s. The location of the reattachment point, confirmed through the oil dot flow visualization method, was maintained consistently between $x_R = 6h$ and $7h$, i.e., $x_R \approx 6.5h$, except in the vicinity of both sides of the plate. The flow was seen to be directed nearly parallel to the x-axis in the redeveloping boundary layer after the reattachment point. The boundary layer over the step edge was transitional and about 2 mm thick, with a local stream velocity of 23 m/s. The experimental data at $x/h = 0$ are shown in Table 2 and those at other measuring points can be found in Baik (1989). The fact that this flow belongs to the regime of transitional separated flow plus turbulent reattachment flow can be also verified from the chart of Adams et al. (1984) for separated and reattached flow regimes. As shown in Fig. 2, the boundary layer thickness δ, defined by the distance from the plate where $U/U_0 = 0.995$, increased steadily after reattachment, while the displacement thickness δ_1 and the momentum thickness θ initially decreased until $x/h = 16$ and $x/h = 20$, respectively, before they began increasing. Particularly, it is noted that the boundary layer thickness δ in the present study is much thicker than the usual equilibrium turbulent boundary layer thickness δ_r corresponding to the same momentum thickness θ. The difference between δ and δ_r is almost constant after $x/h = 35$.

In Fig.3, the distribution of the normalized wall static pressure $(C_p - C_p,\ \min)/(1 - C_p,\ \min)$ as defined in Castro and Haque (1987) is compared with some existing experimental results, which were obtained under different experimental geometries and conditions. The present result shows that the maximum of C_p occurs at $x/h = 8$, slightly downstream of reattachment, which is in qualitative agreement with other results. The reason why C_p still increases after reattachment can be explained by considering the x-momentum equation near the plate:

$$\frac{1}{\rho}\left(\frac{\partial p}{\partial x}\right)=\frac{\partial \tau}{\partial y} \tag{5}$$

In the reattachment region the shear stress increases with y from the value for a boundary layer to that for a mixing layer. Therefore, $\partial\tau/\partial y$ is positive and hence the wall pressure increases with x. On the other hand, after $x/h = 15$, C_p is nearly constant and the effect of the pressure gradient can be negligible.

In Fig. 4, the profiles of u^+ downstream of the reattachment are plotted against y^+, where the wall shear stress, u_τ, was determined by forcing data points to match the logarithmic profile ($u^+ = (1/0.41)\ \ln y^+ + 5.0$) over the range of $50 <$

Table 1 The estimated uncertainties of measured quantities

Measured quantity	Uncertainty estimate	Remarks
U and V	± 0.02	hot wire measurements
$\overline{u^2}$, $\overline{v^2}$ and $\overline{uv}$	$\pm\ 0.03$	
$F_{11}\ (n)$	± 0.06	$\int_0^{10kHz} F_{11}(n)\ dn \approx \overline{u^2}$ within 3 percent
$\overline{u^3}$, $\overline{u^2v}$, $\overline{uv^2}$ and $\overline{v^3}$	± 0.2 ± 0.5	where the magnitudes are large where the magnitudes are small
γ	± 0.05	for $U/U_0 > 0.7$
P	less than 1 percent	
x	± 1 mm	
y	± 0.1 mm	

Table 2 Experimental data at $x/h=0$

y(mm)	U (m/s)	V (m/s)	$\sqrt{\overline{u^2}}$ (m/s)	$\sqrt{\overline{v^2}}$ (m/s)	$\overline{uv}$ (m/s)
0.50	2.996	−0.249	0.682	0.340	−0.254
1.00	9.181	−0.262	0.808	0.113	−0.019
1.50	19.424	−0.373	0.534	0.113	−0.006
2.00	22.917	−0.497	0.259	0.146	0.000
2.50	23.276	−0.400	0.146	0.081	0.013
3.00	23.193	−0.262	0.162	0.113	0.019
3.50	23.179	−0.179	0.178	0.097	0.013
4.00	23.124	−0.083	0.146	0.065	0.013
4.50	23.097	−0.014	0.162	0.081	0.013
5.00	23.110	−0.014	0.146	0.081	0.019
5.50	23.083	−0.009	0.146	0.081	0.013
6.00	23.069	−0.019	0.146	0.097	0.013
6.50	23.000	−0.024	0.146	0.081	0.019

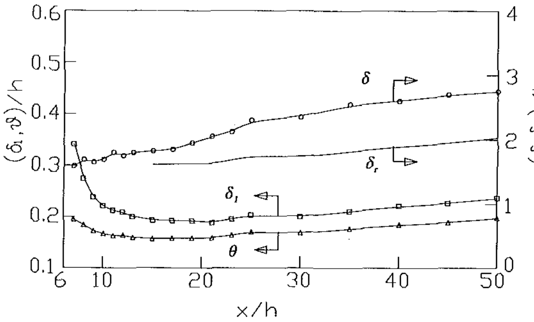

Fig. 2 Boundary layer, displacement, and momentum thicknesses in the redeveloping boundary layer

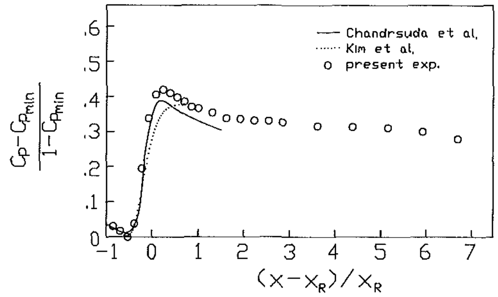

Fig. 3 Distribution of the pressure coefficient: ———— , Chandrsuda and Bradshaw (1981); ------, Kim et al. (1980); o, present experiment

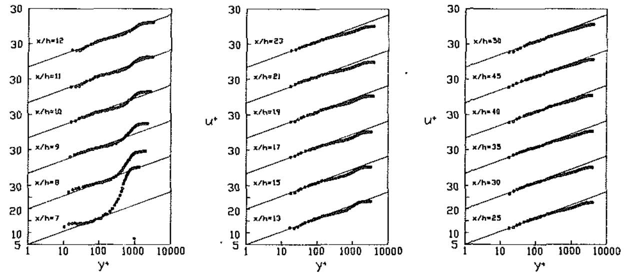

Fig. 4 Mean velocity profiles represented in the semilogarithmic plot

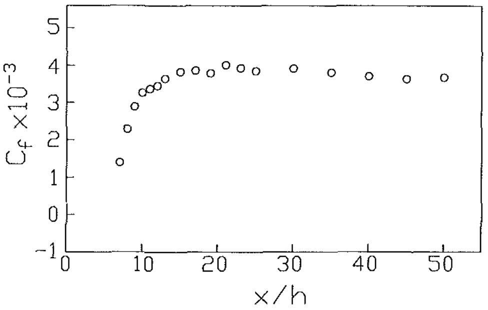

Fig. 5 Distribution of the skin friction

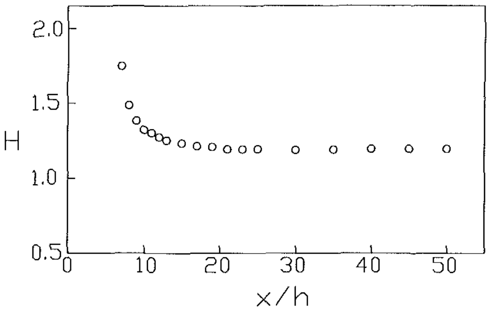

Fig. 6 Distribution of the shape factor

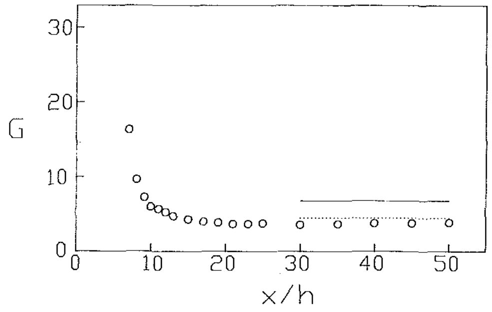

Fig. 7 Distribution of the Clauser parameter: ———— , equilibrium boundary layer data of Coles (1962) ($G=6.8$); -----, purely logarithmic profile data of Bradshaw and Wong (1972) ($G=4.5$); o, present data ($G=3.7$)

$y^+<150$ (Kim et al. (1980) and Chandrsuda and Bradshaw (1981)). The velocity very near the wall increases rapidly, but the velocity recovery is slow in a region slightly farther from the wall. Thus, the mean velocity gradient prominently decreases in the inner region where y^+ is greater than 100, and the mean velocity profile shows a "dip" below the logarithmic profile. As we move downstream, the region matching with the log law is gradually recovered such that the limit of y^+ for this region is extended up to approximately 500 at $x/h = 25$. However, the recovery of the velocity defect is so slow in the outer region that even at $x/h = 50$ the wake structure is not of the form typical in the ordinary equilibrium turbulent boundary layer.

The friction coefficient C_f as deduced from the mean velocity profiles is shown in Fig. 5. After reattachment at $x/h \approx 7$, C_f rapidly increases, reaches a maximum at $x/h \approx 20$ and then decreases gradually to 0.0036 at $x/h = 50$.

The distribution of the shape factor H is plotted in Fig 6. We observe that H decreases rapidly after the reattachment region where the redeveloping boundary layer starts to grow. But after $x/h = 25$ it maintains a constant value 1.20 which is less than 1.29 for one-seventh-power law velocity distribution. In Fig. 7, the distribution of the Clauser parameter G defined by the following equation is plotted:

$$G=\frac{\displaystyle\int_0^1 \frac{(U_0-U)^2}{u_\tau^2}\, d\left(\frac{y}{\delta}\right)}{\displaystyle\int_0^1 \frac{(U_0-U)}{u_\tau}\, d\left(\frac{y}{\delta}\right)} \tag{6}$$

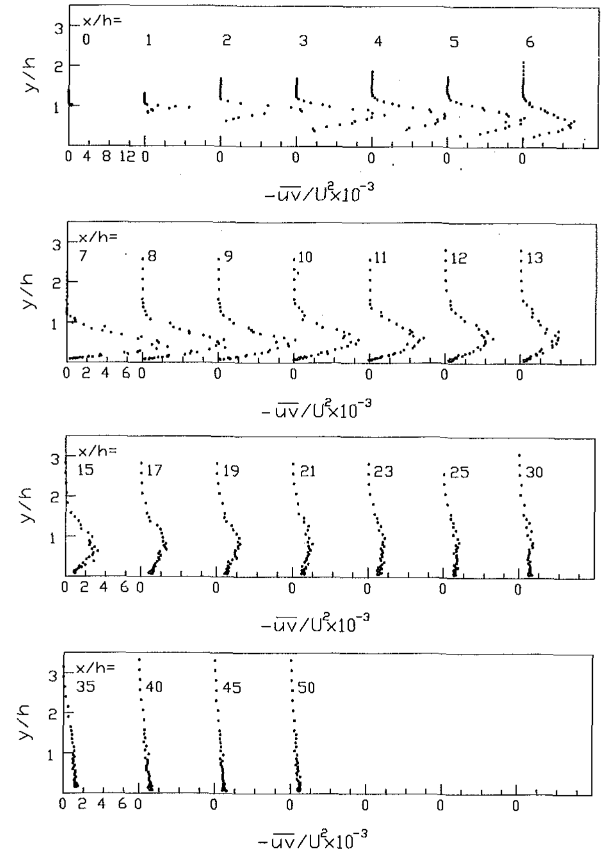

Fig. 8 Distribution of $\overline{uv}/U^2$

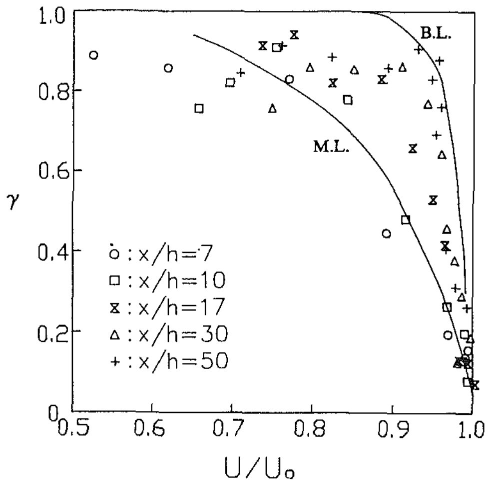

Fig. 9 Intermittency versus U/U_0, where "B.L." implies measurements of Klebanoff (1955) in a constant pressure boundary layer and "M. L." implies measurements of Antonia and Bradshaw (1971) in a mixing layer

This parameter also decreases rapidly after the reattachment region but maintains a constant value 3.7 after $x/h = 25$. It does not simply approach the value 6.8 obtained by Coles (1962) for ordinary turbulent boundary layer, but it rather approaches the value 4.5 obtained for the pure logarithmic profile (Bradshaw and Wong (1972)). The fact that G maintains a constant value in the downstream region implies that the ratio of the pressure force in the boundary layer to the friction force on the wall is constant and that a balance is maintained between these two forces.

Turbulence intensity increased greatly along the flow direction in the separated shear flow before reattachment, and began decreasing shortly before reattachment. The distributions of $\overline{u^2}$, $\overline{v^2}$ and $\overline{uv}$ changed from mixing layer to boundry-layer type along the flow direction. However, to conserve space, in Fig. 8 only the distributions of $\overline{uv}$ are illustrated. For more detailed discussion, including the distributions of $\overline{u^2}$ and $\overline{v^2}$, reference should be made to Baik (1989). The location of the maximum point of $\overline{uv}$ at each cross-section initially approaches the plate but after reattachment it moves farther away from the wall and the maximum value of $\overline{uv}$ decreases, so that after $x/h = 35$ the distribution of $\overline{uv}$ shows characteristics typical of an equilibrium turbulent boundary layer without any pressure gradient where the value of $\overline{uv}$ decreases monotonically from the wall.

In the redeveloping boundary layer after reattachment, the flow near the wall displays the characteristics of the boundary layer while the flow away from the wall displays the characteristics of the mixing layer developed in the separated flow region. Therefore, the intermittency at each streamwise location should display an intermediate characteristic between the boundary layer and mixing layer cases. Figure 9 shows the intermittency obtained by the method described in the previous section. It is readily seen that the distribution of the intermittency, being nearly the same as a mixing layer at $x/h = 7$, approaches the boundary layer case as we move downstream and finally becomes quite similar to a boundary layer at $x/h = 50$. The intermittency at $x/h = 30$ is seen to be closer to that of the boundary layer (Klebanoff, 1955). This is in contrast to the result of Bradshaw and Wong (1972) as their intermittency at $x/h = 30$ was closer to that of the mixing layer (Antonia and Bradshaw (1971)). This suggests that the recovery to the equilibrium boundary layer in the present study takes place at a faster rate than in Bradshaw and Wong, which may have to do with the different experimental geometries and conditions.

Turbulence models which are adopted in Reynolds-averaged calculations of turbulent flows usually involve constants or approximate expressions based on experimental results for equilibrium shear layer flows. Therefore, they may not be appropriate for nonequilibrium flows such as treated in the present study. To select more appropriate turbulence models and to develop better numerical algorithms, it is highly desirable to estimate terms of the transport equations for the turbulent quantities. The transport equation for the turbulent kinetic energy is as follows:

$$\underbrace{\left(U\frac{\partial k}{\partial x}+V\frac{\partial k}{\partial y}\right)}_{\text{convection}}+\underbrace{\left(\overline{uv}\left(\frac{\partial U}{\partial y}+\frac{\partial V}{\partial x}\right)+(\overline{u^2}-\overline{v^2})\frac{\partial U}{\partial x}\right)}_{\text{production}}$$

$$+\underbrace{\left(\frac{\partial}{\partial x}\left(\frac{\overline{pu}}{\rho}+\overline{ku}\right)+\frac{\partial}{\partial y}\left(\frac{\overline{pv}}{\rho}+\overline{kv}\right)\right)}_{\text{diffusion}}+\underbrace{\epsilon}_{\text{dissipation}}=0 \qquad (7)$$

To evaluate the magnitude of respective terms, the first three terms are usually obtained experimentally and then the dissipation term is calculated as a closure term (see Hanjalic and Launder, 1972). In estimating the diffusion term, it is further assumed that the pressure fluctuation term is small compared with other terms and only the term involving $\overline{kv}$ is considered which is obtained from the third order correlations (see Harsha, 1977, and Chandrsuda and Bradshaw, 1981). In the present study the convection and production terms are obtained directly from experiment and the dissipation term is obtained exactly by integrating the dissipation energy spectrum, whereas the diffusion term is calculated in its entirety as a closure term. In addition, the turbulent kinetic energy is approximated by the following formula (Chandrsuda and Bradshaw, (1981):

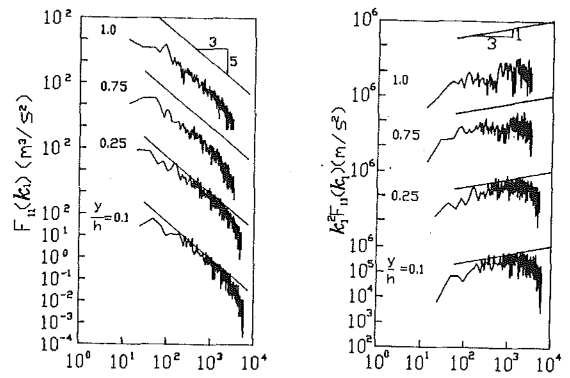

(a) $x/h=7$

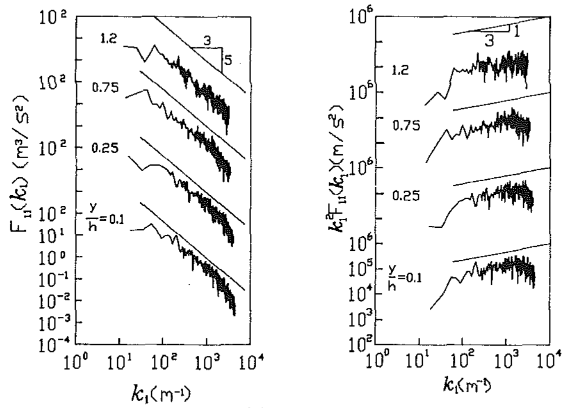

(b) $x/h=10$

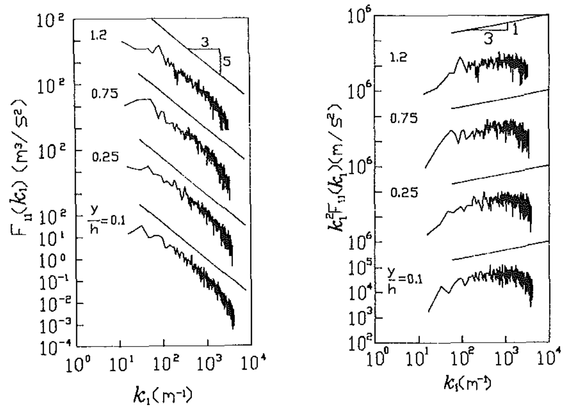

(c) $x/h=17$

$$k=\frac{1}{2}\left(\overline{u^2}+\overline{v^2}+\overline{w^2}\right)=\frac{3}{4}\left(\overline{u^2}+\overline{v^2}\right) \qquad (8)$$

and the spatial differentiation is taken after obtaining an approximate expression through the least squares method.

As a preliminary step toward evaluating the dissipation term, the one-dimensional energy spectrum and the dissipation energy spectrum were measured and calculated at different streamwise locations downstream of the backward-facing step, as shown in Fig. 10. As we move away from the wall at each streamwise location, the magnitude of the one-dimensional energy spectrum decreases and the distribution against wave number also shifts from large wave number to small wave number. Since small wave numbers imply large eddies, x/h = 7 and 10, immediately after reattachment, small size eddies are known to be decaying with distance from the wall. In

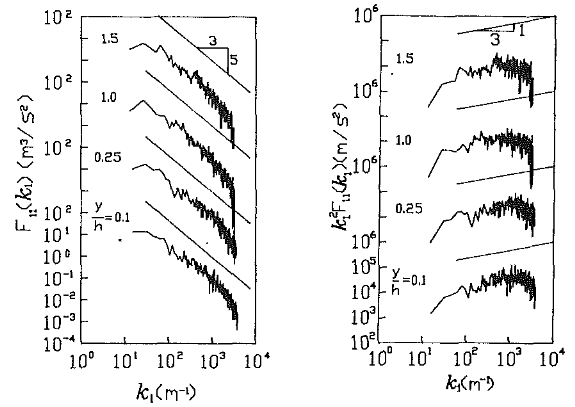

(d) $x/h=30$

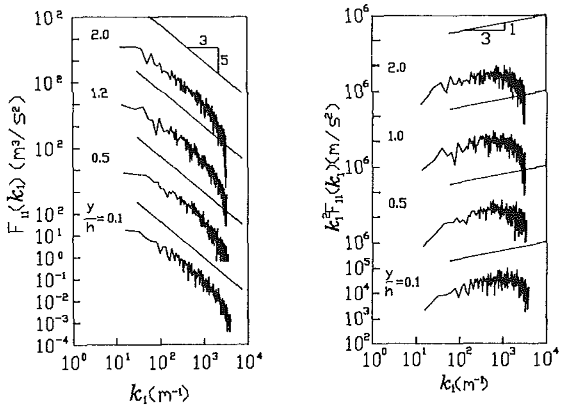

(e) $x/h=50$

Fig. 10 One-dimensional energy and dissipation spectra: *(a)* $x/h=7$, *(b)* $x/h=10$, *(c)* $x/h=17$, *(d)* $x/h=30$, *(e)* $x/h=50$

addition, it is confirmed that an inertial subrange satisfying the Kolmogoroff − 5/3 law exists for the energy spectrum. In the wave number range corresponding to the inertial subrange, the dissipation spectrum increases with a slope of 1/3, reaches a maximum and decreases at a larger wave number range. Thus, it is believed that the wave number range in the present measurement is appropriate.

With the energy dissipation rate ϵ obtained through the numerical integration of Eq. (4), Fig. 11 illustrates the behaviors of the respective terms of Eq. (7). At x/h = 7 the characteristics of a mixing layer developed in the upstream region are prevalent due to the very large convection and diffusion terms, while the production term attains its maximum at $y/h=0.3$ with very small values near the wall. However, near the wall the dissipation term is very large and balanced with the diffusion term, indicating nonequilibrium. Similar trends can be found at x/h = 10. It is quite noteworthy that the present data at x/h = 10 agree qualitatively with the results of Chandrsuda and Bradshaw (1981) at x/h = 8.4 (see their Fig. 14(*c*)), although we used a different approach for evaluating the dissipation term. Therefore, further turbulence measurements are highly desirable, where the dissipation term is obtained through direct integration of the dissipation energy spectrum. As we move farther downstream, the production term near the wall is recovered so that at x/h = 30 it attains a maximum near the wall. In particular, until x/h = 15, the magnitude of the production term $(\overline{u^2}-\overline{v^2})\,\partial U/\partial x$ is not negligible near the wall, unlike the ordinary turbulent boundary layer. At x/h = 50, the production and dissipation terms are balanced, maintaining an equilibrium state and displaying similar distributions to the typical equilibrium turbulent boundary layer.

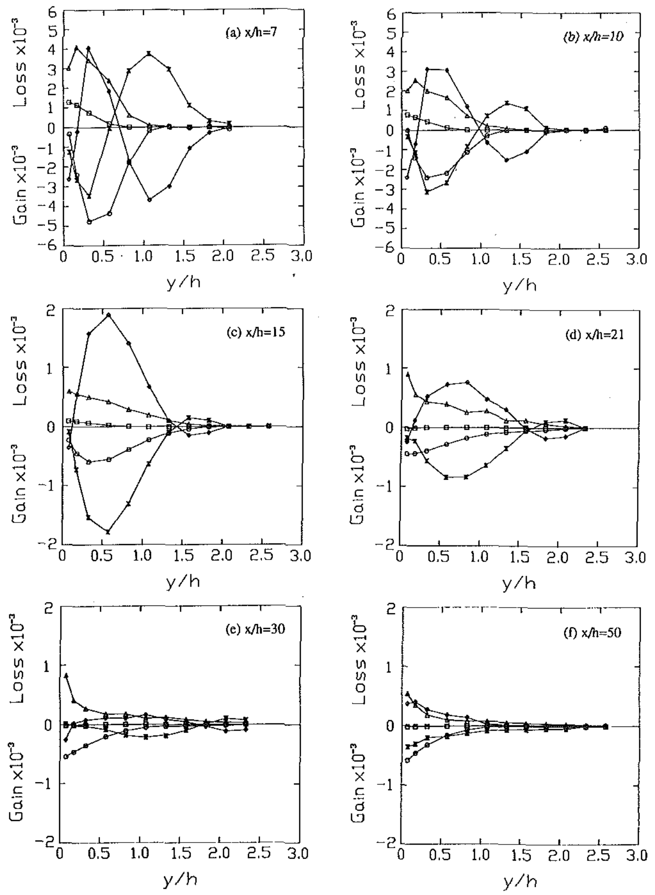

Fig. 11 Turbulent energy balances, where all terms are nondimensionalized by

U_o^3/h (⧖, $U\frac{\partial k}{\partial x}+V\frac{\partial k}{\partial y}$; ○, $\overline{uv}\left(\frac{\partial U}{\partial y}+\frac{\partial V}{\partial x}\right)$; □, $(\overline{u^2}-\overline{v^2})\frac{\partial U}{\partial x}$; ◇, $\frac{\partial}{\partial x}\left(\frac{\overline{pu}}{\rho}+\overline{ku}\right)+\frac{\partial}{\partial y}\left(\frac{\overline{pv}}{\rho}+\overline{kv}\right)$; △, ϵ): *(a) x/h* = 7, *(b) x/h* = 10, *(c) x/h* = 15, *(d) x/h* = 21, *(e) x/h* = 30, *(f) x/h* = 50

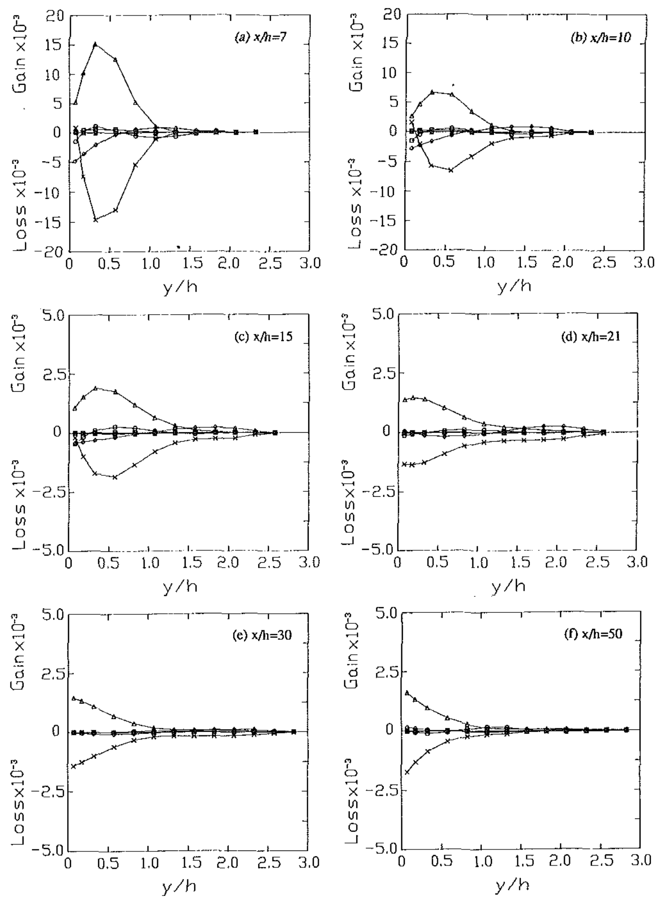

Fig. 12 Shear stress balances, where all terms are nondimensionalized by

U_o^3/h (○, $U\frac{\partial\overline{uv}}{\partial x}+V\frac{\partial\overline{uv}}{\partial y}$; □, $\overline{u^2}\frac{\partial V}{\partial x}$; △, $\overline{v^2}\frac{\partial U}{\partial y}$; ⧖, $\frac{\partial\overline{u^2v}}{\partial x}$; ◇ $\frac{\partial\overline{uv^2}}{\partial y}$; ×, $-\frac{1}{\rho}\overline{p\left(\frac{\partial u}{\partial y}+\frac{\partial v}{\partial x}\right)}$): *(a) x/h* = 7, *(b) x/h* = 10, *(c) x/h* = 15, *(d) x/h* = 21, *(e)* × */h* = 30, *(f) x/h* = 50

The transport equation for the turbulent shear stress is as shown below:

$$\underbrace{\left(U\frac{\partial\overline{uv}}{\partial x}+V\frac{\partial\overline{uv}}{\partial y}\right)}_{\text{convection}}+\underbrace{\left(\overline{u^2}\frac{\partial V}{\partial x}+\overline{v^2}\frac{\partial U}{\partial y}\right)}_{\text{generation}}+\underbrace{\left(\frac{\partial\overline{u^2v}}{\partial x}+\frac{\partial\overline{uv^2}}{\partial y}\right)}_{\text{turbulent diffusion}}-\underbrace{\frac{1}{\rho}\overline{p\left(\frac{\partial u}{\partial y}+\frac{\partial v}{\partial x}\right)}}_{\text{pressure-strain}}+\underbrace{\frac{1}{\rho}\left(\frac{\partial\overline{pv}}{\partial x}+\frac{\partial\overline{pu}}{\partial y}\right)}_{\text{pressure-diffusion}}=0 \quad (9)$$

Figure 12 illustrates the behaviors of respective terms of the above equation, which were measured and calculated at different downstream locations after reattachment. The convection, generation and turbulent diffusion terms are obtained from experiment, while the pressure-diffusion term is neglected and the pressure-strain term is obtained by balancing it with the rest of the terms of Eq. (9). As mentioned in the last part of the previous section, the measurements of the third order moment may involve large errors. Therefore it is not difficult to understand that the turbulent diffusion term obtained by using the third order moment involves a larger error, when compared with other terms. At $x/h = 7$ the generation and pressure-strain terms attain their maxima at $y/h = 0.3$ away from the wall, while the generation and diffusion terms are well-balanced with each other near the wall. As we move farther downstream, and maximum points of the generation and pressure-strain terms approach closer to the wall and the magnitudes of the convection and diffusion terms decrease gradually so that at $x/h = 30$ the generation and pressure-strain terms are nearly balanced with each other and at $x/h = 50$ a typical equilibrium turbulent boundary layer distribution is almost recovered.

A numerical study to compare the predictions of dissipation rate and the individual terms in the turbulent kinetic energy equation is being performed. Preliminary calculations (Baik, 1989) using the standard $k-\epsilon$ model and the Reynolds stress models proposed by Launder et al. (1975) and Daly and Harlow (1978) all predict shorter reattachment lengths than the experimental results. The present experimental study is expected to provide useful information for further research on improved turbulence models and numerical methods.

Conclusion

An experimental study has been performed to investigate a redeveloping turbulent boundary layer downstream of reattachment for a backward-facing step with transitional separated flow. The wall pressure continues to increase even slightly after reattachment, reaches a maximum at $x/h = 8$ and then decreases. The dip below the universal law of the wall occurring after reattachment is gradually recovered so that at $x/h = 25$, the region satisfying the law of the wall is extended up to $y^+ = 500$. However, in the outer region the effect of the upstream mixing layer still exists so that even at $x/h = 50$ the wake form of the equilibrium turbulent boundary layer is not obtained.

The wall friction coefficient C_f reaches a maximum at $x/h = 20$, gradually decreases, and reaches a constant value of 0.0036. The shape factor H and the Clauser parameter G decrease rapidly after reattachment and maintain nearly constant values of 1.2 and 3.7 respectively after $x/h = 25$. The Reynolds stresses decrease monotonically from the wall only after $x/h = 35$.

In the redeveloping boundary layer far downstream from reattachment non-turbulent components carried from the upstream region are still apparent in the fluctuation velocities u and v. The distribution of the intermittency develops from a mixing layer type to a boundary layer type along the streamwise direction after reattachment. This is also consistent with the fact that small eddies are decaying with distance from the wall immediately after reattachment, which is confirmed by the analyses of the one-dimensional energy spectrum and the dissipation spectrum.

The energy dissipation rate has been obtained through numerical integration of the second moment of the energy spectrum and is used in evaluating the balances of the terms in the energy transport equation. A nonequilibrium state is shown to exist near the wall after reattachment, where the dissipation and diffusion terms of the turbulent energy transport equation are balanced with each other. The diffusion and generation terms of the shear stress transport equation are balanced near the wall immediately after reattachment. Farther downstream, the generation and pressure-strain terms are balanced so that at $x/h = 50$ an equilibrium turbulent boundary layer distribution is almost attained.

Acknowledgment

The authors wish to acknowledge the financial support they received from the Korea Science and Engineering Foundation through a grant for an Objective Basic Research Project.

References

Adams, E. W., Johnston, J. P., and Eaton, J. K., 1984, "Experiments on the Structure of Turbulent Reattachment Flow," Rep. MD-43, Thermosciences Div., Dept. of Mech. Eng., Stanford University.

Antonia, R. A., and Bradshaw, P., 1971, Imperial College, London, Aero. Rep. No. 71-04.

Baik, S. J., 1989, "A Study on the Redeveloping Turbulent Boundary Layer Beyond Separation-Reattachment" (in Korean), Ph.D. thesis, Seoul National University, Seoul.

Bradshaw, P., and Wong, F. Y. F., 1972, "The Reattachment and Relaxation of a Turbulent Shear Layer," *J. Fluid Mech.*, Vol. 52, pp. 113-135.

Castro, I. P., 1973, "A Highly Distorted Turbulent Free Shear Layer," Ph.D. thesis, Imperial College, Univ. of London, London.

Castro, I. P., and Haque, A., 1987, "The Structure of a Turbulent Shear Layer Bounding a Separation Region," *J. Fluid Mech.*, Vol. 179, pp. 439-468.

Champagne, F. H., 1978, "The Fine-Scale Structure of the Turbulent Velocity Field," *J. Fluid Mech.*, Vol. 86, pp. 67-108.

Chandrsuda, C. and Bradshaw, P., 1981, "Turbulent Structure of a Reattaching Mixing Layer," *J. Fluid Mech.*, Vol. 110, pp. 171-194.

Coles, D., 1962, RAND Corp. Rep. R-403-PR.

Daly, B. J., and Harlow, F. H., 1970, "Transport Equations in Turbulence," *Phys. Fluids*, Vol. 13, No. 11, pp. 2634-2649.

Hanjalic, K., and Launder, B. E., 1972, "A Reynolds Stress Model of Turbulence and Its Application to Thin Shear Flows," *J. Fluid Mech.*, Vol. 52, pp. 609-638.

Harsha, P. T., "Kinetic Energy Method," *Handbook of Turbulence, Vol. 1 Fundamentals and Applications*, eds., Frost, W. and Moulden, T. H., 1977, Plenum Press, New York.

Hinze, J. O., 1975, *Turbulence, Second Edition*, McGraw-Hill, New York.

Kim, J., Kline, S. J., and Johnston, J. P., 1980, "Investigation of a Reattaching Turbulent Shear Layer: Flow Over a Backward-Facing Step," ASME JOURNAL OF FLUIDS ENGINEERING, Vol. 102, pp. 302-308.

Klebanoff, P. S., 1955, NACA Rep. No. 1247.

Launder, B. E., Reece, G. J., and Rodi, W., 1975, "Progress in the Development of a Reynolds-Stress Turbulence Closure," *J. Fluid Mech.*, Vol. 68, Part 3, pp. 537-566.

Muck, K. C., 1980, "Comparison of Various Schemes for the Generation of the Turbulent Intermittency Function," *Imperial College Aero. Rep.*, No. 80-03.

Murlis, J., Tsai, H. M., and Bradshaw, P., 1982, "The Structure of Turbulent Boundary Layers at Low Reynolds Number," *J. Fluid Mech.*, Vol. 122, pp. 13-56.

Pronchick, S. W., and Kline, S. J., 1983, "An Experimental Investigation of the Structure of a Turbulent Reattaching Flow Behind a Backward-Facing Step," Rep. MD-42, Thermosciences Div., Dept. of Mech. Eng., Stanford University.

Some Characteristics of the Vortical Motions in the Outer Region of Turbulent Boundary Layers

(Data Bank Contribution*)

J. C. Klewicki

Department of Mechanical Engineering,
University of Utah,
Salt Lake City, UT 84112

R. E. Falco

J. F. Foss

Department of Mechanical Engineering,
Michigan State University,
East Lansing, MI 48824-1226

Time-resolved measurements of the spanwise vorticity component, ω_z, are used to investigate the motions in the outer region of turbulent boundary layers. The measurements were taken in very thick zero pressure gradient boundary layers (R_θ = 1010, 2870, 4850) using a four wire probe. As a result of the large boundary layer thickness, at the outer region locations where the measurements were taken the wall-normal and spanwise dimensions of the probe ranged between $0.7 < \Delta y/\eta < 1.2$ and $2.1 < \Delta z/\eta < 3.9$, respectively, where η is the local Kolmogorov length. An analysis of vorticity based intermittency is presented near $y/\delta = 0.6$ and 0.85 at each of the Reynolds numbers. The average intermittency is presented as a function of detector threshold level and position in the boundary layer. The spanwise vorticity signals were found to yield average intermittency values at least as large as previous intermittency studies using "surrogate" signals. The average intermittency results do not indicate a region of threshold independence. An analysis of ω_z event durations conditioned on the signal amplitude was also performed. The results of this analysis indicate that for decreasing R_θ, regions of single-signed ω_z increase in size relative to the boundary layer thickness, but decrease in size when normalized by inner variables.

1 Introduction

A fundamental property of all turbulent flows is an unsteady three-dimensional vorticity field. If the vortical fluid is bounded by an irrotational body of fluid, as is true (for example) for a jet, a wake or boundary layer, then it can be rationalized that a relatively thin and well-defined interface—the viscous superlayer—exists between these two domains.

The original, Corrsin (1943), and pioneering works, Townsend (1948) and Corrsin and Kistler (1955), provide both experimental observations and foundational theories for the interface and the consequences of its existence.

The basis for such an interface is most readily established in terms of the vorticity transport Eq. (1); namely,

$$\frac{\partial \tilde{\omega}_i}{\partial t} + \tilde{u}_j \frac{\partial \tilde{\omega}_i}{\partial x_j} = \tilde{\omega}_j \frac{\partial \tilde{u}_i}{\partial x_j} + \nu \frac{\partial^2 \tilde{\omega}_i}{\partial x_j \partial x_j}. \quad (1)$$

The two terms on the left of Eq. (1) represent the material derivative of the indicated vorticity components. The first term on the right is the reorientation and stretching term, while the last term on the right accounts for the diffusion of vorticity. Nonvortical fluid becomes vortical only through processes described by the viscous diffusion term in Eq. (1). Once a fluid element is vortical, processes described by the stretching and reorientation term may attenuate or amplify this existing vorticity.

Visual images (derived from relatively non-diffusive markers such as an oil fog in air or dye in water), and the inferences from probe measurements suggest that the interface is strongly convoluted with reentrant wedges (Phillips 1972). The passage of the convoluted surface past a fixed probe gives an intermittent character to such a signal. The intermittency function, $I(x,y,z,t)$, is defined such that $I(t) = 1$ if vortical fluid occupies the spatial location, and $I(t) = 0$ if the fluid is irrotational.

Corrsin and Kistler (1955), using a streamwise vorticity probe of the type designed by Kovasznay (1950), were the first to attempt to characterize the intermittent region of a boundary layer using the fundamental definition of $I(t)$. Their study was in a rough wall boundary layer at $R_\theta \approx 7900$. The detail to which their probe could resolve the structure of the viscous superlayer, was however, severely limited by its wire spacing of approximately 70 viscous units. Later studies (Kovasznay et al. 1970; Subramanian et al. 1985) have attempted to characterize outer region spanwise vorticity field, but, once again,

---

*Data have been deposited to the JFE Data Bank. To access the file for this paper, see instructions on p. 705 of this issue.

Contributed by the Fluids Engineering Division for publication in the JOURNAL OF FLUIDS ENGINEERING. Manuscript received by the Fluids Engineering Division December 30, 1991. Associate Technical Editor: D. M. Bushnell.

the probe resolution in these studies significantly limited the analysis to the characterization of larger scale motions. The recently reported measurements of Balint et al. (1991) convincingly demonstrate the capability to make vorticity measurements in a turbulent boundary layer. However, these measurements have not (to the authors' present knowledge) been used to extract intermittency information. Such measurements have, however, been reported for a shear layers. Haw et al. (1989) provide ω_z data from a high R_θ (= 78,000) single stream shear layer. These results exhibit the unexpected pattern wherein periods of non-zero but small fluctuation levels of the $\omega_z(t)$ signals are observed. It was also observed that the indicated intermittency magnitude monotonically decreased with the threshold level. It has been an "article of faith" that a "true" $I(t)$ indicator would be characterized by a plateau with respect to threshold level (i.e., $\partial\langle I\rangle/\partial s_t = 0$, where s_t = threshold level of the conditioning signal, s). The monotonic decrease of $\langle I\rangle$ with the threshold of the conditioning signal was also found in a two stream shear layer by Foss (1991) at a much smaller Reynolds number, $R_\theta = 4{,}600$.

Numerous investigators have used "surrogate" signals in order to define $I(t)$; included in these are the studies by Fiedler and Head (1966), and Hedley and Keffer (1974). In part, surrogate signals have been used because of the difficulties involved in obtaining accurate time resolved vorticity measurements. Conditional sampling and visualization studies of the intermittent region have also been performed. For example, Murlis et al. (1982) and Antonia et al. (1982) used temperature as a marker for the purposes of detecting the turbulent/nonturbulent interface. In both of these studies the Reynolds number dependence of the outer region was investigated. Concerning this issue, Murlis et al. hypothesize that it is "highly probable that at low Reynolds number a large fraction of the outer-layer fluid in the boundary layer is in fact occupied by the viscous superlayer," and conclude (in agreement with the earlier hypothesis of Huffman and Bradshaw 1972) that the main source of low Reynolds number effects is the changing structure of the viscous superlayer. With regard to the structure of the superlayer, the flow visualization studies by Falco (1974, 1977), suggest that the corrugations in the turbulent/nonturbulent interface are the vortex ring-like "typical eddy" motions. The Klewicki and Falco (1990) r.m.s. spanwise vorticity measurements at their lowest R_θ value are consistent with the notion of the changing structure of the superlayer at low Reynolds number. Specifically, the lowest R_θ condition shows larger values of the non-dimensional spanwise vorticity than the two higher R_θ conditions (see Fig. 2).

Given vorticity measurements of sufficient resolution, the issues relating to the thickening of the viscous superlayer with decreasing Reynolds number, and the scale of the corrugations in the turbulent/nonturbulent interface may be reliably investigated. In the present study, spatially and temporally resolved measurements of ω_z in zero pressure gradient boundary layers ($1010 < R_\theta < 4850$) are used to investigate these issues.

2 Experimental Procedures and Conditions

The experiments were performed in the 17 meter low speed wind tunnel located in the Turbulence Structure Laboratory at Michigan State University. The experimental results presented herein are derived from the data base accumulated by Klewicki (1989), and a detailed account of the experimental procedures as well as additional information pertaining to the accuracy of the experiments may be found there as well as in Klewicki and Falco (1990); only a brief summary is presented here.

The measurements were taken at the three Reynolds numbers, R_θ = 1010, 2870, and 4850. The measurements were obtained using a four-wire spanwise vorticity probe similar to that developed by Foss et al. (1986). The probe is comprised of a parallel-array element and an x-array element. The copper-plated 5 μm diameter tungsten hot-wires contained within the probe are 3 mm in length with a center active length of 1 mm. The Δy spacing between the parallel-array wires (pertinent to the measurement of $\partial u/\partial y$) is nominally 1 mm, as is the spacing between the wires contained in the x-array. The Δz spacing between the centers of the parallel and x-arrays is nominally 3.4 mm. For reference 1 mm is equal to about 1.85, 4.75 and 7.75 viscous units at R_θ = 1010, 2870 and 4850, respectively. Experiments quantifying the errors resultant from the spanwise offset between the centers of the parallel and x-arrays are presented by Klewicki and Falco (1990). These experiments indicate that in the worst case (i.e. at the point nearest the wall in the $R_\theta = 4850$ flow) the resulting error in the rms spanwise vorticity, ω_z', is about 6 percent. For the present study, this percentage error is felt to be an upper limit since the measurements considered are in the outer part of the boundary layer. The probe was operated using DISA model 55M01 anemometers at a heating ratio of 1.7. The x-array calibration employed an effective angle technique. The parallel-array elements were calibrated using a two step matching technique. This technique begins by calibrating one of the wires using velocities computed from pressure readings, and then measured velocities from this wire are used to calibrate the other wire. All calibrations were performed under steady conditions, that is, a static calibration technique was employed. Calibrations were performed immediately before and after each experiment.

The components of $\omega_z = \partial v/\partial x - \partial u/\partial y$ were computed using a two point central difference from the parallel-array data, and by differentiating a local (in time) five-point quadratic curve-fit of the x-array data. Taylor's hypothesis was used to convert the time derivative of the x-array data to the

Nomenclature

A/D = analog to digital converter
C_f = skin friction coefficient
f_c = low-pass cut-off frequency
f_K = Kolmogorov frequency, $U/2\pi\eta$
f_s = sampling frequency
H = boundary-layer shape factor
$I(t)$ = intermittency function
LSB = least significant bit in the A/D
pdf = probability density function
R_θ = momentum deficit thickness Reynolds number, $U_\infty\theta/\nu$
u, v, w = streamwise, wall normal, and spanwise velocity components
U = mean streamwise velocity component
U_∞ = free stream velocity
u_τ = friction velocity
x, y, z = streamwise, wall normal, and spanwise Cartesian coordinates
δ = boundary-layer thickness
η = Kolmogorov length
ν = kinematic viscosity
θ = momentum deficit thickness
ω_c = vorticity amplitude used in the event duration analysis
$\omega_x, \omega_y, \omega_z$ = streamwise, wall normal and spanwise vorticity components

Subscripts/Superscripts

$\langle(\ )\rangle$ = denotes time-averaged quantity
$(\ )'$ = denotes r.m.s. value of a fluctuating quantity
$(\ )^+$ = denotes normalization by ν and u_τ

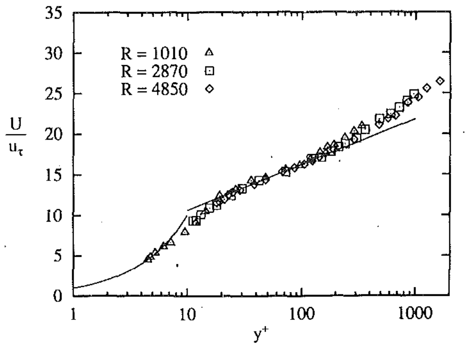

a) Law of the wall representation, straight line given by, $U/u_\tau = 2.44 \ln (yu_\tau/\nu) + 5.0$

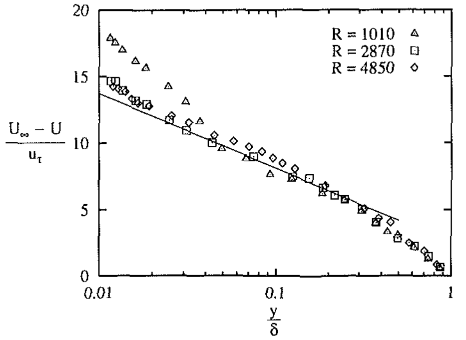

b) Defect law representation, straight line given by, $(U_\infty - U)/u_\tau = -2.44 \ln (y/\delta) + 2.5$

Fig. 1 Logarithmic mean velocity profiles

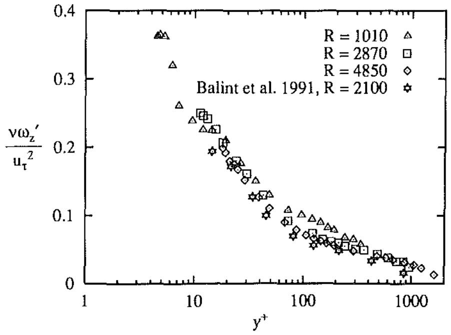

Fig. 2 Inner-normalized spanwise vorticity intensity profiles

Table 1 Principal characteristics of the zero pressure gradient boundary layers of the present study

R_θ	U_∞ (m/s)	δ_{99} (mm)	θ (mm)	H	U_τ (m/s)	C_f	f_c (Hz)	f_s (Hz)
1010	0.607	206	24.8	1.45	0.0282	0.00430	250	500
2870	1.752	205	24.5	1.40	0.0707	0.00325	500	1000
4850	2.981	199	24.3	1.38	0.1125	0.00285	1000	2000

streamwise gradient. A moving 100-point average streamwise velocity was used as the convection velocity in the procedure. Piomelli et al. (1989) have analyzed the validity of Taylor's hypothesis using experimental, large eddy simulation, and direct simulation data. Their study indicates that employing Taylor's hypothesis results in only very small errors for y^+ greater than about 40. For the intermittency analysis, the sample size of the time series was 200,000. This corresponds to observation times between 1200 and 2900 δ/U_∞. The number of points in the time series for the event duration analysis was 600,000.

Mean velocity profiles for the three Reynolds numbers are given in Figs. 1(*a*,*b*) and inner variable normalized r.m.s. spanwise vorticity profiles are given in Fig. 2. The friction velocity used in these profiles was obtained from the Clauser technique using the logarithmic law $U^+ = 2.44 \ln y^+ + 5.0$. Included in Fig. 2 are the ω_z' data of Balint et al. (1991). The integral features of the boundary layers of the present study are given in Table 1. The data at each Reynolds number were analog filtered at the cut-off frequencies and acquired at the sampling frequencies given in Table 1. Furthermore, the acquired voltage time series were digitally low-pass filtered at (or slightly above) the local Kolmogorov frequency, $U/(2\pi\eta)$, at each location. Estimates of η in the computation of f_K were obtained from the approximate formula for the dissipation rate given by Klewicki and Falco (1990). Digital filtering consisted of processing the data twice through a two-pole Butterworth filter. The data were first filtered in the forward direction and then again in the reverse direction in order to remove any phase shifting associated with the Butterworth filters. This additional filtering was executed in order to achieve a greater level of consistency between the data sets for purposes of comparison, since, in general, the analog cut-off frequencies given in Table 1 are significantly higher than the Kolmogorov frequencies at any given location in the boundary layers. The cut-off frequency values ($\approx f_K$) used in the digital filter were 75 Hz, 300 Hz, and 600 Hz at $R_\theta = 1010$, 2870, and 4850, respectively. The effect of the additional digital filtering on the profiles of Fig. 2 was mild. In the worst case, the digitally filtered time series yielded r.m.s. ω_z values about 8, 3, and 2 percent lower than the unfiltered time series at $R_\theta = 1010$, 2870 and 4850 respectively. Examination of the differences between the profiles in Fig. 2 indicates, however, that these changes in the r.m.s. values are not nearly large enough to account for the observed Reynolds number trends in the outer region. An important final note on this filtering process is that since it was performed on the individual hot-wire voltages, the computed ω_z time series continued to contain frequencies significantly higher than the indicated digital cut-off frequencies.

Estimates of the uncertainty level in the zero value of the ω_z time series were required for the purposes of defining an average intermittency. Uncertainties in the ω_z signals may generally be attributed to three major sources: electronic noise, the binary effect due to the random flipping of the least significant bit (LSB) in the A/D, and the background vorticity in the freestream. Because of the additional digital filtering, the effect of the electronic noise had been reduced to negligible levels. Thus, the dominant sources of uncertainty pertained to the LSB of the A/D, and the freestream turbulence. It has been shown (Klewicki 1989) that the local curve fitting procedure used to compute $\partial v/\partial x$ greatly reduces the effects of spurious points. Thus, the estimate of the uncertainty caused by the random flipping of the LSB of the A/D registers was determined by considering this effect on the computation of $\partial u/\partial y$ alone. In order to determine this, an average velocity was computed,

$$U_{\text{avg}} = \frac{U_u + U_l}{2},$$

where U_u and U_l are respectively the average velocities derived from the upper and lower parallel-array elements. U_{avg} was then divided by the total number of A/D bits (4096), to give a velocity increment, ΔV, associated with the LSB. Given that the flipping of the LSB from either of the two signals produced by the parallel-array occurs randomly, one would expect that on average the uncertainty in the vorticity measurement resultant from this error would be close to,

$$\frac{\Delta V}{\Delta y},$$

where Δy is the spacing of the parallel-array elements. On occasion, however, the random flipping of the LSB may cause the maximum uncertainty of two LSB's associated with parallel-array measurements, and thus in order to obtain a con-

Table 2 Normalized signal uncertainty levels associated with the flipping of the least significant bit of the analog to digital converter

$R_\theta = 1010$	0.11 ($y/\delta = 0.62$)	0.16 ($y/\delta = 0.86$)
$R_\theta = 2870$	0.06 ($y/\delta = 0.62$)	0.07 ($y/\delta = 0.87$)
$R_\theta = 4850$	0.05 ($y/\delta = 0.58$)	0.06 ($y/\delta = 0.83$)

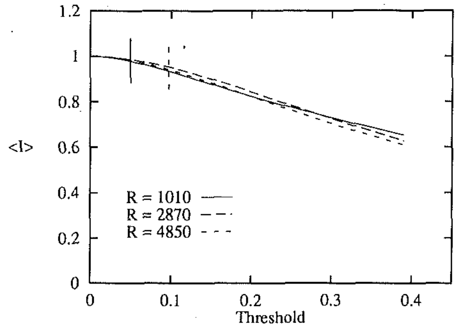

Fig. 3 Average intermittency versus normalized signal threshold at y/δ near 0.60

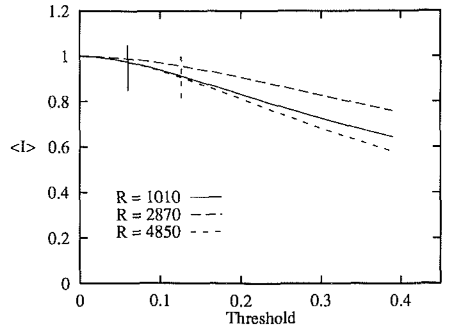

Fig. 4 Average intermittency versus normalized signal threshold at y/δ near 0.85

servative estimate of this effect, the value of $2\Delta V$ divided by Δy was used. Table 2 presents the values of these uncertainty levels normalized by the local r.m.s. values at the locations corresponding to the results in Figs. 3 and 4. Solid vertical hash marks indicating the values for the highest Reynolds number flow are included in Figs. 3 and 4.

Obtaining an estimate of the background spanwise vorticity is typically found by acquiring an ω_z time series in the freestream and computing its r.m.s. (Haw et al., 1989; Vukoslavcevic et al., 1991). This estimate then contains both the background ω_z level, and the uncertainty resultant from the flipping of the LSB. In the present study, however, the calibration time series were not saved, and thus the uncertainty resultant from this effect had to be estimated by a less direct means. For the three flows investigated, the $R_\theta = 4850$ profile contained points at the largest y/δ values, and thus the following extrapolation procedure employed these data. Utilizing the values of the last two points in this profile, a linear extrapolation out to $y/\delta = 1.4$ was performed. The value resulting from this extrapolation provided an estimate of the background ω_z, including the effect of the LSB. At $y/\delta = 0.58$ this value is 9.7 percent of the r.m.s. and $y/\delta = 0.83$ it amounts to 12.6 percent of the r.m.s. These values are indicated by the dashed vertical has marks in Figs. 3 and 4. Based on the fact that this estimate should include both the background ω_z and the effect of the LSB, one would expect it to be greater than the above values based upon the flipping of the LSB. This is the case. Additionally, based upon the assumption that the vorticity fluctuations in the freestream are of large scale, it is expected that a vorticity estimate based upon the axial freestream intensity should be greater than the above estimate. In fact, an estimate based upon the value of $u'/U_\infty = 0.2$ percent and the parallel-array element spacing of 1 mm yields a background vorticity estimate about twice that of the extrapolation based estimate. Thus, from this point of view, the present estimate is also found to be reasonable. The best estimate for the "in-practice" signal zero at $R_\theta = 4850$ is believed to be bracketed on the low end by the LSB estimate, an on the high end by the extrapolation based estimate for the free-stream vorticity level.

Table 3 A comparison of the spanwise vorticity based average intermittency results of the present study, and the turbulence-biased temperature scheme average intermittency results of Murlis et al. (1982)

	$y/\delta = 0.58$	$y/\delta = 0.83$
Present: $R_\theta = 4850$	0.98–0.94	0.97–0.90
Murlis et al.: $R_\theta = 4820$	0.96	0.76

3 Results

Spanwise Vorticity Intermittency. Intermittency, $I(t)$, is the classically defined binary function which takes on the values of 1 when ω_z exceeds the magnitude of the signal threshold level for two consecutive data points, and is 0 when the signal is below this threshold for two consecutive samples.

The average intermittency, $\langle I \rangle$, versus threshold level (normalized by ω_z') for the three Reynolds numbers at $y/\delta \approx 0.6$ and 0.85 are given in Figs. 3 and 4, respectively. The results in Fig. 3 indicate that the dependence of $\langle I \rangle$ on threshold is nearly identical for all three Reynolds numbers. Conversely, Fig. 4 indicates that the $R_\theta = 2870$ results are consistently higher than either the $R_\theta = 1010$ or 4850 results for most of the threshold values. The reason for these results are currently unknown, but it is inferred that the result is not correct. Note that these anomolous values (for $R_\theta = 2870$) indicate a larger $\langle I \rangle$ value for a given normalized threshold level than the cluster of values at $y/\delta = 0.6$.

None of the curves in Fig. 3 and 4 indicate a region of threshold independence, and thus a clear-cut value of $\langle I \rangle$ is not immediately extracted from these data. (These results are consistent with the findings of Haw et al. (1989) and Foss (1991) in single and two stream shear layers, respectively, as indicated in the introduction.) In order to ascertain a value of $\langle I \rangle$ from the curves in Figs. 3 and 4, one must account for the uncertainty in distinguishing the signal zero level. At the lower two Reynolds numbers, uncertainty estimates based on the flipping of the LSB resulted in a lower bound for the signal zero. At the higher Reynolds number, however, the above described extrapolation procedure additionally resulted in an upper bound for the signal zero. These bracketing values are represented in Figs. 3 and 4 by the vertical hash marks.

The study of Murlis et al. (1982) utilized a surrogate signal based upon the detection of temperature fluctuations in a slightly heated boundary layer. In general, their temperature based average intermittency results showed very little variation with Reynolds number over the range $1100 < R_\theta < 4820$. Furthermore, their $\langle I \rangle$ results were nearly independent of threshold for temperature differences greater than about 0.1 K. Since the present vorticity based $\langle I \rangle$ results do not indicate a region of threshold independence, comparisons between the present results and those of Murlis et al. are limited to the higher R_θ results, where reasonable upper and lower bounds on the signal zero were obtained. Table 3 gives the ranges of values of the $R_\theta = 4850$ curves in Figs. 3 and 4 which fall between the upper and lower signal zero uncertainty brackets. Included in this table are the turbulence-biased temperature scheme average intermittency results of Murlis et al. at ap-

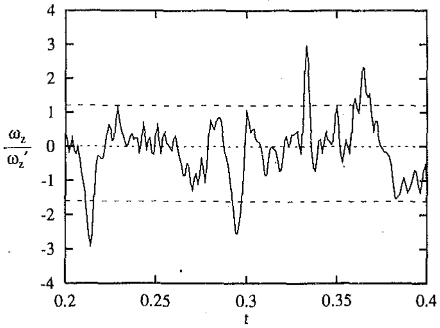

Fig. 5 Normalized ω_z time series at $y/\delta = 0.62$, $R_\theta = 2870$

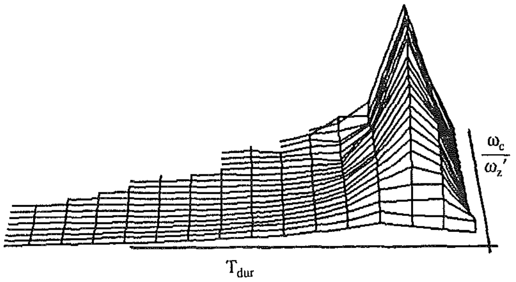

Fig. 6 Positive ω_z event duration probability density functions versus conditioning amplitude at $y/\delta = 0.62$, $R_\theta = 2870$

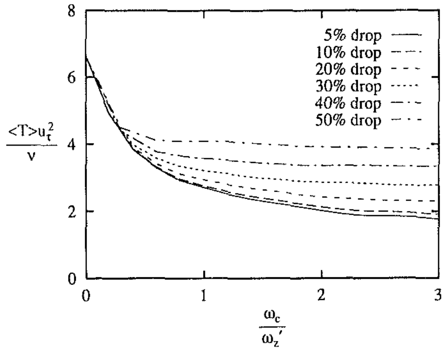

Fig. 7 Inner normalized average positive ω_z event durations versus conditioning amplitude for different percentage drop limits at $y/\delta = 0.83$, $R_\theta = 4850$

proximately the same y/δ values and $R_\theta = 4820$. The results given in this table indicate that at $y/\delta = 0.57$ the vorticity based $\langle I\rangle$ results bracket the temperature based results, while at $y/\delta = 0.83$ the vorticity based $\langle I\rangle$ results are significantly higher than the temperature based results. In connection with this, the results of Haw et al. (1989) indicate that, in general, their ω_z based $\langle I\rangle$ results were larger than the surrogate signal based results of Wygnanski and Fielder (1970). However, a comprehensive comparison between vorticity based and surrogate signal based $\langle I\rangle$ measurements has yet to be performed.

Spanwise Vorticity Event Durations. Previous studies by Murlis et al. (1982) and Antonia et al. (1982) indicate that while the average intermittency shows very little Reynolds number dependence, significant changes in the motions in the outer region occur at low R_θ. In order to examine whether these changes are also evident in the motions bearing ω_z, an event duration analysis was performed. This analysis consisted of determining the duration of either positive or negative ω_z events conditioned on an amplitude, ω_c, for a range of ω_c values. Furthermore, to account for small amplitude deviations from overall trends in the time series, an allowable percentage drop of 20 percent in the peak amplitude of the signal (for a given event) was used to sustain the event—even if the absolute signal amplitude dropped below ω_c.

Figure 5 graphically depicts the procedure for determining the ensemble of event durations at each ω_c value. In this figure a positive and negative ω_c value are represented by the horizontal dashed lines. Consider first the case $\omega_c/\omega_z' = -1.6$. In this case two clear-cut events are defined near $t = 0.21$ and $t = 0.29$, and the durations of these events are represented in this figure by the section of the dashed line bracketed by the downward and upward signal crossings. Consider now the case of $\omega_c/\omega_z' = 1.2$. In this case the signal exceeds ω_c near $t = 0.33$ and $t = 0.36$. As with the two negative events, the event near $t = 0.33$ is unambiguously defined. In the case of the event near $t = 0.36$, however, the distinction between defining one or two events depends upon the percentage drop limit employed. Under the condition of a 20 percent drop of the peak amplitude (after exceeding ω_c), the signal near $t = 0.36$ would define a single event since the downward excursion below ω_c does not exceed 20 percent of the peak signal amplitude for the given event. In the case of a smaller percentage drop limit (say 5 percent), two events would be defined. It is important to note that for the results presented herein, the percentage drop limit is based upon the peak amplitude of the signal for a given event, and not on ω_c. Thus, the results are both a function of the local signal peak characteristics, and the value of ω_c—in comparison to simply a function of ω_c, which is case when the percentage drop limit is defined as a fraction of ω_c. Since, however, the signal must exceed ω_c in order to define the start of an event, it easy to show that for a given percentage drop limit the average event duration based upon the peak amplitude percentage drop will never be greater than that based upon ω_c.

At each value of ω_c (for a given percentage drop limit) a distribution of event durations is obtained. For example, a three dimensional representation of the family of pdf's corresponding to positive event durations for $R_\theta = 2870$ and $y/\delta = 0.6$ are given in Fig. 6. The locus of average values from these pdf's are plotted and discussed below. The pdf's in Fig. 6 demonstrate the trend exhibited by all of the data; namely a dramatic narrowing for larger values of ω_c.

The choice of percentage drop limit affects the individual pdf's at each value of ω_c. The general effect of the value of the percentage drop limit is shown in Fig. 7. In this figure, the locus of the average positive event durations is plotted for different percentage drop limits for the data at $R_\theta = 4850$ and $y/\delta = 0.57$. As can be seen, the major effect of the percentage drop-based event grouping procedure occurs at the larger ω_c values. Also, with increasing percentage drop, the curves in Fig. 7 show less variation with increasing ω_c. This indicates that the ensembles at larger ω_c have many of the same entries. In general, however, all of the curves in Fig. 7 show little variation for ω_c greater than about one r.m.s. For ω_c greater than one r.m.s., the measured duration also exhibits a monotonic increase with increasing percentage drop. Furthermore, for equal increments in percentage drop, the change in the measured duration is, in general, also an increasing function (see, for example, the trend at $\omega_c/\omega_z' = 1$).

The value of 20 percent used in the data presentation below was chosen somewhat arbitrarily. Considerations in making this choice included selecting a value that was a relatively small fraction of the peak magnitude, which still caused a significant number of groupings to be made, but not so many so as to begin to be a dominant factor in the computed average duration. Noting that the 5 and 10 percent curves differ relatively little, the 20 percent curve was chosen since it was near the minimum value of percentage drop which started to cause a significant number of event groupings. In reference to the mean values presented below, the variation of the 5 and 30 percent curves at $\omega_c/\omega_z' = 1$ about the 20 percent curve is approximately ±10 percent.

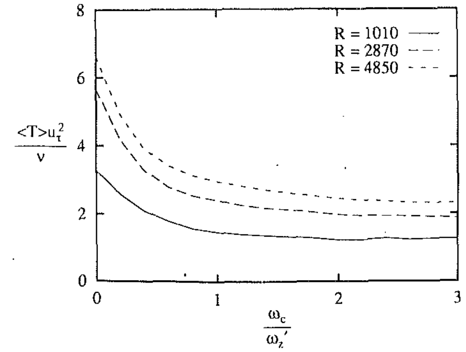

(*a*) **Positive events**

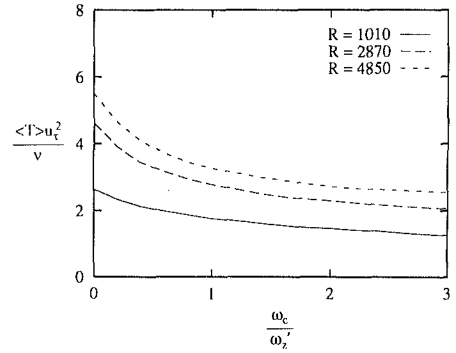

(*b*) **Negative events**

Fig. 8 Inner normalized average ω_z event durations versus conditioning amplitude near $y/\delta = 0.6$, drop limit = 20 percent

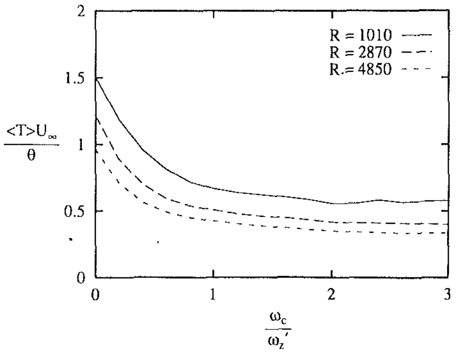

(*a*) **Positive Events**

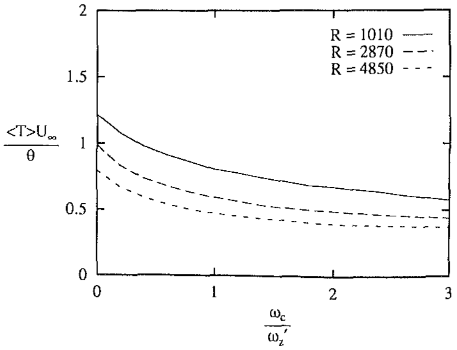

(*b*) **Negative Events**

Fig. 9 Outer normalized average ω_z event durations versus conditioning amplitude near $y/\delta = 0.6$, drop limit = 20 percent

The normalized event duration results at y/δ near 0.6 are given in Figs. 8 and 9. (Nearly identical results were found near $y/\delta = 0.85$.) The curves Figs. 8 and 9 are shown as a function of ω_c/ω_z. In the worst case (positive events and $R_\theta = 1010$) the event duration sample size was 71. Figs. 8(*a*) and 8(*b*) show the inner normalized event durations for positive and negative excursions respectively, and Figs. 9(*a*) and 9(*b*) show these same results under outer normalization. Regardless of the normalization, it can be seen that for ω_c greater than about one r.m.s. the duration curves exhibit very little change. These results are consistent with the large flatness values of ω_z in the outer region (Klewicki, 1989), the narrowing of the event duration pdf's with increasing ω_c, as well as the small values of $\langle I\rangle$ (less than 0.25) for ω_c/ω_z greater than one. In general, these results indicate that at large ω_c the sample of durations becomes relatively small, but have a well-defined mean value. A comparison of the positive and negative results indicates that for small ω_c values the positive events are of longer duration, while for a wide range of ω_c values, starting at those greater than about 0.5, the negative events are longer. These observations are consistent with the large negative skewness of the ω_z pdf in the outer part of the boundary layer, see Klewicki (1989), Balint et al. (1991).

Clear Reynolds number dependencies are exhibited in Figs. 8 and 9. The trends revealed indicate that with increasing R_θ the inner normalized event durations increase, while under outer normalization the event durations decrease. Thus, while the results clearly indicate that the motions bearing ω_z have a well defined time scale, this time scale follows a R_θ dependence intermediate to ν/u^2_τ and θ/U_∞. The analyses of Huffman and Bradshaw (1972) and Murlis et al. (1982) indicate that the increasing influence of viscous effects should result in the extent of the regions of single-signed ω_z in the outer region to increase as a fraction of the total layer thickness with decreasing R_θ. Using the local mean velocity as a convection velocity to convert event durations to outer normalized convected lengths yields curves with magnitudes almost exactly proportional to those shown in Figs. 9. Thus, the present results indicate a feature that is consistent with the hypothesis that at low R_θ viscosity has a significant effect on the outer region vorticity field. The present results do not, however, give evidence indicating that the superlayer thickness increases in viscous units with decreasing R_θ. In fact, the opposite is indicated in Figs. 8.

As discussed in the Introduction, outer region flow visualizations by Falco (1974, 1977) suggest that the corrugations in the turbulent/nonturbulent interface represent the vortex ring-like "typical eddy" motions. In a recent compilation of available flow visualization data (Falco, 1991), these motions are shown to have a characteristic length that exhibits a Reynolds number dependence intermediate to inner or outer scaling. As indicated above, this property is also exhibited by the present ω_z event durations. In order to examine this correspondence more closely, the inner normalized event durations at $\omega_c/\omega_z' = 1.0$ were converted to a convected length by using the mean velocity as a convection velocity, and compared with the characteristic typical eddy lengths as a function of Reynolds number. For the purposes of comparing with the visual results, the choice of $\omega_c/\omega_z' = 1.0$ was made since this is nominally the conditioning amplitude at which the duration values plateaued. Furthermore, combined visual/hot-wire studies (see, for example, Falco 1991) indicate that ensemble averaged ω_z signatures derived from a visual conditioning procedure reach amplitudes well in excess of one long-time r.m.s. Thus, it is expected that events which can be reliably detected by visual means are, in general, of amplitude greater than one r.m.s..

The visually based and probe-based results are compared in Fig. 10. As can be seen, the present data at $R_\theta = 1010$ are about 30 percent lower than the normalized typical eddy dimension, while the higher R_θ data show excellent agreement. In general, the visually determined results indicate a Reynolds number trend that agrees very well with the trend suggested

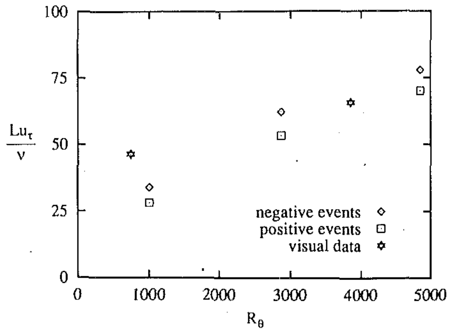

Fig. 10 Comparison of the visually determined typical eddy length scales (from Falco, 1991) with the inner normalized convected length scales derived from the data of Fig. 8

by the $R_\theta = 2870$ and 4850 probe-based results. Overall (and given the experimental difficulties in precisely determining either the visually-based or probe-based length scales), it is felt that the results of Fig. 10 provide a strong consistency argument in favor of the typical eddy motions being the characteristic vortical motion in the outer region.

4 Conclusions

The following conclusions are derived from this investigation:

- The present vorticity based $\langle I \rangle$ measurements in the outer region of a turbulent boundary layer are at least as large as those obtained by Murlis et al. (1982) using a "surrogate" temperature based scheme.
- For the positions in the outer region investigated, $\langle I \rangle$ does not exhibit a region of threshold independence.
- The trends in the outer normalized ω_z event durations indicate that the scale of single-signed ω_z regions increases as a fraction of the total boundary layer thickness with decreasing Reynolds number. In this manner, the present results support previous hypotheses by Huffman and Bradshaw (1972) and Murlis et al. (1982) that in the outer region viscous effects are increasingly significant at low R_θ.
- The trends in the inner normalized ω_z event convected lengths exhibit very good agreement with the typical eddy flow visualization results of Falco (1974, 1977). In this manner, the present results support the notion that the corrugations in the turbulent/nonturbulent interface are resultant from the typical eddy motions.

5 JFE Data Bank Contributions

A number of the results presented herein are being added to the Journal of Fluids Engineering data bank. In particular, all of the data except for the ω_z time series presented in Fig. 5, and the probability density surface of Fig. 6 have been submitted to the data bank. The results from Figs. 5 and 6 were omitted because of their limited use with regard to further analysis and/or comparison with other results. For ease of use, all of the results have been submitted in dimensional form. Thus, in order to recover the results presented herein and/or to create the different nondimensional representations, one is referred to the velocity and length scale information listed in Table 1. To access the file for this paper, see instructions on p. 705 of this issue.

6 Acknowledgment

This work was partially supported by the AFOSR contract 87-0047. The contract monitor was Dr. James McMichael.

References

Antonia, R. A., Rajagopalan, S., Subramanian, C. S., and Chambers, A. J., "Reynolds-Number Dependence of the Structure of a Turbulent Boundary Layer," *Journal of Fluid Mechanics*, Vol. 121, pp. 123-140.

Balint, J. L., Wallace, J. M., and Vukoslavcevic, P., 1991, "The Velocity and Vorticity Vector Fields of a Turbulent Boundary Layer. Part 2. Statistical Properties," *Journal of Fluid Mechanics*, Vol. 228, pp. 53-86.

Corrsin, S., 1943, "Investigation of Flow in an Axially Symmetric Heated Jet of Air," NACA Wartime Rept. W94.

Corrsin, S., and Kistler, A. L., 1955, "Free Stream Boundaries of Turbulent Flows," NACA Rep. no. 1244.

Falco, R. E., 1974, "Some Comments on Turbulent Boundary Layer Structure Inferred from the Movements of a Passive Contaminant," AIAA Paper No. 74-99.

Falco, R. E., 1977, "Coherent Motions in the Outer Region of Turbulent Boundary Layers," *Physics of Fluids*, Vol. 20, p. S124.

Falco, R. E., 1991, "A Coherent Structure Model of the Turbulent Boundary Layer and its Ability to Predict Reynolds Number Dependence," *Philosophical Transactions, Proceedings of the Royal Society A*, to appear.

Fiedler, H., and Head, M. R., 1966, "Intermittency Measurements in the Turbulent Boundary Layer," *Journal of Fluid Mechanics*, Vol. 25, pp. 719-735.

Foss, J. F., 1991, "Vorticity Considerations and Planar Shear Layers," *Proceedings of Experimental Heat Transfer, Fluid Mechanics and Thermodynamics*, J. F. Keffer, R. K. Shah and E. N. Ganic, eds., Elsevier, pp. 240-251.

Foss, J. F., Klewicki, C. L., and Disimile, P. J., 1986, "Transverse Vorticity Measurements Using an Array of Four Hot-Wire Probes," NASA CR 178098.

Haw, R. C., Foss, J. K., and Foss, J. F., 1989, "Vorticity Based Intermittency Measurements in a Single Stream Shear Layer," *Advances in Turbulence 2*, H. H. Fernholz and H. E. Fiedler, eds., Springer-Verlag, Berlin, pp. 90-95.

Hedley, T. B., and Keffer, J. F., 1974, "Some Turbulent/Non-turbulent Properties of the Intermittent Region of a Boundary Layer," *Journal of Fluid Mechanics*, Vol. 64, pp. 645-678.

Huffman, G. D., and Bradshaw, P., 1972, "A Note on Von Karman's Constant in Low Reynolds Number Turbulent Flows," *Journal of Fluid Mechanics*, Vol. 53, pp. 45-60.

Klewicki, J. C., 1989, "On the Interaction Between the Inner and Outer Region Motions in Turbulent Boundary Layers," Ph.D. Dissertation, Michigan State University, East Lansing, MI.

Klewicki, J. C., and Falco, R. E., 1990, "On Accurately Measuring Statistics Associated With Small Scale Structure in Turbulent Boundary Layers Using Hot-Wire Probes," *Journal of Fluid Mechanics*, Vol. 219, pp. 119-142.

Kovasznay, L. S. G., 1950, *Q. Prog. Rep. Aero. Dept. Contract NORD-8036-JHB-3D*, The Johns Hopkins University, Baltimore, MD.

Kovasznay, L. S. G., Kibens, V., and Blackwelder, R. F., 1970, "Large Scale Motions in the Intermittent Region of a Turbulent Boundary Layer," *Journal of Fluid Mechanics*, Vol. 41, pp. 283-325.

Murlis, J., Tsai, H. M., and Bradshaw, P., 1982, "The Structure of Turbulent Boundary Layers at Low Reynolds Numbers," *Journal of Fluid Mechanics*, Vol. 122, pp. 13-56.

Phillips, O. M., 1972, "The Entrainment Interface," *Journal of Fluid Mechanics*, Vol. 51, pp. 97-118.

Subramanian, C. S., Kandola, B. S., and Bradshaw, P., 1985, "Measurements of the Low-Wave-Number Structure of a Turbulent Boundary Layer," Imperial College Aeronautics Report 85-01.

Townsend, A. A., 1948, *Australian Journal of Scientific Research*, Vol. 1, p. 161.

Vukoslavcevic, P., Wallace, J. M., and Balint, J. L., 1991, "The Velocity and Vorticity Vector Fields of a Turbulent Boundary Layer. Part 1. Simultaneous Measurement by Hot-Wire Anemometry," *Journal of Fluid Mechanics*, Vol. 228, pp. 25-51.

Wygnanski, I., and Fiedler, H., 1970, "The Two-Dimensional Mixing Region," *Journal of Fluid Mechanics*, Vol. 41, pp. 327-361.

Turbulent Flow Near a Rough Wall

Yang-Moon Koh
Department of Mechanical Engineering,
University of Ulsan,
Ulsan 680-749, South Korea

By introducing the equivalent roughness which is defined as the distance from the wall to where the velocity gets a certain value ($u/u_\tau \approx 8.5$) *and which can be represented by a simple function of the roughness, a simple formula to represent the mean-velocity distribution across the inner layer of a turbulent boundary layer is suggested. The suggested equation is general enough to be applicable to turbulent boundary layers over surfaces of any roughnesses covering from very smooth to completely rough surfaces. The suggested velocity profile is then used to get expressions for pipe-friction factors and skin friction coefficients. These equations are consistent with existing experimental observations and embrace well-known equations (e.g., Prandtl's friction law for smooth pipes and Colebrook's formula etc.) as special cases.*

1 Introduction

It will not only be the author who has felt some confusion about the displacement height d and roughness functions A, B in the logarithmic law (Eqs. (1) and (2)) of the velocity profile in a turbulent boundary layer, when one tries to use it in fluid flow and heat transfer analysis. Though the displacement height is usually taken to be zero and, hence, the mean-velocity distribution is expressed in terms of the distance y from the wall rather than $y-d$, the effective wall location is not readily apparent. The roughness functions are also functions of the height and shape of roughness elements. But it is not fully understood how they vary, especially when the surface is transitional, i.e., neither smooth nor completely rough.

The roughness function should be estimated accurately not only to predict the mean velocity properly but also to evaluate the friction factor and skin-friction coefficient correctly. The effect of the displacement height seems to be weaker than that of the roughness function; its effect on the mean velocity is confined to the small region very close to the wall only and, hence, there seems to be no correlation between the displacement height and friction factor or skin-friction coefficient. However, inaccurate estimation of the displacement height necessarily causes a big error in computing the velocity near the wall, which can be critical to the problem of convection heat transfer by liquids over a wide range of Prandtl number. Furthermore, as we can see soon, the displacement height is closely related to the roughness function and skin friction.

Though he took a rather different way of reasoning and did not use the term "displacment height" explicitly, Squire (1948) showed that the logarithmic law will give better results when the origin of the y-coordinate is shifted from the (smooth) wall; he considered that the turbulence effect starts just at the outer edge of the laminar sublayer (now the viscous sublayer) and, hence, the eddy diffusivity is related to the distance from there rather than from the wall. Granville (1958) extended the method of Squire to cover the case of rough surfaces and derived a general relation for the frictional resistance of flat plates with arbitrary roughnesses. However, he did not give explicit expressions for the roughness function, and, hence, for the frictional resistance when the surface is transitional. Furthermore, it seems more reasonable to think in terms of the displacement height rather than the thickness of the viscous sublayer; the displacement height can be defined irrespective of surface roughness, but the viscous sublayer itself vanishes when the surface becomes rough.

The present study is to resolve these problems and to provide working formulae for the displacement height, roughness function, and, hence, velocity profile, which are accurate, simple, and general enough to be useful to most engineering problems in various circumstances. In the next section, analyzing Nikuradse's experiment on turbulent flow in sand-grain coated pipes, we will derive equations for the displacement height, roughness function, and, hence, the velocity profile near smooth and completely rough surfaces. Then, modifying these equations, we will get a new equation which can be used for turbulent flows over surfaces with arbitrary roughnesses. Finally, the new equation for the velocity profile is used to get equations for the pressure loss in a pipe and skin friction in a turbulent boundary layer over a flat surface.

2 The Velocity Profile

The logarithmic law of the mean-velocity profile across the turbulent boundary layer is usually written as

$$u^+ = \frac{1}{\kappa} \ln (y^+ - d^+) + A \tag{1}$$

or

$$u^+ = \frac{1}{\kappa} \ln \frac{y^+ - d^+}{k^+} + B \tag{2}$$

and, by differentiating, we get

$$\frac{du^+}{dy^+} = \frac{1}{\kappa(y^+ - d^+)} \tag{3}$$

where u, y, k, d, and κ represent the velocity, distance from the wall, representative height of roughness elements, dis-

---

Contributed by the Fluids Engineering Division for publication in the JOURNAL OF FLUIDS ENGINEERING. Manuscript received by the Fluids Engineering Division June 13, 1991. Associate Technical Editor: T. T. Huang.

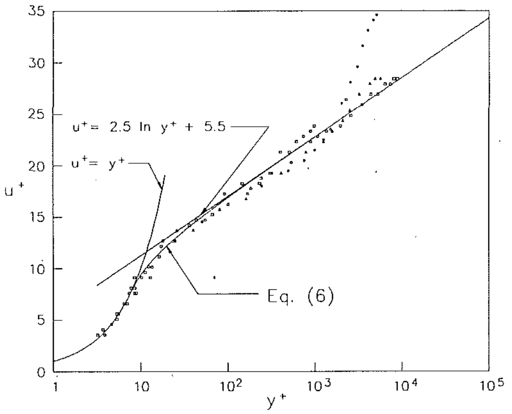

Fig. 1 Mean-velocity profile in the inner region of turbulent boundary layers. Experimental data are after Cebeci and Smith (1974), where the references are given in full.

placement height, and Kármán constant, respectively, and the superscript + means that the variables are made dimensionless by the kinematic viscosity ν and friction velocity u_τ. The roughness functions A, B and displacement height d depend on the respresentative height k and other linear parameters defining the roughness of the wall. Since the problem becomes nearly intractable when all these factors are considered, A, B, and d are usually considered to be functions of the "equivalent sand roughness" only, where the equivalent sand roughness is defined as the roughness of the sand-grained surface which gives the same friction coefficient as the actual surface. Let us assume also that the roughness k means the equivalent sand roughness as well unless specified otherwise and consider the surface covered by uniform sand-grains first. It looks also more convenient to consider cases of smooth and rough surfaces separately at first. Later we will define another "equivalent roughness" and provide a formula which can be applied both to rough and smooth surfaces.

2.1 A Perfectly Smooth Surface: $k^+ = 0$. The simplest approach for this case may be to ignore the buffer layer entirely by assuming that the displacement height d^+ is zero and that the linear velocity profile of the viscous sublayer and the logarithmic profile meet at $y^+ = \delta_v^+$, i.e.,

$$u^+ = \begin{cases} y^+ & \text{for } y^+ < \delta_v^+ \\ \dfrac{1}{\kappa} \ln y^+ + A_s & \text{for } y^+ > \delta_v^+ \end{cases} \tag{4}$$

where A_s means the value of A when the surface is perfectly smooth. As well-known, these formulae give abrupt change of the velocity gradient at $y^+ = \delta_v^+$, and velocity profiles which vary smoothly and fit better to experiments are suggested by several authors (Reichardt, 1951; van Driest, 1965, etc.). However, these formulas are rather complicated and, in some cases, cannot be expressed explicitly, but implicitly in the integral form.

A rather simple expression for the velocity profile which fits well to the experiment and whose derivative is continuous as well can be obtained by adjusting the value of the displacement height. Assuming that the displacement height of a smooth wall is d_s^+, we have

$$\frac{du^+}{dy^+} = \begin{cases} 1 & \text{for } y^+ < \delta_v^+ \\ \dfrac{1}{\kappa(y^+ - d_s^+)} & \text{for } y^+ > \delta_v^+ \end{cases} \tag{5}$$

and, by integrating from $y^+ = 0$,

$$u^+ = \begin{cases} y^+ & \text{for } y^+ < \delta_v^+ \\ \dfrac{1}{\kappa} \ln \dfrac{y^+ - d_s^+}{\delta_v^+ - d_s^+} + \delta_v^+ & \text{for } y^+ > \delta_v^+ \end{cases} \tag{6}$$

From the conditions that the velocity gradient should be continuous at $y^+ = \delta_v^+$ and that Eq. (6) should asymptote to Eq. (4) as y^+ goes to infinity we have

$$d_s^+ = A_s - \frac{1 + \ln \kappa}{\kappa} \tag{7}$$

and

$$\delta_v^+ = A_s - \frac{\ln \kappa}{\kappa} \tag{8}$$

which give 5.3 and 7.8 for the value of d_s^+ and δ_v^+, respectively, if $\kappa = 0.4$ and $A_s = 5.5$ are taken. Equation (6) was obtained by Squire (1948) and is illustrated in Fig. 1 with some experimental results.

Nomenclature

A = roughness function, Eq. (1)
A_s = roughness function, A, for perfectly smooth surface
B = roughness function, Eq. (2)
B_∞ = roughness function, B, for completely rough surface
c_f = skin-friction coefficient
d = displacement height
d_r = displacement height of rough surface
d_s = displacement height of smooth surface
f = pipe friction factor
k = roughness height
k_e = equivalent roughness height, $u^+ = B_\infty$ at $y^+ = k_e^+$
k_{e0} = equivalent roughness height, k_e, for perfectly smooth surface
R = radius of pipe
R_D = Reynolds number based on diameter, VD/ν
R_k = Reynolds number based on roughness height, $u_e k/\nu$
R_x = x Reynolds number, $u_e x/\nu$
R_δ = Reynolds number based on boundary-layer thickness, $u_e \delta/\nu$
u = mean velocity in x-direction
u_e = free stream velocity at the edge of boundary-layer
u_k = x-velocity at $y = k$
u_τ = friction velocity
V = average velocity in pipe flow
x = streamwise coordinate
y = coordinate normal to surface
β = roughness parameter, Eq. (24)
δ = boundary-layer thickness
δ_v = nominal thickness of viscous sublayer
κ = Kármán constant
ν = kinematic viscosity
Π = Cole's profile parameter, Eq. (36)

Other symbols

Δu^+ = velocity defect function, Eq. (26)

Superscripts

$+$ = nondimensionalized by kinematic viscosity and friction velocity

2.2 A Hydrodynamically Smooth Surface: $k^+ < \delta_v^+$.

If the roughness elements are completely immersed in the viscous sublayer, we can assume that Eq. (5) will hold in the region $y^+ > k^+$ and get the velocity profile by integrating Eq. (5) from $y^+ = k^+$, as

$$u^+ = \begin{cases} y^+ - k^+ + u_k^+ & \text{for } k^+ < y^+ < \delta_v^+ \\ \dfrac{1}{\kappa} \ln \dfrac{y^+ - d_s^+}{\delta_v^+ - d_s^+} + \delta_v^+ - k^+ + u_k^+ & \text{for } y^+ > \delta_v^+ \end{cases} \tag{9}$$

where u_k is the velocity at $y = k$. Thus the problem is now reduced to find out the values of u_k^+ as well as d_s^+ and δ_v^+ as functions of k^+.

It does not seem that δ_v^+ will be far from that of the perfectly smooth surface and the condition that the velocity gradient should vary continuously requires that the differences $\delta_v^+ - d_s^+$ should be a constant $1/\kappa$. Thus let us assume that δ_v^+ and d_s^+ will take the same values as those of the perfectly smooth surface.

The apparent mean shear stress in the region $0 < y^+ < k^+$ will vary due to the drag induced by roughness elements and this drag will be proportional to the velocity, since the flow is laminar and slow. Thus we can put

$$\frac{d\tau}{dy} = \frac{\alpha^2 \mu}{k^2} u$$

where τ is the shear stress, α a constant, and μ the viscosity. Thus we have a differential equation for u^+ in the region $0 < y^+ < k^+$ as

$$\frac{d^2 u^+}{dy^{+2}} = \frac{\alpha^2}{k^{+2}} u^+ \tag{10}$$

with boundary conditions

$$u^+ = 0 \quad \text{at } y^+ = 0$$

$$\frac{du^+}{dy^+} = 1 \quad \text{at } y^+ = k^+$$

The solution of Eq. (10) is

$$u^+ = \frac{k^+}{\alpha} \frac{\sinh(\alpha y^+/k^+)}{\cosh \alpha}$$

and u_k^+ becomes

$$u_k^+ = \frac{\tanh \alpha}{\alpha} k^+ \tag{11}$$

where the constant α can be determined from experiment.

Thus we have

$$u^+ = \begin{cases} y^+ - \left(1 - \dfrac{\tanh \alpha}{\alpha}\right) k^+ & \text{for } k^+ < y^+ < \delta_v^+ \\ \dfrac{1}{\kappa} \ln(y^+ - d_s^+) + A_s - \left(1 - \dfrac{\tanh \alpha}{\alpha}\right) k^+ & \text{for } y^+ > \delta_v^+ \end{cases} \tag{12}$$

and

$$B = \frac{1}{\kappa} \ln k^+ + A_s - \left(1 - \frac{\tanh \alpha}{\alpha}\right) k^+ \tag{13}$$

Comparing with Nikuradse's experiments (Schlichting, 1968, Ch. XX), we find that α is about 0.55 (Fig. 2).

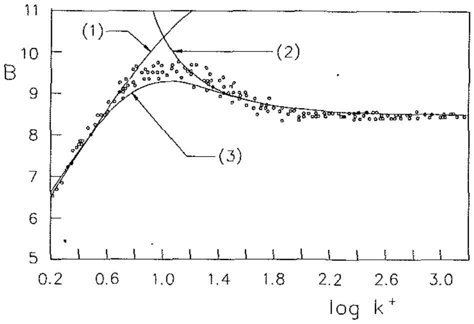

Fig. 2 Roughness function *B* after Nikuradse (see Schlichting, 1968). Curve (1): smooth, Eq. (13); Curve (2): rough, Eq. (19); Curve (3): Eq. (25) with β = 0.12.

2.3 A Completely Rough Surface: $k^+ >> \delta_v^+$.

When the roughness height is much greater than the nominal thickness of the viscous sublayer, we can get the velocity profile by integrating Eq. (3) from $y^+ = k^+$ as

$$u^+ = \frac{1}{\kappa} \ln \frac{y^+ - d^+}{k^+} - \frac{1}{\kappa} \ln \left(1 - \frac{d^+}{k^+}\right) + u_k^+ \tag{14}$$

and

$$B = -\frac{1}{\kappa} \ln \left(1 - \frac{d^+}{k^+}\right) + u_k^+ \tag{15}$$

where u_k^+ is again the velocity at $y^+ = k^+$. Thus, as in smooth surfaces, the velocity profile and, hence, the roughness function B can be estimated, if d^+ and u_k^+ are known as functions of the roughness k^+.

For the displacement height d, we have two conflicting results. Jackson (1981) argues that the expression $d = 0.7k$ gives a good estimate for various types of roughnesses. If we assume, generalizing this argument slightly, that

$$d^+ = rk^+ + d_r^+ \tag{16}$$

then Eq. (14) becomes as

$$u^+ = \frac{1}{\kappa} \ln \left(\frac{y^+}{k^+} - r - \frac{d_r^+}{k^+}\right) + B \tag{17}$$

and the semilogarithmic plot of velocity profile will not give a straight line near $y^+ = k^+$, however large k^+ is. But Nikuradse's results (Schlichting, 1968, Fig. 20.20) give a straight line. The only method to get a straight line in the semilogarithmic plot of Eq. (17) with large k^+ is to put $r = 0$. It is not clear why this discrepancy happens. Note, however, that Jackson defines the displacement height as the level at which the mean drag on the surface appears to act rather than as the virtual origin of the logarithmic velocity profile. In this study, we have assumed that the displacement height d^+ is equal to a constant d_r^+.

It can be easily seen from Eq. (14) that u_k^+ asymptotes to a constant value B_∞ (≈ 8.5 in a sand-roughened surface) as k^+ goes to infinity. If k^+ is large, the boundary condition at the wall $y^+ = 0$ will not affect the flow near $y^+ = k^+$ so much and the drag of roughness elements, being independent of viscosity, will be proportional to the square of u_k. In other words, we can assume that the velocity, $u_k^+ (\equiv u_k/u_\tau)$, at $y^+ = k^+$ will take the constant value B_∞ when $k^+ >> \delta_v^+$.

Thus we have, from Eqs. (14) and (15),

$$u^+ = \frac{1}{\kappa} \ln \frac{y^+ - d_r^+}{k^+} + B \tag{18}$$

and

$$B = B_\infty - \frac{1}{\kappa} \ln \left(1 - \frac{d_r^+}{k^+}\right) \tag{19}$$

where the value of d_r^+ can be determined from experiments.

In Fig. 2, Eqs. (19) and (13) are compared with Nikuradse's experimental results. Agreements between the experimental and theoretical results are excellent. They differ only in the very small transitional region near $k^+ = 10$ ($\approx \delta_v^+$). As the value of d_r^+, it is taken to be 5.3 same as d_s^+.

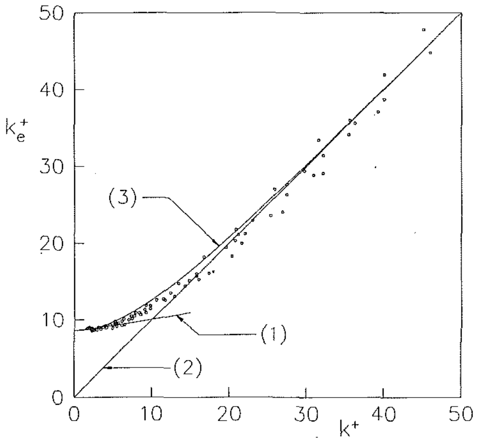

Fig. 3 Equivalent roughness k_e^+ for Nikuradse's sand roughness. Curve (1): smooth, Eq. (20); Curve (2): rough, Eq. (21); Curve (3): Eq. (24) with $\beta = 0.12$.

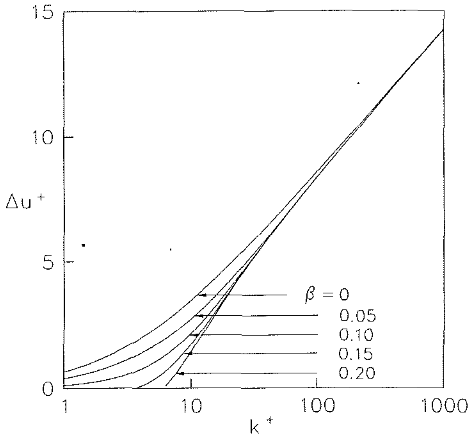

Fig. 4 Effect of wall roughness and β on universal velocity profile

2.4 A Surface With Arbitrary Roughnesses. In the previous section it is found that the dimensionless mean velocity u_k^+ at $y^+ = k^+$ has a constant value B_∞ when $k^+ >> \delta_v^+$. Generalizing this, let us define the (dimensionless) equivalent roughness height k_e^+ as the height from the wall to where the mean velocity is equal to B_∞. Thus, from Eq. (12), we have

$$k_e^+ = d_s^+ + \exp\left\{\kappa\left[B_\infty - A_s + \left(1-\frac{\tanh\alpha}{\alpha}\right)k^+\right]\right\} \tag{20}$$

when the surface is smooth, and

$$k_e^+ = k^+ \tag{21}$$

when the surface is completely rough. If this equivalent roughness height is used, both Eqs. (12) and (18) reduce to the same equation

$$u^+ = \frac{1}{\kappa}\ln\frac{y^+ - d^+}{k^+} + B, \quad y^+ > k_e^+ \tag{22}$$

where

$$B = B_\infty - \frac{1}{\kappa}\ln\frac{k_e^+ - d^+}{k^+} \tag{23}$$

Thus the equivalent roughness height is the lower boundary of the inner layer where the logarithmic velocity profile holds, whether the surface is smooth or not; when a surface is perfectly smooth, k_e^+ is about 8.6 which is very close to 7.8, the nominal thickness of the viscous sublayer.

In Fig. 3 the results of Nikuradse's experiment in Fig. 2 are replotted to see the variation of k_e^+ as a function of k^+ together with Eqs. (20) and (21). It increases continuously from k_{e0}^+ (≈ 8.6) when $k^+ = 0$ and asymptotes to a straight line $k_e^+ = k^+$ and two theoretical curves follow experimental data points very closely except the small region near $k^+ = 10$. It can be seen easily that, instead of these two curves, a single equation of the type

$$k_e^+ = k^+ + k_{e0}^+ \exp(-\beta k^+) \tag{24}$$

will fit data points more closely, if appropriate values are taken for k_{e0}^+ and β.

It has already been shown that the dimensionless displacement height d^+ will take the same value (≈ 5.3) for both the smooth and rough surfaces and its value for transitional surfaces (approximately $6 < k^+ < 15$) only has not yet been determined. However, it is hard to think that it will take a different value in this small region. Then Eq. (23) becomes

$$B = B_\infty - \frac{1}{\kappa}\ln\left[1+\frac{k_{e0}^+ e^{-\beta k^+} - d_s^+}{k^+}\right] \tag{25}$$

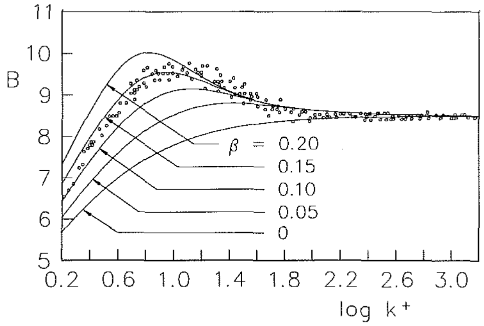

Fig. 5 Effect of β on the roughness function B

In Fig. 2, Eq. (25) is also plotted with $\beta = 0.12$. Again it agrees very well to the experiment in the whole range of k^+.

Equation (22) can be rearranged as

$$u^+ = \frac{1}{\kappa}\ln(y^+ - d_s^+) + A_s - \Delta u^+ \tag{26}$$

where

$$\Delta u^+ = \frac{1}{\kappa}\ln(k^+ + k_{e0}^+ e^{-\beta k^+} - d_s^+) + A_s - B_\infty \tag{27}$$

In Fig. 4 the vertical shift, Δu^+, of the logarithmic curve is plotted as a function of k^+ with β as a parameter. From this figure (compare this with Fig. 11 of Clauser, 1956) we can see that the above formulation can be applicable not only to sand roughened surfaces but also to other rough surfaces by adjusting values of β and B_∞ (or by taking appropriate values for the parameter β and the equivalent sand roughness); the shape of the curve will vary according to the value of β, and B_∞ determines the vertical shift of the curve. Variation of the roughness function B according to the parameter β is also plotted in Fig. 5.

3 The Friction Factor

Integrating Eq. (22) over the cross-sectional area (strictly speaking, from the center of the pipe to $R - k_e$, where R is a radius of the pipe, and then letting k_e/R and d/R go to zero) we obtain the mean velocity V of the flow

$$\frac{V}{u_\tau} = \frac{1}{\kappa}\ln\frac{R}{k} + B - \frac{3}{2\kappa} \tag{28}$$

and the pipe friction factor f

$$\sqrt{\frac{8}{f}}=\frac{1}{\kappa}\ln\frac{R}{k}+B-\frac{3}{2\kappa} \tag{29}$$

Using Eq. (25) and substituting constants by appropriate values ($\kappa = 0.4$, $B_\infty = 8.5$, $k_{e0}^+ = 8.6$, and $d_s^+ = 5.3$), we have from Eq. (29)

$$\frac{1}{\sqrt{f}}=1.68-2.035\log\left[\frac{k}{R}+\frac{48.6\exp\left(-0.1768\beta \mathrm{R}_D\frac{k}{R}\sqrt{f}\right)-30.0}{\mathrm{R}_D\sqrt{f}}\right] \tag{30}$$

where R is the radius of the pipe and R_D the Reynolds number based on the diameter of the pipe and the mean velocity. The experiment, however, requires that the constants 1.68 and 2.035 in Eq. (30) should be adjusted to 1.74 and 2.0, respectively, giving the pipe friction formula as

$$\frac{1}{\sqrt{f}}=1.74-2.0\log\left[\frac{k}{R}+\frac{48.6\exp\left(-0.1768\beta \mathrm{R}_D\frac{k}{R}\sqrt{f}\right)-30.0}{\mathrm{R}_D\sqrt{f}}\right] \tag{31}$$

By putting $k = 0$ in Eq. (31) we get the *Prandtl's universal law of friction for smooth pipes*,

$$\frac{1}{\sqrt{f}}=2.0\log(\mathrm{R}_D\sqrt{f})-0.8 \tag{32}$$

and, by letting R_D go to infinity, the resistance formula for completely rough pipes,

$$\frac{1}{\sqrt{f}}=2.0\log\frac{R}{k}+1.74 \tag{33}$$

If we put $\beta = 0.12$, we have the friction formula for sand-grained pipes, which did not seem to be known before,

$$\frac{1}{\sqrt{f}}=1.74-2.0\log\left[\frac{k}{R}+\frac{48.6\exp\left(-0.0212\mathrm{R}_D\frac{k}{R}\sqrt{f}\right)-30.0}{\mathrm{R}_D\sqrt{f}}\right] \tag{34}$$

Finally, if we put $\beta=0$, we get the well-known *Colebrook's formula* for commercial pipes

$$\frac{1}{\sqrt{f}}=1.74-2.0\log\left[\frac{k}{R}+\frac{18.6}{\mathrm{R}_D\sqrt{f}}\right] \tag{35}$$

There seems no need to confirm Eqs. (32), (33), and (35) any more, which are well-known and have been used satisfactorily for a long time. In Fig. 6, friction factors computed from Eq. (34) are compared with those measured by Nikuradse and Galavics (Schlichting, 1968, Fig. 20.18). The agreement is excellent except when $R/k = 1300$. Note, however, that Galavics' experiment ($R/k = 1300$) is with commercial pipes.

4 The Skin-Friction Coefficient

To get a velocity profile in a boundary layer, we should add an empirical wake function. If we use the Coles' wake function (Coles, 1956), we have

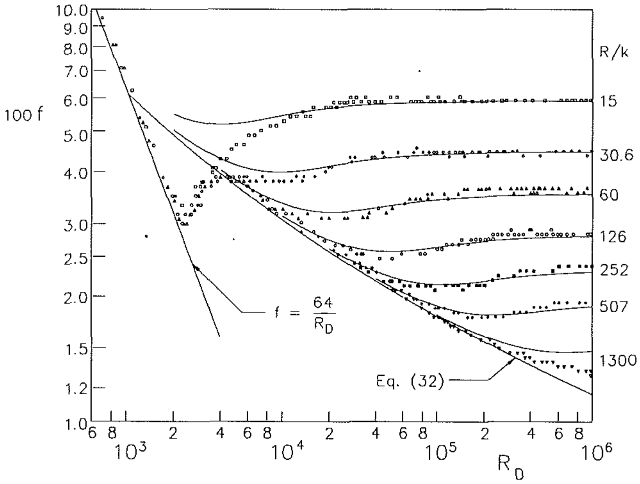

Fig. 6 Pipe-friction factor for rough pipes after Nikuradse and Galavics (Schlichting, 1968). Curves for rough pipes are after Eq. (34).

$$\frac{u}{u_\tau}=\frac{1}{\kappa}\ln\frac{y^+-d_s^+}{k^+}+B+\frac{\Pi(x)}{\kappa}w\left(\frac{y}{\delta}\right) \tag{36}$$

where B is given in Eq. (25). The profile parameter Π is nearly constant when the momentum-thickness Reynolds number is greater than 5000 and the law-of-the-wake function $w(y/\delta)$ is independent of x and has the value of 2 at $y = \delta$, i.e., $w(1)=2$. Thus at the edge of the boundary layer, assuming that $\delta >> d_s$, we have

$$\frac{u_e}{u_\tau}=\frac{1}{\kappa}\ln\frac{\mathrm{R}_\delta\frac{u_\tau}{u_e}}{\mathrm{R}_k\frac{u_\tau}{u_e}+k_{e0}^+\exp\left(-\beta\mathrm{R}_k\frac{u_\tau}{u_e}\right)-d_s^+}+B_\infty+\frac{2\Pi}{\kappa} \tag{37}$$

where u_e is the free stream velocity and R_δ and R_k are Reynolds numbers, i.e., $\mathrm{R}_\delta = u_e\delta/\nu$ and $\mathrm{R}_k = u_ek/\nu$. Assuming further that the boundary layer thickness δ increases proportional to the distance x from the leading edge, i.e.,

$$\delta=b\frac{u_\tau}{u_e}x$$

where b is a constant, and that Π and $w(1)$ are independent of k and x, we have the formula for the skin friction c_f as

$$\frac{1}{\sqrt{c_f}}=\frac{1}{\sqrt{2}\kappa}\ln\frac{\mathrm{R}_xc_f}{\mathrm{R}_k\sqrt{c_f}+\sqrt{2}\,[k_{e0}^+\exp(-\beta\mathrm{R}_k\sqrt{c_f}/\sqrt{2})-d_s^+]}+C \tag{38}$$

where R_x is a Reynolds number ($=u_ex/\nu$) and C is a constant. When $k = 0$, Eq. (38) reduces to

$$\frac{1}{\sqrt{c_f}}=\frac{1}{\sqrt{2}\kappa}\ln \mathrm{R}_xc_f-\frac{1}{\sqrt{2}\kappa}\ln[\sqrt{2}(k_{e0}^+-d_s^+)]+C$$

To fit this equation to the *Kármán's skin-friction formula for smooth plates*

$$\frac{1}{\sqrt{c_f}}=1.8\ln(\mathrm{R}_xc_f)+1.7 \tag{39}$$

we need to put

$$\frac{1}{\sqrt{2}\kappa}=1.8$$

and

$$C-\frac{1}{\sqrt{2}\kappa}\ln[\sqrt{2}(k_{e0}^{+}-d_s^{+})=1.7$$

which give $\kappa = 0.39$ and $C = 4.5$, if $k_{e0}^{+} = 8.6$ and $d_s^{+} = 5.3$ are taken as before. Then Eq. (38) becomes

$$\frac{1}{\sqrt{c_f}}=1.8\ln\frac{\mathrm{R}_x c_f}{\mathrm{R}_k\sqrt{c_f}+12.2\exp(-0.71\beta\mathrm{R}_k\sqrt{c_f})-7.5}+4.5 \qquad (40)$$

If we put $\beta = 0.12$ in Eq. (40), we get the equation for the sand-grained plates

$$\frac{1}{\sqrt{c_f}}=1.8\ln\frac{\mathrm{R}_x c_f}{\mathrm{R}_k\sqrt{c_f}+12.2\exp(-0.085\,\mathrm{R}_k\sqrt{c_f})-7.5}+4.5 \qquad (41)$$

putting $\beta = 0$, the skin-friction formula which may be useful for commercial plates

$$\frac{1}{\sqrt{c_f}}=1.8\ln\frac{\mathrm{R}_x c_f}{\mathrm{R}_k\sqrt{c_f}+4.7}+4.5 \qquad (42)$$

and, finally, for completly rough plates with $\mathrm{R}_k\sqrt{c_f} >> 1$

$$\frac{1}{\sqrt{c_f}}=1.8\ln\left(\frac{x}{k}\sqrt{c_f}\right)+4.5 \qquad (43)$$

5 Conclusions

A simple formula to represent the mean-velocity distribution across the inner layer of a turbulent boundary layer is suggested. The suggested equation is general enough to be applicable to turbulent boundary layers over surfaces of any roughnesses covering from very smooth to completely rough surfaces. This generalization is made possible by introducing the equivalent roughness which is defined as the distance from the wall to where the velocity gets a certain value ($u^{+} \approx 8.5$); the equivalent roughness is, in fact, the lower boundary of the inner layer where the logarithmic velocity profile holds and can be represented by a simple function of the roughness. The suggested velocity profile is then used to get equations for friction factors of fully developed turbulent pipe flows and skin-friction coefficients in constant-pressure turbulent boundary layers. These formulae are consistent with existing experimental observations and embrace equations, which are known to be accurate and have been used widely for a long time in engineering problems but under restricted conditions (say, an equation for smooth surfaces or applicable to completely rough pipes, etc.), as special cases.

Acknowledgment

I am grateful to Prof. P. Bradshaw, FRS, for reading the manuscript and giving valuable comments.

References

Clauser, F. H., 1956, "The Turbulent Boundary Layer," *Advan. Appl. Mech.*, Vol. 4, pp. 1-51.

Coles, D., 1956, "The Law of the Wake in the Turbulent Boundary Layer," *J. Fluid Mech.*, Vol. 1, pp. 191-226.

Granville, P. S., 1958, "The Frictional Resistance and Turbulent Boundary Layer of Rough Surfaces," *J. of Ship Research*, Vol. 2, No. 3, pp. 52-74.

Jackson, P. S., 1981, "On the Displacement Height in the Logarithmic Velocity Profile," *J. Fluid Mech.*, Vol. 111, pp. 15-25.

Reichardt, H., 1951, "Vollständige Darstellung der turbulenten Geschwindigkeitsverteilung in glatten Leitungen," *ZAMM*, Vol. 31, pp. 208-219.

Schlichting, H., 1968, *Boundary-Layer Theory*, 6th ed., McGraw-Hill.

Squire, H. B., 1948, "Reconsideration of the Theory of Free Turbulence," *Phil. Mag.*, Vol. 39, pp. 1-20.

van Driest, E. R., 1965, "On Turbulent Flow Near a Wall," *J. Aero. Sci.*, Vol. 23, pp. 1007-1011.

An Inverse Inner-Variable Theory for Separated Turbulent Boundary Layers

D. K. Das
Associate Professor
of Mechanical Engineering,
University of Alaska Fairbanks,
Fairbanks, AK 99775-0660

An integral method is presented for computing separated and reattached turbulent boundary layers for incompressible two-dimensional flows. This method is a substantial improvement over the inner-variable approach of Das and White (1986), which was based on a direct boundary layer scheme that had several shortcomings. In this new approach, the integral equations have been completely reformulated so that the theory now proceeds in an inverse mode using displacement thickness as input. This new formulation eliminates the need for the second derivative of velocity distribution, which in the past has always been a source of error in all previous inner-variable approaches. Other significant additions are: (a) a single pressure gradient-wake correlation from a large amount of experimental data; and (b) replacement of the wake parameter from the final equations with a more stable parameter, wake velocity. Derivations of integral equations and their final working expressions, in both dimensional and nondimensional forms, are presented in detail. Predictions by this theory for skin friction, freestream velocity, momentum thickness, velocity profile and separation, and reattachment points agree well with experimental data. Sensitivity studies display that the theory is stable against variations in initial conditions, input distributions, and the pressure gradient-wake correlation.

1 Introduction

Turbulent flow separation occurs frequently in many fluid-handling devices. Therefore, research continues on this important class of flow problems on both the analytical and experimental fronts. In modeling the separated flow fields, one may resort to the solution of either the Navier-Stokes equations or a simplified set of boundary layer equations. The boundary layer methods, using both integral and differential approaches, are well documented in the *Stanford Conference Proceedings* by Kline et al. (1968). Newer techniques, including Navier-Stokes solutions, can be found with detailed descriptions and computations in the three volumes of the *Proceedings of 1980–81 AFOSR-HTTM-Stanford Conference on Complex Turbulent Flows* by Kline et al. (1981). In this paper, we will present an integral theory based on a conceptually simple scheme suitable for practical design computations with a minimal amount of computer storage and time.

In the realm of differential theories, Celenligil and Mellor (1985) presented a time dependent finite difference scheme based on the vorticity-stream function approach and found that the wall boundary conditions required further improvement in the separation region. Kwon and Pletcher (1986) computed separated channel flows with a viscous-inviscid interaction procedure. Henau et al. (1990) showed that their modified K-ϵ model predicted separation while the standard K-ϵ model did not. All these differential methods required variations from the original turbulence models for their application to separated flows.

Considering the integral form of the boundary layer equations, Kline et al. (Vol. II, 1981) classified the methods into three categories. All three use the standard Karman momentum integral equation; it is the choice of the second integral equation that distinguishes one method from the other. The second equation can be: (*a*) a moment of momentum equation, (*b*) a kinetic energy equation, or (*c*) an entrainment equation.

However, the inner-variable integral method described in this paper is unique in that it follows a new approach differing from theories based on the Karman relation. Instead of using the equations previously cited, it derives its own integral relation. The detailed derivation of this equation for separated flows is a major objective of this paper.

Reviewing integral theories, we find that Gerhart (1979) employed the moment of momentum integral equation and used the flow angle in place of displacement thickness as the input. Moses et al. (1979; 1982) selected the kinetic energy integral equation and solved the viscous boundary layer equation simultaneously with the inviscid equation in a finite difference form. Whitfield et al. (1981) also used the kinetic energy integral equation, but evaluated the dissipation integral from a three-parameter velocity profile expression. Strawn and Kline (1983) employed the entrainment equation through the correlation of Ferziger et al. (1982). Later, Strawn et al. (1984) adopted Head's entrainment correlation via shape factor to analyze separated flow fields in diffusers. Melnik and Brook (1986) applied a modified Green's entrainment equation with

---

Contributed by the Fluids Engineering Division for publication in the JOURNAL OF FLUIDS ENGINEERING. Manuscript received by the Fluids Engineering Division February 20, 1992. Associate Technical Editor: D. M. Bushnell.

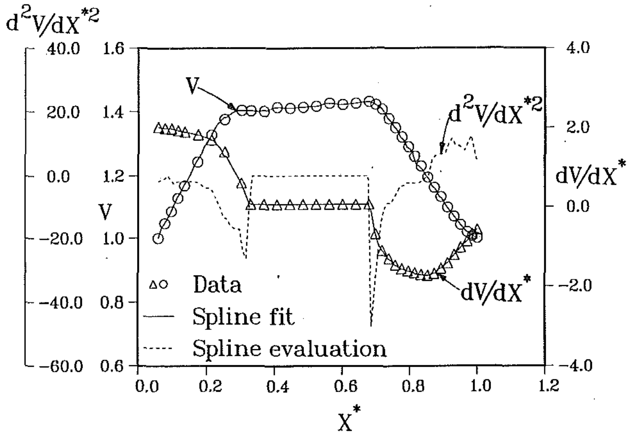

Fig. 1 Distribution of velocity and its derivatives for flow INDENT-2100. Circles represent measured velocities and triangles represent computed data points of the first derivative reported in Coles and Hirst (1968). $V = U/U_0$, U_0 = 34.08 m/s.

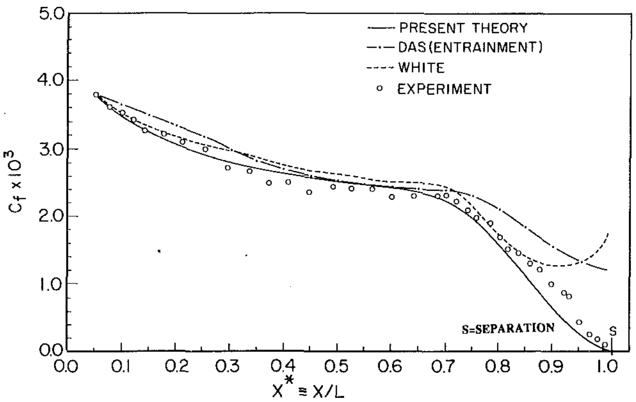

Fig. 2 Prediction via three different theories. White's and Das' are direct schemes; the present theory uses an inverse scheme. Experimental data are from IDENT-2100, Coles and Hirst (1968). S (experiment) reported in Kueth and Chow (1986) = 7.8 ± 0.1 m, S (prediction) = 8.0 m.

a lag scheme to predict separated flow at the trailing edge of airfoils. In Volume III of Kline et al. (1981), Smith presented computations from Green's lag-entrainment method, and interactive calculations with the method of Collyer and Lock. A similar lag-entrainment integral method for the viscous region was formulated by Le Balleur in an interactive scheme to compute transonic flows in Kline et al. (1981). Cousteix has reviewed a number of these integral techniques in Kline et al. (1981, Vol. II, pp. 650–671).

The new method presented in this paper is no more complex than any of the integral methods just discussed, but it is quite different. It is an improvement on White's theory (1974), and is called the inner-variable method because all integral calculations are performed in the inner or wall coordinate y^+. The basic difference lies in the momentum integral equation. The inner-variable integrations yield a differential equation with skin friction as the primary variable, which is a more fundamental parameter than the momentum thickness used in theories based on the Karman relation. Therefore, the inner-variable approach does not require any empirical correlation for skin friction. Rather, it obtains skin friction directly from the solution of a differential equation, and predicts the steady separation point where skin friction approaches zero.

A major deficiency in the original inner-variable method was the need for accurate knowledge of the second derivative of the external velocity distribution, but the evaluation of the second derivatives from discrete data points was highly uncertain, since numerical differentiation is inherently an inaccurate process. Figure 1 displays this behavior for the separating airfoil flow of Schubauer and Klebanoff denoted as FLOW: 2100 in the Stanford Conference Proceedings (Coles and Hirst, 1968). We can obtain a very precise fit by using accurate cubic spline subroutines CSAKM and CSDER of IMSL (1987) for velocity V and dV/dx^* distribution. As evident from Fig. 1, despite these accurate subroutines, the second derivative d^2V/dx^{*2} evaluation is erroneous, with many abrupt changes and wavy characteristics. A consequence of this drawback is the poor prediction by the original White (1974) method as displayed in Fig. 2.

Additional studies conducted by Das (1983; 1987), and Das and White (1986) to overcome this shortcoming revealed that even a different approach with entrainment correlation of Ferziger et al. (1982) as a closure equation did not improve the results significantly. Finally, by reformulating the inner variable theory in the inverse mode, the necessity of the second derivative of velocity was eliminated and the inverse theory predicted separation, as it should, in Fig. 2. This demonstrated its ability to compute separated boundary layers where direct inner-variable schemes had failed. Additional advances were accomplished by refining the pressure gradient-wake correlation and by introducing wake velocity v_β, so that the new

Nomenclature

A_i, B_i, D_i, E_i = coefficients in Eqs. (8), (10), (12), (14)
B = constant in the law-of-the-wall = 5.0
C_f = skin friction coefficient, $2\tau_w/\rho U^2 = 2\zeta|\zeta|$
L = reference length, usually length of the body
P_i, Q_i, R_i = coefficients in Eqs. (22), (23), (24)
p = pressure
R, S = reattachment and separation points
S_{ii} = dimensionless coefficients in Eqs. (28), (29), (30)
y^+ = dimensionless law-of-the-wall variable, $y^+ = y|v^*|/\nu$
U = velocity at the edge of the boundary layer
U_0 = reference velocity, usually the velocity at entrance
V = dimensionless velocity, U/U_o
u, v = velocity components parallel and normal to the wall
v^* = shear velocity, $(\text{sign } \tau_w)\sqrt{\frac{|\tau_w|}{\rho}}$

ζ = dimensionless shear velocity, v^*/U
v_β = wake velocity, $\Pi|v^*|$
V_b = dimensionless wake velocity, v_β/U
x, y = coordinates parallel and normal to the wall
x^* = dimensionless surface distance, x/L
β = Clauser's pressure gradient parameter
δ = boundary layer thickness
δ^+ = value of y^+ at the edge of the boundary layer, $\delta|v^*|/\nu$
δ^* = displacement thickness
δ_n^* = dimensionless displacement thickness, δ^*/L
θ = momentum thickness
θ_n = dimensionless momentum thickness, θ/L
κ = Von Karman's constant in the law-of-the-wall = 0.41
ν = kinematic viscosity
Π = Cole's wake parameter
ρ = density
τ = shear stress
τ_w = shear stress at the wall

formulation had improved the prediction of integral thickness and shape factor, which the earlier direct scheme could not.

For potential users, we have listed the expressions for the final working equations in the Appendix to program this method. Using them, a small computer program can be written and run on the mini- or micro-computers available to small-scale industrial users. In design problems the displacement thickness distribution is not known a priori. Therefore, this integral method must be combined with an inviscid solution code, as done for example, by Whitfield et al. (1981) or Strawn et al. (1984).

2 Development of the Theory

The problem of two-dimensional incompressible turbulent boundary layers is governed by the equations for conservation of mass and momentum.

$$\frac{\partial u}{\partial x}+\frac{\partial v}{\partial y}=0 \tag{1}$$

$$u\frac{\partial u}{\partial x}+v\frac{\partial u}{\partial y}=U\frac{dU}{dx}+\frac{1}{\rho}\frac{\partial \tau}{\partial y} \tag{2}$$

The velocity profile adopted here is the well-known law-of-the-wall and wake. The wake laws of Coles and Moses (White, 1974) are nearly identical, and when integrated for displacement and momentum thicknesses, they yield essentially the same results. There are, however, some advantages with the polynomial function of Moses: (*a*) while deriving the momentum integral equation, the integrations are easiest using this function; and (*b*) it enables us to evaluate all integrals across the boundary layer analytically. Therefore, we use the velocity profile equation with the polynomial wake.

$$u(x,y)=v^*\left[\frac{1}{\kappa}\ln y^+ + B\right]+\frac{2v_\beta}{\kappa}\left[3\left(\frac{y^+}{\delta^+}\right)^2-2\left(\frac{y^+}{\delta^+}\right)^3\right] \tag{3}$$

Das and White (1986) and Das (1990) have successfully applied the velocity equation in this form to flows in unseparated as well as separated regions.

As mentioned earlier, the present theory uses its own momentum integral equation, unlike other integral theories that employ the classical Karman integral equation. The inner-variable momentum integral equation presented by White (1974) will not be accurate because it is based on a crude linear wake model, and that velocity profile is not suitable for separated flows. Therefore, we need to derive an appropriate integral equation. Derivation of this integral equation in terms of inner-variables constitutes the critical part of this theory. It involves lengthy analytical expressions; for clarity, all intermediate results are included for easy comprehension of the theory.

With $u(x, y)$ prescribed by Eq. (3), we can obtain the normal velocity component $v(x, y)$ by integrating the mass conservation Eq. (1).

$$v(x,y)=-\int_0^y \frac{\partial u}{\partial x}\,dy=-\frac{\nu}{|v^*|}\int_0^{y^+}\frac{\partial u}{\partial x}\,dy^+ \tag{4}$$

Note the transformation of integration from the physical y coordinate to the y^+ coordinate, which is the key to the inner-variable approach. The partial derivative in Eq. (4) is obtained from Eq. (3).

$$\begin{aligned}\frac{\partial u}{\partial x}&=\left[\frac{1}{\kappa}\ln y^+ + B\right]\frac{dv^*}{dx}+\frac{v^*}{\kappa|v^*|}\frac{d|v^*|}{dx}\\ &+\frac{2}{\kappa}\frac{dv_\beta}{dx}\left[3\left(\frac{y^+}{\delta^+}\right)^2-2\left(\frac{y^+}{\delta^+}\right)^3\right]+\frac{12v_\beta}{\kappa}\left[\left(\frac{y^+}{\delta^+}\right)-\left(\frac{y^+}{\delta^+}\right)^2\right]\\ &\times\left(\frac{y^+}{\delta^+}\right)\left(\frac{1}{|v^*|}\frac{d|v^*|}{dx}-\frac{1}{\delta^+}\frac{d\delta^+}{dx}\right)\end{aligned} \tag{5}$$

Substituting Eq. (5) into (4), completing the integration, and rearranging the terms, one obtains an important equation. This is the equation that enables one to generate the normal component of the velocity profile at any streamwise location in the boundary layer.

$$\begin{aligned}v(x,y)&=-\frac{\nu y^+}{|v^*|}\left[\frac{1}{\kappa}\ln y^+ + \left(B-\frac{1}{\kappa}\right)\right]\frac{dv^*}{dx}\\ &-\frac{\nu v^* y^+}{\kappa|v^*|^2}\frac{d|v^*|}{dx}-\frac{12\nu v_\beta}{\kappa|v^*|^2}\left[\frac{y^{+3}}{3\delta^{+2}}-\frac{y^{+4}}{4\delta^{+3}}\right]\frac{d|v^*|}{dx}\\ &-\frac{2\nu}{\kappa|v^*|}\left[\frac{y^{+3}}{\delta^{+2}}-\frac{y^{+4}}{2\delta^{+3}}\right]\frac{dv_\beta}{dx}+\frac{12\nu v_\beta}{\kappa|v^*|}\left[\frac{y^{+3}}{3\delta^{+3}}-\frac{y^{+4}}{4\delta^{+4}}\right]\frac{d\delta^+}{dx}\end{aligned} \tag{6}$$

Next, obtain the partial derivative of u with respect to y from Eq. (3) to express the convective acceleration terms in the conservation of momentum Eq. (2).

$$\frac{\partial u}{\partial y}=\frac{v^*|v^*|}{\kappa y^+\nu}+\frac{12v_\beta}{\kappa}\left(\frac{y^+}{\delta^{+2}}-\frac{y^{+2}}{\delta^{+3}}\right)\frac{|v^*|}{\nu} \tag{7}$$

Now Eqs. (3), (5), (6), and (7) are substituted into the momentum Eq. (2). Upon simplification and grouping terms with same x-derivatives, we obtain

$$A_1\frac{dv^*}{dx}+A_2\frac{d|v^*|}{dx}+A_3\frac{dv_\beta}{dx}+A_4\frac{d\delta^+}{dx}=U\frac{dU}{dx}+\frac{1}{\rho}\frac{\partial\tau}{\partial y} \tag{8}$$

The coefficients A_1 through A_4 are analytical functions of v^*, v_β, y^+ and δ^+; these are presented in the Appendix.

Equation (8) is next integrated across the boundary layer, analogous to the Karman method, but the integrations are now performed in the y^+ direction instead of the y direction. The limits at the wall are $y^+ = 0$ and $\tau = \tau_W$, and the limits at the edge of the boundary layer are $y^+ = \delta^+$ and $\tau = 0$. Integration of the right side of Eq. (8) with the shear stress term is simple.

$$\begin{aligned}&U\frac{dU}{dx}\delta^+ +\frac{1}{\rho}\int_0^{\delta^+}\frac{\partial\tau}{\partial y^+}\frac{\partial y^+}{\partial y}\,dy^+\\ &\qquad=U\frac{dU}{dx}\delta^+ +\frac{|v^*|}{\rho\nu}\int_{\tau_w}^{0}\partial\tau=\delta^+ U\frac{dU}{dx}-\frac{|v^*|}{\mu}\tau_w\end{aligned} \tag{9}$$

where $\tau_W = \rho v^*|v^*|$ to account for reverse flow.

The integrals on the left side of Eq. (8) are lengthy, but they are the most crucial part for the correctness of the theory. Fortunately, all integrals can be evaluated analytically, and no numerical integrations were needed to obtain the final form of the momentum integral equation.

$$(B_1\pm B_2)\frac{dv^*}{dx}+B_3\frac{dv_\beta}{dx}+B_4\frac{d\delta^+}{dx}+B_5\frac{dU}{dx}=B_6 \tag{10}$$

Once the integrations are complete, the coefficients B_1 through B_6 are available as universal algebraic functions applicable to all types of unseparated and separated boundary layers under arbitrary pressure gradient conditions. These coefficients are simply analytical functions of relevant parameters v^*, v_β, δ^+, and U. The final expressions for these coefficients are listed in the Appendix, so they are readily available to potential users. A major advantage of having these coefficients in the analytical form translates into considerable savings in computational effort and time. For many other integral theories, the integral coefficients must be obtained via numerical integrations. This effect increases the complexity and computing time at each step, while advancing the boundary layer solution. In Eq. (10), the positive sign on B_2 applies before separation ($v^* > 0$) and the negative sign applies after separation ($v^* < 0$).

To solve for the four unknowns, v^*, v_β, δ^+, and U in Eq. (10), we must seek three additional relations. One comes from the differentiated wall-wake law, a second from the displacement thickness relation, and the third from the pressure-gradient wake correlation. These are derived in the following:

Applying the boundary condition $u(x, y) = U$ at $y^+ = \delta^+$ to Eq. (3), we get

$$U = v^* \left(\frac{1}{\kappa} \ln\delta^+ + B \right) + \frac{2v_\beta}{\kappa} \tag{11}$$

Differentiating Eq. (11) and rearranging the terms like Eq. (10) leads to

$$D_1 \frac{dv^*}{dx} + D_2 \frac{dv_\beta}{dx} + D_3 \frac{d\delta^+}{dx} + D_4 \frac{dU}{dx} = 0 \tag{12}$$

where D_1 through D_4 are listed in the Appendix.

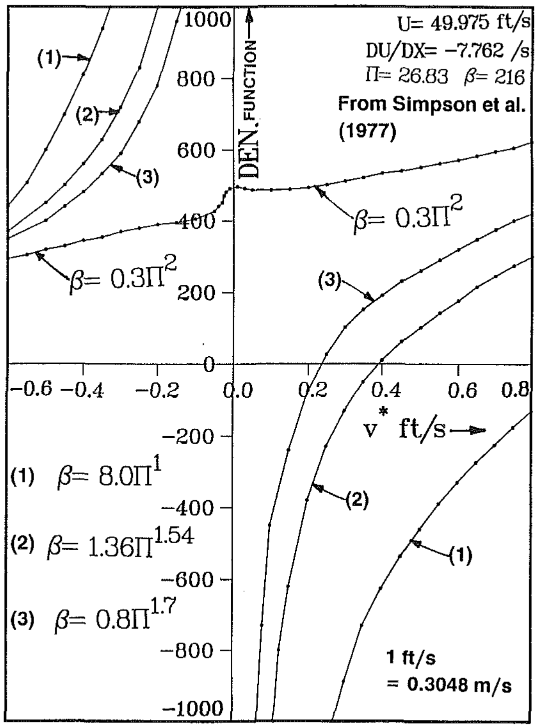

Fig. 3 Effect of various Π-β curve-fits on the theory in the vicinity of separation. The "denominator" function along the ordinate is the principal term in the final working equation as presented in Das (1983) and Das and White (1986).

Using the definition of displacement thickness and integrating the velocity profile Eq. (3), we obtain

$$\frac{\delta^*}{\delta} = \frac{v_\beta + v^*}{\kappa U} \tag{13}$$

Note that we integrated Moses' polynomial wake, and it yields exactly the same expression as that given by Coles with his sine wake in Coles and Hirst (1968), thus demonstrating the similarity between the two wake functions.

Differentiating Eq. (13) and rearranging results in

$$E_1 \frac{dv^*}{dx} + E_2 \frac{dv_\beta}{dx} + E_3 \frac{d\delta^+}{dx} + E_4 \frac{dU}{dx} = E_5 \tag{14}$$

where E_1 through E_5 are given in the Appendix.

Note the improvement over our earlier theory (Das and White, 1986; Das, 1988). We had the wake parameter Π in the momentum integral relation and in all auxiliary equations; we have now replaced it with the wake velocity v_β. As Ghosh and Kline (1978) have shown, at separation, Π goes to infinity as the shear velocity v^* approaches zero. But their product, the wake velocity $v_\beta = \Pi |v^*|$ remains finite. This improvement results in stable computations in the vicinity of separation.

2.1 Pressure Gradient-Wake Correlation. Several empirical correlations to relate Coles' wake parameter Π to Clauser's pressure gradient parameter β have appeared in the literature. White (1974) gave a power-law correlation from the data of some equilibrium and nonequilibrium flows, but they were mostly limited to unseparated boundary layers.

$$\beta = (1.25\ \Pi)^{4/3} - 0.5 \tag{15}$$

In order to extend them to separated flows, Das (1983) compiled a substantial amount of experimental data from eighteen experiments. These included equilibrium and nonequilibrium boundary layers under adverse, as well as favorable pressure gradients. Care was also taken to include several near-separating and fully separated flows. Many functional relationships between β and Π were examined to establish which type of correlation was best suited for separated flows.

Using measured values of free stream velocity, its gradient, Π, and β in the vicinity of separation from the experiment of

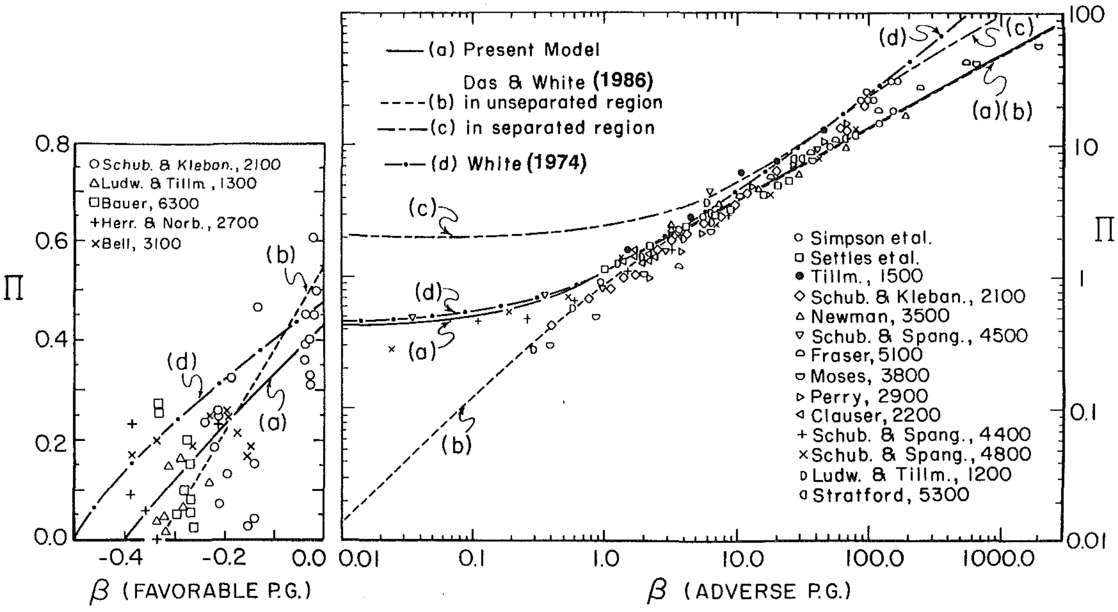

Fig. 4 Π-β correlation. Eighteen data sets have been used. All data sets except Simpson et al. (1977) and Settles et al. (1982) are from Coles and Hirst (1968).

Simpson et al. (1977), computations were made to study the behavior of the theory near separation. The results are displayed in Fig. 3 for several curve-fit functions between β and Π. As separation ($v^* = 0$) is approached, there are substantial changes in the denominator function, which is the main term of the final working equation given in Das (1983) and Das and White (1986). This behavior of the denominator also introduces great changes in computations in the vicinity of separation. As demonstrated in Fig. 3, with the increase in the power of Π from 1 to 2, the zone of instability around separation diminishes. There is only a slight increase with $\beta \sim \Pi^2$ as computation passes through the separation point. Therefore, it is evident that a quadratic form of the curve-fit is the clear choice for modeling separated flows.

Das and White (1986) expressed their Π-β model through three equations. Their equations follow; they have also been plotted against the experimental data in Fig. 4.

$$\beta = 0.76\Pi + 0.42\Pi^2 \quad \text{(adverse gradient unseparated, shown as model } (b) \text{ in Fig. 4)} \tag{16}$$

$$\beta = -5.5 + 2.5\Pi + 0.09\Pi^2 \quad \text{(adverse gradient separated, model } (c)\text{)} \tag{17}$$

$$\beta = 0.6\Pi - 0.33 \quad \text{(favorable gradient, model } (b)\text{)} \tag{18}$$

This approach had several shortcomings. First of all, three correlations were cumbersome to program because computations had to be switched from one mode to the other while passing through different flow regions. This led to discontinuity, or jumps, in calculations. Furthermore, the favorable and adverse gradient equations did not merge smoothly at the zero pressure gradient point (see Fig. 4). Therefore, discontinuity in computation occurred while calculating airfoil-type flow, where the flow is initially under favorable gradient and then gradually changes to adverse gradient.

After examining the data carefully, we have developed a single expression that fits the data well and overcomes all these shortcomings. This model, denoted as model (*a*) in Fig. 4, is shown along with other models for comparison. The new correlation is valid for all flow regions and replaces Eqs. (16), (17), and (18). The final expression is:

$$\beta = c_0 + c_1\Pi + c_2\Pi^2 \text{ where } c_0 = -0.4,\ c_1 = 0.76,\ c_2 = 0.42 \tag{19}$$

We shall adopt Eq. (19) from now on as our standard Π-β correlation. With the Π-β relation established, the third equation can now be derived, which provides closure to our inverse theory. From the definition of the pressure gradient parameter

$$\beta = \frac{\delta^*}{|\tau_w|}\frac{dp}{dx} = -\frac{\delta^*}{|v^*||v^*|}\left(U\frac{dU}{dx}\right) \tag{20}$$

Note that the sign of β is governed by the sign of the pressure or velocity gradient. The absolute value of τ_w is used in Eq. (20) so that the sign of β is not affected when separation occurs and τ_w changes sign. Eliminating δ^* from Eq. (20) through Eq. (13) and substituting for β from the experimental correlation (19), one obtains

$$\frac{dU}{dx} = \frac{-\kappa|v^*|[c_0v^{*2} + c_1v_\beta|v^*| + c_2v_\beta^2]}{\delta^+\nu(v_\beta + v^*)} \tag{21}$$

Equations (10), (12), (14),and (21) can be solved simultaneously for dv^*/dx, $d\delta^+/dx$ and dU/dx, if dv_β/dx can be eliminated. The derivatives of v^*, δ^+ and U are retained for the following reasons. Solving a differential equation in v^* will produce better results for wall shear or skin friction; a differential equation in δ^+ will give better results for integral thicknesses and shape factor; and a differential equation in U will predict the boundary layer edge velocity correctly as necessary in an inverse method. Therefore, dv_β/dx is eliminated in favor of the other derivatives using Eq. (12). Following this elimination, Eqs. (10) and (14) simplify to:

$$P_1\frac{dv^*}{dx} + P_2\frac{d\delta^+}{dx} + P_3\frac{dU}{dx} = P_4 \tag{22}$$

$$Q_1\frac{dv^*}{dx} + Q_2\frac{d\delta^+}{dx} + Q_3\frac{dU}{dx} = Q_4 \tag{23}$$

where coefficients P_1 through P_4 and Q_1 through Q_4 are given in the Appendix. Equation (21) can be viewed in the same form as Eqs. (22) and (23), where the first two coefficients are zero and the right side of Eq. (21) can be denoted as R_4.

There are now three ordinary differential Eqs.—(21), (22), and (23)—which can be solved simultaneously for three variables—v^*, δ^+, and U—after applying Cramer's rule.

The origin of these three relations are:

$$\begin{array}{l} \text{Momentum equation} \\ \text{Displacement thickness equation} \\ \Pi\text{-}\beta \text{ equation} \end{array} \begin{bmatrix} P_1 & P_2 & P_3 \\ Q_1 & Q_2 & Q_3 \\ 0 & 0 & 1 \end{bmatrix} \begin{Bmatrix} dv^*/dx \\ d\delta^+/dx \\ dU/dx \end{Bmatrix} = \begin{Bmatrix} P_4 \\ Q_4 \\ R_4 \end{Bmatrix} \tag{24}$$

After solving them at each spatial step in the streamwise direction, the fourth variable v_β is obtained from the wall-wake law

$$v_\beta = \frac{\kappa}{2}\left[U - v^*\left(\frac{1}{\kappa}\ln\delta^+ + B\right)\right] \tag{25}$$

and the skin friction coefficient follows from $C_f = 2v^*|v^*|/U^2$.

Once v^*, δ^+, U and v_β are computed at any streamwise location, computing the momentum thickness θ and then the shape factor is straightforward. Integration of the velocity profile Eq. (3) yields

$$\theta = \delta^* - \frac{\nu\delta^+}{|v^*|\kappa^2U^2}(2v^{*2} + 3.1667v^*v_\beta + 1.4857v_\beta^2) \tag{26}$$

2.2 Nondimensional Form. It is convenient to nondimensionalize the final working equations following White (1974), before applying them to a set of experiments. This transformation helps free the computations from dependence on any particular unit. For this, the following dimensionless variables have been selected.

$$x^* = \frac{x}{L},\ V = \frac{U}{U_0},\ \zeta = \frac{v^*}{U},\ V_b = \frac{v_\beta}{U},\ \delta_n^* = \frac{\delta^*}{L},\ \theta_n = \frac{\theta}{L} \tag{27}$$

Substituting the nondimensionalized variables into the final set of equations [Eqs. (21), (22), and (23)] and rearranging, three differential equations in dimensionless shear velocity ζ, thickness δ^+, and edge velocity V are obtained.

$$S_{11}\frac{d\zeta}{dx^*} + S_{12}\frac{d\delta^+}{dx^*} + S_{13}\frac{dV}{dx^*} = S_{14} \tag{28}$$

$$S_{21}\frac{d\zeta}{dx^*} + S_{22}\frac{d\delta^+}{dx^*} + S_{23}\frac{dV}{dx^*} = S_{24} \tag{29}$$

$$S_{33}\frac{dV}{dx^*} = S_{34} \tag{30}$$

The coefficient functions S_{ij} are all dimensionless and are listed in the Appendix. The wake velocity V_b and momentum thickness θ_n at each step in the longitudinal direction x^* are calculated from two algebraic equations whose nondimensionlized expressions follow.

$$V_b = \frac{\kappa}{2}\left[1 - \zeta\left(\frac{1}{\kappa}\ln\delta^+ + B\right)\right] \tag{31}$$

$$\theta_n = \delta_n^* - \frac{\delta^+}{\kappa^2VR_L|\zeta|}[2\zeta^2 + 3.1667\zeta V_b + 1.4857V_b^2] \tag{32}$$

Here $R_L = U_0L/\nu$ is the nominal Reynolds number.

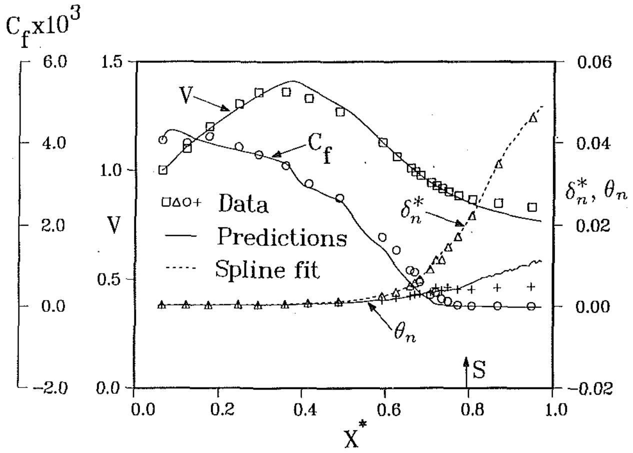

Fig. 5 Comparison between theoretical and experimental results for the flow of Simpson et al. (1981). S (experiment) = 3.4 m, S (prediction) = 3.63 m, L = 4.57 m, U_0 = 16.03 m/s. Measurement uncertainties reported by experimenters (V ±2.4 percent hot-wire, ±3.2 percent cross hot-wire, laser anem. ±0.2 ft/s; C_f ±8.5 percent Preston tube, ±12 percent surface hot-wire).

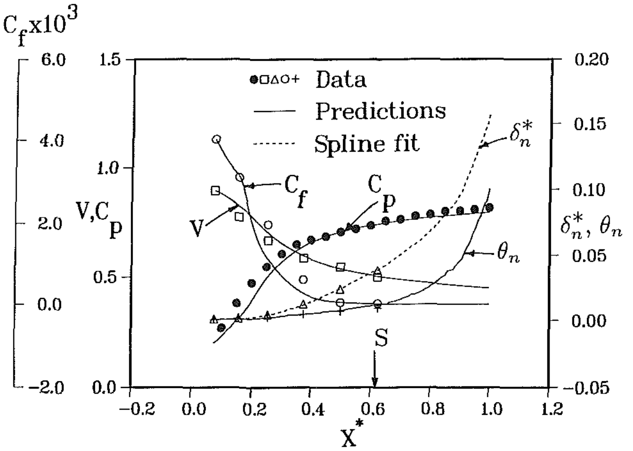

Fig. 6 Comparison between theoretical and experimental results for the flow of Moses. Experimental data are from IDENT-3800, Coles and Hirst (1968). S (experiment) = 0.562 m, S (prediction) = 0.627 m, L = 1.016 m, U_0 = 23.77 m/s.

3 Computational Scheme

The three first-order nonlinear ordinary differential equations (ODE) can be solved using any ODE solver to obtain ζ, δ^+, and V. Notice that a direct output of this solution is ζ, the skin friction parameter that determines the skin friction coefficient via $C_f = 2\zeta|\zeta|$. Thus, our method yields separation and reattachment points directly where the skin friction vanishes. But the Karman-type integral methods must resort to correlations of shape factor and momentum thickness to infer separation.

A simple Runge-Kutta-Gills subroutine, given in the appendix of the text by White (1974), and an approximate polynomial curve-fit equation for δ_n^* distribution took less than one CPU second to calculate the flow IDENT-2100, displayed in Fig. 2, on a VAX 8600 computer. A step size dependence study was conducted by varying Δx^* up to a factor of three (eg. 0.01 to 0.03). The computed results showed imperceptible change—generally in the fourth place after decimal. Several flows were tested with at least two different step sizes to ensure that convergence had been achieved.

For finer computations, the run was repeated with a sophisticated ODE solver (IVPAG of IMSL, 1987) that can handle stiff as well as nonstiff equations. It possesses many niceties (such as automatic step sizing, excellent local and global error control at each step, and stability) that are useful for computations in the vicinity of separation. An accurate δ_n^* distribution was provided as input to this program through IMSL cubic spline subroutines, CSAKM and CSDER. The refined computation took approximately three seconds on the same VAX machine, indicating that the computing costs are very small.

4 Comparison With Experiments

The parameters that are important for comparison with experimental data are: velocity V, skin friction C_f, and momentum thickness θ_n. The distribution of displacement thickness δ_n^*, which is the input to our theory, will also be shown for each test case.

A Separated Flow: Figure 5 presents the results for the separated flow of Simpson et al. (1981), which was a test case for many theories in the 1980–81 Stanford Conference. The overall predictions for all parameters are quite good. There are a number of "wiggles" only on the θ_n curve. This is not due to step size refinements or the failure to converge. It is due to interpolation of values of δ_n^* at close intervals made from unsmoothed discrete experimental data points that we provided as input. Notice that θ_n is not an outcome of the solution of our ODEs; rather, it is calculated as a byproduct from the algebraic Eq. (32). The ragged interpolated values of δ_n^* when used in Eq. (32) give rise to wiggles generally in the high δ_n^* zone where interpolation errors are large. All other curves are smooth and the computational scheme has no problem with convergence at smaller step sizes. As a matter of fact, we imposed a maximum permissible error limit of 10^{-4} to 10^{-5} on the ODE solver IVPAG, so that it automatically selected very fine step sizes near separation or reattachment, and in regions where gradients were large. The code has built in safety features to flag nonconvergence, instability or unforgivable errors, but our ODEs did not experience any such problem and were found to be stable.

The prediction curves in Fig. 5 and all subsequent figures are plotted using the FORTRAN graphics software Disspla (1981) on a VAX 8600. Each curve in these figures contains all the computed points. For example, if we used 100 steps to compute a particular flow, then each curve for this flow contains all 100 computed points. Having so many closely spaced points for θ_n gives rise to repeated interpolation of discrete experimental data and the resulting wiggles in its curves.

Flow Separation on a Cylinder: Figure 6 presents results for the boundary layer separation on a cylinder in axially symmetric flow conducted by Moses. It was denoted as IDENT-3800 in Coles and Hirst (1968) and selected as a mandatory test case for all methods competing in the 1968 Stanford Conference. Since the flow is axisymmetric, and our theory is two-dimensional, slight deviations in skin friction and pressure coefficient C_p curves are observed in the beginning. However, all other parameters show quite good agreement with experimental data. Pressure measurements had been reported well into the separation region, and the pressure coefficient prediction looks excellent in the separated region.

Prediction Through a Complete Separation Bubble; Serpa et al. (1987)—2 Flows: These two flows differ from the other cases in that they entail boundary layer separation and subsequent reattachment on a curved surface. Simulations of these two flows are much more complex than the ones already discussed, because the theory should be able to handle both the separation and the reattachment regions. The computation must be carried through the separation bubble into the reattachment region. To the best of this writer's knowledge, no prediction for these two flows has appeared in the literature to date.

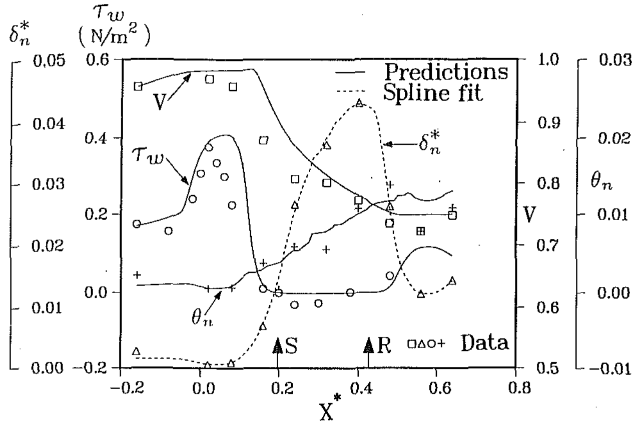

Fig. 7 **Comparison between theoretical and experimental results for the flow of Serpa et al. (1987), Flow 1. S (experiment) = 0.498 m, S (prediction) = 0.504 m, R(experiment) = 1.006 m, R(prediction) = 1.086 m, L = 2.54 m, U_0 = 9.144 m/s. Measurement uncertainties reported by experimenters (V ±5 percent; δ_n^* and θ_n between ±5.5 percent and ±11.2 percent; τ_w between ±2 percent and ±8 percent).**

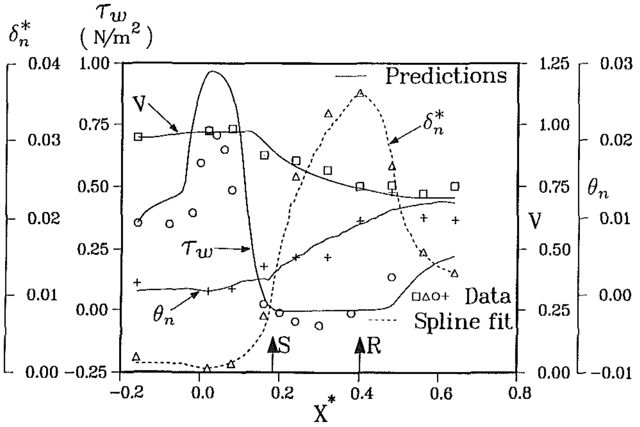

Fig. 8 **Comparison between theoretical and experimental results for the flow of Serpa et al. (1987), Flow 2. S (experiment) = 0.447 m, S (prediction) = 0.468 m, R (experiment) = 0.986 m, R (prediction) = 1.022 m, L = 2.54 m, U_0 = 15.24 m/s. Measurement uncertainties reported by experimenters (V ±5 percent; δ_n^* and θ_n between ±5.5 percent and ±11.2 percent; τ_w between ±2 percent and ±8 percent).**

Flow-1, 9.14 m/s (30 ft/s): Serpa et al. (1987) present surface shear stress τ_w as the experimental data (Fig. 7) instead of skin friction C_f. We compared our theory against this parameter. Our prediction of τ_w is good in the increasing region, but it somewhat overpredicts the data in the decreasing region due to inadequate input of the distribution of displacement thickness. Very few data are available for displacement thickness in that region, even though the flow is undergoing transformation from acceleration to deceleration in that region. There are eight τ_w data points available before $x^* = 0.1$, but only three δ_n^* data points are available from the experiment in the same region. One must input sufficient δ_n^* points to accurately capture the sharp rise and fall of τ_w that occurs in this very narrow region. However, the overall trend of τ_w computation matches with the experiment.

Separation and reattachment (denoted as S and R in Fig. 7) agree very closely with the experimental results. The experimental separation point is at $x = 0.4978$ m, and our computed separation point is 0.5039 m. Similarly, the experimental reattachment point is 1.006 m, whereas our theory computes reattachment at 1.086 m. The overall prediction for V is very good. The maximum deviations between experimental data and predictions in the sharply diminishing τ_w region are only on the order of 9 percent. Calculated values of θ_n agree well with experimental results.

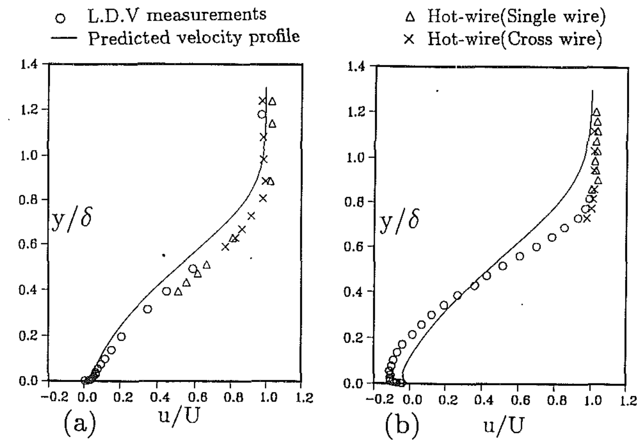

Fig. 9 **Comparison of predicted and experimental velocity profiles at two stations upstream and downstream of separation. Experimental data from Simpson et al. (1980); (*a*) 3.349 m (131.875 in.), (*b*) 3.972 m (156.375 in.). Measurement uncertainties reported by the experimenters (U ±2.4 percent single hot-wire, ±3.2 percent cross hot-wire, ±0.2 ft/s laser Doppler velocimeter; Position from wall y ±0.002 in.).**

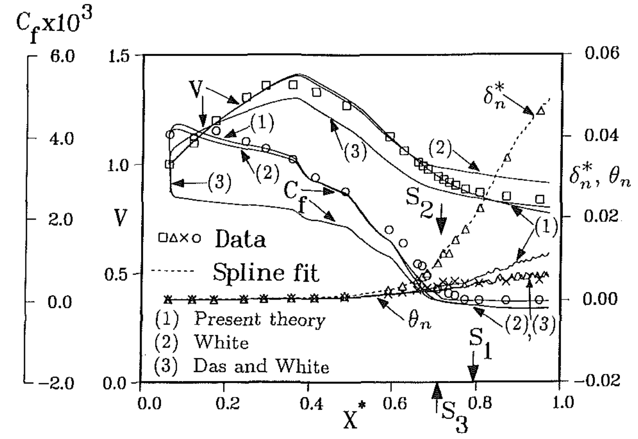

Fig. 10 **Sensitivity of the theory to π-β correlation. The test case is the flow of Simpson et al. (1981). S_1 = 3.63 m, S_2 = 3.26 m, S_3 = 3.24 m. S (experiment) = 3.4 m.**

Flow-2, 15.24 m/s (50 ft/s): This flow is similar to Flow-1 but was conducted at a higher Reynolds number. In Fig. 8, the wall shear stress τ_w rises sharply, almost doubling within a short distance. The theory overpredicts experimental stress data in this region, but comes to agreement after the sharp drop before separation. As described under Flow-1, to accurately simulate this region, many δ_n^* data points are needed at finely spaced intervals rather than the crude input of the available three points. Overall, the trend of the computed shear is similar to experimental results. Location of separation and reattachment points are predicted quite well. Separation and reattachment predicted by our theory are at $x = 0.468$ m and 1.022 m, respectively. The experiment of Serpa et al. (1987) establishes separation at 0.447 m and reattachment at 0.986 m. The prediction for velocity is excellent. The maximum difference from the experimental data is only 6 percent at the last profile where $x^* = 0.64$. The overall prediction of θ_n is good.

Other Flows: In addition to the test cases just discussed, we have tested the theory against a variety of separated and reattached flows. The results have shown good agreement with experimental data. Due to the length limitations of this paper, all test cases could not be presented here. Therefore, we only summarize their performance in locating the separation point in the following table. Complete predictions can be obtained upon request from the author.

Additionally, reattaching flow at a ledge spoiler (Tillman,

Table 1 List of experiments and prediction of separation point (S)

	Experimenter/s and reference	Description of experiments	S Experiment meter	S Theory meter
1	Newman, IDENT-3500 from Coles and Hirst (1968)	Boundary layer separation on an airfoil	1.51	1.55
2	Moses, IDENT-3800 from Coles and Hirst (1968)	Boundary layer on a cylinder under strong pressure gradient with separation	0.562	0.627
3	Schubauer and Spangenberg, IDENT-4400 from Coles and Hirst (1968)	Boundary layer in moderate pressure gradient with separation	1.65	1.69
4	Schubauer and Spangenberg, IDENT-4500 from Coles and Hirst (1968)	Boundary layer in moderate positive pressure gradient with separation	3.49	3.51
5	Schubauer and Klebanoff, IDENT-2100 from Coles and Hirst (1968)	Boundary layer on airfoil-like body with pressure gradient initially mildly negative and then strongly positive, with separation	7.8±0.1	8.1
6	Perry and Fairlie (1975)	A suddenly separating and reattaching boundary layer on a flat surface. Case 1: U_0 = 16.98 m/s	1.062	1.12
7	Perry and Fairlie (1975)	Case 2: U_0 = 24.5 m/s, *analog solution	1.124*	1.15
8	Chu and Young (1975)	Monotonic adverse pressure gradient leading to flow separation. Series II	1.71	1.69
9	Simpson et al. (1977)	Pressure gradient initially favorable, then adverse causing separation. Data available in the separation region.	3.35	3.52
10	Simpson et al. (1981)	Similar in nature to the case of Simpson et al. (1977) with modifications and additional studies on structure of separating boundary layer	3.4	3.63

IDENT-1500, Coles and Hirst, 1968), reattachment of a turbulent shear layer downstream of a backward facing step (Bradshaw and Wong, 1972) and boundary layer developing in an increasingly adverse pressure gradient (dp/dx and $d^2p/dx^2 > 0$) by Samuel and Joubert (1974)—a test case of 1980–81 Stanford Conference—were also predicted well by our theory.

4.1 Profile Prediction. Our theory computes v^*, v_β, δ^+, and V at each streamwise location from which we can easily generate velocity profiles $u(x, y)$ and $v(x, y)$ by using Eqs. (3) and (6). The $u(x, y)$ profile, which is more important, is generally predicted by all differential methods. For our integral method here, we have selected the formula given by Whitfield et al. (1981) which is better than Eq. (3) in the sublayer region. Since our code generates all the parameters necessary for both equations, it behooves us to select the better one. In terms of our computed parameters, the equation can be expressed as

$$\frac{u}{U} = |\zeta| \left[\frac{s}{0.09} \tan^{-1}\left(\frac{0.09 y |\zeta| V U_0}{\nu} \right) + \left(\frac{1}{\zeta} - \frac{s\pi}{0.18} \right) \tanh^{1/2}\left\{ a \left(\frac{y}{\theta_n L} \right)^{b} \right\} \right] \quad (33)$$

where a and b are functions of ζ, θ_n, V, δ_n^*, and s is the sign of skin friction ($C_f/|C_f|$).

We have tested several profiles from the experiment of Simpson et al. (1980) to compare our velocity predictions with experimental data. Due to the space limitations of this paper we have presented two profiles: one from the near-separation and the other from the fully separated regions. The first profile, shown in Fig. 9(a), is just upstream of our computed separation point; the second profile, Fig. 9(b), is after the separation point. The experimental data are collected from several tables presented in the comprehensive report by Simpson et al. (1980). *These predictions are comparable to those presented by other theories in the 1980–81 AFOSR-HTTM-Stanford Conference.*

5 Effect of the Empiricism on the Theory

The single most important empirical relation of our theory is the pressure gradient-wake (Π-β) correlation. Since this is a major factor in the development of our theory, it is imperative that we test how sensitive the theory is to this correlation. For this testing we selected three correlations; the results are shown in Fig. 10. In this figure, prediction (1) is based upon our best-fit present model (Eq. 19), prediction (2) on White's model (Eq. 15), and prediction (3) on the Model-c (Eq. 18), which is a very poor fit as seen from Fig. 4. We deliberately selected this last one to determine if the theory gives any computational problems when using a correlation significantly different from the correct one.

Inclusion of different correlations into the computational scheme is achieved by altering the coefficient function S_{34} of Eq. (30). Prediction (1) in Fig. 10 gives the best overall performance, confirming our proposition. White's correlation, labeled as prediction (2), deviates from the data only in the separation region. This is exactly what one would expect, because White's correlation does not match the Π-β data in this region as observed clearly from Fig. 4.

Due to incompatibility, prediction (3) shows a sudden decrease for C_f right after the starting point. At this point, Π is about 0.2, whereas prediction (3) attains a value of 1.6, an 800 or an eight-fold increase. This abrupt change is consistent with Fig. 4 where model (c) follows a course way above the actual data in the low Π region.

Despite the eight-fold mismatch introduced in the beginning, due to deliberate use of a very poor correlation, the theory quickly retrieves its corresponding compatible value. It then continues to calculate smoothly without any numerical diffi-

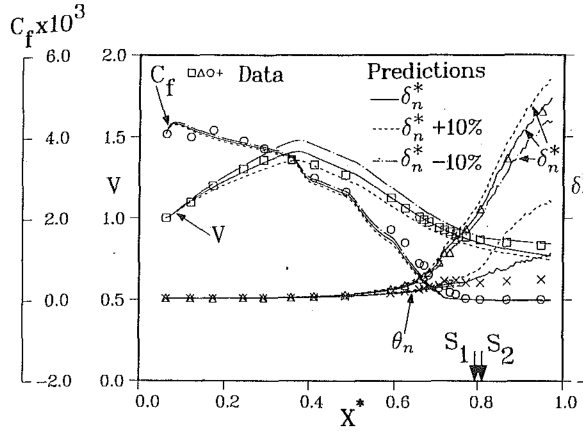

Fig. 11 **Sensitivity of the theory to δ_n^* distribution. S_1 = 3.63 m, S_2 (for δ_n^* − 10 percent) = 3.7 m, S (experiment) = 3.4 m.**

culty. The momentum thickness does not show appreciable changes for these different Π-β correlations. This test showed that small variations in Π-β correlations have only minor effects on the prediction. The theory is amazingly stable for an eightfold mismatch and does not lead to any numerical problem or grossly incompatible computed results.

6 Sensitivity Study

6.1 Sensitivity to Input Distribution. The distribution of displacement thickness δ_n^* is an input to this inverse boundary layer theory. Like any experimental data, these are always subject to some uncertainty. Therefore, we wish to find out the effect of variations in this input on the final calculated results. Figure 11 shows the effect on the final results by varying δ_n^* by ±10 percent. The other inputs (i.e., the initial conditions) were left unchanged. The flow discussed here is that of Simpson et al. (1981). There is very little effect on the overall predictions except θ_n in the separated region, proving that reasonable variations in these inputs do not destroy the predictability and the reliability of the theory.

6.2 Sensitivity to Initial Conditions. The initial conditions needed to start the calculation in this theory are ζ_0, δ_0^+, and V_0. In practical cases, these initial conditions are often unknown, so a designer must input some estimated values. Furthermore, even if experimental values are available, there are always some uncertainties in these numbers. We investigated several test cases by varying ζ_0, δ_0^+, and V_0 to find the sensitivity of the method to the specification of initial conditions. Each parameter was varied separately, and the test flow was that of Simpson et al. (1981).

Figure 12 shows the effect of varying V_0 by ±10 percent. The velocity predictions run parallel to the prediction given by unperturbed V_0. The effect on skin friction is insignificant. Momentum thickness remains unaffected in the attached region, but increases somewhat for the V_0 + 10 percent case in the separated region. Additional sensitivity tests were performed by varying initial conditions C_{fo} and δ_0^+ and the outcomes were similar to that shown in Fig. 12. Due to the space limitations, they could not be included here.

These sensitivity studies revealed that overall, the theory is not very sensitive to initial conditions or input distributions. When they were varied, computed results changed predictably, following a realistic trend. For example, when V_0 was raised by 10 percent, the computed results for that parameter were consistently higher by about that percentage throughout the flow field. Therefore, deviations from correct input do not cause the theory to behave erratically or yield results significantly off the unperturbed predictions; rather, the theory produces stable and predictable outcomes.

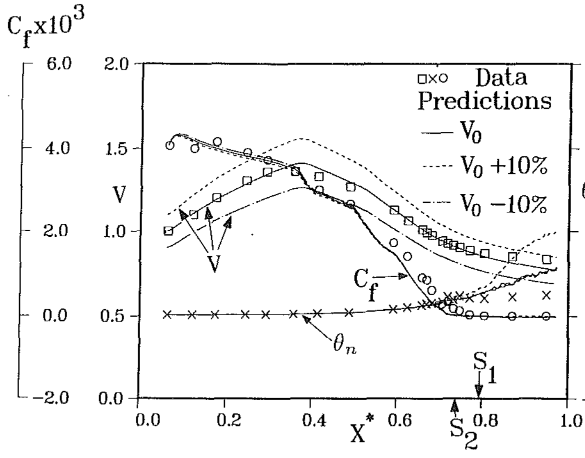

Fig. 12 **Sensitivity of the theory to initial condition; V_0 variation. S_1 = 3.63 m, S_2 (for V_0 − 10 percent) = 3.37 m, S (experiment) = 3.4 m.**

7 Conclusions

(1) A practical integral method has been presented for computing separated and reattached turbulent boundary layer flows. The new inverse inner-variable theory incorporates major improvements over its predecessors: (*a*) an improved pressure gradient-wake correlation valid for attached and separated flows, derived from eighteen sets of experimental data expressed through a single equation; (*b*) elimination of the dependence of the inner-variable theory on the second derivative of velocity distribution; and (*c*) replacement of the unstable wake parameter Π with the stable parameter v_β.

(2) Fifteen validation runs made by the theory for separated flows, reattached flows and flows forming separation bubbles demonstrated good accuracy. Therefore, the method is a viable tool for analyzing practical flow problems that present separation phenomena.

(3) Careful analysis has gone into developing an accurate Π-β correlation from experimental data that yields superior results when compared to similar correlations. Furthermore, the theory proved to be stable against sizeable variations of this correlation.

(4) Sensitivity studies proved that the theory behaves in a stable and predictable manner when introducing variations in initial conditions and input distributions.

(5) Sufficient information has been provided so that a potential user can implement the method. The theory should be useful to industrial designers who can run it on mini or microcomputers for repetitive calculations. Since engineering designs often compare and weigh alternatives, the method may be attractive due to its low computing time and costs.

References

Bradshaw, P., and Wong, F. Y. F., 1972, "The Reattachment and Relaxation of a Turbulent Shear Layer," *Journal of Fluid Mechanics*, Vol. 52, pp. 113–135.

Celenligil, M. C., and Mellor, G. L., 1985, "Numerical Solutions of Two-Dimensional Turbulent Separated Flows Using a Reynolds Stress Closure Model," ASME JOURNAL OF FLUIDS ENGINEERING, Vol. 107, pp. 467–476.

Chu, J., and Young, A. D., 1975, "Measurements in Separating Two-dimensional Turbulent Boundary Layers," *AGARD Conference Proceedings No. 168 on Flow Separation*, Paper 13, pp. 13-1 to 13-12.

Coles, D. E., and Hirst, E. A. (eds.), 1968, *Computation of Turbulent Boundary Layers—1968 AFOSR-IFP-Stanford Conference*, Vol. II, Stanford University, CA.

Das, D. K., 1983, "An Integral Method of Analyzing Impressible Two-dimensional Turbulent Boundary Layers With Separation," Ph.D. thesis, University of Rhode Island, Kingston, 260 pp.

Das, D. K., 1987, "A Numerical Study of Turbulent Separated Flows," *Forum on Turbulent Flows*, ASME FED, Vol. 51, pp. 85–90.

Das, D. K., 1988, "A Simple Theory for Calculating Turbulent Boundary Layers Under Arbitrary Pressure Gradients," *International Journal of Engineering Fluid Mechanics*, Vol. 1, pp. 83–99.

Das, D. K., 1990, "An Improved Turbulent Boundary Layer Theory," *Mechanics Research Communications*, Vol. 17, No. 4/90, pp. 207-216.

Das, D. K., and White, F. M., 1986, "Integral Skin Friction Prediction for Turbulent Separated Flows," ASME JOURNAL OF FLUIDS ENGINEERING, Vol. 108, pp. 476-482.

Disspla, 1981, "Display Integrated Software System and Plotting Language," User's Manual, Integrated Software Systems Corporation, San Diego, CA.

Ferziger, J. H., Lyrio, A. A., and Bardina, J. G., 1982, "New Skin Friction and Entrainment Correlation for Turbulent Boundary Layers," ASME JOURNAL OF FLUIDS ENGINEERING, Vol. 104, pp. 537-540.

Gerhart, P. M., 1979, "An Integral Method for Predicting Subsonic Turbulent Separating Boundary Layers With Specified Free Stream Input," *Turbulent Boundary Layers*, Weber, H. E. (ed.), ASME Fluids Engineering Conference, pp. 69-78.

Ghosh, S., and Kline, S. J., 1978, "The Computation of Optimum Pressure Recovery in Two-Dimensional Diffusers," ASME JOURNAL OF FLUIDS ENGINEERING, Vol. 100, pp. 419-426.

Henau, V. D., Raithby, G. D., and Thompson, B. E., 1990, "Prediction of Flows With Strong Curvature and Pressure Gradient Using the K-ε Turbulence Model," ASME JOURNAL OF FLUIDS ENGINEERING, Vol. 112, pp. 40-47.

IMSL Library Edition 10.0, User's Manual, 1987, Math/library Version 1.0, Customer Relations, Houston, TX, pp. 420-433 and 629-652.

Kline, S. J., Cantwell, B. J., and Lilley, G. M. (eds.), 1981, *Proceedings of the 1980-81 AFOSR-HTTM-Stanford Conference on Complex Turbulent Flows: Comparison of Computation and Experiment*. Vols. I, II and III, Stanford University, CA.

Kline, S. J., Cockrell, D. G., Morkovin, M. V., and Sovran, G. (eds.), 1968, *Computation of Turbulent Boundary Layers—1968 AFOSR-IFP-Stanford Conference*, Vol. I, Stanford University, CA.

Kueth, A. M., and Chow, C., 1986, *Foundations of Aerodynamics*, Fourth Edition, Wiley, NY, pp. 409-412.

Kwon, O. K., and Pletcher, R. H., 1986, "A Viscous-Inviscid Interaction Procedure—Part 1: Method for Computing Two-Dimensional Incompressible Separated Channel Flows," ASME JOURNAL OF FLUIDS ENGINEERING, Vol. 108, pp. 64-70.

Melnik, R. E., and Brook, J. W., 1986, "The Computation of Viscous-Inviscid Interaction on Airfoils with Separated Flow," *Numerical and Physical Aspects of Aerodynamic Flows III*, Cebecci, T. (ed.), Springer-Verlag, New York, pp. 77-101.

Moses, H. L., Jones, III, R. R., and Sparks, J. F., 1979, "An Integral Method for the Turbulent Boundary Layer With Separated Flows," *Turbulent Boundary Layers*, Weber, H. E. (ed.), ASME Fluids Engineering Conference, pp. 69-73.

Moses, H. L., Thomason, S. B., and Jones, R. R., 1982, "Simultaneous Solution of the Inviscid Flow and Boundary Layers for Compressor Cascades," *AIAA Journal*, Vol. 20, No. 10, pp. 1466-1468.

Perry, A. E., and Fairlie, B. D., 1975, "A Study of Turbulent Boundary-Layer Separation and Reattachment," *Journal of Fluid Mechanics*, Vol. 69, pp. 657-672.

Samuel, A. E., and Joubert, P. N., 1974, "A Boundary Layer Developing in an Increasingly Adverse Pressure Gradient," *Journal of Fluid Mechanics*, Vol. 66, pp. 481-505.

Serpa, J. M., Lessmann, R. C., and Hagist, W. M., 1987, "Turbulent Separated and Reattached Flow Over a Curved Surface," ASME JOURNAL OF FLUIDS ENGINEERING, Vol. 109, pp. 403-409.

Settles, G. S., Williams, D. R., Bac, B. K., and Bogdonoff, S. J., 1982, "Reattachment of a Compressible Turbulent Free Shear Layer," *AIAA Journal*, Vol. 20, No. 1, pp. 60-67.

Simpson, R. L., Strickland, J. H., and Barr, P. W., 1977, "Features of a Separating Turbulent Boundary Layer in the Vicinity of Separation," *Journal of Fluid Mechanics*, Vol. 79, pp. 553-594.

Simpson, R. L., Chew, Y.-T., and Shivaprasad, B. G., 1980, "Measurement of a Separating Turbulent Boundary Layer," Project SQUID Report SMU-4-PU, Southern Methodist University, Dallas, TX, 207 pp.

Simpson, R. L., Chew, Y.-T., and Shivaprasad, B. G., 1981, "The Structure of a Separating Turbulent Boundary Layer. Part 1, Mean Flow and Reynolds Stresses," *Journal of Fluid Mechanics*, Vol. 113, pp. 23-51.

Strawn, R. C., and Kline, S. J., 1983, "A Stall Margin Design Method for Planar and Axisymmetric Diffusers," ASME JOURNAL OF FLUIDS ENGINEERING, Vol. 105, pp. 28-33.

Strawn, R. C., Ferziger, J. H., and Kline, S. J., 1984, "A New Technique for Computing Viscous-Inviscid Interactions in Internal Flows," ASME JOURNAL OF FLUIDS ENGINEERING, Vol. 106, pp. 79-84.

White, F. M., 1974, *Viscous Fluid Flow*, McGraw-Hill, NY.

Whitfield, D. L., Swafford, T. W., and Jacocks, J. L., 1981, "Calculation of Turbulent Boundary Layers with Separation and Viscous-Inviscid Interaction," *AIAA Journal*, Vol. 19, pp. 1315-1322.

APPENDIX

Various coefficient functions cited in the main body of the paper while deriving the theory are summarized here for completeness. They should be helpful in programming this theory.

$$A_1 = v^*\left[\frac{1}{\kappa^2}\ln^2 y^+ + B^2 - \frac{B}{\kappa} + \frac{1}{\kappa^2} + \left(\frac{2B}{\kappa} - \frac{1}{\kappa^2}\right)\ln y^+\right]$$

$$+ v_\beta\left[-\frac{6y^{+2}}{\kappa^2\delta^{+2}}\ln y^+ + \frac{8y^{+3}}{\kappa^2\delta^{+3}}\ln y^+ + \left(\frac{-6B}{\kappa} + \frac{12}{\kappa^2}\right)\frac{y^{+2}}{\delta^{+2}} + \left(\frac{8B}{\kappa} - \frac{12}{\kappa^2}\right)\frac{y^{+3}}{\delta^{+3}}\right]$$

$$A_2 = \frac{v^{*2}}{|v^*|}\left(\frac{1}{\kappa^2}\ln y^+ + \frac{B}{\kappa} - \frac{1}{\kappa^2}\right) + \frac{v^* v_\beta}{|v^*|}\left[\frac{12y^{+2}}{\kappa^2\delta^{+2}}\ln y^+ - \frac{12y^{+3}}{\kappa^2\delta^{+3}}\ln y^+\right]$$

$$+ \frac{v^* v_\beta}{|v^*|}\left[\left(\frac{12B}{\kappa} - \frac{10}{\kappa^2}\right)\frac{y^{+2}}{\delta^{+2}} + \left(-\frac{12B}{\kappa} + \frac{11}{\kappa^2}\right)\frac{y^{+3}}{\delta^{+3}}\right] + \frac{v_\beta^2}{|v^*|}\left[\frac{24y^{+4}}{\kappa^2\delta^{+4}} - \frac{36y^{+5}}{\kappa^2\delta^{+5}} + \frac{12y^{+6}}{\kappa^2\delta^{+6}}\right]$$

$$A_3 = v^*\left[\frac{6y^{+2}}{\kappa^2\delta^{+2}}\ln y^+ + \left(\frac{6B}{\kappa} - \frac{2}{\kappa^2}\right)\frac{y^{+2}}{\delta^{+2}} - \frac{4y^{+3}}{\kappa^2\delta^{+3}}\ln y^+ + \left(\frac{1}{\kappa^2} - \frac{4B}{\kappa}\right)\frac{y^{+3}}{\delta^{+3}}\right] + v_\beta\left(\frac{12y^{+4}}{\kappa^2\delta^{+4}} + \frac{4y^{+6}}{\kappa^2\delta^{+6}} - \frac{12y^{+5}}{\kappa^2\delta^{+5}}\right)$$

$$A_4 = \frac{12v_\beta}{\kappa^2\delta^+}\left[-v^*\left\{\frac{y^{+2}}{\delta^{+2}}\ln y^+ - \frac{y^{+3}}{\delta^{+3}}\ln y^+ + \left(B\kappa - \frac{1}{3}\right)\frac{y^{+2}}{\delta^{+2}} + \left(\frac{1}{4} - B\kappa\right)\frac{y^{+3}}{\delta^{+3}}\right\}\right]$$

$$- \frac{12v_\beta^2}{\kappa^2\delta^+}\left(\frac{2y^{+4}}{\delta^{+4}} - \frac{3y^{+5}}{\delta^{+5}} + \frac{y^{+6}}{\delta^{+6}}\right)$$

$$B_1 = \delta^+\left[v^*\left\{\frac{1}{\kappa^2}\ln^2\delta^+ + \left(\frac{2B}{\kappa} - \frac{3}{\kappa^2}\right)\ln\delta^+ + \left(B^2 - \frac{3B}{\kappa} + \frac{4}{\kappa^2}\right)\right\} + \frac{7v_\beta}{6\kappa^2}\right]$$

$$B_2 = \frac{\delta^+}{|v^*|}\left[v^{*2}\left(\frac{1}{\kappa^2}\ln\delta^+ - \frac{2}{\kappa^2} + \frac{B}{\kappa}\right) + v^* v_\beta\left(\frac{1}{\kappa^2}\ln\delta^+ - \frac{7}{6\kappa^2} + \frac{B}{\kappa}\right) + \frac{18v_\beta^2}{35\kappa^2}\right]$$

$$B_3 = \delta^+\left[v^*\left(\frac{1}{\kappa^2}\ln\delta^+ - \frac{5}{6\kappa^2} + \frac{B}{\kappa}\right) + \frac{34v_\beta}{35\kappa^2}\right]$$

$$B_4 = -v_\beta\left[v^*\left(\frac{1}{\kappa^2}\ln\delta^+ - \frac{7}{6\kappa^2} + \frac{B}{\kappa}\right) + \frac{18v_\beta}{35\kappa^2}\right]$$

$$B_5 = -\delta^+ U \text{ and } B_6 = -\frac{|v^*|\tau_w}{\mu} = -\frac{|v^*|\rho v^*|v^*|}{\mu} = -\frac{v^{*3}}{\nu}$$

$$D_1 = \frac{1}{\kappa}\ln\delta^+ + B,\ D_2 = \frac{2}{\kappa},\ D_3 = \frac{v^*}{\kappa\delta^+} \text{ and } D_4 = -1$$

$$E_1 = \nu\delta^+ \mp \kappa\delta^* U,\ E_2 = \nu\delta^+,\ E_3 = \nu(v_\beta + v^*),\ E_4 = -\kappa\delta^*|v^*| \text{ and } E_5 = \kappa U|v^*|\frac{d\delta^*}{dx}$$

$$P_1 = B_1 \pm B_2 - \frac{B_3 D_1}{D_2},\ P_2 = -\frac{D_3 B_3}{D_2} + B_4,\ P_3 = \frac{B_3}{D_2} + B_5 \text{ and } P_4 = B_6$$

$$Q_1 = E_1 - \frac{E_2 D_1}{D_2},\ Q_2 = -\frac{E_2 D_3}{D_2} + E_3,\ Q_3 = \frac{E_2}{D_2} + E_4 \text{ and } Q_4 = E_5$$

$$S_{11} = \frac{U_0 V}{L}\left[B_{1n} \pm B_{2n} - \frac{B_{3n} D_{1n}}{D_{2n}}\right]$$

$$S_{12} = \frac{1}{L}\left[-\frac{D_{3n} B_{3n}}{D_{2n}} + B_{4n}\right]$$

$$S_{13} = \frac{U_0}{L}\left[\left(B_{1n} \pm B_{2n} - \frac{B_{3n} D_{1n}}{D_{2n}}\right)\zeta + \frac{B_{3n}}{D_{2n}} + B_{5n}\right]$$

$$S_{14}=B_{6n},\ S_{21}=\frac{U_0V}{L}\left[E_{1n}-\frac{E_{2n}D_{1n}}{D_{2n}}\right],\ S_{22}=\frac{1}{L}\left[E_{3n}-\frac{E_{2n}D_{3n}}{D_{2n}}\right]$$

$$S_{23}=\frac{U_0}{L}\left[\left(E_{1n}-\frac{E_{2n}D_{1n}}{D_{2n}}\right)\zeta+\left(\frac{E_{2n}}{D_{2n}}+E_{4n}\right)\right]$$

$$S_{24}=E_{5n},\ S_{31}=S_{32}=0$$

$$S_{33}=\frac{U_0}{L},\ \text{and}\ S_{34}=R_{4n}$$

where $B_{in}'s$, $D_{in}'s$, $E_{in}'s$ and R_{4n} are as given below.

$$B_{1n}=\delta^+VU_0\left[\zeta\left\{\frac{1}{\kappa^2}\ln^2\delta^++\left(\frac{2B}{\kappa}-\frac{3}{\kappa^2}\right)\ln\delta^+\right.\right.$$
$$\left.\left.+\left(B^2-\frac{3B}{\kappa}+\frac{4}{\kappa^2}\right)\right\}+\frac{7V_b}{6\kappa^2}\right]$$

$$B_{2n}=\delta^+VU_0\left[\frac{\zeta^2}{|\zeta|}\left(\frac{1}{\kappa^2}\ln\delta^+-\frac{2}{\kappa^2}+\frac{B}{\kappa}\right)\right.$$
$$\left.+\frac{\zeta V_b}{|\zeta|}\left(\frac{1}{\kappa^2}\ln\delta^+-\frac{7}{6\kappa^2}+\frac{B}{\kappa}\right)+\frac{18V_b^2}{35|\zeta|\kappa^2}\right]$$

$$B_{3n}=\delta^+VU_0\left[\zeta\left(\frac{1}{\kappa^2}\ln\delta^+-\frac{5}{6\kappa^2}+\frac{B}{\kappa}\right)+\frac{34V_b}{35\kappa^2}\right]$$

$$B_{4n}=-V_b(VU_0)^2\left[\zeta\left(\frac{1}{\kappa^2}\ln\delta^+-\frac{7}{6\kappa^2}+\frac{B}{\kappa}\right)+\frac{18V_b}{35\kappa^2}\right]$$

$$B_{5n}=-\delta^+VU_0,\ B_{6n}=-\zeta^3(VU_0)^3/\nu$$

$$D_{1n}=\frac{1}{\kappa}\ln\delta^++B,\ D_{2n}=2/\kappa,\ D_{3n}=\zeta VU_0/\kappa\delta^+$$

$$E_{1n}=\nu\delta^+\mp\kappa L\delta_n^*VU_0,\ E_{2n}=\nu\delta^+,\ E_{3n}=\nu VU_0(V_b+\zeta)$$

$$E_{4n}=-\kappa L\delta_n^*VU_0|\zeta|,\ E_{5n}=\kappa(VU_0)^2|\zeta|\frac{d\delta_n^*}{dx^*}$$

$$R_{4n}=\frac{-\kappa(VU_0)^2|\zeta|}{\nu\delta^+(V_b+\zeta)}[c_0\zeta^2+c_1V_b|\zeta|+c_2V_b^2]$$

$$c_0=-0.4,\ c_1=0.76,\ c_2=0.42$$

In E_1, P_1, S_{11}, S_{13}, and E_{1n}, a positive sign applies before separation and after reattachment (v^* and $\zeta > 0$) and a negative sign within the separation region (v^* and $\zeta < 0$).

R. Balachandar
Research Associate,
Concordia University,
Montreal, Canada H3G 1M8
Assoc. Mem. ASME

L. Robillard
Professor,
Ecole Polytechnique,
Montreal, Canada H3C 3A7
Mem. ASME

A. S. Ramamurthy
Professor,
Concordia University,
Montreal, Canada H3G 1M8
Mem. ASME

Some Characteristics of Counter Flowing Wall Jets

Experimental results related to the interaction between a uniform flow and a two-dimensional counter flowing wall jet are presented for various ratios of the jet velocity to the freestream velocity. Both visual observations and wall pressure surveys were made in the jet penetration zone. Attempts were made to choose the proper scaling variables to suitably nondimensionalize the wall pressure distributions. The geometrical characteristics of the dividing streamline were determined for a range of test conditions. Limited tests were also carried out to check the influence of the size of the jet injection device on the flow characteristics.

Introduction

It has been pointed out that one of the methods of effectively diluting industrial effluents in a stream is to inject the former as a counter jet into the stream (Robillard, 1974a). The characteristics of a free jet penetrating a stream of counter flowing fluid have been obtained by several investigators (Beltaos, 1973; Hopkins, 1962; Rajaratnam, 1976; Ramamurthy, 1971; Rao, 1958; Robillard, 1971). In the case of a free counter jet, it has been shown (Robillard, 1974a) that there can be two distinct modes of counter jet flow. In one of the modes, the jet stays on one side of the plane of symmetry, while in the other mode, the jet oscillates about this plane. The latter is characterized by intense mixing which promotes effective dilution. The mode of flow also depends on the ratio of the jet velocity to the freestream velocity. It should be noted that, in the case of free counter jets, fluids from two different sources interact in the absence of solid boundaries. Colin (1968) has obtained some of the characteristics of a wall jet beneath a counter flowing stream.

In the present study, which involves a counter flowing wall jet, the region of jet penetration is bound by a solid wall on one side and the dividing streamline on the other (Fig. 1). In Hopkin's (1962) model based on ideal fluid flow theory for a free counter jet, one can obtain a theoretical model for the wall jet in counter flow, upon replacing the central streamline by a solid wall. In real flows, one should note that the presence of the wall forces the velocity at the wall to be zero. Furthermore, in real flows, the presence of the wall in the rear of the jet acts like a splitter plate and inhibits the formation of an alternate vortex shedding mechanism which is normally present in the case of centrally mounted two-dimensional free counter jets (Robillard, 1974a).

Experimental Setup and Procedures

The device used to inject the wall jet into the counter flowing stream is shown in Fig. 2(*a*). A smooth "S" shaped contraction was designed to obtain a uniform flow at the mouth of the jet. Several honeycombs and grid arrangements were provided ahead of the contraction to reduce the turbulence level in the jet. The jet width was nominally 25.4 mm and streamlined inserts were used to obtain jet sizes of 6.35 and 3.18 mm (Fig. 2(*b*)). Several pressure taps of 0.8 mm diameter were located at close intervals along the bottom brass plate AB (Fig. 2(*a*)) to obtain the wall pressure distribution in the jet penetration region.

A simple schematic of the experimental setup used is shown in Fig. 2(*c*). The central part of the tunnel denoted as the "test section" is 25.4 cm wide, 183 cm high and 244 cm long. The top of the test section is left open in order to permit the upper limit of flow to form an adjustable free surface. The velocity distributions at the exit of the jet were measured and found to be fairly uniform (Robillard, 1974b). The flow in the jet injection device is highly accelerating and this results in a uniform velocity distribution at the jet exit (Daily and Harleman, 1966). To avoid the interference effect of the jet injection

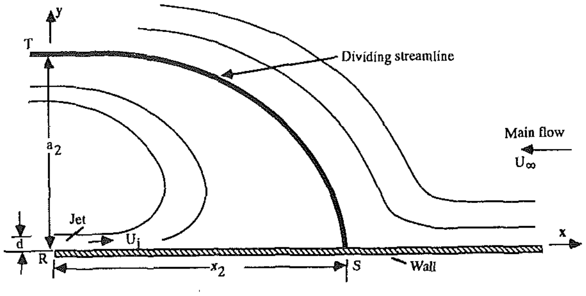

Fig. 1 Definition sketch of counter flowing wall jet

Contributed by the Fluids Engineering Division for publication in the JOURNAL OF FLUIDS ENGINEERING. Manuscript received by the Fluids Engineering Division December 21, 1990. Associate Technical Editor: Cheh-Ming Ho.

device with the main flow, an asymmetrical contraction was adopted. The pressure drop across the jet injection device was calibrated to evaluate the exit jet velocities. Visual observations were made to obtain the geometry of the bubble zone denoted as the region RST in Fig. 1. A dye injection arrangement was designed to visualize the flow. The jet continues to progressively penetrate into the main flow and is ultimately turned back and carried downstream by the approach flow. The jet penetration into the approach flow field is arrested when it reaches a common stagnation point S (Fig. 1) along the wall, which is the starting point of the dividing streamline ST (Fig. 1). The outline of the dividing streamline was fairly well defined in the neighborhood of S. The length of jet penetration x_2 (Fig. 1) was obtained by measuring the distance from the jet exit to the confluence of the dividing streamline with the wall. This length was also confirmed by observing the movements of fine tufts of wool threads placed along the bottom wall. The jet penetration lengths were obtained several times during a given test run and the values reported in the forthcoming sections are the averaged values. The ratio of the size of the counter jet to the height of the free stream flow was maintained small in order to keep blockage effects to a minimum. The jet flow Reynolds number was sufficiently high to minimize viscous effects.

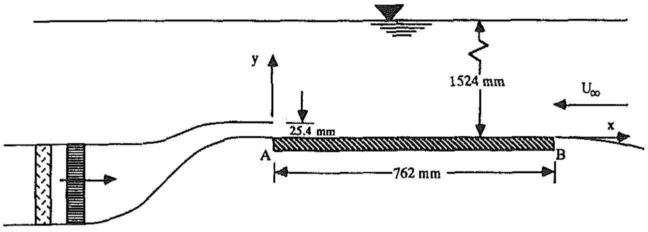

Fig. 2(*a*) **Wall jet injection device**

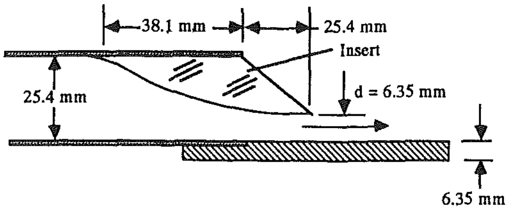

(Not to scale)

Fig. 2(*b*) **Typical streamlined insert for smaller jets**

Nondimensional Test Variables

The following are the nondimensional test variables pertinent to the study:

Wall pressure coefficient $C_p = \dfrac{P - P_\infty}{\frac{1}{2}\rho U_\infty^2}$

Here, P_∞ and U_∞ are the pressure and velocity of the freestream, respectively. P refers to the wall pressure measured at any point along AB (Fig. 2(*a*)).

Modified pressure coefficient $C_p^* = \dfrac{C_p - C_{p\,\min}}{1 - C_{p\,\min}}$

Here $C_{p\,\min}$ refers to the minimum values of C_p measured along AB (Fig. 2(*a*)).

Velocity ratio $\lambda = \dfrac{U_j}{U_\infty}$

Here, U_j refers to the exit jet velocity.

Nondimensional parameter $X^* = \dfrac{x - x_{\text{stg}}}{x_{\text{stg}}}$

where, x refers to the coordinate measured from the jet exit (along AB in Fig. 2(*a*)) and x_{stg} refers to the location of the maximum pressure (stagnation) along the wall. The other important nondimensional test variables are x_2/d and a_2/d. Here

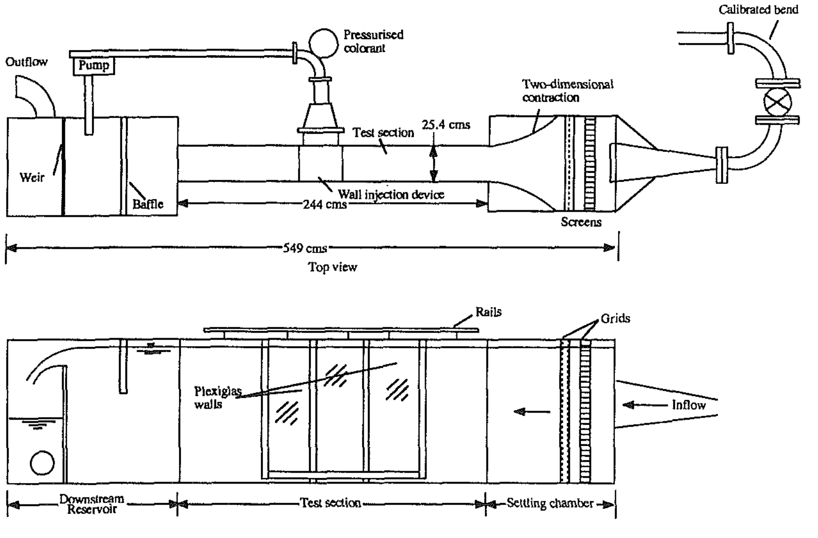

Fig. 2(*c*) **Experimental setup**

Nomenclature

a_2 = width of jet penetration at $x = 0$
C_p = pressure coefficient at any location along AB (Fig. 2(*a*))
C_p^* = modified pressure coefficient
d = jet size at $x = 0$
J_o = jet momentum
P = pressure at any location along the wall AB (Fig. 2(*a*))
P_∞ = freestream pressure (approach flow)
U_∞ = freestream velocity (approach flow)
U_j = jet velocity
x_2 = length of jet penetration zone
λ = ratio of jet velocity to free stream velocity

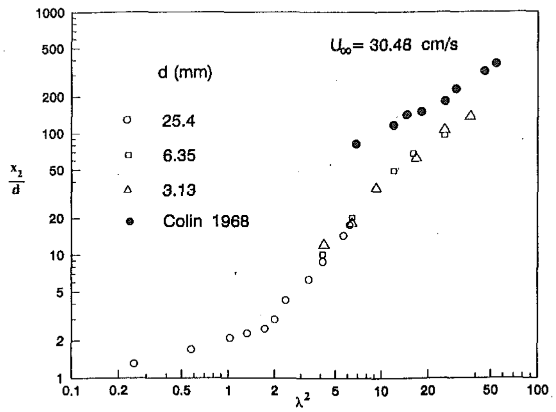

Fig. 3(*a*) Variation of x_2/d with λ^2 (uncertainty in $x_2/d = \pm 5$ percent at 20:1 odds)

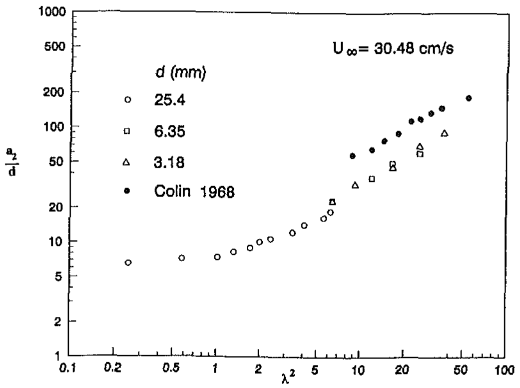

Fig. 3(*b*) Variation of a_2/d with λ^2 (uncertainty in $a_2/d = \pm 5$ percent at 20:1 odds)

a_2 refers to the width of the bubble RT measured at $x = 0$ (Fig. 1). Based on an odds of 20:1, the maximum uncertainty estimates in the evaluation of C_p and x_2/d are of the order of ± 3.5 and ± 5 percent, respectively. The uncertainty estimates were obtained following the standard procedure indicated by Kline (1953, 1985).

Analysis of Results

On observing the wall jet interaction with the main flow, it appears that the jet penetration length x_2 depends on two main mechanisms. An increase in the value of λ^2 increases the jet momentum J_o, which determines the jet expansion. The jet expansion in turn controls the velocities at any section of the jet and indirectly influences the jet penetration. First, for a given value of the freestream velocity U_∞, an increase in the value of λ^2 is reflected as an increase in the jet velocity U_j which promotes deeper jet penetration. Second, it should be noted that the jet expansion is restricted by the opposing main flow. As such, the rate of drop in the mean velocity with increasing distance from the jet exit will be much less for a counter flowing wall jet compared to a wall jet without counter flow.

Figures 3(*a*) and 3(*b*) show the variation of the length and width of the jet penetration zone over a large range of λ^2 for different sizes of initial jet width. One notes from these figures that the use of λ^2 as the abscissa, absorbs size scale effects to a good extent and the present data fall on a single curve. For purposes of analysis, the entire range of λ^2 is divided into two main regions: a lower range ($0 < \lambda^2 < 2$) and an upper range ($\lambda^2 > 10$), bridged by an intermediate transition region ($2 < \lambda^2 < 10$). It can be noted from Figs. 3(*a*) and 3(*b*) that the bubble width a_2 is an order of magnitude larger than the jet penetration length x_2 in the lower λ^2 range, while both these parameters are of the same order of magnitude in the upper λ^2 range. In the lower λ^2 range, the value of the jet penetration length x_2 increases at a moderate rate with increasing λ^2 (Fig. 3(*a*)). On the other hand, the value of the bubble width a_2 is almost constant (Fig. 3(*b*)). In this range of λ^2, since the width of the bubble region is much larger than the jet penetration length, the jet expansion due to flow reversal effects dominate and the rate of increase in x_2 is very limited due to the two opposing mechanisms related to increasing velocities and increasing jet expansions.

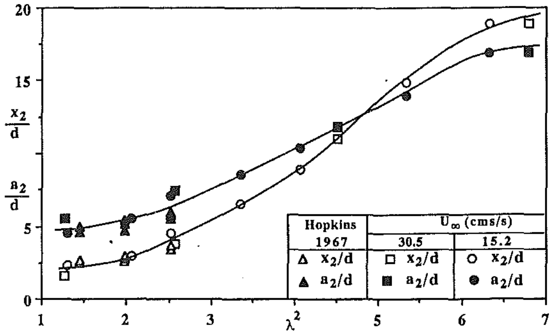

Fig. 4 Variation of jet penetration zone geometry with λ^2 at various freestream velocities (uncertainty in x_2/d and $a_2/d = \pm 5$ percent at 20:1 odds)

In the transition range of λ^2, while the increased jet velocities promote higher jet penetration, the spreading of the jet though not excessive, does dampen the ability of the jet to penetrate. In this λ^2 range, the former appears to dominate and the values of x_2 become quite significant. Consequently, the values of x_2 increase at a rate higher than that found at the lower range of λ^2. Further, an increase in λ^2 can also be perceived as a decrease in freestream velocity, which in turn permits the jet to expand more freely. This in part accounts for the increase in a_2 with λ^2. Hence, the value of a_2 also increases at a rate higher than that found at the lower range of λ^2.

For the same reasons stated in the previous paragraph, when $U_j \gg U_\infty$, the constraint for the jet to expand is less and hence the values of a_2 increase in the upper range of λ^2. However, the relatively large U_j values associated with larger λ^2 enable the jet to penetrate much farther. At larger λ ratios, other factors such as increased boundary friction will also tend to limit the tendency to penetrate the approaching flow field. However, in the limit as $U_\infty \rightarrow 0$, the characteristics of the jet will resemble that of a submerged wall jet without counter flow.

In Figs. 3(*a*) and 3(*b*), the results of Colin (1968) are also shown. They deviate from the present set of data. In the experiments of Colin (1968), it is contended that the visualization techniques adopted could have possibly contributed to errors (Robillard, 1974b). Colin used a mixture of titanium dioxide and oil coated on the side walls to measure the geometry of the counter jet penetration zone. Consequently, his measurements would provide the maximum values of x_2 and a_2 rather than the mean values obtained in the present study. Further, Colin did not use a correction factor to account for the variation of velocity across the width of the jet. From Colin's experimental set-up, one notes that the jet momentum correction factor can be expected to be different from unity.

Figure 4 shows the variation of x_2/d and a_2/d with λ^2 at two different freestream velocities of 30.5 and 15.2 cm/s. These results indicate that no significant differences in the results can be found at the two velocities. Also shown in Fig. 4 are the results of Hopkins (1967) obtained for a free jet in counter flow. For the range of λ indicated in Fig. 4, one notes that the geometric characteristics of a counter wall jet are very similar to that of a free jet in counter flow.

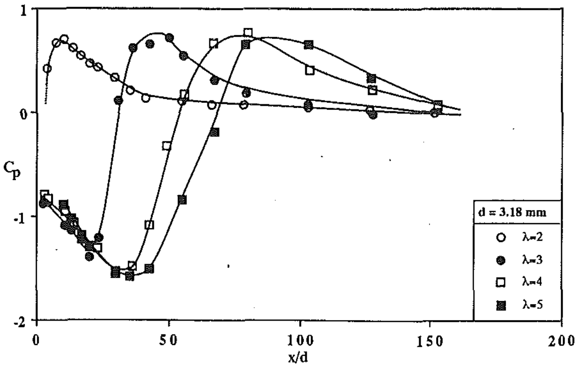

Fig. 5 Variation of C_p with x/d (uncertainty in $C_p = \pm 3.5$ percent at 20:1 odds)

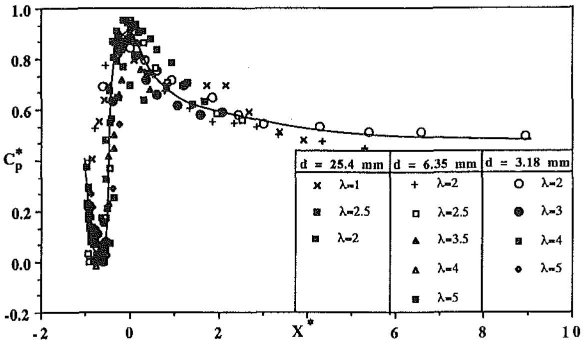

Fig. 6 Variation of C_p^* with X^*

Figure 5 shows a typical variation of the wall pressure distribution downstream of the jet exit at various values of λ. Similar pressure distributions were also obtained at other sizes of jet openings. As noted from Fig. 5, at a typical value of $\lambda = 3$, the values of C_p decrease with increasing x/d, reach a minimum, and thereafter increase to reach a maximum. The values of x_2 corresponding to the location of the stagnation point S (Fig. 1) obtained visually, agree fairly with the estimation of x_2 corresponding to the location of the maximum values of C_p along the wall, based on pressure records. As x/d increases further, $C_p \rightarrow 0$, as the pressures reach the freestream values. Incidentally, the wall pressure distributions indicated in Fig. 5 resemble those obtained downstream of a backward facing step (Ramamurthy, 1990). Following previous experiences (Adams, 1988; Roshko, 1965), an attempt was made to absorb size and velocity scale effects by defining a modified pressure coefficient $C_p^* = C_p - C_{p\min}/(1 - C_{p\min})$. Figure 6 shows the variation of C_p^* with X^*. Here, $X^* = (x - x_{\text{stg}})/x_{\text{stg}}$. The results indicate that the data for all sizes of jet openings and various λ appear to collapse on to a single curve. It should be noted that up to the point of stagnation ($X^* = 0$), the data very clearly fall on a single line. Beyond stagnation or maximum pressure recovery, there is some deviation from the mean curve drawn (Fig. 6); especially at very small values of λ and at large jet openings. Due to equipment limitations, the jet flow range was generally the same for all values of d. However, the lowest range of J_o was associated with the lower values of the jet flow Reynolds numbers associated with higher frictional losses. Furthermore, the ratio of the jet size (d) and the height of the freestream flow was the largest for the larger value of d and hence, a higher value of blockage. These factors could have contributed to the deviation from the indicated mean curve in Fig. 6.

In practice, the jet injection device acts like a protrusion into the main flow and may disturb flow characteristics significantly. To ensure that such is not the case, one can install a protrusion and verify its effects on the counter jet parameters such as x_2 and a_2. The results of such an interference test are included in Fig. 7 which indicates that the protrusion does not disturb the flow. In practice, the type of protrusions encountered vary in size and shape. The optimum size and shape can be chosen by conducting tests and obtaining results similar to the one shown in Fig. 7.

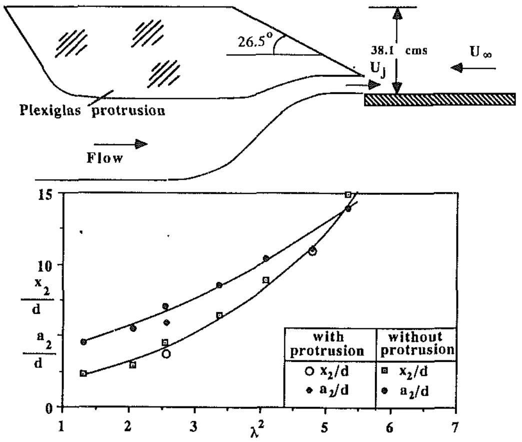

Fig. 7 Jet penetration characteristics with and without protrusion (uncertainty in x_2/d and $a_2/d = \pm 5$ percent at 20:1 odds)

Conclusions

The following conclusions can be drawn from the present counter flowing wall jet study:

1. As the ratio of the jet velocity to the freestream velocity increases, the length and width of the zone of jet penetration increase.
2. The nondimensional wall pressure surveys indicate a similar trend at all values of λ and for the three values of jet sizes tested. The pressures first decrease with increasing distances from the jet exit, reach a minimum and then begin to increase up to the point of stagnation beyond which they decrease and tend toward the freestream value.
3. By proper choice of the scaling variables, the wall pressure data can be collapsed to a single curve for the entire range of λ tested for all sizes of initial jet width.
4. The optimum size and shape of the wall jet injection device can be chosen after conducting simple jet interference tests.

References

Adams, E. W., and Johnston, J. P., "Effects of Separating Shear Layer on the Reattachment Flow Structure, Part 1—Pressure and Turbulence Quantities," *Experiments in Fluids*, Vol. 6, pp. 400–408.

Beltaos, S., and Rajaratnam, N., 1973, "Circular Turbulent Jet in an Opposite Infinite Stream," Canadian Hydraulic Conference, The University of Alberta, Edmonton, May.

Colin, P. E., 1968, "The Wall Jet Beneath a Counter-Flowing Stream," Contract No. DAJA 3767-C-0045 von Kármán Institute for Fluid Dynamics, Mar.

Daily, J. W., and Harleman, D. R. F., 1966, *Fluid Dynamics*, Addison Wesley, New York.

Hopkins, D. F., 1962, "A Study of Fluid Jet Penetration," Ph.D. thesis, Mechanical Engineering, University of Illinois.

Hopkins, D. F., and Robertson, J. M., 1967, "Two-Dimensional Incompressible Fluid Jet Penetration," *J. Fluid Mech.*, Vol. 29, Part 2, pp. 273–287.

Kline, S. J., 1985, "The Purposes of Uncertainty Analysis," ASME JOURNAL OF FLUIDS ENGINEERING, Vol. 107, pp. 153–160, June.

Kline, S. J., and McClintock, F. A., 1953, "Describing Uncertainties in Single Sample Experiments," *Mechanical Engineering*, ASME, pp. 3–8, Jan.

Rajaratnam, N., 1976, "Turbulent Jets," *Developments in Water Science*, Vol. 5, Elsevier Scientific Publ. Co., New York.

Ramamurthy, A. S., Robillard, L., Duong, V. L., and Bhaskaran, P., 1971, "Unstable Characteristics of a Plane Counter Jet," CANCAM, Calgary, May, pp. 569–570.

Ramamurthy, A. S., Balachandar, R., and Govinda Ram, H. S., 1990, "Characteristics of Flow Past Backward Facing Steps Including Cavitation Effects," Under review for possible publication in the ASME JOURNAL OF FLUIDS ENGINEERING, Oct.

Rao, T. R. K., 1958, "Investigation of the Penetration of a Jet into a Counterflow," Master's thesis, State University of Iowa.

Robillard, L., 1971, "Mouvement périodique d'un jet bidimensionnel plan dans un contre-courant et production de tourbillons alternés," *Journal of Mécanique*, Vol. 10, No. 1, mars.

Robillard, L., and Ramamurthy, A. S., 1974a, "Experimental Investigation of the Vortex Street Generated by a Plane Jet in Counter Flow," ASME JOURNAL OF FLUIDS ENGINEERING, pp. 43–48, Mar.

Robillard, L., 1974b, "Contribution a l'etude des jets a contre-courant," Ph.D. thesis, L'Universite Laval, mars.

Roshko, A., and Lau, J. C., 1965, "Some Observations on Transitions and Reattachment of a Free Shear Layer in Incompressible Flow," *Proc. Heat Transfer and Fluid Mech. Inst.*, Stanford University Press, pp. 157–167.

F. J. Pierce
Mechanical Engineering Department,
Virginia Polytechnic Institute and State University,
Blacksburg, VA 24061-0238
Fellow ASME

J. Shin
Aerospace Engineer,
NASA-Lewis Research Center,
Cleveland, OH 44135
Mem. ASME

The Development of a Turbulent Junction Vortex System

(Data Bank Contribution*)

The growth and development of a horseshoe vortex system in an incompressible, three-dimensional turbulent junction flow were investigated experimentally. A streamlined cylinder mounted with its axis normal to a flat surface was used to generate the junction vortex flow. The flow environment was characterized by a body Reynolds number of 183,000, based on the leading edge diameter of the streamlined cylinder. The study included surface flow visualizations, surface pressure measurements, and mean flow measurements of total pressure, static pressure, and velocity distributions in three planes around the base of the streamlined cylinder, and in two planes in the wake flow. Some characterizations of vortex properties based on the measured mean cross-flow velocity components are presented. The results show the presence of a single large, dominant vortex, with strong evidence of a very small corner vortex in the junction between the cylinder and the flat surface. The center of the dominant vortex drifts away from both the body and the flat surface as the flow develops along and downstream of the body. The growth and development of the core of the large, dominant vortex are documented.

1 Introduction

The 1981-82 Stanford Conference on Complex Turbulent Flows (Kline et al., 1981) revealed the need for detailed, experimental studies which could serve as standard test cases for evaluating computational codes developed for complex turbulent flows. In an attempt to respond to this need, a long term project was initiated to provide an extensive, highly detailed, coherent and self-consistent data set for one particular complex turbulent flow. The three-dimensional turbulent separated flow centered about a junction or horseshoe vortex was selected. This is a complex, three-dimensional flow characterized by large scale turbulent fluctuations, by separation, by recirculation, and by vortex structures. This flow is generated by placing a streamlined cylindrical body normal to a flat surface in a thick, turbulent boundary layer. Detailed descriptions of various portions of the work can be found in Harsh (1985), Tree (1986), Pierce et al. (1987a), Pierce et al. (1987b), and Pierce and Nath (1990). This type of flow is encountered in many areas including the wing-fuselage junction of aircraft, the blade-end wall junction of turbomachinery, and the sail-hull junction of submersibles.

The prominent feature of the junction flow is the presence of the horseshoe vortex system formed in the corner between the body and the flat surface. The physical mechanism responsible for the formation of this vortex system is the total pressure gradient near the leading edge of the body, resulting from the upstream boundary-layer flow. The pressure gradient causes a three-dimensional separation in the neighborhood upstream of the body. The separated boundary layer rolls up downstream of the separation line to form a system of vortices, and this system of vortices appears to wrap around the base of the body. This horseshoe vortex system persists downstream and is seen clearly in the body wake flow.

As reviewed in Pierce and Tree (1990), the most frequently presented model for the upstream symmetry plane for a turbulent junction vortex shows a system of four distinct vortices, in two counter rotating pairs, and defining two pairs of separation and attachment lines on the flat surface as presented in Baker (1980) and Hunt et al. (1978). This model is based mainly on surface flow visualizations. In the Reynolds number range of this experiment, the more recent surface flow visualizations of Pierce and Harsh (1983) and Eckerle and Langston (1987), together with their extensive velocity field measurements, confirm the existence of at most one pair of counter rotating vortices with the corresponding pair of one separation and one attachment line for the flow in the forward portions of the junction vortex system. A thorough review of several relevant experiments is presented in Pierce and Tree (1990).

Several studies have investigated the interaction of a streamwise vortex embedded within a turbulent boundary layer. Shabaka et al. (1985) and Metha et al. (1983) studied a single vortex embedded within the boundary layer in a constant pressure flow. Their results showed a strong distortion of turbulent stresses within the boundary layer. Westphal et al. (1987) investigated the development of a fairly weak streamwise vortex within a turbulent boundary layer with and without an adverse pressure gradient. They concluded that the adverse pressure gradient increased the rate of core growth and caused a stronger distortion of the core shape. These studies dealt with an isolated vortex generated by a half-delta wing. Shabaka and Bradshaw (1981), Kubendron et al. (1986), Dickenson (1986), Hazarika et al. (1986), and Moore and Forlini (1984) have made meas-

---

*Data have been deposited to the JFE Data Bank. To access the file for this paper, see instructions on p. 705 of this issue.

Contributed by the Fluids Engineering Division for publication in the JOURNAL OF FLUIDS ENGINEERING. Manuscript received by the Fluids Engineering Division, June 5, 1990. Associate Technical Editor: F. M. White.

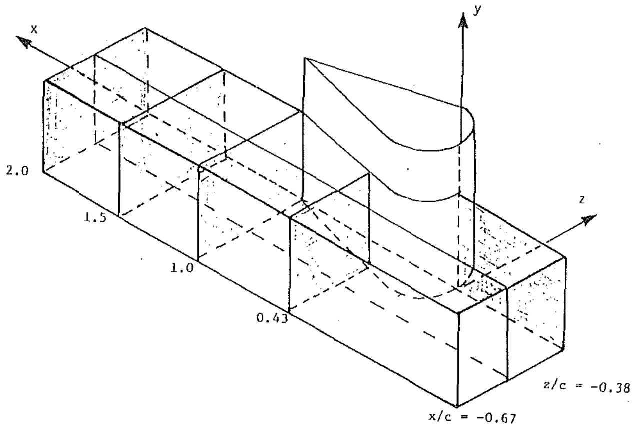

Fig. 1 The body, coordinate system and measurement planes

urements within a horseshoe vortex in a junction flow at cross-sectional planes around a body, but the development of the horseshoe vortex has not been extensively documented quantitatively. The objective of the present study was to document and characterize the growth and development of the horseshoe vortex system in such a flow.

Subsequent to the work reported here, Devenport and Simpson (1990) confirmed many of these earlier results, including the surface flow visualizations, the surface pressure measurements, and the upstream time mean velocity measurements reported earlier in Harsh (1985), Pierce and Harsh (1987), Pierce et al. (1987a) and Pierce et al. (1987b), as well as the LDV velocity measurements and the bimodal character of the probability density function for the velocity field in and around the junction vortex on the upstream symmetry plane reported by Tree (1986). Devenport and Simpson report on measurements of probability density functions over a larger spatial area and map out the regions where bimodal distributions occurred in their flow. They report extensive turbulent stresses and turbulent kinetic energy data. They also offer a time variant physical flow model which they propose is consistent with the observed bimodal probability density functions.

2 Experimental Facilities and Methods

The experiments were conducted in an open circuit, subsonic wind tunnel. The test section, located 5.0 m downstream of the tunnel inlet nozzle exit, has a rectangular cross section 0.91 m by 0.61 m, and a freestream turbulence of 0.5 percent. Dynamic similarity was achieved by maintaining a constant Reynolds number at the tunnel nozzle exit. The Reynolds number per unit length, $\mathrm{Re}/L = \rho V^*/\mu$, was equal to 1,340,000 per meter. Based on the undisturbed test section speed, the body chord and body thickness Reynolds numbers were 429,400 and 183,000, respectively. The boundary layer was tripped on all four sides of the tunnel nozzle exit with 2.8 mm diameter rods. The test section boundary-layer thickness was 81.6 mm, with a displacement thickness of 10.5 mm and a momentum thickness of 8.09 mm. The momentum Reynolds number was 12,500.

The streamlined cylinder has a leading edge diameter (maximum thickness) of 127 mm, an overall length (chord) of 298 mm, and a height of 229 mm. The flat sides of the cylinder terminate in a sharp trailing edge and are tangent to the circular leading edge of the body. The right-hand orthogonal coordinate system used to describe the flow and the body are shown in Fig. 1. The x and z directions are referred to as the streamwise and transverse direction, respectively. All measurements were made with the body fixed at 5.0 m downstream of the tunnel nozzle exit. Measurements were made in five planes, including the upstream centerline plane or upstream plane of symmetry, and four transverse planes at the 43, 100, 150, and 200 percent chord positions, as shown in Fig. 1.

The three components of the mean velocity, the total pressure, and the static pressure were measured using a 3.18 mm diameter, United Sensor Corporation, type DC, five-hole biconic, Prandt-type pressure probe. An automated transverse and digital data acquisition system was used for vertical probe movement, local yaw movement, data collection and preliminary data reduction. Details about the probe, nulling methods, probe calibration, data acquisition system, data reduction methods, and the calculation of uncertainty estimates for individual measurements can be found in Harsh (1985) or Pierce et al. (1987a). Tables of values for all the figures included here are in Harsh (1985), Pierce et al. (1987a), Pierce et al. (1987b), and Tree (1986).

The five-hole probe calibration was arbitrarily limited to a pitch of 15 degrees to minimize the experimental uncertainties. Local regions of flow near separation and in portions of the large vortex structure in the upstream symmetry plane exceeded this pitch angle limit of 15 degrees, making measurements in these regions suspect. A two-color, two-component, frequency shifted laser Doppler velocimeter was used to make extensive additional measurements throughout the separation and vortex region in the plane of symmetry. These methods and measurements are described in Pierce and Tree (1990), with extensive details and tabulated results of all measurements, including uncertainty calculations, in Tree (1986). All other pressure probe measurements presented here were made well within the calibration pitch angle limit.

The transverse or streamwise vorticity was computed for each of the measurement planes from the measured velocity data by using the average of forward and backward difference approximations for the required partial derivatives.

3 Results and Discussion

Figure 2 shows a surface flow visualization of the flow upstream of the body. The original high quality visualization shows only one singular saddle point of separation in the symmetry plane, with a line of ordinary separation radiating from this point and wrapping around the body. The separation point is approximately one leading edge radius forward of the body, in agreement with other studies for such flows (Baker, 1980 and Eckerle and Langston, 1987). No additional lines of sep-

Nomenclature

c_p = static pressure coefficient
$c_{p,T}$ = total pressure coefficient
D = leading edge diameter or body thickness
h = body height
H = floor to vortex center distance
R_D = Reynolds number based on body dimension
R_θ = Reynolds number based on approach boundary-layer momentum thickness
R_y = vortex vertical scale, radius measured up from vortex center
R_z = vortex transverse scale, radius measured left from vortex center
V^* = tunnel inlet nozzle exit speed used to nondimensionalize velocities
U, V, W = components of velocity
x, y, z = coordinates
Y_c, Z_c = distances to the vortex center
δ = boundary-layer thickness
δ^* = boundary-layer displacement thickness
θ = boundary-layer momentum thickness

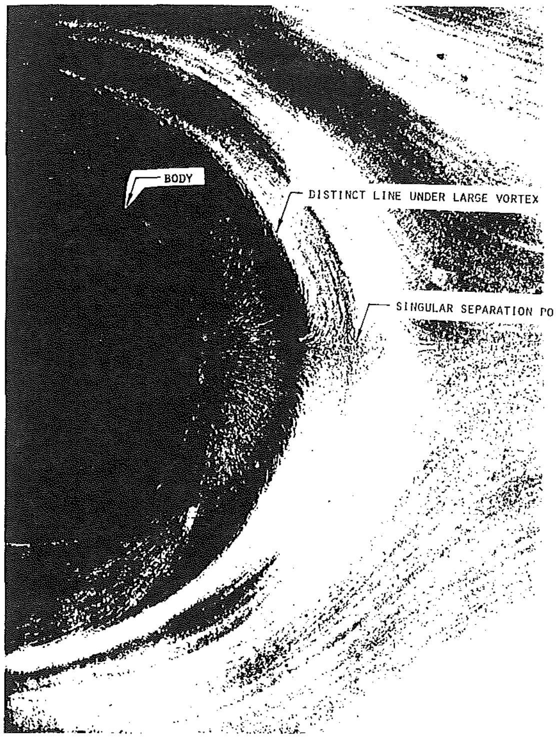

Fig. 2 Surface flow visualization around the upstream symmetry plane

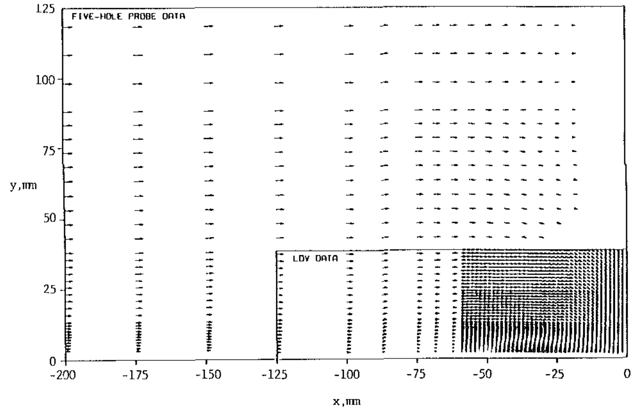

Fig. 3 Combined LDV and pressure probe measured *UV* velocity field in the upstream symmetry plane. Largest calculated uncertainty is ±0.009.

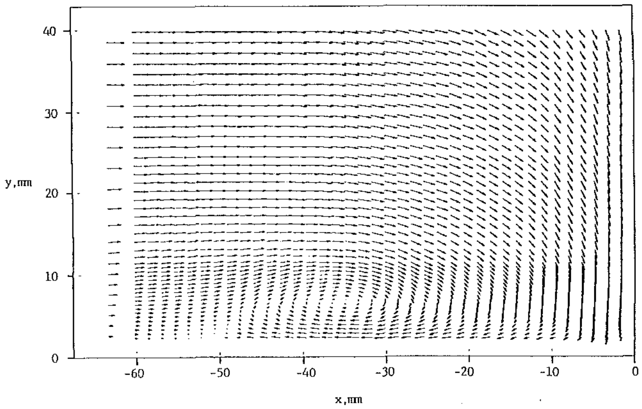

Fig. 4 LDV measured *UV* velocity field in the upstream symmetry plane. Largest calculated uncertainty is ±0.009.

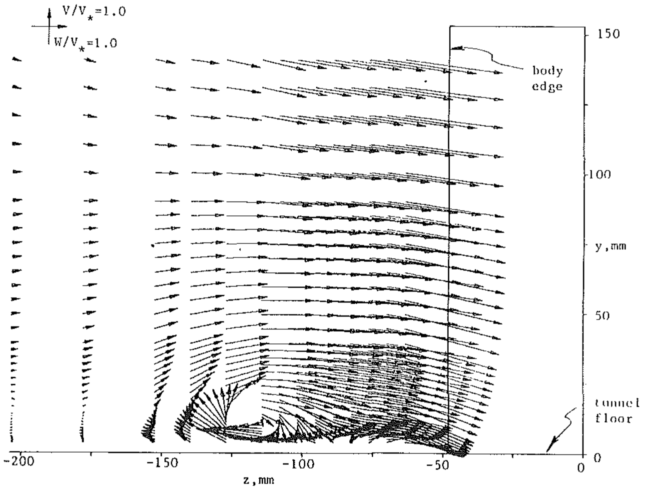

Fig. 5 Measured *VW* velocity field in the 43 percent transverse plane. Largest calculated uncertainty is ±0.008.

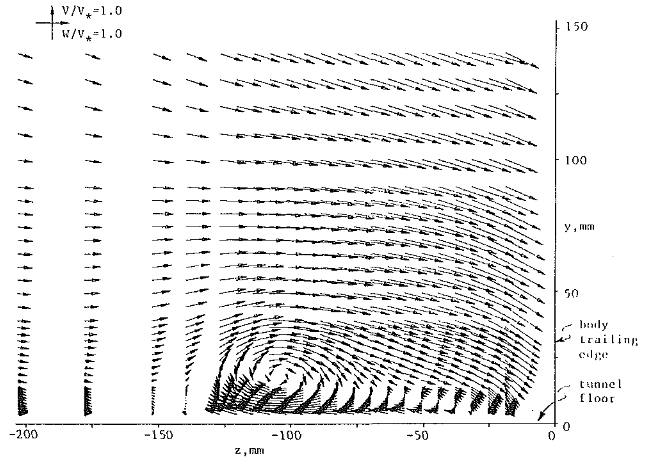

Fig. 6 Measured *UW* velocity field in the 100 percent transverse plane. Largest calculated uncertainty is ±0.008.

aration or attachment are seen in the visualization. A distinct line is seen between the singular separation point and the body, and this is identified as a high wall shear line which lies below the center of the large or principal junction vortex to be described below. Floor surface pressure measurements show this line to be coincident with a local minimum in the floor static pressure. This is particularly clearly seen in the upstream symmetry plane and presented in Pierce and Tree (1990). Additional details on the upstream and surrounding flow are presented in Menna and Pierce (1988) and Pierce and Harsh (1988)

Figures 3 through 8 show the measured velocities in the five planes described earlier. The velocity components *U*, *V*, and *W* were nondimensionalized by the speed at the exit of the tunnel nozzle, V^*.

Figure 3 shows the combined pressure probe and LDV measured *U-V* velocity field in the plane of symmetry, and Fig. 4 shows the details revealed by the more extensive LDV measurements. The *V-W* velocity distributions in the four transverse planes, measured by the five-hole pressure probe, are shown in Figs. 5-8. The velocity distributions in all five planes all show one large vortex structure clearly. Baker (1980) and Hunt et al. (1978) both offer a symmetry plane flow model, base mainly on surface flow visualizations, showing a four vortex model with two pairs of counter rotating vortices. Only one, relatively large, vortex structure is seen in Figs. 4 and 5. The corresponding computed vorticity field in Fig. 9 shows strong

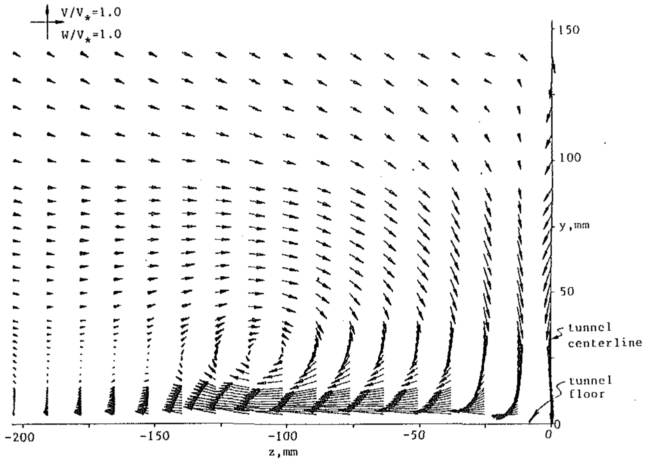

Fig. 7 Measured *VW* velocity field in the 150 percent transverse plane. Largest calculated uncertainty is ±0.008.

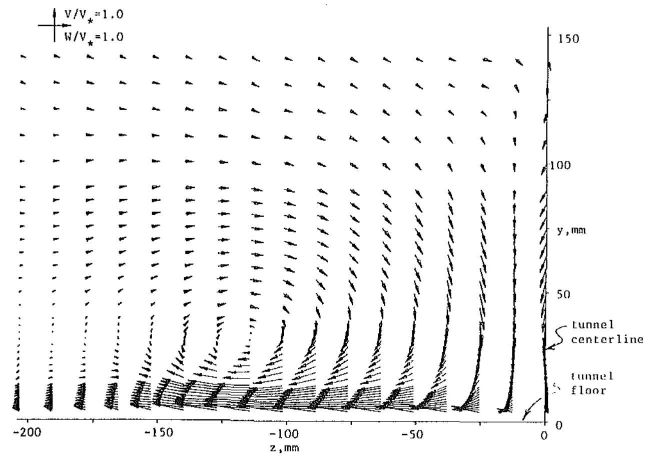

Fig. 8 Measured *VW* velocity field in the 200 percent transverse plane. Largest calculated uncertainty is ±0.008.

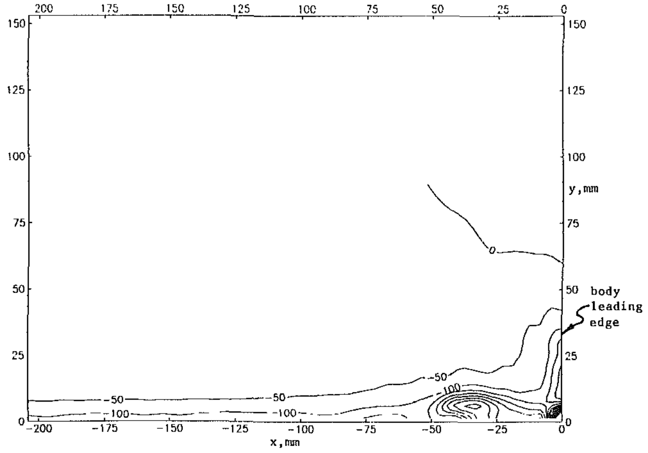

Fig. 9 Vorticity field in the upstream symmetry plane. Estimated uncertainty is ±10 percent.

evidence of a very tightly wound, physically much smaller, counter rotating corner vortex at the body-floor intersection. The presence of such a small corner vortex is also supported by the work of Dickenson (1986) and Hazarika et al. (1986). There is no clear evidence of any second pair of vortices, or multiple separation and attachment lines, in the floor flow visualization, the measured velocity field or the computed vorticity field. Figure 5 at the 43 percent chord position can be interpreted as showing the top portion of a smaller scale, corotating vortex that is positioned closer to both the body and the floor, and Fig. 6 at the 100 percent chord position can be interpreted as showing even more of a smaller scale, corotating vortex, again positioned both nearer to the body and to the floor than the principal junction vortex structure.

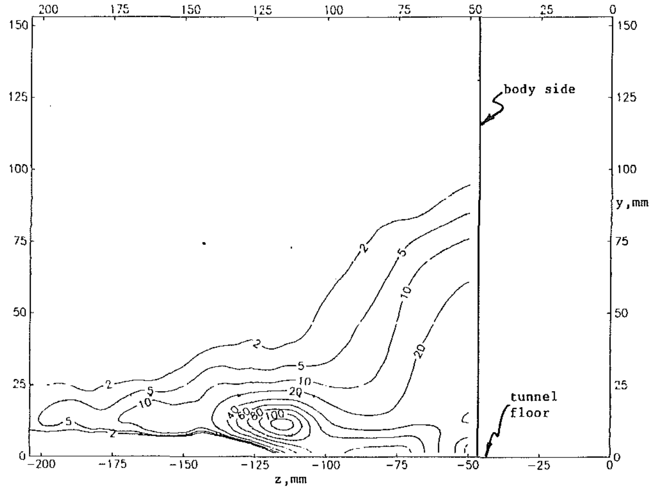

Fig. 10 Vorticity field in the 43 percent transverse plane. Estimated uncertainty is ±10 percent.

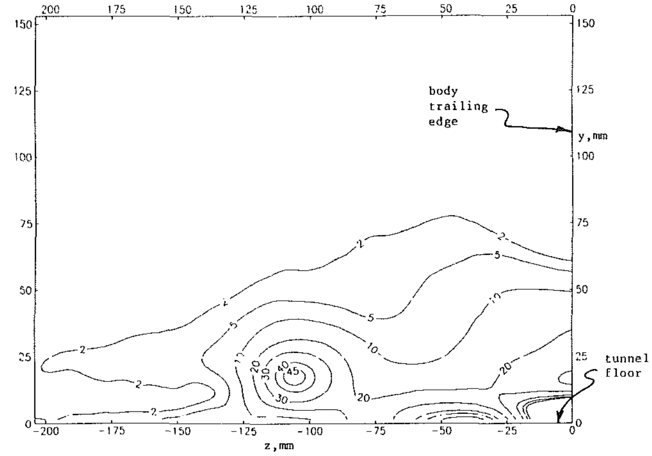

Fig. 11 Vorticity field in the 100 percent transverse plane. Estimated uncertainty is ±10 percent.

The effect of the proximity of the flat surface under the vortex in the wake flow is apparent in the strong *W* velocities measured beneath the vortex centers in Figs. 7 and 8. The secondary flow distributed over the top of the vortex and moving toward the tunnel centerline is confined to a relatively thin layer moving away from the tunnel centerline below the vortex, with relatively large velocities. This results in substantial gradients of the transverse or *W* velocity in the normal or *y* direction in these regions, and results in the computed vorticity peaks being displaced downward from the vortex centers seen in the secondary velocity fields of Figs. 7 and 8.

Figure 9 shows the computed transverse vorticity field for the upstream plane of symmetry. The figure shows one large vortex structure clearly, with strong evidence of a smaller, tightly wound corner vortex. This vortex pair is a counter rotating pair, with approximately equal minimum and maximum values of −400 and 400/s for the principal vortex and the tightly wound corner vortex, respectively.

Figures 10 through 13 show the streamwise vorticity contours for the four transverse planes. The figures show contours that are more or less concentric, and with a local maximum in the vorticity approximately coincident with the spatial position of the large or principal vortex structure seen in the secondary

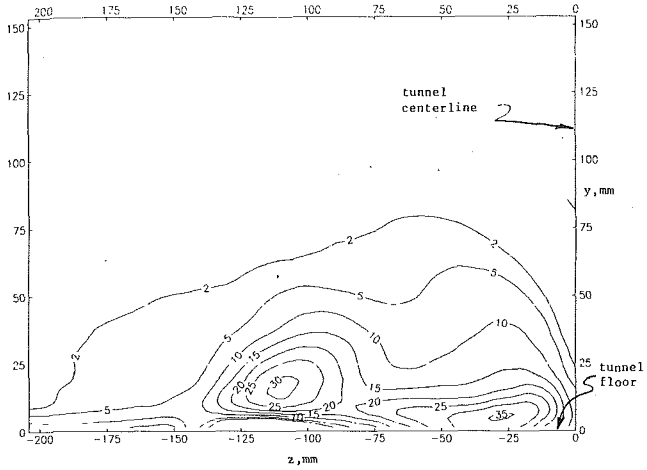

Fig. 12 Vorticity field in the 150 percent transverse plane. Estimated uncertainty is ±10 percent.

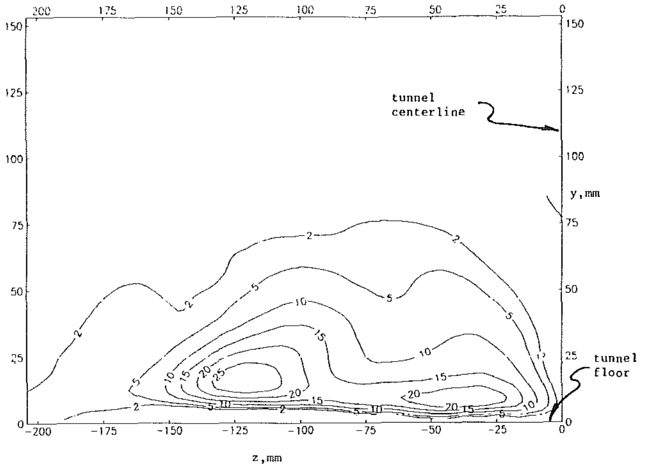

Fig. 13 Vorticity field in the 200 percent transverse plane. Estimated uncertainty is ±10 percent.

velocity figures. Figures 10 through 13 show no evidence of the tightly wound corner vortex, suggested in the upstream plane of symmetry, propagating around the body. Figure 10 for the 43 percent chord position shows a clear local maximum in the vorticity, coincident with the large vortex structure seen in the corresponding secondary velocity field. Relatively large values of positive vorticity persist into the corner of the figure, again consistent with a second, smaller scale, corotating vortex that is suggested by the velocity field. Figure 11 at the 100 percent chord position (the body trailing edge) shows two peaks in vorticity of approximately equal strength. Both of these peaks are of the same sign, indicating a pair of corotating rather than counter rotating vortices. The secondary velocity field in Fig. 6 can also be interpreted to support the existence of a smaller scale, corotating vortex structure closer to both the body and the floor, consistent with the second peak in the computed vorticity field. Other studies done in this tunnel with modified body shapes show the existence of a corner separation vortex in the flow downstream of the body's thickest section and upstream of the body trailing edge. Such a corner separation vortex may be the source of this corotating vortex structure suggested by the vorticity contours at the 100 percent plane in the present study. The conventional wisdom suggests that vortices occur in counter rotating pairs. No evidence of a counter rotating structure is seen in the velocity field figure, nor implied by the computed vorticity field for this plane. However, such structures could exist as very small scale structures in the fluid layer very close to the floor and beyond resolution by the pressure probe used.

Table 1 Mean flow secondary kinetic energy per unit mass

plane	m^2/s^2
43% chord	6.10
100% chord	1.89
150% chord	0.52
200% chord	0.41

Figures 12 and 13 in the wake of the body at the 150 and 200 percent transverse planes also show two vorticity peaks each, both of the same sign and both of nearly the same value. The secondary velocity fields for these planes do not show or strongly imply a second corotating vortex structure. The single, large vortex structure seen in each of Figs. 7 and 8 is identified as the principal junction vortex first identified in the plane of symmetry, and subsequently wrapping around the body and propagating or developing into the wake flow. Vorticity contours and a peak in vorticity approximately coincident with this principal vortex structure are clearly seen in Figs. 12 and 13. It can be argued that the two corotating vortices suggested in Figs. 6 and 11, for the 100 percent or trailing edge transverse plane, have merged in the secondary velocity figures for the 150 and 200 percent chord positions, showing only one large vortex structure clearly, while the computed vorticity field still shows evidence of two structures. As noted for the trailing edge transverse plane, there is no evidence in either the secondary velocity field shown, or in the computed vorticity field, of any counter rotating vortex pairs.

The vortex center, Y_c, Z_c, was located at the approximate geometric center of the concentric vorticity contours. An alternative vortex center can sometimes be defined by the point where the velocity components are zero in the V-W (or U-V) velocity plots. The vortex centers in Figs. 12 and 13 appear to be closer to the floor than indicated by the secondary velocity fields of Figs. 7 and 8. This results from the very large gradients in W with y that occur below the vortex structures as discussed earlier.

The strength of the principal vortex was characterized by the mean secondary flow kinetic energy, MSFKE, and by the peak value of vorticity at the vortex core or center.

The mean secondary flow kinetic energy per unit mass is defined as

$$\text{MSFKE} = \frac{\int_A \left\{ \left(V_i^2 + W_i^2 \right) / 2 \right\} \rho_i \, U_i \, dA_i}{\int_A \rho_i \, U_i \, dA_i}$$

and was computed for the four transverse planes. In each case the numerical integration was made over a window that contained only the large vortex structure. This procedure excluded the large transverse velocities seen in Figs. 5 and 6, and attributed to the bulk flow following the body shape. The results show a large decrease in mean secondary flow kinetic energy from the 43 to 100 percent chord planes, with a continuing decrease from the 100 to 200 percent chord planes. The computed values are tabulated in Table 1.

In the plane of symmetry, the peak value of vorticity is on the order of 400/s. The peak value of vorticity at the 43 percent chord position decreases to 120/s and the peak value decreases further to about 30/s at the 200 percent chord position. Circulation for the principal vortex was computed by integrating the vorticity over the portion of the plane that does not contain the smaller corner vortices in order to exclude contributions of these structures. Circulation of the principal vortex was observed to decrease steadily from a value of 0.0898 m^2/s in the plane of symmetry, to a value of 0.0438 m^2/s at the 200 percent chord position. As the principal vortex develops, it

Table 2 Circulation

plane	m^2/s
plane of symmetry	0.0898
43% chord	0.0683
100% chord	0.0505
150% chord	0.0503
200% chord	0.0438

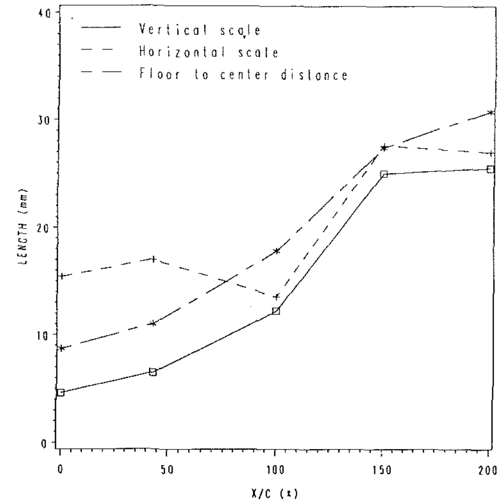

Fig. 14 Vertical scale R_y, transverse scale R_z, and floor to vortex center distance H of the principal vortex.

decreases in strength and increases in cross sectional area, with the vorticity in the core region spreading outward. The values of circulation are tabulated in Table 2.

Vortex length scales are characterized by radial dimensions in both the transverse and vertical directions due to the ellipticity of vorticity contours. Radial scales were measured from the vortex center to where the vorticity had decreased to 50 percent of the maximum value at the vortex center. Because of the interaction between the principal vortex and the adjacent vorticity peaks, the radius measured left from the center and the radius measured right from the center are not equal in the transverse direction. The presence of the flat surface also makes the downward vertical radius different from the upward vertical radius. The radius measured left from the vortex center for the transverse radial dimension, R_z, and the upward radius for the vertical radial dimension, R_y, were used to characterize the growth of vortex core, so that this characterization is free of the constraint of the tunnel floor and interaction between the principal vortex and any possible corner vortices. Figure 14 shows the vertical dimension of the core, R_y, the transverse dimension of the core, R_z, and the distance of the vortex center above the floor, Y_C. The figure shows a rapid growth of R_y until it reaches the value of about 25 mm at the 150 percent chord position, from where R_y stays approximately constant to the 200 percent chord position. The growth of R_z shows a similar trend.

The total pressure distribution and the static pressure distribution in the 100 percent chord plane are shown in Figs. 15 and 16, respectively. These figures indicate that the vortex core consists of both low total pressure and low static pressure fluid. The total pressure and the static pressure distributions at other planes indicate essentially the same results. Figure 17 shows the streamwise velocity distribution at the 100 percent chord plane. The figure shows that the vortex consists of low streamwise momentum fluid. The corner between the tunnel floor and the vertical side of the body is filled with relatively high streamwise momentum fluid, induced into the corner by the vortex. The streamwise velocity distributions at other planes show similar results.

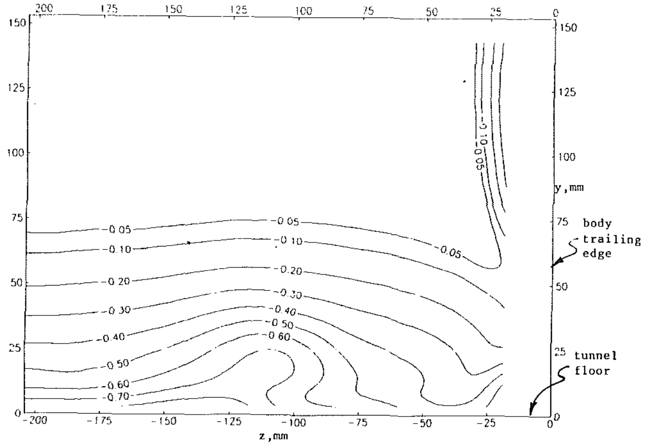

Fig. 15 The total pressure coefficient, c_{pt} in the 100 percent transverse plane. Typical calculated uncertainty is +0.01.

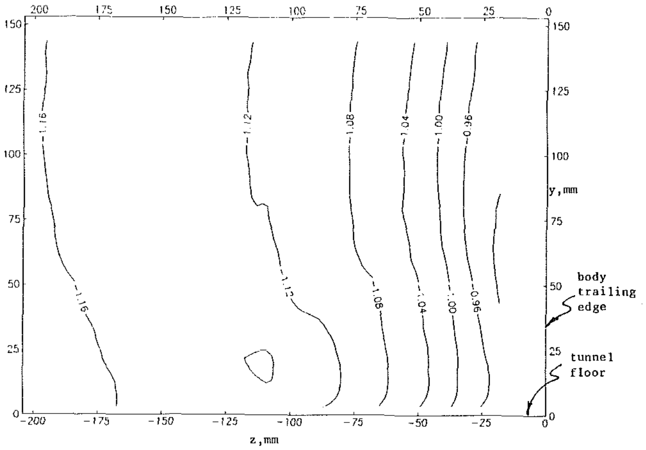

Fig. 16 Static pressure coefficient, c_p, in the 100 percent transverse plane. Typical uncertainty is ±0.02.

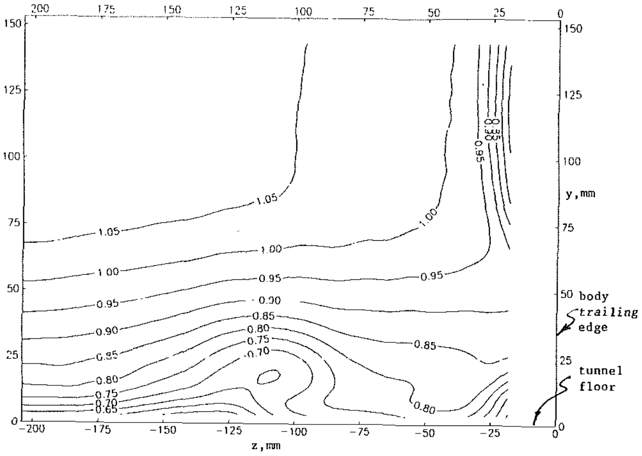

Fig. 17 Streamwise velocity contours in the 100 percent transverse plane. Typical uncertainty is ±0.007.

4 Standard Test Case

The results presented in this paper are part of a large data base documenting the mean flow structure upstream, around, within, and in the near wake of a turbulent junction vortex flow. The data set is a highly detailed, coherent, self-consistent set offered to the computational fluid mechanics community as a standard test case for the evaluation of the capabilities of numerical solvers intended for predicting the flowfield in such a complex, separated, three-dimensional turbulent flow. Measurements of the primitive variables of velocity, static, and total pressure were made on all 10 of the flat surfaces shown in Fig. 1. A statistically meaningful uncertainty is reported for every measurement in the data set.

The complexity of the flow through separation and in the vortex suggests that the full, elliptic, turbulent Navier-Stokes equations would be required in a solution. A well-posed problem governed by elliptic equations requires boundary conditions on all boundaries surrounding the solution domain. In this case, the three transverse and one streamwise plane contained in the interior of the solution domain shown in Fig. 1 would be available for comparison with any computed flow field. The data set is also suitable in evaluating parabolized numerical methods that march through the elliptic flow, while correcting for the elliptic character of the flow. In this latter case, the endmost transverse plane would also be available for comparison with the computed flow field.

5 Conclusions

The horseshoe vortex system in an incompressible, three-dimensional, turbulent junction flow has been investigated experimentally. In the plane of symmetry, the mean flow results indicated that the three-dimensional separation and junction vortex were confined to a region very near the flat surface. In this plane both the floor surface flow visualization and the measured velocity field showed a single dominant vortex, with a tightly wound, smaller length scale, counter rotating, corner vortex of approximately the same strength strongly implied by the computed vorticity field. The smaller scale, corner vortex is not clearly recognized in subsequent downstream measurements.

From the velocity measurements, only one dominant vortex was observed in all the planes around the body in the downstream and wake flow. The secondary velocity fields and the computed vorticity fields suggest a second, smaller scale, corotating vortex structure nearer to both the floor and the body, at the 43 and 100 percent transverse planes. The computed vorticity fields in the wake at the 150 and 200 percent chord position also suggest this additional, physically smaller but approximately equal strength corotating vortex, located both closer to the symmetry plane and the floor. This second vortex is tentatively identified with a corner separation which is thought to occur just downstream of the body at its thickest cross section. The strength of the principal horseshoe vortex, quantified by either its maximum value of vorticity, its circulation, or its mean secondary flow kinetic energy, decreases, while its length scale increases, as the vortex develops downstream.

Data Bank Contribution

Essentially all of the measured data relating to this junction vortex flow are being added to the *Journal of Fluids Engineering* Data Bank. These data are made up of the primitive variables velocity magnitude, velocity components, yaw and pitch angles, and static and total pressure measured by the five-hole, biconic pressure probe for the 10 planes shown in Fig. 1. Similarly detailed velocity data for the upstream symmetry plane and measured with a two-component, two-color frequency shifted LDV system are included. Additionally, extensive floor and body side pressure field data are also included. All the data is in nondimensional form, with statistically meaningful experimental uncertainties reported with each reported measured value. Details on calibration methods, calibration functions, data acquisition and processing methods, including details on the calculation of the individual uncertainty methods, nondimensionalizing methods are discussed in Harsh (1985) and Pierce et al. (1987a) for the pressure probe measurements. Details of the LDV measurements are in Tree (1986). The complete tabulated data set is also available in Pierce et al. (1987a), Pierce et al. (1987b), and Tree (1986). To access the file for this paper, see instructions on p. 705 of this issue.

References

Baker, C. J., 1980, "The Turbulent Horseshoe Vortex," *Journal of Wind Engineering and Industrial Aerodynamics*, Vol. 6, No. 1-2, pp. 9-23.

Devenport, W. J., and R. L. Simpson, 1990, "Time-Dependent and Time-Averaged Turbulent Structure Near the Nose of a Wing-Body Junction," *Journal of Fluid Mechanics*, Vol. 210, pp. 23-55.

Dickinson, S. C., 1986, "An Experimental Investigation of Appendage-Flat Plate Junction Flow Vol. I," David Taylor Naval Ship Research and Development Center, Rpt DTNSRDC-86/051.

Eckerle, W. A., and L. S. Langston, 1987, "Horseshoe Vortex Formation Around a Cylinder," ASME *Journal of Turbomachinery*, Vol. 109, pp. 278-285.

Harsh, M. O., 1985, "An Experimental Investigation of a Turbulent Junction Vortex," Dissertation, Mechanical Engineering, Virginia Polytechnic Institute and State University, Blacksburg, VA, (available University Microfilms).

Hazarika, B. K., R. Raj, and D. R. Boldman, 1986, "Three Dimensional Fluid Flow Phenomena in the Blade End Wall Corner Region," ASME Paper 86-GT-179.

Hunt, J. C., C. J. Abell, J. A. Peterka, and H. Woo, 1978, "Kinematical Studies of the Flows Around Free and Surface-Mounted Obstacles; Applying Topology to Flow Visualization," *Journal of Fluid Mechanics*, Vol. 86, Part 1, pp. 179-200.

Kline, S. J., B. J. Cantwell, and G. M. Lilley, 1981, *1980-1981 AFOSR-HTTM-Stanford Conference on Complex Turbulent Flows*, Vols. I, II, III, Stanford University, 1981.

Kubendran, L. R., H. M. McMahon, and J. E. Hubbartt, 1986, "Turbulent Flow Around a Wing/Fuselage Type Juncture, " *AIAA Journal*, Vol. 24, No. 9, pp. 1447-1452.

Menna, J. D., and F. J. Pierce, 1988, "The Mean Flow Structure Around and Within a Turbulent Junction or Horseshoe Vortex: Part I: The Upstream and Surrounding Three-Dimensional Boundary Layer," ASME JOURNAL OF FLUIDS ENGINEERING, Vol. 110, pp. 4066-414.

Metha, R. O., I. M. M. A. Shabaka, A. Shibl, and P. Bradshaw, 1983, "Longitudinal Vortices Imbedded in Turbulent Boundary Layers," AIAA Paper 83-0378, Reno, NV.

Moore, J., and T. J. Forlini, "A Horseshoe Vortex in a Duct," 1984, ASME *Journal of Engineering for Gas Turbines and Power*, Vol. 106, pp. 668-676.

Pierce, F. J., and M. D. Harsh, 1985, "Three-Dimensional Turbulent Boundary Layer Separation at the Junction of a Streamlined Cylinder with a Flat Plate," *Flow Visualization III, Proceedings of the Third International Symposium on Flow Visualization*, Hemisphere Pubg Corp., pp. 331-335.

Pierce, F. J., and M. D. Harsh, 1988, "The Mean Flow Structure Around and Within a Turbulent Junction or Horseshoe Vortex: Part II: The Separated and Junction Vortex Flow," ASME JOURNAL OF FLUIDS ENGINEERING, Vol. 110, pp. 415-423.

Pierce, F. J., C. M. Kim, and M. D. Harsh, 1987a, "The Mean Flow Structure of a Turbulent Junction Vortex," Rept. VPI-E-87-6, Mechanical Engineering, Virginia Polytechnic Institute and State University, Blacksburg, VA (available NTIS).

Pierce, F. J., C. M. Kim, S. Nath, and J. Shin, 1987b, "The Mean Flow Structure in the Near Wake of a Turbulent Junction Vortex," Rept. VPI-E-87-26, Mechanical Engineering, Virginia Polytechnic Institute and State University, Blacksburg, VA (available NTIS).

Pierce, F. J., and I. K. Tree, 1990, "The Mean Flow Structure on the Symmetry Plane of a Turbulent Junction Vortex," ASME JOURNAL OF FLUIDS ENGINEERING, Vol. 112, pp. 16-22.

Shabaka, I. M. M. A., and P. Bradshaw, 1981, "Turbulent Flow Measurements in an Idealized Wing/Body Junction," *AIAA Journal*, Vol. 19, No. 2, pp. 131-132.

Shabaka, I. M. M. A., R. D. Metha, and P. Bradshaw, 1985, "Longitudinal Vortices Imbedded in Turbulent Boundary Layers. Part I. Single Vortex," *Journal of Fluid Mechanics*, Vol. 155, pp. 37-57.

Tree, I. K., 1986, "Laser Doppler Velocimeter Measurements in a Turbulent Junction Vortex," Dissertation, Mechanical Engineering, Virginia Polytechnic Institute and State University, Blacksburg, VA (available University Microfilms).

Westphal, R. V., J. K. Eaton, and W. R. Pauley, 1987, "Interaction Between a Vortex and a Turbulent Boundary Layer in a Streamwise Pressure Gradient," *Turbulent Shear Flows 5*, ed., F. Durst et al., Springer-Verlag Berlin Heidelbert, pp. 266-277.

Experimental Investigation of a Three-Dimensional Boundary Layer Flow in the Vicinity of an Upright Wall Mounted Cylinder

(Data Bank Contribution*)

J. H. Agui

J. Andreopoulos

Experimental Fluid Mechanics and
Aerodynamics Laboratory,
Department of Mechanical Engineering,
The City College of The City University
of New York,
New York, NY 10031

The flow of a three-dimensional boundary layer approaching an upright wall mounted circular cylinder has been experimentally investigated by means of instantaneous flow visualization techniques using a laser sheet and time resolved measurements of the wall pressure, the gradients of which are related to the vorticity flux away from the wall. The mean separation point of the oncoming boundary layer is located on the plane of symmetry, 0.76 and 0.82 diameters upstream of the cylinder for the two investigated Reynolds numbers, based on the cylinder diameter, of 1.0×10^5 *and* 2.2×10^5*, respectively. The present flow visualization studies have shown that there is always a primary vortex present in the flow which induces an eruption of wall fluid. Very often, this eruption results in the formation of counter rotating or mushroom vortices. A secondary vortex further upstream has been observed occasionally. This vortex, as well as the vortices formed by the fast eruption of wall fluid evolve quickly in time and space and therefore cannot be obtained from time-average measurements. The primary vortex consists of several large scale structures which have originated in the oncoming boundary layer and which have acquired substantial additional vorticity. Point measurements indicate that the r.m.s. pressure fluctuations increase as separation is approached and reach a maximum near reattachment. A low degree of space-time correlation and longer integral time scales were also observed downstream of separation. A bimodal probability density function of the fluctuating pressure was observed in the vicinity of the mean separation point, close to the corner region and in the wake of the cylinder. Quasi periodic vortex shedding from the cylinder with a Strouhal number 0.13 was also observed.*

1 Introduction

The most significant feature of the flow formed when a two-dimensional boundary layer developing over a flat surface encounters a surface mounted protrusion with a bluff nose/leading edge is the appearance of a skew-induced secondary flow generally termed a "horseshoe vortex." Most of the previous work on this problem is associated with wing body junctions i.e., two-dimensional wall flows encountering a wing. Numerous workers have carried out surface-flow visualization and/or single point measurements using hot-wires or Laser Doppler Anemometry (see for example, Sedney, 1972; Dechow, 1977; Shabaka and Bradshaw, 1981; McMahon et al., 1983; Devenport and Simpson, 1988, 1990; Menna and Pierce, 1988; Pierce and Tree, 1990). Mehta (1984) found that the shape of the wing-nose affected the size, position and strength of the vortex. Unlike the time-averaged image that results from the wet-surface technique, Falco (1982) was able to visualize the instantaneous structure of the flow in the boundary layer region upstream of an upright circular cylinder mounted on the wall. His visualization indicated that large eddies present in the oncoming boundary layer were highly distorted. In the reattachment and reverse flow regions jet-like structures were intermittently present. Hunt, et al. (1978) and Baker (1979) interpreted surface flow visualizations around blunt bodies in low speed flows with the aid of kinematic considerations and postulated a four vortex system formed in the area immediately upstream of separation. Time-average measurements by Pierce and Tree (1990) in the flatplate/wing junction and calculations by Lai and Makomaski (1989) in the case of surface-mounted rectangular obstructions indicated the existence of only a two-vortex system. Recently Visbal (1991) carried out a numerical investigation using the three-dimensional, time-dependent Navier-Stokes equations and found a system of six vortices for laminar flows. Experiments by Greco (1990) and Fitzgerald et al. (1991) in laminar flows indicated the existence of multiple vortices in the flow, the number of which depends on the

---

*Data have been deposited to the JFE Data Bank. To access the file for this paper, see instructions on p. 705 of this issue.

Contributed by the Fluids Engineering Division for publication in the JOURNAL OF FLUIDS ENGINEERING. Manuscript received by the Fluids Engineering Division April 8, 1991. Associate Technical Editor: D. M. Bushnell.

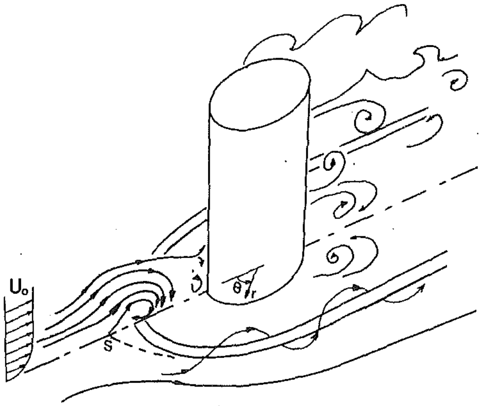

Fig. 1 Flow schematic

Reynolds number. Eckerle and Langston (1987) and Boyle and Langston (1989) experimentally investigated the flow around a single and a pair of wall mounted upright cylinders. Eckerle and Awad (1991) both measured mean velocities inside the separated region and concluded that for high free-stream velocity a vortex is formed off the plane of symmetry.

The objective of the present investigation was to increase our physical understanding of the incompressible flow around the junction formed between a flat plate and an upright wall mounted circular cylinder. This was accomplished by measuring surface pressure fluctuations on the flat wall and the cylinder (see Fig. 1). The Poisson equation indicates that wall pressure fluctuations are a result of momentum fluctuations occurring inside the flow field. Therefore a study of the wall pressure fluctuations may be indicative of the flow field behavior. In addition wall pressure gradients are related to the vorticity flux away from the wall (Lighthill, 1963). Willmarth (1975) has shown experimentally that wall pressure fluctuations provide a direct indication of surface stresses.

Spectral measurements of wall pressure fluctuations in wing-body junctions have been reported by Devenport and Simpson (1986) and Hasan et al. (1986) who found that the low frequency pressure fluctuations in the impingement region of the recirculating flow within the corner region are highly amplified. Dinkelacker et al. (1977), Schewe (1983), Thomas and Bull (1983), and Johansson et al. (1987) used the fluctuating wall pressure field to infer the structure of two-dimensional, zero pressure gradient boundary layers via conditionally sampling techniques. In the present investigation an attempt has been made to improve our understanding on the process by which the flow structure of the approaching two-dimensional boundary layer changes to that of the complex horseshoe vortex system. This, indirectly, may provide additional information concerning the structure of the vortex system, which is still unresolved.

Figure 1 shows a sketch of the time-dependent picture of the present flow which consists of three different regimes: 1) The upstream boundary layer flow including the separated and reattachment region; 2) The junction flow in the vicinity of and around the cylinder; and 3) The wake flow behind the cylinder. This paper describes results from flow visualization and measurements obtained in the upstream flow, in the region around the cylinder which is simply termed here the "corner region" and in the wake. Further details are described by Agui (1989) and by Agui and Andreopoulos (1990).

2 Experimental Setup and Instrumentation

The experiments were performed at the CCNY large scale wind tunnel (shown in Fig. 2(*a*)) which is powered by a 20 bhp frequency controlled motor which provides 40,000 cfm of air at a maximum free-stream velocity of approximately 11 meters per second. The rectangular flow inlet is 12 ft by 12 ft and includes a honeycomb and five mesh screens. The test section is 4 ft by 4 ft and 20 ft long. Preliminary measurements indicate a 0.08 percent turbulence intensity in the free stream at maximum velocity. To minimize vibration, the working section was isolated from the downstream axial fan and motor. In addition the wall of the fan/motor housing section is porous to damp acoustic noise generated by the fan/motor assembly. The present model which was mounted on the tunnel wall, consisted of a circular cylindrical plexiglass tube, 1 ft in diameter by 2 ft in height, rigidly attached to a 3 ft diameter circular flat turn-table also made of plexiglass. The corresponding blockage ratio of the present model was 12.5 percent. Figure 2b shows a diagram of the model configuration including instrumentation locations. Mean and fluctuating wall pressures were recorded using a Metrabyte DASH20 A/D board, configured on an IBM AT computer, and a MASSCOMP 5500 data acquisition computer respectively. Mean pressures were measured using MKS BARATRON type 223B pressure transducers. Fluctuating pressures were measured using two high sensitivity pressure transducers model XCS-062-5-D as supplied by KULITE SEMICONDUCTORS PRODUCTS. The Kulites are differential pressure transducers and were set-up to measure time-resolved pressure against the atmospheric pressure. Long, small diameter, tubing was used to damp atmospheric pressure fluctuations. The resonant frequency of the transducers as stated by the manufacturer was 150 kHz. Shock tube tests, including static and dynamic calibrations, in our laboratory and elsewhere, indicated a frequency response of the transducers close to this value (Honkan and Andreopoulos, 1990; Chung and Lu, 1990).

The approaching boundary layer was tripped by means of a ½ in. wide strip of sand paper glued onto the tunnel wall at the end of the contraction. Table A indicates the nominal mean flow parameters of the incoming wall boundary layer. The skin friction coefficient was measured using the Clausert Chart and Preston tube methods. The spanwise uniformity of the incoming boundary layer was established via Preston tube measurements at several longitudinal and lateral locations on

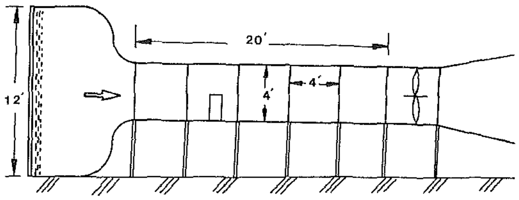

Fig. 2(*a*) Wind tunnel facility

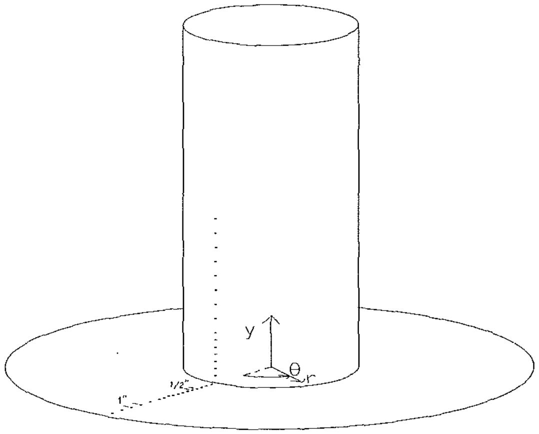

Fig. 2(*b*) Model with linear array of pressure taps. First tap on both surfaces is located at 1/2 in. from the corner. 12 taps on the plate are spaced 1/2 in. apart and 5 are spaced 1 in. apart. 7 taps on the cylinder are spaced 12 in. apart and 8 are spaced 1 in. apart.

Table A Two-dimensional boundary layer flow parameters

U_o	u_τ	δ_o	θ	H	C_f
11 m/s	0.48 m/s	27 mm	2.6 mm	1.3	0.0038

the wall of the present facility. The results indicated that at a longitudinal distance of $x = 180$ cm from the beginning of the working section the skin friction was uniform to within a 5 percent variation over 80 percent of the wind tunnel span. At $x = 500$ cm the skin friction was uniform to within a 2.5 percent variation over 60 percent of the tunnel span. Although we were primarily interested in the analysis of the large-scale low frequency unsteadiness associated with the flow separation, considerable attention has been given to the spatial and temporal resolution of the transducers in the viscous subrange. Their sensing area was circular with a 0.71 mm diameter corresponding to 22 viscous length scales v/u_τ where u_τ is the friction velocity $u_\tau = \sqrt{(\tau_\omega/\rho)}$. Estimates of this length scale were obtained by measuring the skin friction of the incident boundary layer in the absence of the cylinder. It was felt that this arrangement provided a measurement of a typical viscous length in the flow under investigation. The present case includes large portions of separated flows where by definition skin friction is zero, and therefore this kind of scaling fails. Simpson (1981) found that the spanwise wave length of the flow structures in the viscous sublayer of the wall flow, as measured by the viscous scale v/u_τ, is one order of magnitude larger than upstream of the detachment. This indicates that the spatial resolution of the pressure transducers is improved downstream of separation. A typical viscous frequency scale u^2_τ/v of the flow is 14 kHz, a value which is well below the frequency response of the transducers. The results include measurements of the mean and fluctuating wall pressure as well as spectral analysis of the time dependent pressure. Signal conditioning for the analog output of the Kulite transducers was provided by two EG&G model 113 low noise differential amplifiers and a KRON-HITE filter model 3323. The transducers were calibrated frequently in the calibrator model supplied by Thermo-Systems Inc. No blockage correction has been applied to any of the mean or fluctuating pressure data reported here.

Pressure transducers of high frequency response are known to respond to acoustic noise and vibrations as well as pressure fluctuations. In addition, electronic noise may also contaminate the signal. To minimize these effects several measures have been taken. First, almost all instruments were powered by batteries and not by line power with transformers. Second, the model assembly, including the turn-table, was supported externally so that no vibration from the tunnel wall could be transmitted onto the table. Third, the cylinder itself was rather large which helped to avoid vibrations due to vortex shedding. Fourth, as was mentioned earlier the wall of the fan/motor section of the wind tunnel was porous to damp acoustic noise. Despite all these precautions the r.m.s. of the noise level was 2 Pa which corresponds to approximately 2.5 percent of the dynamic pressure of the incoming flow $1/2\rho U_0^2$. The r.m.s. level of the pressure fluctuations of the incoming two-dimensional boundary layer measured far upstream or in the absence of the cylinder is 5 percent of $1/2\rho U_0^2$. This suggests a 2:1 signal to noise ratio at these locations. The signal to noise ratio was increased to 3:1 by recording the a.c. component of the signal only. The cut-off frequency of the high-pass filter was set at 0.01 Hz. Similar values of signal to noise ratio are reported by Johnansson et al. (1987). It should be emphasized that the signal to noise ratio in the separated zone of the flow was 20:1 and therefore it can be safely concluded that noise is practically absent in these experimental data. However in some occasions narrow band spikes were observed in the power spectral densities (p.s.d.) of the signals which were centered at frequencies which were multiples of 60 Hz. These spikes were a result of interference of the Thyristor control of the wind tunnel motor and sometimes could not be eliminated or controlled. Figure 3 depicts a case where this kind of electronic interference is present in the data. The figure shows the p.s.d. of the pressure fluctuations computed through Fast Fourier Transforms (FFT) of the digitized data. They were obtained in the upstream boundary layer and inside the separated zone of the three-dimensional boundary layer at $r/D = 0.74$, at the plane of symmetry. For comparison the noise level, obtained under zero flow velocity, is also recorded. A spectral peak detection technique was developed to detect the spikes in the p.s.d. over different ranges of frequencies in each data record of 2^{13} words length. A notch filter algorithm was used to cut-off the sharp spike and restore a value which was equal to the value of the p.s.d. just outside the frequency window used. The latter spanned one or two digital points about the center frequency. The original pressure signal was restored after an inverse FFT of the data record was performed. Typical p.s.d. of filtered signals are shown in Fig. 4, corresponding to those in Fig. 3 and plotted in terms of the inner wall variables of the upstream boundary layer. The data of Willmarth and Wooldridge (1962), Hasan et al. (1986), Devenport et al. (1990), and Haritonidis et al. (1988) are also plotted for comparison. These boundary layer data have been obtained in different facilities under different conditions and pressure transducer sizes. Table B shows the flow parameters and the size of transducers used in these experiments. Microphones were used in all cases. As can be seen from Fig. 4, the present processed data agree fairly well

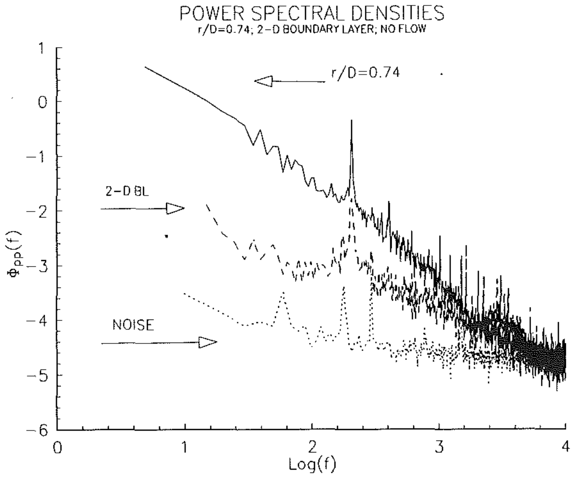

Fig. 3 Power spectral densities

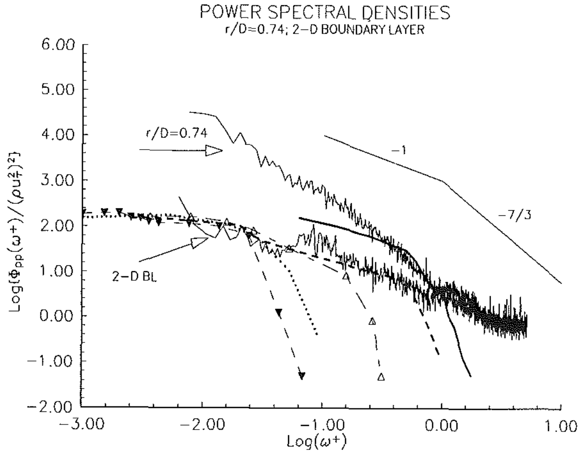

Fig. 4 Power spectral densities: Symbols: ······, Hasan et al. (1986); ···▲··, Willmarth and Wooldridge (1962); -----, Devenport et al. (1990); —, Haritonidis et al. (1988); — present two-dimensional boundary layer and $r/D = 0.74$ data; ▼ present low pass filtered data.

Table B Reynolds numbers of flows and spatial resolution of pressure tranducers used

Investigation:	Present	Willmarth and Wooldridge (1962)	Hasan et al. (1986)	Devenport et al. (1990)	Haritonidis et al. (1988)
Re_θ	1840	29000	3389	7590	4340
d^+ (Transducer size)	21	410	505	33 (estimated)	19

with the results of the above mentioned investigations bearing in mind the uncertainties involved, such as background noise and inadequate spacial resolution in all data. The same figure also shows the f^{-1} and $f^{-7/3}$ variations normally expected in boundary layer flows. The present results suggest a narrow region of $\omega^{-7/3}$ variation for $0.5 < \omega^+ < 0.8$ as measured by Schewe (1983) and a wider range of ω^{-1} for $0.12 < \omega^+ < 0.5$ as suggested by Bradshaw (1967) and Kim (1989). Kim, in his direct numerical simulation of fully developed channel flow also found a broad peak at $\omega^+ = 0.11$ in the p.s.d. of pressure fluctuations, a value which is close to the bursting frequency of $\omega_b^+ = 0.07$ reported by Luchik and Tiederman (1987). Both values fall inside the range of $0.06 < \omega^+ < 0.125$ of the present data where a broader peak in p.s.d. occurs. The fastest decaying region of the p.s.d. (roll-off region) is quite different in each set of the data presented in Fig. 4. This behavior is a consequence of the limited spatial resolution of the pressure transducers used, which is defined by their non-dimensional size as shown in Table B.

Another set of low-pass filtered data, obtained in the range of d.c. to 60 Hz, is also plotted in Fig. 4. The low-pass cutoff frequency of 60 Hz was selected electronically on the analog filters. In this, rather narrow frequency range, which was wide enough to include the Strouhal frequency and its harmonics, no spikes due to electronic interference were observed in the p.s.d. These measurements also agree with the rest of the data shown in Fig. 4.

The agreement of the present data with previous measurements and results provides confidence in the techniques applied and probes used in this investigation and improves credibility on the results obtained in the separated boundary layer.

The uncertainties of the measurements in the present investigation, have been estimated, using the method of Kline and McClintock (1953) and Moffat (1985), as 3 percent for the mean pressure measurements and 12 percent for the pressure fluctuation measurements.

3 Results and Discussion

Figures 5(*a*) and 5(*b*) show the surface-oil visualization for Reynolds numbers of 2.2×10^5 and 1.0×10^5, respectively. The direction of the oil streaks represents the direction of the mean wall shear stress while an indication of shear stress magnitude can be obtained from the amount of oil (white color) deposited on the streaks, this being greater at low shear regions. Thus dark areas are characterized by high shear and may be associated with flow reattachment while light areas indicate low shear stress regions which are closely related to the flow separation. The most distinctive feature of the present visualization is a parabolic like line which wraps around the cylinder. This line represents an imprint of the horse-shoe vortex formed by reorientation of the vorticity of the incoming boundary layer which is strongly decelerated as it approaches the cylinder. The vorticity of the incoming boundary layer is $\omega_z \simeq -\partial U/\partial y$ which is of the order of U_0/δ_0 where δ_0 is the boundary layer thickness. Therefore it is expected that the vorticity of the incoming boundary layer in the case of $Re = 2.2 \times 10^5$ is roughly 2.5 times higher than the vorticity of the boundary layer in the case of $Re = 10^5$ if we assume that $\delta_0 \sim Re_x^{-1/5}$ (Reynolds number variation was obtained by changing free-stream velocity.) This vorticity is stretched in the spanwise direction by the lateral velocity gradient $\partial W/\partial z$ and at the same time is reoriented in the longitudinal direction. In addition to vorticity reorientation, longitudinal acceleration or deceleration can stretch or compress vortex lines respectively, which indicate amplification or attenuation of vorticity respectively. The upstream wall region where strong lateral divergence occurs i.e., $0 \leq \theta < 90$ deg is associated with simultaneous, longitudinal deceleration, $\partial U/\partial x$, which reduces the vorticity of the vortex. In fact in the case of the second experiment with Reynolds number of 10^5, where ω_x is weak (shown in Fig. 5(*b*)), the footprint of the vortex seems to grow substantially in size at $\theta \simeq 60$ deg indicating a sharp decrease in vorticity.

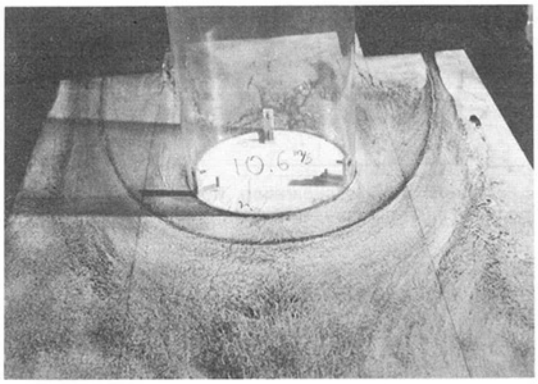

Fig. 5(*a*) Surface-oil visualization picture for $Re = 2.0 \times 10^5$

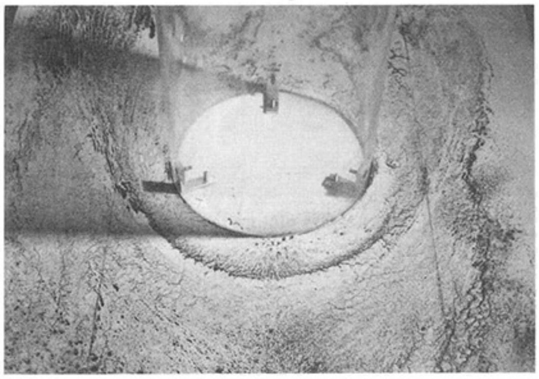

Fig. 5(*b*) Surface-oil visualization picture for $Re = 10^5$

It is also interesting to observe that the location of the vortex "footprint" is not the same at the two Reynolds numbers. At the lower Reynolds number the vortex is formed and wraps around closer to the cylinder than at the higher Reynolds number. The light area upstream of the horseshoe vortex indicates a low shear region which is associated with separation. The so-called separation line seems to be the vaguely visible line passing through the saddle point on the plane of symmetry, wrapping around the cylinder and the vortex and then merging with the footprint of the vortex. This observation is also supported by the mean and fluctuating pressure measurements which indicate that separation occurs close to the end of an adverse pressure gradient region. Figure 6 provides a schematic for the flow separation, the horse-shoe vortex and the associated mean and r.m.s wall pressure distributions. The r.m.s. pressure fluctuations which increase as separation is ap-

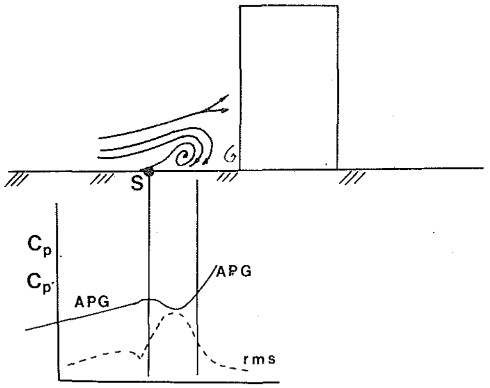

Fig. 6 Schematic of flow separation, horse-shoe vortex and corresponding mean and r.m.s. pressure distribution

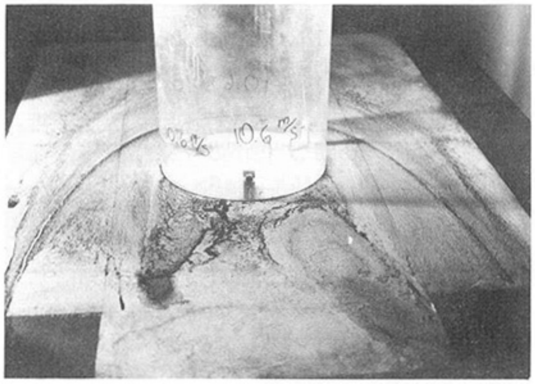

Fig. 7 Surface-oil visualization picture of the wake for Re = 2.2×10^5

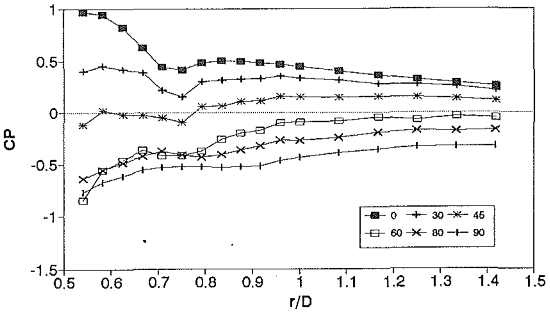

Fig. 8(*a*) Mean pressure distribution on the flat plate for 0 deg ≤ θ ≤ 90 deg

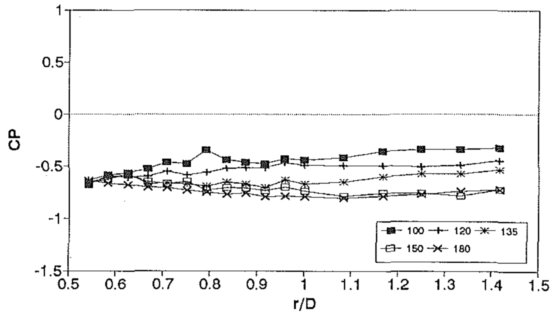

Fig. 8(*b*) Mean pressure distribution on the flat plate for 90 deg < θ ≤ 180 deg

proached, is rather small in the immediate area downstream and below the separated shear layer and reaches very high values in the area considered herein as the reattachment region. The mean separation point located at the end of the adverse pressure gradient region is in agreement with previous investigations by Devenport and Simpson (1990) and Eckerle and Langston (1987). A high r.m.s. level of pressure fluctuations has been found by Farabee and Casarella (1985) in a backward facing step flow.

The interpretation of the present data is based on the notion that the dark parabolic line shown in Fig. 5(*a*) and 5(*b*) is the footprint of the horse-shoe vortexs and not the separation line which lies 0.05 diameters further upstream. This notion is supported by the present pressure measurements and the results of Devenport and Simpson (1988, 1990) who found two distinct lines wrapping around the wing in their wing-body junction. The most upstream imprint is the separation line while the second is associated with low shear. Their LDA measurements indicated that the locus of the horse-shoe vortex is located slightly downstream and above this low shear line. Accordingly, the separation line is probably located at $r/D = 0.82$ and 0.76 upstream of the axis of the cylinder for Re = 2.2×10^5 and 1.0×10^5 respectively.

Figure 7 shows a view of the wake of the cylinder for a Reynolds number 2.2×10^5. Two imprints of large vortical structures are clearly shown in the wake of the cylinder which may be associated with the shear layers separated from the cylinder. The surface streaklines may also be considered as the limiting streamlines which are normal to the surface vortex lines. The picture also indicates a slight asymmetry in these two structures although the flow upstream of the cylinder is, as can be seen in Fig. 4(*a*), quite symmetric. Similar asymmetries have also been observed in the work by Eibeck (1990). It is also interesting that the legs of the horse-shoe vortex which are wrapped around the cylinder do not intersect the vortical imprints in the wake of the cylinder.

Mean pressure plots along various radial positions on the plate at different angles for Re = 2.2×10^5 are shown in Fig. 8(*a*) and 8(*b*). As can be seen in Fig. 8(*a*) there is no adverse pressure gradient at angles greater than 45 deg. The attenuation of the adverse pressure gradient with increasing angle θ most probably indicates that flow separation on the flat plate is confined and does not extend downstream.

The corner area, which is the region close to the cylinder, is strongly affected by the flow separation off the cylinder itself. Mean pressure measurements on the cylinder presented in the thesis by Agui (1989) indicate that separation on the present finite cylinder occurs at about 80 deg. Therefore the corner area immediately upstream and downstream of this angle is dominated by this separation and is characterized by low C_p values and moderate pressure gradients, $\partial p/\partial r$. No appreciable pressure gradients are found in the wake of the cylinder.

Flow separation and reattachment can be very unsteady processes and therefore considerable pressure fluctuations can be expected in regions associated with such phenomena. Figure 9 shows the distribution of the pressure fluctuation coefficient $C_{p'}$, which is defined as $C_{p'} = p'/1/2\rho U_0^2$, at various positions on the flat plate. Willmarth and Wooldridge (1962), Willmarth (1972) and Schewe (1980) have found that in a two dimensional boundary layer with zero pressure gradient, the r.m.s. of the local pressure fluctuations p' is 2 to 3 times greater than the local wall shear stress τ. In the present investigation $C_{p'}$ is roughly 3.5 times greater than the local skin friction coefficient $C_f = \tau_w/1/2\rho U_0^2$ at $r/D = 1.75$. This value is slightly higher than that of the previous investigations on two-dimensional boundary layers, however this is not surprising since the flow at this location is decelerating under the influence of a small adverse pressure gradient.

There are certain regions in the flow which are characterized by large r.m.s. pressure fluctuations. At 0, 30, and 45 deg angles there is a three-fold increase of r.m.s. from the level of the pressure fluctuations at the furthest upstream position.

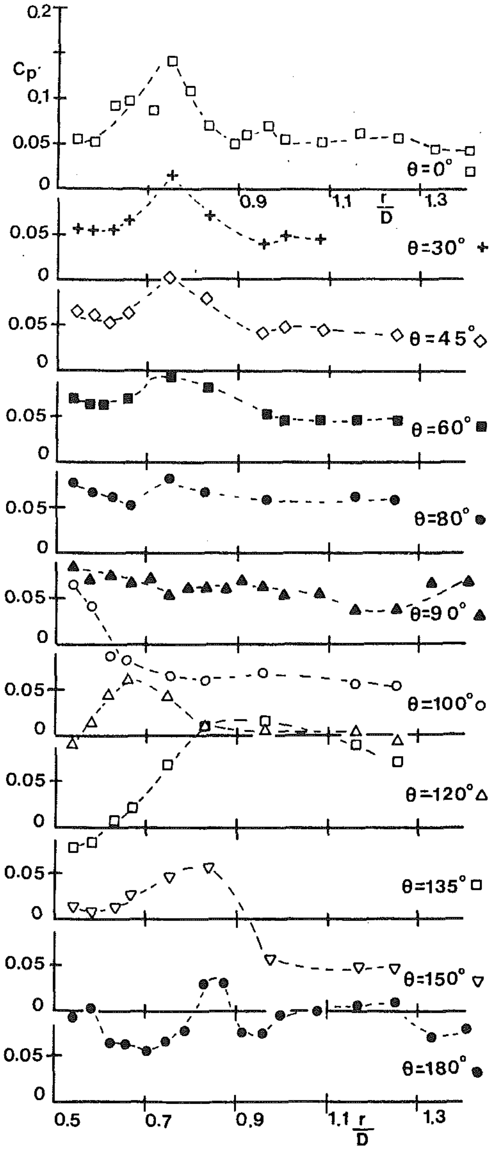

Fig. 9 Distribution of r.m.s. of pressure fluctuations for various θ

The peak values are associated with the horse-shoe vortex and upstream flow separation of the oncoming boundary layer. In fact as was stated earlier, it is the reattachment of the separated shear layers and the unsteady "wandering" of the vortex which produce large pressure fluctuations. At larger than 45 deg angles the r.m.s. values are smaller and the distribution becomes flat indicating a diminishing effect of the phenomena associated with flow separation and reattachment of the oncoming boundary layer. This is another indication that the flow separation does not wrap around the cylinder. The high r.m.s. values found in the corner and wake regions at angles greater than 90 deg are associated with shear layers separated from the cylinder. This is suggested by the fact that these peaks are located at normal distances, $r\sin\theta$, from the plane of symmetry $\theta = 0$ which are roughly equal to one radius, $D/2$, as opposed to the peaks caused by the horseshoe vortex which take place roughly at 1.3 radii from the same plane.

Figures 10(*a*) to 10(*f*) show distributions of the probability density function (p.d.f.) of pressure fluctuations at various positions upstream of the cylinder, on the plane of symmetry and in the near wake. At $r/D = 1$ (Fig. 10(*a*)) and $r/D = 0.833$ (Fig. 10(*b*)) where the nominal separation point is located, the distributions are slightly skewed, so that negative

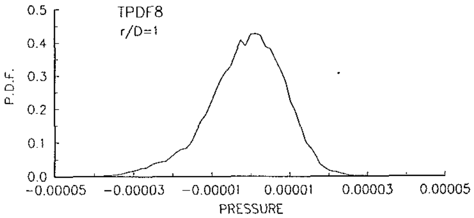

Fig. 10(*a*) Probability density function of pressure fluctuations at *r*/*D* = 1

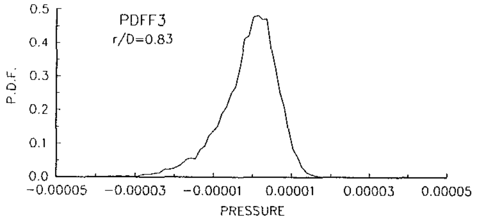

Fig. 10(*b*) Probability density function of pressure fluctuations at *r*/*D* = 0.83

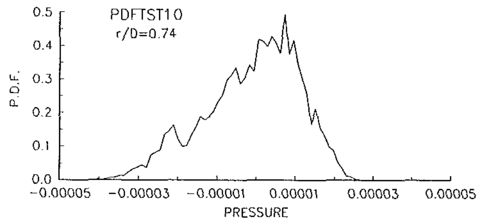

Fig. 10(*c*) Probability density function of pressure fluctuations at *r*/*D* = 0.74

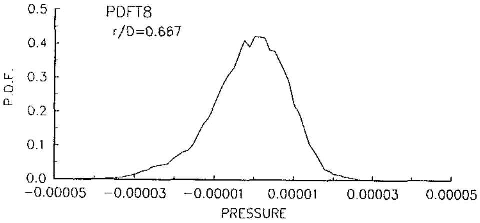

Fig. 10(*d*) Probability density function of pressure fluctuations at *r*/*D* = 0.667

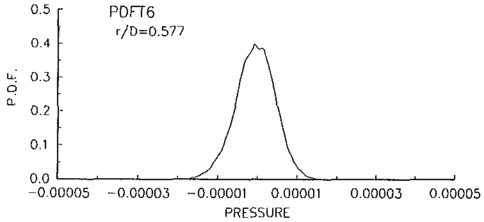

Fig. 10(*e*) Probability density function of pressure fluctuations at *r*/*D* = 0.577

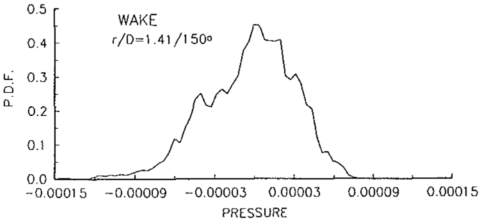

Fig. 10(*f*) Probability density function of pressure fluctuations at *r*/*D* = 1.41 and θ = 150 deg

pressure fluctuations have higher probability of appearance, while at $r/D = 0.74$ (Fig. 10(*c*)), the position of maximum r.m.s., a bimodal distribution is present. A bimodal distribution is also evident in the wake of the cylinder (Fig. 10(*f*)). A bimodal p.d.f. indicates that a highly intermittent, or periodic phenomenon is present in the flow. It should be noted that the p.d.f. of a sinusoidal wave is strongly bimodal with high values around the edges of the distribution. The present flow is probably dominated by two phenomena: the unsteady boundary layer separation off the flat plate and the quasi-regular vortex shedding due to boundary layer separation off the cylinder. Their signatures are expected to be present upstream as well as downstream of the cylinder. The p.d.f. of data low passed filtered at 60 Hz and measured at $r/D = 1.41$ and $\theta = 0$ deg are shown in Fig. 11 where a strongly bimodal distribution is present. A closer examination of the p.s.d. of these data, shown in Fig. 12, suggests a peak at 4.88 Hz, a frequency corresponding to vortex shedding off the cylinder with a Strouhal number $\mathrm{St} = 0.135$. This value has been also obtained in measurements of unsteady pressure in the wake and on the surface of the cylinder. Since there are no convective phenomena propagating in the direction upstream from the cylinder and no vibrations of the model, a possible explanation is that the vortices shed off the cylinder induce an unsteady pressure field which modulates the flow upstream. Greco (1990) and Fitzgerald, Greco and Smith (1991) in a similar experiment with laminar and transitional boundary layer flows have also found a similar phenomenon. Convective phenomena with feedback are present in the separation/recirculation region upstream of the cylinder. However, unsteady separation never reaches the $r/D = 1.417$ location.

The unsteadiness due to the boundary layer separation off the flat plate alone could be also causing bimodal distributions of the p.d.f. In the wing/body experiment of Devenport and Simpson (1988) p.d.f.'s of velocity fluctuations were also bimodal. In fact, for their case there was no vortex-shedding off the wing and therefore this feature was linked to an interaction of low velocity near wall flow coming from upstream and high velocity reverse flow. This intermittent process is part of the unsteady separation phenomenon and it is not clear how it is related to the large-scale structures and the bursting-sweep phenomenon. Simpson (1981) assumes that the bursting frequency, nondimensionalized by outer variables, U_0 and δ_0, should remain constant in flows approaching separation under an adverse pressure gradient. This suggests that the frequency of these events is rather small since the velocity decreases and the boundary layer thickness increases. Power spectra at locations close to separation indicate several peaks. However it is rather difficult to attribute these peaks to separation on the flat plate since higher harmonics of the shedding frequency may also be present. In addition, at positions closer to the cylinder the velocity is reduced while the thickness of the wall flow is increased, and therefore the frequency will be decreased. This results in a broadening of the spectra which makes it difficult to identify any distinct frequency of large scale unsteadiness in this region. Broadening in the lower frequency domain masks even the shedding frequency. A better picture of the events associated with the boundary layer upstream of the cylinder can be obtained by looking at the integral time scale.

$$T_{pp} = \int_0^{\tau_1} R_{pp}(\tau)\,d\tau$$

where R_{pp} is the autocorrelation function. This quantity indicates a typical time sale of the large scale structures. The point where the autocorrelation crosses zero for the first time is the upper limit of the integration τ_1. Figure 13 shows the variation of this time-scale along the plane of symmetry. The results have been nondimensionalized by the cylinder diameter D and free stream undisturbed velocity U_0. The boundary layer thickness δ_0 in the absence of the cylinder was found to be $\delta_0 \simeq 0.088D$. It has been established that the bursting period of a two-dimensional boundary layer over a flat plate when scaled with δ_0 and U_0 is of the order of $T_B U_o/\delta_0 \simeq 3.0$. It has been speculated in the past by Kim, Kline and Reynolds (1971) that a strong relation exists between the large-scale structures and the burst-sweep mechanism, i.e. for a large scale structure there is only one cycle of the bursting phenomenon. Kim and Moin (1986), Spalart (1988) and Robinson (1990) have verified this observation for the case of low Reynolds number channel flow and two-dimensional boundary layer by numerically solving the full Navier-Stokes equations. It has been also found in flows relaxing after reattachment (Kiya and Sasaki, 1985). The data in Fig. 13 indicate a gradual increase in time scales from the furthest upstream location to almost the end of separation

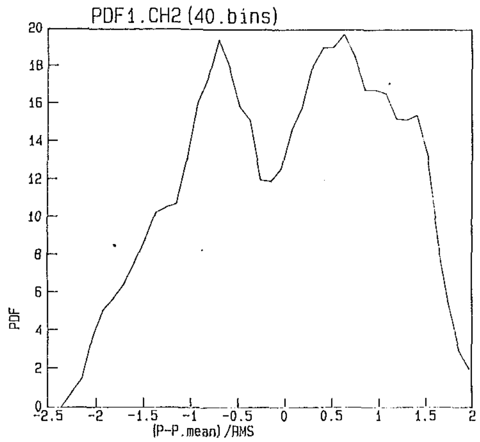

Fig. 11 Probability density function of low-pass filtered pressure fluctuations at $r/D = 1.41$ and $\theta = 0$ deg

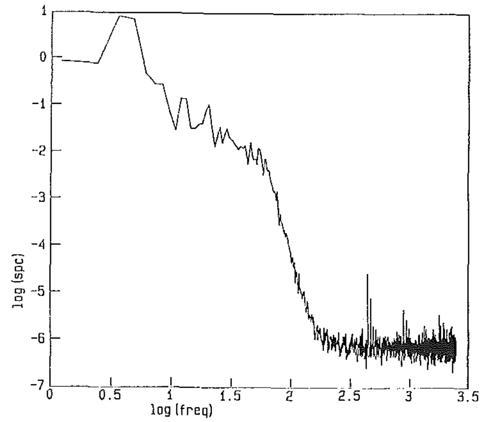

Fig. 12 Power spectral densities of low-pass filtered pressure fluctuations at $r/D = 1.41$ and $\theta = 0$ deg

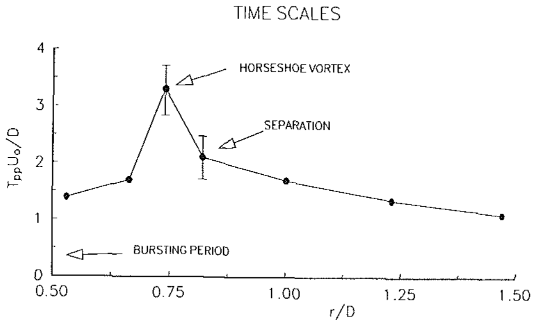

Fig. 13 Integral time-scales along $\theta = 0$ deg

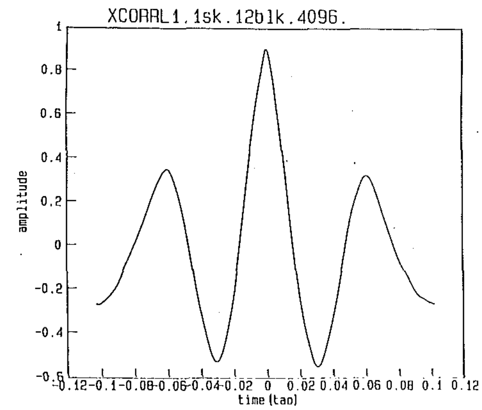

Fig. 14(*a*) **Cross-correlation coefficient of pressure fluctuations; $r_1 = 1.41D$, $r_2 = 1.33D$ ($\theta = 0$ deg)**

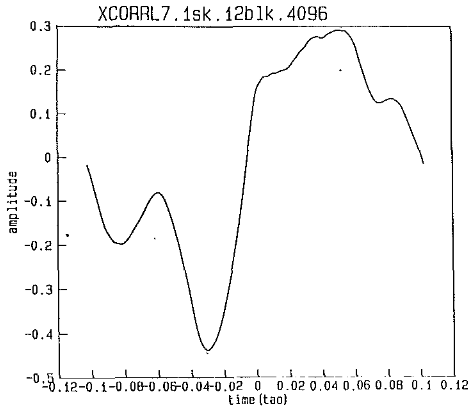

Fig. 14(*c*) **Cross-correlation coefficient of pressure fluctuations; $r_1 = 0.708D$, $r_2 = 0.666D$ ($\theta = 0$ deg)**

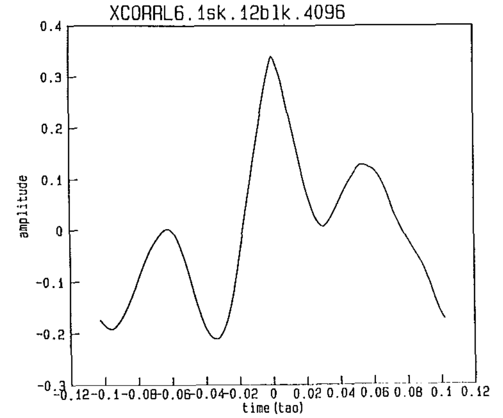

Fig. 14(*b*) **Cross-correlation coefficient of pressure fluctuations; $r_1 = 0.792D$, $r_2 = 0.74D$ ($\theta = 0$ deg)**

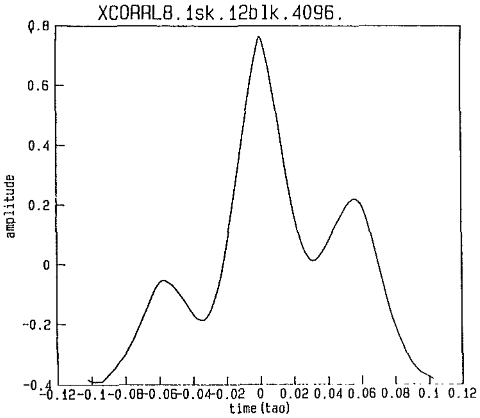

Fig. 14(*d*) **Cross-correlation coefficient of pressure fluctuations; $r_1 = 0.625D$, $r_2 = 0.583D$ ($\theta = 0$ deg)**

followed by a sudden three fold overshoot. This may be a result of pairing of large structures to form a vortex, rather than a slow increase in scales without any interaction among the large structures. This hypothesis is also supported by the reduction in cross correlation which is observed between stations upstream and at $r/D = 0.74$. Figure 14(*a*) shows the space-time correlations coefficients R_{pp} (r_1, r_2, τ) between two points at $r_1 = 1.417D$ and $r_2 = 1.333D$ at $\theta = 0$ deg. Figure 14(*b*) shows the same coefficient R_{pp} between two points $r_1 = 0.792D$ and $r_2 = 0.74D$ well inside the separated zone and under the horse-shoe vortex. In the first case the correlation coefficient has a maximum value close to 0.9 at almost zero time delay, τ, while the same coefficients drops to 0.35 in the second case of Fig. 14(*b*). The loss correlation indicates that a kind of merging among large scale structures is taking place. Similar behavior of R_{pp} (r_1, r_2, τ) is observed immediately downstream at $r_1 = 0.708D$ and $r_2 = 0.667D$ (see Fig. 14(*c*)) while higher values of correlation are found further downstream at $r_1/D = 0.62$ and $r_2/D = 0.583$ (Fig. 14(*d*)). In addition, the p.s.d. at $r/d = 0.74$, shown in Fig. 4 as well as the wing-body results of Hasan et al. (1986), clearly demonstrate that the low frequency range is dynamically more important than the high frequency range of the spectral content of the fluctuating pressure field. This is because the amplitude of the fluctuations is increased substantially more in the low frequency range over that of the undisturbed two-dimensional boundary layer values. This evidence and the loss of cross-correlation suggests that the large scale structures play a very important role in the dynamics of the separated flow and a significant mutual interaction takes place among them which results in scales considerably larger than those of the incoming flow.

4 Instantaneous Flow Structure

Honkan (1991), in a yet unpublished work, carried out flow visualization experiments in the present setup using a laser sheet to illuminate the flow structures. Smoke was introduced into the boundary layer through a small slit located on the wall beneath the flow at $r/D = 4$, $\theta = 0$ deg. The small underpressure inside the tunnel was adequate to drive the smoke into the tunnel without disturbing the flow. The smoke, which entered the boundary flow and marked the large scale structures, never extended into the free stream. A CCD Hi8 video camera was used to record the images with a rate of 30 frames/s. Figure 15 shows an image-processed picture of the flow structures on the plane of symmetry $\theta = 0$ deg, upstream of the cylinder at $\mathrm{Re} = 2.2 \times 10^5$. A primary vortex is undoubtedly evident in the picture, together with four different large scale structures marked by arrows and shown at various stages of the interaction with the vortex. This picture is also indicative of the evolution of a typical large scale structure before and after the interaction. The evolution of these structures, however, has been obtained from a sequence of video frames, rather than from still pictures and can be summarized as follows: The large scale structures, as they approach the separation point, are considerably stretched because the part nearest the wall is substantially decelerated while the outer part continues to be convected downstream with, practically, unchanged velocity. The sudden deceleration in the near wall region allows the

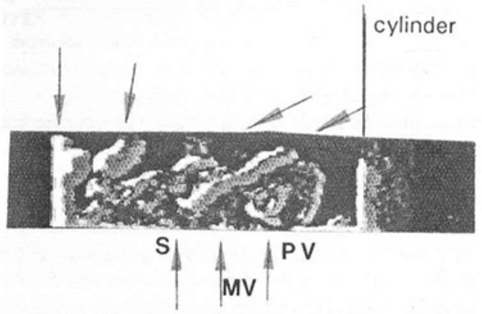

Fig. 15 Image-processed picture of the flow on the plane of symmetry upstream of the cylinder at Re = 2.2 × 10^5

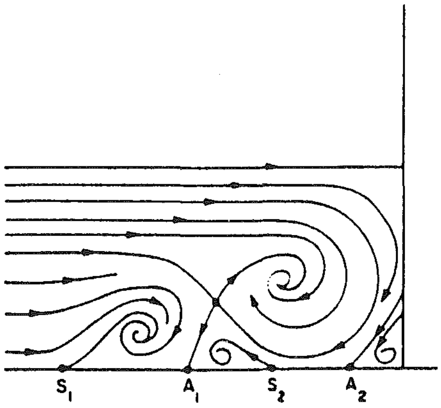

Fig. 16 Mean flow structure proposed by Hunt et al. (1978) and Baker (1980)

structures to interact and possibly undergo a merging of their lower parts before separation occurs. Figure 15 clearly shows three structures with their lower parts amalgamated. This seems to explain the increase of the integral time scales inferred from the pressure fluctuation measurements in this region. At the same time the structure tilts towards the wall because the faster moving outer part starts to merge with the vortex and subsequently is integrated into the primary vortex. Although the primary vortex seems to dominate the flow structure in this region, it also appears that the role of the large scale structure is not passive. They interact strongly with the vortex and they force the latter to "wander" in space, mostly in the longitudinal direction, with an amplitude of the order of δ_0. Several large scale structures were observed inside the vortex as a result of the mutual interaction. Figure 15 shows at least three of them at various positions inside the vortex. It seems, therefore, plausible to assume that the flow in this region consists of several large scale structures which form a new structure, the primary vortex. This scenario is also in agreement with the quantitative measurements shown in Fig. 13, which indicated large values of the integral time scales at the position of the vortex.

There is considerable disagreement in the literature regarding the structure of the vortex system. Falco (1982), for instance, showed that a mushroom vortex is the typical time-dependent structure, while Hunt et al. (1978) and Baker (1980) postulated a four vortex system to be typical of the time-average structure (see Fig. 16) and Pierce and Tree (1990) measured a two-vortex system in a wing-body configuration. Eckerle and Awad (1991) claim that there is no vortex formed on the plane of symmetry at high Reynolds numbers but only a reversed flow going outward, off the plane. This conclusion was based on the fact that the measured V-component of the mean velocity vector was very small at this plane. Along these lines, Honkan's work has provided some new information on the structure of the vortex system which may explain the discrepancies among previous experiments. In this work the term vortex is used to describe a rotational motion of smoke persistent over at least three frames. The major findings of his work can be summarized below:

1. A well defined primary vortex exists on the plane of symmetry, which is present in all recorded frames and at all Reynolds numbers investigated. The fact that the vortex is not evident in the mean velocity measurements of Eckerle and Awad is most probably due to the substantial "wandering" of the vortex. An oscillatory motion of the vortex in the longitudinal direction with an amplitude of one δ is enough to wash out completely the V-component of the mean velocity and therefore to cause the mean streamlines to be parallel to the wall. This argument is also supported by the fact that the measurements of V-component fluctuations, as they are presented in Eckerle and Awad, indicate an r.m.s. level of the order $0.2U_0$ to $0.4U_0$ in this region. This suggests instantaneous excursions of the V-component of the order of $\pm 0.6U_0$ to $\pm 1.2U_0$ if a range of three r.m.s. is assumed. These high values clearly indicate a very large unsteadiness of the vortex.

2. Strong eruption of wall fluid away from the wall was observed upstream of the primary vortex. This led to the formation of either a counter rotating vortex or mushroom vortex. A mushroom vortex is shown in Fig. 15. These vortices were smaller in size than the primary vortex and were never stationary in space. They were moving upwards before they interacted with an oncoming large scale structure or amalgamated with the primary vortex. They were difficult to identify and subsequently trace them because of their small size or because they moved off the plane of observation. They were observed in many frames of the video film but certainly not in all frames. It is rather difficult, if not impossible, to depict them through mean velocity measurements because of their continuous uplift motion and because of their short appearance.

3. A secondary vortex, upstream of the previously mentioned vortices, with clockwise rotation was also occasionally observed.

4. The wall junction vortex, right at the corner, was never observed. Figure 17(*a*) shows an unprocessed image of a flow visualization picture obtained at Re = 2.2×10^4. The lower part of the picture is the reflected image of the flow on the plexiglass. A mushroom vortex appears as a result of an eruption of wall fluid with strong vorticity in the reverse flow region below the center of the primary vortex. The right part of the mushroom vortex with the clockwise rotation seems to be located inside the primary vortex which existed before the formation of the mushroom vortex. The vortex is completely lifted off the wall in the next frame shown in Fig. 17(*b*). This type of mushroom vortex was observed sometimes in the present investigation but not always. Therefore they can not be considered as the prevailing structure of the vortex system at this Reynolds number. Similar observations were made with the single counter-rotating vortex which is also a result of the strong eruption of wall fluid. It seems that the type of vortex formed depends on the strength of the reverse flow below the primary vortex center and the type of vorticity generated on the wall. If the reverse flow region has a velocity distribution similar to a wall-jet i.e., with two inflectional points, then a mushroom vortex should be expected. If a monotonic velocity profile prevails in the region then a single counter-rotating vortex maybe formed. The position of the center of the primary vortex and the amount of carried vorticity seems to dominate the strength of the reverse flow. If the center is located near the wall then the reverse flow is quite strong and mushroom vortices may be formed. If the center is further above the wall then a single counter-rotating vortex may be formed. This mechanism seems to account for the type of vorticity present but is rather incomplete as far as the description of their evolution.

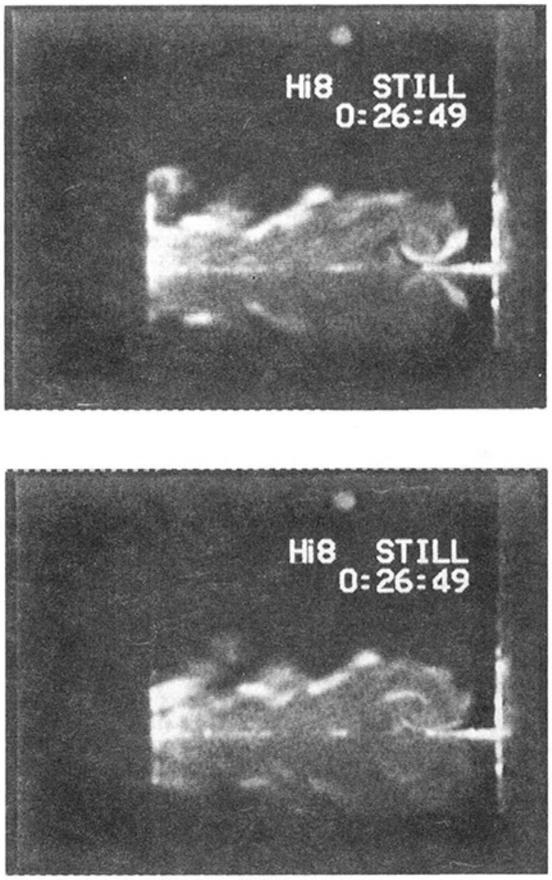

Fig. 17(*a*) and 17(*b*) Sequential frames of unprocessed images of the flow on the plane of symmetry, upstream of the cylinder at Re = 2.2 × 10^4

5 Concluding Remarks

Most of the previous work on three dimensional turbulent boundary layers formed by intersection with a wall mounted protrusion has been restricted to time-average measurements of wall pressure or velocity inside the upstream flow field. In the past, a significant amount of work has been carried out by many researchers in an effort to identify the flow structure inside the vortex system, either through flow visualization or through mean velocity measurements. The results have been rather contradictory. The present work has focussed on the instantaneous structure of the flow which has been inferred from flow visualization data obtained by using a laser sheet to illuminate the flow and single point or two-point measurements of wall pressure fluctuations obtained by high frequency pressure transducers. The results indicate that this structure is very complex and significantly different from the time average structure. The latter is expected to be described by the two vortex model found in the case of wing/body geometries by Pierce and Tree (1990). However, one should be very cautious in extrapolating or generalizing conclusions, based on time-average information, into time-dependent structure and vice-versa.

The present flow visualization studies indicate that there is always a primary vortex present in the flow which induces an eruption of wall fluid away from the wall. Very often, this eruption results in the formation of counter rotating or mushroom type of vortices. One major characteristic of the primary vortex is its quasi-periodic unsteadiness and "wandering" in space with an amplitude of order one boundary layer thickness. This motion seems to be coupled with the arrival or acquisition rate of the large scale structures of the incoming boundary layer by the primary vortex. The role of the large scale structures in the dynamics of this motion requires further investigation.

A secondary vortex upstream of the other vortices has been observed occasionally to exist. This vortex, as well as the vortices formed by the fast eruption of wall fluid, are very quickly evolving in time and space making it impossible to depict through time-average measurements.

Point measurements in the present investigation have indicated that the r.m.s. pressure fluctuations increase from the upstream level as separation is approached and reaches a maximum at reattachment. Farabee and Casarella (1985) have also found high values of r.m.s. pressure fluctuations in the reattachment region of a back and forward facing step flow. The present measurements of mean and fluctuating pressure suggest that the flow separation on the flat plate is confined and does not extend downstream, consequently it does not wrap around the cylinder. The high r.m.s. level at the separation region indicates that separation is associated with considerable unsteadiness. Cross-correlation measurements indicate a loss of correlation in this area. Bimodal histograms and power spectra indicated the existence of quasi-periodicity in the wake which is closely associated with shedding of large scale structures from the cylinder. The area marked by these vortices is characterized by an eight-fold increase in the r.m.s. values of pressure fluctuations above the upstream level. It is not clear yet whether this increase is due to a simple passage of the structure above the measuring location or is due to reattachment of the shear layer which separated from the cylinder perhaps accompanied by a strong flapping in the spanwise direction. Nowhere else on the cylinder are such large r.m.s. levels present. The fact that these structures travel downstream and that the area with high r.m.s. is localized indicates that shear layer flapping and/or reattachment is the most likely cause of these high fluctuating pressure levels.

The frequency of the vortex shedding off the cylinder corresponds to a Strouhal number St = 0.135 ± 0.016. The classical diagram of Strouhal number variation with Reynolds number for two dimensional cylinders (see Massey, 1983) indicates a Strouhal number of 0.2 for the present Reynolds number which falls into the so-called supercritical regime where the vortex Kármán street is rather irregular. However the present lower value of St is attributed to the low aspect ratio of the present finite cylinder ($L/D = 2$) and to the presence of the flat plate/wall (see Zdravkovich et al., 1989; Williamson, 1989). Both effects may result in irregularities in vortex shedding.

The behavior of time scale shown in Fig.13 suggests a considerable increase of T_{pp} in the area upstream of the horseshoe vortex/separation location followed by a sudden increase in the location of the vortex. Decreased time scales are observed subsequently in the region between the cylinder and the vortex.The upstream increase of T_{pp} indicates a growth of the large eddies in the longitudinal direction. This growth is a net growth because the flow is deviated in the spanwise direction which tends to reduce the longitudinal scale. However the sudden increase of T_{pp} in the location of the vortex cannot be explained by a gradual change of scales. Therefore pairing of the large-scale structures may be responsible for this behavior. In fact, instantaneous flow visualization has shown that the primary vortex consists of three to four large scale structures which originate in the boundary layer and which merge with the primary vortex. At the location of the vortex and the downstream region, fluid is swept sideways due to lateral stretching and therefore time-scales fall abruptly in front of the cylinder. The flow visualization indicated that the horseshoe vortex is not directly affecting the near wake of the flow. However if there is any connection between the horse-shoe vortex and the vortices shed off the cylinder, the time-scale of the latter which, if non-dimensionalized by U_0 and D, is 1/St, should be in close relation with the time-scale T_{pp} of the former.

Our measurements indicate that the ratio between the two scales, at maximum, is

$$\frac{T_{pp}}{1/\mathrm{St}} \simeq 2.25$$

This most probably suggests that the two vortical systems are uncorrelated.

JFE Data Bank Contributions

The data presented in the figures of this paper have been edited and deposited on the JFE data bank for future use by any of the readers. The data include mean and r.m.s. fluctuation of pressure, probability density functions and spectral analysis of pressure. In addition to the statistical averages instantaneous raw data are also included in the bank, so that the reader can apply his/her own data analysis. The files also include appropriate instructions on the data format. To access the file for this paper, see instructions on p. 705 of this issue.

Acknowledgment

We would like to acknowledge Mr. Anant Honkan's help with the Masscomp 5500 Data Acquisition computer system and the support provided by O.N.R. under grant #N00014-89-J-1289 monitored by Dr. S. Ramberg.

References

Agui, J. H., 1989, "A Study of the Wall Pressure Fluctuations in Turbulent Three-Dimensional Layer Around a Cylinder and Plate Model," Master's thesis Dissertation, Department of Mechanical Engineering, City College of New York.

Agui, J. H., Andreopoulos, J., 1990, "Boundary Layer/Wake Interaction in a Flow Around a Cylinder and Flat Plate," ASME FED Meeting Toronto.

Baker, C. J., 1980, "The Laminar Horseshoe Vortex," *J. Fluid Mechanics*, Vol. 95, No. 2, p. 347.

Bradshaw, P., 1967, "Inactive Motion and Pressure Fluctuations in Turbulent Boundary Layers," *J. Fluid Mech.*, Vol. 30, p. 241.

Boyle, M. T., and Langston, L. S., 1989, "Asymmetrical Boundary Layer Separation at the Base of a Two Cylinder Geometry." ASME JOURNAL OF FLUIDS ENGINEERING, Vol. 111, p. 443.

Chung, K., and Lu, F., 1990, "Shock-Tube Calibration of a Fast-Response Pressure Transducer" AIAA 16th Aerodynamic Ground Testing Conference, Seattle WA, paper #90-1399.

Dechow, R., 1977, "Mittlere Geschwindigkeit und Reynoldssher Spannungstensor in der Dreidimensionalen Turbulenten Wandgrenzschicht vor einem Stehenden Zylinder," Ph.D. dissertation, University of Karlsruhe.

Devenport, W. J., Agarwal, N. K., Dewitz, M. B., Simpson, R. L., and Poddar, K., 1990, "Effects of a Fillet on the Flow Past a Wing-Body Junction," *AIAA Journal*, Vol. 287, p. 2017.

Devenport, W. J., and Simpson, R. L., 1988, "LDV Measurements in the Flow Past a Wing-Body Junction," *4th International Symposium on Applications of LDA to Fluid Mechanics*, Lisbon, Portugal.

Devenport, W. J., and Simpson, R. L., 1990, "Time-dependent and Time-averaged Turbulence Structure Near the Nose of a Wing-Body Junction," *J. Fluid Mech.*, Vol. 210, pp. 23–55.

Devenport, W. J., and Simpson, R. L., 1986, "Some Time-dependent Features of Turbulent Appendage-Body Junction Flows," *16th Symposium on Naval Hydrodynamics*, July 14–18, Berkeley CA, W. C. Webster, Academic Press, pp. 312–335.

Dinkenlacker, A., Hessel, M., Meir, G. E. A., and Schewe, G., 1977, "Investigation of Pressure Fluctuations Beneath a Turbulent Boundary Layer by Means of an Optical Method," *Phys. of Fluids*, Vol. 20, p. 216.

Eibeck, P. A., 1990, "An Experimental Study of the Flow Downstream of a Circular and Tapered Cylinder," ASME JOURNAL OF FLUIDS ENGINEERING, Vol. 112, p. 393.

Eckerle, W. A., and Awad, J. K., 1991, "Effect of Free Stream Velocity on the Three-Dimensional Separated Flow Region in Front of a Cylinder," ASME JOURNAL OF FLUIDS ENGINEERING, Vol. 113, p. 37.

Eckerle, W. A., and Langston, L. S., 1987, "Horseshoe Vortex Formation Around a Cylinder," ASME *Journal of Turbomachinery*, Vol. 110, p. 278.

Falco, R., 1982, *Album of Fluid Motion*, by Van Dyke, M., Parabolic Press, Stanford, Calif.

Farabee, T. M., and Casarella, M. J., 1985, "Measurements of Fluctuating Wall Pressure for Separated/Reattached Boundary Layer Flows," ASME, NAC-1, pp. 17–25.

Fitzgerald, J. P., Greco, J. G., and Smith, C. R., 1991, "Cylinder Junction Vortex Dynamics," Video Film, Department of Mechanical Engineering, Lehigh University.

Greco, J. G., 1990, "The Flow Structure in the Vicinity of Cylinder-Flat Plate Junction: Flow Regimes, Periodicity, and Vortex Interactions," MSc Thesis, Department of Mechanical Engineering, Lehigh University.

Johansson, A. V., Her, J-Y., and Haritonidis, J. H., 1987, "On the Generation of High-Amplitude Wall Pressure Peaks in Turbulent Boundary Layers and Spots," *J. Fluid Mech.*, Vol. 175, pp. 119-142.

Haritonidis, J. H., Grescko, L. S., and Breuer K. S., 1988, "Wall Pressure Peaks and Spectra," Zoran Zarič Memorial Conference, Ed Kline and Afgan, Hemisphere Publishing Corp., p. 397.

Hasan, M.A.Z., Casarella, M. J., and Rood, E. D., 1986, "An Experimental Study of the Wall Pressure Field Around a Wing-Body Junction," ASME *Journal of Vibrations, Acoustics, Stress and Reliability in Design*, Vol. 108, p. 308.

Honkan, A., 1991, Private Communication.

Honkan, A., and Andreopoulos, J., 1990, "Experiments in a Shock-Wave/Homogeneous Turbulence Interaction," 21st Fluid Dynamics, Plasmadynamics and Lasers Conference, Seattle, WA, paper #90-1647.

Hunt, J. C., Abell, C. J., Peterka, J. A., and Woo, H., 1978, "Kinematical Studies of the Flows Around Free and Surface-Mounted Obstacles; Applying Topology to Flow Visualization," *J. Fluid Mech.*, Vol. 86, No. 1, p. 179.

Kim, J., 1989, "On the Structure of Pressure Fluctuations in Simulated Turbulent Channel Flows," *J. Fluid Mech.*, Vol. 205, p. 421.

Kim, K. T., Kline, S. J., and Reynolds, W. C., 1971, "The Production of Turbulence Near a Smooth Wall in a Turbulent Boundary Layer," *Journal of Fluid Mechanics*, Vol. 50, p. 133.

Kim, J., and Moin, P., 1986, "The Structure of the Vorticity Field in Turbulent Channel Flow Part 2. Study of Ensemble-Average Fields," *Journal of Fluid Mechanics*, Vol. 162, p. 339.

Kiya, M., and Sasaki, K., 1985, "Turbulent Structure and Unsteadiness in a Separation-Reattachment Flow," *5th Turbulent Shear Flow Symposium*, Cornell University.

Kline, S. J., and McClintock, F. A., 1953, "Describing Uncertainties in Single-Sample Experiments," Mechanical Engineering, Vol. 75, p. 3.

Lai, K. Y. M., and Makomaski, A. H., 1989, "Three-Dimensional Flow Pattern Upstream of a Surface-Mounted Rectangular Obstruction," ASME JOURNAL OF FLUIDS ENGINEERING, Vol. 111, p. 449.

Lighthill, M. J., 1963, *Boundary Layer Theory in Laminar Boundary Layers*, ed., Rosenhead, Oxford University Press.

Luchik, T. S., and Tiederman, W. G., 1987, "Timescale and Structure of Injections and Bursts in Turbulent Channel Flows," *J. Fluid Mech.*, Vol. 174, p. 529.

Massey, B. S., 1983, "*Mechanics of Fluid*," 5th ed., Van Nostrand Reinhold UK.

McMahon, H., Hubbartt, J., and Kubendran, L., 1983, "Mean Velocities and Reynolds Stresses Upstream of Simulated Wing Fusellage Juncture," NASA CR 3695.

Mehta, R., 1984, "Effect of Wing Nose Shape on the Flow in a Wing/Body Junction," *Aeronautical Journal*, Vol. 88, p. 456.

Menna, J. D., and Pierce, F. J., 1988, "The Mean Structure Around and Within a Turbulent Junction or Horseshoe Vortex—Part I: The Upstream and Surrounding Three-Dimensional Boundary Layer," ASME JOURNAL OF FLUIDS ENGINEERING, Vol. 110, p. 406.

Mofatt, R. J., 1985, "Uncertainty Analysis in the Planning of an Experiment," ASME JOURNAL OF FLUIDS ENGINEERING, Vol. 107, p. 173.

Pierce, F. J., and Tree, I. K., 1990, "The Mean Flow Structure on the Symmetry Plane of a Turbulent Junction Vortex," ASME JOURNAL OF FLUIDS ENGINEERING, Vol. 112, p. 16.

Robinson, S. K., 1990, "A Perspective on Coherent Structure and Conceptual Models for Turbulent Boundary Layer Physics," AIAA 21st Fluid Dynamics, Plasmadynamics and Lasers Conference, Seattle, WA, paper #90-1638.

Sedney, R., 1973, "A Survey of the Effect of Small Protuberances on Boundary Layer Flows," *AIAA J.*, Vol. 11, No. 6, p. 782.

Shabaka, I. M. M. A., and Bradshaw, P., 1981, "Turbulent Flow Measurements in an Idealized Wing/Body Junction," *AIAA J.*, Vol. 19, p. 131.

Simpson, R. L., 1981, "A Review of Some Phenomena in Turbulent Flow Separation," ASME JOURNAL OF FLUIDS ENGINEERING, Vol. 103, p. 520.

Schewe, G., 1983, "On the Structure and Resolution of Wall-Pressure Fluctuations Associated with Turbulent Boundary Layer Flow," *J. Fluid Mech.*, Vol. 134, p. 311.

Spalart, P. R., 1988, "Direct Numerical Simulation of a Turbulent Boundary Layer up to $\mathrm{Re}_\theta = 1410$," *J. Fluid Mech.*, Vol. 187, p. 61.

Thomas, A. S. W., and Bull, M. K., 1983, "On the Role of Wall-Pressure Fluctuations in Deterministic Motions in the Turbulent Boundary Layer," *J. Fluid Mech.*, Vol. 128, p. 283.

Williamson, C. H. K., 1989, "Oblique and Parallel Models of Vortex Shedding in the Wake of a Circular Cylinder at Low Reynolds Numbers," *J. Fluid Mech.*, Vol. 206, p. 579.

Willmarth, W. W., 1975, "Pressure Fluctuations Beneath Turbulent Boundary Layers," *Ann. Rev. Fluid Mech.*, Vol. 7, p. 13.

Willmarth, W. W., and Wooldridge, C. E., 1962, "Measurements of the Fluctuating Pressure at the Wall Beneath a Thick Turbulent Boundary Layer," *J. Fluid Mech.*, Vol. 14, p. 187.

Zdravkovich, M. M., Brand, V. P., Mathew, G., and Weston, A., 1989, "Flow Past Short Circular Cylinder with Two Free Ends," *J. Fluid Mech.*, Vol. 203, p. 557.

Nonlinear Response of Planar Laminar Flow Over a Flat Plate Vibrating in Different Modes

N. Kolluru Venkat
Consultant,
Spaulding Environmental Associates, Inc.,
Wakefield, RI 02879
Assoc. Mem. ASME

Malcolm Spaulding
Professor,
Department of Ocean Engineering,
The University of Rhode Island,
Kingston, RI 02881
Mem. ASME

A computer model developed by Venkat and Spaulding (1991a) for unsteady flows over vibrating bodies is used to investigate the nonlinear characteristics of external flow over a flat plate, a section of which is subjected to time varying motion of various mode shapes (n). The Reynolds number, Re is fixed at 1000. For the first case, the Strouhal number, St and the vibration amplitude ratio, H_0 are fixed at 0.25 and 0.025, respectively while for the second case, St and H_0 are increased to 1.0 and 0.1, respectively. Simulations are performed for modes varying in the range $1<n<4$. For $n=1$, upstream and downstream pressure wave propagation is very high compared to higher modes. The transfer of energy from the input frequency to the first harmonic is pronounced for higher modes. A source-sink pair exists over the vibrating section for even modes. For high St and H_0 the pressure spectral amplitude of higher harmonics far downstream is quite large for $n=4$ compared to $n=2$ thus indicating more nonlinear interaction between the vibrating body and the external flow for large even modes. The pressure coefficient on either side of the vibrating section is controlled by the gradient of vorticity for odd modes and by the convective acceleration terms for even modes.

Introduction

In unsteady fluid mechanics the response of viscous flows to dynamic disturbances introduced extraneously is an important phenomenon in many engineering applications (Curle, 1955; Goldstein, 1974; Telionis, 1981). The unsteadiness may be caused by the change in shape of the flexible body or by disturbing the free stream flow. Venkat and Spaulding (1991a) developed a numerical model to predict the unsteady flow over a flexible body. They simulated the laminar flow over a flat surfaced body with a section forced in simple harmonic motion. The vibrating motion starts with the plate moving upwards (positive y direction). They found that higher harmonics appear in the flow when the vibrating section is forced to oscillate at high Strouhal numbers (ratio of the fluid time scale to the plate oscillation period) and the Reynolds number, Re and the amplitude of vibration, H_0 (ratio of the plate vibration amplitude to the vibrating plate section length) are maintained at 1000 and 0.1, respectively. They also applied the model to simulate the interaction between the external flow and the vibrating section of the body for different amplitudes and Reynolds numbers (Venkat and Spaulding, 1991b,c). Their results clearly show that for low Strouhal numbers and amplitudes, the response of the external flow to the plate vibration amplitude is linear and there is little up or down stream influence. However for high Strouhal numbers, Reynolds numbers, and amplitudes the higher harmonics of the pressure spectral amplitudes become large. In addition considerable up and down stream influence is observed for high St and low Re.

It was shown by Venkat and Spaulding (1991a) that the nonlinear dynamics of the external flow over a body vibrating transversely, is controlled by the term $v(\partial u/\partial y)$ where v is the vertical velocity of vibration and $(\partial u/\partial y)$ is the gradient of the horizontal velocity u in the y-direction. The latter term is a function of vibration mode and amplitude for a fixed Reynolds number. In this paper Venkat and Spaulding's (1991a,b,c) earlier work is extended to explore the effect of vibration mode on the nonlinear dynamics of the external flow over a vibrating body.

Mathematical Formulation

The mathematical formulation for simulating viscous flow over a vibrating body uses the two dimensional x-y Navier-Stokes equations in vorticity and stream function variables. The nondimensional laminar flow equations are

$$\frac{\partial \omega}{\partial t}+\frac{\partial \psi}{\partial y}\frac{\partial \omega}{\partial x}-\frac{\partial \psi}{\partial x}\frac{\partial \omega}{\partial y}=\frac{1}{\mathrm{Re}}\left[\frac{\partial^2 \omega}{\partial x^2}+\frac{\partial^2 \omega}{\partial y^2}\right] \tag{1}$$

$$\left[\frac{\partial^2 \psi}{\partial x^2}+\frac{\partial^2 \psi}{\partial y^2}\right]=-\omega \tag{2}$$

The coordinate system (physical plane) is shown in Fig. 1. The x and y axes are oriented along and normal to the plate surface, respectively with an origin at point A. The values of vorticity and stream function for a given Reynolds number at the upstream boundary (section FA) are specified using Blasius' boundary layer equations (White, 1991) assuming that the lead-

---

Contributed by the Fluids Engineering Division for publication in the JOURNAL OF FLUIDS ENGINEERING. Manuscript received by the Fluids Engineering Division April 1, 1992. Associate Technical Editor: F. T. Dodge.

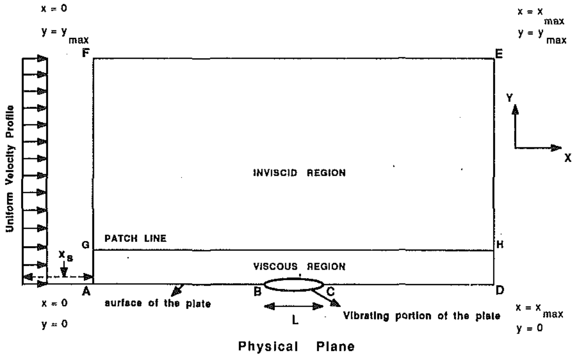

Fig. 1 Physical plane for simulating viscous flow over a vibrating plate

ing edge of the flat plate is located at a distance, $x_s = 1$ upstream from the entry region of the model domain. The normal second order derivatives of the stream function and vorticity are made zero at the downstream boundary (section ED). On the top boundary (section FE) the horizontal velocity $(\partial\psi/\partial y)$ approaches the free stream velocity (U_∞) and the vorticity assumed to be zero (Fletcher, 1988).

On the plate surface, a section vibrates in simple harmonic motion with different modal shapes (section BC). The equation for plate deflection is given by

$$y_w(x, t) = H_0 \sin(2\pi t \mathrm{St}) \sin(n\pi x) \quad x_{LE} \leq x \leq x_{TE} \tag{3}$$

where x_{LE} and x_{TE} are the locations of the leading and trailing edges of the vibrating section BC, n is the mode number of the plate oscillation and the subscript w refers to the wall or plate surface. On the remainder of the plate

$$y_w(x, t) = 0.0 \quad 0 < x < x_{LE} \text{ and } x_{TE} < x < x_{\max} \tag{4}$$

where $x_{\max}$ is the domain exit location. The stream function is obtained by integrating the velocity of vibration along the x axis (U. Ghia and K. N. Ghia, 1990). The no slip boundary condition is simultaneously satisfied. On the non-vibrating surface of the flat plate, the stream function remains constant and satisfies the no slip boundary condition (section AB and CD). Since no direct boundary condition exists for body vorticity, it is obtained using Eq. 2 on the body surface. A detailed description of the boundary conditions is presented in Venkat (1991).

The flow and the associated boundary conditions are transformed to a boundary fitted computational plane (Venkat and Spaulding, 1991) where time dependent boundaries are represented by constant immovable coordinate lines (Thompson, 1982). This transformation allows problems with time dependent boundaries to be solved with relative ease.

Numerical Method

The flow equations (Eqs. (1) and (2)) are solved with an inner-outer method (viscous-inviscid) approach. In the viscous region, adjacent to the body surface, Eqs. (1) and (2) are solved while in the inviscid region Eq. (2) (with $\omega = 0$) is solved. The two solutions are matched at a patch line between the viscous and inviscid regions (Fig. 1). The patch line location from the plate is selected such that the model predicted results are not disturbed by its presence. Test cases were run by moving the patchline from the top boundary towards the plate. The test results showed that the patch line location (segment AG) should beat least 1.2 times the boundary layer thickness calculated at the domain downstream end. A detailed discussion about the patch line location and its effect on the CPU time is given in Venkat (1991) and Venkat and Spaulding (1991). This approach substantially reduces computational costs compared to conventional methods.

The Line Gauss Seidal method of Napolitano and Walters (1986) is adopted for the present numerical simulations. The grid and the flow equations are discretized using second order finite differences (Bringen, 1980; Vemuri and Karplus, 1981). The resulting algebraic equations and the associated boundary conditions are solved using a Thomas Tri Diagonal Matrix Algorithm (Bringen and McMillan, 1980; Napolitano and Walters, 1986) from upstream to downstream for each time step. The evaluation of time step, relaxation factors for the stream function and vorticity and criteria for convergence are based on the approach described in Peyret and Taylor (1983) and Roache (1972). A Von Neumann linear stability analysis was performed on the finite difference form of Eq. (1) in the transformed plane. The vorticity ω is expanded in a Fourier Series. The stability requires that the Fourier modes do not increase with time for a given grid size in x and y directions.

Once the solutions are obtained for the first time step, they are used to calculate the friction and pressure coefficients on the body surface (Venkat and Spaulding, 1991a). Next, the plate is moved to a new time position (next increment in time) and the iteration procedure outlined above is repeated. The

Nomenclature

a = body vibration amplitude, m
C_f = friction coefficient on the plate surface
C_p = pressure coefficient on the plate surface
f = plate vibration frequency, Hz
H_0 = nondimensional body vibration amplitude ratio (a/L)
L = characteristic length of the vibration portion of the body, m
n = plate vibration mode
p = dimensionless pressure $(p = P/\rho U_\infty^2)$
P = fluid pressure, kg/m^2
Re = Reynolds number $(U_\infty L/\nu)$
Re_x = local Reynolds number $(U_\infty x/\nu)$
St = Strouhal number (fL/U_∞)
T = dimensional time (s)
t = dimensionless time $(t = TU_\infty/L)$
u, v = dimensionless horizontal and vertical velocities $(u = U/U_\infty,\ v = V/U_\infty)$
U, V = horizontal and vertical velocities, m/s
U_∞ = free stream velocity, m/s
x, y = nondimensional coordinates in the physical plane $(x = X/L,\ y = Y/L)$
x_{LE}, x_{TE} = leading and trailing edges of the vibrating section of the plate in the physical plane
$x_{\max}$ = length of the computational domain in the physical plane
x_s = nondimensional distance between the leading edge of the plate and the model entry domain
X, Y = dimensional coordinates in the physical plane
$y_{\max}$ = height of the computational domain in the physical plane
Γ = dimensional vorticity, 1/s
ρ = fluid density
Ψ = dimensional stream function, m^2/s
ψ, ω = dimensionless stream function $(\psi = \Psi/LU_\infty)$ and vorticity $(\omega = \Gamma L/U_\infty)$
δ_{LE} = boundary-layer thickness at the leading edge of the vibrating plate section

simulation is continued for subsequent time steps and cycles until there is no change in the cycle calculated values of friction and pressure coefficients.

The model was tested for steady flow in a square cavity (Morris, 1972), oscillating flow through a fixed wavy channel (Sobey, 1982) for Re = 100, Blasius flow over a flat plate (White, 1991) for Re = 1000 and flow through a channel with time dependent indentation (Ralph and Pedley, 1988). The model simulations were tested for the impact of grid size, grid stretching and location of upstream, downstream and top free stream boundaries on the numerically predicted results. In addition, the effect of patch line location on the numerical results was also studied for unsteady flows. These results are presented in detail in Venkat (1991).

Results and Discussions

In this paper, we focus our attention on studying the hydrodynamic response of the external flow over a flat plate, a section of which is subjected to simple harmonic oscillations. The nonlinear response of the flow is controlled by the term $v(\partial u/\partial y)$ where v is a function of plate oscillation frequency while $(\partial u/\partial y)$ is a function of plate oscillation amplitude and mode and flow Reynolds number. In our earlier work we found that the interaction between the vibrating plate and the external flow is nonlinear for low St and high H_0 and for high St and all vibrating amplitudes (Venkat and Spaulding, 1991b). For high St and Re, high amplitude spectral harmonics appear in the downstream pressure. For low Re and high St, considerable up and downstream influence is predicted compared to the low St case.

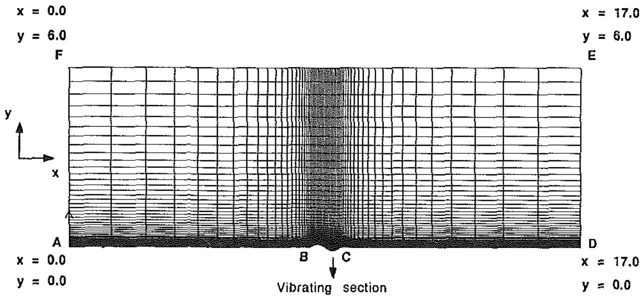

Fig. 2 61 × 41 grid domain for simulating viscous flow over the vibrating plate

In this paper, we control the v and $\partial u/\partial y$ terms by changing the mode number (n) of the vibrating section. The following cases are studied:

Case 1: St = 0.25, $H_0 = 0.025$, Re = 1000, $1 < n < 4$.
Case 2: St = 1.00, $H_0 = 0.100$, Re = 1000, $n = 2$ and 4.

The Reynolds number, based on distance from the leading edge of the plate to the leading edge of the vibrating section ($x = 9$), Re_x for both cases is 9000. This gives a boundary layer thickness ($\delta_{LE} = 0.4743$, based on $\delta/x = 5/\sqrt{\mathrm{Re}_x}$) to vibrating plate length ($L = 1$) ratio of 0.4743 at the leading edge of the vibrating section and hence the boundary layer is relatively thick compared to the plate length. The ratio of H_0 (0.025) to δ_{LE}(0.4743) is 0.0527.

The grid domain shown in Fig. 2 is used for the present simulations. The domain extends 8 vibrating plate lengths up and downstream and 6 lengths normal to the plate. The total length of the domain is 17 vibrating plate lengths. The grid domain has 61 and 41 grids in the x and y directions, respectively. Sensitivity studies have shown that the grid distribution and boundary locations and specification procedure reasonable estimates of the flow field (Venkat, 1991). The plate length between $x = 8.0$ and 9.0 is made to oscillate with different mode shapes.

Case 1. The pressure envelope (defined as the maximum and minimum values within which the value varies with time) versus distance along the plate in the vicinity of the vibrating section of the plate for mode, $n = 1$, 2, 3 and 4 is shown in Fig. 3. For $n = 1$, the entire vibrating section of the plate behaves like a source or sink. The pressure coefficient range increases continuously for $x > 8.5$ along the plate surface. This is due to the existence of large vorticity gradients and fluctuations near the vibrating section. When the mode number is increased to 2, source-sink behavior is introduced in the vibrating section. Hence the C_p envelope increases up to the plate mid section and then decreases to a low range down-

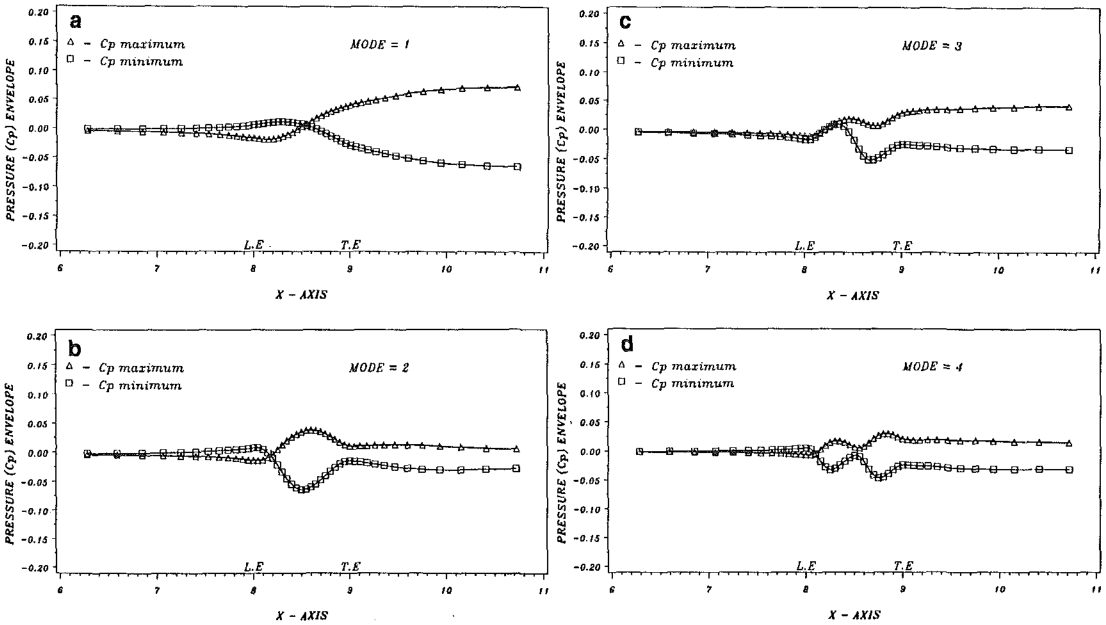

Fig. 3 Variation of pressure coefficient along the vibrating plate for various mode numbers at St = 0.25, Re = 1000 and $H_0 = 0.025$

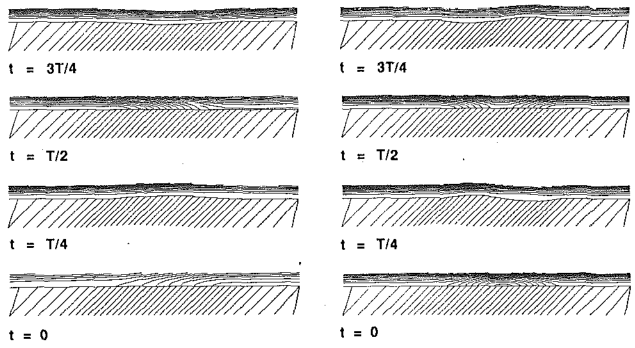

(a) MODE = 1 (b) MODE = 2

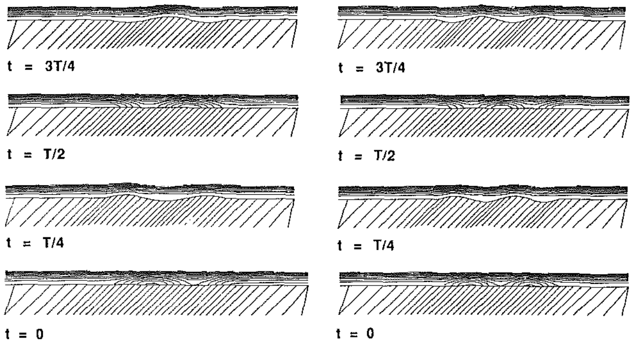

(c) MODE = 3 (d) MODE = 4

Fig. 4(*c,d*)

Fig. 4 Contour plot stream function in the vicinity of the vibrating section of the plate for one complete cycle of vibration at *T*/4 time intervals for St = 0.25, Re = 1000, H_0 = 0.025 and *n* = 1, 2, 3, 4

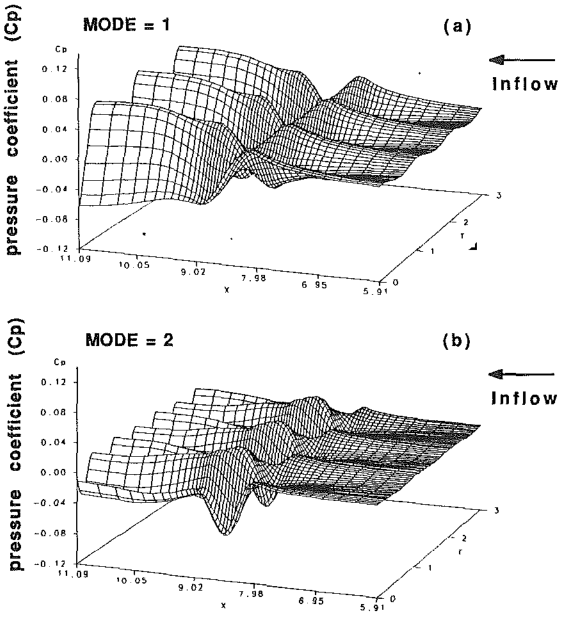

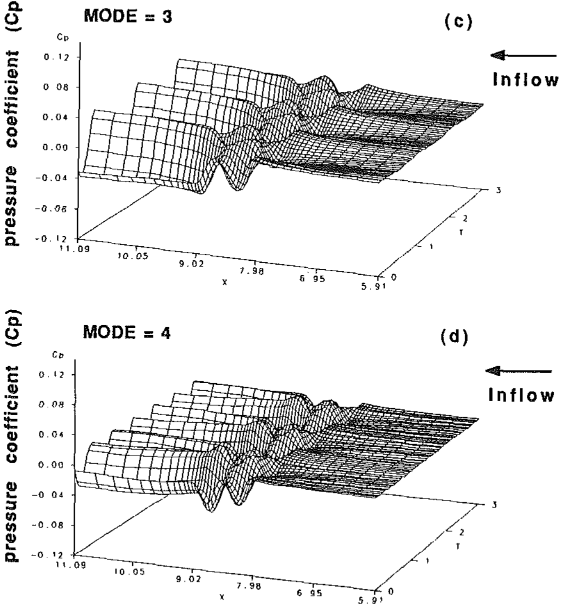

Fig. 5(*c,d*)

Fig. 5 Variation of pressure coefficient along the vibrating plate as a function of time for various mode numbers at St = 0.25, Re = 1000 and H_0 = 0.025

stream. For this case, the vorticity fluctuations are small because of the existence of source/sink pair over the vibrating section. For $n=3$, in addition to a source-sink pair, the last one-third of the vibrating section behaves like a single source or sink similar to $n=1$. At the downstream end, the C_p envelope range is larger than for the $n=2$ results, however, it is smaller than for the $n=1$ case. This is because only one third of the vibrating section behaves like $n=1$. When the mode of vibration is increased to 4, the downstream pressure envelope decreases compared to the $n=3$ results. For this mode, the pressure variation over the vibrating section is due to the combination of two source-sink pairs.

The flow field is further analyzed by plotting stream function contour lines in the vicinity of the vibrating section. They are shown in Fig. 4 for $t=0$, $T/4$, $T/2$ and $3T/4$. At $t=0$, the plate has maximum velocity and zero deflection. For $n=1$, the vibrating section deflects the fluid as shown in Fig. 4(*a*). Since there is no corresponding sink available for the vertically advected fluid, the stream lines over the vibrating section are not closed. Hence, the external fluid is deflected throughout the vibrating section. This flow pattern is similar to the potential flow over a half Rankine body discussed in White (1986). When the mode is increased to 2, the vibrating body behaves like a source-sink pair and hence a fluid cell is formed over the plate (Fig. 4(*b*)). This behaves like a full Rankine body. Because of this, the pressure coefficient decreases for the first half of the vibrating section where the fluid is accelerated and partially recovers for the second half where the flow is decelerated (Fig. 3(*b*)). For $n=3$ (Fig. 4(*c*)), two thirds of the vibrating section forms a fluid cell similar to Fig. 4(*b*) while in the remaining one-third section, the flow pattern is similar to Fig. 4(*a*). The pressure envelope shown in Fig. 3(*c*) for this mode is qualitatively a combination of the $n=1$ (Fig. 3(*a*)) and $n=2$ (Fig. 3(*b*)) cases. When the mode number is increased to 4, two fluid cells are formed over the vibrating section and the external flow is deflected accordingly. At $t=T/4$, the flow follows the plate deflection except near the trailing edge where it is decelerated for $n=1$. For $n=2$, the external flow does not follow the plate deflection in the trough portion of the vibrating section. Similar flow responses are observed for $n=3$ and 4. When the plate reaches $T/2$ position, the external flow is drawn towards the vibration section with its maximum downward velocity. This is exactly opposite to the $t=0$ case where the external fluid is pushed upward by the vibrating section for $n=1$. The flow pattern is similar to that at $t=0$ but reversed. For $n=2$, the flow pattern, similar to $n=1$, occurs in the first half while the flow pattern similar to $n=1$ at $t=0$ is observed on the second half of the vibrating section. In this section, the

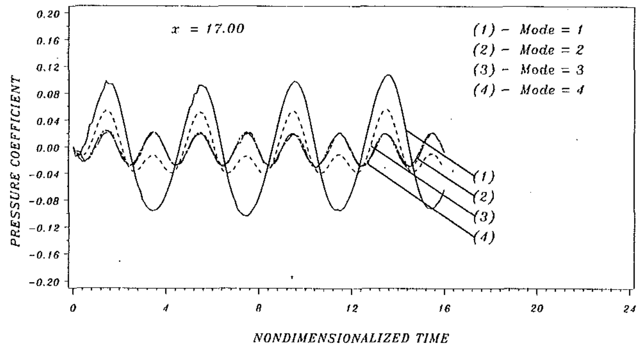

Re = 1000 St = 0.25 Ho = 0.025

Fig. 6(a) Time series plot of pressure coefficient for various mode numbers at $x = 17.0$ (downstream end) with St = 0.25, Re = 1000 and $H_0 = 0.025$

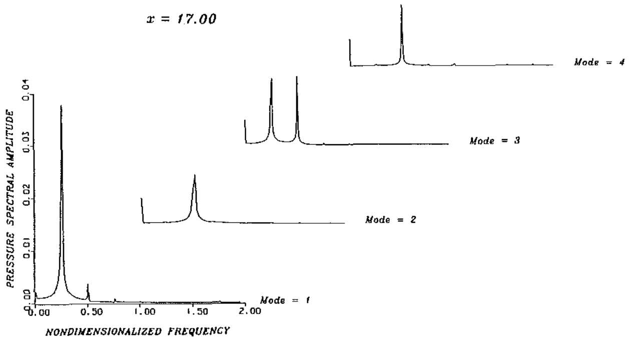

Re = 1000 St = 0.25 Ho = 0.025

Fig. 6(b) Pressure coefficient versus frequency for various mode numbers at $x = 17.0$ (downstream end) with St = 0.25, Re = 1000 and $H_0 = 0.025$

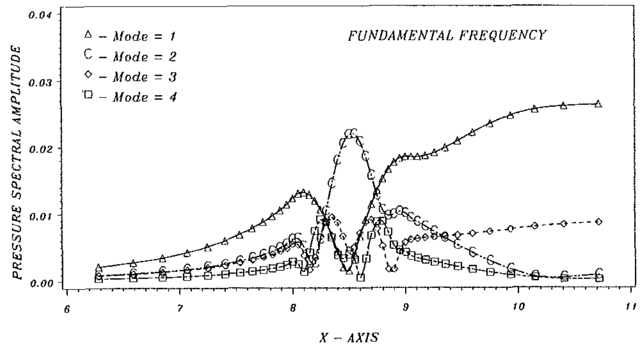

Re = 1000 St = 0.25 Ho = 0.025

Fig. 7 Variation of pressure spectral amplitude (fundamental frequency) along the vibrating plate for various mode numbers at St = 0.25, Re = 1000 and $H_0 = 0.025$

upward vibration velocity displaces the incoming fluid. For $n = 3$, one third of the vibrating section behaves like the $n = 1$ case and hence the flow pattern looks very similar to $n = 1$ result. For the next two-thirds portion of the plate, a circulation cell is observed. This section behaves like a source-sink pair. The flow pattern for $n = 4$ is the combination of $n = 3$ and $n = 1$ results. At $t = 3T/4$, the flow does not follow the trough portions of the vibrating section for any of the modes. Unfavorable pressure gradient exists in the trough portion, and there is a tendency for the flow to separate from the body surface. The flow patterns repeat themselves for subsequent vibration cycles.

The variation of pressure coefficient along the vibrating section of the plate as a function of time for different mode numbers is shown in Fig. 5. The up and downstream amplitude of the pressure wave is higher for $n = 1$ than other modes. The figure clearly shows that the downstream pressure wave frequency and amplitude changes with increasing mode number. The absence of corresponding sink (source) in the vibrating section for the oscillating flow for $n = 1$ is clearly seen in Fig. 5(a). For even modes ($n = 2$ and 4), considerable pressure recovery is seen (Figs. 5(b) and 5(d)) due to the presence of a corresponding sink (source) in the vibrating section. For $n = 3$, the downstream pressure recovery is minimal (Fig. 5(c)).

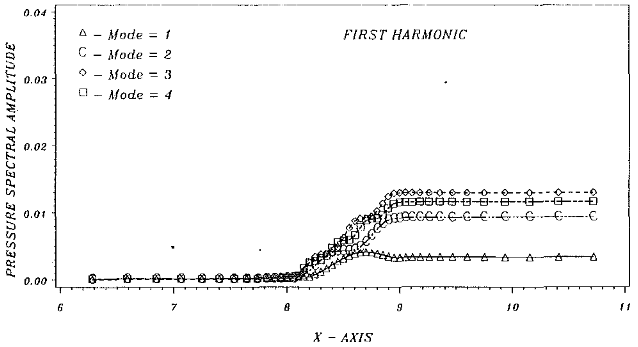

Re = 1000 St = 0.25 Ho = 0.025

Fig. 8 Variation of pressure spectral amplitude (first harmonic) along the vibrating plate for various mode numbers at St = 0.25, Re = 1000 and $H_0 = 0.025$

The time varying pressure coefficient is spectrally analyzed (Newland, 1975) to investigate the nonlinear interaction between the external flow and the vibrating section of the plate. The data (2048 points) for the Fast Fourier Analysis (FFT) use the last cycle (steady state) of the C_p time series. In this approach, sub harmonics created during the transient stage and subsequently damped are not included in the spectral representation. Time series plots of pressure coefficient at the downstream end of the model domain for all modes are shown in Fig. 6(a). The corresponding Fast Fourier Transforms (FFT) are shown in Fig. 6(b). For $n = 1$, a large spectral peak occurs at the forcing frequency (0.038) and a very small peak at the first harmonic (0.0036). The corresponding pressure wave in the time domain has an amplitude of 0.10 (Fig. 6(a)). When the mode number is increased to 2, all the energy is shifted to the first harmonic and hence a spectral peak appears at the first harmonic (0.009). There is no peak at the forcing frequency (Fig. 6(b)). For $n = 3$, the spectral peak appears at both the forcing frequency (0.012) and the first harmonic (0.013). The corresponding pressure wave is shown in Fig. 6(a). This shows that for $n = 3$, two thirds of the vibrating section transfers energy to the first harmonic while the last one third section just receives energy and transfers it to the incoming fluid at the forcing frequency. When n is increased to 4, there is no spectral peak at the forcing frequency. A spectral peak however is present at the first harmonic (0.01156). This shows that for even modes, all the energy is transferred to the first harmonic while for odd modes, in addition to the first harmonic, considerable energy still exists at the forcing frequency.

The variation of the fundamental frequency pressure spectral amplitude along the plate surface for all modes is shown in Fig. 7. For $n = 1$, the energy added to the fluid at the input frequency increases on the downstream and decreases on the upstream sides of the vibrating section. There is minimum energy transfer to the flow around the plate mid section. The figure clearly shows that significant energy has propagated upstream from the vibrating section of the plate for $n = 1$. For $n = 2$, the energy transfer at the forcing frequency decreases on either side of the vibrating section and has a maximum value near the plate mid section. This is in contrast to the $n = 1$ result which has a maximum at the plate mid section. The upstream energy propagation for $n = 2$ is smaller than for $n = 1$. When the mode number increases to 3, the spectral amplitude

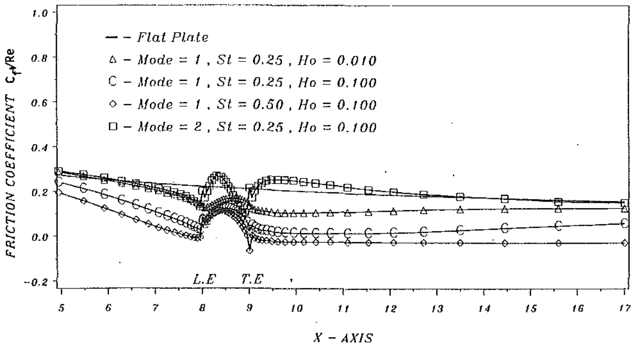

Fig. 9 Variation of friction coefficient along the vibrating plate for various amplitudes, modes and Strouhal numbers at $t = T$ and Re = 1000

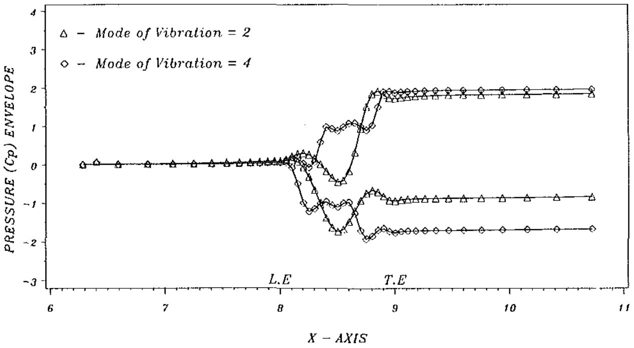

Fig. 10 Variation of pressure coefficient along the vibrating plate for St = 1.0, Re = 1000, $H_0 = 0.10$ and $n = 2$, 4

of the input frequency along the plate surface is the combination of the $n = 1$ and 2 cases. However, its magnitude at the downstream end is less than the $n = 1$ case but higher than the $n = 2$ case. For $n = 4$, the spectral amplitude variation is similar to the $n = 2$ case. Its downstream magnitude is very small. Figure 7 clearly shows that the upstream energy propagation decreases with increasing mode number. The downstream energy propagation increases for odd mode numbers and decreases for even mode numbers.

The first harmonic spectral amplitude variation over the plate surface for all modes is shown in Fig. 8. For all modes, the spectral amplitude is zero upstream of the vibrating section, increases over the vibrating section and reaches a constant value downstream. The increase is pronounced for higher modes ($n > 2$). There is a three fold increase in the first harmonic spectral amplitude of downstream pressure wave when the mode is changed from 1 to 2. For $n = 3$, the first harmonic spectral magnitude increases but decreases for $n = 4$. For $n = 1$, there is a one step increase in the spectral amplitude over the vibrating section (Fig. 8). For increasing modes, the number of step increase is approximately equal to the mode of the vibration. As an example, for $n = 2$, Fig. 8 clearly shows a two step increase in the spectral amplitude over the vibrating section.

Case 2. Venkat and Spaulding (1991b) showed that the existence of high amplitude spectral harmonics is significant for high Strouhal numbers and all vibration amplitudes. In this case study, the Strouhal number and the amplitude of vibration are increased to 1.0 and 0.10, respectively. With odd mode simulations, we found that the flow does not reach the Blasius' results far downstream for large St and H_0. This is clearly shown in terms of the friction coefficient versus along plate distance in Fig. 9. For $n = 1$, St = 0.25 and $H_0 = 0.010$ the flow reaches the Blasius results with minimum deviation. But

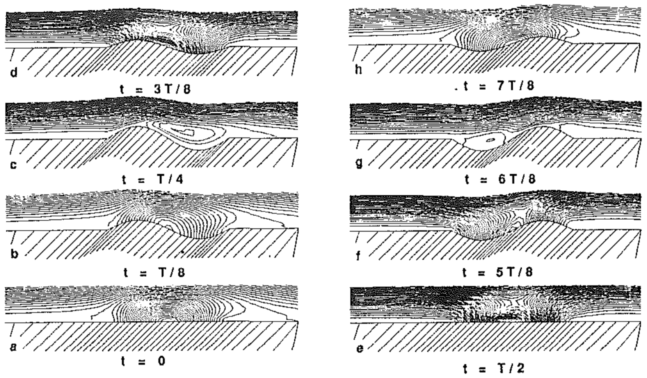

Fig. 11(*a*) Contour plot of stream function in the vicinity of the vibrating section of the plate for one complete cycle of vibration at $T/8$ time intervals with St = 1.0, Re = 1000, $H_0 = 0.10$ and $n = 2$

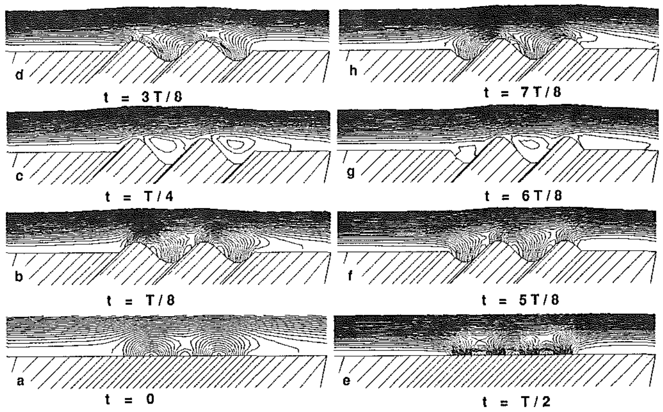

Fig. 11(*b*) Contour plot of stream function in the vicinity of the vibrating section of the plate for one complete cycle of vibration at $T/8$ time intervals with St = 1.0, Re = 1000, $H_0 = 0.10$ and $n = 4$

when the amplitude is increased, there is considerable deviation from the Blasius curve. The flow needs considerable increase in the domain length at the downstream to return to Blasius' flow. However, for even modes the flow reaches the Blasius' results prior to the designated downstream boundary location at $x = 17$. This is due to the existence of source-sink pair at the vibrating section for even modes as explained above. We have selected not to extend the model domain for these simulations and therefore results are presented for the even modes only.

The pressure envelopes for even modes are shown in Fig. 10. The pressure increase in the C_p maximum curve over the vibrating section for $n = 4$ is the summation of two C_p maximum vs. x curve of $n = 2$ but reduced in amplitude. This is obvious since the flow pattern over the vibrating section for $n = 4$ should be the same as $n = 2$ but repeated twice. Similarly, the pressure decrease in the C_p minimum for $n = 4$ is the summation of two C_p minimum vs. x curve of $n = 2$ but reduced in amplitude.

The flow pattern over the vibrating section is shown by plotting the stream function contour lines (Fig. 11) for one complete cycle of vibration at $T/8$ intervals. Figure 11(*a*) and 11(*b*) refer to $n = 2$ and 4, respectively. At the zero deflection and maximum velocity position ($t = 0$), a large circulation cell is formed over the vibrating section for $n = 2$. The shape of the cell resembles a half ellipsoid. This flow pattern suggests that the vibrating section is composed of a series of distributed sources and sinks. The external flow is deflected by the cell and the C_p changes correspondingly. However, for $n = 4$, two similar but smaller circulation cells are formed on the vibrating section. The pressure recovery along the second quarter ($L/4 < x < L/2$) is inhibited by the upward deflection of the fluid by the second circulation cell (Fig. 11(*b*)). This means that

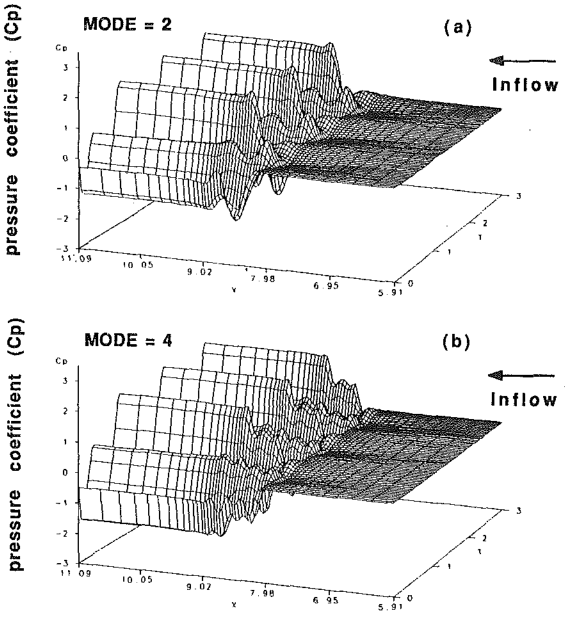

Fig. 12 Variation of pressure coefficient along the vibrating plate as function of time for St = 1.0, Re = 1000, H_0 = 0.10 and n = 2 and 4

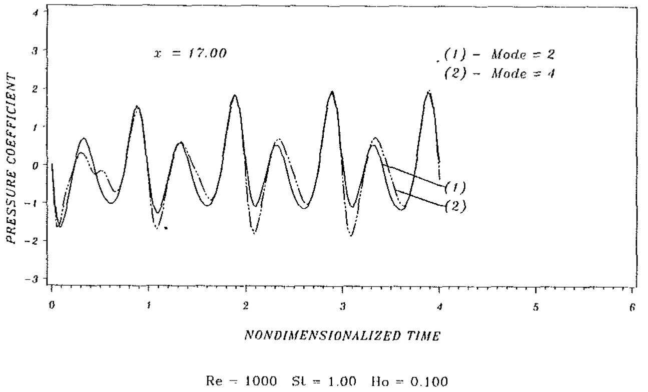

Fig. 13 Time series plot of pressure coefficient at x = 17.0 for St = 1.0, Re = 1000, H_0 = 0.10 and n = 2, 4

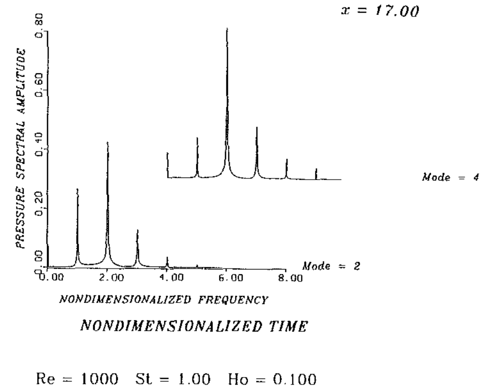

Fig. 14 Pressure coefficient versus frequency at x = 17.0 for St = 1.0, Re = 1000, H_0 = 0.10 and n = 2, 4

the pressure coefficient further decreases and maintains a steady high value at the downstream compared to the $n=2$ case. When the plate reaches the maximum deflection position ($t=T/4$) the external flow separates from the plate near the plat mid-section and reattaches just before the trailing edge of the vibrating section (Fig. 11(a)). Because of this, a large separation cell is formed on the second half of the vibrating section. However for $n=4$, two similar but smaller separation cells are observed in the trough sections of the plate. As the plate moves to the third quarter ($t=T/2$), external fluid is drawn into the first half while some oscillating fluid is pushed downstream from the second half of the vibrating section for $n=2$. In addition, a small circulation cell similar to that at $t=0$ is formed around the vibrating section mid-point. A similar flow pattern is seen for $T/2<t<3T/4$. For $n=4$, three circulation cells are initially formed over the vibrating section at $t=3T/8$. The cells development is clearly depicted in $t=T/2$. At the end of the third quarter ($t=3T/4$), a large separation bubble is formed in the first half and a second, considerably elongated downstream in x-direction, appears near the trailing edge for $n=2$. On the other hand, for $n=4$, a small separation cell appears in the first quarter plate length ($x<L/4$), a second in the third quarter ($L/2<x<3L/4$) and finally a larger one near the trailing edge of the vibrating section. When the plate moves to the fourth quarter, the cells formed at $t=3T/4$ are swept by the upward and downward motion of the first and second halves of the vibrating plate, respectively. This gives rise to the formation of circulation cells similar to $t=0$ case. This flow behavior is seen for $n=2$ and 4 cases. The flow pattern described above repeats itself for subsequent cycles.

The propagation of the pressure wave for both modes is clearly illustrated in Fig. 12. For $n=4$, the energy addition at two levels one in the first half and the other in the second half of the vibrating section is clearly seen in Fig. 12(b). The amplitude of the propagating downstream pressure wave is large for $n=4$. The far downstream pressure variation with time and the corresponding FFT are shown in Figs. 13 and 14, respectively. With an increase in the mode number, the amplitude of the pressure wave and the magnitudes of the first, second and third harmonics increase while the fundamental decreases. This suggests that if the plate vibrates at higher mode numbers the higher harmonics increase in magnitude in the downstream pressure wave.

Conclusion

The model developed by Venkat and Spaulding (1991a) has been successfully applied to investigate the external flow interactions with the section of the flat plate vibrating in different mode numbers (n). The following results are concluded from the above study.

Low St and H_0. There is considerable upstream influence and, the energy added to the forcing frequency over the vibrating plate is transferred to the flow at the same frequency for $n=1$. For this case, large vorticity gradients and fluctuations exist on either side of the vibrating section of the plate. With an increase in the mode number, the upstream influence and the vorticity gradient decrease considerably. The external flow receives energy at the fundamental frequency and simultaneously transfers it to the first harmonic, partially for odd modes ($n>1$) and completely for even modes.

For $n=1$, the flow pattern over the vibrating section is similar to the potential flow over a half-Rankine body (source/sink + free stream). For $n=2$, the vibrating section behaves like a full Rankine body (source/sink + sink/source + free stream). For higher modes, the basic flow pattern can be predicted easily from lower mode ($n=1$ and 2) results. For even modes, the source-sink pair always exists whereas for odd modes there is always complete ($n=1$) or at least one portion of the vibrating section ($n=3$) of the plate that behaves like a source/sink.

High St and H_0. The formation of a half-Rankine body for odd modes is pronounced for high H_0, St and Re. Because of the absence of the corresponding sink/source for odd modes, the flow did not reach the Blasius results at the downstream boundary. An extension of the downstream boundary is therefore required to study these flows. For even modes the flow reaches the Blasius results downstream due to the existence of source-sink pair.

Nonlinear interactions between the vibrating section of the plate and the external flow, as evidenced by the existence of large amplitude higher harmonics in the downstream pressure wave, is considerably large for the $n=4$ compared to $n=2$.

Acknowledgment

This research work was funded by the Office of Naval Research under contract no: 535413.

References

Bringen, S. H., and McMillan, O. J., 1980, "Calculation of Two-Dimensional Inlet Flow Fields in a Supersonic Free Stream-Program Documentation and Test Cases," NASA CP-3221.

Curle, N., 1955, "The Influence of Solid Boundaries Upon Aerodynamic Sound," *Proceedings of the Royal Society of London*, Series A, Vol. 231, pp. 505-514.

Fletcher, C. A. J., 1988, *Computational Fluid Dynamics*, Vols. 1 and 2, Springer-Verlag, New York.

Ghia, U., and Ghia, K. N., 1990, "Analysis and Control of Low-Speed Forced Unsteady Flows," *Second International Conference on Non-Steady Fluid Dynamics*, pp. 321-328.

Goldstein, M. E., 1974, *Aeroacoustics*, NASA SP-346.

Halim, Ahmad A. M., 1986, "Development of an Iterative Boundary Layer Type Solver for Axisymmetric Separated Flow," *AIAA Journal*, Vol. 24, No. 8, pp. 1298-1304, Aug.

Morris, D. J., 1975, "Solution of the Incompressible Driven Cavity Problem by the Alternating-Direction Implicit Method," NASA SP-378, pp. 47-59.

Napolitano, M., and Walters, R. W., 1986, "An Incremental Block Line Gauss Seidal Method for the Navier-Stokes Equations," *AIAA Journal*, Vol. 24, No. 5, pp. 770-776.

Newland, D. E., 1975, *An Introduction to Random Vibrations and Spectral Analysis*, Longman Group Ltd.

Peyret, P., and Taylor, T. D., 1983, *Computational Methods for Fluid Flow*, Springer-Verlag, New York.

Ralph, M. E., and Pedley, T. J., 1988, "Flow in a Channel With a Moving Indentation," *Journal of Fluid Mechanics*, Vol. 190, pp. 87-112.

Roache, P. J., 1972, *Computational Fluid Dynamics*, Hermosa Publishing, Albuquerque, New Mexico.

Sobey, Ian J., 1982, "Oscillatory Flows at Intermediate Strouhal Number in Asymmetric Channels," *Journal of Fluid Mechanics*, Vol. 125, pp. 359-373.

Telionis, D. P., 1981, *Unsteady Viscous Flows*, Springer Series in Computational Physics, Springer-Verlag, New York.

Thompson, J. F., 1982, *Numerical Grid Generation*, North-Holland.

Vemuri, V., and Karplus, W. J., 1981, *Digital Computer Treatment of Partial Differential Equations*, Prentice-Hall.

Venkat, N. K., 1991, "Numerical Simulation of Planar and Axisymmetric Unsteady Flows over Vibrating Bodies," Ph.D. Dissertation, Department of Ocean Engineering, The University of Rhode Island.

Venkat, N. K., and Spaulding, M., 1991a, "A Model to Predict the Nonlinear Response of Laminar Flow Over Vibrating Bodies," ASME JOURNAL OF FLUIDS ENGINEERING, Vol. 113, No. 4, pp. 544-554, Dec.

Venkat, N. K., and Spaulding, M., 1991b, "Influence of Vibration Amplitude on the Laminar Flow Over a Plate Vibrating at Low Strouhal Number," in ASME press.

Venkat, N. K., and Spaulding, M., 1991c, "Hydrodynamic Characteristics of External Laminar Flow Over a Vibrating Body for Varying Reynolds Number," under revision.

White, F. M., 1991, *Viscous Fluid Flow*, McGraw-Hill.

White, F. M., 1986, *Fluid Mechanics*, McGraw-Hill.

Flow Instability in a Curved Duct of Rectangular Cross Section

A. Belaidi

M. W. Johnson

University of Liverpool,
Liverpool, England

J. A. C. Humphrey

University of California at Berkeley,
Berkeley, California

An experimental investigation has been carried out in a curved duct of rectangular cross section in order to study the development of flow instability in such geometries. Hot wire anemometry was used to obtain detailed measurements of velocity on the symmetry plane of the duct for different curvature ratios. As the duct Dean number is increased, a centrifugal instability develops and the Dean vortices are seen to oscillate along the inner wall. To understand the contribution of these vortices to the laminar-turbulent transition, time histories and spectra of the flow were taken on the symmetry plane of the duct for different Reynolds numbers. These data reveal a time-periodic motion along the inner wall where the secondary flows originating from the side wall boundary layers collide. The bend angle where this instability develops depends on the Reynolds number while the frequency of the instability depends on the curvature ratio of the bend.

Introduction

Because of their academic and industrial importance, flows in curved ducts and pipes have been the subject of considerable research initially by Eustice (1911), Dean (1928a,b), Taylor (1929), Wattendorf (1935), Cumming (1952) and, more recently, Pratap et al. (1975), Humphrey (1978), Humphrey et al. (1977), Humphrey et al. (1985), Chang et al. (1983), Arnal (1988), and Hur et al. (1990).

When a fluid enters a curved duct of any cross section, an imbalance occurs between the centrifugal force and the radial pressure gradient. These two factors act in opposing directions on each fluid element. To maintain a momentum balance, the faster moving fluid in the core of the flow moves outwards pushing fluid from the outer wall to the side walls and then inwards, along the side walls, towards the inner wall creating a cross-stream circulation. The fluid in the symmetry plane is thus directed from the inner wall to the outer wall. Stewartson et al. (1980) suggested that the boundary layer first develops on the outer wall and is convected in either direction along the side walls towards the inner wall where the two fluid streams collide. This results in a jet of fluid leaving the inner wall and moving towards the outer wall.

As was observed by Reynolds (1883) in his dye experiment in a straight pipe, transition to turbulence is instantaneous. The dye streaks break down catastrophically as soon as the flow rate exceeds a certain critical value. Whereas, transition to turbulence in curved pipes is preceded by a flow instability. This sort of instability has been investigated extensively in past years, both experimentally and theoretically through numerical simulations. Earlier this century, Taylor (1929) injected dye near the side wall of a coiled pipe and observed the cross-stream circulation in the flow as calculated by Dean (1928a). Taylor found the flow to be steady up to a certain speed, past which an oscillatory motion developed which retained its identity through at least one complete turn of the helix. The oscillatory motion observed by Taylor was not of a turbulent type. Dean's (1928a) investigation on the flow instability in curved pipes showed that the small disturbances which do not persist in a straight pipe are retained in a curved one. Dean relates the phenomenon to the effects of curvature, but most researchers in the field relate the flow instability in curved pipes to the onset of a second vortex pair in the outer region of the bend. Joseph et al. (1975) and Ghia and Sokhey (1977) predicted numerically a weak vortex pair near the outer wall for fully developed flow in a curved duct of square cross-section. Hille et al. (1985) used an LDA system to measure the streamwise and cross-stream velocities in a 180 deg bend of square cross section. Their measurements revealed a second vortex along the outer wall between the 108 and 171 deg planes for Dean numbers ranging between 150 and 300. This finding agrees very well with numerical calculations for a fully developed laminar flow in a curved channel performed by Cheng et al. (1976) where the second vortex pair appeared at $De = 202$. However, Winters (1987) predicted an additional vortex pair by the outer wall for a developed flow in a curved duct of square cross-section for $De = 92$. He also showed that between $92 < De < 136$ no stable solution is obtained. Soh's (1988) computation for the bifurcation problem for developing flow in a curved duct of square cross-section found the critical Dean number at which the second vortex pair develops to be 126.7. In their flow visualization downstream of a 180 deg bend of circular section, Cheng and Yuen (1987)observed the formation of the additional vortex pair at $De = 100$.

Flow visualization performed by Arnal et al. (1987) revealed the presence of unsteadiness occurring in a developing flow through a 180 deg bend of square cross section and curvature ratio $\beta = 6.7$. Cotton threads were placed on the inner and outer walls, and the Reynolds number was varied between 800 and 8100. The authors observed the first sign of unsteadiness

---

Contributed by the Fluids Engineering Division for publication in the JOURNAL OF FLUIDS ENGINEERING. Manuscript received by the Fluids Engineering Division June 15, 1991. Associate Technical Editor: Chih-Ming Ho.

at Re = 1710, along the outer wall in the second half of the bend. As the Reynolds number was increased the unsteadiness gradually moved upstream along the outer wall and developed in the second half of the bend along the inner wall. For 3280 < Re < 4000 unsteadiness was detected everywhere in the bend and the first evidence of intense turbulent fluctuations was observed at Re = 4000.

The same sort of instability has been observed by Tsuda and Ohba (1984) who investigated developing laminar flow in a 180 degree bend of square cross-section. The curvature ratio was $\beta = 19$ and the Reynolds number ranged between 670 and 1340. The authors found alternating high and low frequencies in the region contained between the centerline and the side walls, with frequencies ranging between 0 and 10 Hz.

The frequencies of the large scale oscillations observed by Arnal (1988) in the same geometry as in Arnal et al. (1987) were estimated to range between 0.026 and 0.46 Hz, and were found to develop first on the outer wall for 90 deg $< \theta <$ 180 deg. For low Reynolds number, the author linked the flow unsteadiness with the presence of Goertler vortices which develop as a result of a centrifugal instability on the outer wall.

The numerical calculation by Sankar et al. (1988) on the flow behavior through a coil of square cross section showed the development of a periodic oscillatory solution in the streamwise direction of the flow depending on the Dean number and the radius of curvature. The authors stated that for $R_c/D_h = 100$ and $D_e > 125$ an unstable four cell configuration is obtained, while for $R_c/D_h = 4$, the cell configuration obtained is stable to asymmetric perturbations. However, Winters (1984) showed that for $92 < D_e < 136$ the solution obtained is unstable.

Scarton et al. (1977) used a solution of neutrally buoyant methylene blue to visualize the flow in a developing curved pipe flow with a curvature ratio of 3.2 and a bend angle of 168 degrees. A uniform velocity profile was set at the inlet of the bend and the Reynolds number range investigated was $500 < R_e < 5700$. An additional pair of counter-rotating vortices was observed near the inner wall and the flow appeared to be unsteady in this region with the presence of bursts. The unsteadiness near the inner wall was attributed to the extra pair of vortices.

Stewartson et al. (1980) suggest that flow instability in curved pipes is caused by the boundary layer collision along the inner wall region. The authors solved the boundary layer equations for a developing laminar flow from the entrance of a curved pipe of circular cross section and showed that the streamwise component of the skin friction vanishes on the inner symmetry line at a distance $0.943\ a\beta^{-1/2}$ down the pipe from the entry section, where a is the pipe radius. A collision develops at this position between the side wall boundary layers as they approach the inner wall centerline. This problem was subsequently studied by Humphrey et al. (1985) for the case of a developing laminar flow in bends of circular cross section over a range of Dean number. The authors solved the Navier-Stokes equations numerically in their semi-elliptic form using a considerably finer mesh than earlier studies and adopting a more accurate third-order quadratic upwind differencing scheme. The axial wall shear stress predicted along the inner wall line of symmetry showed a minimum value which decreases gradually as De is raised. This minimum value occurs progressively at smaller values of the downstream location and approaches the behavior predicted by Stewartson et al. (1980), where the point of singularity is fixed. Beyond the point of minimum shear stress, Humphrey et al. predicted a damped oscillatory behavior with a growing amplitude as De is raised, this behavior is in striking contact with Stewartson's result where the shear stress increases sharply beyond the point of singularity with a monotonic approach to an asymptotic level.

A number of fundamental questions concerning flow instability and transition to turbulence in curved ducts remain unanswered. To shed further light on the problem, an experimental investigation was carried out in a 90 deg bend of rectangular cross section. The important nondimensional parameters affecting the flow instability in bends are the curvature ratio β, the duct aspect ratio δ and the flow Reynolds number Re; thus these parameters were varied in the experiments.

Experiment

The test section shown in Fig. 1 is a 90 deg bend with short upstream and downstream tangents all of rectangular cross section (15.24 cm × 30.48 cm). The hydraulic diameter is $D_h = 20.32$ cm, the mean radius of curvature is $R_c = 1.5D_h = 30.48$ cm, giving a curvature ratio $\beta = 3$. The whole section is constructed from transparent Plexiglas for optical accessibility. The test section is placed at the end of a blower wind tunnel. The lowest velocity obtained from the tunnel is 2.52 ± 0.1 m/s corresponding to a Reynolds number of 33,500. A double screen was placed at the outlet of the wind tunnel in order to reduce the velocity to a minimum value of 0.6 ± 0.02 m/s and allow investigations at lower Reynolds numbers. Such an arrangement gives a uniform velocity profile entering the bend with negligible boundary layers. A very clean flow entered the bend with a turbulence level of 0.18 percent, $1D_h$ upstream of the 0 deg plane at the center of the duct for Re = 15,000.

Hot wire anemometry was used for velocity measurements. The signal processing and data collection system were as reported by Johnson (1988) with a minor modification. The output signal from the bridge was linearized and then fed through a DISA 56N20 signal conditioner. Frequencies exceeding 60 Hz were eliminated. The signal was then digitized using an AI13 12 bit a-d converter manufactured by Interactive Inc., and stored in the memory of an Apple 2e microcomputer. The data collection rate was adjustable up to 20 kHz using a rapidly executable data collection program written in machine code. In the present application, a collection rate of 258 Hz was used, giving a sampling time of 31 sec. Each of 8192 data points were stored in 2 consecutive 8 bit memory locations. The computer was interfaced to a dual disk drive so data could

Nomenclature

a = width of the duct
b = height of the duct
D_h = hydraulic diameter of the duct, $2ab/(a+b)$
De = Dean number, $(D_h/2R_c)^{1/2}$ Re
f = nondimensional frequency, $\omega D_h/U_b$
R_c = mean radius of curvature of the duct
Re = Reynolds number, $\rho U_b D_h/\mu$
R^* = nondimensional radial position in a curved duct, $(r - r_i)/(r_o - r_i)$
r_i = inner wall radius in a curved duct
r_o = outer wall radius in a curved duct
U_b = bulk velocity
U_θ = tangential velocity
z = streamwise location in cartesian coordinate system
β = curvature ratio, $2R_c/D_h$
δ = duct aspect ratio, b/a
θ = streamwise angular location in the bend
ρ = fluid density
μ = dynamic viscosity
ω = frequency of the flow instability

be saved for subsequent analyses. Frequencies were obtained using a spectrum analyzer program. The mean velocities of the flow were taken directly from a digital voltmeter while the rms values were taken from a Disa rms unit. Signal time histories were taken from a transient recorder from which the signal could be plotted.

Experimental Methodology

All measurements were confined to the symmetry plane of the duct, at six streamwise locations ($-1D_h$, 0, 26, 49, 68 deg, $0.25D_h$) and were obtained for three Reynolds numbers. The probe was positioned manually and the data were taken at 19 radial locations for each streamwise location. In order to change the aspect ratio of the bend, the spanwise dimension of the duct was reduced using a flat plate which could be placed at any spanwise position. With the plate at the symmetry plane, a new curved duct was configured with $D_h = 12.19$ cm and $\beta = 5$.

Flow visualization experiments were performed in the bend to identify the flow unsteadiness. Two methods of visualizing the flow were used. In the first experiment, paraffin oil smoke was introduced upstream of the bend and a laser beam spread out in a sheet across the bend illuminating the smoke in the test planes. The smoke technique was effective and gave meaningful results only at low Reynolds numbers. In addition, flow visualization using cotton threads was performed in order to investigate high Re. Two long cotton threads of length such that they would not interfere were taped to the side walls with tufts attached to their free ends. The location of the threads which gave the most informative results were found by trial and error.

Experimental Uncertainties

The accuracy of the data is subject to various sources of uncertainty which are systematic and random. The accuracy of the mean and rms velocities is affected by the linearization process for the output signal from the bridge. The rms quantities are most affected in regions where the flow has a high level of unsteadiness. The introduction of the probe itself within the flow presents some disturbance which is very difficult to quantify. For the mean velocity the uncertainty was estimated to be as large as 5 percent while for the rms values the uncertainty was estimated to be 10 percent in regions with a high level of unsteadiness and around 7 percent in steadier regions. The probe was positioned manually to within ±0.3 mm.

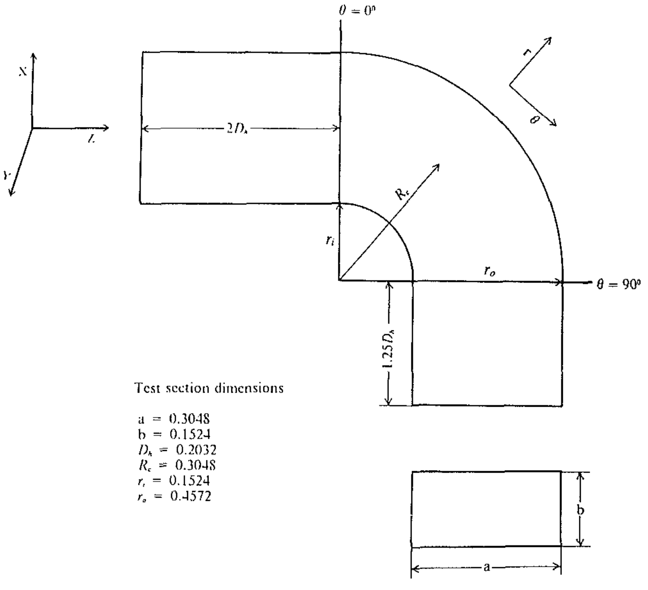

Fig. 1 Test section: defining coordinate systems, relevant notation and geometrical dimensions in meters

Results and Discussion

Streamwise-velocity profiles for the symmetry plane of the duct are shown in Fig. 2 at representative stations for three different Reynolds numbers. Uniform velocity profiles with very thin boundary layers are clearly observed at the upstream streamwise location $z = -1D_h$ for all Reynolds numbers. Additional data were taken in the region of interest near the inner wall of the duct.

As the flow enters the bend it accelerates near the inner wall and, as it travels around the bend, the boundary layers thicken gradually up to the 68 deg plane where the profiles show an inflection point and a rapid thickening occurs.

The rms velocities for the flow along the symmetry plane of the 90 deg bend are normalized by the bulk velocity and presented in Fig. 3(*a*)-3(*c*) in the form of contour plots. Upstream of the bend the flow is steady. The highest fluctuation levels are observed near the inner wall with a peak close to the 68 deg measurement plane.

Around Re = 7000, the flow is steady in the bend. The instability appears near the inner wall and strengthens as the Reynolds number is increased.

Particular attention was given to the inner region of the bend where the strongest instabilities were observed.

Dependence of the Flow Instability on the Reynolds Number. Time histories and spectra, taken at $\theta = 68$ deg and $R^* = 0.18$ as a function of Re, showed the nature and development of the flow instability.

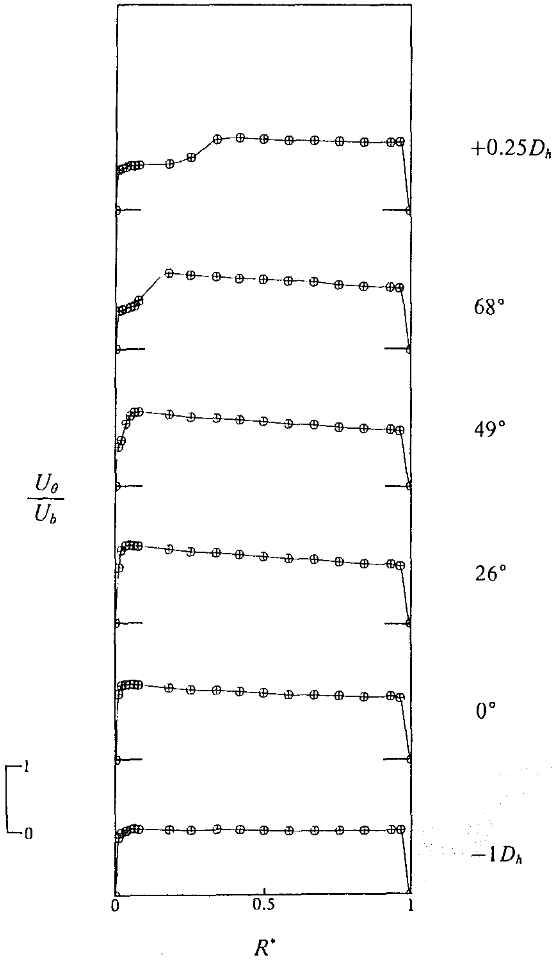

Fig. 2(*a*)

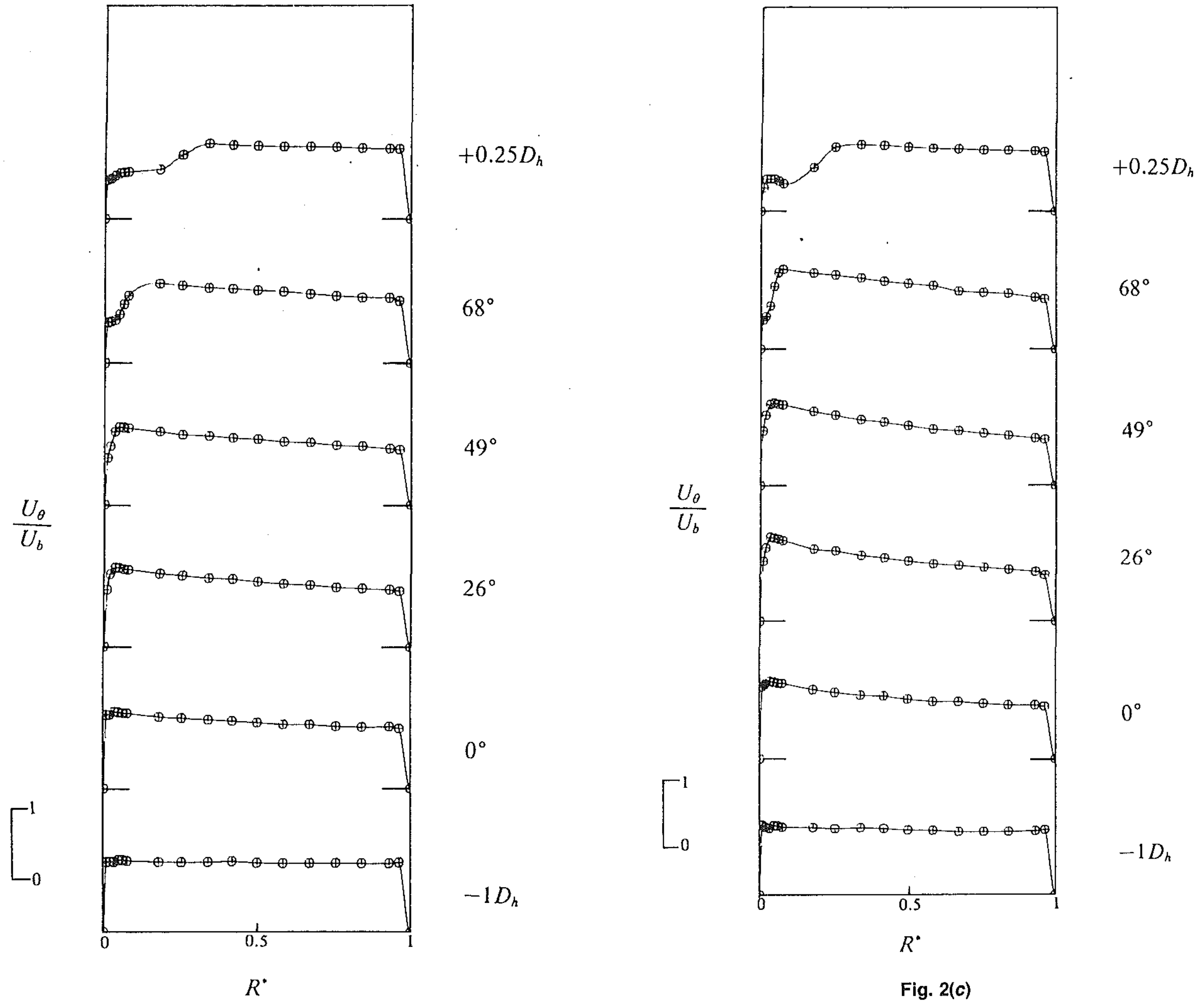

Fig. 2(*b*)

Fig. 2(*c*)

Fig. 2 Mean tangential (streamwise) component of velocity as a function of radius along the symmetry plane of the curved duct at different streamwise locations. (*a*) Re = 15,000; (*b*) 24,000; (*c*) 42,000. Uncertainties: R^* ± 0.01, U_θ/U_b ± 0.062.

Below Re = 24,000 the flow only exhibited very low fluctuation levels. At Re = 24,000 a regular oscillation of a large scale character was observed having a frequency $\omega \approx 25$ Hz corresponding to a nondimensional frequency f of 1.22. The frequency measured by Arnal (1988) was very low, while the one found by Tsuda and Ohba (1985) ranged between 0 and 10 Hz. The differences in the measured frequencies can be related to the differences in curvature ratios. As the Reynolds number is increased the oscillatory motion is amplified until it reaches its maximum amplitude around Re = 42,000; see Fig. 4. Above this value of Re; as is shown in Fig. 5, high frequencies are superimposed on the peaks of the low frequency oscillation; as the flow undergoes transition. These high frequencies amplify with increasing Re until they dominate around Re = 64,000. During this transition the low frequency oscillation weakens in amplitude and increases slightly in frequency.

Such unsteadiness is purely an effect of curvature and is probably due, as suggested by Stewartson et al. (1980), to the effect of the side wall boundary layers colliding at the inner centerline of the bend. This leads to low energy fluid being forced away from the wall and the establishment of an unstable gradient of total pressure which decreases with distance from the wall. Thus, two counter-rotating vortices are developed which carry this low energy fluid back to the wall. The instability arises if there is any slight imbalance in the magnitude of the two vortices, as one will then tend to grow at the expense of the other. However, the stronger vortex will remove fluid from the boundary layer in its half of the passage and hence will eventually start to weaken again. Meanwhile, the boundary layer in the second half of the passage will have thickened, hence the weaker vortex will strengthen once more. This phenomenon is clearly observed in the flow visualization performed in the bend with $\beta = 5$ using the smoke technique. Figure 8 shows the cross-stream circulation of the flow at Re = 4770 in the form of two vortices in the same way as calculated by Dean (1928a). The sequence of photographs in Fig. 8(*b*)–8(*e*) confirms Stewartson's (1980) suggestion, showing the interaction at Re = 5700 of the side wall boundary layers at the inner centerline, and the development of a jet flow directed from the inner wall toward the outer wall of the bend. The interaction observed could be the origin of the flow unsteadiness measured in such geometries. Moreover, the effect of a highly distorted velocity profile cannot be ruled out since it is a very important factor in the contribution to the development of unsteadiness.

In the cotton threads visualization method used in the bend with $\beta = 3$, the threads were steady up to a Reynolds number of 24,000, and then started to oscillate until Re = 56,000 when

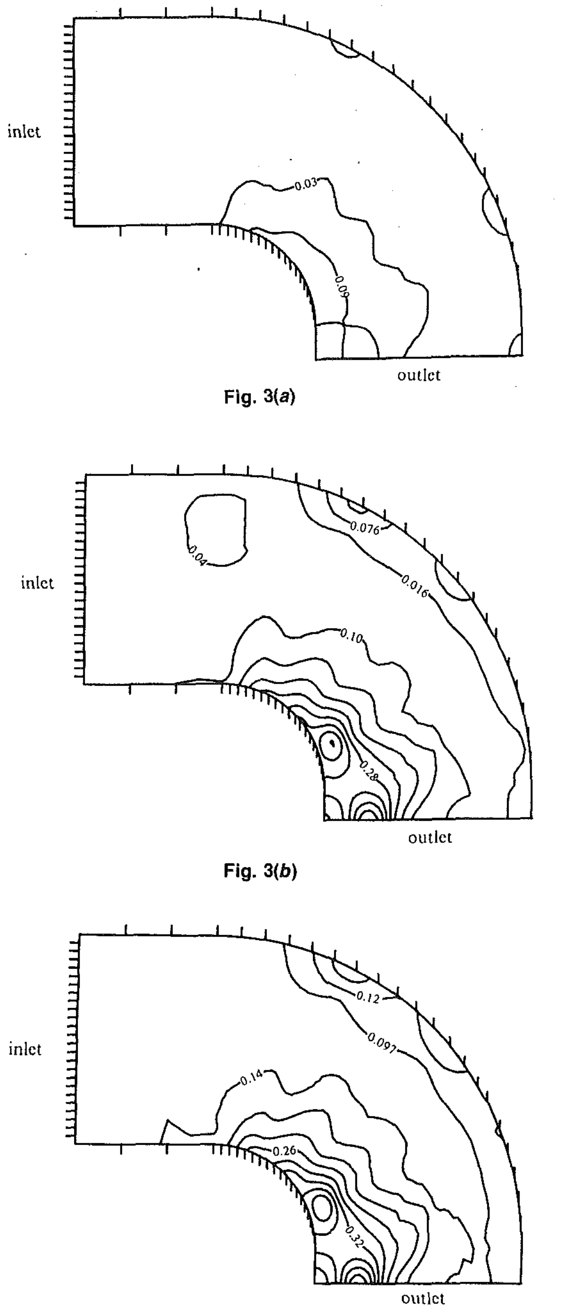

Fig. 3(*a*)

Fig. 3(*b*)

Fig. 3(*c*)

Fig. 3 Contour plots of the rms of the tangential (streamwise) component of velocity on the symmetry plane of the curved duct. (*a*) Re = 15,000; (*b*) 24,000; (*c*) 42,000. Uncertainties: U_θ/U_b ± 0.03 near the inner curved wall and ±0.008 elsewhere.

they clearly start to rotate depicting two counter rotating vortices at the inner side of the bend as observed by Scarton et al. (1977), see Fig. 8(*f*).

Dependence of the Flow Instability on the Streamwise Position. Measurements were made at two stations upstream of the 68 deg plane. The Reynolds number was kept at 42,000 and $R^* = 0.18$, since these values showed the maximum fluctuation amplitude at the 68 deg plane. At the 49 deg plane, the low frequency oscillation was present at lower amplitude than at the 68 deg plane; but at the 26 deg plane the flow was steady again. It appears that, the flow instability is generated after the 26 deg plane and amplifies as the flow travels downstream. The instability could travel from the upstream tangent towards the inner region via the center or the outer regions of the duct. To investigate this, measurements were made as a function of R^* for Re = 42,000 at the 26 deg plane. The results are discussed below.

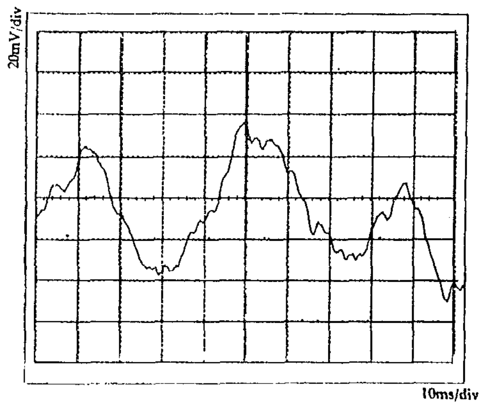

Time history

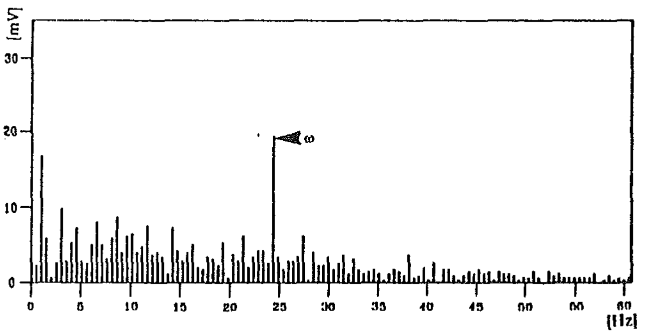

Spectrum

Fig. 4 Time record and spectrum at R^* = 0.18, and θ = 68 deg for the curved duct with β = 3 and Re = 42,000. Uncertainties: ω ± 0.5 Hz, amplitude ±8 mv.

Dependence of the Flow Instability on the Radial Position. The flow unsteadiness is stronger near the inner wall of the bend where it originates, and decays gradually toward the center of the bend.

Time histories and spectra taken across the 26 deg plane for Re = 42,000, show a steady flow with no evidence of oscillatory motion. Therefore, flow unsteadiness is definitely generated in the bend downstream of the 26 deg plane and is not an instability entering through the inlet plane. The angle where the flow instability first appears depends on the Reynolds number. A further set of experimental data was taken at $\theta = 26$ deg and $R^* = 0.18$. As it is shown in Fig. 6, when Re was raised to a value of 45,000, the same frequency appeared again. With a further increase in Re, the high frequencies emerge and dominate again in a similar way to the observation made at the 68 deg station. This observation supports the finding by Humphrey et al. (1985) who predicted the minimum shear stress along the inner line of symmetry to occur progressively at smaller values of the downstream location as the Dean number was raised.

It can be concluded that while the frequency of the instability which develops in the curved duct does not depend on the Reynolds number, the streamwise position where the instability first develops does show such a dependence.

Dependence of the Flow Instability on the Curvature Ratio. In order to investigate the dependence of the frequency of the flow instability on the bend geometrical parameters, the

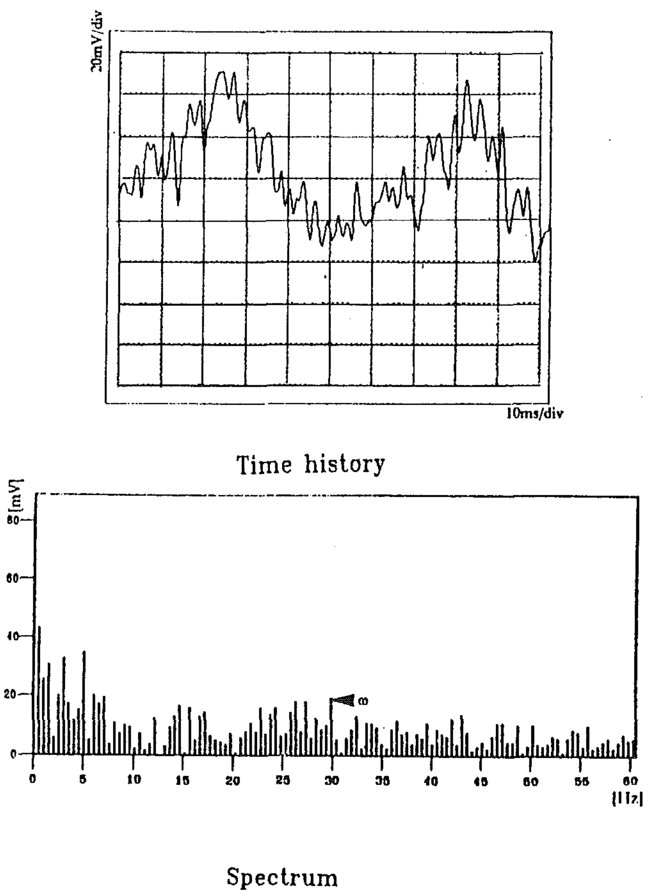

Fig. 5 Time record and spectrum at $R^* = 0.18$, and $\theta = 68$ deg for the curved duct with $\beta = 3$ and Re = 56,000. Uncertainties: $\omega \pm 0.5$ Hz, amplitude = ±22 mv.

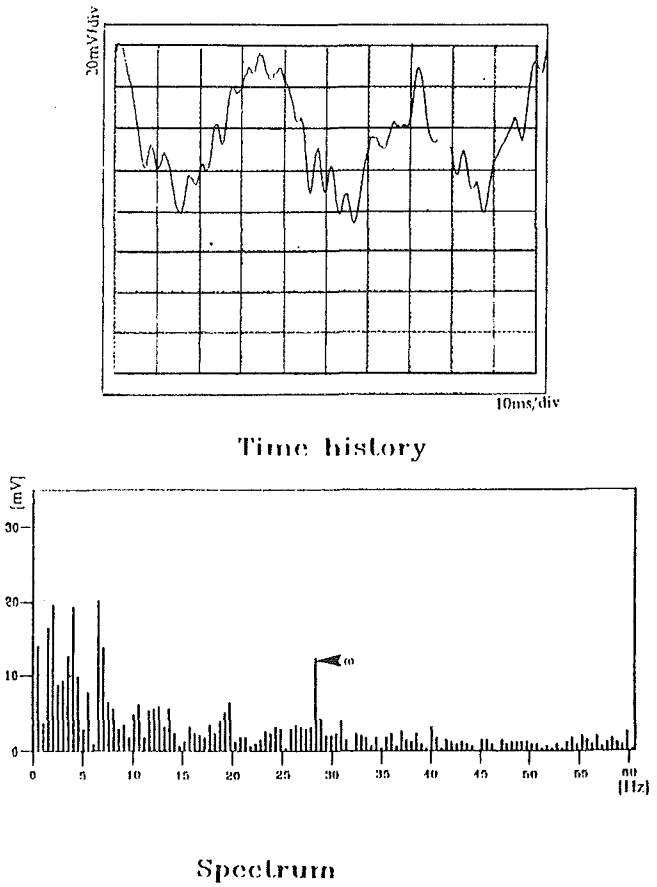

Fig. 6 Time record and spectrum at $R^* = 0.18$, and $\theta = 26$ deg for the curved duct with $\beta = 3$ and Re = 45,000. Uncertainties: $\omega \pm 0.5$ Hz, amplitude ±8 mv.

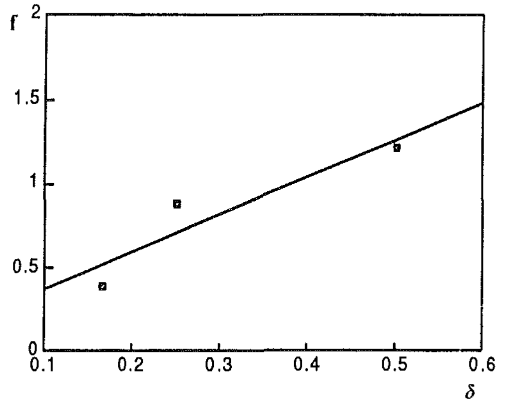

Fig. 7 Variation of the flow instability dimensionless frequency with the curved duct aspect ratio. Straight line corresponds to $f = 2.22\delta + 0.146$.

Table 1 Frequency ranges measured as a function of curved duct parameters

β	δ	R^*	ω [Hz]	range of f	range of Re
3	0.5	0.18	25	1.22–2.85	24000–56000
5	0.25	0.10	13	0.88–1.60	8300–15000
7	0.166	0.078	8.5	0.39–0.86	5140–11370

spanwise dimension of the duct was reduced by half to give a new aspect ratio δ of 0.25, hence a new curvature ratio $\beta = 5$. Experiments similar to those described above were performed with the new geometry, and the results are discussed below.

In this case, the flow instability develops closer to the inner wall and at a lower Reynolds number than for $\beta = 3$. The first evidence of flow unsteadiness appears at the 68 degree plane for Re = 8300 at $R^* = 0.10$. In this case the frequency of the flow oscillation is around 13 Hz accompanied by a lower frequency of 6 ± 1 Hz. This correspond to a non-dimensional frequency of 0.88. In their LDV measurements Tsuda and Ohba (1984) found a peak at 3 Hz for a curvature ratio of 19. As the Reynolds number is increased further, the low frequency oscillation is amplified in the same fashion as for $\beta = 3$, until at a value of Re = 11,500 high frequency fluctuations appear superimposed on the large scale oscillation. At Re = 15,000, the high frequency fluctuations dominate with the appearance of strong peaks having a frequency corresponding to the large scale oscillation. The appearance of such strong peaks agrees with the flow visualization performed by Scarton et al. (1977) who observed this activity near the inner wall of a curved pipe with $\beta = 3.2$.

For Re = 11,500 and $R^* = 0.10$, for which the low scale oscillation has a maximum amplitude, the flow is very steady at the 49 deg plane. At this streamwise position, the unsteadiness appears closer to the inner wall at $R^* = 0.06$ for Re = 5700, and develops in the same way as at the 68 degree station.

A third set of similar measurements was performed with the plate at one third of the spanwise dimension of the duct, giving a third aspect ratio δ of 0.166 (i.e., a curvature ratio $\beta = 7$). Here again, a large scale oscillatory motion appears and develops similarly as in the two previous cases. A fundamental frequency of 8.5 ± 0.5 Hz corresponding to a minimum non-dimensional frequency of 0.39 appeared at the 68 deg plane and $R^* = 0.078$ for a lower value of Re than previously.

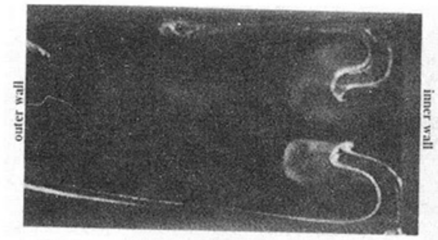

8-a Re=4770, $\beta = 5$, $\theta = 49°$.

8-d Re=5700, $\beta = 5$, $\theta = 49°$.

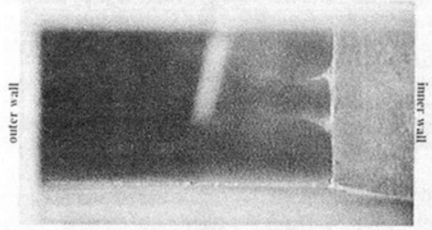

8-b Re=5700, $\beta = 5$, $\theta = 49°$.

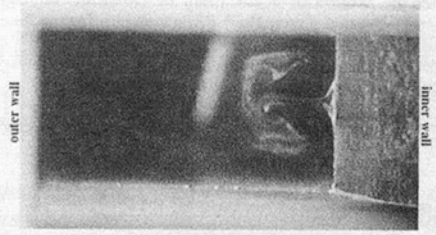

8-e Re=5700, $\beta = 5$, $\theta = 49°$.

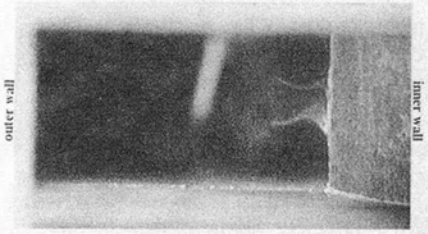

8-c Re=5700, $\beta = 5$, $\theta = 49°$.

8-f Re=56000, $\beta = 3$, $\theta = 49°$.

Fig. 8 Flow visualization in the bend using the laser sheet (*a*, *b*, *c*, *d*, *e*) and the cotton threads (*f*)

The fundamental frequencies of the flow instabilities measured in the bend with different curvature ratios are summarized in Table 1 and Fig. 7 shows a linear variation of the minimum nondimensional frequency as a function of the duct aspect ratio.

Conclusions

The flow instability in a 90 deg curved duct of rectangular cross section has been studied experimentally. The main goal of the study was to understand the origin and the development of the unsteady behavior in such geometries. From hot wire measurement and smoke flow visualization it is understood that the main contributing factors to the generation of flow unsteadiness in curved ducts is the strongly distorted velocity profile caused by the imbalance between the centrifugal forces and pressure gradient, as well as the collision between the side wall boundary layers at the inner centerline. From the experimental work it can be concluded that:

1. A low frequency oscillation of a nonturbulent nature arises in the bend near the inner radius wall where the secondary flows from the side wall boundary layers collide.
2. The streamwise position where the instability is first generated depends on the flow Reynolds number, while its frequency depends on the bend curvature ratio.
3. As the curvature ratio of the bend increases, the flow instability appears at smaller radial positions for lower Reynolds numbers.

References

Arnal, M., 1988, "Investigation of Developing Laminar and Turbulent Flow in Curved Ducts," Ph.D. thesis, University of California at Berkeley.

Arnal, M., Firmino, F., Humphrey, J. A. C., 1987, "Unsteady Motion and Transition to Turbulence in Developing Curved Duct Flow," *Proceedings of the Sixth Symposium on Turbulent Shear Flows*, Toulouse, France, Sept. 7–9.

Chang, S. M., Humphrey, J. A. C., and Modavi, A., 1983, "Turbulent Flow in a Strongly Curved U-Bend and Downstream Tangent of Square Cross-Section," *PhysicoChemical Hydrodynamics*, Vol. 4, p. 243.

Cheng, K. C., Lin, R. C., and Ou, J. W., 1976, "Fully Developed Laminar Flow in Curved Rectangular Channels," ASME JOURNAL OF FLUIDS ENGINEERING, Vol. 98, p. 41.

Cheng, K. C., and Yuen, F. P., 1987, "Flow Visualization Studies of Secondary Flow Patterns in Straight Tubes Downstream of a 180 Deg Bend and in Isothermally Heated Horizontal Tubes," *Journal of Heat Transfer*, Vol. 109, p. 49.

Cumming, H. G., 1952, "The Secondary Flow in Curved Pipes," Aero. Res. Council, Reports and Memoranda No. 2880, Ministry of Supply, London.

Dean, W. R., 1928a, "The Streamline Motion of Fluid in a Curved Pipe," *Philosophical Magazine*, Vol. 5, p. 673.

Dean, W. R., 1928b, "Fluid Motion in a Curved Channel," *Proceedings of the Royal Society*, Series A 121, p. 402.

Eustice, J., 1911, "Experiments on Streamline Motion in Curved Pipes," *Proceedings of the Royal Society*, Series A 85, p. 119.

Ghia, K. N., and Sokhey, J. S., 1977, "Laminar Incompressible Viscous Flow in Curved Ducts of Regular Cross-Sections," ASME JOURNAL OF FLUIDS ENGINEERING, Vol. 99, p. 640.

Hille, P., Vehrenkamp, R., and Schulz-Dubois, E. O., 1985, "The Development and Structure of Primary and Secondary Flow in a Curved Square Duct," *Journal of Fluid Mechanics*, Vol. 151, p. 219.

Humphrey, J. A. C., 1978, "Numerical Calculation of Developing Laminar Flow in Pipes of Arbitrary Curvature Radius," *The Canadian Journal of Chemical Engineering*, Vol. 56, p. 151.

Humphrey, J. A. C., Iacovides, H., and Launder, B. E., 1985, "Some Numerical Experiments on Developing Flow in Circular-Sectioned Bends," *Journal of Fluid Mechanics*, Vol. 154, p. 357.

Humphrey, J. A. C., Taylor, A. M. K., and Whitelaw, J. H., 1977, "Laminar Flow in a Square Duct of Strong Curvature," *Journal of Fluid Mechanics*, Vol. 83, p. 509.

Hur, N., Thangam, S., and Speziale, C. G., 1990, "Numerical Study of Turbulent Secondary Flows in Curved Ducts," ASME JOURNAL OF FLUIDS ENGINEERING, Vol. 112, p. 205.

Johnson, M. W., 1988, "Boundary Layer Transition Measurements Using a Hot Wire Anemometer and Digital Signal Processing," Report FM/122/88 Mech. Eng. Dept., The University of Liverpool, England.

Joseph, B., Smith, E. P., and Adler, R. J., 1975, "Numerical Treatment of Laminar Flow in Helically-Coiled Tubes," *American Institute of Chemical Engineers Journal*, Vol. 21, p. 965.

Pratap, V. S., and Spalding, D. B., 1975, "Numerical Computation of the Flow in Curved Ducts," *Aeronautical Quarterly*, Vol. 26, p. 219.

Reynolds, O., 1883, "On the Experimental Investigation of the Circumstances Which Determine Whether the Motion of Water Shall be Direct or Sinuous, and the Law of Resistance in Parallel Channels," *Philosophical Transactions of the Royal Society*, Vol. 174, p. 935.

Sankar, S. R., Nandakumar, K., and Masliyah, J. H., 1988, "Oscillatory Flow in Coiled Square Ducts," *Physics of Fluids*, Vol. 31, p. 1358.

Scarton, H. A., Shah, M. P., and Tsapogas, M. J., 1977, "Relationship of the Spatial Evolution of Secondary Flow in Curved Tubes to the Aortic Arch," in *Mechanics in Engineering*, ASCE-EMD, May 26–28, 1976, University of Waterloo Press.

Soh, W. Y., 1988, "Developing Fluid Flow in a Curved Duct of Square Cross-Section and its Fully Developed Dual Solutions," *Journal of Fluid Mechanics*, Vol. 188, p. 337.

Stewartson, K., Cebeci, Y., and Chang, K. C., 1980, "A Boundary Layer Collision in a Curved Duct," *Quarterly Journal of Mechanics and Applied Mathematics*, Vol. 33, p. 59.

Taylor, G. I., 1929, "The Criterion for Turbulence in Curved Pipes," *Proceedings of the Royal Society*, Series A 124, p. 243.

Tsuda, N., and Ohba, K., 1984, "Laser Doppler Measurement of Developing Laminar Flow in a Moderately Curved U-Bend of Square Cross-Section," *Proceedings of the Second Osaka Symposium on Flow Measuring Techniques*, July 13, Osaka, Japan.

Wattendorf, F. L., 1935, "A Study on the Effect of Curvature on Fully Developed Turbulent Flow," *Proceedings of the Royal Society*, Series A 148, p. 565.

Winters, K. H., 1987, "A Bifurcation Study of Laminar Flow in a Curved Tube of Rectangular Cross-Section," *Journal of Fluid Mechanics*, Vol. 180, p. 343.

Yukimaru Shimizu
Professor,
Department of Mechanical Engineering,
Mie University,
Tsu-shi, Mie-ken, 514 Japan

Yoshiki Futaki
Yamaha Co. Ltd,
Boat Ship Factory,
Hamamatsu-shi, Japan

C. Samuel Martin
Professor,
School of Civil Engineering,
Georgia Institute of Technology,
Atlanta, GA 30332

Secondary Flow and Hydraulic Losses Within Sinuous Conduits of Rectangular Cross Section

This paper describes the relationship between hydraulic losses and secondary flow within sinuous conduits with complicated bends. It has been found that the nature of secondary flow present in the bends is quite sensitive to the geometric configuration of the bend and the actual aspect ratio of the conduit section. Indeed, many different secondary flow patterns have been found to exist as the bend geometry is altered. A wide range of experiments has been conducted for various aspect ratios of a rectangular conduit with different curvatures.

1 Introduction

For more than a century, hydraulic engineers and researchers have recognized the peculiar nature of flow around a pipe bend, as noted in the review by Berger et al. (1983). Indeed, there has been considerable research, albeit principally for single-bend geometries. For laminar flow around curved rectangular ducts, recent investigations have been conducted by Cheng et al. (1974), Humphrey et al. (1977), Hille et al. (1985), and Thangam and Hur (1990). Experimental studies into the nature of turbulent flow were performed by Melling and Whitelaw (1974) and Humphrey et al. (1981). Numerical analysis of turbulent flow in bends by Nakayama et al. (1983) and Hur et al. (1990) should also be cited. The more complicated single-bend flow afforded by a turbine draft tube has been approached numerically by Vu and Shyy (1990).

Investigations on the nature of the flow in double- or triple-bend flow have been limited to those by Melling and Whitelaw (1974) and collection of papers by the principal author, Murakami and Shimizu (1969, 1973), Shimizu et al. (1982, 1985, 1986a, 1986b). Studies on flow in multiple-bend conduits have been quite meager, solely conducted by the authors Murakami and Shimizu (1969, 1973) and Shimizu et al. (1982, 1985). In all of these papers, there has been only limited attention directed towards the nature of the flow through the sinuous conduits, with the exception of measurements and correlations of such gross parameters as overall head loss and heat transfer. Detailed investigations into secondary flow phenomena in more complicated geometries have been particularly meager.

This paper emphasizes the relationship between the hydraulic losses and the secondary flow in conduits with complicated bends—to be referred to as sinuous conduits. It has been found that the nature of secondary flow present in the bends is quite sensitive to the configuration of the bend and the cross-section shape of the conduit. Indeed, many different secondary flow patterns can exists as the bend geometry is altered. Using rectangular cross sections, measurements of hydraulic losses and descriptions of the secondary flow patterns have been performed. Experiments were conducted to determine the sensitivity of these parameters to the aspect ratio of the rectangular cross section as well as to the curvature ratios of the respective bends. The experimental results clearly indicate that the very complicated secondary flow occurring in sinuous conduits with rectangular cross section can not be deduced from corresponding results obtained in sinuous pipes with circular cross section.

2 Definition of Losses and Secondary Velocities

The total head loss associated with the entire four-bend sinuous conduit drawn in Fig. 1 is defined in a conventional manner. In terms of the cross-sectional average velocity in the conduit V_m the head loss coefficient for the bend ζ_n is defined as

$$(P_u - P_d)/\rho g = [\lambda(L/D) + \zeta_n](V_m^2/2g) \tag{1}$$

where P_u and P_d are the upstream and downstream pressures measured at locations of 8 and 80 diameters, respectively (see Fig. 1). The total length $L = L_u + L_d$ for the conduit with mean hydraulic diameter D and Darcy-Weisbach resistance coefficient λ. For a sinuous conduit system of n bends, for each of which the head loss coefficient is ζ_1 a mutual interference head loss coefficient m is defined as

$$m = \zeta_n / n\zeta_1 \tag{2}$$

From Euler's equation the pressure difference across an individual bend is expressed in terms of the centrifugal force as a nondimensional integral

$$\Delta P_w = \left[\int (V^2/r)dr\right] / (V_m^2/r_w^2) \tag{3}$$

3 Experimental Apparatus

The bend loss and the velocity distribution were measured

Contributed by the Fluids Engineering Division for publication in the JOURNAL OF FLUIDS ENGINEERING. Manuscript received by the Fluids Engineering Division October 24, 1990. Associate Technical Editor: F. T. Dodge.

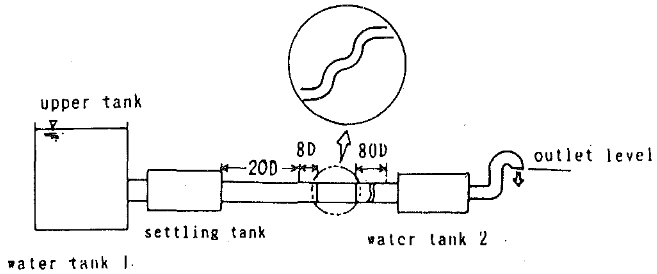

Fig. 1(*a*) Schematic diagram of experimental apparatus

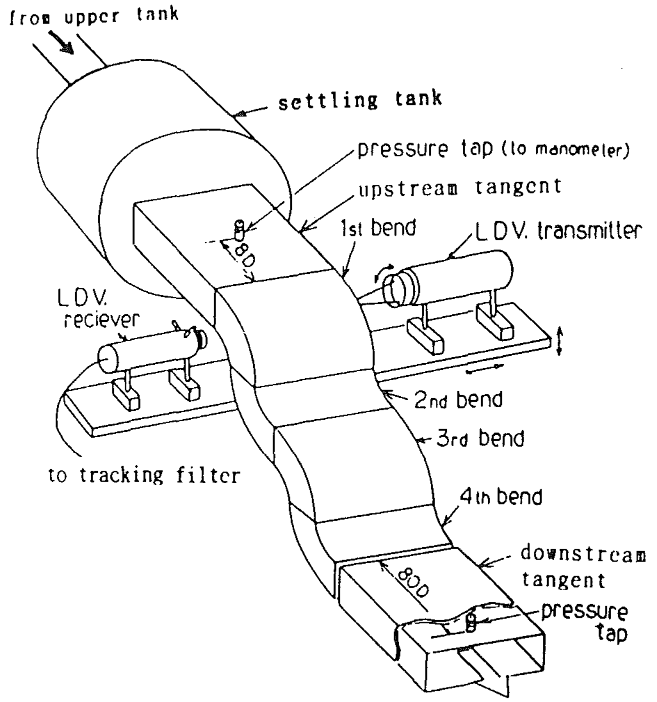

Fig. 1(*b*) Sinuous conduit of rectangular cross section and LDV setup

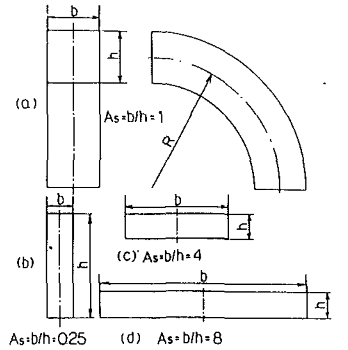

See Table 1 for list of bend dimensions tested

Fig. 2(*a*) Definition of bend geometry

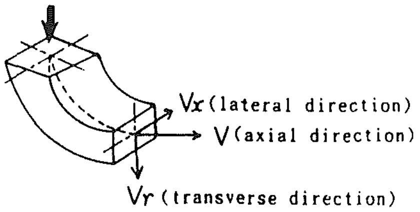

Fig. 2(*b*) Definition of coordinate system

Table 1 Dimensions of bend elements tested

As=b/h	h (mm)	b (mm)	D (mm)	R/r_w	l (mm)	cross-sec. area (cm²)
0.25	131.6	32.9	52.6	6	247.8	43.29
1	52.6	52.6	52.6	6	247.8	27.67
4	32.9	131.6	52.6	6	247.8	43.29
8	16.5	131.6	29.3	6.1	141.4	21.65
circular	—	—	53.2	6	252.1	22.22

$D(=2r_w)$: Hydraulic mean diameter

by the apparatus shown in Fig. 1(*a*) and (*b*). To reduce the uncertainty for the head loss coefficient and velocity, the water level in the upper tank shown in Fig. 1(*a*) was maintained constant by constant attention, and the outlet of the pipe was fixed to suppress vibration. The flow rate was controlled by the difference between upper and lower reservoir levels. The detailed geometric features of each bend are shown in Fig. 2. Eight different configurations of the four-bend layout were tested. For individual bend angles β_0 equal to 90 and 180 deg cross-sectional aspect ratios of 1/4, 1, 4, and 8 comprised the

Nomenclature

$As = b/h$ = aspect ratio of conduit cross section
b = width of rectangular conduit
$D = 2r_w$ = mean hydraulic diameter
g = gravitational acceleration
h = height of rectangular conduit
L = total length of conduit
L_d = length of conduit to downstream pressure tap from last bend element
L_u = length of conduit to upstream pressure tap from first bend element
m = mutual interference coefficient of bends defined by Eq. (2)
n = number of bend elements
N = bend number
P_d = downstream pressure at $L_d = 80D$
P_u = upstream pressure at $L_u = 8D$
ΔP_w = nondimensional pressure difference between inner and outer conduit walls as determined by Eq. (3)
R = radius of conduit curvature
$Re = V_m D/\nu$ = Reynolds number based on hydraulic diameter
r_w = mean hydraulic radius
V = axial velocity component
V_m = mean axial velocity in conduit
V_r = radial velocity component of secondary flow as determined by Eq. (4)
v' = axial turbulence intensity Eq. (5); $v_r'^2 \simeq v_x'^2 \simeq 0$
β = angle through individual bend element
β_0 = total angle of individual bend element
γ = specific weight of fluid
λ = Darcy-Weisbach resistance coefficient
ζ_n = total bend loss coefficient as defined by Eq. (1)

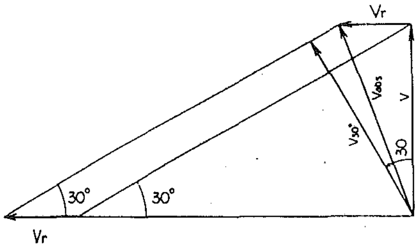

Fig. 3(*a*) Vector diagram utilized to compute secondary flow velocities from Eq. (4)

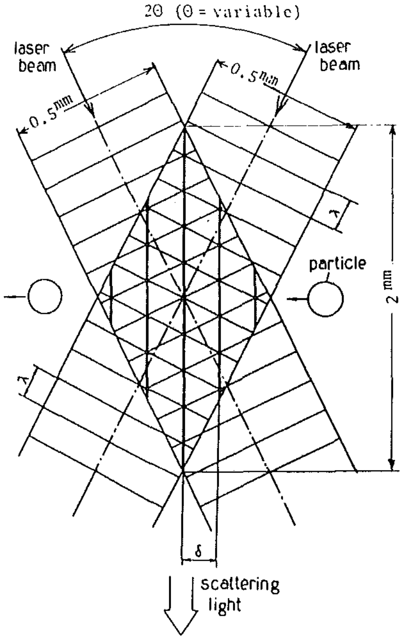

Fig. 3(*b*) Cross section of two laser beams

eight geometrical setups. The experiment was carried out on Reynolds number, $\mathrm{Re} = V_m D/\nu \simeq 10^5$ ($V_m \simeq 2 \sim 3$ m/s).

The velocity distributions in the bends were determined by means of a two-component laser Doppler velocimeter (LDV). By using two laser beams in a single plane that could be rotated 30°, the two velocity components can be determined as follows with reference to Fig. 3(*a*). The secondary velocity component of the radial velocity is given by

$$V_r = (V_{30}\mathrm{deg}/\sin 30\ \mathrm{deg}) - (V/\tan 30\ \mathrm{deg}) \qquad (4)$$

where V is the axial velocity component.

The rectangular fringe volume generated by the laser beams is 0.5 mm × 0.5 mm × 2 mm in size (see Fig. 3(*b*)). The seeding material consisted of aluminum powder mixed with alcohol. This mixture of clear alcohol and aluminum particles was poured into the flowing water, providing a quite effective seeding technique for the LDV. The cross section of two laser beams was rotated 30 deg because of convenience and ease of calculation.

As shown in Fig. 4, flow visualization was accomplished by utilizing small air bubbles and cotton tufts (about 5 mm). Compressed air was admitted upstream of the bend on opposite walls through 0.3 mm diameter openings. By proper lighting and back ground coloring and reduction of light refraction, photography of air bubble trajectory and tuft orientation was accomplished. This technique only allowed the investigation of flow separation and secondary flow patterns in the bends.

4 Experimental Results and Analysis

4.1 Hydraulic Losses. All tests were conducted for Reynolds numbers $\mathrm{Re} = V_m D/\nu \simeq 10^5$ ($V_m \simeq 2 \sim 3$ m/s). The results for the head-loss characteristics of the multiple-bend conduits are shown in Fig. 5 in terms of the total head-loss coefficient ζ_n defined in Eq. (1). The ratio of ζ_n to a single bend loss coefficient ζ_1 is correlated with the number of bends n for ($1 \le n \le 6$) bend angles $\beta_0 = 90$ and 180 deg, and for four aspect ratios ($b/h = 1/4$, 1, 4, and 8). The ratio ζ_n/ζ_1 for all four aspect ratios of the rectangular conduit is greater than that for a circular pipe for both 90 and 180 deg bend angles, Shimizu (1982). Six numbers of 90 deg bends, $n = 6$, are used in the experiment.

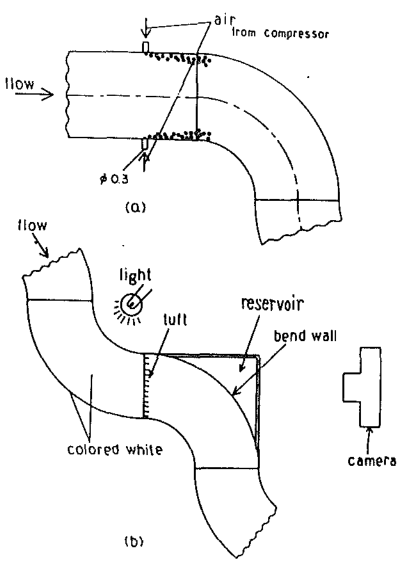

Fig. 4(*a*) Air bubble injection

Fig. 4(*b*) Use of cotton tuft

Fig. 4 Flow visualization techniques

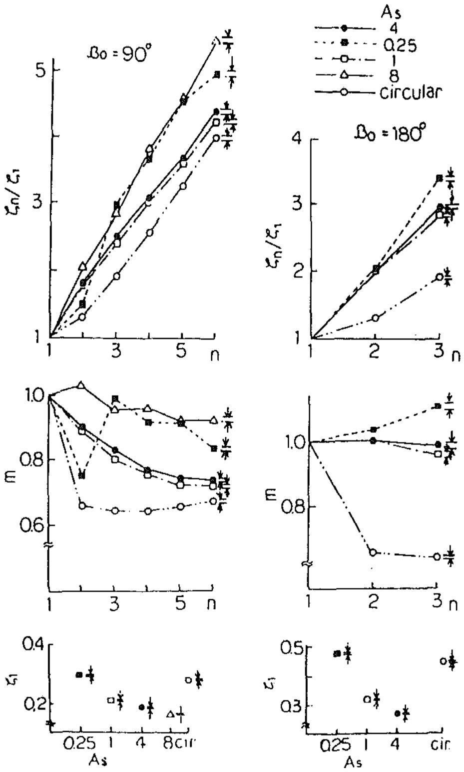

Fig. 5 Variation of loss coefficient ζ_n/ζ_1 and mutual interference coefficient m with number of bends n. Correlation of single bend loss coefficient ζ_1 with b/h. $\mathrm{Re} \simeq 10^5$ ($V_m \simeq 2 \sim 3$ m/s). (Uncertainty estimates: $\zeta_1 = 0.4 \pm 0.002$, $\zeta_n/\zeta_1 = 4.0 \pm 0.04$, $m = 1.0 \pm 0.01$ and $b/h = 1.0 \pm 0.01$)

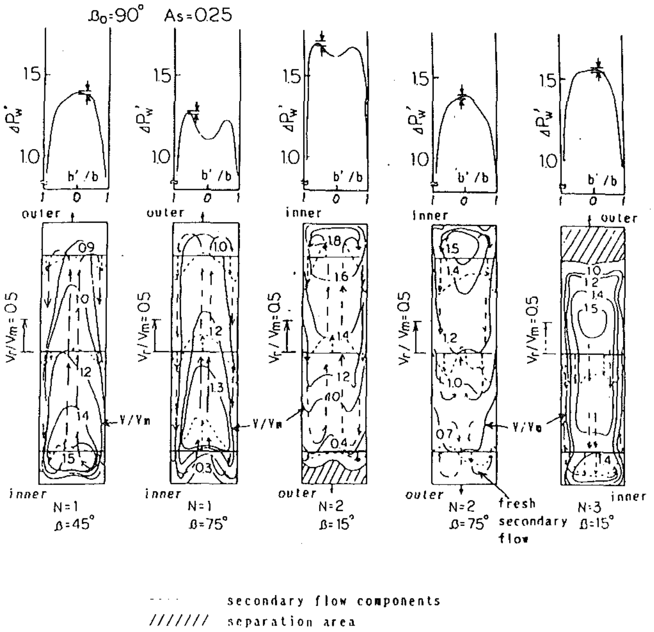

Fig. 6 Relationship between velocity distribution as measured by LDV and pressure difference. The velocity distribution was measured on seven cross stream planes. [$A_s = 0.25$ ($b/h = 1/4$) and $\beta_0 = 90$ deg] (Uncertainty estimates: $V/V_m = 1.5 \pm 0.015$, $V_r/V_m = 1.0 \pm 0.01$, and $\Delta P_w' = 1.5 \pm 0.015$)

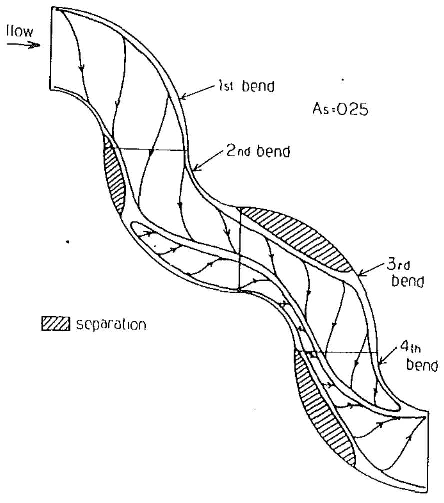

Fig. 7 Secondary flow pattern in sinuous conduit [$A_s = 0.25$ ($b/h = 1/4$) and $\beta_0 = 90$ deg]

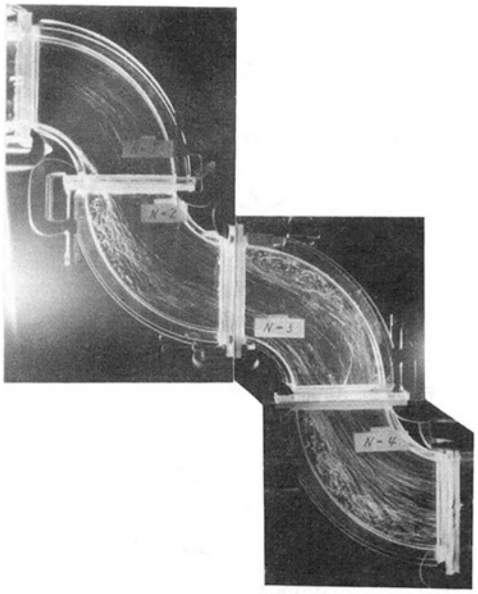

Fig. 8 View of flow pattern with air bubble trajectory method [$A_s = 0.25$ ($b/h = 1/4$) and $\beta_0 = 90$ deg]

For aspect ratios $b/h = 1$ and 4, the correlations of ζ_n/ζ_1 versus number of bends n are nearly identical. Curiously, the same conclusion—but with higher losses—can be drawn for the aspect ratios of 1/4 and 8. There is a tendency for the normalized loss coefficient to increase as n increases from 2 to 3 for $b/h = 1/4$, and for the circular pipe data.

The mutual interference coefficient m as defined in Eq. (2) would yield a value of unity if there were no bend interference and the losses per bend were identical. As shown by Fig. 5, that bends with aspect ratios $b/h = 1$ and 4 and $\beta_0 = 90$ deg indicate a gradual decrease in the parameter m as the number of bends increases. For these two geometries m appears to approach an asymptotic value as n attains a value of 6. In contrast, for a circular pipe there is an abrupt drop from $n = 1$ to $n = 2$, followed by a gradual increase. For $b/h = 1/4$ there is large change in m, while for $b/h = 8$ the value of m remains nearly constant for $\beta_0 = 90$ deg. A complete explanation of these trends is given in the section on the results of flow visualization.

An inspection of the results in Fig. 5 reveals that the general tendency of the correlation curves for $\beta_0 = 180$ deg is similar to that just discussed for $\beta_0 = 90$ deg. For the three rectangular conduits tested ($b/h = 1/4$, 1, and 4) the results for ζ_n/ζ_1 and m are nearly identical. Indeed, the mutual interference factor m is not far from unity for $b/h = 1$ and 4 for $\beta_0 = 180$ deg. Interestingly, the mutual interference factor m is greater than unity for $b/h = 1/4$, in contrast to very low values for the circular pipe. For purposes of comparison, plots of the head-loss coefficient ζ_1 for a single bend are also presented in Fig. 5. Due to quite large separation (see Figs. 6, 7, and 8) at the corners of the bends, ζ_1 is largest for $b/h = 1/4$ for rectangular cross sections for $\beta_0 = 90$ and 180 deg. The associated flow separation to be discussed later is shown in Fig. 8.

4.2 Flow Patterns in Right-Angle Sinuous Conduits ($\beta_0 = 90$ deg)

4.2.1 Aspect Ratio $b/h = 1/4$. For an aspect ratio of $b/h = 1/4$ the distributions of the axial velocity component V and the secondary (radial) velocity component V_r were measured by the LDV. The pressure difference ΔP_w referred to the inner wall surface was determined from the measured velocity distribution by the integral in Eq. (3). For bends numbered $N = 1$, 2, and 3, the nondimensional pressure distributions across the channel are plotted in terms of ΔP_w in the upper portion of Fig. 6 for various bend angles β. The pressure difference across the bend clearly reflects the effect of centrifugal force on reversal of streamline curvature caused by bend reversal.

The lower illustrations in Fig. 6 are both the isovels of nondimensional axial velocity component V/V_m (solid lines) and secondary radial velocity component V_r/V_m (dashed lines). The long dashed lines indicate the direction of secondary flow while the cross-hatched area outlines the region of separated flow. The plots show that the flow in the region of higher velocity deflects towards the inner side of the respective bend. Indeed, the higher nondimensional axial velocity V/V_m (solid lines) attains a value of more than 1.2. The pressure distribution indicates two distinct flow patterns. The first pattern shows the maximum value of ΔP_w in the center of the channel, while the other displays the local minimum value in the center of the channel. The secondary flow in the bends is reflected by the ΔP_w distributions. For this case of $b/h = 1/4$ the secondary

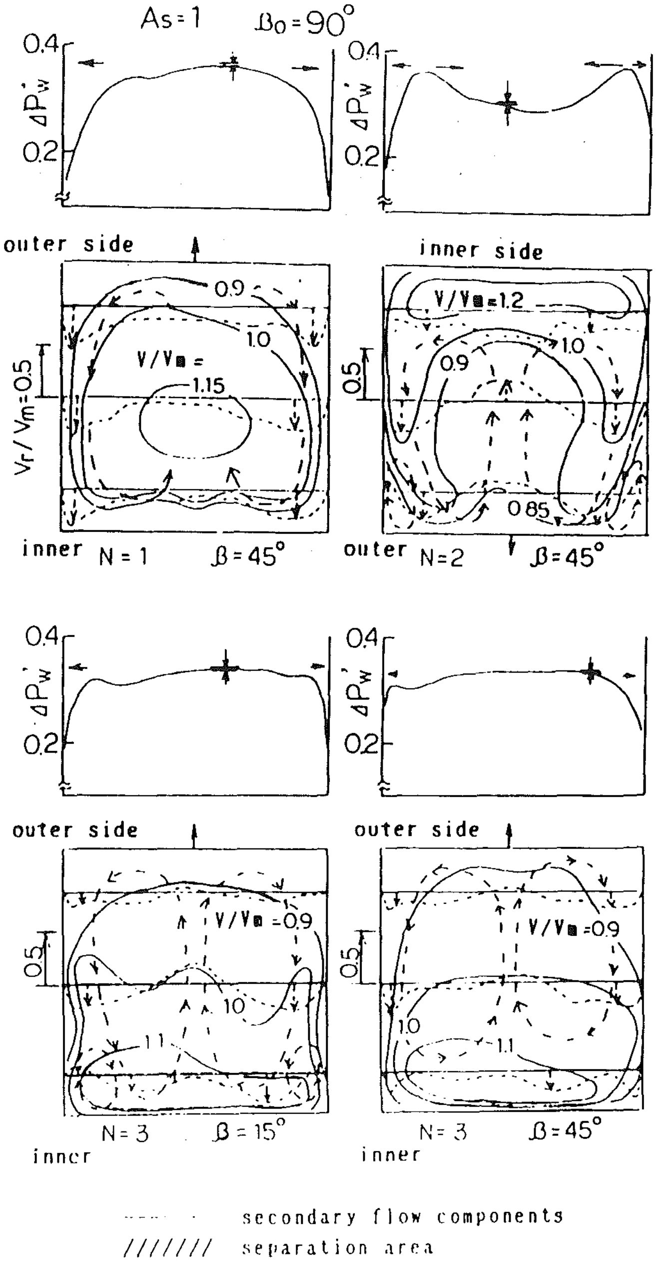

Fig. 9 Relationship between velocity distribution as measured by LDV and pressure difference. The velocity distribution was measured on nine cross stream planes. [$A_s = 1$ ($b/h = 1$) and $\beta_0 = 90$ deg] (Uncertainty estimates: $V/V_m = 1.1 \pm 0.011$, $V_r/V_m = 1.0 \pm 0.01$, and $\Delta P_w' = 0.3 \pm 0.003$)

flow pattern is quite strong and indeed very complicated. The separation occurs at the location where the low velocity fluid is swept out and thereby enveloped by the secondary flow. The secondary flow that occurs in the first bend ($N=1$) persists into the second bend ($N=2$). However, for $\beta = 75$ deg in the second bend ($N=2$), a newly formed secondary flow can be recognized. Two regions of two counter rotating secondary flow eddies continue into the third bend ($N=3$) and on into the fourth ($N=4$). Moreover, these two regions of secondary flow become large at first, then small, and again reform. This complicated flow pattern is illustrated in Fig. 7 for four bend elements. The separation regions depicted in Fig. 7 were determined from the photograph of the air bubble trajectory shown in Fig. 8. Clearly, Figs. 7 and 8 show that the separation zone spreads from the outlet of the bend elements into the inlet of the next bend element. The separation zones in the first and second bend elements are relatively small compared to those in the third and fourth elements. Consequently, the interference coefficient m plotted in Fig. 5, which reflects separation losses, is small for $n=2$ but large for $n=3$.

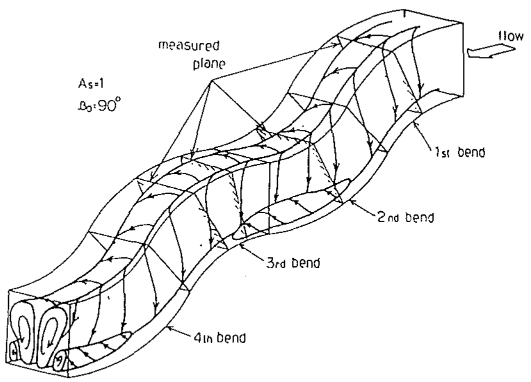

Fig. 10 Secondary flow pattern in sinuous conduit [$A_s = 1$ ($b/h = 1$) and $\beta_0 = 90$ deg]

4.2.2 Aspect Ratio b/h = 1. Figure 9 shows the nondimensional isovels of axial and secondary velocity components V/V_m and V_r/V_m and the distribution of the nondimensional pressure ratio ΔP_w for the aspect ratio of $b/h = 1$. The three primary characteristics of the flow are as follows. First, flow separation does not occur in all four elements of the sinuous conduit. Secondly, the direction of the secondary flow established in the first bend element is maintained into the fourth element. Namely, circumferential direction of secondary flow remains constant in the sinuous conduit for $b/h = 1$ and $R/r_w = 6$, where R is the radius of curvature and r_w is the mean hydraulic radius. The strength of the main secondary flow alternates from weak to strong. Last, two additional rather weak secondary vortices with counter flow with respect to the main secondary flow occur at the corners of the second and third bend elements. It can be noted that these weak corner vortices disappear at the outlet of the third bend element, subsequently reappearing in the middle portion of the fourth bend element. This phenomenon of alternating weak and strong secondary flow can be explained with reference to the wall pressure difference ratio ΔP_w.

The secondary flow in the wall boundary layer is generated by the wall pressure difference ΔP_w. Indeed, the secondary flow produced in the first bend element is accelerated by the magnitude of ΔP_w distribution in the second bend element; namely, fluid in the boundary layer is forced from the peak to the trough of the ΔP_w distribution. When the direction of this force due to the ΔP_w difference in the second bend element coincides with the direction of secondary flow in the first bend element, then the secondary flow becomes strong. On the other hand, in the reverse situation, the secondary flow becomes weak. Figure 10 depicts the secondary flow pattern as ascertained from velocity measurements and flow distribution observations. The main features of the flow are the absence of flow separation zones and the comparative weakness of the secondary flow.

4.2.3 Aspect Ratio b/h = 4. For the rather large aspect ratio of $b/h = 4$ several pair of secondary flow cells occur in the sinuous conduit. The wall pressure difference ΔP_w and the nondimensional isovels of axial and secondary velocity components plots are illustrated in Fig. 11. Each of the pressure difference ΔP_w diagrams ($N=1$, $\beta = 75$ deg; $N=2$, $\beta = 15$ deg; $N=3$, $\beta = 30$ deg; and $N=4$, $\beta = 30$ deg) shown in Fig. 11 has three distinct peaks. The pressure difference between a peak and a trough is smaller than for the case of $b/h = 1$ because the distance between the inner and outer walls of the bend is relatively small. The arrows depicted on the ΔP_w distribution indicate the direction of the secondary flow on the side wall of the bend curvature. The arrow direction is from a peak to

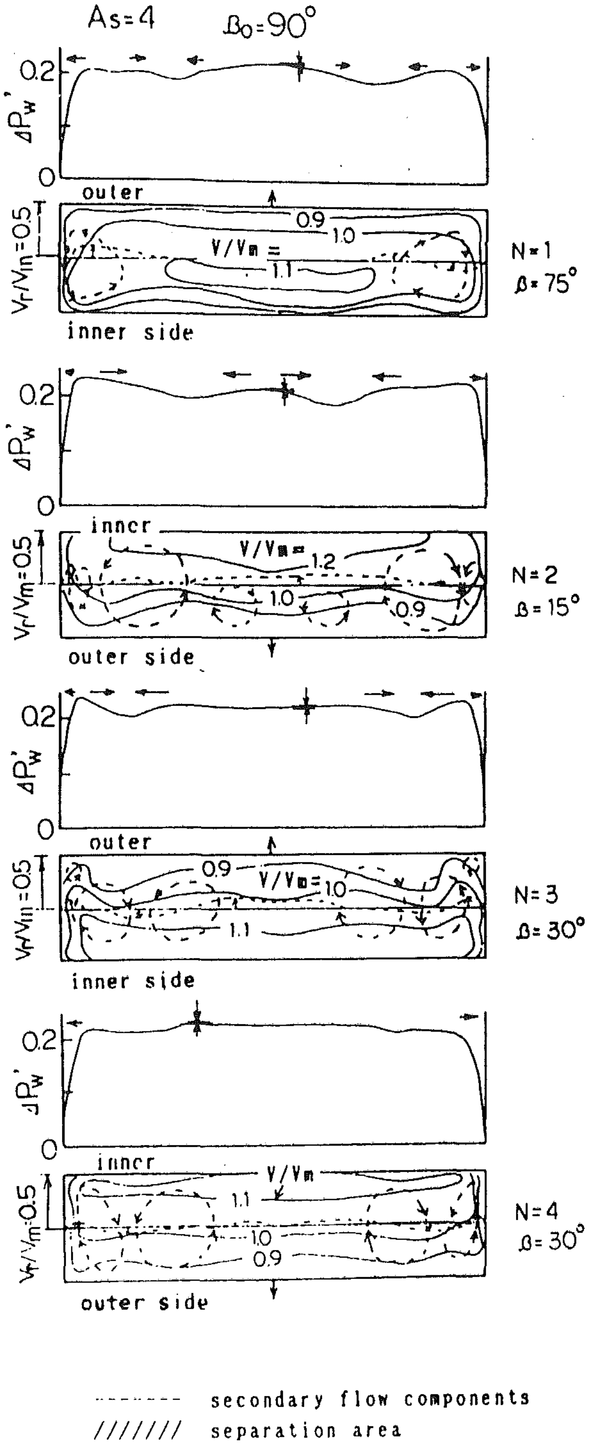

Fig. 11 Relationship between velocity distribution as measured by LDV and pressure difference. The velocity distribution was measured on seven cross stream planes. [$A_s = 4$ ($b/h = 4$) and $\beta_0 = 90$ deg] (Uncertainty estimates: $V/V_m = 1.1 \pm 0.011$, $V_r/V_m = 0.5 \pm .0.05$, and $\Delta P_w' = 0.2 \pm 0.002$)

a trough. In fact, the direction of swirling vortices generated in each bend section coincides with the direction of the arrow.

The flow pattern generated from both velocity measurements and the flow visualization technique utilizing air bubble trajectory is shown by the sketch in Fig. 12 for the aspect ratio $b/h = 4$ and $\beta_0 = 90$ deg. A pair of secondary flow cells occurs near both the left and right walls on the first bend element at $\beta = 75$ deg. As described earlier for $b/h = 1$, pairs of secondary flow cells persist from the first bend element all the way to the fourth, as clearly seen in Fig. 12. Moreover, other small

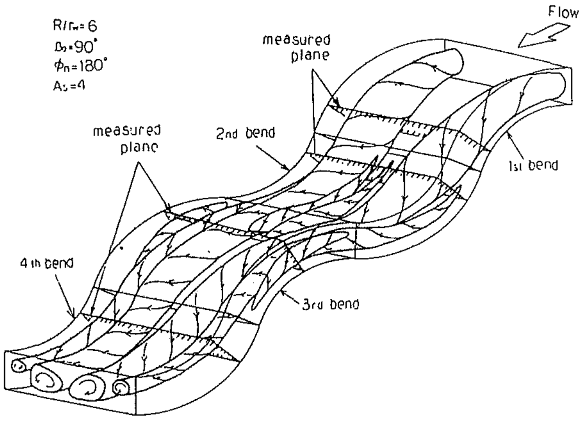

Fig. 12 Secondary flow pattern in sinuous conduit [$A_s = 4$ ($b/h = 4$) and $\beta_0 = 90$ deg]

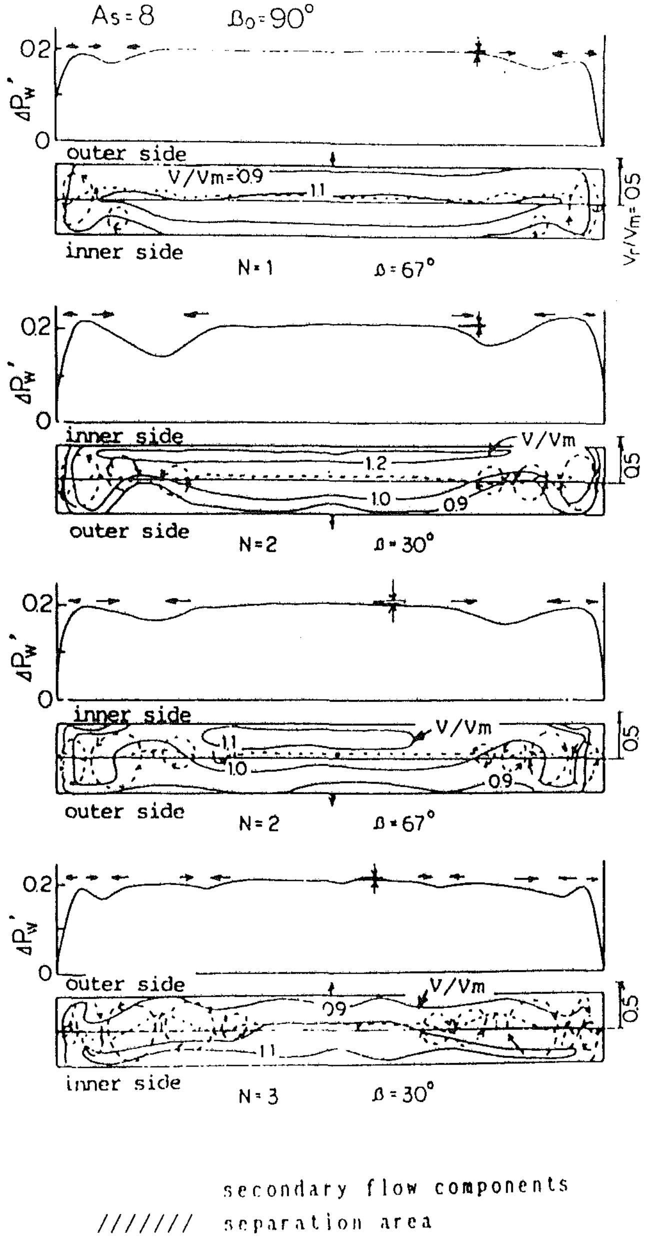

Fig. 13 Relationship between velocity distribution as measured by LDV and pressure difference. The velocity distribution was measured on four cross stream planes. [$A_s = 8$ ($b/h = 8$) and $\beta_0 = 90$ deg] (Uncertainty estimates: $V/V_m = 1.1 \pm 0.011$, $V_r/V_m = 0.5 \pm .0.05$, and $\Delta P_w' = 0.2 \pm 0.002$)

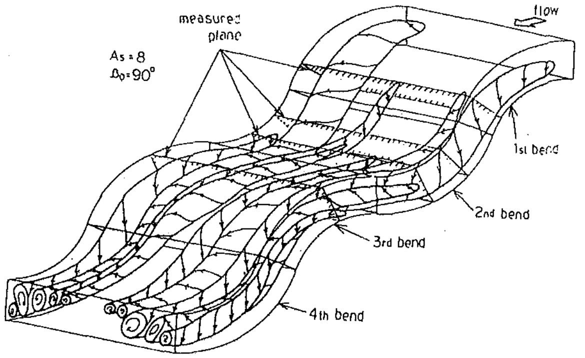

Fig. 14 Secondary flow pattern in sinuous conduit [$A_s = 8$ ($b/h = 8$) and $\beta_0 = 90$ deg]

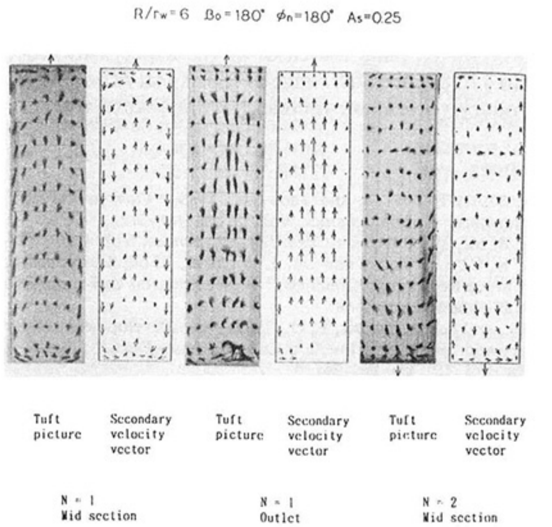

Fig. 15 Photographs of tuft and secondary velocity vectors in sinuous conduit [$A_s = 0.25$ ($b/h = 0.25$) and $\beta_0 = 180$ deg]

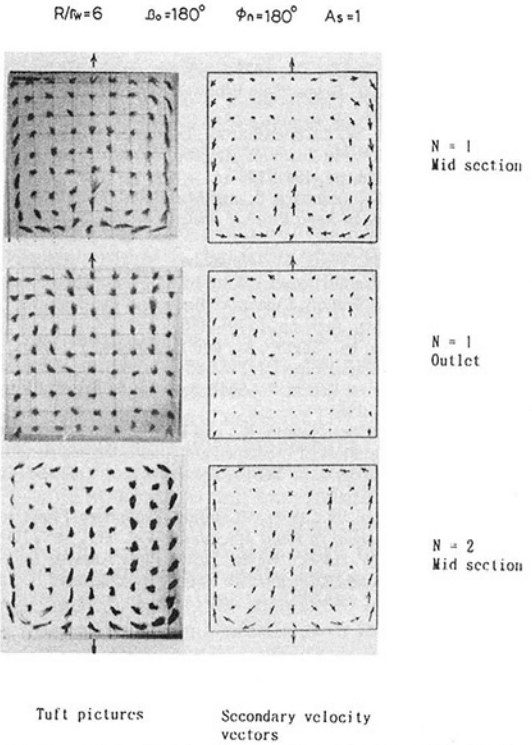

Fig. 16 Photographs of tuft and secondary velocity vectors in sinuous conduit [$A_s = 1$ ($b/h = 1$) and $\beta_0 = 180$ deg]

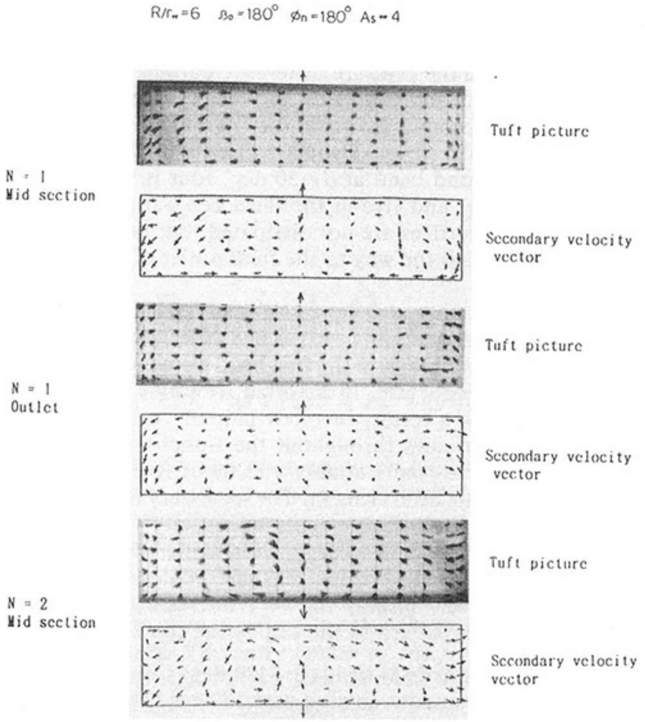

Fig. 17 Photographs of tuft and secondary velocity vectors in sinuous conduit [$A_s = 4$ ($b/h = 4$) and $\beta_0 = 180$ deg]

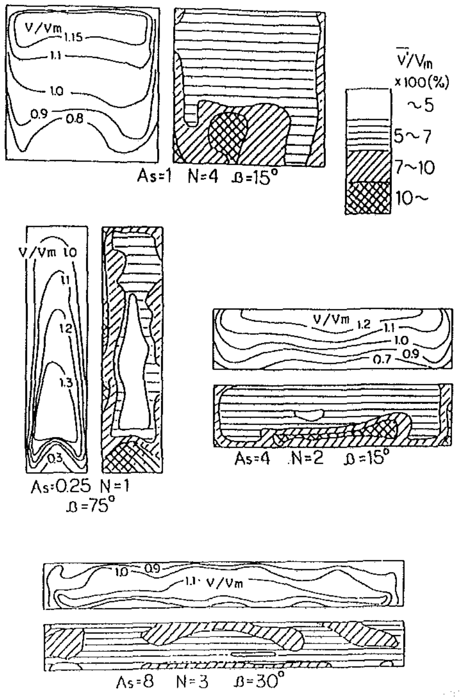

Fig. 18 Plot of isovels (V/V_m) and turbulence intensities $\sqrt{\overline{v'^2}}/V_m$ at representative cross sections β for each sinuous conduit tested (Uncertainty estimates: $V/V_m = 1.2 \pm 0.012$, and $\overline{v'^2}/V_m = 10 \pm 0.1$)

secondary vortices appear and then disappear in the middle of the second bend element and on both the left and right sides of the third bend element; namely, three pair of secondary vortices appear in the second and third bend elements. It can be deduced that such patterns of secondary flow will be repeated in quite long sinuous conduits.

4.2.4 Aspect Ratio $b/h = 8$. The normalized pressure and velocity distributions defined earlier are plotted in Fig. 13 for the case of aspect ratio $b/h=8$. Again, it can be demonstrated that secondary vortices are produced from the maximum to minimum values in the pressure difference parameter ΔP_w, as shown by the peaks and valleys on Fig. 13. Furthermore, the actual number of secondary vortices for $b/h=8$ is much greater than for the case of $b/h=4$. There are three pair of secondary vortices in the second bend at $\beta=30$ deg, four in the second bend at $\beta=67$ deg, and five in the third bend at $\beta=30$ deg. These secondary vortices are not dissipated, but rather maintain their strength all the way to the final outlet of the fourth bend.

The mechanism that is believed to generate much of the secondary vortex motion can be explained as follows. Initially, one pair of vortices appears in the first bend element, for which the pressure difference ΔP_w is distorted, resulting in the two pressure peaks. As a result, two new pair of vortices occur. This tendency continues throughout the sinuous bends, and the number of vortex pairs attains a value of five at the exit of the fourth and last bend element. The secondary flow pattern constructed from the measurements of velocity is shown in Fig. 14 for $b/h=8$ and $\beta_0=90$ deg. At the outlet of the fourth bend element five pair of vortex cells can be definitely seen. These rows decisively display the very interesting and truly complicated vortex pattern in the serpentine conduit.

4.3 Flow Patterns in U-bend ($\beta=180$ deg) Conduit. The flow pattern in the sinuous conduit with 180 deg bend elements was determined by using the tuft grid technique. Figure 15 shows the tuft orientation and the secondary velocity vector maps ascertained from the tuft photographs of the left side of the bend. The vector map of the secondary velocity as viewed from the right side are also shown for this case of $b/h=1/4$ and $R/r_w=6$. Significantly, the pattern of secondary flow represented in Fig. 15 is nearly identical to that referred to earlier for $\beta_0=90$ deg and $R/r_w=6$. However, only limited separation occurs in the first bend element for $\beta_0=180$ deg.

For an aspect ratio $b/h=1$ the tuft and secondary velocities are mapped in Fig. 16 for the 180 deg sinuous conduit. In this geometry, additional secondary flow occurs in the central portion of the middle cross section of the first bend element. Moreover, the secondary flow becomes very weak at the outlet of the first bend element, resulting in reversal of the circumferential secondary velocity component in the second bend element. The mutual interference between bend elements is weak, yielding a value of m approximately equal to unity.

Figure 17 shows the result of the U-bend configuration for an aspect ratio $b/h=4$. Although a pair of secondary vortices can be found at the $\beta=90$ deg cross section within the first bend element, the vortices dissipate at the exit of this bend. A pair of secondary vortices reappears in the second bend element, followed by the growth of another pair. Two pair of secondary vortices occupy the middle cross section within the second bend element. However, m is nearly equal to unity in each bend element as the total strenght of the secondary flow is not only weak but also constant.

4.4 Turbulence Intensity for Sinuous Conduit With $\beta_0=90$ deg. The nondimensional axial velocity isovels and the turbulence intensity of representative cross sections as measured by the LDV are plotted in Fig. 18. The nondimensional ratio V/V_m and the turbulence intensity v'/V_m (in percentage) were measured in the fourth bend element ($N=4$) at $\beta=15$ deg for $A_s=1$ ($b/h=1$), in the first bend ($N=1$) at $\beta=75$ deg for $A_s=0.25$ ($b/h=1/4$), in the second bend ($N=2$) at $\beta=15$ deg for $A_s=4$ ($b/h=4$), and in the third bend ($N=3$) at $\beta=30$ deg for $A_s=8$ ($b/h=8$). The measurement locations were chosen to correspond to situations for which the secondary flows were strong and many vortices appeared. Notably, the turbulence intensities become strong in the zones of separation where the velocities are relatively low.

5 Conclusions

- Hydraulic losses in sinuous conduits are quite sensitive to the aspect ratio of the cross section, b/h. The trend is for the losses to decrease as the aspect ratio increases.
- For the smallest aspect ratio tested, $b/h=1/4$, flow separation occurs at each downstream section of the sinuous conduit, resulting in large hydraulic losses. Furthermore, secondary vortices align themselves in rows in the direction of bend curvature in a definitely complicated pattern.
- For sinuous conduits with large aspect ratios (relatively flat bends) no separation occurs and the resulting number of secondary vortex pairs increases as the aspect ratio increases from 1 to 4 to 8. Over this range of the aspect ratio, the number of secondary vortex pair increases from two to five.

References

Berger, S. A., Talbot, L., and Yao, L-S., 1983, "Flow in Curved Pipes," *Annual Review of Fluid Mechanics*, Vol. 15, pp. 461-512.

Chang, S. M., 1983, *Physico-Chem Hydrodynamics*, Vol. 4, pp. 243-269.

Cheng, K. C., Lin, R. C., and Ou, J. W., 1976, "Fully Developed Laminar Flow in Curved Rectangular Channels," ASME JOURNAL OF FLUIDS ENGINEERING, Vol. 98, March, pp. 41-48.

Hille, P., and Schulz-Dubois, E. O., 1985, "The Development and Structure of Primary and Secondary Flow in a Curved Square Duct," *Journal of Fluid Mechanics*, Vol. 151, pp. 219-241.

Humphrey, J. A. C., Taylor, A. M. K., and Whitelaw, J. H., 1977, "Laminar Flow in a Square Duct of Strong Curvature," *Journal of Fluid Mechanics*, Vol. 83-3, pp. 509-527.

Humphrey, J. A. C., Whitelaw, J. H., and Yee, G., 1981, "Turbulent Flow in a Square Duct with Strong Curvature," *Journal of Fluid Mechanics*, Vol. 103, pp. 443-463.

Hur, N., Thangam, S., and Speziale, C. G., 1990, "Numerical Study of Turbulent Secondary Flows in Curved Ducts," ASME JOURNAL OF FLUIDS ENGINEERING, Vol. 112, pp. 205-211.

Melling, A., and Whitelaw, J. H., 1976, "Turbulent Flow in a Rectangular Ducts," *Journal of Fluid Mechanics*, Vol. 78, pp. 289-315.

Murakami, M., and Shimizu, Y., 1969, "Studies on Fluid Flow in Three-Dimensional Bend Conduits," *Bulletin of the JSME*, Vol. 12-54, Dec., pp. 1369-1375.

Murakami, M., and Shimizu, Y., 1973, "Studies on the Hydraulic Loss in Pipe Bends (Results for 90°-Screw Type Elbows)," *Bulletin of the JSME*, Vol. 16-96, June, pp. 981-989.

Nakayama, A., Chow, W. L., and Sharma, D., 1983, "Calculation of Fully Developed Turbulent Flows in Ducts of Arbitrary Cross-section," *Journal of Fluid Mechanics*, Vol. 128, pp. 199-217.

Shimizu, Y., Sugino, K., Kuzuhara, S., and Murakami, M., 1982, "Hydraulic Losses and Flow Patterns in Bend Pipes," *Bulletin of the JSME*, Vol. 25-199, Jan., pp. 24-31.

Shimizu, Y., Sugino, K., Yasui, M., Hayakawa, Y., and Kuzuhara, S., 1985, "Flow Patterns and Hydraulic Losses in Quasi Coil Pipes (The Effects of Configuration of Bend Cross Section, Curvature Ratio and Bend Angle)," *Bulletin of the JSME*, Vol. 28-241, July, pp. 1379-1386.

Shimizu, Y., Nagafusa, M., Sugino, K., and Nakamura, F., 1986a, "Studies on Performance and Internal Flow of Twisted S-shaped Bend Diffuser—The So Called Bend Diffuser: 1st Report," ASME JOURNAL OF FLUIDS ENGINEERING, Vol. 108, Sept., pp. 289-296.

Shimizu, Y., Nagafusa, M., Sugino, K., and Kubota, T., 1986b, "Studies on Performance and Internal Flow of U-Shaped and Snake-Shaped Bend Diffusers: 2nd Report," ASME JOURNAL OF FLUIDS ENGINEERING, Vol. 108, Sept., pp. 297-303.

Thangam, S., and Hur, N., 1990, "Laminar Secondary Flows in Curved Rectangular Ducts," *Journal fo Fluid Mechanics*, Vol. 217, pp. 421-440.

Vu, T. C., and Shyy, W., 1990, "Navier-Stokes Flow Analysis for Hydraulic Turbine Draft Tubes," ASME JOURNAL OF FLUIDS ENGINEERING, Vol. 112, pp. 199-204.

A Power-Law Formulation of Laminar Flow in Short Pipes

M. Sherman
Staff Scientist,
Applied Science Division,
Lawrence Berkeley Laboratory,
University of California,
Berkeley, CA 94720

In the quantification of air flow through penetrations in buildings, it is necessary to be able to characterize the flow without detailed knowledge of the geometry of the paths. At the conditions typical of buildings, the flow regime is partially developed laminar flow. This report develops a theoretical description of the hydrodynamic relationship based on a power-law representation between the air flow and applied pressure for laminar flow in short pipes. It is found that short pipes can be described with a simple power law dependence on pressure, but that the exponent of the power law is itself a function of pressure. The entry length of the flow is derived based on a formulation for short, sharp-edged pipes. The theoretical formulation is compared to measured data. A dimensionless quantity, S, *is defined to account for the power law behavior and maps simply to the flow exponent. The exponent or* S *number can be used to infer many of the characteristics of the flow and may prove useful in the inverse problem of determining flow geometry from fluid properties and the measured pressure and flow.*

Introduction

Since the energy crisis of the 1970s, energy conservation and energy efficiency research have been an active area of study. Up to ten percent of energy used in the developed world can be attributed to air flow through building envelopes. In the United States, the cost of this leakage is on the order of thirty-billion dollars annually. Because most buildings are ventilated by air leakage, overzealous reduction could cause indoor air quality problems. Thus, it is necessary to be able to quantify the impact that building leakage has on ventilation, implying a need for a physical understanding of air leakage.

Air flows into and out of buildings occur through a variety of paths. Some of the paths such as flues or window openings are relatively large and well-defined. Most of the paths are leaks having widths on the order of millimeters—i.e., cracks or other pathways caused by the building construction or wear. Because in a real building the location and geometry of these leaks is virtually unknowable, the only practical measurement is to determine the flow through the ensemble of leaks as a function of applied pressure.

The technique in general use is ASTM Standard E779 (1987), and uses a fan (usually door-mounted) to pressurize the building to a set of steady-state pressures and measure the flow rate. Because of measurement uncertainties, fan pressurization tests are usually conducted at higher pressures (i.e., 10–50 Pa) and the results are extrapolated down to the pressures more typical of the undisturbed air leakage process (i.e., 1–5 Pa). Sherman and Modera (1986 and 1988) have developed techniques using time-varying pressures to improve the accuracy of the measurement.

Many thousands of buildings have been measured using these techniques and it has been empirically determined that flow vs. pressure curve follows a two-parameter power law quite well,

$$Q = C\Delta P^{n} \tag{1}$$

with the exponent falling between the two physical limits of inertial flow ($n = 1/2$) and fully developed laminar flow ($n = 1$).

Although the power law is recognized as an empirical representation, the leakage is often quoted as a single parameter. Although the leakage is sometimes quoted at the flow at a pressure of 50 Pa, most commonly the single parameter used is the Effective Leakage Area (ELA):

$$\mathrm{ELA} = CP_{\mathrm{ref}}^{n-(1/2)}\sqrt{\frac{\rho}{2}} \tag{2}$$

where the reference pressure is typical of the leakage process (e.g., 4 Pa).

Sherman et al. (1986) have compiled leakage areas and exponents from a variety of different house types and have found that, while there is a broad distribution of ELAs, the exponent tends to cluster near a value of 2/3 (with a standard deviation of .09).

Although the power law model has been used extensively in the field, open questions remain: Why does the measured data follow a power law? Why does the exponent of the power law cluster around 2/3? Is the power-law formulation an acceptable model for extrapolation? If not, is there useful information in the deviation? It is the intent of this report to help supply answers to these questions.

The problem faced in air leakage research is one of *inverse modeling*, namely that the response of the system must be

---

Contributed by the Fluids Engineering Division for publication in the JOURNAL OF FLUIDS ENGINEERING. Manuscript received by the Fluids Engineering Division March 10, 1992. Associate Technical Editor: D. P. Telionis.

measured and some system parameters inferred from that data. Tarantola (1987) points out that inverse modeling cannot go very far without *forward modeling* to determine the role of the physics on the observables and a *system parameterization* to discover the minimal set of model parameters needed to adequately describe the system. The focus of this report is to derive a sufficiently accurate model (i.e., system parameterization) to link the well-studied physics of laminar flow (i.e., forward modeling) to the power law approach (i.e., inverse modeling).

Laminar Entry Flow. The model development starts from the physical paradigm of developing laminar flow in a circular pipe. Since the typical Reynold's number for leaks in buildings is below the transition region, laminar flow is appropriate; similarly, since the path length of most leaks is insufficient to ignore entry effects, developing flow is appropriate. The choice of circular geometry, however, is somewhat more arbitrary.

Because of the large variability in leak geometries, no single one would be an accurate representation of the ensemble, but because we are interested in finding the system response, (and not in determining the crack geometry), we can represent the system by the equivalent parameters for a single geometry. We have chosen circular pipes because it is the most well studied and because the cross-section is defined by a single parameter (i.e., the diameter or area) rather than two parameters as would be the case for parallel plates.

Before proceeding with the circular geometry it should be noted that other geometries such as parallel plates, could have been used. One of the best such effects for numerically determining the velocity profile in parallel plates is that of Nguyen and Maclaine (1988). Baker et al. (1987) have developed an expression analogous to the one below for parallel plate geometry including right angle bends. Their work suggests ways of increasing the entry loss to account for bends. Since we are using the forward model as a defining relationship for equivalent parameters, there is no advantage to considering these geometries.

The problem of laminar flow in (short, circular) pipes has been investigated for over a century. Boussinesq (1891), Schiller and Agnew (1922), and Langharr (1942) have all elected to treat it by linearizing the Navier–Stokes equation and all have come up with an equation of the following form:

$$\Delta P = \frac{32\mu l v}{d^2} + m^{1/2}\rho v^2 \tag{3}$$

The first term can be recognized as the Hagen-Poiseuille equation for (fully developed) laminar flow. As described in detail in the references, the second term results from acceleration of the fluid into its exit profile and the excess viscous losses resulting therefrom.

The factor m[1] can be calculated from the linearized theory and has also been measured. For pipes long enough for the exit profile to be parabolic, the parameter m can be treated as a constant; and the literature contains a range of values for it, $2.16 < m < 2.41$, which depend on the details of the linearization (and to a small extent on Reynolds number and passage length).

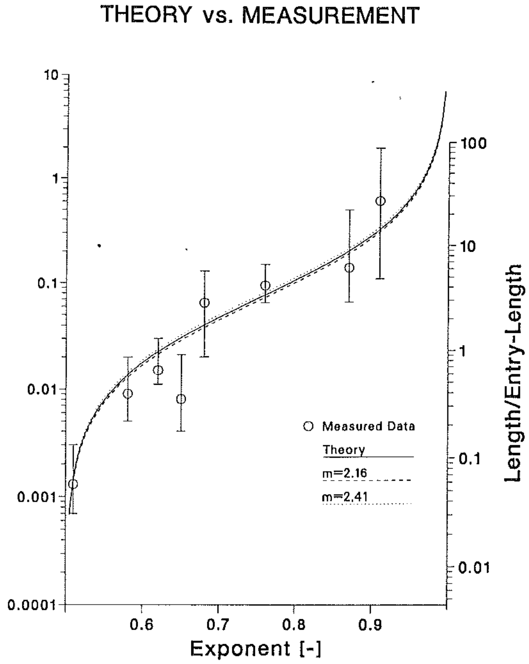

Fig. 1 Kreith's data with their error bars shown as function of exponent. Left-hand axis is the normalized length from the original reference. Right-hand axis is pipe length divided by the entry length. Theoretical curve uses $m = 2.28$ as derived in text.

Inherent in the derivation of Eq. (3) are assumptions regarding the inlet flow and outlet flow conditions. As Prandtl and Tietjens (1934)—among others—have pointed out, these assumptions can become suspect when pipe length become shorter than the entry length. Schiller (1922) introduced a correction to m for very short pipes with bell-mouthed inlets. A correction in the opposite sense, however, is required to account for flow contraction due to separation at (a sharp-edged) inlet.

The experiments and theory assumed a square inlet profile with no flow separation. For such a case, the corrections such as Schiller's are needed, but its often difficult to keep separation from occurring—especially outside a well-conducted laboratory situation. For a more detailed review of flow (and heat transfer) in laminar ducts of various shapes see Shah and London (1978).

Kreith and Eisenstadt (1957) have measured the flow characteristics of pipes of different dimensions (e.g., $0.45 < l/d < 17.25$). Figure 1 contains a plot of the original data overlaid with some constant-m curves. The measurements were made for square inlet capillary tubes, rather than the bell-mouthed inlets assumed by Schiler, Boussinesq and Langharr. Although this data is not accurate enough to improve the estimate of m, it does indicate that the constant-m assumption is reasonable. In this report we shall assume m need not be corrected and is a constant even for very short pipes; the estimate of $m = 2.28$ by Langharr will be used herein as being most representative.

Nomenclature

A = open area of pipe [m^2]
C_d = discharge coefficient [-]
d = diameter of pipe [m]
C = power-law coefficient [m^3/s-Pa^n]
l = length (along flow path) of pipe [m]

n = power-law exponent
Q = fluid flow through pipe [m^3/s]
Re = Reynolds number [-]
S = S number [-]
ΔP = pressure drop across pipe [Pa]
δP = pressure range of interest [Pa]

v = mean velocity of fluid [m/s]
μ = viscosity of fluid [kg/m-s]
υ = kinematic viscosity (η/ρ) of fluid [m^2/s]
ϕ = power-law factor [-]
ρ = density of fluid [kg/m^3]

---

[1] Rather than m some more recent works (e.g., Shah and London (1978), p. 42) use the term pressure defect, K, which is equal to $m - l$.

Power-Law Formulation

Although power laws are often used in to describe turbulent flow situations such as Jeppson's (1977) description of pipe-networks, Blasius's (1913) friction factors at moderate Reynolds numbers, or Schilicting's (1968) skin-resistance solutions, power-law approaches to the solution of laminar flow problems are not generally used. Nevertheless, any smooth function can be locally represented by a power law where the exponent is allowed to vary. For Eq. (1) this implies

$$n \equiv \frac{d\log(Q)}{d\log(\Delta P)} \tag{4}$$

Equation (3) is our physical description of the relationship between the velocity and the pressure. Although the velocity is usually considered one of the fundamental observables in laminar flow theory, it is not even an observable in air leakage research; it is, rather, the total flow which is the fundamental observable—they are of course just related through the pipe area:

$$\frac{Q}{\nu} = A = \frac{\pi d^2}{4} \tag{5}$$

Solving Eq. (3) for the flow yields

$$Q = \frac{8\pi\nu l}{m}\left(\left(1 + \frac{md^4\Delta P}{512\nu^2\rho l^2}\right)^{1/2} - 1\right) \tag{6}$$

and the exponent becomes,

$$n = 1/2\left[1 + \left(1 + \frac{mA^2\Delta P}{32\pi^2\rho\nu^2 l^2}\right)^{-1/2}\right] \tag{7}$$

As we can see from this equation, in terms of the geometry (i.e., the forward model) the exponent depends only on the ratio of pipe *area* to length.

Equations (6 and 7) suggest that prior to finding the power law, we should non-dimensionalize the pressure. We can define the *S number* so that it will be unity when the two terms in Eq. (3) are equal:

$$S \equiv \frac{mA^2\Delta P}{256\pi^2\nu^2\rho l^2} \tag{8}$$

In which case the exponent can be directly related to the S number:

$$n = 1/2(1 + (1 + 8S)^{-1/2}) \tag{9}$$

and the flow can be expressed using either:

$$Q = \frac{8\pi\nu l}{m}(\sqrt{1+8S} - 1) = \frac{8\pi\nu l}{m}\,\frac{1-n}{n-1/2} \tag{10}$$

To get the flow in the form of a power law in S, we can use the last two equations iteratively:

$$Q = \frac{16\pi\nu l}{m}\,\phi S^n \tag{11}$$

where the power-law factor, ϕ, factor is a slowly varying function of exponent (and, hence, pressure) that varies between one and two, defined as follows:

$$\phi \equiv (2/n)^n(1-n)^{1-n}(2n-1)^{2n-1} \tag{12}$$

Equation (11) is not a true power law because both the exponent, n, and the coefficient (specifically ϕ) have a pressure dependence, albeit small; it is, however, a power law *locally*. The power-law factor is an artifact of the equation of interest not being a true power law. When the S number is near unity, the power-law factor is also unity and is slowly-varying. As the S number deviates significantly from unity, ϕ begins to slowly increase and approaches the limit for either laminar or inertial flow.

The range of acceptable pressures of the power law formulation depends upon the deviation from a true power acceptable. The deviation is primarily caused by variation of the exponent with pressure:

$$\frac{dn}{d\log(\Delta P)} = n(1-n)(2n-1) \tag{13}$$

If, for example, we can accept a 5 percent maximum variation from a true power law the upper value of the pressure range can be three times the lower value near an exponent of 2/3. (Note that $n = 2/3$ is the place where the exponent varies the fastest.)

Power-Law Exponent as a Pipe Characteristic. In forward modeling a pipe is characterized by its geometry (i.e., length, diameter, and perhaps the shape of the entry). In inverse modeling these are not necessarily the appropriate parameters to characterize the system of the pipe and the fluid. The system parameterization represented by Eqs. 9–12 suggest that the exponent (or equivalently the S number) is a key system characteristic. This section demonstrates the usefulness of this representation.

The *S number*, which is a nondimensionalized pressure, is a good indicator of the shortness of the pipe. For large values of S the pipe is very short and can be characterized as an orifice in the limit. At small values of S the pipe is very long and is well-described by viscous flow equations. Since the S number can be represented as a function only of the exponent

$$S = \frac{1}{8}\,\frac{(1-n)n}{(n-1/2)^2} \tag{14}$$

either one represents a characteristic of the system.

The standard *Reynolds number* is based on the pipe diameter and fluid velocity. We can eliminate the fluid velocity to get an equivalent expression involving the aspect ratio and either the exponent or S number:

$$\mathrm{Re} = \frac{32l}{md}(\sqrt{1+8S} - 1) = \frac{32l}{md}\,\frac{1-n}{n-1/2} \tag{15}$$

This equation is the basis for the curves plotted in Fig. 1. l/d divided by the Reynold's number is a characteristic of the system and is the left hand axis of Fig. 1.

The *discharge coefficient* is often used to describe the actual flow in terms of the equivalent perfect nozzle.

$$C_d \equiv \nu\left(\frac{2\Delta P}{\rho}\right)^{-1/2} = \sqrt{\frac{1-n}{mn}} \tag{16}$$

From this expression it is clear that value of m may have to change only slightly for very short pipes (i.e., $n \rightarrow 1/2$) to reflect the shape of the inlet.

The concept of *entry length* is often used to determine if the flow has reached its steady-state behavior. For lengths less than the entry length the flow is said to be developing, for lengths greater than the entry length the flow is developed (because the exit profile is parabolic) and for pipe length much greater than the entry length the flow is said to be fully developed because entry effects can be ignored.

One common approach to defining the entry length is as that length at which the profile becomes (approximately) parabolic, leading to an entry length of $d\mathrm{Re}/16$. An examination of Eq. (3), however, suggests a slightly different value; namely, we choose the entry length such that the frictional losses due to laminar flow of a pipe of length equal to the entry length is equal to the entry loss (i.e., the two terms in Eq. (3) are equal). Thus,

$$l_e \equiv m\,\frac{\mathrm{Re}}{64}\,d \tag{17}$$

This definition leads to a somewhat smaller value for the entry

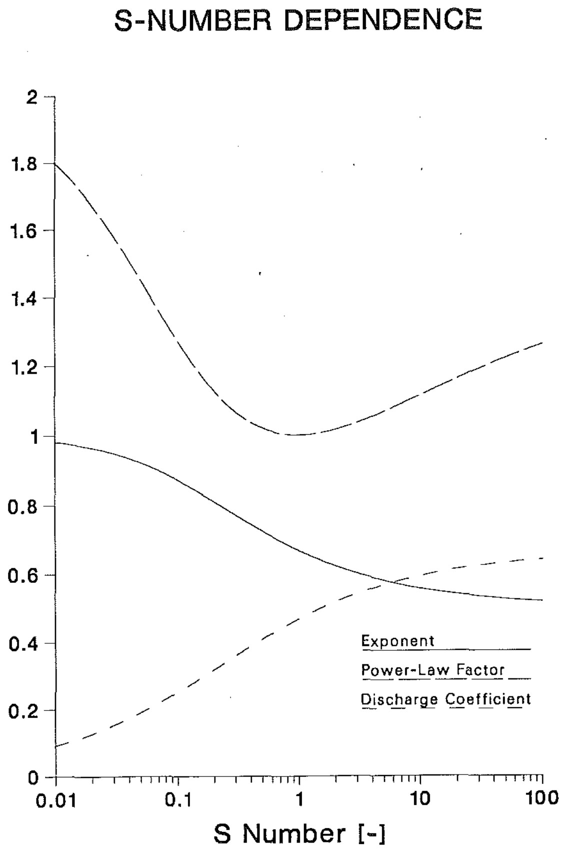

Fig. 2 Dependence of length, discharge coefficient, and power-law factor with *S* number

length than the conventional definition and it can be expressed in terms of the exponent as follows:

$$\frac{l_e}{l}=\frac{1-n}{2n-1}=\frac{(\sqrt{1+8S}-1)}{2}\,\frac{m/64}{(l/d)/\mathrm{Re}} \tag{18}$$

Thus the exponent and the length of the pipe relative to its entry length are uniquely related. As can be seen from the vertical axes of Fig. 1, the entry length is quite sensitive to the exponent near the limits of its range.

Figure 2 shows the *S*-number dependence of the (dimensionless) length, discharge coefficient, and power-law factor.

Application to Building Leakage

The power-law formulation can be used to characterize a system from measured data. Assume that we have measured the flow vs. pressure response of a building and determined the power law parameters (of Eq. (1), C (or ELA) and n, at or around a particular pressure, ΔP. We can apply our model to calculate (the S-number and) a set of equivalent geometric parameters that would produce the measured results:

$$l=C\Delta P^{n}\,\frac{m}{8\pi v}\,\frac{n-1/2}{1-n} \tag{19}$$

$$A=C\Delta P^{n-1/2}\sqrt{\frac{\rho m n}{2(1-n)}}=\frac{\mathrm{ELA}}{C_d}\left(\frac{\Delta P}{P_{\mathrm{ref}}}\right)^{n-1/2} \tag{20}$$

If we apply these equations to typical building leakage (e.g., Sherman, Wilson, Kiel data), the pipe length comes out quite large. Specifically, it is orders of magnitude longer than is reasonably possible. As an example consider a case in which the measurements determine $n=2/3$ and ELA $=.1$ m^2 for the case of $\Delta P=25$ Pa, $P_{\mathrm{ref}}=4$ Pa. Equation (20) would yield a reasonable area, $A=.22$ m^2, but Eq. (19) yields an unreasonably large length, $l=9.2$ km.

This result does not hinder the ability to use them as system characteristics, but it does imply, not unsurprisingly, that there must be many parallel leakage paths in a building envelope. If there were many identical leaks the total area would remain unchanged but the implied length would be reduced by the number of such leaks. There is no reason, however, to expect the various leakage paths in a building to have the same properties. It is far more likely that there will be a distribution of geometries spanning the physically possible range.

No information about the distribution of leak geometries can be gleaned from the measurements at a single pressure. If it were possible, however, to measure the properties as a function of pressure, information about the distribution could be inferred.

Although a detailed development of this relationship is beyond the scope of this report, an example can demonstrate the importance. If distribution is very narrow (i.e., made up of almost identical leaks) the flow vs. pressure curve would closely resemble that of a single leak following the derivation herein and the exponent will monotonically decrease as a function of applied pressure (Eq. 7). If the distribution is broadly bi-modal (e.g., suitably made up of orifices and long pipes), the exponent will have the opposite pressure dependence, because the fully developed pipe flow will dominate as the pressures increase. Thus a measurement of the pressure dependence of the exponent is a direct indication of the spread of geometries involved in the leakage.

Currently practice in field measurement is insufficiently accurate to determine the pressure dependence of the exponent for real buildings. Uncertainties are on the order of 10 percent for individual flow and pressure measurements. Not only does this deny us the opportunity to learn about the geometries of envelope leaks, but it indicates that the practice of extrapolating high pressure measurements to lower pressures can have significant uncertainties.

Temperature Dependence. Temperature does not explicitly enter this problem. The fluid properties of density and viscosity, however, are functions of temperature (as may be the driving pressure). As temperature increases density will decrease and viscosity will usually increase, thus offsetting their effects in Eq. (3). It is interesting to note that for air at atmospheric conditions, the percentage change in the two terms of Eq. (3) are approximately equal and opposite. Thus C is independent of temperature for air at normal conditions, when $n\approx 2/3$. Although the air flow rate may be independent of temperature under these conditions, the exponent and those quantities derived from it are not.

Conclusions

This report has presented a power-law formulation of laminar flow in short pipes that is equivalent to more standard representations, in order to help understand the field of air leakage in buildings. A system parameterization developed the concept of an S number as a dimensionless pressure that characterizes the shortness of the pipe (i.e., the entry pressure loss relative to the laminar pressure loss). The local power-law exponent is directly related to the S number and is a characteristic of the inverse model. Either of these two parameters can be used to help characterize the leakage process with some of the more familiar concepts being directly calculable from them (e.g., the discharge coefficient of the leak from Eq. (16) or the length of the leak relative to its entry length from Eq. (18)).

In the introduction several questions were posed, which we are now in a position to answer. We have shown that for a single leak the flow versus pressure curve can be represented by a (constant-exponent) power law over a limited pressure range. Depending on the desired level of accuracy, the power-law formulation is acceptable over a factor of three pressure range, and interpolation over this range is reasonable.

Although $n = 2/3$ has special characteristics (i.e., the inertial and laminar pressure drops are equal, and there is almost no temperature dependence), theory does not tell us why the measured exponents of buildings should cluster near 2/3. This fact undoubtedly is linked to the area and length distribution of building envelope leaks, but measurements taken to date are sufficiently uncertain that no conclusions can be drawn.

The extrapolation of data to lower pressures has uncertainties of two different and important kinds. Since the individual measurements have some uncertainty, the estimate of the power-law parameters will be uncertain and cause significant extrapolation error. Secondly, the underlying exponent can in fact be changing either positively or negatively depending on the distribution of leak geometry. Thus, extrapolation is unreliable and methods that measure the behavior at the pressures of interest should be used preferentially.

Acknowledgment

This work was supported by the Assistant Secretary for Conservation and Renewable Energy, Office of Building Technology Building Systems Division of the U.S. Department of Energy under Contract No. DE-AC03-76SF00098.

References

ASTM, 1987, "Standard Test Method for Determining Air Leakage Rate by Fan Pressurization," ASTM E779-87, American Society for Testing and Materials.

Baker, P. H., Sharples, S., and Ward, I. C., 1987, "Air Flow Through Cracks," *Building & Environment*, Vol. 22, No. 4, pp. 293-304.

Blasius, H., 1913, "Das Aehnlichkeitsgesetz bei Reibungsvorgaengen in Fluessigkeiten," Forschg. Arb. Ing.-Wes, No. 131, Berlin.

Boussinesq, J., 1891, Mem. Pres. Acad. Sci. Paris, pp. 23:46.

Jeppson, J. W., 1977, "Analysis of Flow in Pipe Networks," *Ann Arbor Science*, pp. 53-69.

Kreith, F., and Eisenstadt, R., 1957, "Pressure Drop and Flow Characteristics of Short Capillary Tubes at Low Reynolds Numbers," *American Society of Mechanical Engineers, Transactions*, p. 1070.

Langharr, H., 1942, "Steady Flow in the Transition Length of a Straight Tube," ASME *Journal of Applied Mechanics*, Vol. 9, p. A55.

Nguyen, T., and Maclaine, I., 1988, "Incremental Pressure Drop Measurements in Parallel Plate Heat Exchangers," ASME JOURNAL OF FLUIDS ENGINEERING, Vol. 110, pp. 93-96.

Prandtl, L., and Tietjens, O. G., 1934, *Applied Hydro- and Aeromechanics*, McGraw-Hill, NY, p. 28.

Schiller, L., and Agnew, Z., 1922, *Math. Mech.*, Vol. 2, p. 96.

Schlichting, H., 1968, *Boundary-Layer Theory*, McGraw-Hill, pp. 598-602.

Shah, R. K., and London, A. L., 1978, *Laminar Flow Forced Convection in Ducts*, Academic Press.

Sherman, M. H., and Modera, M. P., 1986, "Low-Frequency Measurement of Leakage in Enclosures," *Reviews of Scientific Instruments*, Vol. 57, No. 7, p. 1427.

Sherman, M. H., and Modera, M. P., 1988, "Signal Attenuation Due to Cavity Leakage," *J. Acoustical. Society of America*, Vol. 84, No. 6.

Sherman, M. H., Wilson, D. J., and Kiel, D. E., 1986, "Variability in Residential Air Leakage," *Measured Air Leakage of Buildings*, Trechsel/Lagus, ed., STP 904, American Society for Testing and Materials, Philadelphia, PA, p. 348.

Tarantola, A., 1987, *Inverse Problem Theory*, Elsevier, New York.

T. Cader
Graduate Student.

O. Masbernat
Research Associate.

M. C. Roco[1]
Professor.

Department of Mechanical Engineering,
University of Kentucky,
Lexington, KY 40506-0046

LDV Measurements in a Centrifugal Slurry Pump: Water and Dilute Slurry Flows

A two-component LDV system was used to investigate single and two-phase flow in a representative section at the impeller outlet of a centrifugal slurry pump. Measurements were performed at Q_n and 0.5 Q_n with water and dilute slurry flows ($C = 0.04$ and 0.16 percent by volume). The solids consist of 0.8 mm glass beads. Particle Reynolds number is 65. The point liquid and solid velocities were determined with a Doppler signal amplitude discrimination approach. A rotary shaft encoder was used to represent the velocity as a function of the impeller angular position, and to investigate the effect of a finite number of blades on the flow. The data on liquid and slip velocity distributions show large scale flow structures which dominate the two-phase turbulent flow. Overall, solid particles have a larger radial velocity than the carrier fluid at the impeller outlet, but they lag the fluid in the circumferential direction.

1 Introduction

Most of the experimental studies on particle-fluid flows using Laser Doppler Velocimetry (LDV) have been performed in relatively simple geometries, such as round jets (Levy and Lockwood, 1981; Modaress et al., 1984a and 1984b; Parthasarathy and Faeth, 1987) and pipe flows (Lee and Durst, 1982; Tsuji and Morikawa, 1982; Tsuji et al., 1984; Nouri et al., 1987; Hamdullahpur et al., 1987; Zisselmar and Molerus, 1979; Gore and Crowe, 1989). Several specific methods have been adopted in order to discriminate between the signals originating from the two phases, such as Doppler signal amplitude discrimination techniques in gas-solid flows. Refractive index matching methods have been adopted in dense liquid-solid flows. However, there is no generally recommended approach for processing Doppler signals in two-phase flows, and a full understanding of particle-fluid, particle-particle and particle-wall interaction mechanisms is far from complete, even in simple geometries. Studies of liquid-solid flows in complex geometries (such as turbomachinery) are not generally available.

Previous work on the LDV and Particle Image Velocimetry (PIV) measurements in pumps (Adler and Levy, 1979; Hamkins and Flack, 1987; Paone et al., 1989; Dong et al., 1991) have been performed for single fluid flow using various micron sized trasors. This study deals with LDV measurements on particulate two-phase flow in centrifugal slurry pumps, and includes the determination of the slip velocity between phases and the effect of the impeller angular position. LDV results on slurry pumps have not been previously reported in literature. Only a dilute system is considered here. The overall objective is to offer primary data needed for the development of new theories and validation of numerical methods. A long term goal of this work is the performance prediction of centrifugal slurry pump performance, including the calculation of the pump head, energy loss, and wear rate of the pump. The present paper is a continuation of the previous study performed with water flow in the same pump (Roco et al., 1990).

The velocity distributions have been measured in water and dilute slurry flows with a two-color Argon-Ion TSI LDV. We have used a simple method to measure the solid phase velocity field of dilute slurries based upon discrimination between the signals originating from the micron size particles (which follow the carrier fluid) and millimeter size particles (solid phase). This technique allowed for the computation of the velocity moments for solid phase and liquid, without extensive processing of the digitized signal.

The main features of the two-phase velocity and turbulence profiles are presented in a representative section at the impeller outlet (window #2, line E in Fig. 2), for two flowrates (nominal flowrate Q_n, and $Q_n/2$). Other measurements performed in the whole radial cross-section, and for the whole circumference of the impeller, are reported elsewhere (Roco et al., 1992). The point instantaneous velocities were averaged over the largest time scale of the flow corresponding to a full impeller rotation, as well as over all measurements performed for small angular intervals ($\Delta\phi = 5$ degrees). The equations of motion are commonly formulated for averaged variables.

Large amplitudes of the velocity fluctuations can be observed in casing because of the finite number of blades. These large, nonturbulent, periodic fluctuations caused by the blade displacement were correlated with the blade angular position. The averaging over an intermediate time scale permits differentiation between the periodic and random motion. This type of

---

[1] Presently at NSF, Engineering Directorate, Washington, D.C. 20550.

Contributed by the Fluids Engineering Division and presented at the Fourth International Conference on Laser Anemometry, Cleveland, Ohio, Aug. 1991, of THE AMERICAN SOCIETY OF MECHANICAL ENGINEERS. Manuscript received by the Fluids Engineering Division May 23, 1991. Associate Technical Editor: W. Tabakoff.

averaging was made using the TSI rotary shaft encoder and LDV software.

2 Experimental Facility

2.1 The Centrifugal Slurry Pump. A schematic of the centrifugal pump tested in laboratory is shown in Fig. 1. The casing is quasi-concentric with the impeller. The pump has a discharge diameter of $D_2 = 76.2$ mm and an inlet diameter of $D_1 = 2 \bullet R_{1i} = 100$ mm. The impeller shrouds are planar (Fig. 1(*b*)), and the blades have simple curvature. The impeller outlet diameter is $D_{2i} = 2 \bullet R_{2i} = 280$ mm. The power is transmitted to the pump from a variable speed 15 kW motor ($N = 0$–2000 rpm). The best efficiency point flowrate at 1000 rpm is $Q_n = 63.6$ m^3/h = 280 GPM corresponding to a pump head of 9.7 m. The pump was mounted in a closed circuit, which includes a feeder for solids and a phase separation system in order to control the concentration.

In a previous paper (Roco et al., 1986), three parameters were identified to affect the change of the pump head by the presence of solids: the pump specific speed, particle Reynolds number and particle-fluid Froude number at the impeller outlet. The dimensionless pump specific speed is 0.46, which is a typical value for a radial centrifugal pump. The particle Reynolds number in flow, calculated at the impeller outlet diameter, is 355. This indicates a significant convective velocity of a solid particle relative to fluid, with a significant effect on the pump head. The particle-fluid Froude number at the impeller outlet diameter, defined as the ratio between the turbulence dispersive force and particle inertial force, is much larger than unity (about 400). This indicates that the particles are fully in suspension, without persistent contact with the pump channel walls.

The impeller is closed with three blades. The width of each shroud is 25 mm, and the blade width is $B_{2i} = 35$ mm. The inlet clearance between the front impeller shroud and casing is about 5 mm. The flow cross-section in casing is rectangular ($\Delta r_{\max} = 60$ mm and $B_c = 100$ mm in Fig. 2).

The laser beams have access through eight optical grade quartz windows mounted flush with the casing wall. The quartz windows were chosen instead of plexiglas in order to obtain a better signal-to-noise ratio and to increase wear resistance. The surface of the 0.8 mm glass beads were made opaque in order to increase the amount of light back-scattered. The surface opacity was obtained by increasing the roughness in a mixing vessel with highly concentrated beads and fine abrasive particles. The size distribution of the glass beads used in experiments has remained practically unchanged after their use. The pump is lined with soft rubber, and the elbows made of aluminum have a five to one aspect ratio. In this paper, we present results obtained at window #2, which is located upstream of the pump discharge nozzle (Fig. 2).

2.2 The Laser Doppler Velocimeter. Two-dimensional point velocity measurements were performed with a two-color LDV (TSI) system. A 5W Argon-Ion laser (Coherent Innova 70) generates a multi-line beam containing both the 488 nm blue and 514.5 nm green lines. The mixed beam goes through a beam splitter producing two mixed beams. One of them passes through a Bragg Cell, where it is shifted appropriately for the flow being measured. A dichroic color separator is used to separate the shifted mixed beam into blue and green beams. The blue beams are inclined at an angle of 3.85 degrees from their median line and create a probe volume of 0.155 mm in diameter and 2.3 mm long, with 45 fringes. The green beams, at their turn, are at the same angle, and create a probe volume of 0.163 mm in diameter and 2.42 mm long, also with 45 fringes. A three-beam system (mixed, green and blue) was selected for the velocity measurements near the impeller outlet. With this system it was possible to perform measurements in a control volume at about 1 mm from the impeller periphery, as well as along the casing wall. In order to obtain all three velocity components, the measurements were performed along of two directions at right angle (along the *z* and *r* directions in Fig. 2). Light back-scattered provides information on particle velocities, and the incident beam orientations determine their directions. There were two kinds of particles in suspension: the micron size tracers usually found in tap water, and 0.8 mm glass beads. The output signals of the two photo-

Nomenclature

A_{2i} = impeller outlet cross-section
B_c = casing width
B_{2i} = blade width at the impeller outlet
C = volumetric solids concentration
D_{2i} = outlet impeller diameter
k = kinetic energy per unit mass
N = pump rotational speed
r, θ(degrees)$, z$ = coordinates
$\mathrm{R_f}$ = Reynolds stress factor
Q, Q_n = flow rate, and its nominal value
u = velocity $\overline{V}$ normalized by U_{2i}
U = average of u over $\Delta\phi_b$
U_{2i} = peripheral impeller tip velocity
v = instantaneous point velocity
$\overline{V}$ = time average point velocity at a given ϕ
$\overline{\overline{V}}$ = average of $\overline{V}$ over $\Delta\phi_b$ (Eulerian temporal average of V over time and all impeller angles)
v_∞ = terminal fall velocity of solids at $C = 0$
Z = number of blades on impeller
β = flow angle, defined in Fig. 5
$\Delta r_{\max}$ = maximum radial gap (Fig. 2)
ϕ, ϕ_0 = impeller angle, and its value at window #2, respectively
$\Delta\phi, \Delta\phi_b$ = angular interval, and blade-to-blade angular interval, respectively
ν = kinematic viscosity

Subscripts

av = averaged around the impeller (over $\theta = 0$ to 360 degrees)
A = averaged over the area of a radial cross-section
L, s = liquid and solids, respectively
p = periodic value
r, θ, z = radial, circumferential and axial direction, respectively
$\langle\ \rangle_b$ = average over B_{2i}
$\langle\ \rangle_c$ = average over B_c

Superscripts

r^*, θ^*, z^* = normalized coordinates
v_∞^* = normalized v_∞
U', V' = randomly fluctuating U and V as compared to their periodic values, respectively
ϕ^* = normalized impeller angle measured from window #2 (defined in Eq. (1))

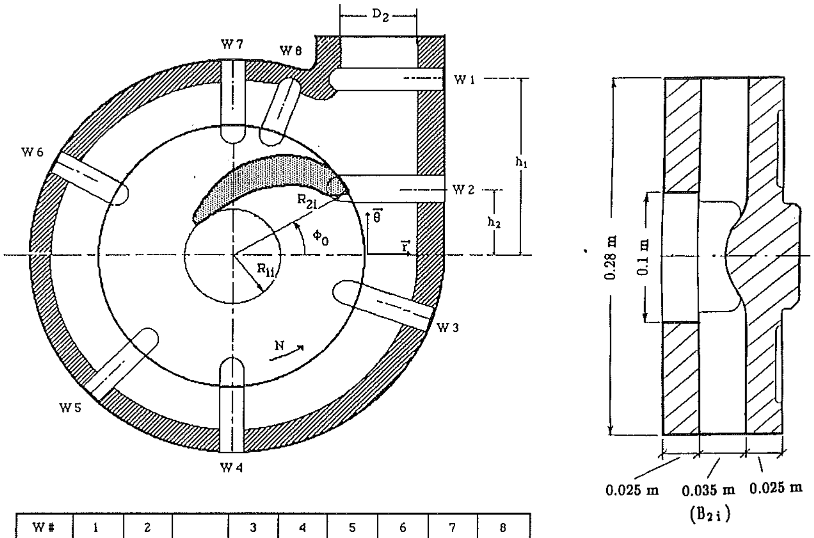

W#	1	2		3	4	5	6	7	8
h (mm)	180.6	61.2	θ (Deg)	-20	-90	-135	-210	-270	-295

(*a*) Casing (*b*) Impeller

Fig. 1 Schematic of the centrifugal slurry pump

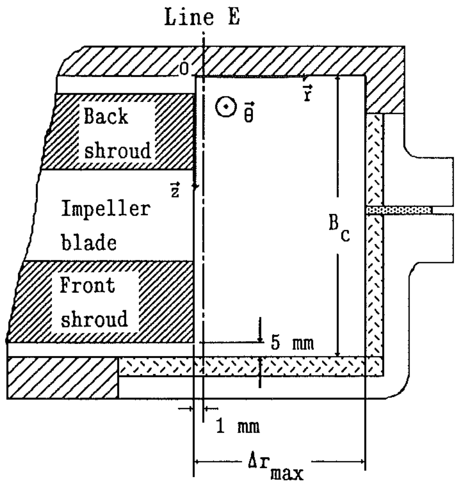

Fig. 2 Locations of the LDV measurements in a pump cross section

detectors were sent to two counter-type signal processors (TSI model 1980B) where the Doppler frequency was determined, digitized and then sent to the data acquisition system for storage and later data reduction. The first two moments of the velocity components and fluctuation cross-correlations have been calculated.

3 LDV Measurements in the Centrifugal Pump

3.1 Principle of LDV in a Dilute Slurry. In order to obtain the local slip velocity between the phases, it is necessary to measure the solids velocity and the carrier liquid velocity in the presence of the solids. The slip velocity is calculated by subtracting this last velocity from the solids velocity. Since the solids concentration is very low ($C<0.2$ percent), one may expect that the carrier liquid mean velocity should not be very different from the mixture mean velocity, defined by $V_M=(1-C)V_L+CV_S$.

Previous two-phase flow measurements have been performed using slight variations of the amplitude discrimination technique by several researchers (see Modaress et al,, 1984, a and b, for turbulent two-phase jets). When measuring the *fluid phase velocity* for a low particle mass loading in gas-solids systems, they reported that signal overload rejection and sometimes bandpass filtration sufficed to reject the signal from solids. Velocity biasing errors were addressed by using sufficiently high seeding concentrations and operating in a continuous wave mode (two or more seeding particles are present in the measuring volume at all times). Barlow et al. (1990) applied a variation of that technique for two-phase flow measurements in dense particle-laden jets, by combining the amplitude discrimination and velocity filtering (post-processing using the velocity histograms). They reported that in regions of low particle data rate (i.e., of low particle concentrations), simple amplitude discrimination is effective in the measurement of the gas phase velocity. The few misidentified particle signals did not significantly affect the mean and variance of the gas velocity. Our study has used the accepted method of lowering laser power and photo-multiplier gain to measure the solids velocity. With low solids concentrations and large solids of 0.8 mm as compared to water seeding, the amplitude discrimination technique was effective in measuring the liquid phase velocity in the presence of solids. The analysis of the velocity histogram peaks was not effective because the slip velocity was less than 10 percent of the water velocity, and the velocity variance was of the same order of magnitude with the mean velocity.

Given the large particle size and increased reflectivity of the bead surfaces, the amplitude of the solids signal was several orders of magnitude larger than that of the liquid phase, resulting in some PM saturation when measuring liquid velocity. The low solids concentration coupled with a high data rate for the liquid phase prevented the PM saturation from significantly hindering the liquid measurements. In order to estimate the effect of solids in the whole signal, a variable amplitude threshold was used. The measuring volume was made to traverse the flow section, while the threshold was set at several different levels. The real time histograms and their statistics were analyzed for each location, but no significant variations were seen in the histograms or their statistics as the threshold was varied.

In order to accomplish the *solids velocity measurements*, the PM gain was reduced to a point where the contribution of the signal arising from the water alone was negligible. This condition was satisfactorily achieved when the data rate from water was 10–15 Hz. Addition of the solid phase at this point caused, on the average, a 25–30 fold increase of the data rate. Reducing the gain any further to completely remove any contribution from the water (signal not exceeding the burst trigger) would have significantly reduced the data rate for solid phase measurements.

This simple method to measure the solid phase velocity presents several limitations. Indeed, not all the particles of the solid phase (glass beads) are taken into account because of the random nature of the solids trajectories across the measuring volume (particles crossing the edge of the volume). However, this will not affect the results for the calculation of the velocity moments of the solid phase. Another limitation of the method concerns the size distribution of the solid phase. For a broad size distribution, the choice of a constant amplitude limit might be too restrictive to discriminate between phases. Thus a more sophisticated method should be considered such as the one proposed by Modaress et al. (1984a, 1984b). This paper considers only the case of a narrow size distribution. The LDV measurements are limited by the concentration of the solid phase. Beyond 0.5 percent by volume the signal loss caused by the beam interruption and increasing noise become too significant to provide good results.

There is an uncertainty for individual velocity measurements attached to the device itself, and another caused by the sampling size. The optical system and the Doppler frequency processor have an error of 1 percent for an individual measurement. The uncertainties for velocity fluctuations and cross-correlations can be derived from the velocity uncertainty and their expressions (Hamkins and Flack, 1987). In our experiments, the uncertainty of velocity fluctuations for an individual measurement is 1 percent of the mean velocity, and the uncertainty of the cross-correlation of the velocity fluctuations in the r and θ directions is 2 percent of the square of the mean velocity.

If the confidence level is set to 95 percent for an Eulerian average, the sampling error (for 1400 samples) is variable between 0.1 and 1 percent as a function of the local variance of the velocity frequency distribution function. At the impeller outlet, the ratio of the standard deviation to mean was between 0.1 (for circumferential velocity component) and 1 (for the radial component).

The uncertainty of the measuring volume location within the flow is a function of the windows quality and optical system used to focus the beams. In our tests, the water measurements were repeated twice at several locations and the differences have been found to be less than 1 percent in average.

3.2 Principle of LDV With the Rotary Shaft Encoder. A periodic mean velocity fluctuation develops at any location in the casing because of the finite number of impeller blades. The frequency is 50 Hz, equal to the product of the number of blades ($Z=3$) and the rotation speed of the impeller (16.7 Hz or 1000 rpm). In order to separate the periodic fluctuating component from the random fluctuations, the measurements have been correlated to the angular position of the impeller using a rotary shaft encoder and a rotating machinery resolver (RMR) produced by TSI.

The shaft encoder is a notched metallic disk mounted on the pump shaft (see Fig. 3). A light source and a photo-detector are mounted on respective sides of the disk. A once-per-revolution (OPR) signal is generated each time the notch is positioned between the light source and photo detector.

This signal is then sent to the RMR where it is multiplied by 3600 in a PLL circuit (Phase-Locked-Loop), so that each pulse corresponds to an increment of 0.1 degrees. The resolver is controlled by an internal micro-processor which in turn is driven by an external micro-computer, the same as that used for the data acquisition. TSI's rotating machinery program (RMP) software package allows for the settings of designated windows in the rotation cycle (see Fig. 3). By setting three windows (one for each blade-to-blade interval) for a full revolution, one observes minor differences between the corresponding point time averages measured between different blades. Accordingly, the experimental data presented in this paper were averaged over all three blade-to-blade windows, and presented in a single 120 degree window. The resulting mean velocity was displayed in real time as a function of the angular position of the impeller.

The impeller angle ϕ^* is measured from window #2, and is normalized by the blade-to-blade interval of $\Delta\phi_b = 120$ degrees:

$$\phi^* = (\phi - \phi_0)/120 \text{ degrees} \qquad (1)$$

where $\phi_0 = 23.7$ degrees is defined in Fig. 1(a).

4 Experimental Results

The experiments were run at one rotational speed ($N = 1000$ rpm) and two flowrates ($Q_n = 63.6$ m^3/h and $Q_n/2 = 31.8$ m^3/h). The pump Reynolds number based upon the linear

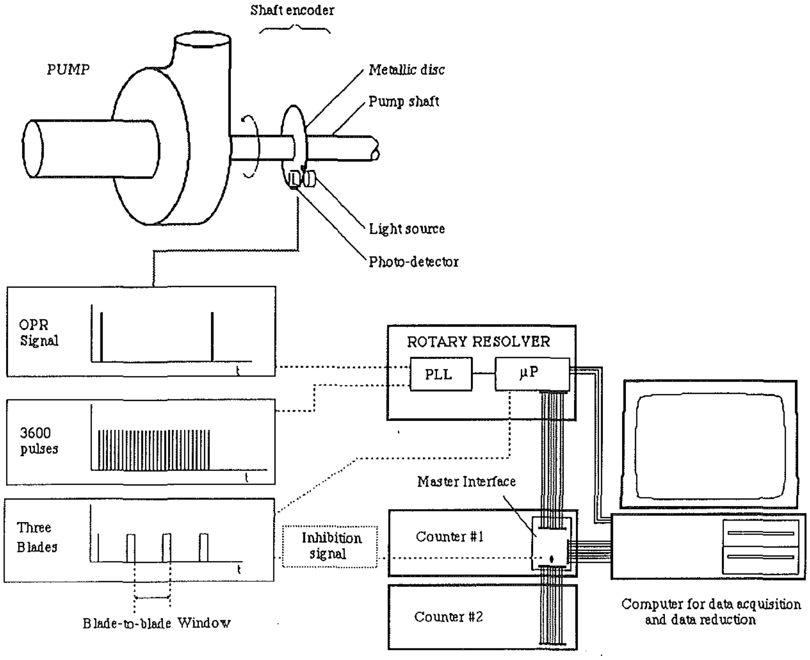

Fig. 3 Schematic of the rotary shaft encoder

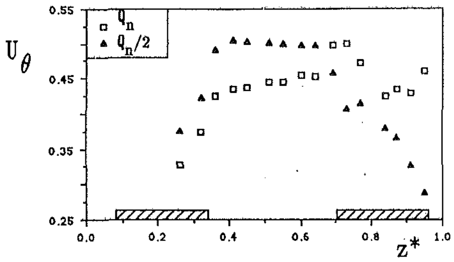

(*a*) Circumferential mean velocity, U_θ

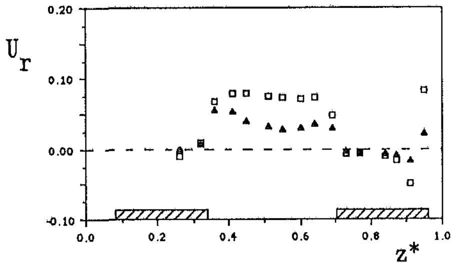

(*b*) Radial mean velocity, U_r

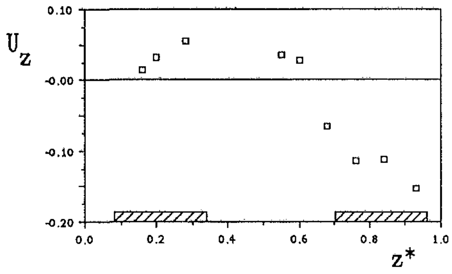

(*c*) Axial mean velocity, U_z

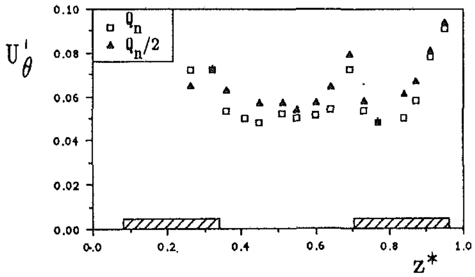

(*d*) Circumferential fluctuating velocity, U'_θ

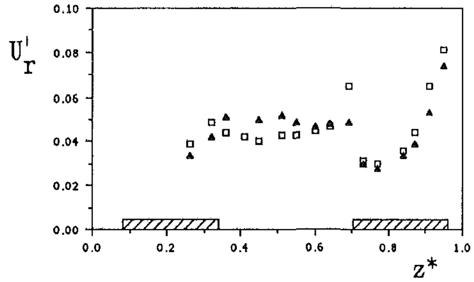

(*e*) Radial fluctuating velocity, U'_r

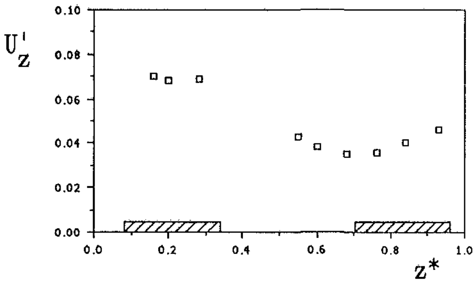

(*f*) Axial fluctuating velocity, U'_z

Fig. 4 Water velocity distribution at Q_n and $Q_n/2$ (all velocities are normalized by U_{2i})

linear velocity of the impeller ($U_{2i}=\pi D_{2i}$ N/60 = 14.67 m/s) and the impeller diameter ($D_{2i}=0.28$ m) was $\mathrm{Re}_{\mathrm{pump}}=4\cdot 10^6$. The water temperature was $20\pm 0.5°\mathrm{C}$ ($\nu\approx 1.01\ 10^{-6}\ \mathrm{m^2/s}$). The coordinate system is represented in Fig. 1. The θ-axis is tangential to the impeller circumference, and the r-axis is directed radially outwards from the impeller center. The z-axis is directed from the impeller back shroud to its front shroud (Fig. 2). The measuring locations along the z-axis start at 5 mm away from the front wall and continue up to 75 mm from the same wall. Measurements were performed at intervals of 5 to 8 mm in single phase and two-phase flows. The axial and radial coordinates were normalized by the axial width of the casing ($B_c=100$ mm) and radial gap ($\Delta r_{\max}=60$ mm), respectively. The two-phase flow experiments were conducted using two glass bead concentrations: $C=0.04$ and 0.16 percent by volume. The glass beads have a narrow distribution about 0.8 mm diameter. The density ratio was $\rho_s/\rho_L=2.48$.

4.1 Time Averaged Local Velocity Field. The Eulerian time averaged velocity distributions are presented along a line (E) parallel to the z-axis of the pump, for single and two-phase flows. $\overline{V}$ defines the measured time-averaged velocity at a point in the casing, and at the same blade-to-blade angular position:

$$\overline{V}=\frac{1}{\Delta t}\sum_{n}(V_j\cdot\Delta t_j),\quad \Delta t=\sum_{n}\Delta t_j \qquad (2)$$

where n is the sample size, and V_j and Δt_j are the velocity and burst time of the jth particle recorded, corresponding to the same angular interval between two successive blades (i.e., same $\Delta\phi$). The sample size was $n=1400$. The velocities were normalized by the peripheral impeller velocity at D_{2i}:

$$u=\overline{V}/U_{2i} \qquad (3a)$$

The normalized average velocity over the blade-to-blade interval is denoted

$$U=\overline{\overline{V}}/U_{2i} \qquad (3b)$$

where $\overline{\overline{V}}$ is the average of $\overline{V}$ over $\Delta\phi_b=120$ degrees.

Measurements for Water Flow. The mean and random fluctuating velocity components are shown in Fig. 4(*a–f*), for the two designated flowrates Q_n and $Q_n/2$. The location of the impeller shrouds is represented on the horizontal axis $0z^*$ (the front shroud is shown on the right side of the axis and the back shroud on the left side).

(*a*) *Mean Flow.* The mean flow U_θ (Fig. 4(*a*)) is asymmetric at Q_n. This asymmetry is due to the circumferential momentum transported from the casing core toward the inlet clearance (in the z direction) by the inlet clearance recirculation stream. Inlet clearance is represented on the z^* axis by the gap between $z^*=0.95$ and 1. The asymmetry of the same velocity profile almost disappears when the flowrate is reduced at $Q_n/2$, presumably due to the reduction of the inlet clearance recirculation at window #2.

The corresponding radial component of the mean velocity is displayed in Fig. 4(*b*). In front of the blade, between the impeller shrouds, the radial flow is quasi-symmetric for both flowrates. Here the profiles are almost flat, which recalls the velocity profile in a turbulent channel flow. The normalized velocity in the radial direction, averaged over the blade width at the trailing edge, is about 0.09 for Q_n and 0.045 for $Q_n/2$. The radial velocity is close to zero along line E in the proximity

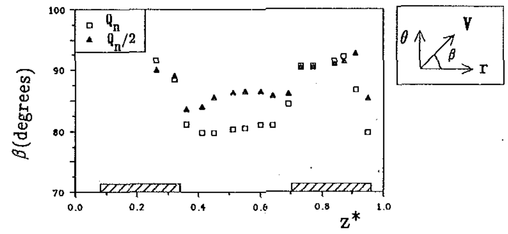

(*a*) β

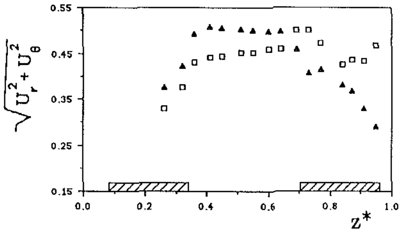

(*b*) $(U_r^2+U_\theta^2)^{0.5}$

Fig. 5 Velocity vector at the impeller outlet, at Q_n and $Q_n/2$

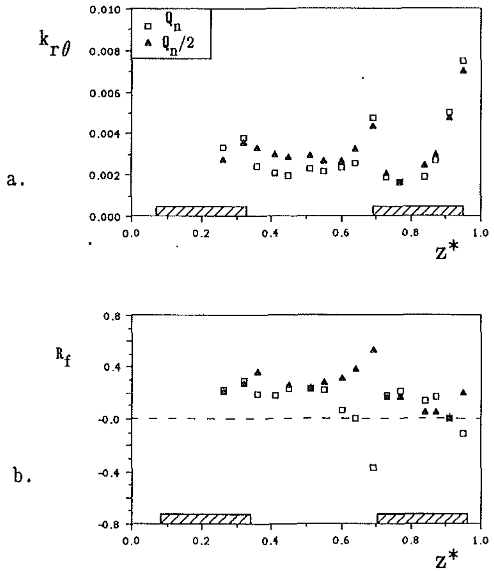

Fig. 6 Normalized turbulent kinetic energy and Reynolds stress factor at Q_n and $Q_n/2$

of the impeller shrouds. Approaching the front wall, the values decrease continuously, becoming slightly negative, then increase suddenly. This suggests the existence of a strong gradient of the velocity at the wall in the proximity of the inlet clearance. Further measurements in the front wall region were almost impossible to achieve because of the diminishing of the signal to noise ratio there, due to the strong light reflection from the window. The projection of the velocity vector in the z (axial) direction is shown in Fig. 4(*c*). The axial velocity U_z becomes negative at a location away from the center of the blade width, closer to the front shroud, at about $z^*=0.63$. This supports our previous measurements which indicate that the double helicoidal flow in casing is not symmetrical, but inclined toward the front shroud. The mean angle of the velocity with respect to the r direction in the (r,θ) plane is shown in Fig. 5(*a*). Along the impeller shrouds the angle is about 90 deg, i.e., the flow is almost circumferential. In front of the blade, the angle decreases, and the flow is more radially oriented. The asymmetry of the velocity distribution in the (r,θ) plane shown in Fig. 5(*b*) suggests the existence of a secondary flow in the cross section at Q_n.

(*b*) *Fluctuating Motion.* The velocity fluctuation averaged over $\Delta\phi_b$ has two parts: one periodic $(U_p=\overline{V}_p/U_{2i})$, and the other random $(U'=V'/U_{2i})$. The circumferential fluctuating velocity U_θ' seems to be symmetric for both flow rates, at Q_n and $Q_n/2$ (Fig. 4(*d*)). The velocity fluctuations U_θ' are larger near the shrouds and smaller in the core. Two local maxima are located at the extremities of the blade opening near the shrouds, which is a common distribution for a turbulent flow in a sudden expansion (Durrett et al., 1990). Another maximum is reached close to the casing front wall. The velocity fluctuations are slightly higher for $Q_n/2$. The radial fluctuations U_r' have almost the same shape as the circumferential fluctuations, but with a smaller magnitude. The fluctuating kinetic energy profile calculated from both random velocity components is shown in Fig. 6(*a*). It has a similar shape to the velocity fluctuations, and its magnitude is larger for $Q_n/2$ than for Q_n. The Reynolds stress factor $\mathrm{R_f}=\overline{U_\theta' U_r'}/(U_{\theta,\mathrm{rms}}U_{r,\mathrm{rms}})$ shown in Fig. 6(*b*) illustrates the change of the flow regimes between the two flowrates, with a complete inversion of the gradient at the edge of the front shroud. The index rms denotes root-mean-square of a velocity fluctuation. The coincidence window for the two velocities was brought down to an acceptable value of 100 μs. Further reduction of the coincidence window did not affect $\mathrm{R_f}$ in a sensible manner.

Measurements for Dilute Slurry Flow. The profiles of the solid phase velocity components (U_θ and U_r) and velocity angle (β) as compared to the corresponding water profiles ($C=0$) at Q_n along line E are shown in Figs. 7 and 8. These measurements were performed for slurry flow at a concentration of $C=0.16$ percent by volume. The asymmetry observed in the circumferential component profile in single phase was maintained in the solid phase profile, and one can notice the similarities between the curves (see Fig. 7(*a*)). The slip velocity is of the order of the settling velocity of the particles. The settling velocity can be estimated by the relation of Richardson and Zaki (1954) for a dilute concentration of a narrow-size particle distribution. The particle terminal fall velocity (at $C\approx 0$) is $v_\infty=0.082$ m/s, and its dimensionless value is $v_\infty^*=v_\infty/U_{2i}=0.0056$. The maximum slip velocity average a full impeller rotation is about 5 times v_∞, and occurs in front of the blade outlet (along line E, $z^*\approx 0.3$ to 0.7).

The radial velocity component distribution is shown in Fig. 7(*b*). The solid phase profile seems to coincide with the single phase one, except in front of the blade trailing edge, where the solid phase leads the single phase. This difference is probably due to the centrifugal and Coriolis forces. Because of the impeller geometry, these forces reach a maximum at the impeller outlet, and are much larger than gravity. The density difference between the phases ($\rho_s/\rho_L=2.48$) produces a noticeable positive slip velocity between the solid phase and the single phase (Fig. 7(*b*)). As a result, the orientation of the solid phase velocity vector is different from that of the single phase in front of the blade trailing edge, their trajectory making a smaller angle in (r,θ) plane (see Fig. 8, where β was defined in Fig. 5(*a*)). In the proximity of both shrouds, the particles almost follow the mean water flow streamlines.

In order to gain more insight, the differences between the water velocity profiles at different solids concentrations, and between water and solids for same concentrations, were analyzed at the impeller outlet in front of the blade (Figs. 9–10). Two low concentrations are considered, $C=0.04$ and 0.16 percent by volume.

The water velocity distributions at $C=0$ coincide with those of the liquid at $C=0.04$ and 0.16 percent, by volume, if the measuring point is in the proximity of the LDV access window at $z^*\geq 0.5$. The deviations which appear in the other half of the domain ($z^*<0.5$) increases slightly with solids concentration, as well as with the distances $(1-z)$ measured from the

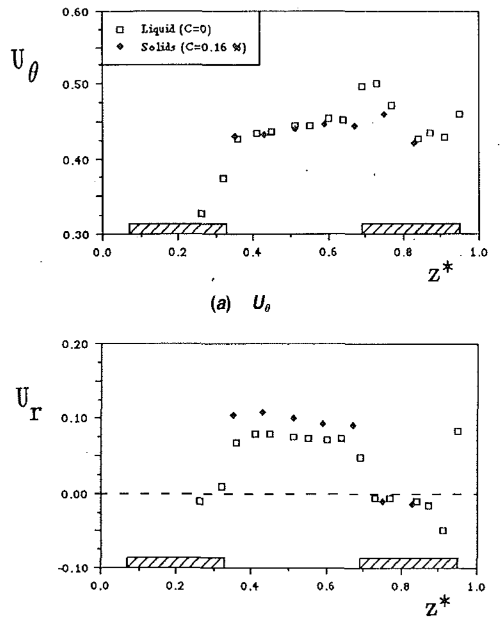

(*a*) U_θ

(*b*) U_r

Fig. 7 Water and solids velocity distributions at Q_n

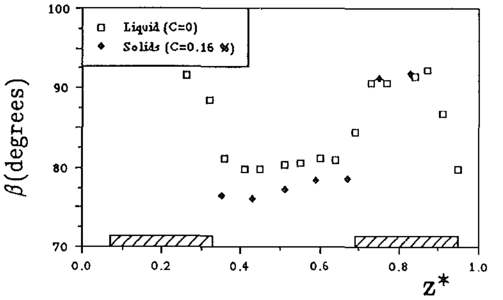

Fig. 8 Flow angle β in the ($r\theta$) plane for water and solid velocities, at Q_n

LDV access window is located. The maximum difference between the measured water velocities at $C=0$ and $C=0.16$ percent is about 10 percent. One reason might be the increase in noise in the back scattered Doppler signal in the presence of the solids as the measuring volume moves deeper into the pump. The water velocity at $C=0$ was used as reference in Figs. 9 and 10.

This error, inherent in the measuring technique, does not affect the solids velocity distributions shown in Figs. 9 and 10 because, in this case, the noise levels of the signals were kept well below the thresholds of the signal processors. While the particle slip velocity as compared to water velocity is relatively small in the θ direction, the slip velocity is larger in the radial direction (Figs. 9(*a*) and (*b*)). As a result, the solids and water velocity vectors have relative inclinations up to 5 degrees in this case (Fig. 9(*c*)).

The components of slip velocity between the solid and liquid phases, averaged over the blade-to-blade interval ($\phi^*=0$ to 1), are illustrated in Figs. 10(*a* and *b*). The slip velocity is normalized by the terminal fall velocity of the particles. In average over the blade width and over a full impeller rotation, the normalized slip velocity is negative and of order 1 in the circumferential direction, and is positive and close to 3 in the radial direction. The effect of solids concentration on the slip velocity plays a minor role at $C<0.2$ percent.

4.2 Results Presented Per Encoder Position. The results presented here illustrate the effect of the displacement of a single blade past the measuring section on the velocity profiles. Previous experiments (Roco et al., 1990) have shown that the blade displacement by the measuring location superimposes a quasi-periodic component on the overall velocity signal. There are small differences between blades, which are assumed negligible in the present study. The measured amplitude of the quasi-periodic signal is a function of the blade geometry as well as the operating parameters (impeller rotational speed, flowrate). It is also a function of the position within the casing. The periodic component decreasing in the radial direction, as one moves from the impeller outlet toward the casing circum-

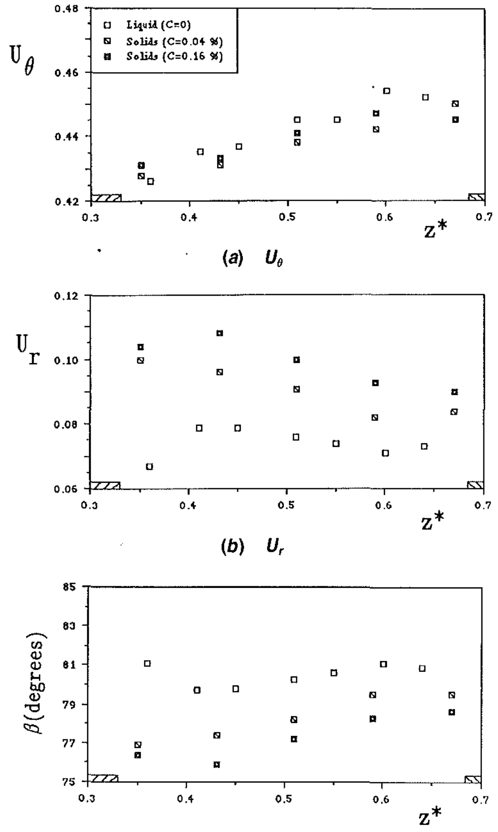

(*a*) U_θ

(*b*) U_r

(*c*) β

Fig. 9 Water and solids velocities at Q_n

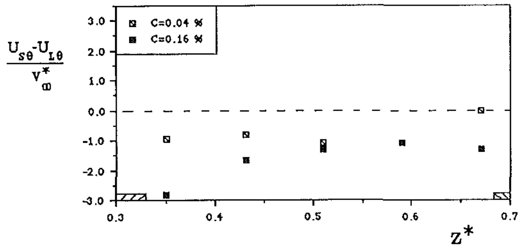

(*a*) In the circumferential direction

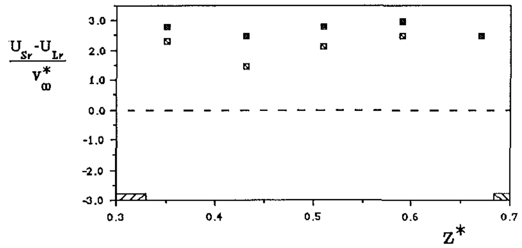

(*b*) In the radial direction

Fig. 10 Normalized slip velocity

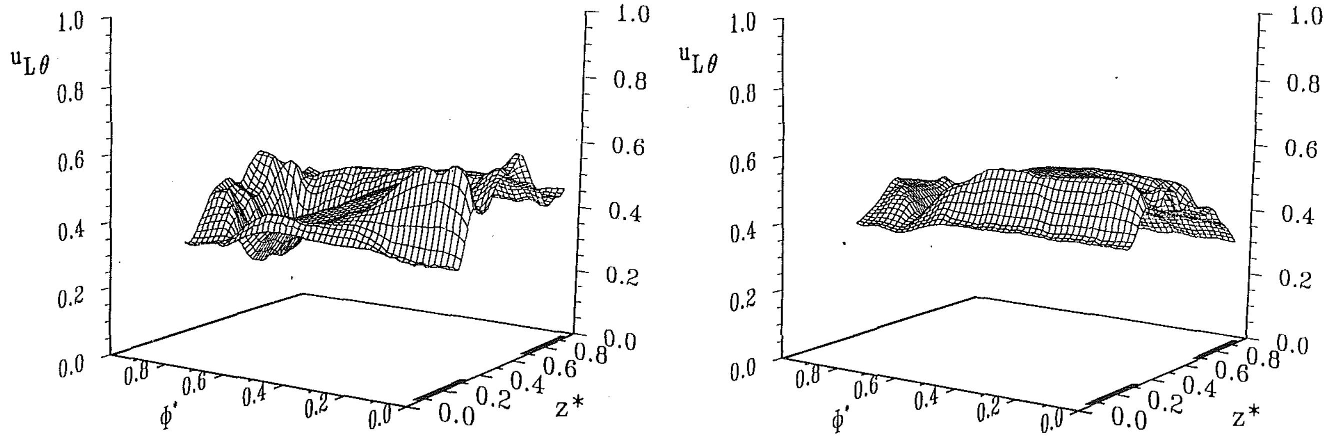

(*a*) Normalized circumferential velocity at Q_n (*c*) Normalized circumferential velocity at $Q_n/2$

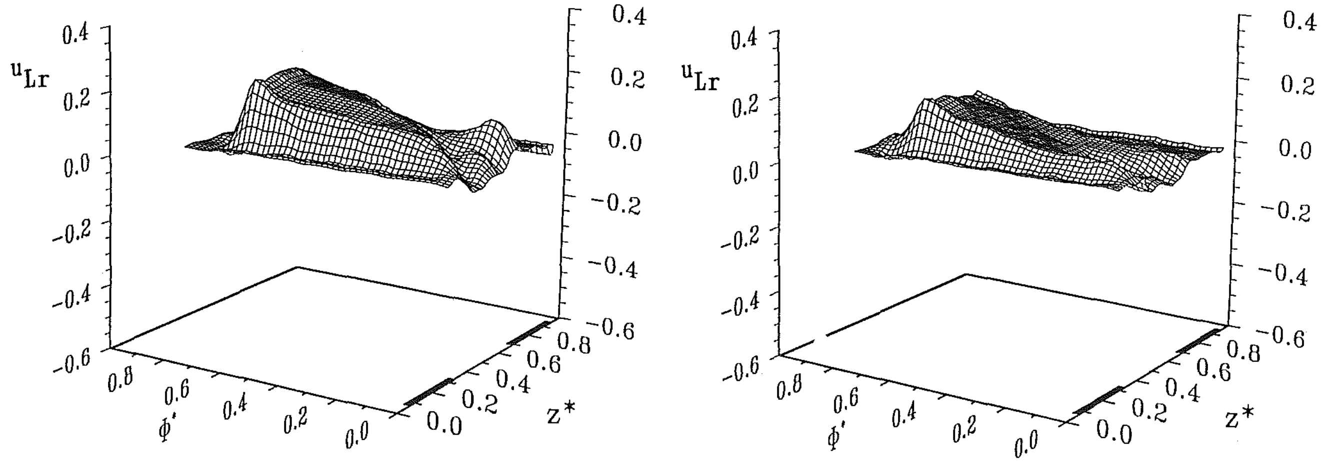

(*b*) Normalized radial velocity at Q_n (*d*) Normalized radial velocity at $Q_n/2$

Fig. 11 Effect of the impeller position on the water velocity

ferential wall. In this paper, the velocities measured over three windows of 120 degrees each (corresponding to the number of blades on impeller) were averaged over a single window of 120 degrees.

Measurements for Water Flow. Figure 11 represents the velocity components along the line E of window #2, normalized by U_{2i}, as a function of the impeller angular position (ϕ^*) and axial position (z^*). Each data point represents an average of 1400 measurements. The blade angle is measured with respect to ϕ_0 (Fig. 1). The angular position is normalized by the blade-to-blade interval (Eq. (1)).

Figure 11 shows that the effect of blade displacement is larger in front of the blade, between the shrouds ($z^* \approx 0.3$ to 0.7). At Q_n, the circumferential velocity reaches a maximum at $\phi^* = 0 - 0.2$ immediately after the blade passage, and a minimum at about $\phi^* = 0.85$ just before the arrival of the next blade. This would suggest a wake pattern behind the blade. The decrease of the circumferential velocity component (Fig. 11(*a*)) tends to be continuous from $\phi^* = 0$ to 0.85. The flow angle β is about 90 degrees at $\phi^* = 0$, and diminishes as the blade moves away. At $\phi^* = 0.85$, one notices a strong negative gradient on the circumferential component profile, immediately followed by a positive one. The radial velocity component (Fig. 11(*b*)) increases steadily with ϕ^* (from $\phi^* = 0$ to $\phi^* \approx 0.8$), and it is almost zero during the passage of the trailing edge (at $\phi^* > 0.85$).

The corresponding curves obtained at $Q_n/2$ are shown in Figs. 11(*c*) and (*d*). The effect of the blade displacement is much less pronounced at this flowrate than at Q_n, because the average inflow from impeller is about half of that at Q_n. The shape of the circumferential component is more uniform for all values of ϕ^* up to 0.9. At $\phi^* = 0.85$, one notices the same minimum for $u_{L\theta}$ and same maximum for u_{Lr} as it was observed at Q_n. However, their absolute magnitude is smaller and only for a small interval $\Delta\phi^* \approx 0.15$. The periodic velocity fluctuations induced by the blade displacement have the same order of magnitude as the turbulent fluctuations about the periodic velocity distribution.

Measurements for Dilute Slurry. The components of the normalized slip velocities, $(u_{s\theta} - u_{L\theta})/v^*_\infty$ and $(u_{sr} - u_{Lr})/v^*_\infty$, at a point $z^* \approx 0.35$ are plotted versus the impeller angle ϕ in Fig. 12. The solids concentration is 0.16 percent, and the flowrate is Q_n. It is obvious the tendency of the slip velocity components to decrease in both circumferential and radial directions, while the average absolute slip velocity is negative in the circumferential direction and positive in the radial one. Three-dimensional plots for the variation of the normalized slip velocity with the normalized coordinates ϕ^* and z^* are given in Fig. 13. The slip velocity is only a small proportion relative to the local mean velocity (about 2 percent for the circumferential component, and about 20 percent for the radial component at Q_n). Large slip velocity gradients can be observed at $\phi^* \approx 0.1$ and $\phi^* = 0.85$. The effect of the blade passage results in a sudden acceleration of the solids. The highest fluctuation is obtained for the radial component, the maximum amplitude reaching 8 times the settling velocity. These radial accelerations induced by the blades have important consequences on the wear rate of the pump casing wall. Modification of the tur-

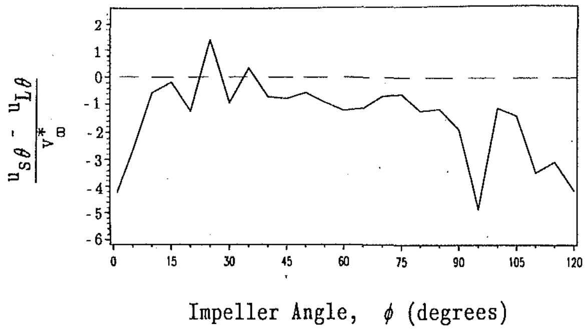

(*a*) **Circumferential slip velocity**

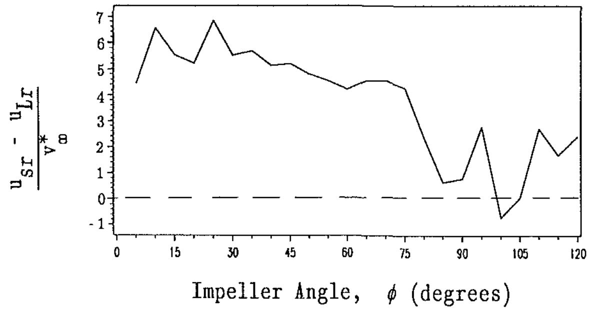

(*b*) **Radial slip velocity**

Fig. 12 Effect of the impeller position on the slip velocity at a point on line E, at Q_n

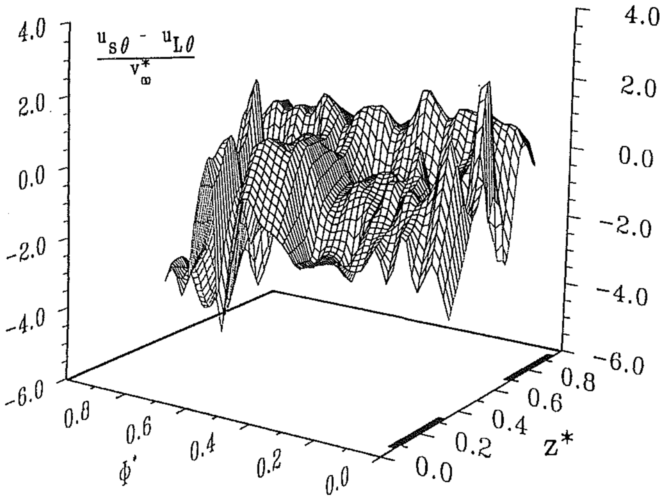

(a) **Circumferential slip velocity**

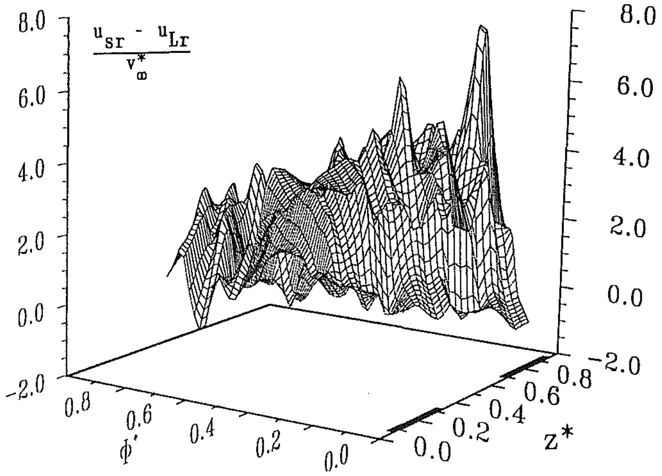

(*b*) **Radial slip velocity**

Fig. 13 Effect of the impeller position on the normalized slip velocity along line E, at Q_n

bulence of the continuous phase is also expected to occur. Preliminary data show that the fluctuations of the solids velocity may decrease the cross correlation of the continuous phase and increase the root-mean-square of the velocity components.

4.3 Discussion. The velocity fluctuations measured as a function of the blade angular position provide useful information, otherwise hidden when only averaging over a full impeller rotation is performed. The angle ϕ was discretized in 72 intervals of $\Delta\phi = 5$ degrees for a full rotation. Because of the periodicity, the data are presented for a blade-to-blade interval 360 degrees/3 blades = 120 degrees, which has 24 intervals. The normalized angle at the beginning of each angular interval n is

$$\phi^*(n) = (n = 1)\Delta\phi/120 \tag{4}$$

For all measurements performed in this study the impeller rotational speed was maintained constant, $N = 1000$ rpm. To each angular increment $\Delta\phi$ corresponds a time increment Δt

$$\Delta t = 60\ \Delta\phi/(360\ \mathrm{N}) = 0.83\ 10^{-3}\mathrm{s} \tag{5}$$

If Δt is normalized by 60/(NZ), one obtains that the normalized blade angular representation is equivalent to a normalized temporal representation, with

$$\Delta t^* = \Delta\phi^* \text{ and } t^*(n) = \phi^*(n) \tag{6}$$

The typical sampling frequency of the velocity signal was 400 Hz. The evolution of the velocity signal as a function of the blade angular position includes most of the turbulent fluctuations. The discrimination between random and periodic motion is not easy to achieve, since the blade passage frequency is equal to 50 Hz. Therefore, such a signal falls in the inertial range of the turbulence spectrum and the "reverse correlation" of the two signals in the frequency domain requires the explicit identification of the periodic signal induced by the blades displacement.

Any point instantaneous velocity $V(t)$ can be decomposed into three components:

$$V(t) = \overline{\overline{V}} + \overline{V}_p(t) + V'(t) \tag{7}$$

where $\overline{\overline{V}}$ is the Eulerian temporal average of V over time and all impeller angles. $\overline{V}_p(t)$ is the periodic signal induced by the blades passage, with a periodicity of 360 degrees/Z, whose average over all impeller angles is zero. $V'(t)$ is the measured random velocity fluctuation superimposed on $\overline{\overline{V}} + \overline{V}_p(t)$, and its average over all measurements at the same impeller angle ϕ is zero.

Since the periodic fluctuations $\overline{V}_p(t)$ are independent of random fluctuations $V'(t)$, the kinetic energy per unit mass of the total fluctuation may be separated into two parts

$$k = k_p + k_t = (\overline{V}^2_{std,p} + V^2_{std,t})/2 \tag{8}$$

where $\overline{V}_{std,p}$ denotes the standard deviation of the periodic fluctuation when the impeller angle changes, and $V_{std,t}$ is the standard deviation of the random fluctuation in time at a chosen impeller angle ϕ. The ratio between the turbulent kinetic energy and the total kinetic energy, $k_t/(k_t + k_p)$, as a function of the impeller angle is illustrated in Fig. 14 for a point at $z^* = 0.60$, in average around the impeller. The minimum ratio was obtained at $\phi = 90$ degrees, about 10 degrees before the arrival of the pressure side of the blade tip at that location in casing. The average proportion of k_t in the total kinetic energy over $\Delta\phi = 120$ degrees is 0.47 at $z^* = 0.6$. The same proportion is 0.42 if averaged over the blade opening. That is, the kinetic energy of the periodic motion is larger than the turbulent

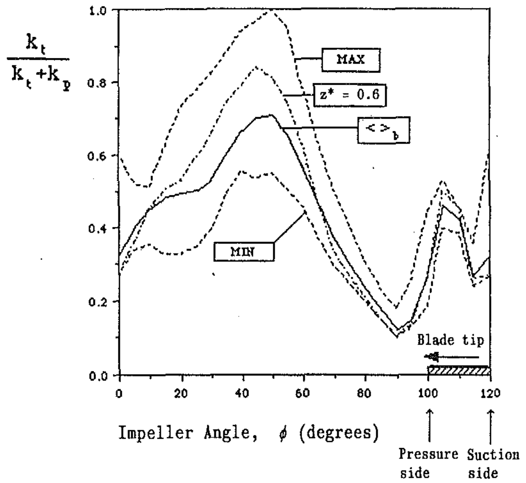

Fig. 14 The proportion of the turbulence kinetic energy k_t of the carrier fluid in the total fluctuation energy (k_p is the kinetic energy of the periodical motion; $\langle\ \rangle_b$ denotes the average over the blade width at the impeller outlet)

kinetic energy in this flow area. Figure 14 also shows the mean ratio over the blade width ($\langle\ \rangle_b$), as well as the maximum and minimum envelopes for all curves. Indeed, the effect of periodic fluctuations cannot be neglected in modeling. In the case of a slurry flow, the periodic and random velocity fluctuations, including fluctuation modulation by solid particles, should be a key element in future simulations.

5 Concluding Remarks

Back-scattering LDV has been used to investigate single liquid and dilute particulate two-phase flows in a centrifugal slurry pump at the impeller outlet. The results obtained with water at a representative section at the impeller outlet show an important change of the flow pattern between Q_n and $Q_n/2$.

The slip velocity was determined for a slurry flow at two low concentrations, using a discrimination method based on the Doppler signal amplitude. The profiles obtained suggest that the particle trajectories deviate from the fluid flow streamlines: in average, they lag the fluid in the circumferential direction, and lead the fluid in the radial direction.

The effect of the finite number of blades was evaluated by recording the velocity distribution as a function of the impeller angle. Periodic fluctuations of relatively high amplitude create a specific, flow microstructure, which is superimposed on the mean fluid and solids velocities. As a result, the velocity fluctuations and the kinetic energy of the total fluctuation increase. This effect is more pronounced at Q_n that at $Q_n/2$. In slurry flow, the effect of the finite number of blades results in a sudden acceleration of the particles, particularly in the radial direction. Hence, the number of blades has a direct consequence on the energy loss in the pump and potentially on wear, by increase the fluctuation level of both phases and the relative velocity of solid phase.

The measurements show a complexity of the flow which is not fully reflected in the present flow simulations.

Acknowledgments

This study was partially sponsored by Dresser Pump and NSF at the University of Kentucky.

References

Adler, D., and Levy, Y., 1979, "A Laser-Doppler Investigation of the Flow Inside a Backswept, Closed, Centrifugal Impeller," *J. of Mechanical Engineering Science*, Vol. 21, No. 1, pp. 1–6.

Barlow, R. S., and Morrison, C. O., 1990, "Two-Phase Velocity Measurements in Dense Particle-Laden Jets," *Experiments in Fluids*, Vol. 9, pp. 93–104.

Dong, R., Chu, S., and Katz, J., 1991, "Quantitative Visualization of the Flow within the Volute of a Centrifugal Pump," *Proc. Joint ASME-JSME Fluids Eng. Conf.*, Portland, OR.

Durrett, R. P., Stevenson, W. H., and Thompson, H. D., 1988, "Radial and Axial Turbulent Flow Measurements with an LDV in an Axisymmetric Sudden Expansion Air Flow," ASME JOURNAL OF FLUIDS ENGINEERING, Vol. 110, pp. 367–372.

Gore, R. A., and Crowe, C. T., 1989, "Effect of Particle Size on Modulating Turbulent Intensity," *Int. J. Multiphase Flow*, Vol. 15, No. 2, pp. 279–285.

Hamdullahpur, F., Pegg, M. J., and MacKay, G. D. M., 1987, "A Laser-Fluorescence Technique For Turbulent Two-Phase Flow Measurements," *Int. J. Multiphase Flow*, Vol. 13, pp. 79–385.

Hamkins, C. P., and Flack, R. D., 1987, "Laser Velocimetry Measurements in Shrouded and Unshrouded Radial Flow Pump Impellers," ASME *Journal of Turbomachinery*, Vol. 109, pp. 70–76.

Lee, S. L., and Durst, F., 1982, "On the Motion of Particles in Turbulent Duct Flows," *Int. J. Multiphase Flow*, Vol. 8, pp. 125–146.

Levy, Y., and Lockwood, F. C., 1981, "Velocity Measurements in a Particle Laden Turbulent Free Jet," *Combustion and Flame*, Vol. 40, pp. 333–339.

Modaress, D., Wuerer, J., and Elghobashi, S., 1984a, "An Experimental Study of a Turbulent Round Two-Phase Jet," *Chem. Eng. Commun.*, Vol. 28, pp. 341–354.

Modaress, D., Tan, H., and Elghobashi, S., 1984b, "Two-Component LDA Measurement in a Two-Phase Turbulent Jet," *AIAA Journal*, Vol. 22, pp. 624–630.

Nouri, J. M., Whitelaw, J. H., and Yianneskis, M., 1987, "Particle Motion and Turbulence in Dense Two-Phase Flows," *Int. J. Multiphase Flow*, Vol. 13, pp. 729–739.

Paone, N., Riethmuller, M. L., and Van den Braembussche, R. A., 1989, "Experimental Investigation of the Flow in the Vaneless Diffuser of a Centrifugal Pump by Particle Image Displacement Velocimetry," *Experiments in Fluids*, Vol. 7, pp. 371–378.

Parthasarathy, R. N., and Faeth, G. M, 1987, "Structure of a Turbulent Particle Laden Water Jet in Still Water," *Int. J. Multiphase Flow*, Vol. 13, pp. 699–716.

Richardson, J. F., and Zaki, W. N., 1954, "Sedimentation and Fluidization," *Trans. Inst. Chem. Eng.*, Vol. 32, pp. 5–12.

Roco, M. C., Marsh, M., Addie, G. R., and Maffet, J. R., 1986, "Dredge Pump Performance Prediction," *J. of Pipelines*, Vol. 5, pp. 171–190.

Roco, M. C., Hamelin, P., Cader, T., and Davidson, G., 1990, "Animation of LDV Measurements in a Centrifugal Pump," ASME Vol. FE, ASME-CSME Conf., Toronto, pp. 5–8 (also in *Int. Video J. of Engineering Research*, 1991, Vol. 1, pp. 25–40).

Roco, M. C., Cader, T., and Masbernat, O., 1992, "Periodic Liquid-Solid Flow Microstructure in a Centrifugal Pump," *Particulate Two-phase Flow*, Chapter 13, Butterworth, Boston.

Tsuji, Y., and Morikawa, Y., 1982, "LDV Measurements of an Air-Solid Two-Phase Flow in a Horizintal Pipe," *J. Fluid Mech.*, Vol. 120, pp. 385–409.

Tsuji, Y., Morikawa, Y., and Shiomi, H., 1984, "LDV Measurements of an Air-Solid Two-Phase Flow in a Vertical Pipe," *J. Fluid Mech.*, Vol. 139, pp. 417–434.

Zisselmar, R., and Molerus, O., 1979, "Investigation of Solid-Liquid Pipe Flow with Regard to Turbulent Modification," *Chem. Eng. J.*, Vol. 18, pp. 233–239.

Optimization of the Parameters for a Rotating, Mixed-Phase Reactor

J. G. Cleland
Research Triangle Institute,
Research Triangle Park, NC 27709

D. M. Kornfeld
NASA Marshall Space Flight Center,
Huntsville, Ala 35812

The motion of small, monodisperse particles in fluid was studied in a horizontal, cylindrical container rotating about its axis. One instigation for the study was the common requirement for mixed-phase, chemical or biological reactors to maintain particles in suspension for extended periods. A cylindrical, rotating reactor can allow long-term particle suspension without particle collisions and resulting agglomeration. The purpose of this study was to verify parametric effects and optimize the time of particle suspension. The theoretical and experimental results were obtained for inert, constant-diameter particles of nearly neutral buoyancy. The centrifugal buoyancy and gravitation terms were both included in the equations of motion. Laser illumination, photography and computer imaging were used to measure experimental particle concentration.

1 Introduction

The ability to keep particles suspended in a fluid without settling or interparticle collisions can be important for reacting systems. For example, this is necessary in the emulsion polymerization of styrene spheres to very precise diameters (e.g., 30 μm ± 0.3 μm) for use as microscopy calibration standards. Such spheres have been produced under low-Earth-orbit, "microgravity" conditions, as described by Kornfeld (1985) and Vanderhoff et al. (1987). An Earth-based, cylindrical, rotating reactor can allow long-term particle suspension without particle collisions and resulting agglomeration. The rotation rate can be adjusted to produce a slow, outward migration of particles which have a density near that of the fluid. The particles are also maintained in the same relative position as migration occurs.

The objectives of this study have been to 1) verify the theory of particle motion with experimental results, and 2) optimize the rate of rotation to maximize concentration of particles in suspension over time.

2 Mathematical Formulation

The following description of the behavior of uniform particles in a fluid medium, rotating inside a horizontal cylinder, follows that of Roberts et al. (1991). The theory assumes constant and similar densities for both particles and fluid, isothermal conditions, a solid body rotation of the mixture, a constant rate of cylinder rotation, and monodisperse particles of singular radius, a.

The classical solution of flow about a sphere is described by Stokes (1851) and Lamb (1945). The phenomenon of particle motion in a uniformly rotating cylindrical flow field was qualitatively described by Otto and Lorenz (1978). A more complete study of the particle orbit problem has been presented by Briegleb et al. (1971), but this study neglects the centrifugal buoyancy term. Greenspan (1983) and Ungarish (1988) have modeled mixtures in cylinders of infinite and finite length, respectively, but only in high rotational velocity ranges where the gravitational term is neglected.

In this experiment we consider a fixed coordinate system relative to the rotating cylinder, with particle position, w, relative to the cylinder center on the complex plane, such that

$$m_p \frac{d^2\overline{w}}{dt^2} = -m_p\overline{g}_y + \overline{F}_n + \overline{F}_t. \tag{1}$$

$\overline{F}_n$ is the "reduced" pressure or normal forces on the spherical particle, including the expression for pressure distribution from the Stokes solution and the centrifugal force contribution for liquid displacement by the particle, as follows

$$\overline{F}_n = \frac{4}{3}\,\pi a^3\overline{g}\rho_f - 2\pi\mu a\overline{U} + \frac{4}{3}\,\pi a^3\rho_f(\overline{w}-\overline{w}_0)\Omega^2. \tag{2}$$

The shear stresses acting tangentially at each point on the surface are integrated to give $\overline{F}_t = -4\pi\mu a\overline{U}$, where $\overline{U}$ is the relative particle velocity.

After combining terms and normalizing, the nondimensional form of Eq. (1) is

$$\frac{d}{d\mathbf{t}}\left(\frac{d\mathbf{w}}{d\mathbf{t}} + w\right) + i\left(\frac{\alpha}{1+\alpha}\right)\left(\frac{\beta}{F_r}\right)\left(\frac{w}{w_0} - 1\right) = 0 \tag{3}$$

where

$$\beta = \left[\frac{2}{9}\,\frac{\rho_p a^2\Omega}{\mu}\right]^2; \quad F_r = \left(\frac{r_0\Omega^2}{8}\right); \quad \text{and} \quad \alpha = \frac{\rho_p - \rho_f}{\rho_p}$$

are the Taylor number, rotational Froude number, and densities ratio, respectively.

The general solution to Eq. (3) represents the superposition of two spiral motions about the equilibrium position, w_0, which is a shift of the center of spiral rotation away from the cylinder axis. The expression for w_0 corresponds to the condition $d\mathbf{w}/d\mathbf{t} = 0$ and illustrates that particles along the singular axis of

---

Contributed by the Fluids Engineering Division for publication in the JOURNAL OF FLUIDS ENGINEERING. Manuscript received by the Fluids Engineering Division June 5, 1991. Associate Technical Editor: F. T. Dodge.

particle rotation are stationary with time. The shift is expressed $w_0 = -(\alpha\sqrt{\beta}/F_r)\ [i\sqrt{\beta} + (1 + \alpha)]^{-1}$. For the purposes of this study, $\beta \ll 1$, and so

$$w_0 \simeq x_0 = -\frac{\alpha\sqrt{\beta}}{F_r(1+\alpha)}. \tag{4}$$

The sign of x_0 is dependent on the relative values of ρ_f and ρ_p, and on the observed direction of rotation. Only large particles, rapidly centrifuged, possess any significant y_0 shift. The final solution takes the form

$$w = w_0 + \delta_1 e^{\alpha\beta\mathbf{t}}\cos(\sqrt{\beta}\mathbf{t}+\omega) + i\delta_1 e^{\alpha\beta\mathbf{t}}\sin(\sqrt{\beta}\mathbf{t}+\omega)$$
$$+ \delta_2 e^{-\mathbf{t}}\cos(-\sqrt{\beta}\mathbf{t}+\omega) + i\delta_2 e^{-\mathbf{t}}\sin(-\sqrt{\beta}\mathbf{t}+\omega) \tag{5}$$

The term $\Omega\alpha\sqrt{\beta}$ is the growth or decay rate for the first spiral, and $-\Omega/\sqrt{\beta}$ represents the much more rapid decay rate for the second spiral, which becomes negligibly small in a few rotations.

Therefore, the solution for any particle's position is approximated by

$$x = x_0 + \delta e^{\alpha\beta\mathbf{t}}\cos(\sqrt{\beta}\mathbf{t}+\omega) \tag{6}$$

and

$$y = \delta e^{\alpha\beta\mathbf{t}}\sin(\sqrt{\beta}\mathbf{t}+\omega), \tag{7}$$

where δ and ω are determined by the initial ($t = 0$) displacement from the center of the spiral,

$$\omega = \arctan\left[\frac{y_i}{x_i - x_0}\right] \tag{8}$$

and

$$\delta = \frac{y_i}{r_0 \sin\omega}. \tag{9}$$

The rotation rate of the spiral about point w_0 is Ω, which is the same rotation rate as the fluid. Particles lighter than the fluid spiral inward, heavier particles outward. The loss of particles from suspension in the field occurs by two mechanisms:

1) Particles are centrifuged out where they stick to the cylinder wall, or inward where they mass along the axis of rotation, and

2) The spiral shift, x_0 (which is established almost instantaneously), reduces the effective outer spiral radius to $r_0 - |x_0|$, causing more particles to collide with the wall on the shift side.

3 Experimental Procedure

3.1 Rotating Cylinder Apparatus. In the experimental evaluation monodisperse (uniform size and density) polystyrene latex microspheres were injected into a small-scale rotating cylindrical chamber and observed (Fig. 1). The cylindrical chamber containing the fluid is made of glass approximately 10.8 cm long with an inside diameter of 5.4 cm. The chamber is rotated about its axis on a shaft driven by a variable speed motor and is immersed in a constant-temperature water bath to maintain isothermal operation. Monodisperse particles of diameter 56 μm or 100 μm were used in separate tests. Particles were injected into the chamber using a hollow probe. Visual and photographic inspection showed a statistically even distribution in central cross sections (Fig. 2). These polymerized,

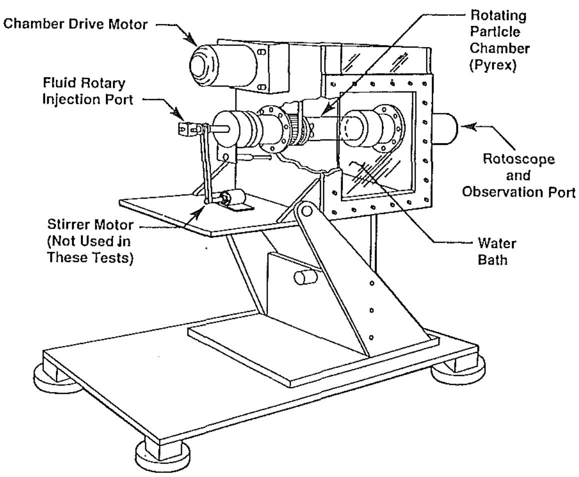

Fig. 1 Rotary reactor for particle motion studies

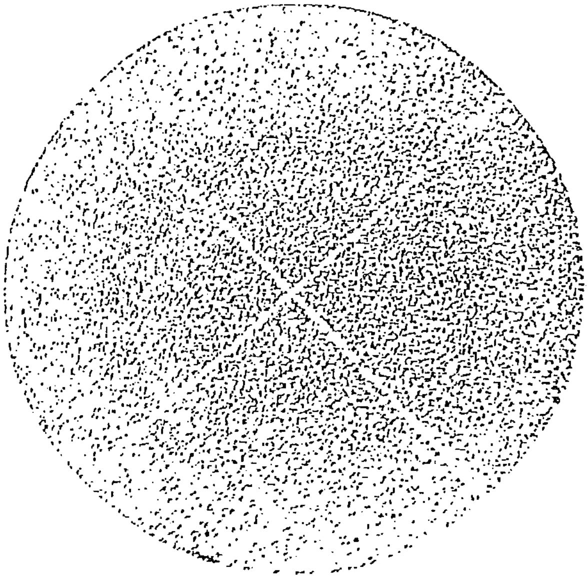

Fig. 2 Digitized and processed image of particle distribution

Nomenclature

C = particle concentration, number/cm^2
$\mathbf{C}$ = fraction remaining, $\mathbf{C} = C/C_i$
F_n = normal forces on particle, dynes
F_t = tangential forces on particle, dynes
F_r = rotational Froude number, $(r_o\Omega^2/g)$
U = relative fluid or particle velocity, as in $|d\bar{r}/dt - \bar{r}X\bar{\Omega}|$ cm/s
a = particle radius, μm
g = gravitational constant, 981 cm/s^2
m_p = particle mass, g
r_o = cylinder inside radius, cm
t = time, s
$\mathbf{t}$ = $t\Omega/\sqrt{\beta}$
w = particle position on x-iy plane, cm
$\mathbf{w}$ = w/r_o
w_o = shift of spiral center from cylinder center, cm
x = horizontal position, cm
y = vertical (parallel to gravity vector) position, cm
α = $(\rho_p - \rho_f)/(\rho_p)$
β = Taylor number, $(2\Omega a^2\rho_p/9\mu)^2$
δ = initial relative position, Eq. (9)
μ = viscosity, poise
ρ = density, g/cm^3
Ω = rate of cylinder rotation, s^{-1}
ω = initial position angle, Eq. (8)

Subscripts

f = fluid
i = initial condition @ $t = 0$
p = particle
0 = denoting spiral shift

inert spheres had a typical particle concentration of 0.02 percent by weight of particles in water. Therefore, about 100,000 particles of 100 μm size were contained in the volume, and approximately 700,000 of the 56 μm size particles. A glass observation port at one end of the cylindrical chamber allows the observer to view and photograph the particles' motion about the axis. Particles always migrated outward because only heavier-than-water particles were used. Particles in a 1-mm thick disk of fluid near the center of the rotating chamber were illuminated for observation and photography. This was accomplished by passing the beam of a 200 mW, Argon ion laser (5145 Å wavelength) through the chamber near the center of the axis, after rectifying the light to a vertical, narrow (1 mm) beam, orthogonal to the horizontal axis of the rotating cylinder. The vertical beam was obtained using a cylindrical lens. Particles in the laser-illuminated slice of fluid were well defined, although some masking and attenuation occurred. The closest average spacing of particles was 12 to 16 particle diameters, for both particle sizes at the given concentrations.

In addition, a Dove prism was mounted just outside the observation port and inside a tube centered on the axis of the rotating cylinder. The tube and prism were rotated about the prism axis, at half the angular rate of the particle-containing cylinder and in the same direction. Therefore, when viewed through the prism, the particles appeared to be standing still. This allowed simplified observation and eliminated any streaking of photographic images during high velocity rotation. The entire apparatus was mounted on a self-leveling optics table in a room shielded against light, heat and acoustic interference.

3.2 Particle Visualization and Analysis. The optical configuration and the nature of particle motion did not allow tracking of the position and mean velocities of individual particles. Although the overall particle field appeared to maintain a relatively uniform behavior, observation of individual particles was hampered by very slight nonuniformity of illumination, as well as by short-term axial migration and masking by other particles.

Particle motions were photographed and digitized using a digital imaging camera. The combination of field of view and camera resolution was such that each pixel was not more than 1.5 to 3.0 particle diameters. Flaring, differences in light refraction, and other distortion of the reflected light caused irregularities in both brightness and apparent size for individual particles. Therefore, a Laplacian treatment of the light intensity gradients was used to reduce the effects of light scattering and to improve resolution.

The Laplacian program approximated a second order gradient by assigning to any given pixel its light value minus the average of the light values of the surrounding 8 pixels, where light is measured from 0 (white/background) to 254 (black/particle). The binary image data were then computer analyzed for the contour of each image, each particle's apparent area, the position of each particle's centroid, and the total number of particles. Computer codes developed for this experiment were then used to determine particle sizes, concentration, and distributions. Figure 2 illustrates the first step of processing of the raw particle images. (Raw particle images are shown in Fig. 6.)

Experimental tests were conducted with constant angular speeds ranging from 0.05 to 2.4 rad/s (0.5 to 23 rpm). Test times were from 1 to 18 hours through about 90 percent depletion of the particles, the point at which particles finally coated the interior wall of the cylindrical vessel.

The estimated uncertainty for absolute particle count and concentration, C, is $+5$ percent, -15 percent, based on the uncertainty of the total number of particles injected for each test and the uncertainty in the imaging analysis. However, the uncertainty for $\mathbf{C}$ ($=C/C_0$) is ± 3 percent of full scale. This represents the precision of measurement by photography during each test. Uncertainties for other parameters are estimated to be: a ±1 percent; α ±4 percent; Ω ±1 percent; μ ±4 percent; and a cumulative uncertainty for the Taylor number, β, is ±8 percent.

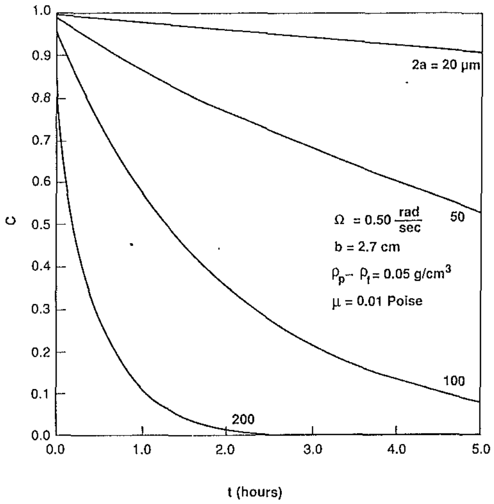

Fig. 3 Influence of particle size on particles concentration

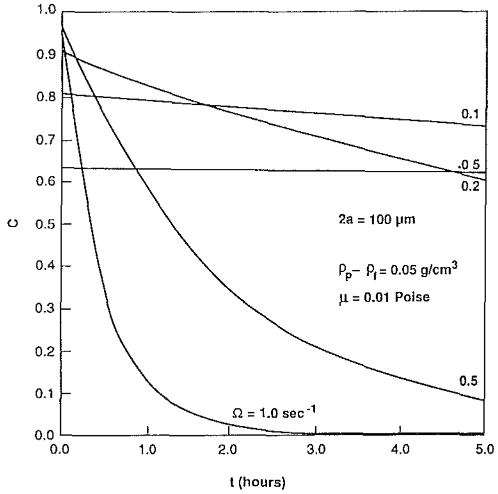

Fig. 4 Influence of angular velocity on particles concentration

4 Results and Conclusions

Baseline parameters for the evaluations were $\rho_f = 1.0$ g/cm^3, $\rho_p = 1.05$ g/cm^3, and $\mu = 0.01$ poise. The radial outward rate of particle migration is slow, relative to the rotation rate. If purely spiral motion is maintained, then monodisperse particles will maintain their relative positions without colliding, except at the outer radius or the axis boundaries.

The fraction of particles remaining in suspension is $\mathbf{C} = C/C_i$ with C_i being the initial concentration (particles/cm^2) in each cross section of the cylinder. C is influenced by particle size as a function of the second power, a^2, representing the particle drag area or profile, as shown in Fig. 3.

Figure 4 shows the effects on concentration of varied angular velocity. The concentration drops almost instantaneously for a significant x_0 shift to the right (lowest values of Ω) and particles with an initial position greater than $|r_0 - x_0|$ hit the wall in the first revolutions.

Decreasing $|\rho_p - \rho_f|$ and increasing viscosity always tends to slow particle migration *and* to reduce the shift in the spiral center. On the other hand, varying the angular velocity, Ω, results in competing effects to reduce or increase particle concentration. Reducing Ω increases spiral shift, but reduces centrifugation. The opposite effects on **C** of these 2 results lead to the optimization problem discussed in Section 4.2.

4.1 Comparison of Theory With Experiment. Uniform particle distribution during centrifuging was confirmed by experimental observation. When illuminated, the complete field of particles and individual particles could be observed (but not continuously tracked) by the naked eye. The particles stuck to the cylinder wall at impact and were not re-entrained by the fluid.

Theoretical predictions were compared with experimental results under conditions of "high" angular velocity, where most particles were removed by centrifugation within 1 to 8 hours. Figure 5 represents the results of comparison. The experimental data agreed well in almost all cases with theoretical predictions. However, the 56 μm particles, centrifuging at about 2.4 s^{-1} resulted in concentration reduction rates somewhat slower than those predicted by theory.

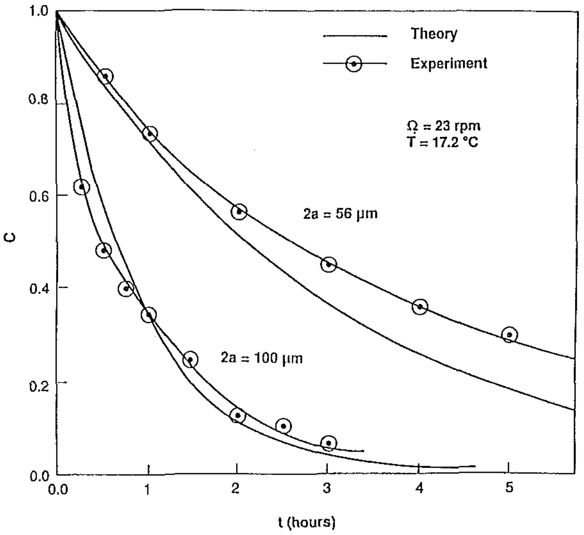

Fig. 5 Predicted concentrations compared with experiment. (Uncertainty in C = ±.03, in t = .008 hour, in a = ±1 μm, in Ω ± .2 rpm, in T = ±.5°C)

The experiments also showed that the assumptions of the theory begin to break down at low rotational velocities. For $2a = 56$ μm and $\Omega \approx 0.1$ s^{-1}, experiment and theory show that the shift of the spiral center, w_0, begins to surpass 0.1, or tens of particle diameters. With 100 μm particles, and Ω reduced to 0.15 s^{-1} ($w_0 \approx .25$), the crescent of clear volume to one side of the cylinder becomes quite apparent (Fig. 6(a)). At $\Omega = 0.10$ s^{-1} (Fig. 6(b)), the crescent grows as the theory predicts for the spiral shift. However, as Ω approaches 0.06 s^{-1} or less ($w_0 > 0.6$) the motion of the particles becomes much less predictable. Swirls and settling of particles were seen. Flow eventually became almost random, or possibly chaotic (Fig. 6(c)).

The eventual buildup of particles near the wall opposite the crescent may induce boundary effects, slip, and loss of solid-body rotation, that may manifest itself over long times even when x_0 is small.

The degree of shift resulting in the breakdown of solid body rotation has yet to be determined for various time periods. Also, crescents observed during experiments appear slightly more exaggerated than predicted by theory. These phenomena will be investigated in later studies.

4.2 Optimization of Rotating Reactor Operation. For purposes of this study, the rotating reactor operation was optimized by maintaining a maximum concentration of particles in suspension over a period of time. Since particles are migrating at rate $|\alpha\sqrt{\beta}\Omega|$ and the decreased spiral area caused by the center shift reduces concentration by the factor $\pi(r_0 - |x_0|)^2/\pi r_0^2$, then concentration is expressed

$$\mathbf{C} = [1 - |w_0|]^2 e^{-2|\alpha|\beta t}. \tag{10}$$

To optimize, $d\mathbf{C}/d\Omega = 0$ defines a maximum C in given t and

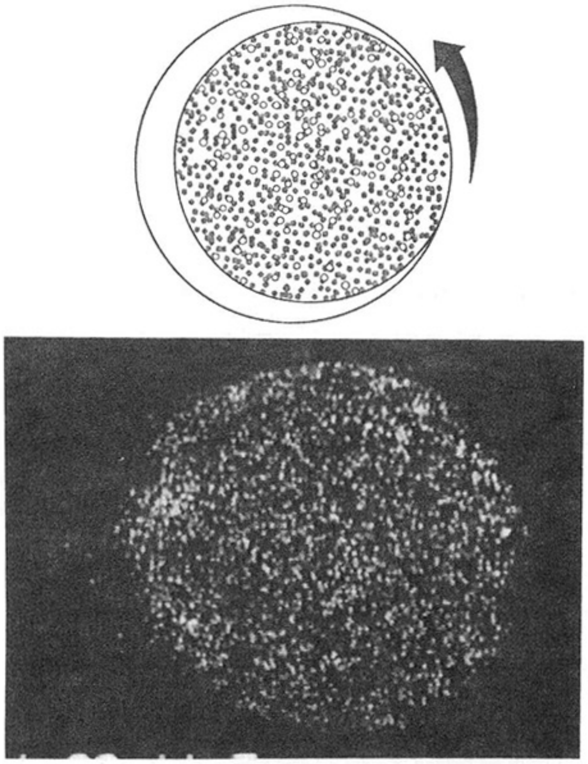

Fig. 6(a) Particle distribution pattern (freeze frame), small depletion crescent ($2a$ = 100 μm; Ω = .16 s^{-1})

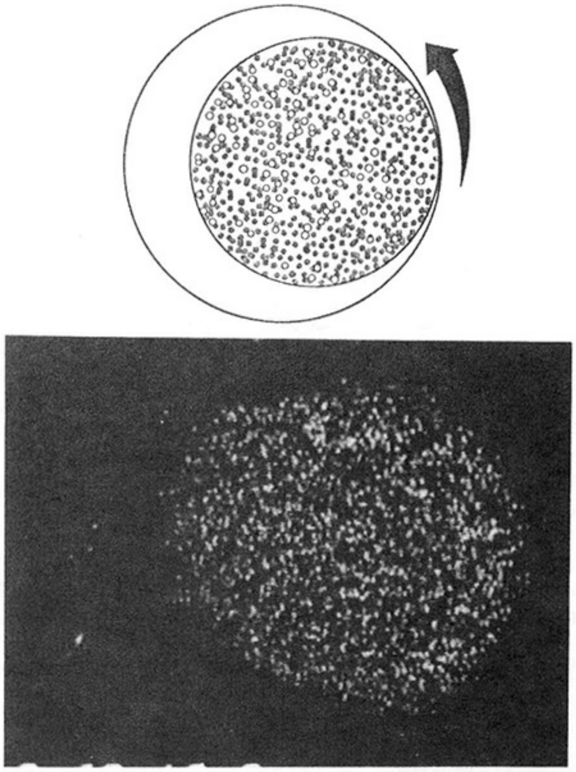

Fig. 6(b) Particle distribution pattern (freeze frame), large depletion crescent ($2a$ = 100 μm; Ω = .10 s^{-1})

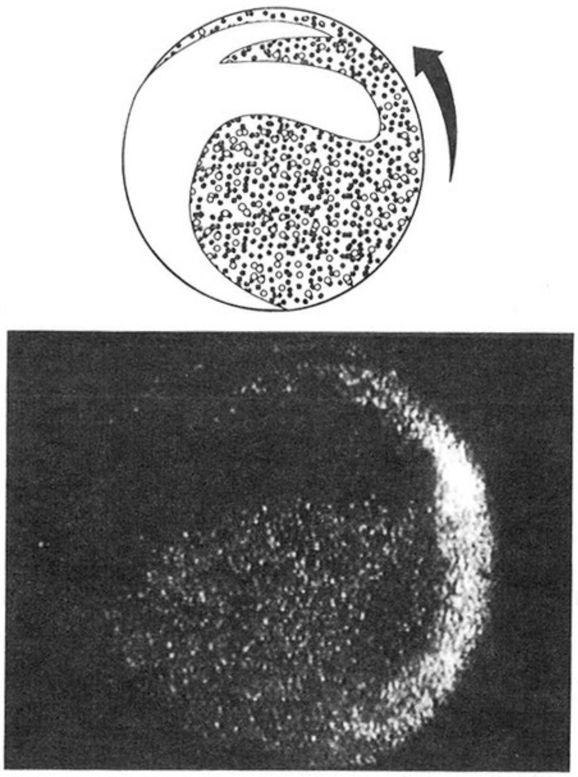

Fig. 6(*c*) Particle distribution pattern (freeze frame), random "chaotic" flow ($2a = 100\ \mu m$; $\Omega = .06\ s^{-1}$)

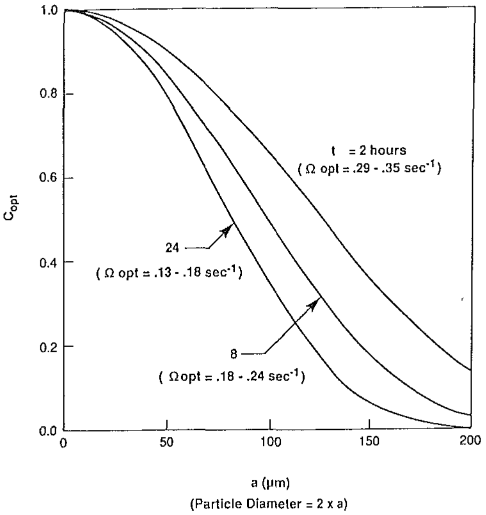

Fig. 7 Optimum particle concentrations as a function of particle size

allows derivation of an optimum rotation rate over a particular time, such as that required for polymerization. Expanding and differentiating Eq. (10) results in a cubic expression for Ω, with a single real root that may be closely approximated by

$$\Omega_{\text{opt}} = \left(\frac{8}{2r_0 t}\right)^{1/3} + \frac{2}{27}\,\frac{g\alpha a^2 \rho_p}{r_0 \mu}. \tag{11}$$

The second term is small, relative to the first, for the range of parameters in this study so that Ω_{opt} is primarily a function of r_0 and t. Large particles and large density differentials can cause the second term to become large, increasing Ω_{opt}.

Figure 7 shows values of $\mathbf{C}_{\text{opt}}$ when operating with Ω_{opt} and various particle sizes. Viscosity, densities, and other parameters are the same as the experimental values. The Ω_{opt} values used to compute $\mathbf{C}$ ranged from 0.13 rad/s (1.25 rpm) to 0.35 rad/s (3.35 rpm).

There are two problems associated with attempting to optimize concentration by speed control. First, Ω_{opt} values may be depressed until solid body rotation is disrupted (e.g., $w_0 > 0.1$). Second, for a selected t, optimum $\mathbf{C}$ values may not be sufficiently high. There are ways to maximize concentrations without relying on sped controls. One obvious method is to increase the chamber radius, r_0, which lowers Ω_{opt} but also decreases w_0, because $w_0 \propto r_0^{-2/3}$. Reactor chamber radius must be increased significantly, however, to maintain high concentrations. For example, to keep 100-μm diameter polystyrene spheres at $\mathbf{C} > 0.95$ in water for 8 hours, r_0 must be increased over 5 times (>15 cm). Another way to improve final concentration levels is to increase the fluid viscosity and reduce $|\rho_p - \rho_f|$. If initial collisions can be tolerated, another option is to first inject and concentrate particles along the chamber axis, and net migration outward would take longer than dispersed particles.

More work is needed to clarify the results obtained thus far. In addition, several problems remain to be investigated, such as variation with time in rotation rate, particle density or particle size; behavior of dense mixtures where particle interaction or mixed-phase viscosity complicate the model; and the complex phenomena that occur at the wall boundary.

Acknowledgments

The authors gratefully acknowledge the cooperation and assistance of W. K. Witherow, NASA Marshall Space Flight Center; G. O. Roberts, Roberts & Associates, Inc.; J. W. Dunn, B. W. Crissman and J. Antley, Research Triangle Institute; J. W. Vanderhoff, Lehigh University; and C. A. Stone, Accutool Corporation.

References

Briegleb, W., Schatz, A., and Tenchert, G., 1971, "Further Theoretical and Experimental Contributions to the Degree of Acceleration Dependencies of the Organisms using O-G Simulation and Hyper-G," *Proceedings of the International Astronautical Congress* (21st), North-Holland, pp. 252-263.

Greenspan, H. P., 1983, "On Centrifugal Separation of a Mixture," *Journal Fluid Mechanics*, Vol. 127, pp. 91-101.

Kornfeld, D. M., 1985, "Monodisperse Latex Reactor—A Materials Processing Space Shuttle Mid-Deck Payload," NASA TM-86487, Marshall Space Flight Center, AL.

Lamb, H., 1945, *Hydrodynamics*, Dover, New York, First American Edition, pp. 602, et seq.

Otto, G. H., and Lorenz, A., 1978, "Simulation of Low Gravity Conditions by Rotation," AIAA Paper Number 78; 273.

Roberts, G. O., Kornfeld, D. M., and Fowlis, W. W., 1991, "Particle Orbits in a Rotating Liquid," *Journal of Fluid Mechanics*, Cambridge University Press, Vol. 229, pp. 555-567.

Stokes, G. G., 1851, "On the Effect of the Internal Friction of Fluids on the Motion of Pendulums," *Transaction Cambridge Philosophical Society*, Vol. 9, Part II, pp. 8-106 or Collected Papers III, 55.

Ungarish, M., 1988, "Two-Fluid Analysis of Centrifugal Separation in a Finite Cylinder," *International Journal of Multiphase Flow*, Great Britain, Vol. 14, No. 2, pp. 233-243.

Vanderhoff, J. W., El-Aasser, M. S., Kornfeld, D. M., Micale, F. J., Sudol, E. D., Tseng, C. M., and Sheu, H. R., 1987, *Materials Research Society Symposium Proceedings*, Vol. 87, pp. 213-223.

Prediction of Rotor Dynamic Destabilizing Forces in Axial Flow Compressors

J. Colding-Jorgensen
Ødegaard & Danneskiold-Samsøe ApS,
1, Kroghsgade
DK-2100 Copenhagen, Denmark

It has been shown by Thomas (1958) and Alford (1965), that axial flow turbomachinery is subject to rotor dynamic destabilizing gas forces produced by the circumferential variation of blade-tip clearance when the rotor is whirling. However, the magnitude and direction of these forces have yet to be clarified. For example, it is still uncertain, under which circumstances the rotor whirl direction will be forward, and when it will be backward, with respect to the rotation. In the present paper, a simple analysis of the perturbed flow in an axial compressor stage with whirling rotor is presented, based on the actuator disc analysis of Horlock and Greitzer (1983), and the gas force on the rotor is calculated on this basis. It appears that in the normal operation range of an axial compressor, the whirl direction is predicted to be forward always. Backward whirl is predicted to take place only at very low flow rates, well below the normally expected stall limit. Experimentally, forces were indeed found in direction of backward whirl for low flow rates, and in direction of forward whirl for high flow rates, in the results reported by Vance and Laudadio (1984), as analyzed by Ehrich (1989). While this experimental evidence supports the present theory qualitatively, a direct comparison of the measured and predicted destabilizing force has yet to be carried out.

Introduction

Highly loaded turbomachinery frequently exhibits self-excited rotor whirl where one of the rotor natural precession frequencies becomes unstable.

One of the possible causes for this is a work-fluid force, depending on the instant position and velocity of the rotor axis during shaft precession. Ehrich and Childs (1984) have reviewed some know and hypothesized mechanisms responsible for this rotor dynamic stability problem.

For axial turbomachinery, the mechanism described by Thomas (1958) and Alford (1965) is the most widely accepted destabilizing mechanism. However, there is still considerable discussion with regard to the magnitude and direction of the destabilizing force, as depending on the different process parameters, primarily speed, load and flow rate. Both Alford and Thomas postulated the destabilizing force to be given by a cross-coupling stiffness coefficient:

$$K_{XY} = -K_{YX} = \frac{T\beta_A}{D_m H} \tag{1}$$

That is, the destabilizing force is proportional to the torque. β_A can be interpreted as the change in thermodynamic efficiency per unit change in clearance, since the force is hypothesized to be caused by the circumferential efficiency variation due to asymmetric blade tip clearance when the rotor axis is deflected.

Alford (1965) argued that the absolute value of torque should be used in Eq. (1), to predict forward whirl (see Fig. 3), both for compressors and turbines. Ehrich (1989) has suggested that it would be more stringent to use the algebraic value of the torque, predicting forward whirl for a turbine, and backward for a compressor.

There has, however, been a considerable mismatch between available empirical data and this simple theory.

If the theory was valid, β_A should be equal to the change in efficiency that one could in fact observe when the clearance was changed in a given machine, but this is far from the case. Therefore, β_A has become a kind of "fudge factor" used to bring empirical data into agreement with the theory.

For example, an empirical study of an axial blower by Vance and Laudadio (1984) showed that β_A is not at all constant, but varies considerably in magnitude, and even in sign, when process parameters are changed. The change in sign means that the same machine could exhibit forward or backward whirl, depending on the process conditions.

To get away from the "fudge factor" approach, it is necessary to abandon the simplified theory, where β_A is interpreted as a proportionality constant between stage torque and destabilizing force, and look in more detail at the flow perturbation in the blade row of an axial turbo machine when the rotor axis is deflected with respect to the housing and stator. Then, armed with this analysis, calculate the resulting fluid force on the rotor, and compare it with empirical data, and with the simplified theory of Eq. (1). This is the scope of the present paper. The flow model used in this study is essentially

---

Contributed by the Fluids Engineering Division for publication in the JOURNAL OF FLUIDS ENGINEERING. Manuscript received by the Fluids Engineering Division April 18, 1990. Associate Technical Editor: U. S. Rohatgi.

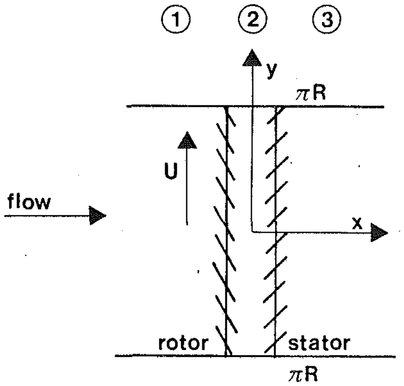

Fig. 1 Actuator disks and coordinate system for flow analysis

that presented by Horlock and Greitzer (1983), that is, an actuator disk model.

Their analysis was aimed at studying the flow perturbation arising from blade defects in rotor and stator of an axial compressor, but they did not calculate the force on the rotor. This analysis was extended by Qiu and Martinez-Sanchez (1989) to calculate the destabilizing force on an axial turbine rotor, but so far the analysis of an axial compressor has not been presented. Also, the investigation of the force as a function of flow rate has not yet been presented, and, as we shall see, this is quite essential.

Physical Model

Alford (1965) made the assumption that the blade tip clearance variation did not affect the flow field, but only the force on the blade, which would then be proportional to the local efficiency.

Contrary to this assumption, the clearance variation is bound to affect the whole flowfield. A simplified calculation of this flow field variation is the actuator disk model presented by Greitzer and Horlock (1983), which is used in the present analysis. In this model, each blade row is represented as an actuator disk across which the local axial velocity is continuous, but the flow angle and pressure is discontinuous. A high hub/tip ratio is assumed, so that a two-dimensional analysis is possible. The fluid is taken to be incompressible and inviscid outside the blade row.

The actuator disk and flow field geometry is treated in a coordinate system, where the row is unwrapped, so that the y-direction is the tangential direction, see Fig. 1.

The particular configuration examined is that of a compressor stage with rotor and stator, but the method can be applied to any configuration with any number of rotor and stator rows, and also for a turbine.

For simplicity, only stationary rotor eccentricities are examined here, so we limit ourselves to a quasi-stationary approach. In this situation, the flow is steady in the x-y system, outside the blade rows. The perturbation velocities are defined in terms of a perturbation stream function:

$$c_x' = \frac{\partial \psi}{\partial y} \tag{2}$$

$$c_y' = -\frac{\partial \psi}{\partial x} \tag{3}$$

Since the tip clearance variation is caused by a small eccentricity of the rotor, it can be written as $t = \bar{t} + \Delta t$, where

$$\Delta t = e_o \exp(iy/R) \tag{4}$$

Consequently, the perturbation stream function must also be of the same form, and it can be formulated outside the blade rows as:

Upstream:

$$\psi_1(x, y) = A \exp(iy/R + x/R) \tag{5}$$

Between rotor and stator:

$$\psi_2(x, y) = F \exp(iy/R - x/R) + G \exp(iy/R - \tan\bar{\alpha}_2 ix/R) \tag{6}$$

Downstream of stator:

$$\psi_3(x, y) = B \exp(iy/r - x/R) + D \exp(iy/R - \tan\bar{\alpha}_3 ix/R) \tag{7}$$

Nomenclature

A = constant in stream function Eq. (5)
B = constant in stream function Eq. (7)
C_p = specific heat coefficient for constant pressure
$\bar{C}_x$ = mean axial velocity
C_x' = perturbed axial velocity
$\bar{C}_y$ = mean tangential velocity
C_y' = perturbed tangential velocity
D = constant in stream function Eq. (7)
D_m = mean tip diameter
e_o = shaft eccentricity
f_T' = perturbed tangential force on blade
F_T = tangential force on rotor
F = constant in stream function Eq. (6)
G = constant in stream function Eq. (6)
H = blade length
$K_{XY} = -K_{YX}$ = cross coupling coefficient
$\bar{p}$ = static pressure
p = mean value of p
p_o = total pressure
$\bar{p}, \bar{p}_o$ = mean values of p and p_o, respectively
Q_1 = defined after Eq. (14)
Q_2 = defined after Eq. (14)
R = $R = D_m/2$
T = torque on shaft (positive for compressor, negative for turbine)
T_o = stagnation temperature
t = tip clearance
t = mean tip clearance
Δt = local variation of clearance
U = rotor tangential speed
(x, y) = coordinate system in flow analysis
(X, Y) = coordinate system for rotor force analysis
α = absolute flow angle
$\bar{\alpha}$ = mean value of α
βA = Alfords constant defined after Eq. (1)
β = blade angle
γ = isentrope coefficient
η = local efficiency
$\bar{\eta}$ = mean value of η
λ = overall efficiency decrease per unit global clearance increase
ρ = density
ϕ = flow coefficient
ψ = perturbation stream function
ω = rotational angular frequency

Subscripts

1 = upstream
2 = between rotor and stator
3 = downstream

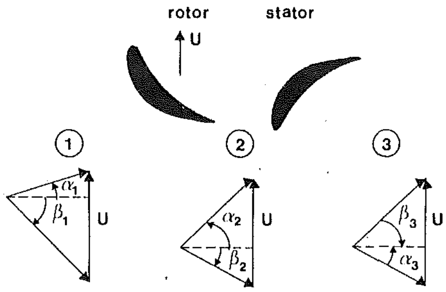

Fig. 2 Flow angles and velocity diagrams

where $\overline{\alpha}_2$ and $\overline{\alpha}_3$ are the mean absolute flow angles, between the rows and downstream respectively, see Fig. 2.

Upstream the flow is irrotational, while downstream the flow is rotational. The first terms in expressions (6) and (7) describe irrotational disturbances, and the second, the rotational disturbances.

The rows are assumed to be infinitely thin, as is the spacing between them. Therefore $x=0$ at all the three rows, and Eq. (6) is only valid for $x \simeq 0$, whereas Eqs. (5) and (7) are valid for $-\infty < x \geq 0$ and $0 \leq x < \infty$, respectively.

Basic Equations

There are two matching conditions across each blade row:

(*a*) The axial velocity is continuous:

$$C'_{x1} = C'_{x2} = C'_{x3} \tag{8}$$

(*b*) The fluid follows the blades perfectly at the outlet of each blade row:

$$\frac{\partial \psi_2}{\partial y}(0, y)\tan\beta_2 = -\frac{\partial \psi_2}{\partial x}(0, y) \tag{9}$$

and

$$\frac{\partial \psi_3}{\partial y}(0, y)\tan\overline{\alpha}_3 = -\frac{\partial \psi_3}{\partial x}(0, y) \tag{10}$$

A third condition is based on the postulate that the local variation of efficiency resulting from a local variation of clearance is the same as the change in overall efficiency resulting from a similar global changes of clearance. The latter can then be obtained for a given machine, testing it with different tip clearance. The total to static compressor efficiency can be written:

$$\eta = \frac{c_p T_{01}\left(\left(\frac{p_3}{p_{01}}\right)^{\gamma-1/\gamma} - 1\right)}{(\mathrm{C}_{y2} - \mathrm{C}_{y1})\mathrm{U}} \tag{11}$$

The third condition can be expressed:

$$\frac{\partial \eta}{\partial y} = \frac{\partial \eta}{\partial t}\frac{\partial t}{\partial y} \tag{12}$$

where $\partial\eta/\partial t = -\lambda$ is taken as the overall efficiency change per unit global clearance increase.

Finally, the momentum balance of the fluid in the tangential direction is:

$$\frac{\partial p}{\partial y} = -\rho\left(\overline{C}_x \frac{\partial C'_y}{\partial x} + \overline{C}_y \frac{\partial C'_y}{\partial y}\right) \tag{13}$$

It should be noted that, contrary to the simplified theory leading to Eq. (1), a tangential variation in discharge pressure is allowed by Eqs. (13) and (11).

Solution of the Equations

When Eqs. (2)-(3) and (11) are perturbed to 1st order in y and inserted into Eq. (13), we get:

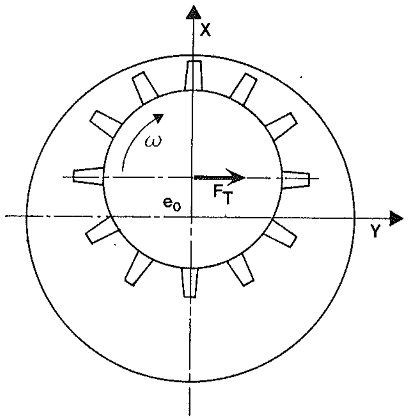

Fig. 3 Tangential force on eccentric rotor

$$\lambda \frac{\partial \Delta t}{\partial y}\frac{Q_1}{\overline{\eta}^2} + \frac{Q_2}{\overline{\eta}^2}\left(\overline{C}_x \frac{\partial^2 \psi_3}{\partial x^2} + \overline{C}_y \frac{\partial^2 \psi_3}{\partial x \partial y}\right) = \left(\frac{\partial^2 \psi_2}{\partial x \partial y} - \frac{\partial^2 \psi_1}{\partial x \partial y}\right) U \tag{14}$$

where

$$Q_1 = C_p T_{01}\left(\left(\frac{\overline{p}_3}{\overline{p}_{01}}\right)^{(\gamma-1)/\gamma} - 1\right)$$

and

$$Q_2 = \overline{\eta} C_p T_{01} \frac{\gamma - 1}{\gamma}\left(\frac{\overline{p}_3}{\overline{p}_{01}}\right)^{(\gamma-1)/\gamma}$$

Equation (14) is reduced to an algebraic equation with the help of Eqs. (4)-(7):

$$\frac{i\lambda e_0 Q_1 R}{\overline{\eta}^2} = -\frac{Q_2}{\overline{\eta}^2}\overline{C}_x B(1 - i\tan\overline{\alpha}_3) - G\tan\overline{\alpha}_2 U + i(F + A)U \tag{15}$$

The matching conditions, Eqs. (8), (9), and (10) are now used to determine the constants B, F, and G in terms of A, and we get:

$$B = 0$$

$$F = A\frac{\tan\overline{\alpha}_2 - \tan\beta_2}{\tan\overline{\alpha}_2 + 1}$$

$$G = A\frac{\tan\beta_2 + i}{\tan\overline{\alpha}_2 + i}$$

These are inserted into (15) which is then solved for A. The result is:

$$A = \frac{R\lambda e_0 Q_1}{U\overline{\eta}^2(1 + i\tan\beta_2)} \tag{16}$$

The perturbation of the flow in the blade rows is now given by:

$$C'_x(x=0) = \frac{\partial \psi_1}{\partial y} = \frac{iA}{R}\exp(iy/R) \tag{17}$$

and the fact that the flow follows the blades perfectly as assumed in actuator disk theory.

Calculation of Destabilizing Force

The perturbation of the tangential force on a rotor blade is obtained from the Euler turbine equation, which is the momentum balance on a control volume around the blade passage:

$$f'_T = -\rho H(C'_{x1}(x=0)(\overline{C}_{y2} - \overline{C}_{y1}) + \rho\overline{C}_x(C'_{y2}(x=0) - C'_{y2}(x=0) - C'_{y1}(x=0))$$

(positive in the direction of rotation). Using Eqs. (2), (3), and (9), we get:

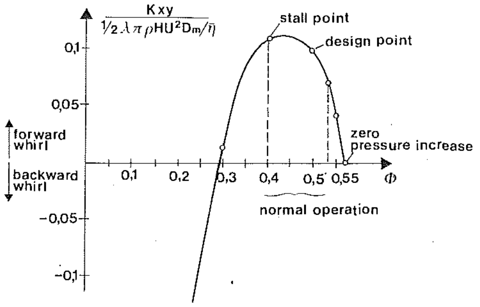

Fig. 4 Nondimensional cross coupling coefficient as a function of nondimensional flow rate

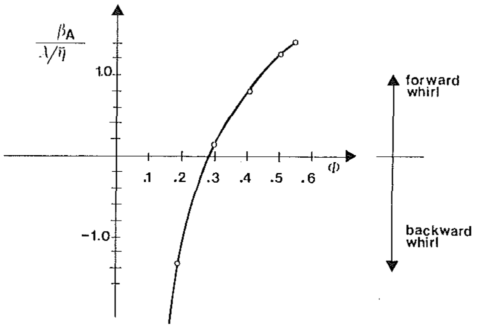

Fig. 5 Revised Alford constant according to Eq. (21)

$$f_T' = \rho H C_{x1}'(x=0)\,(U + 2\overline{C}_x(\tan\beta_2 - \tan\alpha_1)) \qquad (18)$$

Equations (16) and (17) are now inserted in Eq. (18) and integrated around the rotor, bearing in mind that Eq. (4) gives the rotor eccentricity as $-e_0 \exp(iy/R)$. This gives the total tangential force in the direction of rotation on a rotor, which center is moving on a circle with radius e_0:

$$F_T = \frac{\lambda Q_1 \pi e_0}{U\overline{\eta}^2} R \sin\beta_2 (U + \overline{C}_x(2\tan\beta_2 + \cot\beta_2 - \tan\overline{\alpha}_1)) \qquad (19)$$

(see Fig. 3), and the cross coupling stiffness coefficient:

$$K_{XY} = \frac{\partial F_T}{\partial e_0} = \frac{\lambda Q_1 \pi R}{U\overline{\eta}^2} \sin\beta(\rho H)\,(U + \overline{C}_x(2\tan\beta_2 + \cot\beta_2 - \tan\overline{\alpha}_1)) \qquad (20)$$

When K_{XY} is positive, forward whirl will be excited. When K_{XY} is negative, backward whirl will be excited by the destabilizing fluid force.

Using Eq. (11), Eq. (20) can be rewritten as:

$$K_{XY} = \frac{\lambda\pi}{\overline{\eta}} \sin\beta_2 \rho H U^2 R (1 + \phi^2(2\tan^2\beta_2 + 1 - 3\tan\overline{\alpha}_1 \tan\beta_2 - \tan\overline{\alpha}_1 \cot\beta_2 + \tan 2\overline{\alpha}_1) + \phi(3\tan\beta_2 + \cot\beta_2 - 2\tan\overline{\alpha}_1) \qquad (20a)$$

Results and Discussion

In order to get a view of the destabilizing force as a function of process parameters, we study a nondimensional coefficient:

$$\frac{K_{XY}}{\lambda\pi\rho H U^2 R/\overline{\eta}}$$

as a function of the nondimensional flow rate

$$\phi = \frac{\overline{C}_x}{U}.$$

A number of typical compressor stage types have been examined, and in all cases the results predict forward whirl for a compressor, except for flow rates well below the normally expected stall limit. Also, β_A is far from constant as it should be according to the Alford-Thomas formula, Eq. (1).

An example is shown in Fig. 4, for no inlet swirl ($\overline{\alpha}_1 = 0$), and $\beta_2 = -60$ deg.

We can, however, still use the simple Alford expression (1), if we interpret β_A, not as a constant, but as given by:

$$\beta_A = \frac{\lambda \sin\beta_2}{\overline{\eta}}(1/\phi + 2\tan\beta_2 + \cot\beta_2 - \tan\overline{\alpha}_1) \qquad (21)$$

This is found, inserting the torque equation:

$$T = 2\pi R^2 H q \overline{C}_x (\overline{C}_{y2} - \overline{C}_{y1})$$

into Eq. (1) and combining it with Eqs. (11) and (20). In this case, β_A will be a function of ϕ, as shown in Fig. 5 for the case of $\overline{\alpha}_1 = 0$ and $\beta_2 = 60$ deg.

The prediction should also be compared with available experimental evidence. Such data were presented by Vance and Laudadio (1984), for an axial blower. The analysis of such an isolated rotor ends in an expression slightly different from the rotor-stator case presented here, but the β_A-values predicted behave essentially in the same way, so it seems relevant to compare the experimental results of Vance and Laudadio to the β_A-values predicted by the present analysis.

Unfortunately, Vance and Laudadio did not report axial velocity or flow rate-data, but only torque and speed. However, an analysis of their data by Ehrich (1989) suggests that their measurements of negative β_A were with low flow rates, and their measurements of positive β_A were with higher flow rates. This agrees with the present analysis. However, Ehrich (1989) suggested that a compressor should exhibit backward whirl for normal flow rates, and only forward whirl when it approaches turbining, where the torque reverses. This is contradicted by the present analysis, which predicts forward whirl in the normal operating range of a compressor. Also, Eq. (21) and Fig. 5 show that β_A is of the same order of magnitude as λ, in the normal operation range. Since λ is normally measured to be around 2.0, we would expect a $\beta_A \simeq 2.0$ in the normal operation range.

This is precisely what is measured by Vance and Laudadio, and it agrees well with most field experience with axial compressors: backward whirl is hardly ever seen, only forward whirl is observed in the normal operating range, and β_A-values measured as usually reported to lie between 1.0 and 4.0.

Conclusion

A quasi-stationary analysis of the perturbed flow and rotor force in an axial compressor stage has been presented.

The destabilizing force is not predicted to be simply proportional to stage torque as claimed by the simple theory Eq. (1), but a function of flow rate and blade angles. Within the normal operation range of both axial compressors and turbines, the present theory predicts destabilization of forward whirl, whereas backward whirl is predicted for a stalling compressor.

The present theory is in better agreement with experimental data and field experience than the Alford-Thomas formula Eq. (1), and it is therefore claimed to be a better, but still very simple starting point for analytical work aimed at predicting the work-fluid influence on rotor dynamic behavior of axial turbomachinery.

Acknowledgment

The author wishes to thank Dr. F. Ehrich, General Electric Co., for an important contribution to the formulation of the problem treated in this paper, and useful suggestions in regard to its theoretical treatment.

References

Alford, J., "Protecting Turbomachinery from Self-excited Rotor Whirl," ASME *Journal of Engineering for Power*, Oct., 1965.

Ehrich, F., "A State-of-the-Art Survey in Rotor Dynamics—Nonlinear and Self-Excited Vibration Phenomena, Dynamics of Rotating Machinery," *Proceedings of the Second International Symposium on Transport Phenomena, Dynamics, and Design of Rotating Machinery*, Hemisphere Publishing Corporation, 1989.

Ehrich, F., and Childs, D., "Self-Excited Vibration in High Performance Turbomachinery," *Mechanical Engineering*, May 1984.

Horlock, J. H., and Greitzer, E. M., "Non Uniform Flows in Axial Compressors Due to Tip Clearance Variation," *Proceedings of the Institutions of Mechanical Engineers*, Vol. 1976, I. Mech. E. September, 1983.

Thomas, J. J., "Instabile Eigenschwingungen von Turbinenlaufern angefacht durch die Spaltströmungen Stopfbüschen und Beschaufelungen, AEG Sonderdruck, 1958.

Vance, J. M., and Laudadio, F. J., "Experimental Measurement of Alfords Force in Axial Flow Turbomachinery," ASME IGTI Paper No. 1984-GT-140.

Qui, Y. J., and Martinez-Sanchez, M., "The Prediction of Destabilizing Blade Tip Forces for Shrouded and Unshrouded Turbines," Progress Report on NASA Contract NAS8-35018, Mass. Inst. of Technology, 1989.

M. Marini
Research Engineer.

A. Massardo
Associate Professor.
Mem. ASME

A. Satta
Professor.

M. Geraci
Graduate Student.

Dipartimento di Ingegneria Energetica,
Università di Genova,
Genoa, Italy

Low Area Ratio Aircraft Fuel Jet-Pump Performances With and Without Cavitation

The experimental analysis performed on several small size low area ratio aircraft fuel jet pumps in JP4 is outlined. The variables investigated were area ratio, nozzle and throat diameters, nozzle and suction pressures. The experimental values of head ratio were compared to a one-dimensional theoretical prediction method previously found to be applicable to moderate and high area ratio pumps. The results show the necessity of making some modifications in the model at low flow coefficient values. Measured wall static pressures were also compared with the results of an axisymmetric finite difference turbulent calculation; the comparisons are generally in good agreement. The development of cavitation and related parameters were also investigated. In order to enhance cavitation resistance, which is particularly important in the field of aeronautics, some studies were carried out on two stage jet pumps. The results obtained are outlined and discussed.

Introduction

The jet pump is a low pressure high flow rate volume pump. It utilizes the energy of a low mass flow, high velocity stream to induce a large mass flow, low velocity stream. The pump consists of a suction chamber, a mixing throat, an outlet diffuser, and a motive flow nozzle (Fig. 1). With rigid mounting and no moving parts, the pump is immune to vibration and can be designed with minimum weight. The jet pump for fuel transfer in aircraft makes use of the power generally wasted in excess capacity of boost pumps. The boost pump excess flow, instead of being relieved back to tank with all pressure energy lost, is bypassed to the jet pump at boost pump pressure. The use of the jet pump in this manner avoids the weight, reliability penalty, and cost of additional electrical transfer pumps, and jettisonable tank pressurization. In addition, it has a very good resistance to cavitation compared to the other types of pumps, and the maintenance cost it practically nil.

An experimental and theoretical analysis on several small size low area ratio jet pumps is outlined. One of the major objectives of this work is the experimental analysis of low area ratio jet pumps designed to be installed on an executive type airplane (Filippi et al., 1986), and particularly the analysis of the parameters that influence the cavitation resistance (area ratio, nozzle and throat diameters, suction and jet pressures, temperature of fluid). Another objective is the development of theoretical models for the design and analysis of single and two stage jet pumps.

The pumps work with JP4 fuel as in aircraft operation conditions (Filippi et al., 1986). There is little information available in the open literature on this type of pump and application (Cunningham, 1954; Sanger, 1970). Therefore this project was started to develop high cavitation resistance, small size low area ratio jet pumps to be used in aircraft. The experimental studies were carried out with the DINE jet pump facility (Massardo and Satta, 1985), which allows the analysis of simulated aircraft operations (hot day climb). At the same time two theoretical analyses were developed: the first was a one-dimensional model proposed by Cunningham (1954)—modified for low area ratio pumps—and the second was an axisymmetric turbulent jet-mixing calculation developed by Massardo (1989).

In order to obtain high resistance against cavitation, two stage jet pumps were also investigated.

Apparatus and Procedure

The test facility was a closed loop, continuous, or open circulation system having a total fuel capacity of 0.5 m^3. A schematic diagram is shown in Fig. 2 and a complete description is given by Massardo and Satta (1985). The working fluid is JP4 fuel. A high pressure fuel stream, pumped by a gear pump ① flows into the primary nozzle via the flow measuring system (magnetic flow meter) ②. It then discharges at the throat inlet of the jet pump ⑤. The suction line (secondary flow) consists of the suction pipe ③ connected with the fuel depressurizable tank ⑥. The primary fuel and secondary stream mix together in the throat and flow out along the de-

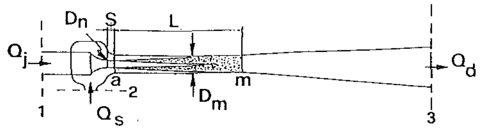

Fig. 1 Schematic representation of jet pump

Contributed by the Fluids Engineering Division for publication in the JOURNAL OF FLUIDS ENGINEERING. Manuscript received by the Fluids Engineering Division March 13, 1990. Associate Technical Editor: U. S. Rohatgi.

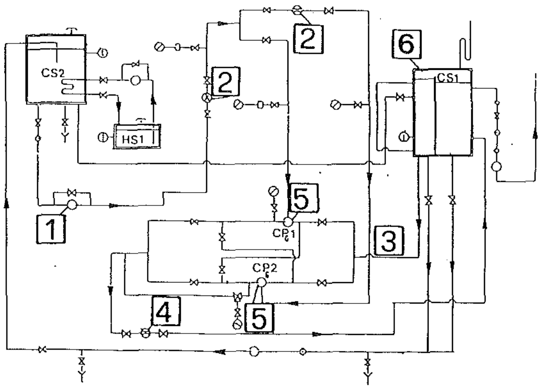

Fig. 2 Schematic drawing of fuel jet pump test facility of the University of Genoa

TAP	1	2	3	4	5	6	7	8
$\bar{X}$	.009	.033	.060	.096	.133	.176	.218	.253
TAP	9	10	11	12	13	14	15	16
$\bar{X}$	.311	.349	.389	.430	.468	.508	.546	.587

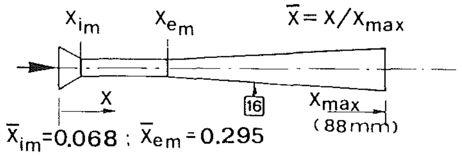

Fig. 3 Schematic diagram of test pump and static pressure tap locations ($\bar{x} = 0.009 + 0.002$)

Table 1 Estimated errors (instrumentation and readability combined) of the principal measured variables

Head rise and static pressure	<0.7%
Inlet pressure, primary stream	<0.6%
Flow rate, primary stream	<2.0%
Flow rate, secondary stream	<2.5%
Temperature	<1.0°C
Vapor pressure	<2.0%

Table 2 Dimensions of twenty-one kinds of pump used

Test N°	D_m (mm)	D_n (mm)	b	L_m/D_m	D_d/D_m
1	5.00	0.50	0.010	4.20	2.460
2	4.44	0.50	0.013	4.50	2.770
3	3.50	0.50	0.020	5.57	3.514
4	5.00	0.75	0.022	4.20	2.460
5	4.44	0.75	0.028	4.50	2.770
6	5.00	0.90	0.032	4.20	2.460
7	4.44	0.90	0.041	4.50	2.770
8	5.00	1.02	0.042	4.20	2.460
9	5.00	1.06	0.045	4.20	2.460
10	3.50	0.75	0.046	5.57	3.514
11	4.44	1.02	0.053	4.50	2.770
12	5.00	1.16	0.054	4.20	2.460
13	4.44	1.06	0.057	4.50	2.770
14	3.50	0.90	0.066	5.57	3.514
15	4.44	1.16	0.068	4.50	2.770
16	5.00	1.45	0.084	4.20	2.460
17	3.50	1.02	0.085	5.57	3.514
18	3.50	1.06	0.092	5.57	3.514
19	4.44	1.45	0.107	4.50	2.770
20	3.50	1.16	0.110	5.57	3.514
21	3.50	1.45	0.172	5.57	3.514

livery line, after recovering pressure in the diffuser. On the delivery line another flow meter ④ is installed.

The instrumentation used in this investigation is discussed in detail in Massardo and Satta (1985). Pressures were measured by precision Bourdon tube gauges and mercury manometers. The flow passage in the mixing and diffuser zones was surveyed at selected axial locations with static pressure taps (Fig. 3). The facility makes it possible to control the working fluid temperature (20-80°C), the primary pressure (0-3000 kPa), and the suction pressure (10-101 kPa). During the tests the vapor pressure of the fluid is measured with the RIED method as described in Massardo and Satta (1985). The facility was designed to preserve the vapor pressure during the tests, by means of separation between virgin and already used JP4.

The estimate errors (instrumentation and readability combined) of the principal measured variable are presented in Table 1.

The performance of many pumps with various configurations were investigated for various jet quantities (p_j or Q_j) and suction pressures (p_s), while the area ratio was changed by using nozzles and throats of various diameters. The range of operation for the tests is presented in Table 2. Each test was conducted at constant values of primary flow rate and secondary inlet pressure. The secondary flow rate and, therefore, the flow ratio was varied.

Analysis of the Results

The overall performance of pumps illustrated in Table 2 was investigated. The results are presented as head ratio ψ, defined as $(p_d - p_s)/(p_j - p_d)$ plotted as a function of flow ratio $\varphi = Q_s/Q_j$. Figure 4 shows the head ratio versus φ assuming b as a parameter at sea level, and Fig. 5 at about 8000 m of ceiling from sea level. Each one shows the difference in allowable head and flow ratios between a very small area ratio ($b_{\min} = 0.01$) and a higher area ratio ($b_{\max} = 0.172$). The cavitation influence is quite evident: the difference between the figures quoted correlates with the cavitation, which is enhanced by low secondary pressure values (Fig. 5).

At selected geometry and flow ratios, wall static pressure surveys were conducted (Fig. 6). At low flow ratios, in the first part of the throat, the wall static pressures are close to suction pressure, while in the second part of the throat (see also Fig. 11) the data have a sharp increase, which continues, but less sharply, in the diffuser. At higher φ values the wall static pressures are lower than p_s in the first part of the throat;

Nomenclature

A, D = area, diameter, respectively
b = area ratio (A_n/A_m)
c = velocity
E = friction loss
k_1 = nozzle friction coefficient
k_{34} = throat and diffuser friction coefficient
p = pressure
Q = flow rate
S = spacing between nozzle and throat inlet

T = temperature
x, y = axial and radial coordinate
φ = flow ratio (Q_s/Q_j)
ψ = head ratio $(p_d - p_s)/(p_j - p_d)$
ρ = density
μ = viscosity
σ_L = cavitation coefficient $(p_s - p_v)/(p_s - p_a^*)$

Subscripts

a = throat inlet
j, s, d = jet, suction, delivery, respectively
f, g = fluid, geometric, respectively
n, m = nozzle, throat, respectively
v = vapor

Superscripts

* = cavitation limit condition

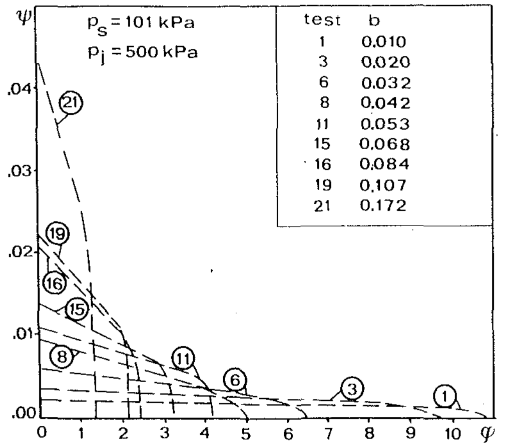

Fig. 4 Head ratio versus flow and area ratio coefficient for pumps of Table 2 and $p_s = 101$ kPa

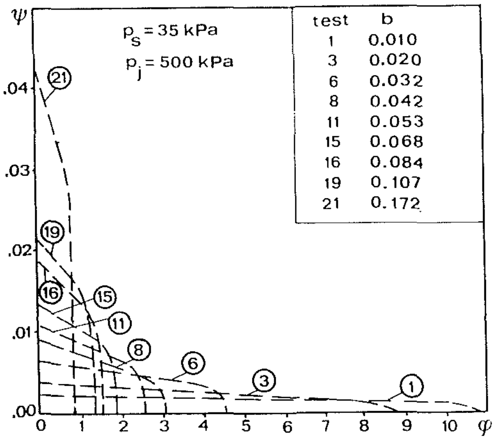

Fig. 5 Head ratio versus flow and area ratio coefficients for pumps of Table 2 and $p_s = 35$ kPa

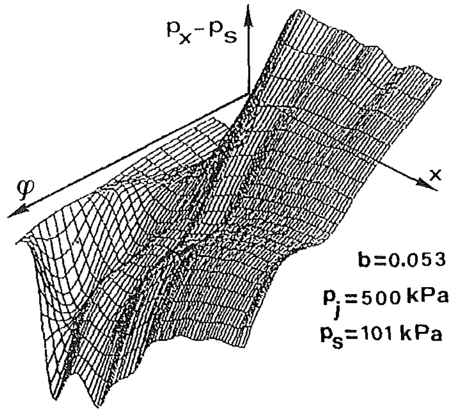

Fig. 6 Static pressure surface versus flow ratio and abscissa x for pump with $b = 0.053$ at $p_s = 101$ kPa and $p_j = 500$ kPa

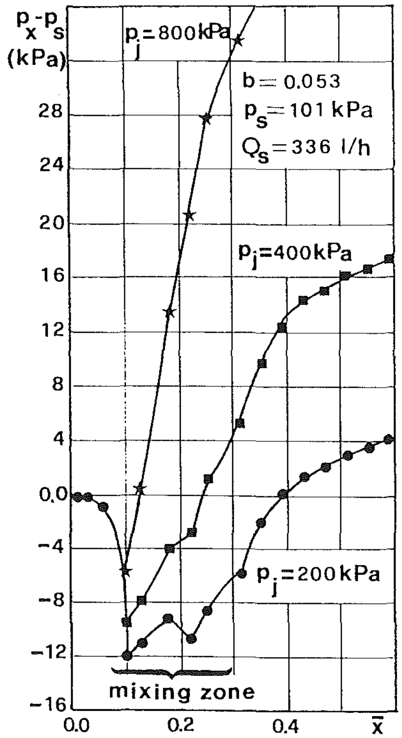

Fig. 7 Jet pressure influence on separation in mixing zone

the pressure recovery is obtained, almost with the same behavior, in the second part of the mixing region and in the diffuser. At the highest φ values ($\varphi > 4$) a zone of separation is present in the mixing. Figure 7 shows that by increasing primary pressure (i.e., jet velocity) at fixed geometry and Q_s value the separation is gradually reduced and then disappears. The same result is obtained by lowering suction pressure as may be seen from the comparison between Fig. 6 and $\varphi = 6$ line of Fig. 11.

Theoretical Analysis

Two different theoretical analyses for jet pumps performance calculation were utilized: the first was a one-dimensional method proposed by Cunningham (1954) (see Appendix); the second was an axisymmetric jet-mixing turbulent model developed by the authors (Massardo, 1989).

Figure 8 shows the comparison between measured and calculated head ratio, using the Cunningham's one-dimensional method. The mean values of the friction coefficients K_{34} and K_1 were evaluated experimentally: $K_{34} = 0.35$ and $K_1 = 0.13$. Cunningham (1954) proposed similar values ($K_{34} = 0.30$ and $K_1 = 0.10$). When φ is greater than 2 ($Q_s > 2Q_j$) the calculation is very close to the data, while if φ is less than 2 the calculation gives head ratio values lower than the data. That happens for all the b values investigated here. As shown clearly in Fig. 8, also assuming $K_{34} = 0.0$ (no losses in the throat-diffuser region), the theoretical analysis underestimates the head ratio values when $\varphi < 2.0$. The influence of Q_d on K_{34} was then investigated in detail; the results are presented in Fig. 9. The solid line represents the K_{34} values obtained using pipes and diffuser friction losses equation, the dotted line represents the K_{34} value necessary to obtain complete agreement between theory and data for all the flow ratio values here investigated. Variations in the delivery flow rate do not influence the solid line, while dotted line is influenced by cavitation at high Q_d values (this is evident when $p_s = 35$ kPa), and at low flow rate where K_{34} assumes also negative values (inconsistent with Cunningham's theory). This phenomenon, which exists only for low area ratio jet pumps ($b < 0.3$) (Sanger, 1970) correlates with the hypothesis used in Cunningham's one-dimensional theory. In fact when $Q_s < Q_j$ ($\varphi < 1$), since $A_m >> A_n$ ($A_m = 100A_n$ if $b = 0.01$), the spread of the primary jet cannot completely fill the throat area in the mixing zone of the pump. The area filled by the fluid, defined as fluid throat area A_{mf}, is lower than geometrical throat area, and therefore b can be considered higher ($b_f > b_g$). It justifies, under fixed conditions (φ, p_s, p_j), the higher values of the measured head ratio at low flow ratios, compared with theoretical data (Fig. 8). Figure 10 shows the influence of flow ratio φ, at various area ratio coefficients b_g, on fluid area ratio

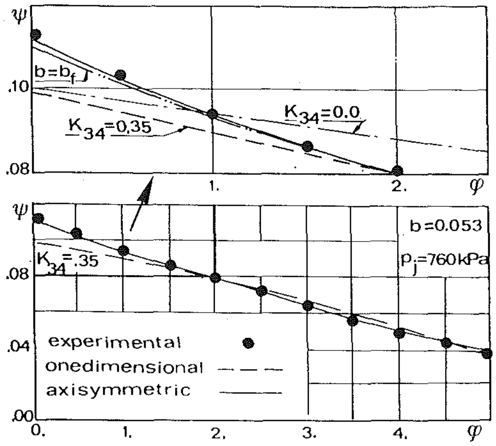

Fig. 8 Experimental and theoretical head ratio for pump having $b = 0.053$

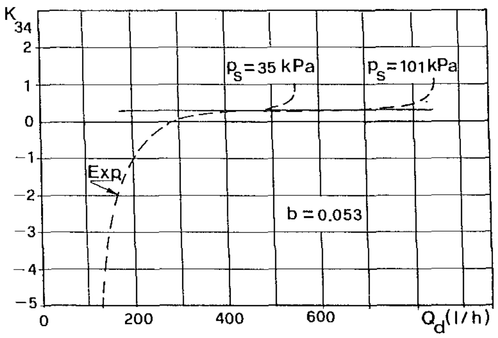

Fig. 9 Effect of delivery flow rate Q_d on coefficient K_{34} at two different suction pressure values

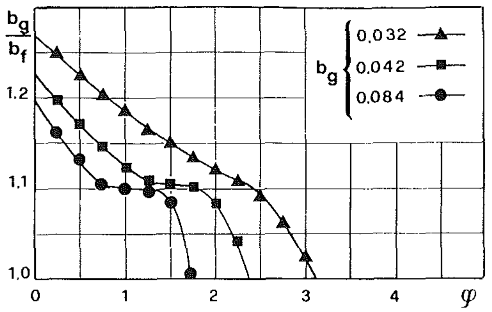

Fig. 10 Fluid area ratio coefficient b_f versus flow ratio and geometrical area ratio b_g

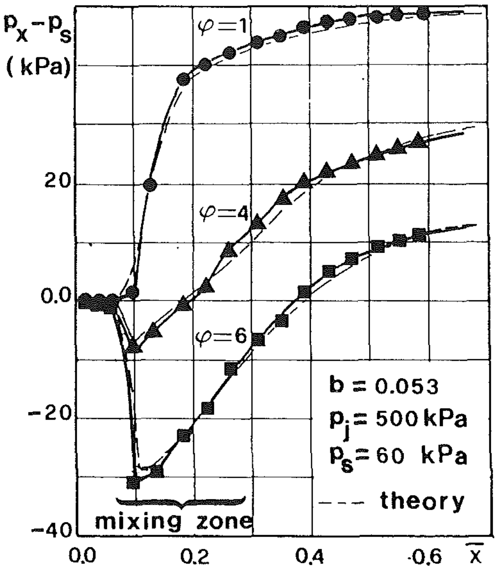

Fig. 11 Comparison between measured and calculated wall static pressure at different flow ratio values

coefficients b_f previously described. The zones where b_f is different from b_g are reduced when b_g increases. The results shown in Fig. 10 confirm that the disagreement between data and Cunningham's theory is greatly present when the area ratio is very low.

A good agreement between data and theoretical analysis can be obtained for all the values of φ (see Fig. 8) using in the head ratio equation (see Appendix) the values proposed in Fig. 10 for the area ratio.

This approach is useful for pump performance overall estimation and also the pump preliminary design (Filippi et al., 1986). However, to improve pump's performance, taking into account mixing phenomena and cavitation influence a finite difference computer program was developed. The channel geometry variation along the axis of the pump was assumed to be gradual, so that wall curvature was neglected and, on all planes normal to the axis, the static pressure was assumed to be uniform. Details of the method were outlined in Massardo (1989). The flow was assumed axisymmetric and incompressible; the equations in boundary layer form were transformed using the Denny and Landis (1971) transformation, and then they were solved with a finite difference technique. The turbulent terms in the governing equations were evaluated using a mixing length model since the primary purpose of the project was to develop a fast and reliable numerical solution procedure for the jet-mixing analysis in jet pump applications. In the various regions of stream field the mixing length was evaluated by appropriate equation (Gibert and Hill, 1975).

There is a good agreement (Fig. 11) between experimental wall static pressures (shown as data points) and the analytical static pressures (dotted line). The comparison is generally excellent. The areas where some disagreements occur are the entrance region of the throat and the exit zone of the diffuser. The difference in the rounded entrance section occurs because the program calculates a centerline static pressure and assumes the static pressure to be constant at each distance from the nozzle discharge, whereas the experimental data are wall static pressures and can be influenced by curving streamlines. At the exit of the diffuser, for the higher flow rate tests, the difference could be due to an underestimation of the pressure losses (wall friction, mixing, and diffusion). The code calculation time, at fixed flow ratio value is about 2 minutes on a IBM-PS2-80. The extensive use of the code makes it possible also to obtain jet pump overall performance (ψ versus φ Fig. 8) and the agreement with the data is generally good.

Cavitation Analysis

For aircraft jet pumps a good resistance to cavitation is very important, because cavitation limits the maximum allowable ceiling.

A cavitation analysis conducted on a $b = 0.06$ jet pump in JP4 was presented by Massardo and Satta (1985); the most important results were:

(I) An optimum spacing between nozzle and throat inlet ($S/D_m = 1.35$) exists with regard to cavitation resistance. External shape and internal to external diameter ratio of the nozzle greatly influence the optimum spacing value.

(II) A JP4 temperature increment reduces the cavitation coefficient σ_L, defined as $(p_s - p_v)/(p_s - p_a^*)$ (Cunningham et al., 1970) where p_a^* is the pressure at throat inlet in cavitation limit condition. This means an improvement of cavitation re-

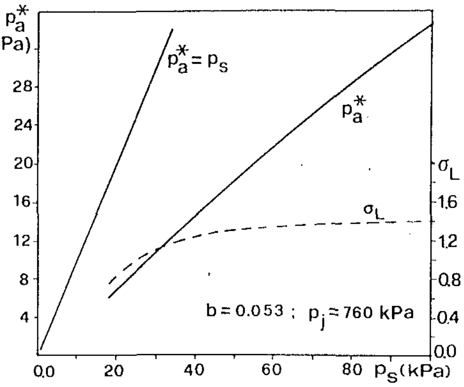

Fig. 12 Influence of suction pressure on σ_L coefficient

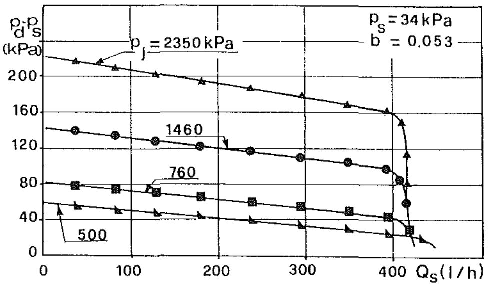

Fig. 13 Effect of suction flow rate Q_s and nozzle pressure p_j on cavitation

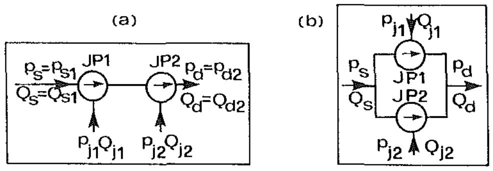

Fig. 14 Two stage jet pumps scheme: *(a)* cascade; *(b)* parallel

sistance and confirms the results of Kudirka and De Coster (1979) (large size jet pumps in hot water).

(III) Cavitation coefficient σ_L is reduced when the ceiling rises (suction pressure falls). This corresponds to an increase in cavitation resistance.

(IV) Cavitation presents two subsequent stages: noise and performance cavitation (Kudirka and De Coster, 1979). This means a gradual reduction of the head ratio when cavitation is taking place.

The analysis conducted here on 21 jet pumps in JP4 (Table 2) confirms the previous results of Massardo and Satta (1985); moreover, the shape of the head ratio lines in the cavitation zone becomes sharper when b increases (Figs. 4 and 5). The influence of suction pressure on σ_L was confirmed as shown in Fig. 12, where also the pressure at throat inlet in cavitation limit condition p_a^* is presented. The reduction of σ_L and, consequently, the improvement in the pump cavitation resistance can be explained taking into account the more rapid reduction of p_a^* compared with p_s.

Furthermore, the dimensional plot of Fig. 13 shows that cavitation always takes place at a constant suction flow rate Q_s, while nozzle pressure has a second order effect (only low values of p_j have a significant influence).

Two Stages Pumps

In order to improve further on the high cavitation resistance of single stage jet pumps, two stage configurations were studied (series and parallel arrangement), Fig. 14. Taking into account

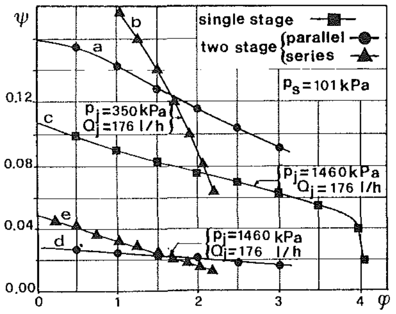

Fig. 15 Nondimensional performance of single and two stage jet pumps

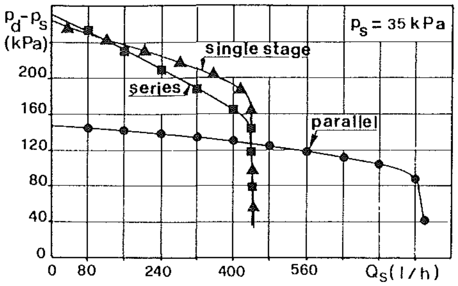

Fig. 16 Dimensional performance of single and two stage jet pumps

the particular aircraft application constraints (Filippi et al., 1986), the tests were conducted at fixed total primary flow rate in both cases (single and two stage pumps). The results are shown in Fig. 15 as dimensionless parameters (a, b, c lines). Each stage of the two-stage configuration is identical with single stage pump of test 11 ($b = 0.053$). To obtain the same primary flow rate the nozzle pressure was greatly reduced from 1460 kPa (single stage) to 350 kPa (two stage). The two kinds of lines (a, b, or d, e) differ for the p_j values employed in two stage pump head ratio calculation (350 or 1460 kPa). It would be better therefore to utilize dimensional plots: pressure rise ($p_d - p_s$) versus suction flow rate Q_s.

Figure 16 shows the performance of two identical pumps ($b = 0.053$; $D_n = 1.02$ mm; test 11 of Table 2) in series or parallel configuration and the performance of a single stage pump ($b = 0.107$; $D_n = 1.45$ mm; test 19 of Table 2). Therefore the total nozzle area was the same in all cases. This made it possible to work with a constant total primary flow rate using the same value of p_j (1460 kPa) for all the nozzles.

The series arrangement has no advantage respect to the single stage pump; in particular the cavitation takes place at the same suction flow rate ($Q_s = 440$ l/h). On the other hand, with the parallel arrangement the cavitation occurs at a double value of Q_s (about 830 l/h). However, in this case the pressure rise ($p_d - p_s$) was lower.

Another comparison between single and two stage jet pumps is shown in Fig. 17. The single stage pump has the geometry of test 8 (Table 2), while the two stage pump, parallel arrangement, has for the single part, the same b value (test 8, Table 2), but A_m and A_n areas halved ($D_m = 3.5$ mm). The pressure rises were similar as it was to be expected. The suction flow rate at cavitation onset was also similar, while the development of cavitation was quite different: for the single stage pump it was sharp, while for the two stage it was gradual.

Conclusion

The results of tests conducted on several small size low area ratio aircraft fuel jet pumps have been presented.

The experimental data were presented as head ratio versus flow ratio φ and area ratio coefficients (Figs. 4 and 5); also

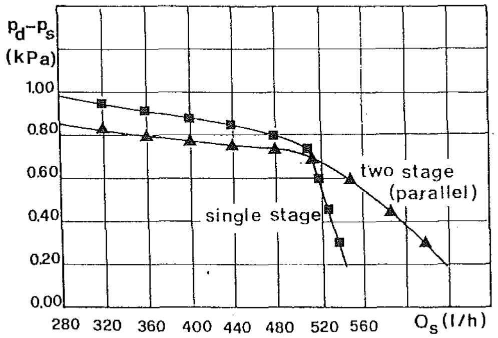

Fig. 17 Dimensional performance of single and two stage (parallel) jet pumps ($b = 0.042$, $p_j = 1460$ kPa, $p_s = 35$ kPa)

wall static pressure surface versus flow ratio and abscissa x was shown (Figs. 6, 7, and 11). The data show that the separation area present in the mixing zone (Fig. 6) disappears by increasing primary pressure (Fig. 7) or by decreasing suction pressure (Fig. 11).

Experimental values of head ratio were compared to a one-dimensional theoretical prediction method (Cunningham, 1954); the results (Figs. 8 and 9) show the necessity of making some modifications in the model at low flow ratio values, as shown in Fig. 10. In this manner the agreement with the data has increased. The data were also compared with the results of a finite difference turbulent jet-mixing model (Massardo, 1989), also for wall static pressure (Fig. 11), and the agreement was generally good.

Cavitation, which is particularly important when the fluid is JP4 (the vapor pressure of JP4 at 43°C—hot day climb condition—is about 23 kPa (Filippi et al., 1986)), was investigated and the results agree well with previously published data (Cunningham, 1954; Sanger, 1970; Massardo and Satta, 1985; Kudirka and De Coster, 1979; Shimizu et al., 1987). Moreover, for very low area ratio pumps the analysis conducted shows that the cavitation depends only on the suction flow rate, while nozzle pressure has a second order effect (Fig. 12); p_j only has a significant influence at low value ($p_j < 500$ kPa).

To enhance cavitation resistance, which is particularly important in the field of aeronautics, some studies were carried out on two stage jet pumps (Fig. 14). The need to illustrate the results in a dimensional way was established (Fig. 15). The possibility of obtaining a higher cavitation flow rate with two stage parallel arrangement pumps instead of with single or two-stage cascade arrangement pumps was also shown (Fig. 16).

Two stage parallel arrangement is also useful to reduce the evolution and the effect of dissolved gas from the liquid, a phenomenon which can be taking place in addition to cavitation at high ceiling values where suction pressure is very low.

Finally, by using single and two stage parallel pumps with the same values of b, p_j, Q_j (Fig. 17) it was seen that the onset of cavitation appeared at the same Q_s value but its development was more gradual in the two stage arrangement.

The analysis here presented and the work done in collaboration with R. Piaggio S.p.A. (Filippi et al., 1986; Massardo and Satta, 1985) allows the knowledge on small size (nozzle diameter about 1 mm) low area ratio jet pumps to be improved. For example with a new design of the external shape of the nozzle and an optimized distance between nozzle and throat inlet the maximum ceiling for the Piaggio P180 aircraft (with two PT6 engines) using jet pump in JP4 (hot day climb simulation with $T_{JP4} > 43°C$), has been improved of over 3500 m compared to the original design results (Filippi et al., 1986).

Moreover, the finite difference turbulent method (Massardo, 1989) can now be utilized to predict the performance of existing pumps (analysis problem), or to design new pumps (inverse problem). In fact, the method allows the pump geometry to be obtained using as input a preassigned axial static pressure distribution. In this way it is possible to improve the performance of the jet pumps (flow separation reduction) and to accommodate the cavitation problem.

Acknowledgments

This work was supported by grant CT/91/02814/11 of National Research Council of Italy, and by MPI.

The authors wish to thank Ing. G. Parodi and Ing. E. Filippi of R. Piaggio S. p. A. for their support in the development of this work.

References

Cunningham, R. G., 1954, "The Jet Pumps as a Lubrification Oil Scavenge Pump for Aircraft Engines," Penn. University, WADC TR SS-143.

Cunningham, R. G., Hansen, A. G., and Na, T. Y., 1970, "Jet-Pump Cavitation," ASME *Journal of Basic Engineering*, Sept., pp. 483–494.

Denny, V. E., and Landis, R. B., 1971, "An Improved Transformation of the Patankar-Spalding Type for Numerical Solution of Two-Dimensional Boundary Layer Flows," *Int. J. Heat Mass Transfer*, Pergamon Press, Vol. 14, pp. 1859–1862.

Filippi, E., Massardo, A., Parodi, G., and Satta, A., 1986, "Jet Pumps Dynamic Performances During Hot Day Climb" (in Italian), XLI ATI Conference, Naples (see also *La Termotecnica 5/90*).

Gilbert, G. B., and Hill, P. G., 1975, "Analysis and Testing of Two-Dimensional Slot Nozzle Ejector with Variable Mixing Sections," *2nd Symposium on Jet Pumps and Ejectors and Gas Lift Techniques*, BHRA, England.

Kudirka, A., and De Coster, M., 1979, "Jet Pump Cavitation with Ambient and High Temperature Water," ASME JOURNAL OF FLUIDS ENGINEERING, Vol. 101.

Massardo, A., 1989, "Confined Jet Mixing Calculation: Ejector and Jet Pump Applications" (in Italian), XLIV ATI Conference, Cosenza, Itlay.

Massardo, A., and Satta, A., 1985, "Experimental Analysis of an Aeronautical Jet Pump" (in Italian), XL ATI Conference, Trieste (see also *La Termotecnica 9/88*).

Sanger, N. L., 1970, "An Experimental Investigation of Several Low Area Ratio Water Jet Pumps," ASME *Journal of Basic Engineering*, Mar., pp. 11–20.

Shimizu, Y., Nakamura, S., Kurahara, S., and Kurata, S., 1987, "Studies of the Configuration and Performance of Annular Type Jet Pumps," ASME JOURNAL OF FLUIDS ENGINEERING, Vol. 109, pp. 205–212.

APPENDIX

The assumptions in the Cunningham's theory (1970) are:

- the flow streams are one-dimensional at throat entrance and exit.
- mixing is completed in the constant-area throat, against an adverse pressure gradient.
- primary and secondary fluids are incompressible and of equal density.

The dimensionless pressure ratio is:

$$\psi = [2b + (1-2b) \qquad \varphi^2 b^2 (1-b)^{-2} - (1+K_{34}) b^2 (1+\varphi)^2]/ [1 + K_1 - \text{numerator}] \tag{A.1}$$

and the friction losses are:

$$\text{Nozzle loss: } E_j = k_1 Q_j c^2 j/2 \tag{A.2}$$

$$\text{Throat loss: } E_m = k_3 b_2 (1+\varphi)^3 \, Q_j c^2 j/2 \tag{A.3}$$

$$\text{Diffuser loss: } E_{\text{dif}} = k_4 b^2 (1+\varphi) 2 Q_j c^2 j/2 \tag{A.4}$$

Where the friction loss coefficients are:

$$k_1 = [(p_j - p_s)/(0.5\,\rho c^2{}_j)] - 1 \tag{A.5}$$

$$k_{34} = k_3 + k_4 = \ [-2(p_a - p_s)/(\rho Q_j) + 2b + b^2 \varphi^2 (1-2b)/(1-b)^2]/[b^2(1+\varphi)^2] - 1 \tag{A.6}$$

Some Unsteady Fluid Forces on Pump Impellers

R. S. Miskovish

C. E. Brennen

California Institute of Technology,
Pasadena, Calif. 91125

Spectral analyses of all the forces and moments acting on a typical centrifugal pump impeller/volute combination are presented. These exhibit shaft frequencies, blade passing frequencies, and beat frequencies associated with a whirl motion imposed on the shaft in order to measure rotordynamic forces. Among other features the unsteady thrust was found to contain a surprisingly large blade passing harmonic. While previous studies have explored the magnitudes of the steady fluid-induced radial forces and the fluid-induced rotordynamic forces for this typical centrifugal pump impeller/volute combination, this paper presents information on the steady bending moments and rotordynamic moments due to the fluid flow. These imply certain axial locations for the lines of action of the radial and rotordynamic forces. Data on the lines of action are presented and allow inferences on the sources of the forces.

1 Introduction

In previous publications (Chamieh et al., 1985, Jery et al., 1985, Adkins and Brennen 1986, Franz et al., 1990) considerable information has been presented on the flow induced radial and rotordynamic forces in centrifugal and axial (Arndt and Franz, 1986) flow pumps. The effect of cavitation on these forces has also been explored (Franz, 1989). The forces in question can be visualized by reference to Fig. 1, which is in a plane perpendicular to the axis of rotation. Steady radial forces which result from asymmetries in the volute, the discharge flow or the inflow are denoted by F^*_{ox} and F^*_{oy}. If, in addition, the axis of rotation undergoes a small displacement given by $x(t)$, $y(t)$ from some mean position then the instantaneous fluid forces on the impeller, $F^*_x(t)$ and $F^*_y(t)$, can be expressed by

$$\begin{Bmatrix} F^*_x(t) \\ F^*_y(t) \end{Bmatrix} = \begin{Bmatrix} F^*_{0x} \\ F^*_{0y} \end{Bmatrix} + [A^*] \begin{Bmatrix} x(t) \\ y(t) \end{Bmatrix} \tag{1}$$

where $[A^*]$ is the rotordynamic matrix. In addition to the radial forces, the corresponding bending moments should be divided into steady radial moments and a rotordynamic moment matrix as follows:

$$\begin{Bmatrix} M^*_x(t) \\ M^*_y(t) \end{Bmatrix} = \begin{Bmatrix} M^*_{ox} \\ M^*_{oy} \end{Bmatrix} + [B^*] \begin{Bmatrix} x(t) \\ y(t) \end{Bmatrix} \tag{2}$$

The forces and moments are presented in dimensionless form denoted by the same symbols without the asterisk. The steady radial forces and moments are nondimensionalized by $\rho\pi\Omega^2 r_2^3 b_2$ and $\rho\pi\Omega^2 r_2^4 b_2$ respectively, the matrices $[A^*]$ and $[B^*]$ by $\rho\pi\Omega^2 r_2^2 b_2$ and $\rho\pi\Omega^2 r_2^3 b_2$ and the displacements are non-dimensionalized by r_2. If for simplicity we focus on a circular whirl orbit (see Fig. 1) of eccentricity ϵ and frequency ω, then $x = \epsilon\cos\omega t$ and $y = \epsilon\sin\omega t$, and

$$\begin{Bmatrix} F_x(t) \\ F_y(t) \end{Bmatrix} = \begin{Bmatrix} F_{ox} \\ F_{oy} \end{Bmatrix} + \epsilon[A] \begin{Bmatrix} \cos\omega t \\ \sin\omega t \end{Bmatrix} \tag{3}$$

$$\begin{Bmatrix} M_x(t) \\ M_y(t) \end{Bmatrix} = \begin{Bmatrix} M_{ox} \\ M_{oy} \end{Bmatrix} + \epsilon[B] \begin{Bmatrix} \cos\omega t \\ \sin\omega t \end{Bmatrix} \tag{4}$$

Virtually all of the previous experimental data confirms the reasonable supposition that the matrices $[A]$ and $[B]$ should be independent of the particular choice of axes, x and y. Such rotational invariance requires that

$$\begin{aligned} A_{zz} = A_{yy} = F_n;\ A_{yx} &= -A_{xy} = F_t \\ B_{xx} = B_{yy} = M_n;\ B_{yx} &= -B_{xy} = M_t \end{aligned} \tag{5}$$

where F_n, F_t, M_n, M_t are the rotordynamic forces and moments normal and tangential to the whirl orbit non-dimensionalized by $\rho\pi\Omega^2 r_2^2 b_2 \epsilon$ in the case of the forces and by $\rho\pi\Omega^2 r_2^3 b_2 \epsilon$ in the

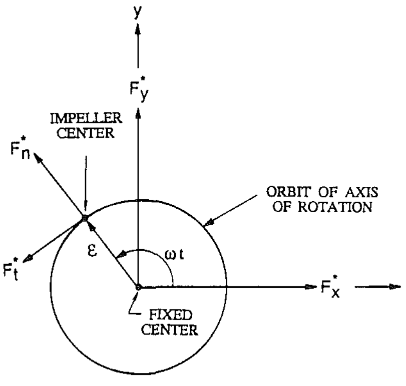

Fig. 1 Schematic defining the radial forces F^*_x and F^*_y and the rotordynamic forces F^*_n and F^*_t in a plane perpendicular to the axis of rotation of the impeller. The instantaneous position of the impeller center and its locus on a circular whirl orbit are shown.

Contributed by the Fluids Engineering Division for publication in the JOURNAL OF FLUIDS ENGINEERING. Manuscript received by the Fluids Engineering Division April 16, 1991. Associate Technical Editor: U. S. Rohatgi.

case of the moments. Like [*A*] and [*B*], the rotordynamic forces and moments will be functions of the whirl frequency and mean operating condition but independent of ϵ if the displacement is within a linear regime. Furthermore, presentation of F_n, F_t, M_n, M_t specifies the entire matrices and has the advantage of ease of physical interpretation. For example, if F_t is in the same direction as the whirl motion, then it represents a fluid-induced destabilizing force from a rotordynamic perspective.

2 Spectra of Forces on a Centrifugal Impeller

During the present investigation a comprehensive examination was undertaken of all the unsteady fluid-induced forces and moments acting upon a typical centrifugal pump impeller. The specific impeller and volute was that combination designated Impeller X/Volute A (see Jery et al., 1985). Impeller X is a five-bladed centrifugal pump with a discharge radius of 8.1 cm. and a design specific speed of 0.57 made by Byron Jackson Pump Company. Volute A is a vaneless, spiral volute made to match Impeller X at a flow coefficient $\phi = 0.092$.

A sketch of the volute and of the impeller mounting is included in Fig. 2. Note that since the impeller moves on an eccentric orbit the clearances between the impeller and the volute vary with time.

The forces described in the preceding section were evaluated from measurements of the radial forces, F_1 and F_2, and moments, M_1 and M_2, in the coordinate frame of the shaft-mounted rotating balance to which the impellers were directly mounted. This balance measured the unsteady components of all six forces and moments, including the torque M_3, and the axial thrust, F_3.

As part of the present investigation, the dynamic signals associated with all six forces and moments during operation of the pump at a particular flow coefficient, ϕ, shaft frequency, Ω, and whirl frequency, ω, were closely examined and revealed at least one surprise which we shall come to shortly. To discuss the results (of which Fig. 3 represents a typical example), it is necessary to describe briefly how the motions are controlled in the experiment. A generator produces a low frequency signal denoted by Ω/J where J is an integer typically 10 or 20. This is then multiplied by J to produce the signal which drives the main shaft motor. The basic signal is also multiplied by a second integer, I, and this is used to drive the whirl motion so that $\omega = I\Omega/J$. Both motions are closely controlled and monitored as part of the data acquisition system. It follows that in the frame of reference of the rotating balance the radial forces and moments which are steady in the laboratory frame will show up at the frequency, Ω. The rotordynamic forces and moments will be represented by signals at frequencies of $(\Omega \pm \omega)$ or $\Omega(J \pm I)/J$. Blade passage frequencies will also be manifest; in the case studied here the Impeller X had five blades and, in combination with the vaneless volute, would generate a blade passage signal at 5Ω. Fourier components were obtained by cross-correlation for all integer multiples of Ω/J up to about 6Ω; tests revealed no significant amplitudes above this frequency.

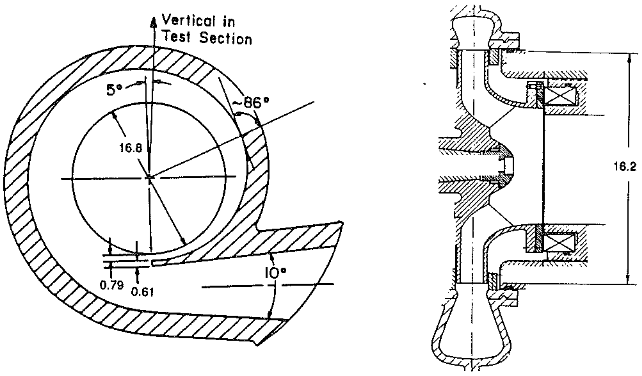

Fig. 2 Sketches of Volute A (left) and Impeller X mounted in the facility (right). Note sketches are two different scales (dimensions in cm.).

Spectra like this were obtained at a number of shaft speeds, whirl ratios, I/J, and operating conditions represented by the flow coefficient, ϕ. They all had similar characteristics exemplified by Fig. 3, in which the results for each of the six forces and moments are normalized with respect to the maximum component occurring in that particular spectrum. Those normalizing values are attached to each spectrum and should be compared with the later data of Figs. 6, 7, and 8 in order to assess whether the amplitudes are significant or not. The following conclusions can be drawn from Fig. 3 and other similar spectra:

(*a*) The strong peak at Ω in all of the radial forces and bending moments (F_1, F_2, M_1, and M_2) is generated by steady radial forces and bending moments due to the asymmetry of the volute.

(*b*) The peaks at $(J \pm I)\Omega/J$ in F_1, F_2, M_1, and M_2 are generated by nonzero F_n, F_t, M_n, and M_t. It is particularly noticeable that the $(J - I)\Omega/J$ component is usually much larger than the $(J + I)\Omega/J$ component and hence

Nomenclature

A_2 = impeller discharge area $= 2\pi r_2 b_2$
b_2 = impeller discharge width
F_1, F_2 = radial forces on the impeller observed in the rotating frame of the balance
F_3 = thrust on the impeller
F_{ox}, F_{oy} = normalized mean radial forces acting on the impeller where x is the direction of the volute cutwater and y is a perpendicular direction rotated in the direction of shaft rotation. Unless otherwise stated, all forces are normalized by $0.5\rho u_2^2 A_2$ and all moments by $0.5\rho u_2^2 A_2 r_2$.
F_n, F_t = mean forces normal to and tangential to the whirl orbit; these are normalized using $0.5\rho u_2^2 A_2 \epsilon / r_2$
M_1, M_2 = bending moments observed in the rotating frame of the balance
M_3 = torque on the impeller
M_{ox}, M_{oy} = normalized mean bending moments acting on the impeller
M_n, M_t = mean moments normal to and tangential to the whirl orbit; these are normalized using $0.5\rho u_2^2 A_2 \epsilon$
r_2 = impeller discharge radius
u_2 = impeller tip speed at discharge $= \Omega r_2$
ϵ = radius of the eccentric whirl orbit
ϕ = flow coefficient $= Q/u_2 A_2$, where Q is the volume flow rate through the pump
ψ = head coefficient $= g\Delta h/u_2^2$, where Δh is the total head rise across the pump
Ω = pump rotational speed (rad/s)
$\omega = I\Omega/J$ = whirl rotational speed (rad/s) where I and J are integers
$\omega/\Omega = I/J$ = whirl ratio

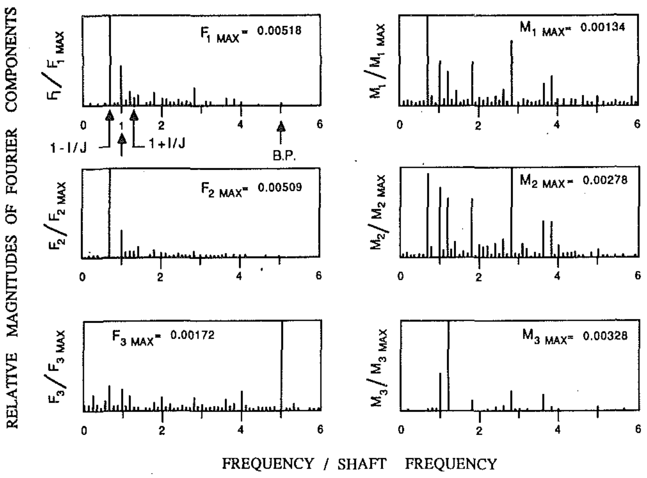

Fig. 3 Typical frequency content of F_1, F_2, F_3, M_1, M_2, M_3 for Impeller X/Volute A for tests at 3000 rpm, φ = 0.092, and I/J = 3/10. Note the harmonics Ω, $(J \pm I)\,\Omega/J$ and the blade passing frequency, 5Ω. Uncertainty in force components is ± 0.0005, in moment components is ± 0.0003.

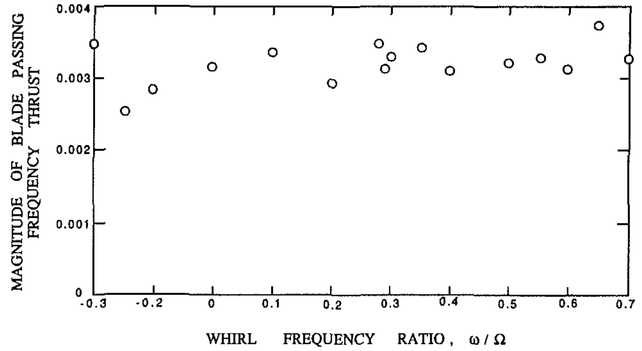

Fig. 4 The blade passing frequency component of thrust oscillation as a function of whirl frequency ratio, ω/Ω, for Impeller X/Volute A operating at 3000 rpm and φ = 0.092. Uncertainty in ordinate is ± 0.0005.

the former frequency provides the major contribution to F_n, F_t, M_n, M_t, and the rotordynamic matrices.

(*c*) The moments M_1 and M_2 seem substantially noisier than the forces F_1 and F_2. This is rather misleading; it is due to the fact that the moments are small since the origin of the force/moment coordinate system is in the center of the discharge of the impeller and the line of action of the radial forces is close to this axial location.

(*d*) The unsteady axial thrust, F_3 contains a surprisingly large component at the blade passing frequency, 5Ω, though other multiples of the impeller rotation frequency are also present. Note that since the balance only records unsteady forces, neither the steady thrust or torque can be measured by this device.

(*e*) The unsteady torque, M_3, was usually quite small compared with the steady torque which was estimated using separate strain gauges on the drive shaft. As demonstrated by Fig. 3, no consistent pattern was observed in the frequency content of this unsteady torque. In all cases, the largest harmonic is 60 Hz, which corresponds to frequency of the electrical input to the balance. In light of the blade passing frequency content in the thrust, one might have expected a similar contribution to the torque. However this was not observed.

3 Unsteady Thrust at Blade Passage Frequency

In the previous section we have noted the significant component in the unsteady thrust at the blade passing frequency. In this section we shall examine the relative magnitude of this unsteady force. Since the balance does not record the steady thrust and since we do not have independent means of measuring the thrust, we shall compare the magnitude of the measured unsteady thrust with an estimate of the steady thrust based on measurement of the pressure rise across the pump and of the pressure distribution around the impeller.

From the geometry of the five-bladed centrifugal pump impeller, Impeller X, and assuming (i) that the discharge pressure acts on the back-face of the impeller and (ii) that the pressure on the exterior of the shroud varies linearly with radial position between the inlet tip and the discharge tip, we find by integration of the pressure distribution on the impeller that

$$\frac{\text{Mean Thrust}}{0.5\rho u_2^2 A_2} = F_{03} = 3.09\phi^2 - a\psi \qquad (6)$$

in which a = 3.0. This provides values which are acceptably close to those of Beitz and Küttner (1981) who recommend a value of a in the range 3.6–4.6. With this estimate of steady thrust, ratios of the magnitude of the unsteady thrust at the blade passing frequency to the steady thrust were evaluated for a range of flow coefficients, ϕ, and whirl ratios. With respect to the latter, Fig. 4 demonstrates that, as expected, the ratio is independent of the whirl ratio since the interaction mechanism occurs irrespective of whirl. Indeed Fig. 4 merely indicates the typical scatter in the magnitude of the unsteady thrust.

The variation with operating point is exemplified by the values in the following table:

Table 1 Steady and unsteady thrust

Operating point		Steady thrust F_{03}	Unsteady thrust magnitude/ steady thrust	θ_m
ϕ	ψ			
0.060	0.510	−1.52	0.0069	−17°
0.092	0.425	−1.25	0.0028	17°
0.104	0.375	−1.09	0.0065	23°

The nominal design flow coefficient of this impeller/volute combination is 0.092. Note that, as might be expected, the unsteady thrust at the blade passing frequency is smallest at the design flow coefficient. Though the magnitude of unsteady thrust is less than one percent of the steady thrust, it is possible to envisage circumstances in which it could cause serious axial resonance problems.

Finally, the relative location of the impeller blades to the volute cutwater at the time of the peak thrust is of interest in attempting to understand the origins of this unsteady thrust. Since Impeller X is five-bladed the angle between the tips of the five blades is 72 deg. If we define an angle between the line from the impeller center to the volute cutwater and the line from the impeller center to the discharge blade tip *at the time when the instantaneous thrust is a maximum* then this angle would take values of $\theta_m^* = \theta_m \pm 72n$ deg (n = 0, 1, 2, etc.) where the observed values of θ_m are as listed in Table 1. The positive direction of θ_m is defined as being in the direction of rotation of the impeller. Note that in all three cases listed in Table 1 the maximum instantaneous thrust occurs when the discharge tip of a blade is close to the volute cutwater.

4 Origins of the Radial and Rotordynamic Forces

Previous publications, (Chamieh et al., 1985; Jery et al., 1985; Adkins and Brennen, 1988; Franz et al., 1990) have presented data on the steady radial forces and on the rotordynamic forces for a number of impellers, diffusers and volutes. Visualizing the centrifugal pump impeller as a control volume, one can recognize that there exists the possibility of contributions to the radial force from three different sources. First, circumferential variation in the impeller discharge pres-

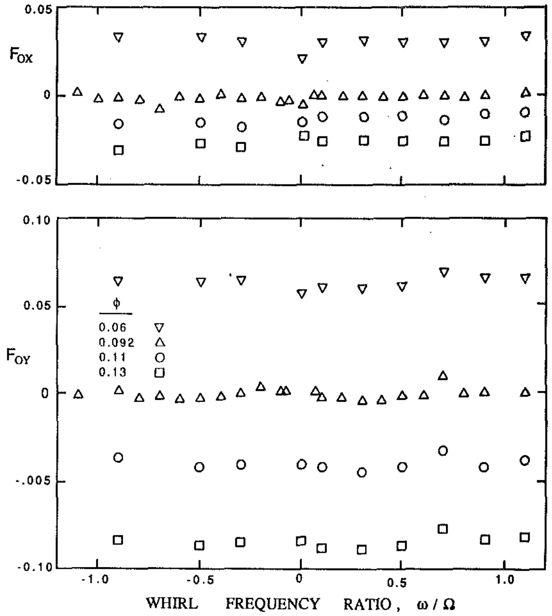

Fig. 5 Steady radial forces, F_{ox} and F_{oy}, for Impeller X/Volute A at a speed of 1000 rpm and various flow coefficients. Uncertainty expressed as a standard deviation: F_{ox}, F_{oy} ± 0.0008.

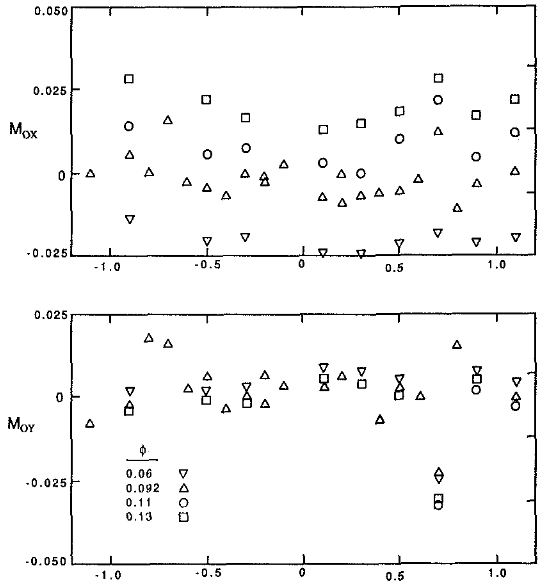

Fig. 6 Steady radial moments, M_{ox} and M_{oy}, for Impeller X/Volute A at a speed of 1000 rpm and various flow coefficients. Uncertainty expressed as a standard deviation: M_{ox}, M_{oy} ± 0.0005.

sure (or volute pressure) will clearly result in a radial force acting on the impeller discharge area. A second contribution could be caused by the leakage flow from the impeller discharge to the inlet between the impeller shroud and the pump casing. Circumferential nonuniformity in the discharge pressure could cause circumferential nonuniformity in the pressure within this shroud/casing gap and therefore a radial force acting on the exterior of the pump shroud. For convenience we shall term this second contribution the leakage flow contribution. Thirdly, a circumferential nonuniformity in the flow rate out of the impeller would imply a force due to the nonuniformity in the momentum flux out of the impeller. Adkins and Brennen (1988) used an impeller flow model in conjunction with a one-dimensional volute flow model to predict the circumferential non-uniformity in the pressure acting on the impeller discharge and found that these pressure distributions were in accord with experimental measurements. Also, integration of the experimental pressure distributions yielded radial forces in good agreement with both the overall radial forces measured using the force balance and the theoretical predictions of the theory. These results demonstrate that it is primarily the circumferential non-uniformity in the pressure at the impeller discharge which generates the radial forces, but that the non-uniformity in the pressures acting on the exterior of the shroud may also contribute.

The origins of the rotordynamic forces were also explored by Adkins and Brennen (1988) who used the same model to evaluate the rotordynamic forces acting on the impeller discharge. It was found that the theoretical values for the impeller discharge contributions were significantly smaller than the total measured forces. Thus it was concluded that the leakage flow around the shroud exterior can be an important contributor to the rotordynamic forces. To confirm this, Adkins and Brennen (1988) made experimental measurements of the pressure distributions in both the impeller discharge flow and in the leakage flow.

None of these previous experimental or theoretical studies addressed the issue of the location of the lines of action of either the radial or the rotordynamic forces. Clearly, a discussion of the lines of action or of the moments requires a definition of the axial location of the origin of the reference frame of the forces and moment. In this paper we arbitrarily choose the origin to be in the center of the impeller discharge. If the radial forces F_{ox}, F_{oy} acted at this location, then the moments M_{ox} and M_{oy} would be zero. It is one of the purposes of this paper to present data on both the steady radial moments and the rotordynamic moments and in doing so to provide information of the location of the lines of action of the radial and rotordynamic forces.

5 Forces and Moments

Typical data on the radial forces and moments are presented in Figs. 5 and 6, respectively, for the Impeller X/Volute A combination at a shaft speed of 1000 rpm and four different flow coefficients. Note that the forces are independent of the whirl ratio as they should be. The data of Fig. 5 correspond to data presented previously by Jery (1987). The moments in Fig. 6 are new. It should be noted that they follow a righthand rule in which the z-axis points toward the inlet. Thus a radial force in the x or y direction whose line of action is closer to the inlet than the origin in the center of the impeller discharge, leads to a positive M_{oy} or a negative M_{ox}. Though the data in Fig. 6 contains a few anomalous points, it does suggest that there exists a steady moment, primarily in the x-direction and that this changes with the flow coefficient. The following example illustrates the typical magnitude of these steady moments. At a flow coefficient of $\phi = 0.06$, the steady force vector $\mathbf{F}_o = F_{ox}\mathbf{x} + F_{oy}\mathbf{y}$ has components $F_{ox} \approx 0.03$ and $F_{oy} \approx 0.06$ (see Fig. 5); it has a magnitude of about 0.067 and an angle from the x-axis, θ_f, of 63 deg. The steady moment vector $\mathbf{M}_o = M_{ox}\mathbf{x} + M_{oy}\mathbf{y}$, where $M_{ox} \approx -0.02$ and $M_{oy} \approx 0$, has a magnitude of 0.02 and an angle from the x-axis, θ_m, of 180 deg. The position of the line of action on the z-axis can be computed from $\mathbf{r} * \mathbf{F} = \mathbf{M}$, (or, in scalar terms $F * r = M\perp$, where $M\perp = M * \sin(\theta_m - \theta_f)$), and the resulting value of r when $\phi = 0.06$ is 0.27 or 2.2 cm (compared with an impeller discharge radius of 8.1 cm). Thus the line of action in this instance is 2.2 cm forward from the center of the discharge. For $\phi = 0.13$, a similar estimate gives a location 1.3 cm forward of the center of the discharge.

In conclusion, the steady moments indicate that the line of action of the steady radial force is some distance ahead of the center of the discharge, though it moves backward with in-

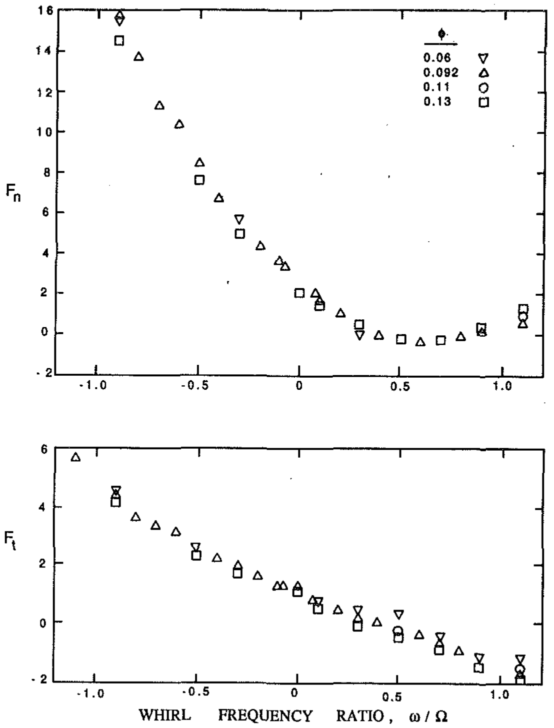

Fig. 7 Normal and tangential rotordynamic forces, F_n and F_t, for Impeller X/Volute A at 1000 rpm and various flow coefficients as in Figs. 5 and 6. Uncertainty expressed as a standard deviation: F_n, F_t ± 0.05.

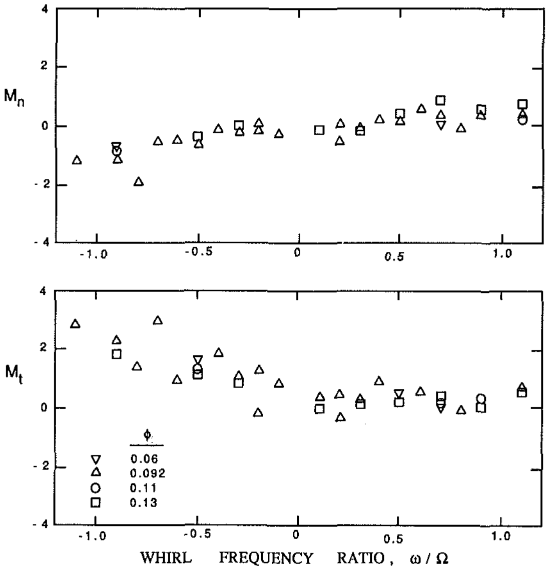

Fig. 8 Normal and tangential rotordynamic moments, M_n and M_t, for Impeller X/Volute A at 1000 rpm and various flow coefficients as in Figs. 5 and 6. Uncertainty expressed as a standard deviation: M_n, M_t ± 0.1.

creasing flow coefficient. The reason the lines of action are forward of the impeller discharge is the contribution to the steady radial force from the pressure distribution on the exterior of the shroud which combines with the force on the discharge to yield the total steady radial force. Since the force on the exterior of the shroud is comparable with that on the discharge, it follows that the line of action of the combination will be forward of the center of the discharge. The present observations are consistent with that previous analysis.

Now we examine the rotordynamic moment matrices. Figure 8 indicates that the values of M_n and M_t are very small and this accounts for the larger scatter in this data. The location of the lines of action of F_n and F_t relative to the center of the discharge can be computed in a manner similar to that used for computation of the lines of action of the steady forces. Typical values from Figs. 7 and 8 indicate that these displacements are much smaller than for F_{ox} and F_{oy} and are less than 1 cm. Thus we conclude that the line of action of the rotordynamic force matrix is close to the center of the discharge. This, too, is consistent with previous analysis which suggest that for the impeller/volute combination used in these experiments the shroud force contributions to the rotordynamic matrices are quite small.

6 Conclusions

The conclusions drawn from this study of the fluid forces on a typical centrifugal impeller are:

(i) The spectral analysis of the forces shows the largest peaks at the frequencies Ω and Ω ± ω for F_1, F_2, M_1, and M_2. These frequencies correspond to the steady forces and moments, and the rotordynamic force and moments respectively. In addition, the spectra of the unsteady thrust was found to contain a strong harmonic at the blade passing frequency.

(ii) On closer examination, the magnitude of the unsteady thrust at blade passing frequency is shown to be less than one percent. Although small, this component of the unsteady thrust could lead to axial resonance problems. It has also been shown that the maximum instantaneous thrust occurs when the discharge tip of a blade is near the volute cutwater.

(iii) The steady radial moments are equivalent to a line of action for the steady radial forces which is as much as 0.25 radii from the center of the impeller discharge (radius 8.1 cm) in the direction of the inlet. This is consistent with the conclusion of Adkins and Brennen (1988) that the forces on the shroud provide important contributions to the radial forces. The line of action moves closer to the center of impeller discharge as the flow coefficient increases.

(iv) The rotordynamic moment matrices are close to the rotationally invariant form that has been used to describe the rotordynamic force matrix. Thus, it suffices to present the moment matrices in terms of M_n and M_t without loss of information. In comparing the steady and unsteady moments with the steady and unsteady forces, the line of action in the z-direction is shown to be close to the center of the impeller discharge (within about 0.1 radii).

Acknowledgments

This work was performed under Contract NAS 8-33108 from NASA George Marshall Space Flight Center, Huntsville, Alabama; the authors are very grateful for their support. We should also like to express our thanks to R. Franz, N. Arndt, A. J. Acosta, and T. K. Caughey for their help during the conduct of this research program.

References

Adkins, D. R., 1986, "Analysis of Hydrodynamic Forces on Centrifugal Pump Impellers," Ph.D. Thesis, Division of Engineering and Applied Science, California Institute of Technology.

Adkins, D. R., and Brennen, C. E., 1988, "Analysis of Hydrodynamic Radial Forces on Centrifugal Pump Impellers," ASME JOURNAL OF FLUIDS ENGINEERING, Vol. 110, pp. 20–28.

Arndt, N., and Franz, R., 1986, "Observations of Hydrodynamic Forces on Several Inducers Including the SSME-LPOTP," California Institute of Technology, Division of Engineering and Applied Science, Rep. No. E249.3.

Beitz, W., and Küttner, K.-H. (eds.), 1981, *Dubbel: Tachenbuch für den Maschinenbau* Springer-Verlag, Heidelberg, pp. 897–899.

Brennen, C. E., Acosta, A. J., and Caughey, T. K., 1986, "Impeller Fluid Forces," *Proceedings of Advanced Earth-to-Orbit Propulsion Technology* Congress, Huntsville, AL, May, NASA Conf. Publ. 2436, pp. 270–295.

Chamieh, D. S., 1983, "Forces on a Whirling Centrifugal Pump-Impeller," Ph.D. thesis, Division of Engineering and Applied Science, California Institute of Technology.

Chamieh, D., Acosta, A. J., Brennen, C. E., and Caughey, T. K., 1985, "Experimental Measurements of Hydrodynamic Radial Forces and Stiffness Matrices for a Centrifugal Pump-Impeller," ASME JOURNAL OF FLUIDS ENGINEERING, Vol. 107, No. 3, pp. 307-315.

Franz, R., Arndt, N., Caughey, T. K., Brennen, C. E., and Acosta, A. J., 1987, "Rotordynamic Forces on Centrifugal Pump Impellers," *Proceedings of the Eighth Conference on Fluid Machinery*, Akademiai Kiado, Budapest, Vol. 1, pp. 252-258.

Franz, R., 1989, "Experimental Investigation of the Effect of Cavitation on the Rotordynamic Forces on a Whirling Centrifugal Pump Impeller," Ph.D. thesis, Division of Engineering and Applied Science, California Institute of Technology.

Franz, R., Acosta, A. J., Brennen, C. E., and Caughey, T. K., 1990, "The Rotordynamic Forces on a Centrifugal Pump Impeller in the Presence of Cavitation," ASME JOURNAL OF FLUIDS ENGINEERING, Vol. 112, No. 3, pp. 264-271.

Jery, B., and Franz, R., 1982, "Stiffness Matrices for the Rocketdyne Diffuser Volute," Report No. E249.1, California Institute of Technology.

Jery, B., Acosta, A. J., Brennen, C. E., and Caughey, T. K., 1985, "Forces on Centrifugal Pump Impellers," *Second International Pump Symposium*, Houston, TX, April 29-May 2.

Jery, B., Acosta, A. J., Brennen, C. E., and Caughey, T. K., 1986, "Hydrodynamic Impeller Stiffness, Damping and Inertia in the Rotordyammics of Centrifugal Pumps," Third Workshop on Rotordynamics Instability Problems in High Performance Turbomachinery, Texas A&M University, NASA Conference Publication 2338, pp. 137-160.

Jery, B., 1987, "Experimental Study of Unsteady Hydrodynamic Force Matrices on Whirling Centrifugal Pump Impellers," Ph.D. thesis and Report No. 200.22, California Institute of Technology.

A. Asai
Associate Scientist,
Canon Research Center,
Canon, Inc.,
Kanagawa 243-01, Japan

Three-Dimensional Calculation of Bubble Growth and Drop Ejection in a Bubble Jet Printer

The three-dimensional Navier-Stokes equation for the motion of ink both inside and outside the nozzle of a bubble jet printer is numerically solved, for the first time, to predict the bubble behavior and the drop ejection. The results of calculation for three types of ink agreed well with experimental data. The effect of initial bubble pressure, viscosity and surface tension on the volume and the velocity of the drop is numerically investigated. The three-dimensional calculation is very useful to the design of bubble jet printers because it saves a lot of time and cost to make and evaluate prototypes.

Introduction

The bubble jet is a new type of drop-on-demand ink jet printing technology, in which vapor bubbles, generated by a rapid heating of ink in nozzles, act as pressure generators (Hara and Endo, 1982). Ink drops are ejected from the outlet of nozzles by the action of high pressure due to boiling under extremely high superheat. A great merit of the bubble jet is that small pitched multiple nozzle arrangements, which are difficult to obtain using piezoelectric transducers, can be achieved by using thin-film resistors as the heating means.

In designing bubble jet printers, it is necessary to know the relation between design parameters (such as ink property and head structure) and the performance characteristics. Numerical simulation of the drop ejection is desired for this purpose, since building prototypes and evaluating their performance are expensive and time-consuming tasks.

For piezoelectric ink jets, Kawamura et al. (1982) and Fromm (1984) presented axisymmetric calculations to predict the drop behavior outside the nozzle. In these calculations, time dependent history of pressure or velocity field is assumed at the outlet of the nozzle. Such method is not satisfactory for bubble jets because the pressure history at the nozzle outlet is not known a priori but should be determined by the behavior of the bubble in the nozzle.

For bubble jets, Allen et al. (1985) presented an axisymmetric calculation of bubble growth and drop formation. But the bubble dynamics law, which is very important for the calculation, is not shown. Further, an axisymmetric calculation is not satisfactory because the three-dimensional effect of the nozzle shape cannot be neglected in many practical situations.

In this paper, a three-dimensional finite difference algorithm based on the VOF method (Hirt and Nichols, 1981 and Flow Science, 1988) is used to predict the bubble behavior and the drop ejection in a bubble jet printer. The results of calculation for three types of ink are compared with experimental data. Further, the effect of ink property on the drop size and velocity is numerically investigated.

Method of Calculation

Fluid Dynamic Equations. The motion of ink is described by the three-dimensional Navier-Stokes equation for an incompressible liquid:

$$\begin{aligned}&\rho(\partial\mathbf{u}/\partial t+(\mathbf{u}\cdot\nabla)\mathbf{u})+\nabla p-\mu\nabla^2\mathbf{u}=0,\\&\nabla\cdot\mathbf{u}=0,\end{aligned}\tag{1}$$

where ρ, μ, p, and $\mathbf{u}$ are density, viscosity, pressure, and velocity of the liquid, respectively. The effect of compressibility is neglected because the characteristic time of bubble growth and drop ejection ($\sim 10\ \mu s$) is long compared to the time of sound propagation to the inlet and the outlet of the nozzle.

Several boundary conditions are imposed in the calculation. At the inlet of the nozzle, the constant pressure boundary condition is imposed:

$$p=p_{\mathrm{res}},\tag{2}$$

where p_{res} is the pressure of the ink reservoir. At the nozzle wall, the no slip boundary condition is imposed:

$$\mathbf{u}=0.\tag{3}$$

At the outlet of the nozzle and the surface of the drop, the free surface boundary condition is imposed:

$$p=p_{\mathrm{amb}}+\sigma(1/r_1+1/r_2),\tag{4}$$

where p_{amb} is the atmospheric pressure, σ is the surface tension of the liquid, and r_1 and r_2 are principal radii of the surface. The contribution of viscosity at the surface is neglected (Harlow and Welch, 1965) because it does not have significant effect as long as the viscosity is not large. The shape of the surface is tracked by the volume of fluid (VOF) function defined at each computational mesh (Hirt and Nichols, 1981). At the bubble surface, a similar boundary condition is imposed:

Contributed by the Fluids Engineering Division for publication in the JOURNAL OF FLUIDS ENGINEERING. Manuscript received by the Fluids Engineering Division October 3, 1991. Associate Technical Editor: R. K. Agarwal.

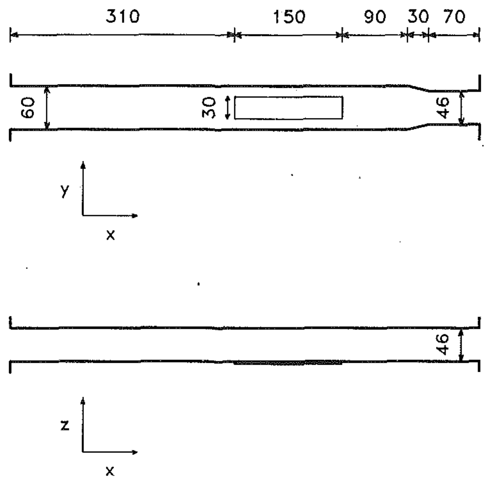

Fig. 1 Nozzle shape of a prototype bubble jet printer. Unit: μm.

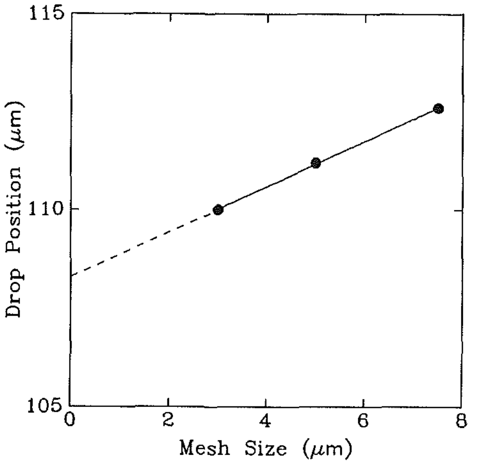

Fig. 2 Calculated drop position at t = 40μs, for various mesh size

$$p = p_v + \sigma(1/r_1 + 1/r_2), \tag{5}$$

where p_v is the bubble pressure described below.

Bubble Model. Since the ink in the nozzle is heated by an extremely high heat flux pulse ($\sim 10^8$ W m^{-2}) with a very short duration ($1 \sim 10$ μs), the bubble generation temperature is close to the superheat limit ($\sim$300°C, for water) and the initial bubble pressure is estimated to be very high (Asai et al., 1987; Asai et al., 1988; Asai, 1989; and Asai, 1991). The temperature and the pressure rapidly decrease in a few microseconds because the thickness of the heated ink is very thin. Thus the bubble pressure can be modeled by an impulsive function:

$$p_v \approx P\delta(t) + p_s, \tag{6}$$

where P is the pressure impulse and p_s is the bubble pressure in the later stage. Numerically, such impulsive pressure change can be described by a rapidly decreasing function of time t:

$$p_v = p_g f(t/t_0), \tag{7}$$

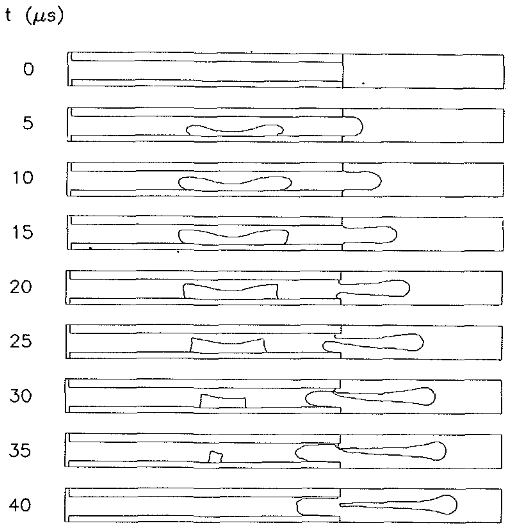

Fig. 3 Calculated cross section of bubble and drop in the xz plane, using 3μm mesh. p_g = 7.5MPa, t_0 = 0.17μs, μ = 4.5mPa s, σ = 50mN m^{-1}.

or bubble volume V:

$$p_v = \begin{cases} p_g g(V/V_0), & \text{for } dV/dt \geq 0 \\ p_s, & \text{for } dV/dt < 0 \end{cases} \tag{8}$$

where p_g is the initial bubble pressure, and t_0 and V_0 are constant parameters. In this paper the following function is used (Asai, 1991):

$$\begin{aligned} p_v &= (p_g - p_s)\exp[-(t/t_0)^{1/2}] + p_s \\ p_g &\gg p_s. \end{aligned} \tag{9}$$

This expression has the property that $p_v = p_g$ at $t = 0$ and $p_v \approx p_s$ at $t \gg t_0$. The pressure impulse, P, and the work done by the bubble, W, are calculated by Eq. (9) as:

$$\begin{aligned} P &\approx 2p_g t_0, \\ W &\approx P^2/(2A_l), \end{aligned} \tag{10}$$

where A_l is the inertance of the nozzle (Asai et al., 1987 and Asai, 1991).

Vectorization. The three-dimensional finite difference scheme requires a great amount of computation. We used vectorizable algorithms for CPU consuming loop calculations in order to reduce the CPU time. The most CPU consuming part of the calculation was the determination of the pressure field by the SOR method. Since the conventional SOR algorithm cannot be vectorized, we used the even-odd SOR technique.

The numerical calculation was done by the HITAC S820/60 super computer. The rate of vectorization was about 90 percent and the CPU time was reduced to about 1/7. The typical CPU time for a calculation was several minutes ~ several hours, depending on the number of mesh cells.

Nomenclature

A_l = inertance of the nozzle, kg m^{-4}
P = pressure impulse, Pa s
p = pressure, Pa
p_{amb} = ambient pressure, Pa
p_g = initial bubble pressure, Pa
p_{res} = reservoir pressure, Pa
p_s = bubble pressure in later stage, Pa
p_v = bubble pressure, Pa
r_1, r_2 = principal radii of the surface, m
S_h = area of heater, m^2
t = time, s
t_0 = time constant, s
$\mathbf{u}$ = velocity, m s^{-1}
V = bubble volume, m^3
V_0 = volume constant, m^3
W = work done by the bubble, J
μ = viscosity, Pa s
ρ = density, kg m^{-3}
σ = surface tension, N m^{-1}

Table 1 Composition of the ink used in the experiment

Ink	Water ratio [Mass %]	Density [g cm^{-3}]	Viscosity [mPa s]	Surface tension [mN m^{-1}]
A	55	1.0	4.5	53.8
B	29	1.0	11.8	49.0
C	9	1.0	16.7	45.7

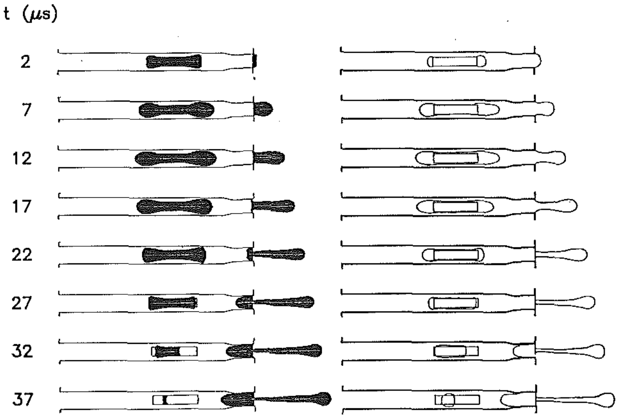

Fig. 4(*a*) Ink A: p_g = 7.5MPa

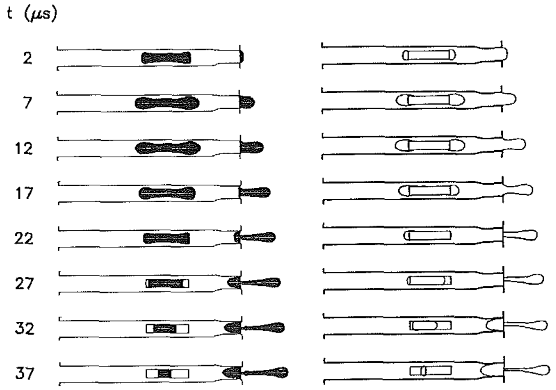

Fig. 4(*b*) Ink B: p_g = 7.3MPa

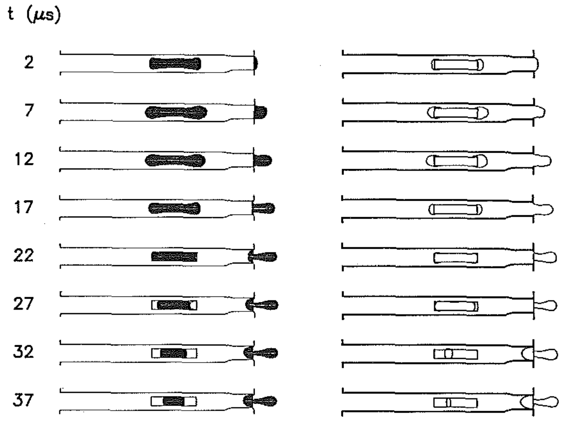

Fig. 4(*c*) Ink C: p_g = 6.6MPa

Fig. 4 Comparison of the calculated (left) and the experimental (right) top views of bubbles and drops

Results and Discussion

Mesh Size. In order to determine the appropriate mesh size for the calculation, the results for different mesh sizes are compared. The calculation was done for a nozzle shown in Fig. 1, which is a prototype nozzle for the BJ-80 bubble jet printer. The calculation was done only in the region $y \geq 0$ because of the symmetry of the nozzle. The initial bubble pressure, p_g, was taken to be 7.5MPa (saturated vapor pressure of water at ~300°C) and the time constant, t_0, which is estimated by the bubble dynamics (Asai et al., 1987 and Asai, 1991), was taken to be 0.17μs. The pressure p_s was chosen to be 16kPa and 101kPa (the saturated water vapor pressure for the ambient temperature and the boiling point), before and after the ink touch the heater surface, respectively. The boundary pressures, p_{res} and p_{amb}, are taken to be 101kPa.

The dependence of the calculated results on the mesh size is shown in Fig. 2. The discretization error can be estimated by extrapolating the result to the 0 μm mesh (dashed line in Fig. 2). In the following calculations, we use the 3 μm mesh, because the discretization error is estimated to be small enough (~2 percent) for this mesh size. The result of calculation for the 3μm mesh is shown in Fig. 3.

Comparison With an Experiment. In order to verify the validity of the calculation, the results are compared with an experiment (Asai et al., 1987) using three types of ink shown in Table 1 and the nozzle shown in Fig. 1. The time constant, t_0, was chosen to be 0.17μs, as above. The initial bubble pressure, p_g, was chosen to be 7.5, 7.3, and 6.6 MPa for ink A, B, and C, respectively, so that the calculated drop velocity agrees with the experiment. These values are reasonable considering the fraction of water in ink. The comparison of the calculation with the experiment is shown in Fig. 4. The drop is ejected for ink A and B, and is not ejected for ink C. The calculated shapes of the bubble and the drop agree well with the experiment.

Effect of Ink Property. The effect of the initial vapor pressure, p_g, viscosity, μ, and the surface tension, σ, on the volume and the velocity of the ejected drop is numerically investigated. The results are shown in Fig. 5. It is shown that the drop volume and velocity increase as the initial pressure increases and decrease as the viscosity or the surface tension increases.

The calculation shown above gives a basic guide to the design of ink, in that it predicts the effect of ink property on the volume and the velocity of the ejected drop, which greatly affect the printing quality (Shioya et al., 1989). Such calculation is very useful compared to the experiment, because each ink property (initial vapor pressure, viscosity and surface tension) cannot be changed independently in the experiment.

Application to the Nozzle Design. The three-dimensional calculation can be applied also to the design of the nozzle shape. In this case, the time constant, t_0, should be determined by an experiment or a theory (Asai, 1991). But once the value of t_0 or V_0 is determined for a nozzle, the calculation can be done for variety of nozzles, by changing the value so that the work done by the bubble to the ink, W, becomes approximately proportional to the size of the heater, S_h. If we use the bubble model (7), the value of t_0 should be adjusted proportionally to $(A_l S_h)^{1/2}$, because the work, $W \approx (\int p_v dt)^2/(2A_l)$, calculated by the model, is approximately proportional to t_0^2/A_l. If we use the bubble model (8), adjustment is simply done by changing the value of V_0 proportionally to S_h, because the work, $W = \int p_v dV$, calculated by the model, is approximately proportional to V_0.

The merit of the numerical study is that the nozzle shape is easily changed in the calculation, while the experimental study requires a lot of time and cost to make prototypes of many kinds. It is noted that the calculation will not produce enough information to the design of the nozzle shape, if it is done only outside the nozzle.

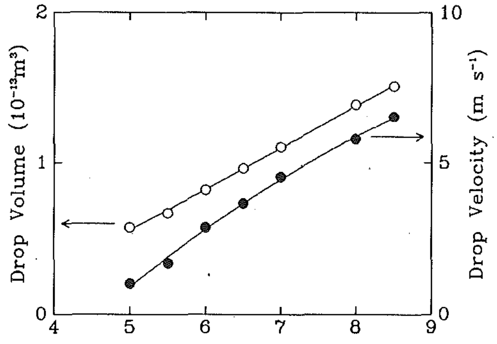

Fig. 5(*a*) Effect of initial bubble pressure

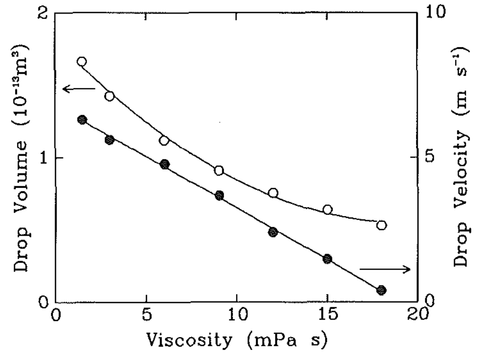

Fig. 5(*b*) Effect of viscosity

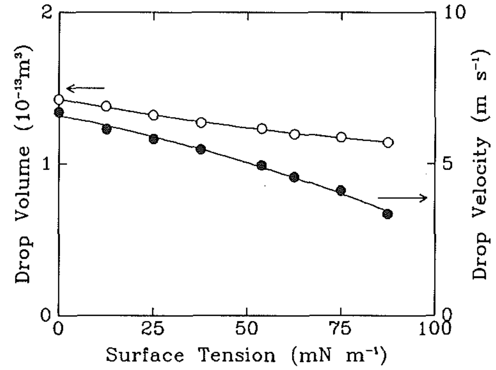

Fig. 5(*c*) Effect of surface tension

Fig. 5 Effect of ink property on the drop volume and the drop velocity

Conclusions

The numerical method to solve the three-dimensional Navier-Stokes equation for the motion of ink both inside and outside the nozzle of a bubble jet printer, presented in this paper, is successfully applied to the prediction of the bubble growth and the drop ejection phenomena. The results of calculation for three types of ink agreed well with experimental data. Further, the effect of ink property (initial bubble pressure, viscosity and surface tension) on the drop size and velocity is numerically investigated. It is concluded that the three-dimensional calculation is very useful to the design of bubble jet printers, because a lot of time and cost to make and evaluate prototypes are saved.

Acknowledgment

The author is grateful to Takeshi Sawada, Canon, Inc., for continual encouragement during the work. The numerical calculation was done on the HITAC S-820/60 supercomputer at the System Engineering Center, Canon, Inc.

References

Allen, R. R., Meyer, J. D., and Knight, W. R., 1985, "Thermodynamics and Hydrodynamics of Thermal Ink Jets," *Hewlett-Packard J.*, Vol. 36, No. 5, pp. 21-27.

Asai, A., 1989, "Application of the Nucleation Theory to the Design of Bubble Jet Printers," *Jpn. J. Appl. Phys.*, Vol. 28, pp. 909-915.

Asai, A., 1991, "Bubble Dynamics in Boiling under High Heat Flux Pulse Heating," *Proc. 3rd ASME-JSME Thermal Eng. Conf.*, Rino, Vol. 2, pp. 269-274, and ASME *Journal of Heat Transfer*, Vol. 113, pp. 973-979.

Asai, A., Hara, T., and Endo, I., 1987, "One-Dimensional Model of Bubble Growth and Liquid Flow in Bubble Jet Printers," *Jpn. J. Appl. Phys.*, Vol. 26, pp. 1794-1801.

Asai, A., Hirasawa, S., and Endo, I., 1988, "Bubble Generation Mechanism in the Bubble Jet Recording Process," *J. Imaging Technol.*, Vol. 14, pp. 120-124.

Flow Science, Inc., 1988, "FLOW-3D/88: Computational Modeling Power for Scientists and Engineers," Flow Science, Inc., Los Alamos.

Fromm, J. E., 1984, "Numerical Calculation of the Fluid Dynamics of Drop-on-Demand Jets," *IBM J. Res. Develop.*, Vol. 28, pp. 322-333.

Hara, T., and Endo, I., 1982, "Bubble Jet Recording," *J. Inst. Image Electron. Engrs.* Jpn., Vol. 11, pp. 66-71 (in Japanese).

Harlow, F. H., and Welch, J. E., 1965, "Numerical Calculation of Time-Dependent Viscous Incompressible Flow of Fluid with Free Surface," *Phys. Fluids*, Vol. 8, pp. 2182-2189.

Hirt, C. W., and Nichols, B. D., 1981, "Volume of Fluid (VOF) Method for the Dynamics of Free Boundaries," *J. Comput. Phys.*, Vol. 39, pp. 201-225.

Kawamura, T., Takami, H., and Ebi, Y., 1982, "Numerical Study of Droplet Formation from Liquid Jet," *J. Jpn. Soc. Fluid Mech.*, Vol. 1, pp. 285-298 (in Japanese).

Shioya, M., Iwata, K., Matsui, S., and Ohta, T., 1989, "Ink and Paper for Excellent Ink Jet Printing—Factors Controlling Print Quality," *J. Imaging Technol.*, Vol. 15, pp. 217-219.

Non-Darcy Couette Flow in a Porous Medium Filled With an Inelastic Non-Newtonian Fluid

A. Nakayama
Department of Energy and
Mechanical Engineering,
Shizuoka University,
Hamamatsu, 432 Japan

Newtonian and non-Newtonian Couette flows through inelastic fluid saturated porous media due to a moving plate boundary have been investigated analytically. The momentum equation which includes both the viscous and inertia terms is solved to examine the effects of the pseudoplasticity, boundary friction, and porous inertia on the velocity profile and wall shear stress at the moving wall. Closed-form exact solutions are presented for three distinct cases of practical interest. A simple expression for the wall shear stress valid for all Newtonian and non-Newtonian cases of small Darcy number has been also derived through an integral treatment, and found to agree closely with the exact values obtained from direct numerical integrations of the momentum equation. The analytical results presented here can be used for possible applications to highly sensitive viscosity measuring devices.

Introduction

In many of practical systems, highly porous media such as foam metals and fibrous media are used. When the Reynolds number based on the pore size is greater than unity, and there is a bounding impermeable wall, the non-Darcy effects, namely, the inertia and boundary effects should be included in the momentum equation. The inertia effects can be considered through the so-called Forchheimer's extention (1901), while the boundary effects can be modeled through the inclusion of a viscous shear stress term, which is known as Brinkman's extention (1947). These non-Darcy effects have been investigated extensively in free convective flows (e.g., Plumb and Huenefeld, 1981; Kaviany and Mittal, 1987; Chen et al., 1987; and Nakayama et al., 1989) and forced flows (Vafai and Tien, 1981; Beckermann and Viskanta, 1987; Kaviany, 1987; and Nakayama et al., 1990).

Studies on Darcy and non-Darcy flow in non-Newtonian fluid-saturated porous medium, on the other hand, just began, due to a broad range of applications in ceramic processing, enhanced oil recovery and filtration. Chen and Cheng (1988a, 1988b) attacked the problem of free convection of power law type fluids in a porous medium. A class of possible similarity solutions for the problem has been found by Nakayama and Koyama (1991) through a generalized similarity transformation. Shenoy (1992) pointed out that the non-Darcy inertia effects can be significant even in non-Newtonian fluids with comparatively high consistency, and modified the Forchheimer's extention to include non-Newtonian effects for his comprehensive study on non-Darcy mixed convection in non-Newtonian fluid-saturated porous medium. None of these previous papers on non-Newtonian fluids, however, deals with the boundary effects which may become as significant as the porous inertia effects within a moderately highly porous medium.

In this article, we shall treat what seems to be the most fundamental shear flow in a saturated porous medium, and yet has been overlooked, namely, non-Newtonian Couette flow through a saturated porous medium, due to a moving plate. The momentum equation which includes both the viscous and inertia terms is proposed, and solved to investigate the boundary and inertia effects on Couette flows through Newtonian and non-Newtonian fluid saturated porous media. The analytical results may be useful for possible applications to highly sensitive viscosity measurement devices.

Governing Equations and Boundary Conditions

As illustrated in Fig. 1, an infinite non-Newtonian fluid-saturated porous medium is bounded by two infinite parallel plates which are h apart, and the lower plate at $y=0$ moves at speed u_w relative to the upper at $y=h$. The boundary conditions are independent of x, hence, it follows that the only nonvanishing Darcian (apparent) velocity component is $u=u(y)$. So as to treat this Couette flow in a non-Newtonian fluid-saturated porous medium in a most general fashion, we shall propose a generalized momentum equation.

The Darcy's law for power law fluids in porous media, as proposed by Christopher and Middleman (1965), is given by

$$-\frac{dp}{dx}=\frac{\mu^*}{K^*}u^n$$

where p is the pressure, μ^* is the consistency index, and K^* is the modified permeability of the non-Newtonian power-law fluid. The expressions for the modified permeability K^* in the

---

Contributed by the Fluids Engineering Division for publication in the JOURNAL OF FLUIDS ENGINEERING. Manuscript received by the Fluids Engineering Division July 17, 1991. Associate Technical Editor: C. J. Freitas.

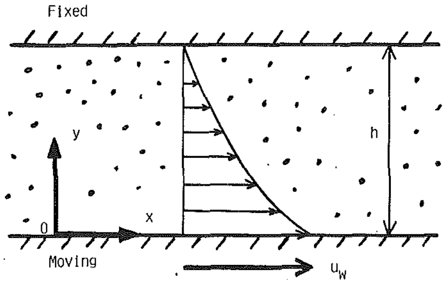

Fig. 1 Physical model and its coordinates

case of packed spheres can be found in Nakayama and Koyama (1991) based on the works by Christopher and Middleman (1965) and Dharmadhikari and Kale (1985). The Darcy's law breaks down for flows at high velocity, in which the flow inertia is no longer negligible. Forchheimer (1901) proposed a velocity square term to be added to the Darcy term. This Forchheimer's modification should be equally valid for non-Newtonian inelastic fluids, since the inertial drag force should not depend on the viscous stress-strain rate relationship. Thus, as in the recent analytical study of Shenoy (1992), the Forchheimer extended Darcy model can be modified for the power-law fluids as

$$-\frac{dp}{dx}=\frac{\mu^*}{K^*}u^n+\rho bu^2$$

where ρ is the fluid density and b is the Forchheimer's constant. For flow through a highly porous medium, the boundary frictional effect becomes appreciable. In order to model such boundary frictional effect, Brinkman (1947) argued that the governing equation must be reduced to the viscous flow limit, and suggested the addition of a macroscopic viscous term. Thus, the Brinkman-Forchheimer extended Darcy's law can be modified for the power-law fluids as

$$\frac{\mu^*}{\epsilon^n}\frac{d}{dy}\left(\left|\frac{du}{dy}\right|^{n-1}\frac{du}{dy}\right)=\frac{\mu^*}{K^*}u^n+\rho bu^2 \tag{1}$$

where ϵ is the porosity. Note that the pressure gradient term vanishes for the present Couette flow problem:

$$-\frac{dp}{dx}=0 \tag{2}$$

In fact, along in the line of Vafai and Tien (1981), the microscopic momentum equation for a power-law fluid can be integrated over a local control volume to derive the volume averaged momentum equation (1). The boundary conditions are as follows:

$$y=0:\quad u=u_w \tag{3a}$$

$$y=h:\quad u=0 \tag{3b}$$

Equation (1) may be rewritten in a dimensionless form as

$$\frac{d}{dy^*}\left(\left|\frac{du^*}{dy^*}\right|^{n-1}\frac{du^*}{dy^*}\right)=\frac{u^{*n}+\mathrm{Re}_K u^{*2}}{\mathrm{Da}^{(1+n)/2}} \tag{4}$$

where

$$u^*=u/u_w \tag{5a}$$

$$y^*=y/h \tag{5b}$$

$$\mathrm{Re}_K=\rho bK^*u_w^{2-n}/\mu^* \tag{5c}$$

and

$$\mathrm{Da}=(K^*/\epsilon^n)^{2/(1+n)}/h^2 \tag{5d}$$

Re_K and Da are the modified Reynolds number and Darcy number. In this analysis, the power-law index n is assumed to be less than 2, since shear flows with $n>2$ are not of much practical interest, as pointed out by Acrivos et al. (1960). The transformed boundary conditions are

$$y^*=0:\quad u^*=1 \tag{6a}$$

$$y^*=1:\quad u^*=0 \tag{6b}$$

For a given set of n, Re_K and Da, Eq. (4) subject to (6) can be integrated to find the velocity profile $u^*(y^*)$ and the dimensionless quantity associated with the viscous shear,

$$\Lambda(y^*)\equiv\mu^*\left|\frac{du}{dy}\right|^n\Big/\mu^*\left(\frac{u_w}{h}\right)^n=\left|\frac{du^*}{dy^*}\right|^n \tag{7}$$

which is unity throughout in the absence of the porous structure, and

$$\Lambda(1)\ll 1\ll\Lambda(0) \tag{8}$$

in the presence of the porous structure. Consider a possible viscometer which measures the torques on a constant-speed rotating cylinder embedded in a fluid-saturated porous medium. We may expect this viscometer to be highly sensitive, since $\Lambda(0)$ is directly related to the sensitivity of the device.

Brinkman-Darcy Flow in a Newtonian Fluid Saturated Porous Medium: $n=1$ and $\mathrm{Re}_K=0$

For the Brinkman-Darcy Newtonian flows, Eq. (4) reduces to

$$\frac{d^2u^*}{dy^{*2}}=\frac{u^*}{\mathrm{Da}} \tag{9}$$

The solution to the foregoing equation subject to (6) is given by

$$u^*=\frac{\sinh\left(\frac{1-y^*}{\mathrm{Da}^{1/2}}\right)}{\sinh\left(\frac{1}{\mathrm{Da}^{1/2}}\right)} \tag{10}$$

Hence,

$$\Lambda(0)=1/\mathrm{Da}^{1/2}\tanh\left(\frac{1}{\mathrm{Da}^{1/2}}\right) \tag{11a}$$

and

$$\Lambda(1)=1/\mathrm{Da}^{1/2}\sinh\left(\frac{1}{\mathrm{Da}^{1/2}}\right) \tag{11b}$$

For $\mathrm{Da}\ll 1$ which is usually the case, $\Lambda(0)=1/\mathrm{Da}^{1/2}\gg 1$. This suggests that a highly sensitive viscosity measuring device is

Nomenclature

b = Forchheimer constant
Da = Darcy number
h = channel height
K^* = intrinsic permeability of the porous medium for flow of power-law fluid
n = power-law index of the inelastic non-Newtonian fluid
Re_K = modified Reynolds number
u = Darcian or superficial velocity component
u_w = velocity of the moving wall
u^* = u/u_w; dimensionless velocity
x, y = Cartesian coordinates
y^* = y/h, dimensionless vertical coordinate
ϵ = porosity of the medium
η = $y^*/\mathrm{Da}^{1/2}$; dimensionless vertical coordinate
μ^* = fluid consistency of the inelastic non-Newtonian power-law fluid
ρ = density of the fluid

possible by simply measuring the torque of a rotor immersed in a fluid-saturated porous medium. Fortunately, in such a system in a porous medium, the measured torque is insensitive to the outer boundary configuration (i.e., h), since $\mu^*(|du/dy|)_{y=0}=\Lambda(0)u_w/h=u_w/(K^*/\epsilon)^{1/2}$.

Brinkman-Forchheimer-Darcy Flow in a Newtonian Fluid Saturated Porous Medium With a Low Permeability: $n=1$, $\mathrm{Re}_K>0$ and $\mathrm{Da}\ll 1$

For the case of nonvanishing Re_K, we must integrate

$$\frac{d^2u^*}{dy^{*2}}=\frac{u^*+\mathrm{Re}_K u^{*2}}{\mathrm{Da}} \tag{12}$$

subject to Eqs. (6). A simple analytical expression for u^* does not seem to exist for this general Newtonian case. However, the assumption $\mathrm{Da}\ll 1$ of practical importance, allows us to replace the outer boundary condition, Eq. (6b) by

$$y^*/\mathrm{Da}^{1/2}\rightarrow\infty:\quad u^*=0 \tag{13}$$

and then, Eq. (4) can readily be integrated to give the following approximate expression for $\mathrm{Da}\ll 1$:

$$u^*=\frac{6}{\mathrm{Re}_K}\,\frac{\dfrac{\left(1+\frac{2}{3}\mathrm{Re}_K\right)^{1/2}-1}{\left(1+\frac{2}{3}\mathrm{Re}_K\right)^{1/2}+1}\,e^{-y^*/\mathrm{Da}^{1/2}}}{\left\{1-\dfrac{\left(1+\frac{2}{3}\mathrm{Re}_K\right)^{1/2}-1}{\left(1+\frac{2}{3}\mathrm{Re}_K\right)^{1/2}+1}\,e^{-y^*/\mathrm{Da}^{1/2}}\right\}^2} \tag{14}$$

and

$$\Lambda(0)=\left(\frac{1+\frac{2}{3}\mathrm{Re}_K}{\mathrm{Da}}\right)^{1/2} \tag{15a}$$

or

$$\tau_w\equiv\mu^*\left(\left|\frac{dy}{dy}\right|\right)_{y=0}=\mu^*\,\frac{u_w}{(K^*/\epsilon)^{1/2}}\left(1+\frac{2}{3}\,\frac{\rho bK^*u_w}{\mu^*}\right)^{1/2} \tag{15b}$$

For given apparatus constants ϵ, K^* and b, the foregoing equation may be used to determine the viscosity μ^*. After transforming Eq. (15b) into a quadratic equation with respect to μ^*, we can solve it to obtain

$$\mu^*=\frac{\tau_w(K^*/\epsilon)^{1/2}}{u_w}\left[\left(1+\left\{\frac{b(K^*\epsilon)^{1/2}\rho u_w^2}{3\tau_w}\right\}^2\right)^{1/2}-\frac{b(K^*\epsilon)^{1/2}\rho u_w^2}{3\tau_w}\right] \tag{16}$$

where τ_w is the wall shear stress at the moving wall evaluated from the measured torque at the rotational speed u_w. Note that the shear stress at the upper stationary wall is negligibly small, namely, $\Lambda(1)\doteq 0$.

Brinkman-Forchheimer-Darcy Flow in a Newtonian Fluid Saturated Porous Medium With a High Permeability: $n=1$, $\mathrm{Re}_K>0$ and $\mathrm{Da}>1$

For the case of moderately high permeability (i.e., Da is of the order of unity or more), we must discard the assumption $\mathrm{Da}\ll 1$. In order to seek an approximate solution for this case, we shall integrate Eq. (12) as

$$\Lambda(0)-\Lambda(1)=\int_0^1\frac{u^*+\mathrm{Re}_K u^{*2}}{\mathrm{Da}}\,dy^* \tag{17}$$

Assuming that a one-parameter fourth order polynomial is flexible enough to describe the velocity profile within a comparatively highly porous medium:

$$u^*(y^*)=1-y^*+(3y^{*2}-5y^{*3}+2y^{*4})\,\frac{1+\mathrm{Re}_K}{6\mathrm{Da}}-(y^*-2y^{*3}+y^{*4})\{\Lambda(0)-1\} \tag{18}$$

Equation (18) automatically satisfies Eqs. (6a), (6b) and the auxiliary conditions implicit in the original differential Eq. (12), namely,

$$\left(\frac{d^2u^*}{dy^{*2}}\right)_{y^*=0}=\frac{1+\mathrm{Re}_K}{\mathrm{Da}} \tag{19a}$$

and

$$\left(\frac{d^2u^*}{dy^{*2}}\right)_{y^*=1}=0 \tag{19b}$$

Integrations in Eq. (17) can be carried out using the velocity profile given by Eq. (18). After some manipulation, we obtain the following quadratic equation for determining the dimensionless wall shear stress at the moving wall $\Lambda(0)$:

$$\begin{aligned}62\mathrm{Re}_K\{\Lambda(0)-1\}^2-\Bigg\{&252(1+10\mathrm{Da})\\&+\left(252+95\,\frac{1+\mathrm{Re}_K}{6\mathrm{Da}}\right)\mathrm{Re}_K\Bigg\}\{\Lambda(0)-1\}\\&+63\left\{10+(3+20\mathrm{Da})\,\frac{1+\mathrm{Re}_K}{6\mathrm{Da}}\right\}\\&+2\left\{210+84\,\frac{1+\mathrm{Re}_K}{6\mathrm{Da}}+19\left(\frac{1+\mathrm{Re}_K}{6\mathrm{Da}}\right)^2\right\}\mathrm{Re}_K=0\end{aligned} \tag{20}$$

For known $\Lambda(0)$, the dimensionless shear stress at the upper stationary wall $\Lambda(1)$ can readily be evaluated from

$$\Lambda(1)=2-\Lambda(0)+\frac{1+\mathrm{Re}_K}{6\mathrm{Da}} \tag{21}$$

These approximate results will be compared against the exact solution.

Brinkman-Darcy Flow in a Non-Newtonian Fluids Saturated Porous Medium With a Low Permeability: $n\neq 1$, $\mathrm{Re}_K=0$ and $\mathrm{Da}\ll 1$

When $n\neq 1$, analytical integrations of Eq. (4), in general, become quite formidable. Fortunately, an exact solution is possible, for the Brinkman-Darcy non-Newtonian flow through a porous medium with a low permeability of practical interest (i.e., $\mathrm{Re}_K=0$ and $\mathrm{Da}\ll 1$). Equation (4) for this case transforms itself into

$$\frac{d}{d\eta}\left(\left|\frac{du^*}{d\eta}\right|^{n-1}\frac{du^*}{d\eta}\right)=u^{*n} \tag{22}$$

subject to

$$\eta=0:\quad u^*=1 \tag{23a}$$

and

$$\eta\rightarrow\infty:\quad u^*=0 \tag{23b}$$

where

$$\eta=y^*/\mathrm{Da}^{1/2}=y/(K^*/\epsilon^n)^{1/(1+n)} \tag{24}$$

The solution to the equation is given by

$$u^*=\exp\left\{-\left(\frac{1}{n}\right)^{1/(1+n)}\eta\right\} \tag{25}$$

and

$$\Lambda(0)=\left(\frac{1}{n}\right)^{n/(1+n)}/\mathrm{Da}^{n/2} \tag{26a}$$

or

$$\tau_w\equiv\mu^*\left(\left|\frac{du}{dy}\right|^{n}\right)_{y=0}=\left(\frac{1}{n}\right)^{n/(1+n)}\cdot\frac{\mu^* u_w{}^{n}}{(K^*/\epsilon^n)^{n/(1+n)}} \tag{26b}$$

The wall shear stress at the upper stationary wall, on the other hand, is expected to be vanishingly small.

Brinkman-Forchheimer-Darcy Flow in a Non-Newtonian Fluid Saturated Porous Medium With a Low Permeability: $n\neq 1$, $\mathrm{Re}_K>0$ and $\mathrm{Da}<<1$

For $\mathrm{Re}_K>0$, we must appeal to numerical integrations. To avoid singularities during integration, we arrange Eq. (4) into

$$\frac{d}{dy^*}\left(\frac{du^*}{dy^*}\right)^2=-\frac{2(u^{*n}+\mathrm{Re}_K u^{*2})}{n\mathrm{Da}^{(1+n)/2}}\left|\frac{du^*}{dy^*}\right|^{2-n} \tag{27}$$

A standard numerical integration scheme (such as Runge-Kutta-Gill scheme) may be used to solve the equation subject to Eqs. (6*a*) and (6*b*). Again, when $\mathrm{Da}\ll 1$, we may rewrite the foregoing equation in terms of $\eta=y^*/\mathrm{Da}^{1/2}$ as

$$\frac{d}{d\eta}\left(\frac{du^*}{d\eta}\right)^2=-\frac{2}{n}\,(u^{*n}+\mathrm{Re}_K u^{*2})\left|\frac{du^*}{d\eta}\right|^{2-n} \tag{28}$$

which then, can be integrated using the boundary conditions given by Eqs. (23*a*) and (23*b*). Numerical solutions can be obtained by first converting the boundary-value problem to an initial-value problem, and with a systematic guessing of the velocity gradient at the wall by the shooting method. Such numerical results will be presented later.

An alternative way to attach the formidable Eq. (28) is to appeal to the integral method. Focussing on the practically important case of $\mathrm{Da}\ll 1$, an integral expression can be obtained by integrating Eq. (4) as

$$\left(\left|\frac{du^*}{d\eta}\right|^{n}\right)_{\eta=0}=\int_0^\infty(u^{*n}+\mathrm{Re}_K u^{*2})d\eta \tag{29}$$

The integral equation states that the wall shear force at the moving wall balances with the sum of the Darcy and inertial resistance forces. (Note that the shear stress at the upper stationary wall is negligibly small.) The velocity profile function

$$u^*(\eta)=\exp\left\{-\left(\left|\frac{du^*}{d\eta}\right|\right)_{\eta=0}\eta\right\} \tag{30}$$

which conforms with Eq. (25) for the case of $\mathrm{Re}_K=0$, may be substituted into Eq. (29) to find

$$\left(\left|\frac{du^*}{d\eta}\right|\right)_{\eta=0}=\left(\frac{1}{n}+\frac{1}{2}\mathrm{Re}_K\right)^{1/(1+n)} \tag{31a}$$

Thus, a useful approximate expression for the dimensionless wall shear stress at the moving wall of the present concern is obtained as

$$\Lambda(0)=\left(\frac{1}{n}+\frac{1}{2}\mathrm{Re}_K\right)^{n/(1+n)}\Big/\mathrm{Da}^{n/2} \tag{31b}$$

The foregoing approximate expression will be examined against the exact solution.

Results and Discussion

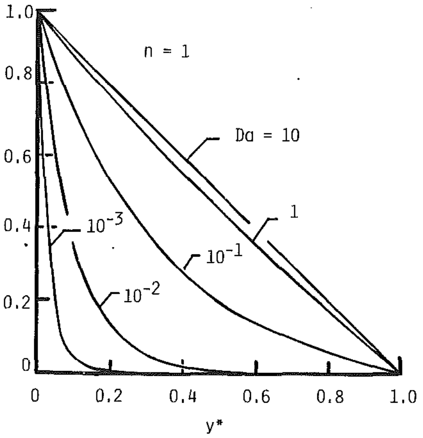

Fig. 2 **Effects of the Darcy number on the velocity profile; $n=1$ and $\mathrm{Re}_K=0$**

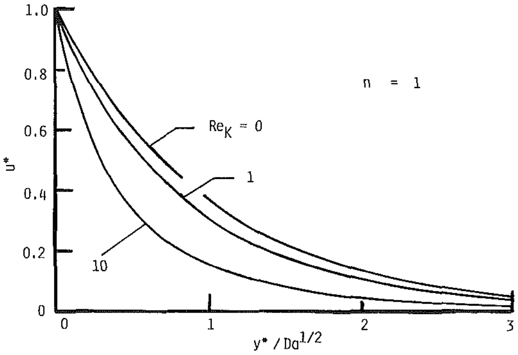

Fig. 3 **Effects of porous inertia on the velocity profile; $n=1$ and $\mathrm{Da}\ll 1$**

The velocity profiles of Newtonian Darcy flows generated from Eq. (10) are plotted in Fig. 2 for comparatively high Darcy numbers such as $\mathrm{Da}=10^{-3}$, 10^{-2}, 10^{-1}, 1 and 10. The velocity profile at $\mathrm{Da}=10$ appears to be almost linear as in the absence of the porous structure, while the profiles at small Da show that the Darcy resistance suppresses the fluid motions even in the vicinity of the moving wall. The velocity profiles for $\mathrm{Da}=10^{-2}$ and 10^{-3} closely follow the asymptotic profile for $\mathrm{Da}\ll 1$ implicit in Eq. (10), namely,

$$u^*=\exp(-y^*/\mathrm{Da}^{1/2}) \tag{32}$$

The equation suggests that the boundary layer thickness is proportional to $h\mathrm{Da}^{1/2}$. Thus, decrease in Da results in thinning the boundary layer. According to Eq. (32), the torque measured from a rotor immersed in a Newtonian fluid-saturated porous medium will be $\mathrm{Da}^{-1/2}$ times greater than that from the conventional viscometer without a porous medium, operated at the same rotational speed. To gain some feeling of the magnitude of the relative sensitivity $\Lambda(0)$, consider a porous layer to thickness 1.5 cm, packed closely with spheres of diameter 1 mm. Since $\mathrm{Da}\fallingdotseq 4\times 10^{-6}$, we may expect the relative sensitivity as high as $\Lambda(0)\fallingdotseq 500$!

The effects of the porous inertia (i.e., Re_K) on the velocity profiles are investigated in Fig. 3, in which the profiles of Newtonian fluids based Eq. (14) are plotted against $y^*/\mathrm{Da}^{1/2}$, assuming the case $\mathrm{Da}\ll 1$, of practical interest. It can be seen that the porous inertia which increases with Re_K, tends to suppress the fluid motions in a fashion similar to the Darcy resistance. Sufficiently away from the moving lower wall, Eq. (14) may well be approximated by

$$u^*=\frac{4}{\left\{\left(1+\frac{2}{3}\mathrm{Re}_K\right)^{1/2}+1\right\}^2}\,e^{-y^*/\mathrm{Da}^{1/2}} \tag{33}$$

Thus, the effect of Re_K is to reduce the velocity level throughout the porous medium.

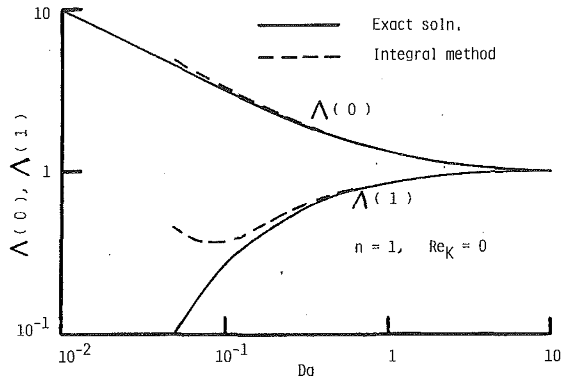

Fig. 4 Effects of the Darcy number on the wall shear stresses; $n=1$ and $Re_K=0$

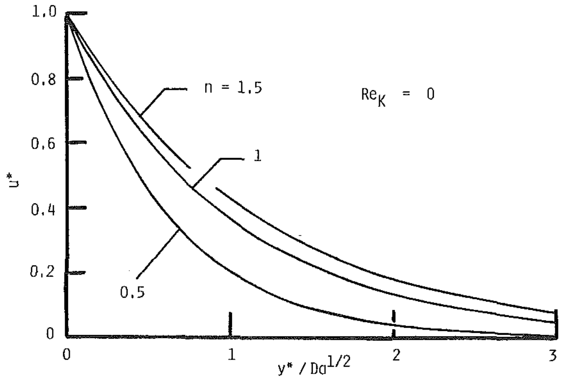

Fig. 5 Effects of the power-law index on the velocity profile; $Re_K=0$ and $Da \ll 1$

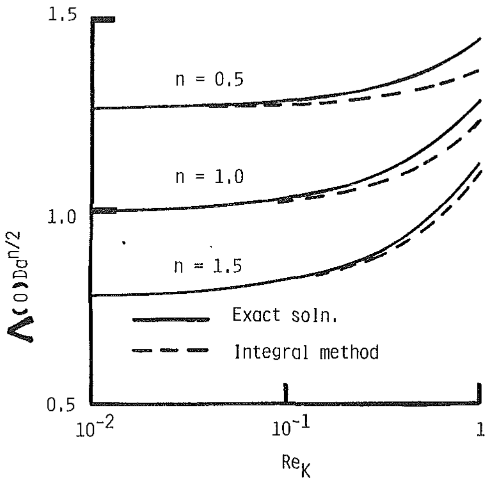

Fig. 6 Effects of the porous inertia on the wall shear stress; $Da \ll 1$

The dimensionless wall shear stresses acting on the moving lower wall (at $y^*=0$) and the stationary upper wall (at $y^*=1$) are evaluated from Eqs. (11*a*) and (11*b*) for Newtonian fluids varying Da from 10^{-2} to 10, and presented in Fig. 4 along with the approximate results from Eqs. (20) and (21) based on the integral treatment. A tremendous difference in the wall shear stresses on the moving and stationary walls can be seen as Da decreases. (Note that, at $Da=10^{-1}$, $\Lambda(0)$ is roughly 12 times greater than $\Lambda(0)$.) The approximate solution curves based on the integral method closely follow the exact solutions up to 0.1, but deviate away from them, as Da decreases further. Difficulties in treating a wide range of Da lie in the fact that the effect of the porous inertia reflects on the velocity profile so drastically that a simple polynomial function such as Eq. (18) cannot cope with changes in the velocity profile (from a linear profile to an exponential profile) as already shown in Fig. 2.

Typical velocity profiles of non-Newtonian fluids, generated from Eq. (25) for pseudoplastic ($n=0.5$) and dilatant ($n=1.5$) fluids are compared against the profile of Newtonian fluid ($n=1$) in Fig. 5, where it can be seen that the boundary layer becomes thinner as the pseudoplasticity increases (i.e., as n decreases). The velocity profile function given by Eq. (25) reveals that the boundary layer thickness varies in proportion to $n^{1/(1+n)}hDa^{1/2}$. Thus, the effect of the pseudoplasticity (shear thinning) is to make the boundary layer thinner and thinner, in a fashion similar to Da. The velocity profile departs from the Newtonian profile ($n=1$) more markedly in the pseudoplastic fluid ($n=0.5$) than in the dilatant fluids ($n=1.5$).

Extensive numerical integrations have been carried out to solve the differential Eq. (28) with (23), for $n=0.5$, 1 and 1.5, varying Re_K in the range of $10^{-2} \leq Re_K \leq 1$, under the practical limiting condition $Da \ll 1$. The boundary problem has been converted into the initial problem, iterating on $du^*/d\eta$ at the wall by integrating Eq. (28) with Eq. (23*a*) and a guessed value of $du^*/d\eta$ at the wall, such that Eq. (23*b*) is satisfied eventually. The upper bound of the integration, namely, $\eta \rightarrow \infty$, was replaced by $\eta=20$, since it was found sufficiently far from the wall in all cases treated here. An increment of $\Delta\eta=0.01$ was used. Convergence was measured in terms of the change in the value of $du^*/d\eta$ at the wall during an iteration. The maximum change allowed for the convergence check was set to 10^{-6}. The numerical integration results are presented in Fig. 6, in terms of $\Lambda(0)Da^{n/2}$, along with the curves based on the approximate formula, Eq. (31*b*) obtained from a simple integral treatment. The effects of Da, Re_K, and n on the velocity profile, discussed above, can be confirmed from the figure. The pseudoplastic fluid maintains a higher level of $\Lambda(0)Da^{n/2}$, as can be expected from the velocity profiles shown in Fig. 5, whereas the dilatant fluid appears to be more sensitive to the porous inertia effect. Agreement between the exact and approximate solutions appears to be reasonable. Especially for $Re_K \leq 0.1$, the difference of the two solutions are hardly discernible.

Conclusions

An analytical study was made on non-Darcy Couette flows through porous media filled with Newtonian and non-Newtonian fluids. The general momentum equation which accounts for both the boundary friction and porous inertia was considered for the Newtonian and non-Newtonian cases. Exact expressions in closed form are found to exist for all Newtonian Brinkman-Darcy flows, Newtonian Brinkman-Forchheimer-Darcy flows and non-Newtonian Brinkman-Darcy flows under small Da. Integral approximate solutions are also obtained for Newtonian and non-Newtonian Brinkman-Forchheimer-Darcy flows. An extensive investigation on the effects of Da, Re_K, and n on the velocity profiles reveals that the effects of Da and n are very much alike in the sense that the decrease in either Da or n results in thinning the velocity boundary layer, whereas the effect of Re_K is to lower the velocity level throughout the porous medium. The present analytical results should be verified experimentally through a possible development of highly sensitive viscosity measuring devices.

Acknowledgment

The author would like to express his sincere thanks to Professors A. V. Shenoy and F. Kuwahara for helpful discussions on this paper.

References

Acrivos, A., Shah, M. J., and Peterson, E. E., 1960, "Momentum and Heat Transfer in Laminar Boundary-Layer Flow of Non-Newtonian Fluids Past External Surfaces," *AIChE Journal*, Vol. 6, pp. 312-317.

Beckermann, C., and Viskanta, R., 1987, "Forced Convection Boundary Layer Flow and Heat Transfer Along a Flat Plate in a Porous Medium," *Int. J. Heat Mass Transfer*, Vol. 30, pp. 1547-1551.

Brinkman, H. C., 1947, "A Calculation of the Viscous Force Exerted by a Flowing Fluid on a Dense Swarm of Particles," *Appl. Scient. Res.*, Vol. A1, pp. 27-34.

Chen, C. K., Hung, C. I., and Cleaver, J. W., 1987, "Non-Darcian Effects on Vertical Plate Transient Natural Convection in Porous Media with High Porosities," *Proc. of The ASME-JSME Thermal Engineering Joint Conf.*, Vol. 2, pp. 313-318.

Chen, H. T., and Chen, C. K., 1988a, "Free Convection of Non-Newtonian Fluids Along a Vertical Plate Embedded in a Porous Medium," ASME *Journal of Heat Transfer*, Vol. 110, pp. 257-260.

Chen, H. T., and Chen, C. K., 1988b, "Natural Convection of a Non-Newtonian Fluid About a Horizontal Cylinder and a Sphere in a Porous Medium," *Int. Communications in Heat and Mass Transfer*, Vol. 15, pp. 605-614.

Christopher, R. V., and Middleman, S., 1965, "Power-Law Flow Through a Packed Tube," *Ind. Engng. Chem. Fundls.*, Vol. 4, pp. 422-426.

Dharmadhikari, R. V., and Kale, D. D., 1985, "Flow of non-Newtonian Fluids Through Porous Media," *Chem. Engng. Sci.*, Vol. 40, pp. 527-529.

Forchheimer, P., 1901, "Wasserbewegung Durch Boden," *Forschtlft. Ver. D. Ing.*, Vol. 45, pp. 1782-1788.

Kaviany, M., 1987, "Boundary Layer Treatment of Forced Convection Heat Transfer from a Semi-Infinite Flat Plate Embedded in Porous Media," ASME *Journal of Heat Transfer*, Vol. 109, pp. 345-349.

Kaviany, M., and Mittal, M., 1987, "Natural Convection Heat Transfer from a Vertical Plate to High Permeability Porous Media; An Experiment and An Approximate Solution," *Int. J. Heat Mass Transfer*, Vol. 30, pp. 967-977.

Nakayama, A., Kokudai, T., and Koyama, H., 1990, "Non-Darcian Boundary Layer Flow and Forced Convective Heat Transfer Over a Flat Plate in a Fluid-Saturated Porous Medium," ASME *Journal of Heat Transfer*, Vol. 112, pp. 157-162.

Nakayama, A., and Koyama, H., 1991, "Buoyancy-Induced Flow of Non-Newtonian Fluids Over a Non-Isothermal Body of Arbitrary Shape in a Fluid-Saturated Porous Medium," *Appl. Scient. Res.*, Vol. 48, pp. 55-70.

Nakayama, A., Koyama, H., and Kuwahara, F., 1989, "Similarity Solution for Non-Darcy Free Convection From a Non-Isothermal Curved Surface in a Fluid-Saturated Porous Medium," ASME *Journal of Heat Transfer*, Vol. 111, pp. 807-811.

Plumb, O. A., and Huenefeld, J. C., 1981, "Non-Darcy Natural Convection From Heated Surfaces in Saturated Porous Media," *Int. J. Heat Mass Transfer*, Vol. 24, pp. 765-768.

Shenoy, A. V., 1992, "Darcy-Forchheimer Forced, Natural and Mixed Convection Heat Transfer in Non-Newtonian Power-Law Fluid-Saturated Porous Media," (to appear in *Trans. Porous Media*).

Vafai, K., and Tien, C. L., 1981, "Boundary and Inertia Effects on Flow and Heat Transfer in Porous Media," *Int. J. Heat Mass Transfer*, Vol. 24, pp. 195-203.

Swirling, Particle-Laden Flows Through a Pipe Expansion

M. Sommerfeld

A. Ando

D. Wennerberg[1]

Lehrstuhl für Strömungsmechanik,
Universität Erlangen/Nürnberg,
8520 Erlangen, Germany

The present study concerns a particle-laden, swirling flow through a pipe expansion. A gas-particle flow enters the test section through a center tube, and a swirling air stream enters through a coaxial annulus. The swirl number based on the total inflow is 0.47. Numerical predictions of the gas flow were performed using a finite-volume approach for solving the time-averaged Navier-Stokes equations. The predicted mean velocity profiles showed good agreement with experimental results when using the standard k-ε turbulence model. The turbulent kinetic energy of the gas phase, however, is considerably underpredicted by this turbulence model, especially in the initial mixing region of the two jets. The particle dispersion characteristics in this complex flow were studied by using the Lagrangian method for particle tracking and considering the particle size distribution. The influence of the particle phase onto the fluid flow was neglected in the present stage, since only low particle loadings were considered. The particle mean velocities were again predicted reasonably well and differences between experiment and simulation were only found in the velocity fluctuations, which is partly the result of the underpredicted turbulent kinetic energy of the gas phase. The most sensitive parameter for validating the quality of numerical simulations for particle dispersion is the development of the particle mean number diameter which showed reasonable agreement with the experiments, except for the core region of the central recirculation bubble. This, however, is attributed again to the predicted low turbulent kinetic energy of the gas phase.

Introdution

The special features of swirling flows are utilized in combustion systems in order to provide flame stabilization and good mixing between fuel and oxidizer. This is achieved by the central recirculation bubble developing in front of the burner exit. Swirl burners are usually operated with liquid or pulverized fuels, and a detailed understanding of the behavior of droplets or particles in such a swirling flow is necessary for the optimization of the combustion process. The typical characteristic of swirling flows, the influence of the flow properties, and the geometrical configuration of the burner on the shape of the central reverse flow region have been already reported in a number of papers (Altgeld et al., 1983; Escudier and Keller, 1985; Lilley, 1977). However, very limited information is available on the dispersion and behavior of particles or droplets in a swirling flow (Blümcke et al., 1988; Hardalupas et al., 1990).

Therefore, a study of the dispersion of solid particles in a non-reacting swirling flow was recently initiated (Sommerfeld and Krebs, 1990; Sommerfeld and Qiu, 1991). Gas and particle velocity characteristics were measured by using a phase-Doppler anemometer which additionally allows the measurement of particle size-velocity correlations. This measuring technique enables studies of the behavior of different particle size classes within the size spectrum of the particle material used. Furthermore, the change of particle size distribution throughout the flow field was studied which indicated strong separation effects due to radial transport, turbulent dispersion, and the action of centrifugal forces.

This paper presents numerical simulations based on the detailed measurements performed in order to give more insight into the behavior of solid particles in confined swirling flows and to validate the results of the numerical code used.

Flow Configuration and Conditions

The flow configuration of the model combustion chamber is a sudden pipe expansion with a centered and coaxial jet discharging into the test section (Fig. 1) which is connected to a stagnation chamber at the downstream end. Such a config-

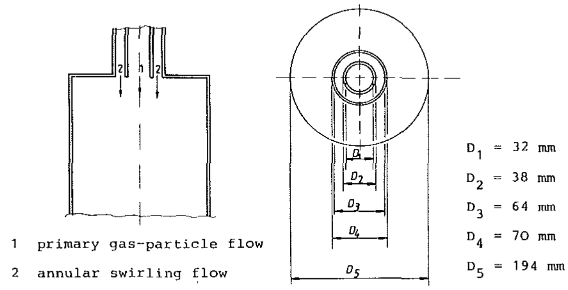

Fig. 1 Inlet geometry of the test section (length 1.5 m)

---

[1] Battelle Europe, Energie-, Umwelt- und Systemtechnik, 6000 Frankfurt 90, Germany.

Contributed by the Fluids Engineering Division for publication in the JOURNAL OF FLUIDS ENGINEERING. Manuscript received by the Fluids Engineering Division May 13, 1991. Associate Technical Editor: E. E. Michaelides.

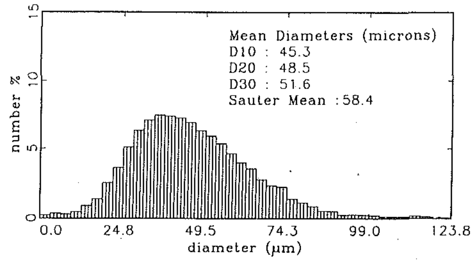

Fig. 2 Particle size distribution (D_p = 45 μm)

uration has the advantage that the inlet conditions could be easily measured which is important for performing numerical calculations. The central primary jet is loaded with spherical glass beads, and the annular jet provides the swirling air stream (Sommerfeld and Qui, 1991). The swirl is introduced by a radial swirl generator which is located above the test section. The flow conditions for the present study are given in Table 1 together with the properties of the glass beads. The size distribution of the glass beads is shown in Fig. 2.

Measurements of air velocity and particle size-velocity correlations were performed at a number of cross sections downstream of the inlet by employing a phase-Doppler anemometer (PDA). All optical parts of the one-component PDA-system are mounted on a three-dimensional traversing system which allows the measurement of all three velocity components (axial, radial, and tangential velocity) by changing the optical setup. Further information about the measuring technique and a discussion of the experimental results are given by Qiu et al. (1990) and Sommerfeld and Qiu (1991).

Numerical Method

The particle-laden, swirling flow was calculated using an Eulerian/Lagrangian method for the gas and particle phases, respectively. The fluid flow calculation is based on the time-averaged Navier-Stokes equations in connection with a closure assumption for the turbulence modelling. The general form of the elliptic differential equations governing a axisymmetric swirling of flow can be expressed as

$$\frac{\partial}{\partial x}(\rho U\phi)+\frac{1}{r}\frac{\partial}{\partial r}(\rho r V\phi)-\frac{\partial}{\partial x}\left(\Gamma\frac{\partial\phi}{\partial x}\right)-\frac{1}{r}\frac{\partial}{\partial r}\left(r\Gamma\frac{\partial\phi}{\partial r}\right)=S_\phi \qquad (1)$$

The source terms, S_ϕ, and the effective viscosity, Γ, for the different variables, ϕ, are given in Table 2.

The solution of the above equations is obtained by using the so-called FASTEST-code (Dimirdzic and Peric, 1990) which incorporates the well-known k-ϵ two-equation turbulence model and uses a finite-volume approach to discretize the equations. In order to minimize the effects of numerical diffusion in the present calculations, the quadratic, upwind-weighted differencing scheme (QUICK) was used for differencing the convection terms in Eq. (1). Furthermore, flux-blending techniques, where the convective flux can be calculated as a weighted sum of the flux expressions from the "upwind" and QUICK differencing schemes (Peric et al., 1988), was used to avoid instabilities and convergence problems that sometimes appear when using higher order schemes.

Table 1 Flow conditions and particle properties

Air flow:		
Mass flow rate of primary jet	9.9	g/s
Mass flow rate of secondary jet	38.3	g/s
Inlet Reynolds number (obtained with $D=64$ mm)	52400	
Swirl number	0.47	
Particle phase:		
Particle mass flow rate	0.34	g/s
Particle loading	0.034	
Particle properties:		
Particle mean number diameter	45	μm
Particle material density	2500	kg/m^3
Stokesian particle response time	15.2	ms

Table 2 Source term expressions for the different independent variables in Eq. (1) and constants in turbulence model

ϕ	Source Term	Γ
1	–	–
U	$\frac{\partial}{\partial x}\left(\Gamma\frac{\partial U}{\partial x}\right)+\frac{1}{r}\frac{\partial}{\partial r}\left(\Gamma r\frac{\partial V}{\partial x}\right)-\frac{\partial P}{\partial x}$	$\mu_{\rm eff}$
V	$\frac{\partial}{\partial x}\left(\Gamma\frac{\partial U}{\partial r}\right)+\frac{1}{r}\frac{\partial}{\partial r}\left(\Gamma r\frac{\partial V}{\partial r}\right)-\frac{\partial P}{\partial r}-2\Gamma\frac{V}{r^2}+\frac{\rho W^2}{r}$	$\mu_{\rm eff}$
W	$-\frac{\rho VW}{r}-\frac{W}{r^2}\frac{\partial}{\partial r}(r\Gamma)$	$\mu_{\rm eff}$
k	$G_k-\rho\epsilon$	$\frac{\mu_{\rm eff}}{\sigma_k}$
ϵ	$\frac{\epsilon}{k}(C_1G_k-C_2\rho\epsilon)$	$\frac{\mu_{\rm eff}}{\sigma_\epsilon}$

$$G_k=\mu_{\rm eff}\left\{2\cdot\left[\left(\frac{\partial U}{\partial x}\right)^2+\left(\frac{\partial V}{\partial r}\right)^2+\left(\frac{V}{r}\right)^2\right]+\left(\frac{\partial W}{\partial x}\right)^2+\left[r\frac{\partial}{\partial r}\left(\frac{W}{r}\right)\right]^2+\left(\frac{\partial U}{\partial r}+\frac{\partial V}{\partial x}\right)^2\right\}$$

$$\mu_{\rm eff}=C_\mu\rho\frac{k^2}{\epsilon}$$

$C_\mu=0.09$	$C_1=1.44$	$C_2=1.92$	$\sigma_k=1.0$	$\sigma_\epsilon=1.3$

Nomenclature

c_d = drag coefficient
d_p = particle diameter
k = turbulent kinetic energy
L_E = eddy length scale
Re_p = particle Reynolds number
T_L = eddy time scale
u, v, w = instantaneous velocity components
u', v', w' = velocity fluctuations
U, V, W = mean velocity components
$\mathbf{U}$ = instantaneous velocity vector
x, r = coordinates
ϵ = turbulence dissipation
ν_f = kinematic viscosity
ρ_f = fluid density
ρ_p = particle material density
σ = r.m.s. value of the Gaussian velocity distribution
τ_p = particle relaxation time

Subscripts

f = fluid
p = particles

The choice of the solution procedure described above is based on the conclusions drawn by Durst and Wennerberg (1991), who performed a number of numerical tests on the prediction of swirling flows by using different integration schemes. The comparison of these numerical results with different measurements in swirling flows indicated that the k-ϵ turbulence model performs reasonably well for moderate swirl intensities.

The present calculations have been performed on a mesh of 80 by 78 grid points in the streamwise and radial directions, respectively. The computational domain in the streamwise direction was extended up to 1.0 m downstream from the inlet, and zero-gradient outflow conditions have been assumed.

The converged solution of the gas flow field was used for the simulations of the particle phase based on a Lagrangian formulation of the basic equations, and a stochastic model was used for simulating the interaction of the particles with the fluid turbulence (Durst et al., 1984; Milojevic, 1990). For the calculation of the particle phase mean properties, a large number of particles were traced through the flow field, typically around 100,000.

In order to take into account the effect of the wide size spectrum of the glass beads used in the experiments on the particle mean velocities, the velocity fluctuations, and the dispersion process, the numerical calculations were performed considering the particle size distribution shown in Fig. 2. The procedure for simulating the particle size distribution by a log-normal distribution function was described by Sommerfeld (1990).

The effect of the particle phase on the fluid flow was neglected in the present calculations since only very small particle loadings were considered. Furthermore, some simplifications in the equation of motion for the particles have been made, since a gas-solid two-phase flow with a density ratio of $\rho_p/\rho \sim 2000$ was considered. This implies that the added mass effect and the Basset history force have been neglected in the present calculations. Hence, the individual particle trajectories were obtained by solving the following instantaneous particle equations for each particle in the flow field:

$$\frac{d\mathbf{x}}{dt}=\mathbf{U}_p \tag{2}$$

$$\frac{d\mathbf{U}_p}{dt}=\frac{3\rho_f}{4\rho_p D_p}\,C_d(\mathbf{U}_f-\mathbf{U}_p)\,|\mathbf{U}_f-\mathbf{U}_p|+\mathbf{F} \tag{3}$$

where the drag coefficient for a spherical particle is obtained by the following correlation:

$$C_d=\frac{24.0}{\mathrm{Re}_p}\left[1.0+\frac{1}{6}\,\mathrm{Re}_p^{0.66}\right],\quad \mathrm{Re}_p<1000$$
$$C_d=0.44,\quad \mathrm{Re}_p\geq 1000 \tag{4}$$

with:

$$\mathrm{Re}_p=\frac{D_p\,|\mathbf{U}_f-\mathbf{U}_p|}{\nu_f} \tag{5}$$

The term $\mathbf{F}$ in Eq. (3) denotes external forces, i.e., gravity (g), corriolis ($v_p\,w_p/r_p$) and centrifugal forces (w_p^2/r_p). The above equations (Eqs. (2) to (5)) were solved by the Euler method, where the maximum allowable time step was set to be 10 percent of the following characteristic time scales:

- The Stokesian response time of the particle
- The time required for a particle to cross the mesh
- The local eddy life-time

The instantaneous fluid velocity components in the above equations are obtained from the local mean fluid velocities and the velocity fluctuations which are randomly sampled from a Gaussian distribution function characterized by and the fluid r.m.s. value, σ. The latter is evaluated from the turbulent kinetic energy by assuming isotropic turbulence.

$$\sigma=\sqrt{\frac{2}{3}\,k} \tag{6}$$

The instantaneous fluid velocities are assumed to influence the particle movement during a certain time period, the interaction time, before new instantaneous fluid velocities are sampled from the Gaussian distribution function. In the present model, the successively sampled fluid velocity fluctuations and the individual components are assumed to be uncorrelated.

The interaction time of a particle with the individual eddies is limited by two criteria, namely the turbulent eddy life-time and the time required for a particle to cross the eddy. In the present study, the eddy life time is taken into account by defining an eddy disappearance probability which is the ratio of time step size, Δt, to the Lagrangian time scale, T_L (Ormancey and Martinon, 1984). If a uniformly distributed random variable, RN, becomes smaller than the ratio, $\Delta t/T_L$, it is assumed that the turbulent structure around the particle vanishes, and a new turbulent eddy is assumed to become active. The Lagrangian time scale of the turbulence is estimated from the turbulent kinetic energy, k, and the dissipation rate, ϵ, in the following manner:

$$T_L=c_T\,\frac{k}{\epsilon} \tag{7}$$

The constant, c_T, was determined to be 0.3 by comparing numerical simulations of the particle dispersion in a grid turbulence with the experiments of Snyder and Lumley (1971).

The crossing trajectory effect was accounted for by integrating the distance traveled by the particle within one eddy and comparing it with the eddy length scale, L_E, obtained from:

$$L_E=T_L\cdot\sigma \tag{8}$$

The integration of the distance travelled by the particle within the eddy is performed by considering all three velocity components.

$$\Delta x_E=\int_0^t u_{\mathrm{rel}}\,dt \tag{9}$$

$$u_{\mathrm{rel}}=\sqrt{(u_f-u_p)^2+(v_f-v_p)^2+(w_f-w_p)^2} \tag{10}$$

When the distance traveled by the particle becomes larger than the eddy length scale, a new fluctuation velocity is assumed to act on the particle.

The boundary conditions for the particle tracking procedure are specified as follows. At the inlet, the particle velocities and the mass flux are specified according to the experimental conditions. A particle crossing the centerline is replaced by a particle entering at this location with opposite radial velocity. For the particle interaction with the solid wall, elastic reflection is assumed (i.e., $v_{p2}=-v_{p1}$).

Numerical Results for the Gas Phase

An overview of the ability of the present numerical method to predict the considered swirling flows is given by a comparison of stream functions calculated from the numerical simulations and the experiments (Fig. 3), where the latter were obtained by integrating the measured axial velocity profiles and applying an interpolation procedure. The locations of the two recirculation zones, the corner recirculation zone, and the central recirculation bubble may be identified by the dividing stream line. It is obvious that even for such a complex flow, the numerical calculations show good agreement with the experimental results for the locations of the recirculation zones.

The numerical results for the mean velocity distributions of the gas phase in comparison to the experimental data are presented in Fig. 4(a)–(c). Considering the development of the axial gas velocity, it is obvious that the spreading of the two

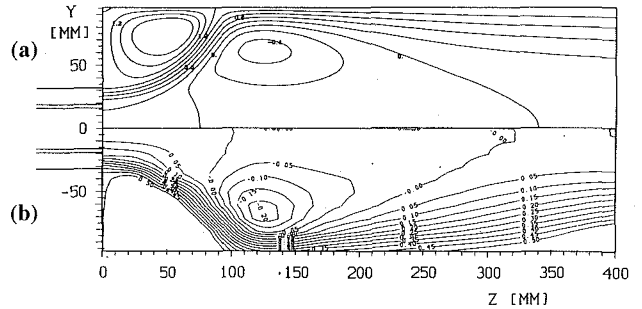

Fig. 3 **Gas phase stream function (*a*) numerical simulation; (*b*) experiment**

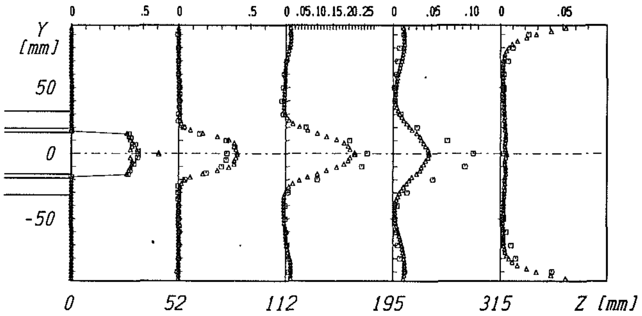

Fig. 5 **Radial profiles of particle mass flux (kg/m²/s), (□ experiment, △ calculation)**

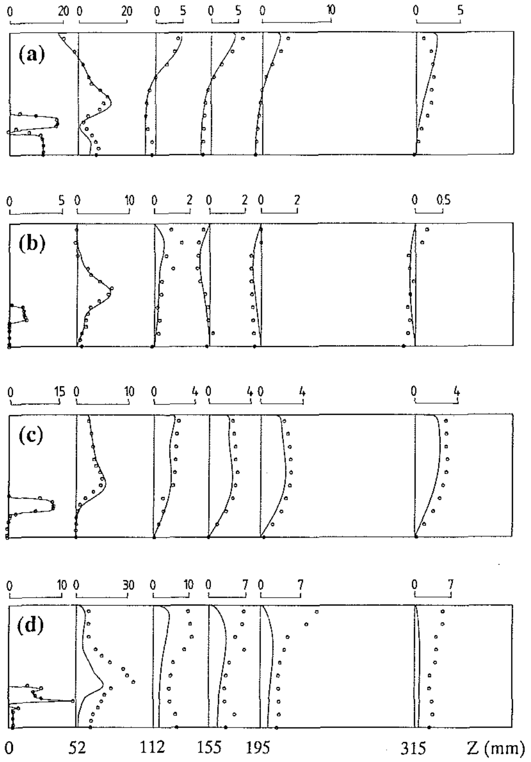

Fig. 4 **Comparison of numerical simulations with measurements for the gas flow, (o experiment, – prediction). (*a*) Axial velocity [m/s]; (*b*) radial velocity [m/s]; (*c*) tangential velocity [m/s]; (*d*) turbulent kinetic energy [m²/s²]**

jets at the upstream end of the recirculation bubble is slightly underpredicted. Further downstream, the agreement is fairly good. In Fig. 4(*b*), the large radial velocity in the outward direction at $z = 52$ mm indicates the strong spreading of the inlet jets which is a special feature of swirling flows. The agreement of the predicted radial and the tangential mean velocity profiles with the measurements is also very good (Fig. 4(*b*) and (*c*)).

The results for the turbulent kinetic energy are shown in Fig. 4(*d*). Contrary to the excellent agreement for the mean velocity distributions, a significant underprediction is observed throughout the flow field. Especially at the location $z = 52$ mm which corresponds to the initial development of the flow and is associated with strong mixing between the two inlet jets the turbulent kinetic energy is considerably underpredicted. This tendency was also observed in the calculations of other investigators (see: Sommerfeld and Wennerberg, 1991) and is mainly attributed to the deficiencies of the applied k-ϵ turbulence model which assumes isotropic turbulence. It is expected that this problem may be overcome by applying a Reynolds stress turbulence model which was recently completed by Hogg and Leschziner (1989).

Numerical Results for the Particle Phase

Integral information about the ability of numerical methods to predict the particle dispersion characteristics in a swirling flow may be achieved by considering the development of the particle mass flux distribution (Fig. 5). With increasing distance from the inlet, the particles are rapidly dispersed in the radial direction. From $z = 112$ mm, the particles begin to accumulate near the wall which is a result of the increasing tangential particle velocity (see Fig. 8(*a*)) and the associated centrifugal effects. The agreement between the numerical calculation and the experimental result is reasonably good. The underprediction of the particle mass flux within the core region of the central recirculation bubble (i.e., at $z = 112$ and 195 mm) indicates that in the numerical simulations, the particles are transported too rapidly out of the core region. This also results in a slightly higher particle mass flux in the outer, near wall region compared to the experiments. However, measurement errors also contribute to the difference between prediction and experiment where the integration of the measured particle mass flux gives differences in the mass flow rate at the various profiles of about ±10 percent.

Figures 6-8 show the comparison of measured and numerically predicted particle mean velocity distributions and the development of the associated velocity fluctuations. Please note that for the cross-section $z = 315$ mm, no experimental data are available for the core region, since the particle rate was too low here. The mean velocity distributions are generally well predicted, and only at $z = 52$ mm, a slight overprediction of the axial particle velocity component is observed in the region between the primary and the secondary jet. Furthermore, the radial particle mean velocity is underpredicted in the near wall region for the cross-section $z = 112$ mm. The predicted tangential mean velocity of the particle phase is in good agreement with the measurements. The scatter of the numerical results in the core region of the flow at the downstream locations $z = 195$ and 315 mm and within the recirculation region of the pipe expansion is due to the low number of particles sampled in these regions.

The particle velocity fluctuations are underpredicted, especially for the axial velocity component. The predicted fluctuations of the radial and tangential particle velocities are closer to the experimental values. This is also correlated with the underprediction of the turbulent kinetic energy of the gas phase, associated with the assumption of isotropic turbulence incorporated by the k-ϵ turbulence model.

Furthermore, the simulated development of the particle mean number diameter throughout the flow field is compared with the experiments (Fig. 9(*a*)) showing some differences in the

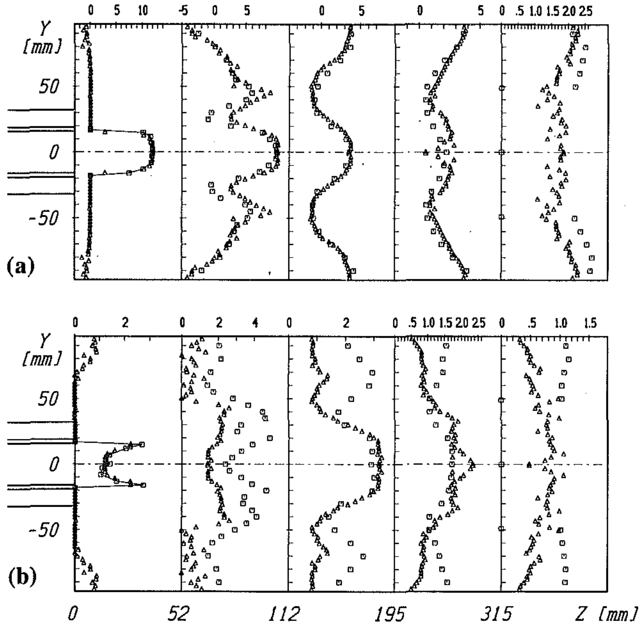

Fig. 6 Development of particle axial velocity (m/s), (□ experiment, △ calculation). (*a*) Mean velocity; (*b*) fluctuating component

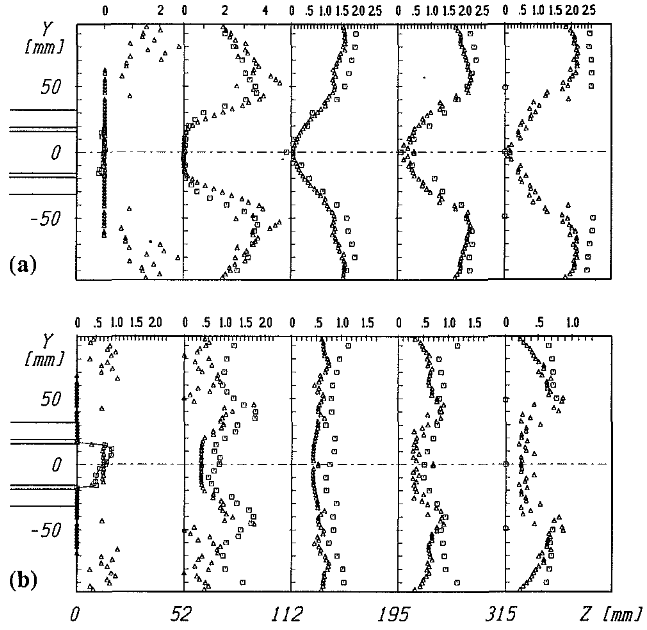

Fig. 8 Development of particle tangential velocity (m/s), (□ experiment, △ calculation). (*a*) Mean velocity; (*b*) fluctuating component

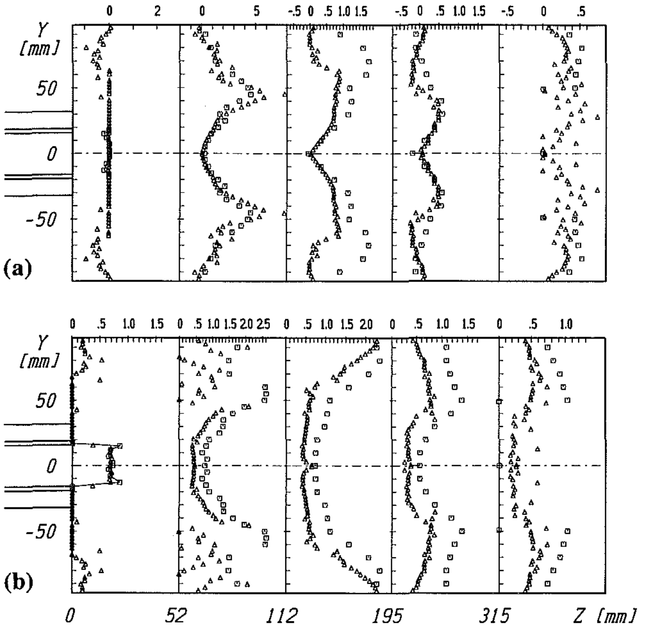

Fig. 7 Development of particle radial velocity (m/s), (□ experiment, △ calculation). (*a*) Mean velocity; (*b*) fluctuating component

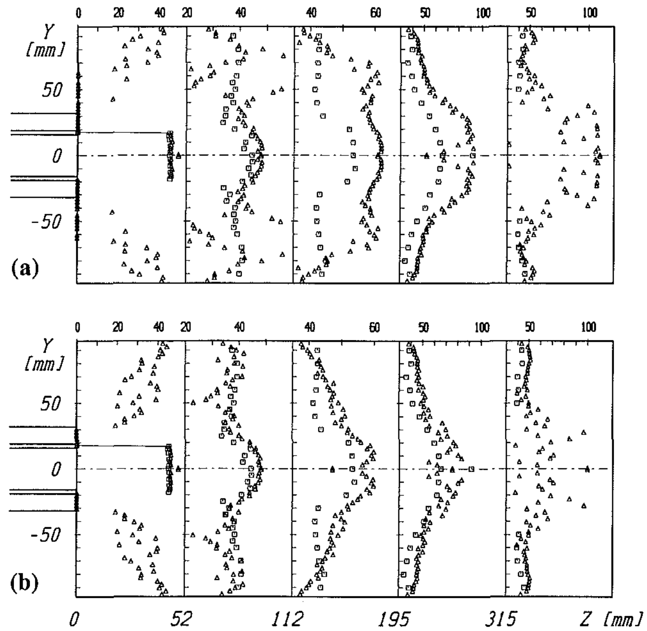

Fig. 9 Profiles of the particle mean number diameter (μm), (□ experiment, △ calculation). (*a*) Simulation with turbulent kinetic energy as given in Fig. 4(*d*); (*b*) doubled turbulent kinetic energy

core region of the central recirculation bubble where the predicted particle mean diameter is about 20 μm larger than the measured one. This may be the result of a too rapid radial transport of the small particles due to centrifugal effects or insufficient turbulent dispersion of the larger particles. Both may be caused by the underprediction of the gas phase turbulent kinetic energy as compared to the experiments and the assumption of isotropic turbulence. The calculations yield instantaneous fluid velocities that are too low which are then used for the calculation of the particle trajectories. Therefore, some of the larger particles are not radially dispersed in the present calculation but would be dispersed if a higher fluid velocity fluctuation is assumed. For the small particles a higher fluid fluctuation could result in an increasing number of particles being entrained in the central recirculation bubble which again would result in a decreasing particle mean diameter. In the near wall region, the agreement between experiment and simulation is good except for $z = 52$ mm where the calculated particle mean diameter shows some scatter due to the low number of particles sampled in this region.

The effect of the fluid fluctuation intensity is shown with a hypothetical numerical simulation by doubling the gas-phase turbulent kinetic energy which results in increased fluctuating components acting on the particles. The length and time scales of the turbulence are not modified in this case. For such a calculation, the agreement of the particle mean number di-

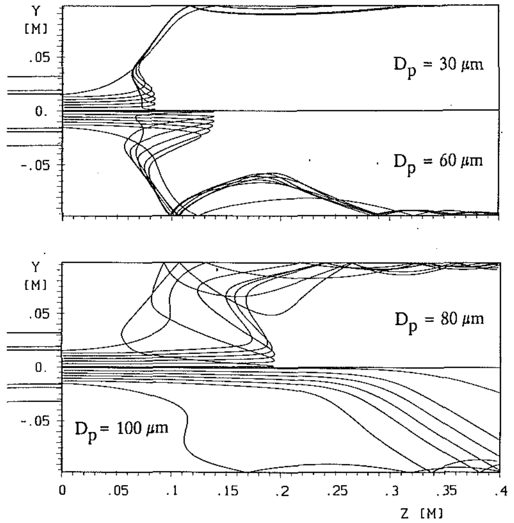

Fig. 10(*a*) Calculation without turbulent dispersion

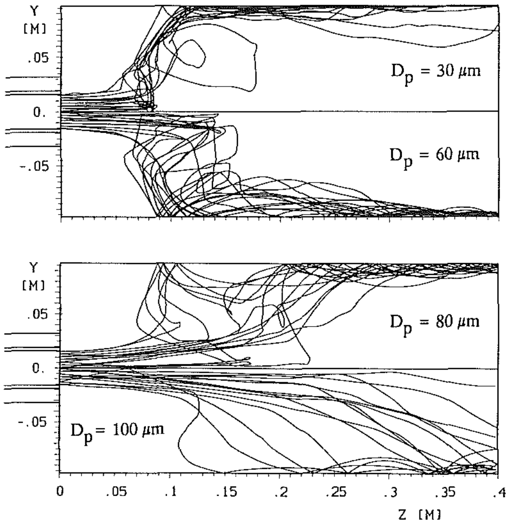

Fig. 10(*b*) Calculation with turbulent dispersion

Fig. 10 Examples of particle trajectories; (D_p = 30 μm, D_p = 60 μm, D_p = 80 μm and D_p = 100 μm

ameter profiles with the measurements is much better (Fig. 9(*b*)), which exhibits the need of more improved turbulence models for the gas phase in order to account for turbulence anisotropy. This fact would additionally require new models for particle-turbulence interaction which take into consideration the anisotropy of the fluid turbulence.

Furthermore, the deficiencies in predicting the dispersion of the larger particles may result in a different development of the particle size distribution throughout the flow field. This effect may additionally have yielded the underprediction of the particle velocity fluctuations. As pointed out by Sommerfeld (1990), the particle velocity fluctuations are increased when the particle size distribution becomes wider which results from the response of the different sized particles to mean flow and fluid turbulence.

Particle Dispersion Characteristics in a Swirling Flow

In order to provide a better understanding of the particle dispersion process in a swirling flow, some examples of particle trajectories for different particle size classes and for calculations with and without turbulence effects on the particle motion are given in Fig. 10. The calculations of the particle motion without turbulence demonstrate the particle response to the mean flow. It is clearly seen that particles with a diameter up to 80 μm are decelerated to zero velocity within the central recirculation bubble. Then, they begin to move toward the inlet while being radially transported outward due to radial transport and centrifugal forces. This is a result of the low axial particle velocity which they acquire after some distance moving through the recirculation bubble and, hence, yields more time for the particles to follow the radial and tangential mean fluid motion. After the particles which move toward the inlet leave the recirculation bubble, they are entrained into the air stream coming from the annular inlet. This phenomenon also causes the existence of an annular recirculation region for the particle phase (see Fig. 6). With increasing particle diameter, the distance from the inlet where the particles are decelerated to zero velocity increases due to their larger inertia. The largest particles (in the present case 100 μm) penetrate the recirculating bubble without stopping their downward motion. When the particles collide with the wall, they are bounced back whereby they may be captured again within the recirculation bubble. However, due to the centrifugal force, they move toward the wall again while moving downstream. This effect results in a spiral motion of the particles along the wall of the test section.

The particle trajectories for the turbulent case show the strong effect of turbulent dispersion on the particle motion (Fig. 10(*b*)). It becomes obvious that the particle recirculation within the central reverse flow region is only caused by flow turbulence and results in much longer residence times of the particles within the recirculation. Even the large particles (D_p = 100 μm) are affected by the turbulence and spread out much faster than in the non-turbulent case. This result demonstrates that the effect of turbulence on the particle motion is very important and considerably alters the particle phase properties (e.g., particle mass flux distributions).

The behavior of particles with different diameters in a swirling flow with a central recirculation bubble may be characterized by introducing two time scale ratios based on the particle response time. The first one is for the region from the primary jet exit to the stagnation point at the top of the recirculation bubble, located at about 73 mm downstream of the inlet in the numerical calculations. This time scale ratio is calculated from the time the particle needs to move from the inlet to the stagnation point, τ_s, and the particle response time, τ_p:

$$S_1 = \frac{\tau_p}{\tau_s} \tag{11}$$

where τ_s is obtained from the distance between jet exit and stagnation point, Δx_s = 73 mm and the particle velocity at the jet exit, U_{p0}.

$$\tau_s = \frac{\Delta x_s}{U_{p0}} \tag{12}$$

The Stokesian particle response time is defined by

$$\tau_p = \frac{d_p^2(1 + 2\rho_p/\rho_f)}{36\nu_f} \tag{13}$$

where d_p, ρ_p, ν_f, and ρ_f are the particle diameter, particle material density, fluid kinematic viscosity, and fluid density, respectively.

Within the central recirculation bubble, the particle response may be characterized by the time scale ratio, S_2, which is the ratio of the time, t_{p0}, which the particle needs to be decelerated to zero axial velocity and the time, t_{int}, within which the particle is assumed to be able to interact with the recirculation bubble.

$$S_2 = \frac{t_{p0}}{t_{\text{int}}} \tag{14}$$

Table 3 Dependence of S_1 and S_2 on particle diameter

d_p [μm]	τ_p [ms]	S_1 [−]	S_2 [−]
20	3.00	0.51	0.01
30	6.76	1.16	0.07
40	12.02	2.06	0.21
50	18.77	3.22	0.42
60	27.03	4.63	0.68
70	36.80	6.30	0.99
80	48.06	8.23	1.37
90	60.83	10.42	1.79
100	75.09	12.86	2.26
110	90.86	15.56	2.78
120	108.13	18.52	3.35

Here, t_{p0} is estimated in the following manner. If the particle had a velocity of U_{ps} at time $t = 0$ in a flow field of velocity U_f, the particle velocity U_p at time $t = \Delta t$ can be expressed as:

$$U_p = U_f - (U_f - U_{ps}) \exp\left(-\frac{\Delta t}{\tau_p}\right) \tag{15}$$

Therefore, the time needed to reach $U_p = 0$ is:

$$t_{p0} = \tau_p \ln\left(\frac{U_f - U_{ps}}{U_f}\right) \tag{16}$$

In the present case, $U_f = -2.15$ m/s is the maximum negative velocity in the recirculating bubble, and U_{ps} is the particle velocity at the stagnation point. The value for U_{ps} is obtained by solving Eq. (15) for the first flow field region up to the stagnation point:

$$U_{ps} = U_{p0} \exp\left(-\frac{1}{\tau_p} \frac{\Delta x_s}{U_{p0}}\right) \tag{17}$$

where, $U_{po} = 12.5$ m/s is the mean axial particle velocity at the primary jet exit and t_{int} is defined as:

$$t_{\text{int}} = \frac{L}{U_{p,av}} \tag{18}$$

$$U_{p,av} = \frac{\int_0^{t_{p0}} U_p dt}{t_{p0}} \tag{19}$$

In these equations, $L = 252$ mm is the length of the recirculation bubble on the axis of symmetry obtained from the numerical results.

The values of S_1 and S_2 for several particle sizes are given in Table 3. For particles smaller than 30 μm, the time scale ratio, S_1, is smaller than one which indicates that the particles are able to follow the deceleration of the fluid in this region. As a result (see Fig. 10), these particles begin to respond to the reverse flow within the recirculation bubble as soon as they enter it and move backward until they are entrained into the main stream emanating from the annulus.

Particles with $S_1 > 1$ still have considerably larger axial velocities at the stagnation point of the recirculating bubble and, as a result, move into the recirculation bubble. However, if $S_2 \leq 1$, these particles are decelerated to zero velocity within the recirculating bubble (e.g., $D_p \leq 80$ μm). This behavior is also confirmed by the simulated particle trajectories (Fig. 10). On the other hand, if S_2 is larger than 1, the residence time of the particles (e.g., $D_p = 100$ μm) in the recirculation bubble is too short and their inertia is too large to be decelerated to zero axial velocity. However, near the end of the recirculation zone, the larger particles are also centrifuged out of the core region due to the increasing tangential velocity. The above considerations show that with the knowledge of the dimensions of the central recirculation bubble and the characteristic flow velocities, it is possible to estimate the expected particle behavior.

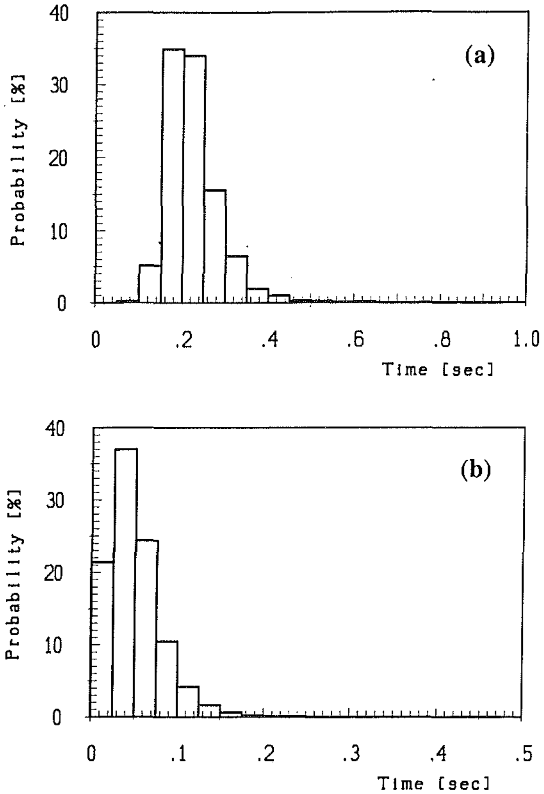

Fig. 11 Calculated particle residence time distribution. (*a*) Within the whole flow field; (*b*) within the recirculation bubble

For practical purposes (e.g., combustion systems), the particle residence time within the flow field is of great importance. Such particle residence time distributions may be easily obtained from the numerical simulations. Two characteristic residence times may be defined: the particle residence time in the whole flow field and within the recirculation bubble. The residence time distribution of particles within the whole flow field (up to $z = 400$ mm) is shown in Fig. 11(*a*) and has the highest probability around 0.2 s. The mean residence time is 0.23 s. The particle residence time within the reverse flow region is less than 0.1 s (Fig. 11(*b*)).

Furthermore, the correlation between particle size and residence time in the whole flow field (Fig. 12(*a*)) and the recirculation bubble (Fig. 12(*b*)) may be obtained from the numerical calculations. In these figures, the close line represents the mean residence time of the different sized particles, and the vertical bars show the standard deviation of the residence time distribution for each size class. As expected from the numerical simulations of the particle trajectories, the larger particles have the shortest residence time in the whole flow field, and small particles (around 20 μm) have the highest residence time (about 0.3 s) due to their better response to the flow turbulence.

An interesting effect is observed for the dependence of residence time in the central recirculation region on the particle diameter which indicates that particles with a diameter between 70 and 80 μm remain in the recirculation bubble for the longest time period. This phenomenon becomes clear when the calculated particle trajectories are considered (Fig. 10). The medium-sized particles have the largest residence time in the recirculation bubble, since they are decelerated to zero velocity in the center of the recirculation and then move back towards the inlet before they are entrained into the main stream coming

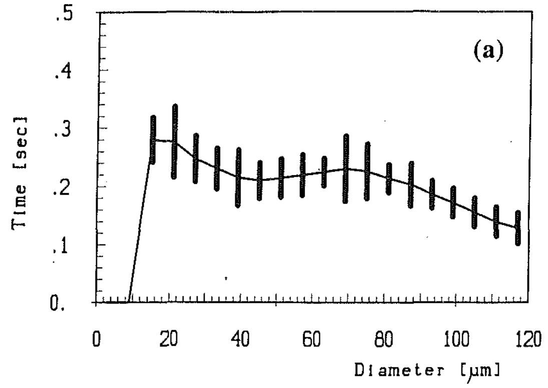

Fig. 12(*a*) Within the whole flow field

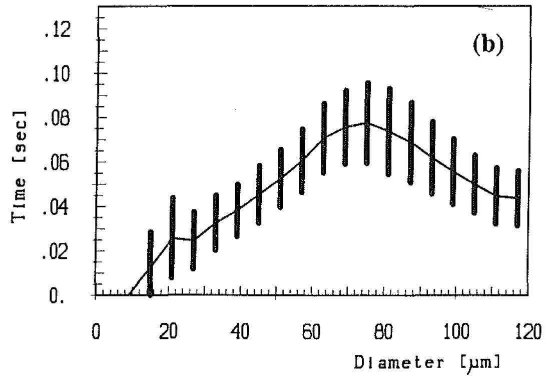

Fig. 12(*b*) Within the recirculation bubble

Fig. 12 Correlation between particle size and residence time

from the annular inlet. Larger particles pass almost straight through the recirculation zone, and small particles are entrained into the main stream quite early and move around the upper edge of the reverse flow region.

The particle velocity characteristics and the resulting separation effects in the swirling flow are also explained by the calculated particle size-velocity correlations for the axial particle velocity at some remarkable locations in the flow field (Fig. 13).

Immediately downstream the inlet (z/y = 52 mm/30 mm), only very few particles have negative axial velocities. Within the central recirculation bubble at z/y = 112 mm/40 mm, the probability of negative axial particle velocities has increased considerably for the particle size range between 40 and 90 μm. In the center of the recirculation bubble, no particles below 50 μm were sampled (z/y = 155 mm/0 mm and z/y = 195 mm/0 mm), and the number of particles with negative velocity decreased. The majority of larger particles (i.e., larger than 60 μm) have positive velocities, but there still exists a strong correlation between particle size and velocity.

Conclusions

A numerical study of a particle laden swirling flow was performed based on the Eulerian/Lagrangian approach by taking into account the particle size distribution. In general the calculated results show good agreement with the experiments for the mean gas and particle velocities. The velocity fluctuations of the gas and particle phase were, however, underpredicted. This is supposed to be mainly caused by the deficiencies of the k-ϵ-turbulence model which assumes isotropic turbulence. It is nevertheless surprising that even though the turbulent kinetic energy of the gas phase is underpredicted, the particle dispersion characteristics are predicted reasonably well by using a rather simple particle dispersion model.

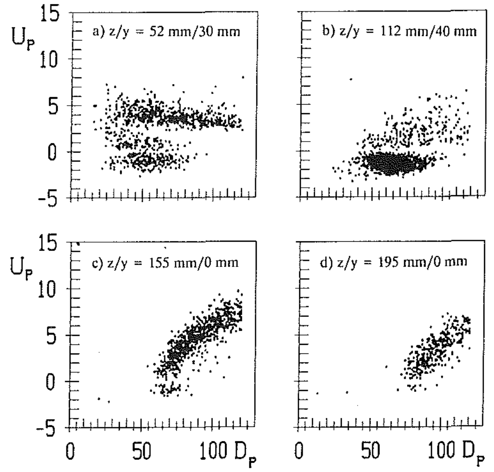

Fig. 13 Calculated particle size-velocity correlations. (*a*) z/y = 52 mm/30 mm; (*b*) z/y = 112 mm/40 mm; (*c*) z/y = 155 mm/0 mm; (*d*) z/y = 195 mm/0 mm

The response of particles with different sizes in the swirling flow, especially within the recirculation bubble, could be characterized by introducing two time scale ratios. These two time scales characterize the particle response to the mean flow in the initial region just downstream of the inlet and within the recirculation bubble and allow estimation of the expected particle behavior in a swirling flow with a central recirculation bubble. Numerically simulated particle trajectories for particles of different size demonstrated the particle response characteristics estimated by two time scale ratios.

Furthermore, the numerical predictions revealed the particle velocity characteristics by considering the particle size-velocity correlations and the correlations between particle size and residence time. The latter is an important parameter for the design of combustion systems.

Acknowledgment

The experimental and numerical studies were performed within the framework of the project "Heterogeneous Combustion in Swirling Flows: Particle Dispersion with Heat and Mass Transfer." The financial support for this project from the Stiftung Volkswagenwerk is gratefully acknowledged. Furthermore, the authors would like to thank H.-H. Qiu and D. Koubaridis who performed the measurements with great care.

References

Altgeld, H., Jones, W. P., and Wilhelmi, J., 1983, "Velocity Measurements in a Confined Swirl Driven Recirculating Flow," *Experiments in Fluids*, Vol. 1, pp. 73-78.

Blümcke, E., Eickhoff, H., and Hassa, C., 1988, "Dispersion of Monosized Droplets in a Turbulent Swirling Flow," *Proceedings of the 4th International Conference on Liquid Atomization and Spray Systems*, pp. 89-96.

Demirdzic, I., and Peric, M., 1990, "Finite Volume Method in Arbitrarily Shaped Domains with Moving Boundaries," *International Journal for Numerical Methods in Fluids*, Vol. 10, pp. 771-790.

Durst, F., Milojevic, D., and Schönung, B., 1984, "Eulerian and Lagrangian Predictions of Particle Two Phase Flows," *Applied Mathematical Modelling*, Vol. 8, pp. 101-115.

Durst, F., and Wennerberg, D., 1991, "Numerical Aspects on Calculation of Confined Swirling Flows with Internal Recirculation," *International Journal for Numerical Methods in Fluids*, Vol. 12, pp. 203-224.

Escudier, M. R., and Keller, J. J., 1985, "Recirculation in Swirl Flow: A Manifestation of Vortex Breakdown," *AIAA Journal*, Vol. 23, pp. 111-116.

Hardalupas, Y., Taylor, A. M. K. P., and Whitelaw, J. H., 1990, "Veclocity and Size Characteristics of Liquid-Fuelled Flames Stabilized by a Swirl Burner," *Proceedings of the Royal Society London*, Vol. A428, pp. 129-155.

Hogg, S., and Leschziner, M. A., 1989, "Computations of Highly Swirling Confined Flow with a Reynolds Stress Turbulence Model," *AIAA Journal*, Vol. 27, p. 57.

Lilley, D. G., 1977, "Swirl Flow in Combustion: A Review," *AIAA Journal*, Vol. 15, pp. 1063–1078.

Milojevic, D., 1990, "Lagrangian Stochastic-Deterministic (LSD) Prediction of Particle Dispersion in Turbulence," *Particle and Particle Systems Characterization*, Vol. 7, pp. 181–190.

Ormancey, A., and Martinon, J., 1984, "Prediction of Particle Dispersion in Turbulent Flow," *Physico Chemical Hydrodynamics*, Vol. 5, pp. 229–244.

Peric, M., Kessler, R., and Scheurer, G., 1988, "Comparison of Finite-Volume Numerical Methods with Staggered and Co-located Grids," *Computers and Fluids*, Vol. 6, pp. 389–403.

Qiu, H.-H., Sommerfeld, M., and Durst, F., 1990, "High Resolution Data Processing for Phase-Doppler Measurements in a Complex Two-Phase Flow," *Measurement Science and Technology*, Vol. 2, pp. 455–463.

Sommerfeld, M., and Krebs, W., 1990, "Particle Dispersion in a Swirling Confined Jet Flow," *Particle and Particle Systems Characterization*, Vol. 7, pp. 16–24.

Sommerfeld, M., 1990, "Particle Dispersion in Turbulent Flow: The Effect of Particle Size Distribution," *Particle and Particle Systems Characterization*, Vol. 7, pp. 209–220.

Sommerfeld, M., and Qiu, H.-H., 1991, "Detailed Measurements in a Swirling Particulate Two-Phase Flow by a Phase-Doppler Anemometer," *International Journal of Heat and Fluid Flow*, Vol. 12, pp. 20–28.

Sommerfeld, M., and Wennerberg, D., (eds.) 1991, *Proceedings of the Fifth Workshop on Two-phase Flow Predictions*, Erlangen, March 19–22, 1990, Bilateral Seminars of the International Bureau, Forschungszentrum Jülich.

F. Wen

N. Kamalu

J. N. Chung

C. T. Crowe

T. R. Troutt

Department of Mechanical
& Materials Engineering,
Washington State University,
Pullman, Wash. 99164

Particle Dispersion by Vortex Structures in Plane Mixing Layers

The dispersion of particles in a plane mixing layer between two air streams is investigated using experimental and numerical techniques. The results show that large-scale spanwise vortices strongly influence the particle dispersion process. Particles with aerodynamic response times on the order of the large scale vortex time scales are found to concentrate near the outer edges of the vortex structures. Time average velocity measurements also demonstrate that these particles tend to move away from the center of the mixing layer. Substantial changes in the lateral particle dispersion are producible by controlled forcing of the vortex structures. Comparisons between the experimental particle dispersion patterns and numerical simulations show striking similarities. A two-part model involving stretching and folding is suggested as a particle dispersion mechanism.

1 Introduction

Fundamental improvements in the understanding of free shear flow phenomena have created the possibility for beneficial applications. One area in which applications of this new knowledge could have considerable potential is in the dispersion of solid or liquid particles. Examples of important technological processes involving free shear flow particle dispersion include liquid droplet fueled gas combustors and particle feed jets for coal-fired power plants.

One of the primary recent findings concerning the behavior of free shear flows has been the observation that orderly vortex patterns control the dynamics of these flows. For the case of the plane mixing layer two dominant types of vortex structures are apparent. A large-scale spanwise structure, which is generally aligned in a direction normal to the velocity gradient plane, appears to coexist with a highly three-dimensional structure of somewhat smaller cross-sectional scale.

Studies describing and quantifying the quasi two-dimensional nature of the large-scale spanwise structures can be found in Brown and Roshko (1974), Winant and Browand (1974), and Browand and Troutt (1980, 1985) and more generally in the review by Ho and Huerre (1984). Investigations concerning the more complex geometry of the three-dimensional vortex patterns are presented in Breidenthal (1981) and Bernal (1981). Recent experimental investigations by Lasheras et al. (1986) and Lasheras and Choi (1988) visualize and characterize in detail the development of the smaller scale three-dimensional structures and the complex interactions between the smaller structures and the large spanwise vortices.

The existence of organized vortex structures in free shear flows has important implications concerning the possibilities for prediction and control of these flows. Current capabilities in the experimental control of free shear flows can be found in the review by Ho and Huerre (1984). The capabilities of time dependent numerical techniques for simulating turbulent shear flows are discussed in reviews by Leonard (1985) and Hussaini and Zang (1987).

To predict the effect of organized vortex structures on the particle dispersion process Crowe et al. (1985) proposed the use of a time scale ratio (Stokes number) $\gamma_\tau = \tau_A/\tau_F$, where τ_A is the particle aerodynamic response time and τ_F is a time scale associated with the large-scale organized vortex structures. The particle aerodynamic response time is conventionally defined here as $\tau_A = \rho_p d_p^2/18\mu$ where ρ_p is the particle density, d_p is the particle diameter and μ is the dynamic viscosity of the fluid. This definition is derived from the Stokes flow result for solid spheres so it is implicitly assumed that the local particle Reynolds number is less than one. For small values of γ_τ the particles should closely follow the turbulent dispersion of the fluid and the particle/fluid dispersion ratio should be approximately unity. Conversely for large values of γ_τ the particles should be little affected by the fluid motion and the particle/fluid dispersion ratio should approach zero.

For intermediate values of this time scale ratio, however, particles might be dispersed significantly faster than the fluid as a consequence of a centrifugal effect created by the organized nature of the large scale vortex structures. The particle/fluid dispersion ratio could then potentially exceed unity. A schematic representation illustrating this concept is presented in Fig. 1.

Recent efforts at employing time dependent discrete vortex simulation models to predict the dispersion of solid particles in free shear flows have been made by Chein and Chung (1988) for a plane mixing layer and by Chung and Troutt (1988) for an axisymmetric jet. The results from these simulations strongly supported the physical concept developed and discussed by Crowe et al. (1985). Although no direct time dependent experimental results were available for comparison to these models, averaged results from the simulations were in good agreement with previous experimental data. An overall review concerning particle dispersion in free shear flows has recently been compiled by Crowe et al. (1988).

Contributed by the Fluids Engineering Division for publication in the JOURNAL OF FLUIDS ENGINEERING. Manuscript received by the Fluids Engineering Division June 24, 1991. Associate Technical Editor: Cheh-Ming Ho.

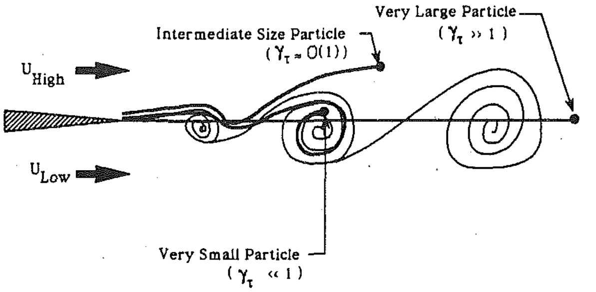

Fig. 1 Hypothesized model for particle dispersion in a plane mixing layer

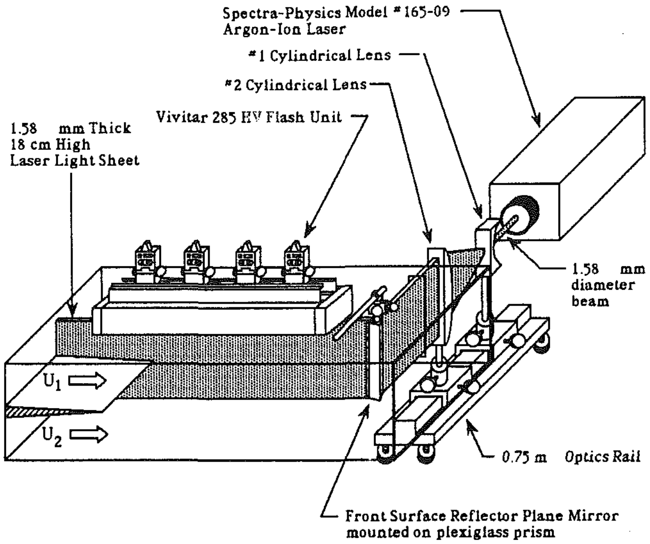

Fig. 2 Schematic of experimental facility

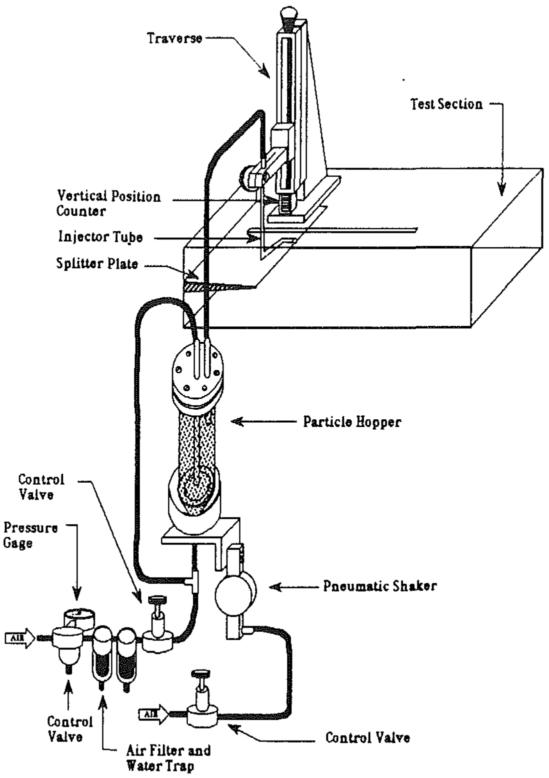

Fig. 3 Schematic of particle injection system

The primary purpose of the present work is to experimentally and numerically examine the role of organized spanwise vortex structures in the particle dispersion process and to determine if modifications in the particle dispersion are possible by forcing the vortex structures in the flow. The experimental results presented here concentrate primarily on particles with small to intermediate time scale ratios since gravitational effects become important as particle size increases. The numerical results, however, are not limited and therefore cover the entire size range of γ_τ's from much less than 1 to much greater than 1.

2 Experimental Apparatus and Techniques

An open return wind tunnel with a test facility of cross section 46 cm × 61 cm and of length 198 cm is used for the experiments. A schematic of the tunnel test section is shown in Fig. 2. The tunnel is fitted with a splitter plate enabling independent control of the free-stream velocities on either side of the plate. The freestream velocities are altered through the insertion of flow resistance screens upstream of the flow management section. Freestream velocities from 0.5 to 25 m/s with high quality flow conditions can be generated by this facility. Typical turbulence intensity levels are approximately 0.1 percent with mean flow uniformity within ±1 percent. By controlling the freestream velocities on either side of the splitter plate, a range of the velocity ratio parameter, $\lambda = U_H - U_L/U_H + O_L$ where U_H is the high speed velocity and U_L is the low speed velocity can be produced. Both plane wakes, $\lambda = 0$, and mixing layers, $\lambda > 0$ can thus be investigated with this facility.

For the conditions of the experiments presented here the boundary layers on both sides of the splitter plate were in a laminar state. The initial momentum thickness of the resulting mixing layer was on the order of 1 mm. The initial naturally occurring instability waves were found to be in the neighborhood of 100 Hz.

Modification of the initial instability waves and the subsequent vortex interaction region was accomplished using a high power loud speaker. A commercial 25 cm diameter woofer was used to generate the acoustic pressure waves. The woofer was connected to the wind tunnel by a length of flexible tubing. The flexible tubing was ported to the test section through a 10 cm diameter hole located in the test section roof above the splitter plate trailing edge. The effective low frequency range of the loud speaker was approximately 30 Hz which enabled forcing at the fundamental frequency and its first subharmonic. Sound levels at the plate trailing edge under typical forced conditions were approximately 90-92 dB. Since the acoustic forcing wavelengths in this frequency range are long compared to the facility dimensions the forcing perturbation can be assumed to be approximately two-dimensional at the plate trailing edge. The acoustic forcing used in the experimental study has a length scale of meters, neither particles (of a length scale of microns) nor large-scale vortices (of a length scale of centimeters) are directly affected by the sound. The weak large-scale sound field does generate small perturbations in the vorticity field. This perturbation, however, has profound impact on the initial Helmholtz instability of a mixing layer and on the resulting large scale structures Crighton (1981) discussed the details of vorticity generated by the sound. The acoustic forcing has been used widely in mixing layer experiments to control large scale structures via the control of the instability (Ho and Huerre, 1984).

Solid glass bead particles of density 2.4g/cm^3 can be introduced into the shear flow using a particle injection device. This device uses a combination pneumatic shaker with air transport concept to achieve adjustable particle flow rates. Spherical particles over a range of diameters can be injected in a controlled fashion using this device. The experiments presented here cover particles from 10 to 40 μm in diameter. The particle size range for an individual experiment was typically ±20

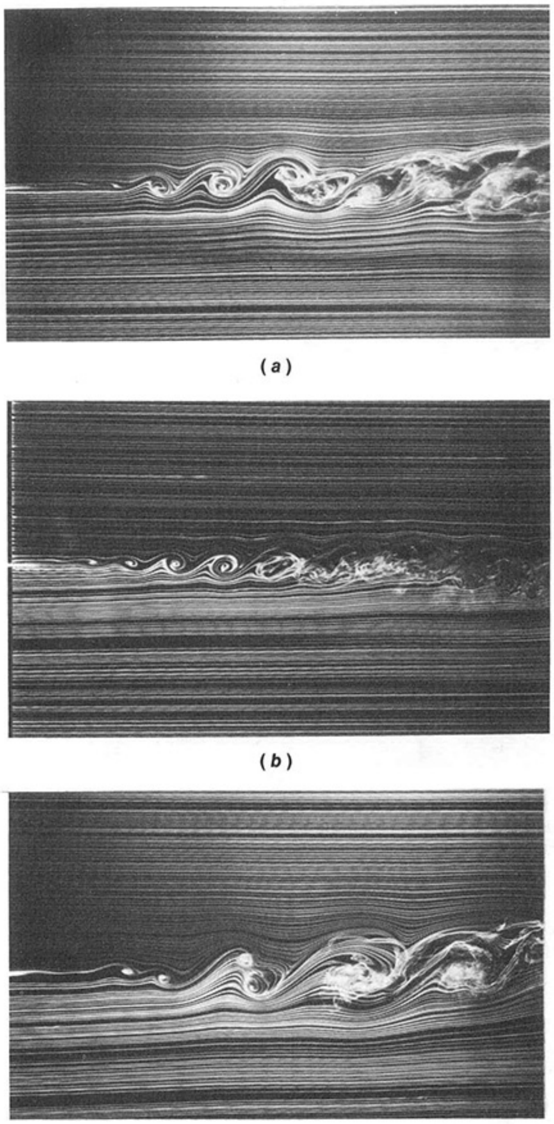

Fig. 4 Visualization of mixing layer flow with smoke wire technique: (*a*) nonforced condition, (*b*) forced near dominate instability frequency, and (*c*) forced at first subharmonic of natural instability

percent around the nominal diameter. These particle sizes give γ_T's between O(.01)–O(10) for the typical flow conditions of these experiments. A schematic of the particle injection system is shown in Fig. 3.

The injector tube is bent in two planes to minimize its downstream effect in the plane of measurement and observation. The injector tube has an outer diameter of approximately 2.3 mm and an inner diameter of approximately 1.6 mm. Smaller diameter injector tubes were tried but steady injection rates were difficult to achieve because of particle clogging tendencies. Efforts were also made to approximate the particle injection velocity with the local freestream flow velocity, however, due to limitations in our present injection system it was only possible to match these velocities within ±20 percent over an extended period of time. The particle injection rate was maintained in the range of 0.01 g/s, which gives relatively low loading ratios over most of the flow region under study.

Mean velocity profiles for the solid particles and the air flow were obtained using a Dantec two-component Laser Doppler Anemometer System with a 5 watt Argon-Ion laser operating in the back scatter mode. Frequency shifting for enhancing the measurement of flow velocities was also employed using acousto-optical Bragg cells. Signal processing was done with two Disa 55 L90A counters. The flow velocity measurements were obtained using an oil smoke generator to seed the air. The generated smoke particles were estimated to be in the 1 μm diameter range. Each mean flow or particle velocity measurement was obtained by averaging over 3000 individual realizations. The particle concentration profiles were obtained using interdata validation rates from the Laser Doppler Anemometer System following the techniques of Fleckhaus et al. (1987). The typical system uncertainty level in the LDA measurements was at ±2 percent for the mean velocities and ±5 percent for the turbulence intensities. The particle concentration was measured by the reciprocal of the LDA sample interdata time. The uncertainty for interdata time was ±0.0001 s. The resulting uncertainty for the relative concentration C/C_{ref} was smaller than ±0.1 everywhere in the flow. However, exceptions were found for a few measurement points near the particle injector where the uncertainties increased to ±0.2 as a result of the higher local particle concentration levels because the uncertainty increases with the particle concentration.

The visualization results reported involve four distinct situations. Two types of visualizations are used to depict the fluid motion in the mixing layer. One type employs a smoke wire technique as described by Corke et al. (1977). The smoke particles produced using this technique can be expected to be in the submicron diameter range and thus closely follow the air motion. Estimated γ_T's for these particles are on the order of 10^{-3}. For the experiments presented here the smoke wire was aligned in the x-y plane and positioned approximately 2mm downstream of the plate trailing edge. Illumination for the smoke wire photographs was supplied using a bank of 4 Vivitar 285 HV flash units.

The other type of flow visualization technique involves the injection of atomized vapor droplets into the boundary layer upstream of the plate trailing edge. The droplets are created using a water and fluorescence dye mixture which is atomized by a commercial ultrasonic vibrational humidifier. The droplet diameters are in the range of a few microns and can be expected to also closely follow the fluid motion. The injected droplets are illuminated using a light sheet produced by a 5 watt Argon-Ion laser aligned in the x-y plane. The dye in the vapor droplets fluoresces when excited by the Argon-Ion laser light and gives off enough illumination to allow reasonably short exposure times.

The two techniques for visualizing the glass bead particle dispersion employed illumination from the diffuse flash units and illumination from the Argon-Ion laser light sheet. The glass beads were injected into the flow using a 1mm diameter tube at a position approximately 1 cm above the plate trailing edge at the outer edge of the splitter plate boundary layer.

A Nikon F-3 35 mm camera and a Graphflex 6 × 4 large format camera were used for acquiring the flow visualization and particle photographs. Film sensitivities up to ASA 12000 were required for obtaining some of the images. Film exposure times ranged from 1/250 second for some of the laser sheet illumination photographs to 1/10,000 second for the diffuse flash illumination photographs. Image analysis of the visualization results were carried out using an Imaging Technologies SDP 151 Processing system.

3 Results

3.1 Experimental Results. Visualizations of the plane mixing layer using the smoke wire technique under natural and forced conditions are shown in Fig. 4. The freestream flow velocities are 5 m/s above the plate and 2 m/s below the plate. The velocity ratio λ is 0.43 for this flow. The visualizations cover approximately the first 35 cm of the flow development. The Reynolds number of the mixing layer based on vorticity

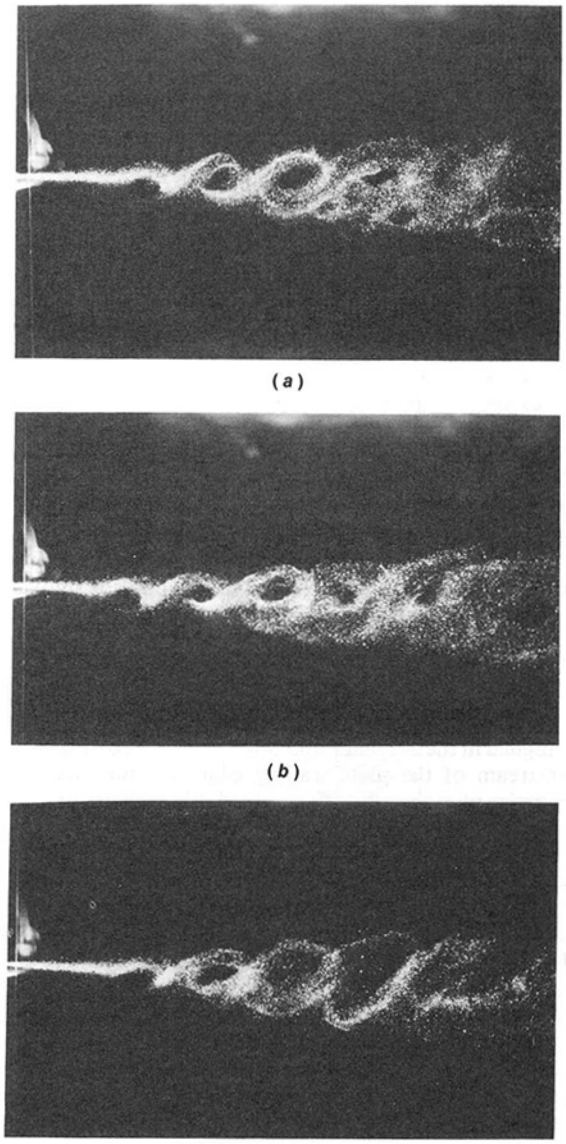
(a)

(b)

(c)

Fig. 5 Dispersion patterns of 40 μm diameter particles: (*a*) nonforced condition, (*b*) forced near dominate instability frequency, and (*c*) forced at first subharmonic of natural instability

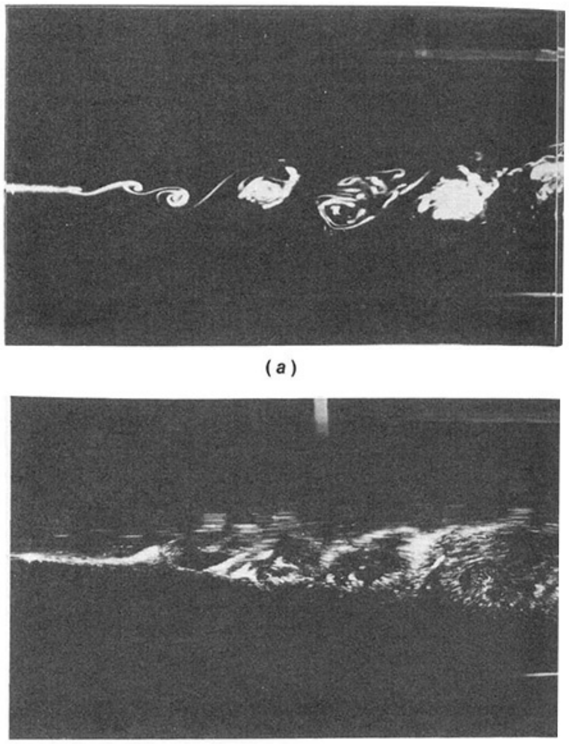
(a)

(b)

Fig. 6 Photographs of nonforced flow visualization and particle dispersion pattern using laser sheet illumination: (*a*) flow visualization and (*b*) 40 μm particle dispersion pattern

thickness and the free stream velocity difference ranges from approximately 1000 to 4500 over the span of the photograph.

Figure 4(*a*) shows the downstream development of the mixing layer under nonforced conditions. The photograph shows a wave like instability near the plate trailing edge which develops into organized vortex structures. These vortex structures are then observed to engage in intermittent pairing interactions as they convect downstream. As these pairing interactions occur three-dimensional complexities become apparent in the smoke dispersion patterns. The underlying large spanwise vortex structures, however, have been shown by multisensor hotwire experiments to retain their quasi two-dimensionality as they develop downstream (Browand and Troutt, 1980, 1985).

Figure 4(*b*) shows the mixing layer with acoustic forcing near the natural initial instability frequency of 120 Hz. A nondimensionalization of this forcing frequency using the average of the freestream velocities and the local mixing layer vorticity thickness gives a value of 0.17. This value is in good agreement with previous experimental observations by Browand and Troutt (1985) of the dominant instability wave in a mixing layer at approximately this λ and with theoretical predictions of Monkewitz and Huerre (1982) for the maximally amplified instability frequency for this flow. For this forced situation the initial vortex structures occur earlier in the flow development but downstream pairing interactions appear suppressed.

Figure 4(*c*) demonstrates the significant change in growth and scale of the mixing layer under subharmonic forcing at 60 Hz. This type of forcing enhances the initial pairing interactions but then suppresses later interactions due to the regularity of the paired structures. Effects on the mixing layer development observed in these visualizations are similar to those discussed in detail by Ho and Huerre (1984).

In the proceding visualizations the smoke particles were small enough, $\gamma_\tau \approx 0.001$, such that it could be reasonably expected that they would closely follow the motion of the fluid. The question of interest here is what happens to the dispersion patterns if significantly larger particles are introduced into the mixing layer flow.

Instantaneous dispersion patterns for the 40 μm diameter solid particles with $\gamma_\tau \sim O(1)$ are shown in Fig. 5. The local γ_τ value actually changes since the mixing layer grows in the downstream direction. If the mixing layer vorticity thickness is used for the local length scale and the free stream velocity difference for the velocity scale the calculated γ_τ varies from approximately 4 to 1 over the range of the photograph.

The nonforced 40 μm solid particle dispersion situation is shown in Fig. 5(*a*). The obvious organized dispersion patterns near the center of the figure demonstrate the importance of the large scale flow structures in the particle dispersion process. Farther downstream the particle patterns appear more disorderly due probably to the intermittent nature of the vortex pairing interactions in this region. The particle patterns near the center of the photograph also indicate strongly enhanced particle concentration levels near the outer edges of the vortex structures. The interior regions of the structures in this area of the photograph appear almost devoid of particles indicating

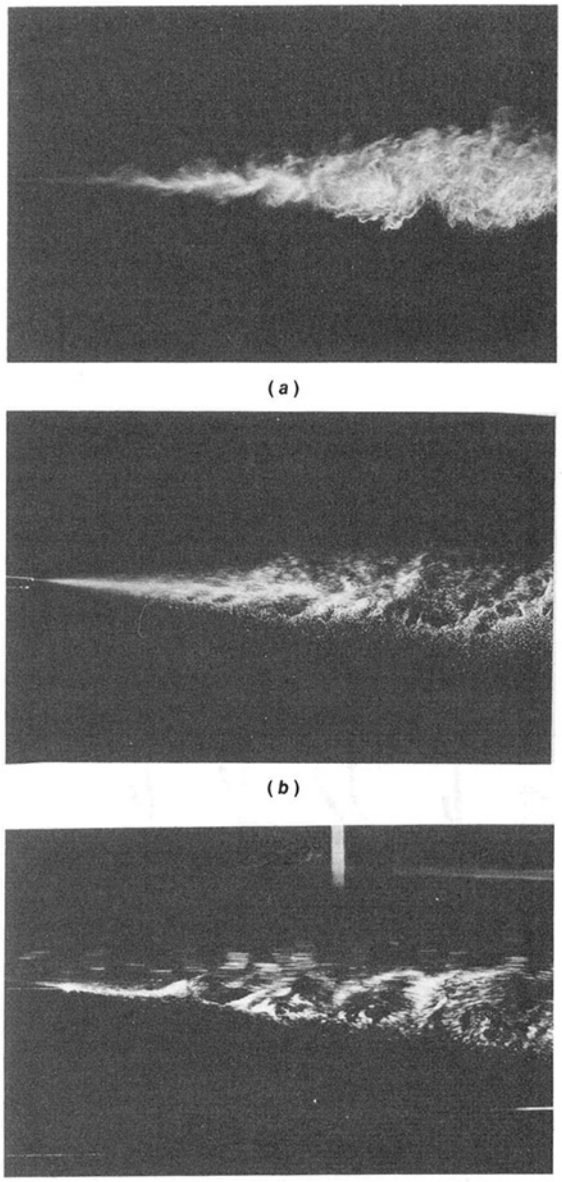

Fig. 7 Dispersion patterns of different diameter particles: (*a*) 10 μm diameter particles, (*b*) 30 μm diameter particles, and (*c*) 40 μm diameter particles

the vortex structures work apparently like mobile centrifuges displacing the particles radially from their centers as they convect downstream.

Figure 5(*b*) displays particle dispersion patterns with the mixing layer forced at the initial instability frequency. In this figure the particle dispersion patterns appear similar in size to the nonforced patterns but somewhat more regularity is apparent in the downstream region of the photograph. This enhanced regularity is probably created by the inhibition of the pairing process which is a result of forcing near the vortex passage frequency. The ability of the vortex structures to disperse the particles radially from the vortex centers is even more apparent in this figure.

Figure 5(*c*) shows the effect on the particle dispersion pattern of forcing at the subharmonic of the fundamental frequency. A large increase in the lateral spread of the particle dispersion pattern is apparent. In a subharmonically forced mixing layer, vortices undergo the first pairing interaction earlier and quickly "lock" on the forcing frequency. Flow is dominated by the well-organized vortex structures with this forced frequency and the new flow time scale for some distance downstream. It was demonstrated that the pairing interaction would result in an increase in the particle dispersion (Chein and Chung, 1987). Because the first pairing interaction is hastened, particle dispersion is increased near the splitter plate as shown in Fig. 5(*c*). Hence, particle dispersion in a forced mixing layer is fundamentally different from that in an unforced one. For practical applications in a spray combustion system, it means that the droplets would get to the hot region faster leading to enhanced vaporization and mixing.

An alternative visualization of the flow using fluorescent vapor droplets illuminated by laser light sheet is shown in Fig. 6. This image was obtained at somewhat lower free-stream velocities, $U_H = 2.0$ m/s and $U_L = 0.5$ m/s, than the previous experiments to alleviate film exposure requirements. The injection of the vapor in a localized region in the boundary layer is similar to the particle injection technique and thus gives a more direct qualitative comparison between the particle and flow dispersion patterns. Photograph 6(*a*) demonstrates that the droplets, with their much smaller time scale ratios, are indeed able to closely follow the fluid patterns and thus tend to fill in the central regions of the large scale vortices.

Figure 6(*b*) shows a photograph of the 40 μm solid particle dispersion patterns also illuminated by laser light sheet. Because of the lower light illumination intensity levels the film exposure time is increased for this photograph so that the particle images appear as traces. The particle traces blur the image somewhat, however, the organized patterns observed in the diffuse flash photographs are still obvious.

Comparisons between the dispersion patterns of the smoke particles, the droplets and the solid glass particles indicate that the patterns are strongly dependent on the time scale ratios of the particles and are not strongly influenced by the injection techniques.

To more directly demonstrate the dependence of the results on particle size Fig. 7 shows laser sheet instantaneous particle dispersion patterns for three different diameter glass bead particles. Figure 7(*a*) shows 10 μm diameter particles injected under the same conditions as the 40 μm diameter particle results discussed previously. The time scale ratios associated with the dispersion of these particles should be different by a factor of 16 from the 40 μm results. Thus γ_τ would vary from approximately 0.25 to 0.06 over the range of the picture. Obviously the dispersion pattern has changed substantially from the 40 μm case shown for comparison in 7(*c*). The particles are now observed to be distributed almost uniformly throughout the vortex structures in a similar fashion to the smoke and vapor droplet results discussed previously. Figure 7(*b*) shows an instantaneous dispersion pattern for 30 μm diameter particles injected under the same conditions as the previous results. The 30 μm particle results appear closely analogous to the 40 μm results with large particle free holes showing up in the vortex structure centers. These results are also clearly quite different from the 10 μm case shown in Fig. 7(*a*).

The qualitative independence of the particle dispersion process to slight changes in the cross-section (*y*-direction and also the vertical direction in our horizontal wind tunnel) location of the particle injector is shown in Figs. 8(*a*) and (*b*). Figure 8(*a*) shows an instantaneous result for the 40 μm particles with the injector in the position used for the previous results (which is slightly above the plate boundary layer), approximately 1 cm above the plate surface. Figure 8(*b*) shows a dispersion pattern for the 40 μm particles with the injector tube resting on the plate trailing edge. The similarities in the dispersion patterns demonstrate that the results are not strongly dependent on the precise injector position under the stipulation that the particles do get entrained into the mixing layer in a region where γ_τ is of O(1).

The effect of the vortex structures on the particle dispersion can also be seen in quantitative time average velocity meas-

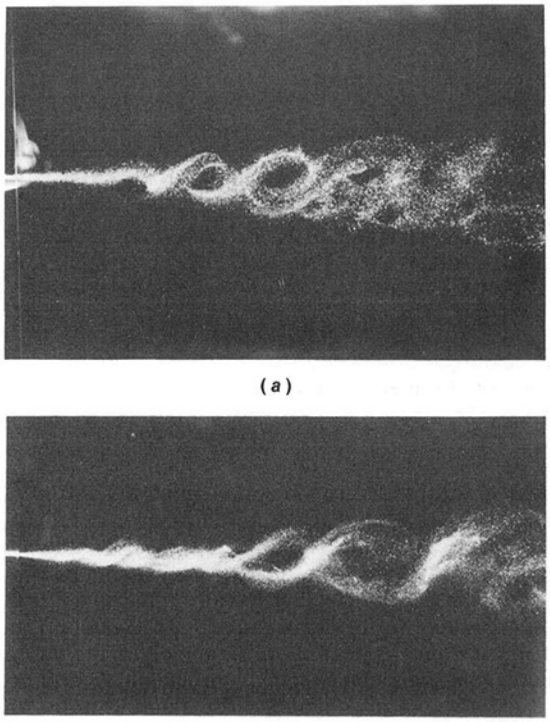

Fig. 8 Dispersion patterns of 40 μm diameter particles with injector at different cross-stream (y-direction) locations: (a) injector located 1 cm above plate and (b) injector located on top surface of plate

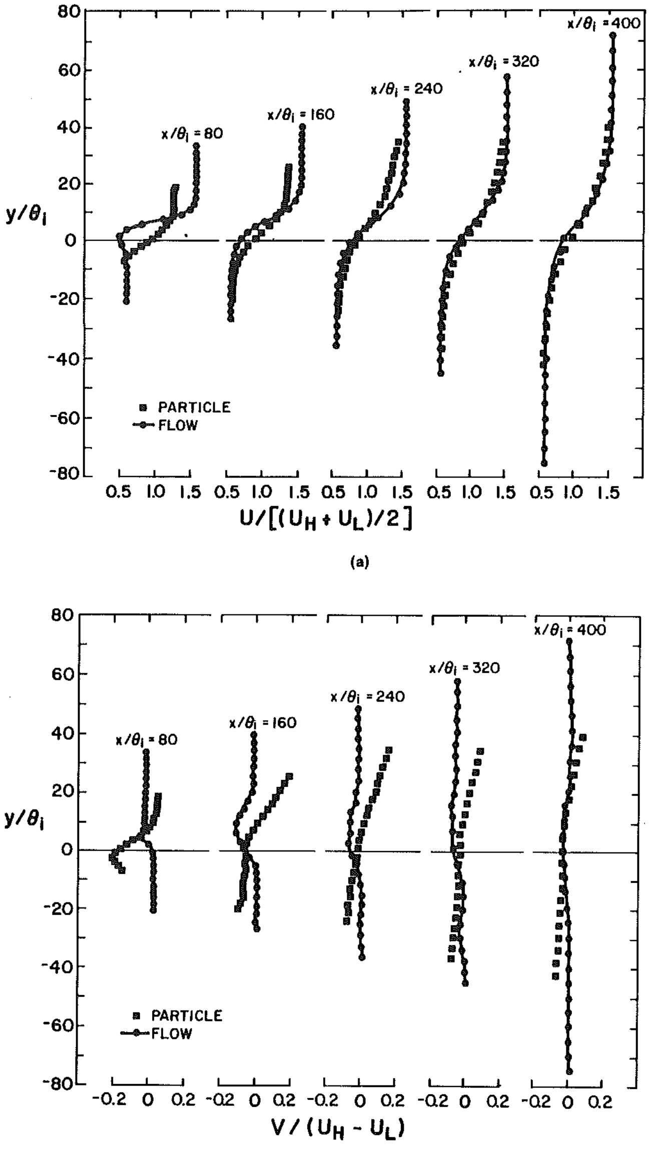

Fig. 9 Time average velocity profiles for flow and particles: (a) downstream velocity component and (b) cross-stream (y-direction) velocity component. (Uncertainty in velocity = ±2 percent, in y/θ_i = ±1 at 20:1 odds)

urements. Experimental velocity profiles for the flow and the 40 micron particles acquired using laser doppler velocimetry techniques are compared in Figs. 9(a) and (b). The results for the downstream velocity component, presented in Fig. 9(a) show that particle velocity profiles gradually approach the fluid velocities until no major qualitative or quantitative differences exist between the velocity profiles for the particles and fluid.

A significantly different situation however is observed for the time average cross-stream component (y-direction) of the flow and particle velocities shown in Fig. 9(b). These experimental measurements reveal an interesting quantitative difference between the flow and particle cross-stream (y-direction) velocity profiles. The cross-stream (y-direction) velocities of the fluid tend to be negative (downward) on the high speed side of the flow and positive (upward) on the low speed side indicating, as expected, a net entrainment of fluid particles into the mixing layer. The cross-stream (y-direction) 40 μm particle velocities, however, display exactly the opposite trend, indicating that the solid particles are being predominantely flung outward from the center of the mixing layer. This time average result strongly supports our physical model and our interpretations of the visualization results. A similar experimental result has also been observed by Kobayashi et al. (1987) for a vertically oriented mixing layer flow with particles seeded throughout one air stream.

Profiles of time averaged experimental particle concentration levels at several downstream positions are presented in Fig. 10 for nonforced and subharmonically forced conditions. These quantitative concentration levels were measured using laser doppler velocimetry interdata validation rates as discussed by Fleckhaus et al. (1987). At each downstream position the local particle concentration estimate is scaled by the concentration at the level of the splitter plate. Since the measurements can not cover the entire region in which particle dispersion occurs, the total number of particles at that downstream position is not available. However, the concentration profiles in Fig. 10 will differ from the probability density functions at corresponding positions only by a scaling factor so the important features of the concentration distribution are preserved. The profiles demonstrate that significant changes in the time average particle distribution patterns can be produced by subharmonic forcing of the mixing layer flow. The particles in these distributions were released 1 cm or approximately one boundary layer velocity thickness, δ_i, above the plate trailing edge. The position of maximum concentration moves below the plate trailing edge vertical position ($y = 0$) at $x = 24\ \delta_i$ for the forced case, whereas the nonforced concentration level peak does not cross the $y = 0$ position until approximately twice this downstream distance. The enhancement of the dispersion and transport of particles produced by the forcing does not persist in the profiles downstream of this location since vortex pairing interactions are inhibited in this downstream region due to the regularity of structures resulting from the initial pairing interaction.

Two important questions arising from the experimental results concern the dependence of the results on the particular experimental situation and the possibility for developing pre-

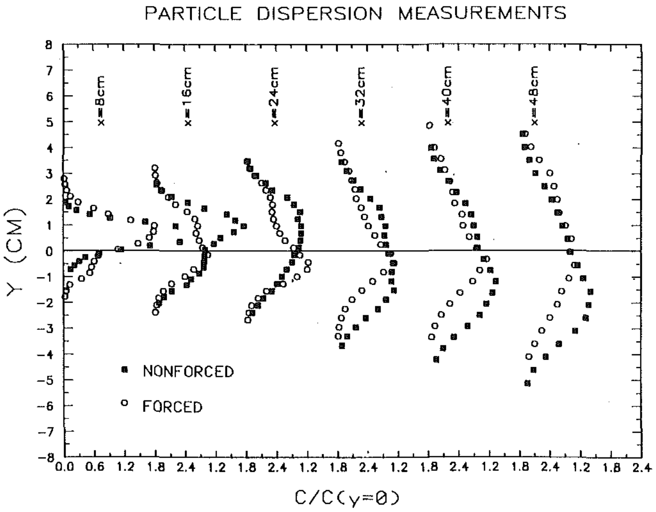

Fig. 10 Profiles of time average particle concentration for nonforced and subharmonic forced conditions. (Uncertainty in *c*/*c*(*y* = 0) is ±0.1, in *y* = 0.1 cm at 20:1 odds)

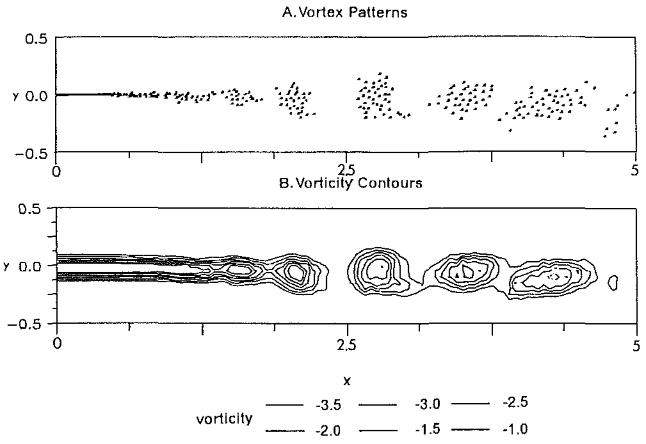

Fig. 11 Instantaneous discrete vortex patterns and contours: (*a*) vortex patterns, (*b*) vorticity contours

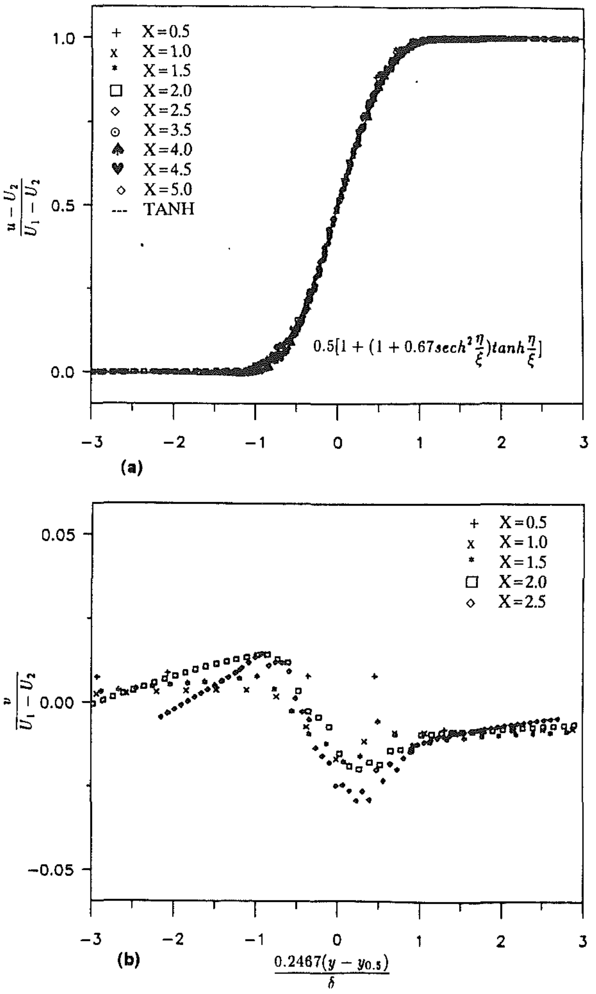

Fig. 12 Time average downstream mean velocity profiles from numerical simulations: (*a*) downstream component, (*b*) cross-stream (*y*-direction) component

dictive or modeling techniques. Both of these questions can be addressed with the use of direct simulation techniques to visualize and quantify the particle dispersion process.

3.2 Numerical Results. Following the numerical simulation efforts of Chung and Troutt (1988) and Chein and Chung (1988) a two-dimensional, inviscid discrete vortex numerical technique was developed to simulate the mixing layer flow. The particle motion was then computed using a modified Stokes force relationship (Crowe et al. 1987). Details concerning the numerical procedures can be found in Chein and Chung (1988) and Chung and Troutt (1988). In the numerical simulation of incompressible flow, external forcing was introduced as a small periodic flow perturbation at the origin of the mixing layer where the instability begins. This perturbation is equivalent to that of the acoustic forcing used in the experiment. The simulation results employed here in addition used a conformal mapping technique such that the effects of the bounding tunnel walls could also be included in the model through a zero normal velocity condition following Ghoniem and Ng (1987). The numerical effort was also aimed at simulating the test facility geometry and experimental conditions as closely as possible under the limitations of the basic assumptions in the discrete vortex model. In addition to simulating more closely the experimental boundary conditions, the current numerical effort also examined dispersion patterns with multiple particle release positions for comparison to the experimental smoke wire results and for evaluating the influence of particle release position on the numerical dispersion patterns. Moreover, vorticity contours were computed from the present results to illustrate more explicitly the exact connections between the vortex structure development and the particle dispersion mechanisms. To insure that numerical dispersion effects were small the numerical integration times were kept at levels much smaller than the characteristic large scale flow time scales.

Results from the numerical simulation are shown in Fig. 11. A discrete vortex pattern is shown in Fig. 11(*a*) at a particular instant in time. The associated contours of negative z direction vorticity are shown in Fig. 11(*b*). From these figures, the development of large scale vortex structures and their pairing interactions can be clearly observed. Although these two-dimensional simulations do not model the full three-dimensional nature of an experimental plane free shear flow (Lasheras et al., 1986 and Lasheras and Choi, 1988) their representation of the large scale features is quite accurate (Hussaini and Zang, 1987). Bernal and Roshko (1986) stated that in the early mixing layer development region, the streamwise structures once formed, preserve their spanwise scale and position for some distance downstream. If there is dispersion associated with three-dimensional structures, it would be of a very smaller magnitude and uniform across the studied region. The scale of the streamwise vortices is very small as indicated by a referee and it is probably of the order of the Taylor microscale as suggested by Lin and Corcos (1984). Therefore, the corresponding Stokes number for the particle dispersion by the streamwise vortices at the Reynolds numbers in our study would

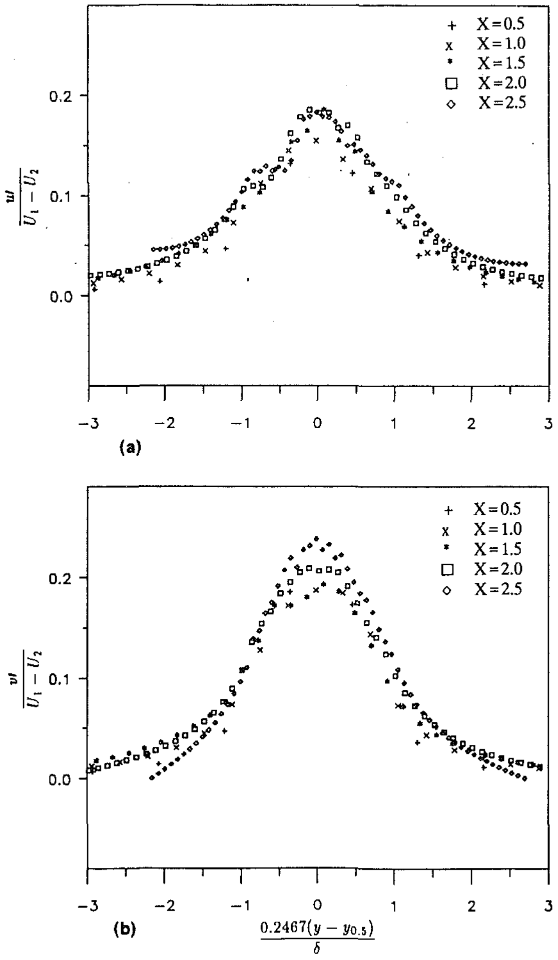

Fig. 13 RMS velocity fluctuation levels from numerical simulations: (*a*) downstream component and (*b*) cross-stream (*y*-direction) component

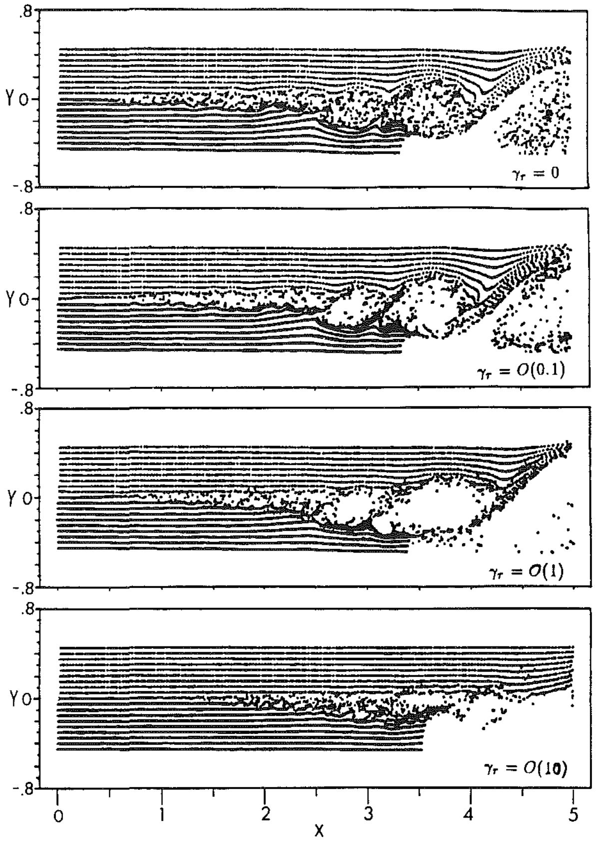

Fig. 14 Instantaneous particle dispersion patterns for tracers and particles with γ_r of O(0.1), O(1) and O(10) (from top to bottom)

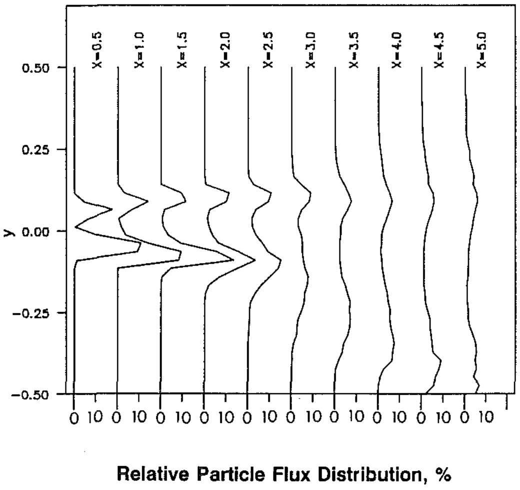

Fig. 15 Profiles of time average particle concentration from numerical simulations

be at least one order of magnitude larger than the order of unity for the spanwise rollers. With such a large Stokes number, the dispersion is negligible.

The numerical results can also be evaluated from a quantitative time average sense. Figure 12 shows time average downstream mean flow velocity profiles. The profiles are nondimensionalized by local flow properties and compared to a curve fit involving the tanh function and its derivative previously employed by Gaster et al. (1985), for fitting mixing layer experimental data. This functional form provided a better fit for the experimental data than the conventional simple tanh profile used previously by numerous investigators.

Root mean square velocity fluctuation levels for downstream and cross-stream (*y*-direction) velocity components are shown in Figs. 13(*a*) and (*b*). The maximum intensity of the nondimensional downstream velocity fluctuation, $u'/\Delta U = 0.18$, is somewhat higher than Browand and Latigo (1979)'s value of 0.15. However, it is in good agreement with Oster and Wygnanski (1982)'s results of 0.18. Furthermore, the maximum nondimensional turbulence energy in the two-dimensional simulation of 3.83×10^{-2} compares well with previous experimental measurements (Oster and Wygnanski, 1982) of 3.84×10^{-2} involving all three velocity components.

Particles of monosize distribution were released uniformly from cross-stream (*y*-direction) positions at $x = 0$ into the flow simulation. To evaluate the effect of Stokes number, γ_r, the large scale structure characteristic time is chosen as the reciprocal of the natural initial instability frequency, calculated from the downstream velocity fluctuation component near the mixing layer origin. Figure 14 shows the instantaneous patterns for tracers and particles with γ_r's of the order of 0.1, 1 and 10 (from top to bottom). Similar to smoke visualizations, the tracers become entrained into the mixing layer and fill in the vortex cores. Larger particles with γ_r's of O(0.1) tend to move towards the edges of the large scale structures. Particles with γ_r's of O(1) are clearly thrown to the vortical structures boundaries and yield the largest dispersion. Further increase in γ_r results in a sharp decrease in the dispersion, as shown in the case of γ_r's of O(10). The particle dispersion patterns from the numerical simulations are qualitatively in good agreement with the visualization pictures and indicate that the Stokes number, γ_r, is indeed a controlling parameter for describing

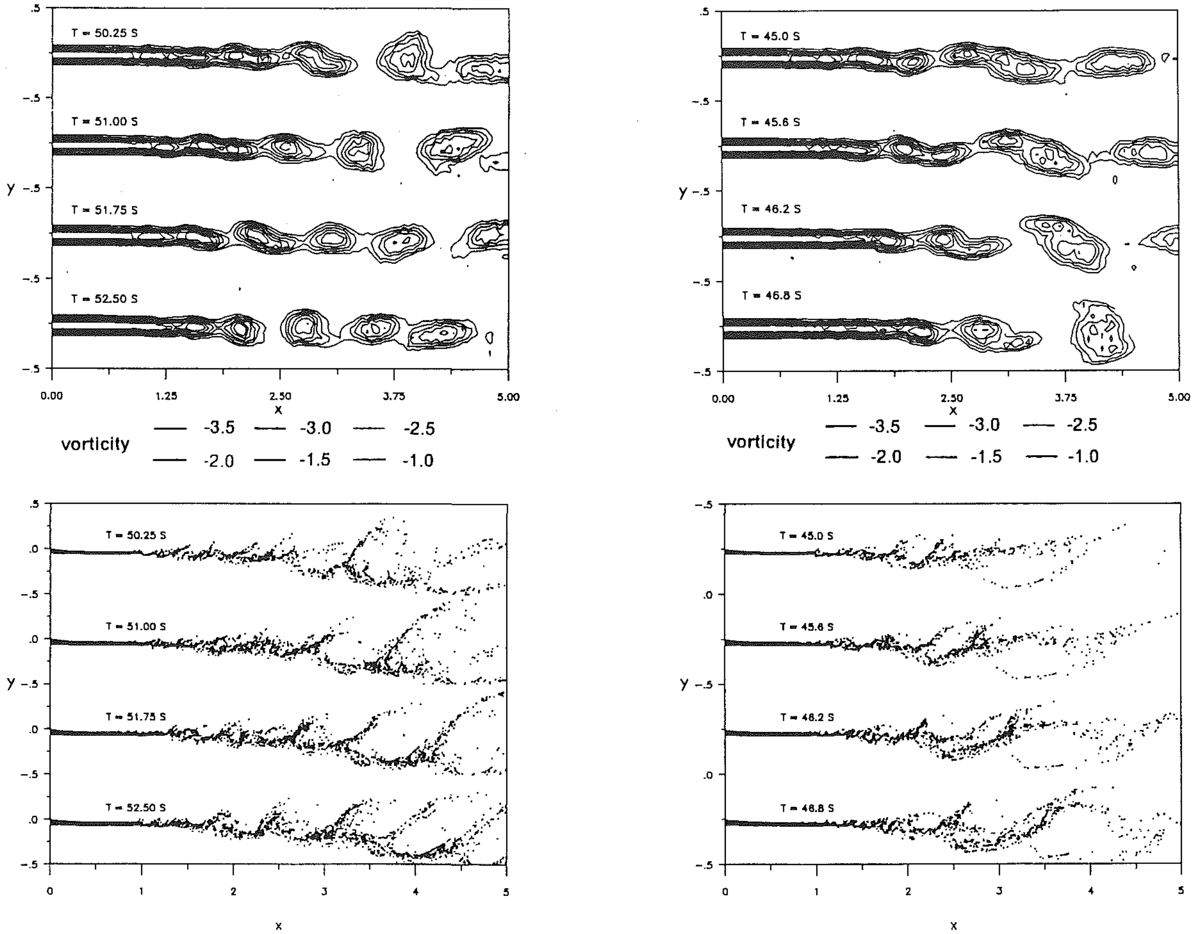

(a)

(b)

Fig. 16 Instantaneous vorticity contours and particle streaklines with γ_T's of O(1) at successive times: (*a*) stretching process, (*b*) folding process

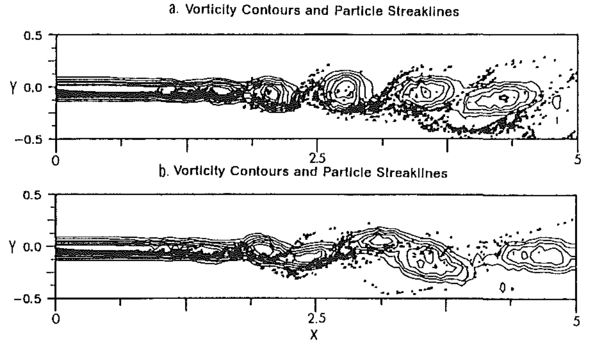

Fig. 17 Instantaneous superimposed vorticity contours and particle patterns: (*a*) stretching process, (*b*) folding process streaklines

the particle dispersion in the large scale structures, as proposed by Crowe et al. (1985).

Time average particle concentration profiles with γ_T's of O(1) were also obtained from the numerical simulations by releasing numerous particles in the neighborhood of the mixing layer origin $x = 0$, $y = 0$. The results of these simulated concentration profiles are shown in Fig. 15. The simulated profiles show much of the same character as the experimental profiles, developing a double peak nature at early downstream positions followed by the movement of a single peak gradually below the centerline.

To examine more closely the particle mixing mechanism successive instantaneous vorticity contours and particle patterns are shown in Fig. 16. Detailed observation of the particle patterns appear to indicate that the dispersion mechanism can be divided into two parts. One part appears to be a stretching mechanism associated with the high velocity gradient regions near the high and low speed boundaries of adjacent vortex structures. The rotational nature of the large vortex structures tends to rapidly separate neighboring particles in these regions. The stretching mechanism primarily involves a focussing of the particles into a thin region as represented by the white stripe which constitutes the lower half of the outer boundary of the preceding vortex and the upper half of the outer boundary of the following vortex as shown in Fig. 5 and as illustrated in Fig. 18. And a stretching of the distance between the particles located in the thin region is also taking place. This mechanism, therefore, tends to produce sheets of particles which ride on the upstream side of the large scale vortices or are flung centrifugally into the high speed stream (Fig. 16(*a*)). The stretching process occurs basically on the high speed boundary of the large scale structures. The folding mechanism follows the stretching mechanism. The stretched thin particle sheets will then fold down on top of each other as a result of the vortex pairing. These pairing interactions tend to fold the particle sheets down onto themselves towards the low speed side of the mixing layer (Fig. 16(*b*). The folding mechanism will not occur in the absence of the vortex pairing (i.e., the wake flow).

Direct connections between the vortex structure development and the $\gamma_T = O(1)$ particle dispersion process are shown in Fig. 17 by superimposing instantaneous particle patterns on their associated vorticity contours. In Fig. 17(*a*) the large-scale vortices are separated in a regular arrangement with the particles concentrated in sheets located on the outer boundaries

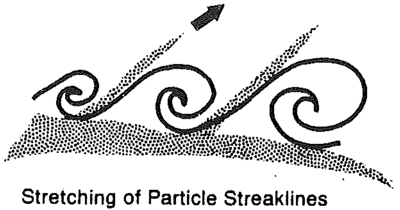

Stretching of Particle Streaklines
Near Boundaries of Vortices

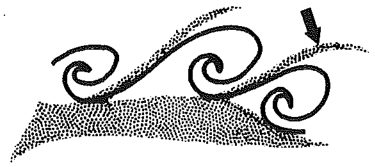

Folding of Particle Streaklines
During Vortex Pairing

Fig. 18 Schematic illustrating particle dispersion mechanism: (*a*) stretching of particle streaklines, (*b*) folding of particle streaklines

of the vortex structures. In Fig. 17(*b*) the vortex structures are caught engaging in a pairing interaction with the particle sheets being folded into the center of the mixing layer. These two figures thus directly illustrate the connection between the instantaneous vortex structure arrangement and the stretching and folding dispersion process for intermediate scale particles. A schematic illustrating these concepts is also shown in Fig. 18.

One important point concerning the stretching and folding mechanism described here is that it is qualitatively identical to the stretching and folding mechanism associated with chaotic dynamic systems occurring in phase space. Moreover Ottino (1990) has recently pointed out that mixing of fluid interfaces may be closely connected to chaotic stretching and folding processes, and turbulent flow processes. This is, however, the first time this mechanism has been directly attributed to particle dispersion in a free shear flow.

4 Conclusions

The experimental results displayed here demonstrate that the dispersion of solid particles in a plane mixing layer is closely connected to the large scale organized vortex dynamics. These results are in general consistent with two-phase mixing layer experiments recently reported by Lazaro and Lasheras (1989) for a single stream air-droplet flow. Experimental and numerical flow visualization results show that intermediate size particles tend to concentrate near the outer edges of the vortex structures. Time average laser doppler velocimetry measurements also demonstrate that intermediate size particles tend to migrate away from the center of the mixing layer. In addition, substantial changes in the particle dispersion are found to result from the use of subharmonic flow forcing techniques. The experimental visualization results also display striking similarity to the numerical simulation results demonstrating the potential for developing accurate new predictive techniques.

A two part model for the particle dispersion process involving a stretching and folding mechanism associated with the large scale vortex dynamics is suggested based on close examination of the numerical results.

Acknowledgment

The authors gratefully acknowledge the support of this research by the Department of Energy under grant no. FG06-86ER1333567. The shear flow wind tunnel was designed by Mr. R. Hanle.

References

Bernal, L. P., 1981, "The Coherent of Turbulent Mixing Layers," PhD thesis, California Institute of Technology, Pasadena, CA.

Bernal, L. P., and Roshko, A., 1986, "Streamwise Vortex Structure in Plane Mixing Layer," *Journal of Fluid Mechanics*, Vol. 170, pp. 499-527.

Breidenthal, J., 1981, "Structures in Turbulent Mixing Layers and Wakes Using a Chemical Reaction," *Journal of Fluid Mechanics*, Vol. 109, pp. 1-24.

Browand, F. K., and Latigo, B. O., 1979, "Growth of the Two-Dimensional Mixing Layer from a Turbulent and Non-turbulent Boundary Layer," *Physics of Fluids*, Vol. 22, pp. 1011-1019.

Browand, F. K., and Troutt, T. R., 1980, "A Note on Spanwise Structure in the Two-dimensional Mixing Layer," *Journal of Fluid Mechanics*, Vol. 97, pp. 771-781.

Browand, F. K., and Troutt, T. R., 1985, "The Turbulent Mixing Layer: Geometry of Large Vortices," *Journal of Fluid Mechanics*, Vol. 158, pp. 489-509.

Brown, G., and Roshko, A., 1974, "On Density Effects and Large Structure the Turbulent Mixing Layers," *Journal of Fluid Mechanics*, Vol. 64, pp. 693-704.

Chein, R., and Chung, J. N., 1987, "Effects of Vortex Pairing on Particle Dispersion in Turbulent Shear Flows," *International Journal of Multiphase Flow*, Vol. 13, pp. 785-802.

Chein, R., and Chung, J. N., 1988, "Simulation of Particle Dispersion in a Two-dimensional Mixing Layer," *American Institute of Chemical Engineering Journal*, Vol. 34, pp. 945-954.

Chung, J. N., and Troutt, T. R., 1988, "Simulation of Particle Dispersion in an Axisymmetric Jet," *Journal of Fluid Mechanics*, Vol. 186, pp. 199-222.

Corke, T., Koga, D., Doubka, R., and Nagib, H., 1977, "A New Technique for Introducing Controlled Sheets of Smoke Streaklines in Wind Tunnels," ICIASF report.

Crighton, D. G., 1981, "Acoustics as a Branch of Fluid Mechanics," *Journal of Fluid Mechanics*, Vol. 106, pp. 261-298.

Crowe, C. T., Gore, R. A., and Troutt, T. R., 1985, "Particle Dispersion by Coherent Structures in Free Shear Flows," *Particulate Science and Technology Journal*, Vol. 3, pp. 149-158.

Crowe, C. T., Chung, J. N., and Troutt, T. R., 1988, "Particle Mixing in Shear Flows," *Progress of Energy Combustion Science Journal*, Vol. 14, pp. 171-194.

Fleckhaus, D., Hishida, K., and Maeda, M., 1987, "Effect of Laden Solid Particles on the Turbulent Flow Structures of a Round Free Jet," *Experiments in Fluids*, Vol. 5, pp. 323-331.

Gaster, M., Kit, E., and Wygnanski, I., 1985, "Large-scale Structures in a Forced Turbulent Mixing Layer," *Journal of Fluid Mechanics*, Vol. 150, pp. 23-39.

Ghoniem, A. F., and Ng, K. K., 1987, "Numerical Study of the Dynamics of a Forced Shear Layer," *Physics of Fluids*, Vol. 30, pp. 706-721.

Ho, C. M., and Huerre, P., 1984, "Perturbed Free Shear Layers," *Annual Review of Fluid Mechanics*, Vol. 16, pp. 365-424.

Hussaini, M. Y., and Zang, T. A., 1987, "Spectral Methods in Fluid Dynamics," *Annual Review of Fluid Mechanics*, Vol. 19, pp. 339-367.

Kobayashi, H., Masutani, S. M., Azuhata, S., Arashi, N., and Hishinuma, Y., 1987, "Dispersed Phase Transport in a Plane Mixing Layer," *2nd International Symposium Transport Phenomena in Turbulent Flows*, Tokyo, Oct. 25-29.

Lasheras, J. C., Cho, J. S., and Maxworthy, T., 1986, "On the Origin and Evolution of Streamwise Vortical Structures in a Plane Free Shear Layer," *Journal of Fluid Mechanics*, Vol. 172, pp. 231-256.

Lasheras, J. C., and Choi, H., 1988, "Three-dimensional Instability of a Plane Free Shear Layer: An Experimental Study of the Formation and Evolution of Streamwise Vortices," *Journal of Fluid Mechanics*, Vol. 189, pp. 53-86.

Lazaro, B. J., and Lasheras, J. C., 1989, "Particle Dispersion in a Turbulent, Plane, Free Shear Layer," *Physics of Fluids*, Vol. A1, pp. 31-52.

Leonard, A., 1985, "Computing Three-dimensional Incompressible Flows with Vortex Elements," *Annual Review of Fluid Mechanics*, Vol. 17, pp. 523-559.

Lin, S. J., and Corcos, G. M., 1884, "The Mixing Layer: Deterministic Model of a Turbulent Flow. Part 3. The Effect of Plane Strain on the Dynamics of Streamwise Vortices," *Journal of Fluid Mechanics*, Vol. 141, pp. 139-178.

Monkewitz, P. A., and Huerre, P., 1982, "The Influence of the Velocity Ratio on the Spatial Instability of Mixing Layer," *Physics of Fluids*, Vol. 27, pp. 1137-1156.

Òster, D., and Wygnanski, I., 1982, "The Forced Mixing Layer Between Parallel Streams," *Journal of Fluid Mechanics*, Vol. 123, pp. 91-130.

Ottino, J. M., 1989, "Mixing, Chaotic Advection and Turbulence," *Annual Review of Fluid Mechanics*, Vol. 22, pp. 207-253.

Winant, C. D., and Browand, F. K., 1974, "Vortex Pairing, the Mechanism of Turbulent Mixing Layer Growth at Moderate Reynolds Number," *Journal of Fluid Mechanics*, Vol. 63, pp. 237-255.

Turbulent Diffusion of Heavy-Particles in Turbulent Jets

A. A. Mostafa
Faculty of Engineering,
Cairo University,
Giza, Egypt

The turbulent dispersion of heavy suspended particles in turbulent shear flows is analyzed when crossing trajectory effects are important. A semiempirical expression for particle diffusion coefficient is developed via a comparison with experimental data of two-phase turbulent jet flows. This expression gives the particle momentum diffusion coefficient in terms of the gas diffusion coefficient, mean relatively velocity, and root mean square of the fluctuating fluid velocity. The proposed expression is used in a two-phase flow mathematical model to predict different particle-laden jet flows. The good agreement between the predictions and data suggests that the developed expression for particle diffusion coefficient is reasonably accurate in predicting particle dispersion in turbulent free shear flows.

I Introduction

Considerable effort has been recently directed toward explaining and modeling the complex interaction between turbulent fluid and dispersed particles (Elghobashi et al., 1984; Crowe et al., 1988; and Faeth, 1983). Because of the complexity and lack of understanding of this class of two-phase flow, there are many reported approaches to formulate the system of differential equations that govern particle behavior in a coupled manner with the carrier fluid (Crowe, 1982). Among these models is the two-fluid approach in which the particles are treated as an interacting and interpenetrating continuum. Hence, they are governed by similar equations to Navier-Stokes with some extra source/sink terms. Among the shortcomings of this approach is the unavailability of a reliability expression to calculate the particle diffusion coefficient, which is needed to close the system of modeled equations. It is the purpose of this paper to develop such an expression and to use it in the prediction of particle-laden jet flows.

Unlike gas flow diffusion that results from inter-molecular collisions, particle diffusion is much more complex because it results from the interaction between the momentum of both particles and gas flow in the vicinity of the particles. Among the parameters that determine particle dispersion are particle properties, turbulence properties, relative velocity between the particle and the surrounding gas, and gas-phase transport properties. Due to this complexity, most of the theoretical studies on particle dispersion were based on several restrictive assumptions. The earliest analytical work on this subject was reported by Tchen (1947), who considered stationary, homogeneous turbulent fields. He assumed, however, that the fluid element should continue to contain the same discrete particle at any time. Several other improvements were made to Tchen's model and can be found in Chao (1964), and Gouesbet et al. (1984).

Peskin (1971) performed an analysis that relaxed the assumption made by Tchen concerning the particle and turbulent eddy. However, he restricted his analysis to small distances between the discrete particles and the "originally surrounding fluid." Peskin predicted that the ratio of particle diffusivity to fluid diffusivity was always less than unity and that it depends on the ratio of Lagrangian to Eulerian microscales of the fluid and on the particle inertia.

Reeks (1977) and Pismen and Nir (1978) have presented more sophisticated analytical studies of particle diffusion in homogeneous, isotropic, and stationary turbulence. Reeks assumed that a linear drag force and a body force acted on the particle. His results show that the effect of particle inertia on long-time diffusion of heavy particles is weak. However, the long-time diffusion will increase with particle size and exceed that of a fluid. Lumley and Shih (1986) derived a set of second-order modeled equations for the motion of particles. They considered the influence of inertia and the crossing-trajectories effect on the particle diffusion. A simple case of a particle mixing layer in a decaying homogeneous turbulence was calculated. The results show that the cross-trajectories effect on particle dispersion is very significant.

The majority of the experimental studies of particle dispersion due to turbulence reported on particle or droplet-laden flows. Goldschmidt and Eskinazi (1986) measured the concentration of liquid aerosol in a plane turbulent jet. They reported a Schmidt number slightly smaller than unity, indicating a lower spreading rate of the droplet concentration profile than that of the velocity profile. Later, Goldschmidt et al. (1972) observed that increasing the droplet size leads to Schmidt numbers higher than one. This result is different from the experimental observations of Hedman and Smoot (1975); Memmot and Smoot (1978), and Wells and Stock (1983). Hedman and Smoot (1975) noticed a decrease of the Schmidt number with the increase of particle diameter in coaxial jets confined in a tube. Memmot and Smoot (1978), using a laboratory-scale test chamber, observed a decrease in the value of the Schmidt

---

Contributed by the Fluids Engineering Division for publication in the JOURNAL OF FLUIDS ENGINEERING. Manuscript received by the Fluids Engineering Division June 9, 1989. Associate Technical Editor: E. E. Michaelides.

number with the increase of particle size. Wells and Stock (1983) reported a rapid decrease of the Schmidt number of heavy particles in a grid-generated turbulent flow.

It was observed experimentally (Modarress et al., 1984; and Shuen et al., 1983) that adding even small amounts of particles cause a significant change in the turbulence structure of the carrier fluid. These observations have motivated many researchers to introduce mathematical models of different levels to account for the presence of dispersed particles (Faeth, 1983). Mostafa and Mongia (1988) proposed a turbulence model for turbulence two-phase flows that simulates the extra energy dissipation caused by the inability of the heavy particles to respond to the whole spectrum of the carrier phase turbulence. This model is used here to validate the proposed particle diffusion coefficient versus the experimental data.

In the present analysis, a semiempirical expression for the particle diffusion coefficient is provided. This expression is based on Csanady's theory (1963) for heavy particle dispersion in turbulent flow and was developed via a comparison with the data of Fleckhaus et al. (1987). As a validation to the proposed expression, it is used in the mathematical model of Mostafa and Mongia (1988) to predict the two-phase jet flows of Bulzan et al. (1988) and Shuen et al. (1983).

II Particle Diffusion Coefficient

In this section, the physical parameters that control the particle behavior in a turbulent flow are discussed, and a semiempirical expression for calculating the particle diffusion coefficient is provided.

II-1 The Semiempirical Expression. The behavior of a single spherical particle suspended in a turbulent field depends on the properties of both the particle and the turbulent flow. The first parameter that controls the particle dispersion is the ratio between the particle relaxation time, τ_P and the fluid Lagrangian integral time scale, τ_L (Crowe et al., 1988). This ratio is a measure of the influence of particle inertia on dispersion of particles by fluid turbulence. If the ratio $\tau_P/\tau_L < 1$, the particle will be able to respond to the entire spectrum of fluid motion and will tend to follow fluid velocity fluctuations. On the other hand, if $\tau_P/\tau_L > 1$, the particles have insufficient time to respond to the turbulent fluctuations.

The second parameter that characterizes the particle dispersion is the relative mean velocity between the particle and the surrounding fluid, U_t. Yudine (1959) pointed out that the dispersion process depends upon U_t in three ways: (i) it determines the vertical displacement of the center of dispersion of the particle; (ii) it is a measure of inertia and, as such, the particle does not follow completely the high frequency of fluctuations of turbulent fluid velocity; and (iii) if it has appreciable value, a particle will fall from one eddy to another, whereas a fluid point would remain in the same eddy throughout the lifetime of the eddy. This phenomenon has been labeled "the effect of crossing trajectories" by Yudine who concluded that, at large U_t, the dispersion coefficient takes on an asymptotic form inversely proportional to it. Reeks (1977), Pismen and Nir (1978) have presented theories and Wells and Stock (1983) have carried out experiments that suggest that the effects of inertia are small compared to the crossing trajectory effect. They also concluded that particle dispersion is reduced due to the crossing trajectory effects.

Based on Yudine's theory, Csanady (1963) has shown that the ratio U_t^2/u^2, where u is the fluctuating velocity of the surrounding fluid, is the main controlling parameter for heavy particle dispersion. He constructed two relations for the particle diffusivity parallel to and normal to the direction of the relative velocity. Lumley (1978), in his discussion on the diffusion of heavy particles, argued that Csanady's model predicts

$$\sigma_P = (1 + \beta U_t^2/u^2)^{-1/2} \tag{1}$$

where β is the ratio of the Eulerian to Lagrangian integral length scales and is determined here through a comparison with experimental data. Peskin (1974) indicated that this parameter depends on the turbulence scales of the flow around the particle. Both experimental observations and theoretical analysis show that particles change turbulence structures, especially in their vicinity. This change is a function of the particle loadings, particle properties, as well as the flow properties. Accordingly, one would expect that β depends on turbulence scales of the flow as well as the particle properties (Peskin, 1974), which determine the particle Reynolds number. It should be noted that Eq. (1) was developed to predict dispersion in the atmosphere where the fluid scales are large. However, it includes the main parameters that determine particle dispersion; U_t/u and the β coefficient. It is also noteworthy to indicate that in homogeneous flows, Eq. (1) is based on:

$$\sigma_P \sim \beta(U_t/u) \tag{2}$$

In Stokes flow β is the ratio of the Eulerian to Lagrangian length scales. For particles with higher Reynolds number, one can linearize the equation of motion, so that in the frame of reference moving with the mean particle velocity

$$\frac{dv}{dt} = -\alpha v + f(\underline{x}, t); \quad \frac{d\underline{x}}{dt} = v \tag{3}$$

Nomenclature

$c_\mu, c_{\epsilon 1}, c_{\epsilon 2}, c_{\epsilon 3}$ = coefficients in the turbulence model
C_D = drag coefficient
d = particle diameter
D = tube diameter
F = interface friction coefficient
g = gravitational acceleration
K = kinetic energy of turbulence
$m^\cdot$ = particles mass flux
P = static pressure
r = distance in the radial direction
U, u = mean and fluctuating velocity of the carrier phase
U_t = mean relative velocity between the particle and the fluid
V, v = mean and fluctuating velocity of the particles
z = distance in the axial direction
β = ratio between the Lagrangian and Eulerian integral length scales
ϵ = kinetic energy dissipation rate
μ = dynamic viscosity of the carrier phase
ν_t = turbulent diffusivity of the carrier phase
ν_p = turbulent diffusivity of the particles
ρ = material density
τ_p = particle relaxation time
τ_L = carrier phase Lagrangian time scale
$\sigma_k, \sigma_\epsilon$ = coefficients in the turbulence model
Φ = volume fraction

Subscripts

0 = conditions at the nozzle exit
1 = carrier phase
2 = dispersed phase
c = conditions of the jet centerline
i = ith direction
r = radial direction
z = axial direction

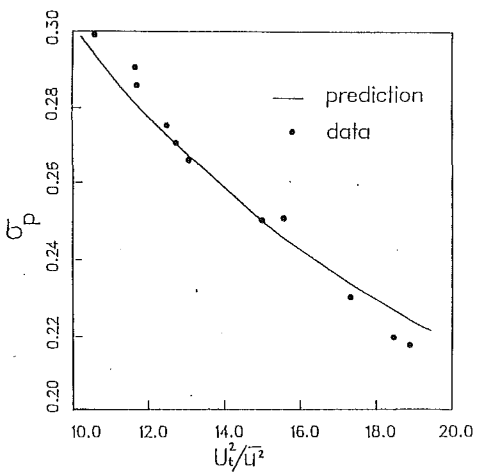

Fig. 1 Measured and predicted momentum diffusivity ratio

for a particle of velocity $\underline{v}$ and position $\underline{x}$ at time t where $\underline{f}$ is a fluctuating aerodynamic driving force (per unit particle mass). Both α and $\underline{f}$ will depend upon the particle Reynolds number but it is expected that $\underline{f} > \alpha\ \underline{v}$ reaching some constant value 0(1) as the particle Reynolds number tends to infinity, σ_P then approximates to

$$\sigma_P \sim \left(\frac{U_t}{u}\right)\left(\frac{u\alpha}{f'}\right)^2 \beta_s \tag{4}$$

where β_S is the value of β for Stokes drag. σ_P is therefore expected to be less than its equivalent value based on Stokes drag, the ratio approaching some finite limit of order 1 as the particle Reynolds gets bigger.

The approach considered in this work is to determine the value of β for a narrow range of heavy particle sizes ($\rho \simeq 1000$ kg/m^n and $d \sim 100$ μm) suspended in a certain class of flow (fully developed free air jets).

II-2 The Value of β. Turbulent dispersion of both particles and carrier fluid can be handled by the concept of an eddy diffusion coefficient. In this approach, the carrier phase shear stress is determined by:

$$\overline{u_z u_r} = -\nu_t \frac{dU_z}{dy} \tag{5}$$

where ν_t is the momentum diffusion coefficient of the carrier phase. Similarly, the particles' shear stress is determined by:

$$\overline{v_z v_r} = -\nu_p \frac{dV_z}{dy} \tag{6}$$

where ν_p is the particle momentum diffusion coefficient. It should be noted that Eq. (6) is based on the continuum assumption for the suspended particles. In this analysis, the ratio between ν_t and ν_p is defined as momentum diffusivity ratio, i.e.,

$$\sigma_p = \frac{\nu_p}{\nu_t} \tag{7}$$

Fleckhaus et al. (1987) measured the radial profiles of $\overline{u_z u_r}$, U_z, u^2, $\overline{v_2 v_r}$, and V_z in a turbulent round jet laden with glass beads at three axial locations downstream of the nozzle exit ($z/D = 10, 20$, and 30). Mostafa (1989) used these profiles and Eqs. (5)-(7), to obtain and plot the experimental value of σ_p against U_t^2/u^2 as shown in Fig. 1. The calculated distribution from expression (1) with an optimized value of $\beta = 1$ is also plotted in the same figure. This figure shows that the optimized value for the coefficient β gives good agreement with the diffusivity ratio obtained from the experimental data. As a validation of expression (1) it is implemented in the mathematical model of Mostafa and Mongia (1988) and used to predict the flow properties of two turbulent particle-laden jets (Bulzan et al., 1988, and Shuen et al., 1983).

III Mathematical Model

In the Eulerian-Eulerian approach both the carrier and particulate phases are treated as two interacting continua. Then, separate continuity and momentum equations are written for each phase. The modeled governing equations for turbulent gaseous jet laden with evaporating liquid droplets are given by Mostafa and Mongia (1987). In the equations of the carrier phase, the volume fraction of that phase is approximated to unity. This is a valid assumption for dilute suspensions where the volume fraction of the particles is less than 0.01. Having used this assumption, the present turbulence model is quite simple and involves less empiricism, since all turbulent correlations between volume fraction and particles velocity are cancelled. For the case of dilute, isothermal, nonreacting solid particles, the governing equations are summarized here.

<u>Carrier Phase:</u>

$$\rho_1 U_{z,z} + \frac{\rho_1}{r}\,(rU_r)_{,x} = 0 \tag{8}$$

$$\rho_1 U_z U_{z,z} + \rho_1 U_r U_{z,r} = -P_{,z} + \frac{1}{r}\,(\rho_1 r \nu_t U_{z,r})_{,x} - \sum_k \Phi^F F^k (U_z - V_z^k) \tag{9}$$

$$\rho_1 U_z U_{r,z} + \rho_1 U_r U_{r,r} = -P_{,r} - \sum_k \Phi^k F^k (U_r - V_r^k) - \frac{2}{3}\frac{\rho_1}{r}\,(rK)_{,r} \tag{10}$$

<u>Particles of Size Class k:</u>

$$\rho_2(\Phi^k V_z^k)_{,z} + \frac{\rho_2}{r}\,(r\Phi^k V_r^k)_{,r} - \rho_2\left(\frac{\nu_p^k}{\sigma_v}\,\Phi,{}^k_z\right)_{,z} - \frac{\rho_2}{r}\left(r\,\frac{\nu_p^k\,\Phi,{}^k_r}{\sigma_v}\right)_{,r} = 0 \tag{11}$$

where σ_v is a constant of order unity. It represents the ratio of particle mass to momentum diffusivity

$$\rho_2 \Phi^k V_z^k V_{z,z}^k + \rho_2 \Phi^k V_r^k V_{z,r}^k = \Phi^k P_{,z} + F^k \Phi^k (U_z - V_z^k) + (\rho_2 - \rho_1) g \Phi^k + \frac{1}{r}\,(\Phi^k r \rho_2 \nu_p^k \nu_{z,r}^k)_{,r} \tag{12}$$

The turbulence model chosen to close the governing equations is the two-equation turbulence model for two-phase flows (Mostafa and Mongia, 1987). The model takes into account the effects of suspended particles on the dissipation of the carrier phase turbulence energy.

IV Numerical Results and Discussion

To assess the expression proposed here for heavy particle diffusion coefficient, it was used in the mathematical model presented in Section III to predict the particle-laden jets of Shuen et al. (1983) and Bulzan et al. (1988). The numerical calculations were performed using a modified version of Spalding's marching finite-difference technique (Spalding, 1979). The dispersed phase required modifications to the standard solution procedure as described by Mostafa and Elghobashi (1985). The computations were started where the radial profiles of the dependent variables were measured. All calculations were performed using 40 grid points in the radial direction. The marching step sizes were limited by 3 percent of the current radial grid width or an entrainment increase of 3 percent, whichever is smaller.

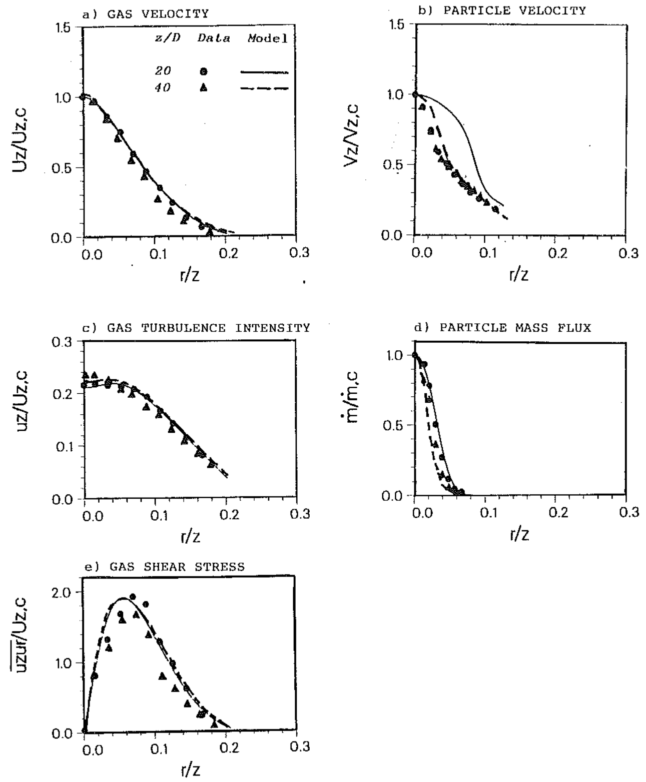

Fig. 2 Predicted flow properties compared to experimental data of Shuen et al., 1983

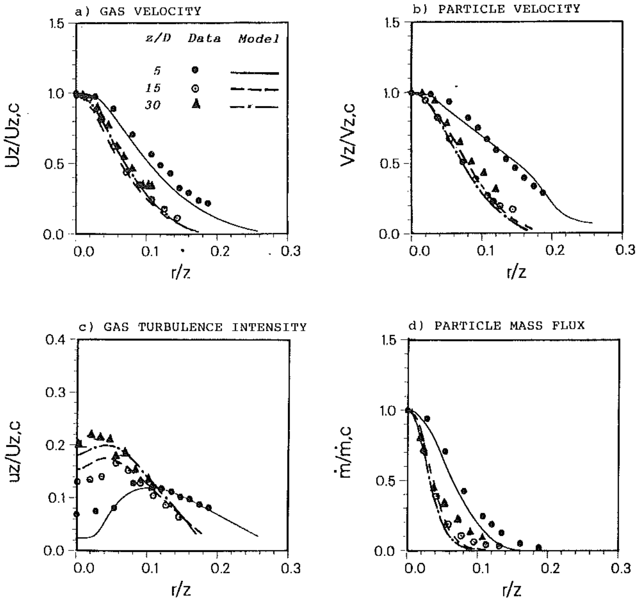

Fig. 3 Predicted flow properties compared to experimental data of Bulzan et al., 1988

The particles were divided into seven size classes. Each class covers particles of certain diameter range. The measured averaged particle velocity was assigned to the averaged diameter size class, and the smallest size class was assumed to have a velocity equal to the gas component. The axial velocity of the remaining five classes was determined by extrapolation.

Shuen et al. (1983) reported measurements of particle-laden round jet discharging into a stagnant environment. They used three sizes of sand particles and various loading ratios, while employing LDA to measure the velocities of both phases. The case corresponds to a loading ratio of 0.2, and a particle diameter of 79 μm is considered in this paper.

Figure 2 shows comparison between predictions and measurements of the flow properties at two axial stations: z/D = 20 and 40. The gas quantities include the mean axial velocity, kinetic energy of turbulence, and shear stress. The mean axial particle velocity and mass flux distribution are number-averaged over all particle sizes. Figure 2 shows that the mathematical model yields good overall agreement with measurements; however, the gas phase jet width is slightly overestimated at $z/D = 40$. This discrepancy is probably caused by the underestimation of turbulence modulation due to the particles. Previous experimental work (Elghobashi et al., 1984, and Shuen et al., 1983) shows that the effects of particles on the continuous phase include decreasing the jet spreading rate and the centerline velocity decay. These effects, as well as the interaction between the continuous phase and the particles, depend on the particle size and their loading ratio. Although the mathematical model used in calculations presented in Fig. 2 accounts for turbulence modulation effects, both the kinetic energy and shear stress are slightly overestimated. This might be caused by the underestimation of these effects by the mathematical model. The dispersed phase results indicate that the concentration of solid particles vanishes at a radial distance approximately equal to half that of the gas width. This narrow distribution reflects the low turbulent diffusion coefficient of the particles compared to that of air, which supports the conclusion of Section II.

The second part of the results covers the measurements of Bulzan et al. (1988). Glass particles with a Sauter mean diameter of 39 μm and a standard deviation of 15 μm were used in a free round jet. Measurements were made at a single value for the particle mass loading ratio of 0.2 and three swirl numbers, ranging from zero to 0.3. The nonswirling case is considered here.

Mean and fluctuating velocity profiles of both phases and particle mass flux distribution were performed at four axial locations: z/D = 0.5, 5, 15, and 30. Calculations were started at z/D = 0.5 and the results were compared with data at the other three axial locations.

Figure 3 presents the measurements of the radial profiles of the mean flow properties at the different axial locations and indicate the extent to which the mathematical model allows reasonable calculations. The agreement between predictions and measurements of mean gas axial velocity and turbulence intensity is satisfactory at the three axial locations.

In contrast to the 79 μm data of Shuen et al. (1983), the 39 μm particles of Bulzan et al. (1988) spreads in most of the radial width of the gaseous jet. This behavior can be seen clearly by comparing the radial distribution of the particle mass flux compared to the distribution of the gas velocity shown in Fig. 3. Smaller particles attain smaller particle relaxation time; τ_p and hence respond better than the larger particles to the different spectrum of fluid motion. This behavior means that the relative mean velocity, U_t decreases with the decrease of the particles diameter and hence yields a higher particle diffusion coefficient (Eq. (1)).

Aside from the experimental uncertainty in the mass flux distribution, the discrepancies between predictions and measurements of this quantity may be attributed to the coefficient β in Eq. (1). As discussed before, the value of this coefficient depends on many factors; such as the fluid scales and particle Reynolds number. However, the approach considered in this work is to determine the value of β for a certain set of flow conditions. It covers heavy particles (material density ~ 10^3 kg/m^3) of diameters in the range of 100 μm suspended in turbulent air jet flow. The overall good agreement with the different experimental data supports this approach, which may serve as a reliable dispersion model for two-phase jet flows.

V Summary and Conclusion

Numerical predictions have been performed for turbulent round gaseous jet flows laden with heavy particles. The present investigations emphasize dispersion of heavy particles when crossing trajectory effects are important. A semiempirical expression for particle diffusion coefficient is developed through a comparison with experimental data. Because of the significance of crossing trajectory effects, the developed expression predicts that the particle diffuses less than the fluid. This expression is used in a recently developed mathematical model for turbulent two-phase flows to predict particle-laden round jets. In conclusion, the present approach yields encouraging results and may serve as a sound basis for predicting turbulent gaseous jets laden with heavy solid particles.

References

Bulzan, D. L., Shuen, J. S., and Faeth, G. M., 1988, "Particle-laden Weakly Swirling Free Jets: Measurement and Predictions," NASA Report No. TM-100920.

Chao, B. T., 1964, "Turbulent Transport Behavior of Small Particles in Dilute Suspension," *Osterreichisches Ingenieur-Archiv*, Vol. 18, pp. 7–21.

Crowe, C. T., 1982, "Review-Numerical Models for Dilute Gas-Particle Flows," ASME JOURNAL OF FLUIDS ENGINEERING, Vol. 104, pp. 297–303.

Crowe, C. T., Chung, J. N., and Trout, T. R., 1988, "Particle Mixing in Free Shear Flows," *Prog. Energy Combust. Sci.*, Vol. 14, pp. 171–194.

Csanady, G. T., 1963, "Turbulent Diffusion of Heavy Particles in Atmosphere," *J. Atmos. Sci.*, Vol. 20, pp. 201–208.

Elghobashi, S., Abou-Arab, T., Rizk, M., and Mostafa, A., 1984, "Prediction of the Particle-Laden Jet With a Two-Equation Turbulence Model," *Int. J. Multiphase Flow*, Vol. 10, pp. 697–710.

Faeth, G. M., "Recent Advances in Modeling Particle Transport Properties and Dispersion in Turbulent Flow," *ASME-JSME, Thermal Engineering Joint Conference Proceedings*, Vol. 2, Y. Mori and W. J. Yang, eds., ASME, New York, 1983, pp. 517–534.

Fleckhaus, D., Hishida, K., and Maeda, M., 1987, "Effect of Laden Solid Particles on the Turbulent Flow Structure of a Round Free Jet," *Experiments in Fluids*, Vol. 5, pp. 323–333.

Goldschmidt, V. W., Householder, M., Ahmadi, G., and Chuang, S. C., 1972, "Turbulent Diffusion of Small Particles Suspended in Turbulent Jets," *Progress in Heat Mass Transfer*, Hetsroni, G., Sideman, S., and Hartnett, J. P., eds., Pergamon Press, New York, G, pp. 487–508.

Goldschmidt, V. W., and Eskinazi, S., 1986, "Two-Phase Turbulent Flow in a Plane Jet," ASME *Journal of Applied Mechanics*, Vol. 33E, pp. 735–747.

Gouesbet, G., Berlemont, A., and Picart, A., 1984, "Dispersion of Discrete Particles by Continuous Turbulent Motions: Extensive Discussion of the Tchen's Theory Using a Two-Parameter Family of Lagrangian Correlation Functions," *Phys. Fluids*, Vol. 27, p. 827.

Hedman, P. O., and Smoot, L. D., 1975, "Particle-Gas Dispersion Effects in Confined Coaxial Jets," *AIChE J.*, Vol. 21, pp. 372–379.

Lumley, J. L., and Shih, T. S., 1986, "Second-Order Modeling of Particle Dispersion in a Turbulent Flow," *JFM*, Vol. 163, pp. 349–363.

Lumley, J. L., 1978, "Two-Phase and Non-Newtonian Flows," *Turbulence* (*Topics in Applied Physics, Vol. 12*), Bradshaw, P., ed., Springer, New York, pp. 290–324.

Memmot, V. J., and Smoot, L. D., 1978, "Cold Flow Mixing Rate Data for Pulverized Coal Reactors," *AIChE J.*, Vol. 24, pp. 466–474.

Modarress, D., Tân, H., and Elghobashi, S., 1984, "Two-Component LDA Measurement in a Two-Phase Turbulent Jet," *AIAA J.*, Vol. 22, p. 624–630.

Mostafa, A. A., 1989, "Turbulent Diffusion in Particle-Laden Flows," *Proc. Int. Symp. on Turbulence Modification in Dispersed Multiphase Flows*, San Diego, CA.

Mostafa, A. A., and Elghobashi, S. E., 1985, "A Two-Equation Turbulence Model for Jet Flows Laden with Vaporizing Droplets," *Int. J. Mutiphase Flow*, Vol. 11, pp. 515–533.

Mostafa, A. A,. and Mongia, H. C,. 1987, "On the Modeling of Turbulent Evaporating Sprays: Eulerian Versus Lagrangian Approaches," *Int. J. Heat Mass Transfer*, Vol. 30, pp. 2583–2593.

Mostafa, A. A., and Mongia, H. C., 1988, "On the Interaction of Particles and Turbulent Fluid Flow," *Int. J. Heat Mass Transfer*, Vol. 31, pp. 2063–2075.

Mostafa, A. A., Mongia, H. C., McDonnell, V. G., and Samuelsen, G. S., 1989, "On the Evolution of Particle-Laden Jet Flows: A Theoretical and Experimental Study," *AIAA J.*, Vol. 27, pp. 167–183.

Peskin, R. L., 1971, "Stochastic Estimation Applications to Turbulent Diffusion," *International Symposium on Stochastic Hydraulics*, Chiu, C. L., ed., University of Pittsburgh, Pa., pp. 251–267.

Peskin, R. L., 1974, "Comments on Studies of the Behavior of Heavy Particles in a Turbulent Fluid Flow," *J. Atmos. Sci.*, Vol. 31, pp. 1167–1168.

Pismen, L. M., and Nir, A., 1978, "On the Motion of Suspended Particles in Stationary Homogeneous Turbulence," *J. Fluid Mech.*, Vol. 84, pp. 193–206.

Reeks, M. W., 1977, "On the Dispersion of Small Particles Suspended in an Isotropic Turbulent Fluid," *J. Fluid Mech.*, Vol. 83, pp. 529–546.

Shuen, J. S., Solomon, A. S. P., Zhang, Q. F., and Faith, G. M., 1983, "A Theoretical and Experimental Study of Turbulent Particle-Laden Jets," NASA-CR- 168293.

Spalding, D. B., 1978, *Genmix: A General Computer Program for Two-Dimensional Parabolic Phenomena*, Pergamon Press, Oxford.

Tchen, C. M., 1947, "Mean Value and Correlation Problems Connected with the Motion of Small Particle Suspended in a Turbulent Fluid," Ph.D. thesis, Delft.

Wells, M. R., and Stock, D. E., 1983, "The Effects of Crossing Trajectories on the Dispersion of Particles in a Turbulent Flow," *J. Fluid Mech.*, Vol. 136, pp. 31–32.

Yudine, M. I., 1959, *In Advances in Geophysics*, Vol. 6, pp. 185–191.

Freestream Nuclei and Traveling-Bubble Cavitation

R. S. Meyer
Research Assistant.

M. L. Billet
Senior Scientist.

J. W. Holl
Professor Emeritus of Aerospace Engineering.

Applied Research Laboratory,
The Pennsylvania State University,
State College, PA 16804

Traveling-bubble cavitation inception tests were conducted in a 30.48 cm water tunnel with a Schiebe headform. A computer code was developed to statistically model cavitation inception on a Schiebe headform, consisting of a numerical solution to the Rayleigh-Plesset equation coupled to a set of trajectory equations. Using this code, trajectories and growths were computed for bubbles of varying initial sizes. An initial off-body distance was specified and the bubble was free to follow an off-body trajectory. A Monte Carlo cavitation simulation was performed in which a variety of random processes were modeled. Three different nuclei distributions were specified including one similar to that measured in the water tunnel experiment. The results compared favorably to the experiment. Cavitation inception was shown to be sensitive to nuclei distribution. Off-body effect was also found to be a significant factor in determining whether or not a bubble would cavitate. The effect of off-body trajectories on the critical bubble diameter was examined. The traditional definition of critical diameter based on the minimum pressure coefficient of the body or the measurement of liquid tension was found to be inadequate in defining cavitation inception.

Introduction

The importance of freestream nuclei to the cavitation process has been well documented. In the mid-1960's, comparative experiments involving cavitation inception on a standard headform (Lindgren and Johnson, 1966) were conducted at many facilities around the world. Figure 1 shows some results taken from that report of cavitation number as a function of water speed at the various facilities. Cavitation number, σ is defined by

$$\sigma = \frac{P_\infty - P_v}{1/2\ \rho V_\infty^2} \tag{1}$$

where P_∞ is the freestream pressure, P_v is the vapor pressure, ρ is the density, and V_∞ is the velocity of the freestream. A large variance in the incipient cavitation number data was noted. Subsequent analysis by Johnsson (1969) and Acosta and Parkin (1970) attributed this variance primarily to viscous effects and freestream nuclei. As a direct result, many definitive experiments have been conducted that clearly demonstrate the role of viscous effects (Arakeri and Acosta, 1973 and Van der Meulen, 1976) and freestream nuclei (Kuiper, 1981; Gates and Billet, 1980; and Katz, 1981).

The impetus for much of the research in freestream nuclei-or microbubbles-has been the problem of modeling ocean conditions in man-made environments. Figure 2 shows some nuclei distributions measured in various man-made and natural surroundings. The number density distribution function is defined as the number of bubbles per unit volume in a specific band divided by the bandwidth. Significant progress has been made in developing measuring techniques that determine either the nuclei distribution or cavitation susceptibility of a liquid (Billet, 1986). This instrumentation has been used in the ocean (O'Hern et al., 1985, Shen et al., 1986; and Gowing and Shen, 1987) as well as in water tunnels. In general, a comparison of data indicates that high dissolved air contents and free air levels are needed in water tunnels to produce the same incipient cavitation number in a venturi (Shen et al., 1986) as measured at deep oceans depths. However, many questions remain as to the application of these data in the prediction and scaling of incipient cavitation number. Numerous scale effects occur when

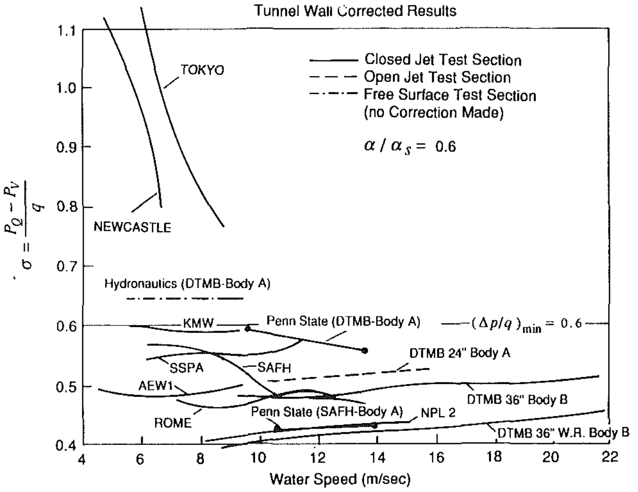

Fig. 1 Cavitation inception results on ITTC standard headform from various facilities (from Lindgren and Johnson, 1966)

Contributed by the Fluids Engineering Division for publication in the JOURNAL OF FLUIDS ENGINEERING. Manuscript received by the Fluids Engineering Division July 15, 1991. Associate Technical Editor: A. Prosperetti.

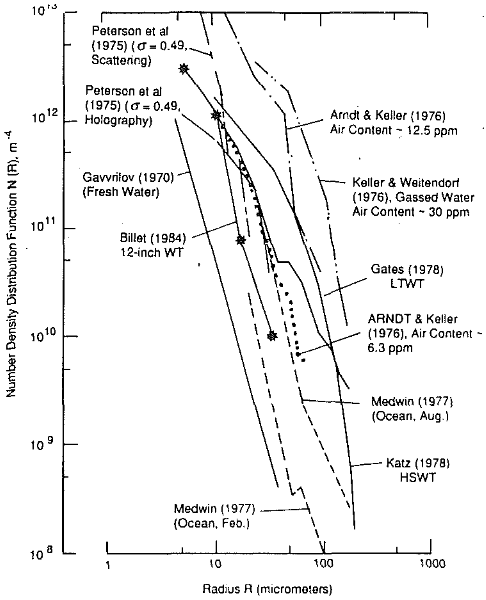

Fig. 2 Sample nuclei distributions measured in various manmade and natural surroundings

a model is tested in a water tunnel. For a discussion of the sources of these scale effects, see a paper by Billet and Holl (1979).

The importance of initial bubble sizes on traveling-bubble cavitation inception has been shown by many investigations via application of the Rayleigh-Plesset equation. The most often used criterion for relating bubble size to cavitation inception is the critical bubble diameter defined by Dergarabedian (1953). The critical diameter is the diameter at which a bubble will become statically unstable and exhibit vaporous growth for a given pressure. It is given by

$$D_{\mathrm{crit}}=\frac{8}{3}\frac{s}{P_v-P_l} \tag{2}$$

where s is the surface tension. Equation (2) is often rewritten as a function of the incipient cavitation number, σ_i, and the minimum pressure coefficient of the body, $C_{p\min}$

$$D_{\mathrm{crit}}=-\frac{8}{3}\frac{s}{1/2\rho_f V_\infty^2(\sigma_i+C_{p\min})} \tag{3}$$

where V_∞ is the freestream velocity of the flow and ρ_f is the mass density of the liquid. Pressure coefficient, C_p is defined by

$$C_p=\frac{P_l-P_\infty}{1/2\rho V_\infty^2} \tag{4}$$

The critical bubble diameter is often used as basis in determining bubble sizes necessary in seeding water tunnels. However, Eq. (3) cannot be utilized to determine the effect of bubble distributions on cavitation. Cavitation inception is a statistical process and is determined not only by the size of the cavitation bubbles but also by the number of events.

Le Goff and Lecoffre (1983) have noted that the number of cavitation events is important to scaling and have suggested a scaling relation for relative numbers of nuclei in the form

$$\frac{c_m}{c_p}=\lambda^3 \tag{5}$$

where c_m and c_p represent model and prototype concentrations, respectively, and λ is the geometrical scale ratio, i.e., prototype length to model length. Applying Eq. (5) with typical prototype concentrations, ($\approx$ 2 cm^{-3}) and typical water tunnel model scales ($\approx 1/10-1/20$th) gives water tunnel nuclei concentrations of approximately 2,000-4,000 cm^{-3}! This scaling relationship does not address the question of number of events required to define cavitation inception.

In order to address the question of nuclei distribution modeling, we must determine the importance of nuclei distribution on cavitation inception. An analytical and experimental investigation has been conducted into the statistics of traveling-bubble cavitation.

Description of the Numerical Analysis

A computer code was developed at ARL Penn State to compute the dynamics of a single bubble traveling in the flow around a Schiebe half-body. A Schiebe half-body is a nearly flat-faced axisymmetric body generated by the addition of a disk source and a uniform flow (Schiebe, 1972). It was chosen because it has demonstrated resistance to laminar separation (Gates et al., 1979) and exhibits traveling-bubble cavitation if a sufficient number of microbubbles is present in the water. The minimum pressure coefficient of the body was $C_{p\min}=-0.75$. An isobar contour map of the body is shown in Fig. 3 (from Schiebe, 1972), and its pressure distribution on the body is shown in Fig. 4. S represents the arc length along the body beginning from the axis of symmetry. R and D are the asymptotic limits of the body radius and diameter, respectively. The dynamics of the change in bubble size are determined from a solution of the Rayleigh-Plesset equation is a second-order non-linear ordinary differential equation for

Nomenclature

$\mathbf{V}$ = velocity vector
$\mathbf{g}$ = gravity acceleration vector
A_b = projected area of bubble
C_p = drag coefficient of bubble
c_m = nuclei concentration-model conditions
c_p = nuclei concentration-prototype conditions
C_p = pressure coefficient
$C_{p\min}$ = minimum pressure coefficient of a body
D = diameter
D_{crit} = critical bubble diameter
D_{eq} = equivalent spherical diameter
D_H = hemispherical major axis length
P_g = partial pressure of dissolved gas in liquid
P_l = local fluid pressure
P_v = vapor pressure
P_∞ = freestream pressure
R = radius
Re_b = bubble Reynolds number
s = surface tension
S = arc length coordinate
t = time
V_b = bubble volume
V_l = local fluid velocity
V_∞ = freestream fluid velocity
η = off-body distance
λ = geometrical scale ratio $=\dfrac{\text{prototype length}}{\text{model length}}$
σ = cavitation number
σ_i = cavitation number at inception
ρ = mass density
μ = dynamic viscosity

Subscripts

f = fluid quantity
b = bubble quantity

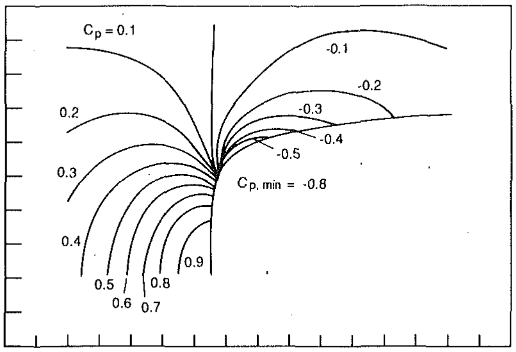

Fig. 3 Constant pressure contours for Schiebe headform with minimum pressure coefficient of −0.8 (from Schiebe, 1972)

R which governs the growth of a spherical bubble in liquid. It takes the form

$$R\ddot{R}+\frac{3}{2}\dot{R}^2=\frac{1}{\rho_f}\left(P_v-P_\infty+P_g-\frac{2s}{R}-4\mu_f\frac{\dot{R}}{R}\right) \qquad (6)$$

where R is the instantaneous bubble radius, $(\dot{\ })$ and $(\ddot{\ })$ indicate first and second time derivatives, respectively, P_v is the vapor pressure of the liquid, P_∞ is the freestream pressure of the liquid, P_g is the partial pressure of the dissolved gas, μ_f is the dynamic viscosity of the liquid, and s is the surface tension. Equation (6) is solved numerically using a predictor-corrector method. The predictor-corrector method is not self-starting; therefore, a Runge-Kutta method was used for the first several time steps.

The trajectory equation for a rigid sphere in a uniform flow was first proposed by Tchen (1947). Lumley and Corrsin (1956) improved upon Tchen's work, and later, Maxey and Riley (1983) extended the work to unsteady Stokes flow. An unsteady bubble growth term has been added from Johnson and Hsieh (1966). The momentum equation for the bubble in vector form is given by

$$\begin{aligned}\rho_b V_b\frac{d\mathbf{V}_b}{dt} &= V_b\,(\rho_b-\rho_f)\,\mathbf{g}+\rho_f\,V_b\frac{D\mathbf{V}_f}{Dt}\\ &+\frac{1}{2}\,\rho_f\,(\mathbf{V}_f-\mathbf{V}_b)\,|\mathbf{V}_f-\mathbf{V}_b|\,C_D\,A_b\\ &+\frac{1}{2}\,\rho_f\,V_b\left(\frac{D\mathbf{V}_f}{Dt}-\frac{d\mathbf{V}_b}{dt}\right)+\frac{3}{2}\,\rho_f\,V_b\,(\mathbf{V}_f-\mathbf{V}_b)\,\frac{dR/dt}{R}\\ &+6\,A_b\sqrt{\frac{\rho_f\mu_f}{\pi}}\int_0^t\frac{\dfrac{D\mathbf{V}_f}{D\tau}-\dfrac{d\mathbf{V}_b}{d\tau}}{\sqrt{t-\tau}}\,d\tau \qquad (7)\end{aligned}$$

where the subscripts f and b denote the ambient fluid and the bubble, respectively, and V_b = bubble volume = $4/3\pi R^3$. The left-hand side of Eq. (7) is the bubble mass $(\rho_b V_b)$ times its acceleration $(d\mathbf{V}_b/dt)$ and the right-hand side comprises the various force terms described below:

Term 1: Gravity force (i.e., buoyancy) which is neglected in this study.

Term 2: Force on the bubble due to pressure gradients in the flowfield.

Term 3: Drag force due to viscosity where

$$C_D=\frac{24}{Re_b}\,(1+0.197\,\mathrm{Re}_b^{0.63}+2.6\times10^{-4}\mathrm{Re}_b^{1.38}) \qquad (8)$$

where $\mathrm{Re}_b=2R\,|\mathbf{V}_f-\mathbf{V}_b|/v$ is a Reynolds number based on the relative motion between the bubble and the surrounding fluid. The expression for C_D is from Johnson and Hsieh (1966).

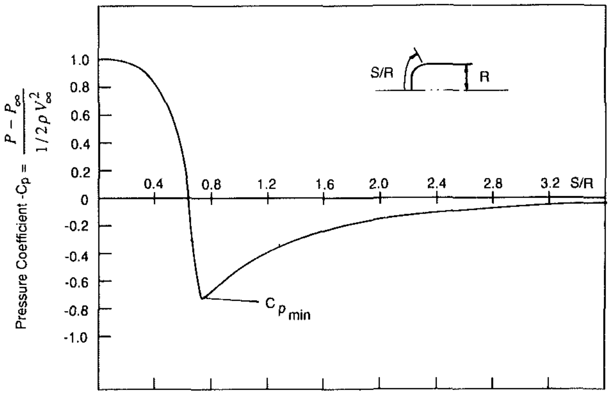

Fig. 4 Pressure distribution on the Schiebe headform

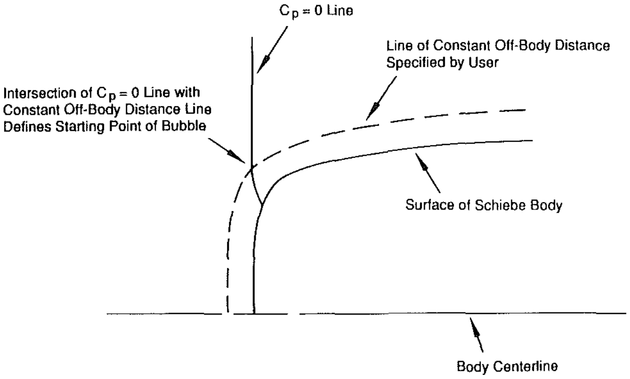

Fig. 5 Illustration of the procedure for finding the starting location of the bubble in the Rayleigh-Plesset code

Term 4: Added mass term in its conventional form which is discussed in great lengths in the literature (e.g., Panton, 1984).

Term 5: Lesser known added mass term due to the growth of the sphere found in Johnson and Hsieh (1966) and explained very well by Garrison in his review comments Holl and Kornhauser (1970).

Term 6: Basset force term discussed by Hinze (1975) and developed by Basset (1888) due to the unsteady disturbance of the streamlines introduced by a particle moving through an otherwise steady flowfield with a relative difference in velocities. The Basset force term was solved via an algebraic transformation developed by Hoffman (1988). Because at every time step the Basset term required integrating over every previous time step, the computational time was significantly increased by the presence of this term. An analysis of its relative effect showed that in the region of strong pressure gradients around the body, its effect was negligible; therefore, it was subsequently neglected.

In addition, it was found that if the bubble was started in the freestream ahead of the body, then the majority of the computational time was taken up just to get the bubble to the low pressure region of the body. Thus, an alternative method of starting the bubble was devised. The bubble was "released" at the point where the local pressure coefficient was equal to zero along the specified off-body distance. Figure 5 illustrates this procedure. The initial translational velocity of the bubble was zero; however, it was found that within a few steps, the bubble had assumed nearly the velocity of the surrounding flow. The bubble response was found to be insensitive to the

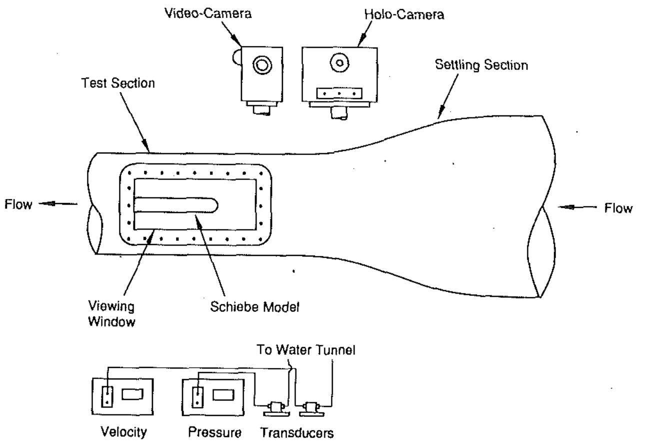

Fig. 6 Schematic of the experimental setup

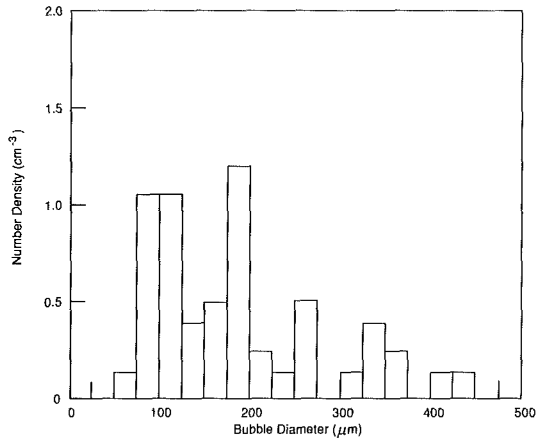

Fig. 7 Freestream microbubble distribution for 9.1*m/s* velocity condition in a seeded flow

initial bubble wall velocity, so the parameter $\dot{R} = 0$ was used in every case. The implication of this start-up procedure was that the nuclei distribution at the $C_p = 0$ point on the body was the same as that of the freestream. This ignores any natural selection effects where bubbles above a certain size are pushed away from the body due to pressure gradients. This is demonstrated in Johnson and Hsieh (1966).

The input parameters for the computer code included water temperature to define fluid properties (20°C in every case), cavitation number, body geometry, and initial bubble parameters, i.e., size, initial location relative to the body, and the first time derivative of the bubble radius (i.e., bubble wall velocity). The code then marched in time and bubble parameters (position, velocity, radius, etc.) were calculated at every time step.

The following approximations were necessary in the computer code:

1. No boundary layers
2. The bubble experiences a uniform pressure distribution in the flowfield (i.e., the bubble is approximated to be a point)
3. All bubbles remain spherical
4. No bubble-to-bubble interactions
5. Growing bubbles do not perturb the pressure field

The first approximation is justified by the fact that no separation occurs on the Schiebe headform and, due to the favorable pressure gradient along the initial portion of the body, boundary layers remain very thin. The second approximation is valid as long as the bubble is very small compared to the characteristic region of the flowfield near the body. This may indeed become violated at some point, however, only when the bubble becomes very large. This leads to the third approximation. Studies (e.g., Kang and Leal, 1988) indicate that large bubbles will break apart in a turbulent shear flow. Also, as will be discussed later, in reality, bubbles on the body display a hemispherical shape rather than a purely spherical shape (Brennen and Ceccio, 1989). In the fourth approximation, for cavitation inception, bubbles are not so closely spaced that multi-bubble interactions are significant as in Chahine (1991); therefore, they are not considered. Finally, the expanding bubbles are assumed not to influence the pressure field around the body. Despite these limitations, the results from this computer simulation still prove useful in showing the general relationship between nuclei distribution and cavitation inception.

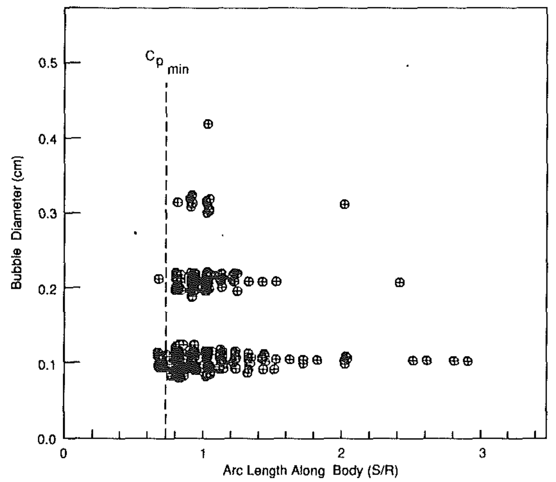

Fig. 8 Cavitation bubbles observed on a 5.08 cm diameter Schiebe headform for 9.1 *m/s* velocity condition in a seeded flow at a cavitation number of 0.552

Description and Results of the Experiment

An experiment was conducted in the 30.48 cm water tunnel of ARL Penn State in which the flow over a 5.08 cm diameter Schiebe nose was seeded with microbubbles. With the tunnel operating at a constant velocity, 9.1 m/s, the pressure was lowered until cavitation inception occurred on the headform. The freestream microbubble distribution was then recorded with holography and the cavitation on the headform was recorded with a video camera. The headform is of the same type as that used in the numerical analysis with $C_{p\text{min}} = -0.75$ in a 30.48 cm water tunnel. A schematic of the experimental setup is shown in Fig. 6. Several conditions were recorded and from those a single representative case was chosen. The tunnel velocity in this case was 9.1 m/s and the incipient cavitation number was 0.552. The nuclei distribution as determined by holography is shown in Fig. 7. The flow was artificially seeded with bubbles in this experiment by pumping an aerated water mixture into the flow upstream of the body. The air content of the water was kept as low as possible to reduce the number of ambient nuclei. The resulting cavitation data for this case are shown in Fig. 8. Each datum represents one bubble as viewed from the videotape and is plotted as an equivalent spherical diameter. The equivalent spherical diameter was calculated from the observed shape that the bubbles on the body display (as found in this study and a similar one by Brennen and Ceccio, 1989) by the following relation

$$D_{\text{eq}} = \left(\frac{1}{2}\right)^{1/3} D_H \tag{9}$$

where D_{eq} is the equivalent spherical diameter, and D_H is the major axis length of the hemisphere. The total time interval

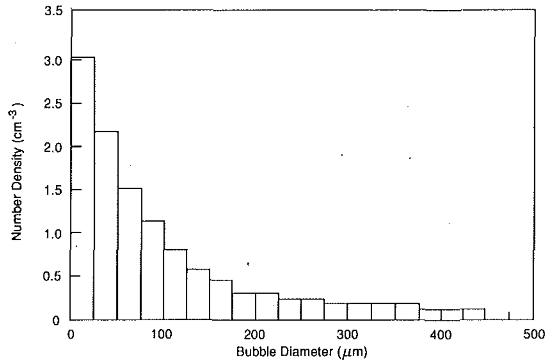

Fig. 9 Arbitrary nuclei distribution weighted toward smaller bubbles

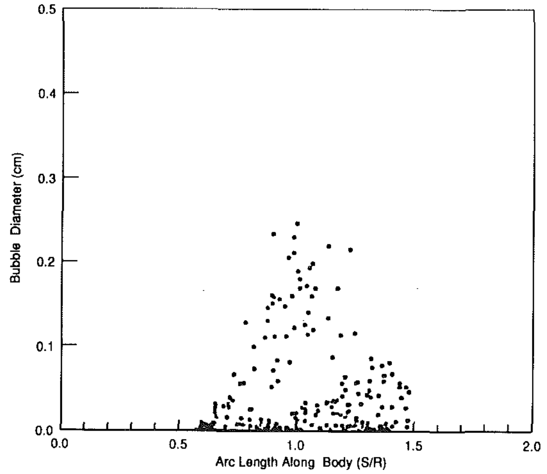

Fig. 10 Results of simulation for distribution weighted toward smaller bubbles for 5.08 cm diameter Schiebe headform at 9.1 m/s and a cavitation number of 0.552

for the bubbles shown in Fig. 8 was eight seconds. The resolution of the videotape was limited so it was necessary to coarsely discretize the data. Where there appear to be large numbers of points at slightly different locations, these are actually points that lie on top of one another and were moved slightly for the purpose of displaying them on the graph. The total number of bubbles on the plot is 379. In addition, some bubbles were observed downstream of the cavitation region. This is due to either rebounding cavitation bubbles or large freestream bubbles.

The purpose of the experimental portion of this investigation was to demonstrate that traveling bubble cavitation does show a sensitivity to microbubble distribution. A numerical analysis is now required to couple the experimental data and to provide guidance as to a definition of cavitation inception. Additional experimental results can be found in Meyer (1989).

Numerical Results

Monte Carlo Simulation of Cavitation. A procedure was developed for simulating cavitation on a headform given a known nuclei distribution. In an actual experiment, multiple random processes exist; therefore, in order for the simulation to be accurate, each had to be replicated. This type of simulation is known as a Monte Carlo simulation. The steps in the simulation are as follows:

1. A nuclei size distribution was specified and an ensemble of bubbles was generated accordingly. The total number of bubbles was typically in the range of 150-200.

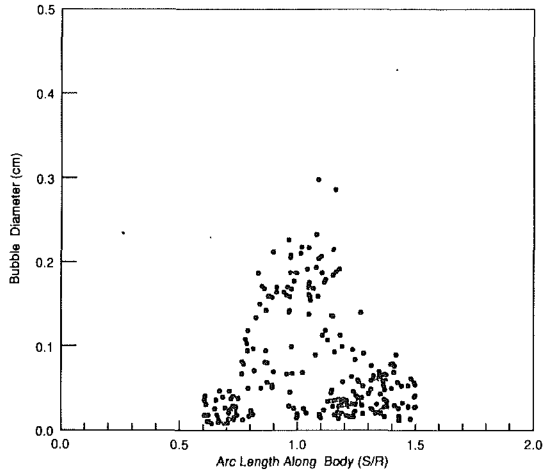

Fig. 11 Results of simulation with the same nuclei distribution as experiment for 5.08 cm diameter Schiebe headform at 9.1 m/s and a cavitation number of 0.552

2. For each bubble, an off-body distance was chosen randomly between zero and the maximum distance that would permit the bubble to exhibit growth. The probability density function (PDF) was assumed to be uniform (i.e., an equal probability exists of finding the bubble at any particular off-body distance).
3. The manner in which the strobe light captures the bubbles was modeled. Under continuous lighting, it is impossible for the eye to resolve discrete bubbles. A pulsed lighting source is necessary in an experiment in order for inception to be determined visually. The strobe rate necessary for the video system used in this investigation was 60 flashes per second. The bubble transport time is much faster than the 1/60 of a second between flashes; consequently, each bubble may appear on only a single frame of the videotape. Moreover, there is no guarantee that the bubble will be at its maximum diameter when it appears. There is an equal probability of the bubble being observed anywhere along its trajectory. The simulation modeled this random process the same way. Each bubble was observed only once, and the position at which it was observed was chosen randomly according to a uniform PDF.

The first Monte Carlo simulation modeled an arbitrary distribution weighted toward smaller bubbles, whose numbers decreased in approximately an inverse-square relation with size. This is illustrated in Fig. 9. The smallest bubbles were 10 μm in diameter and the largest were 450 μm. The code was executed for each bubble in the distribution with its appropriate random parameters. The results of the simulation are shown in Fig. 10. The majority of the bubbles are grouped at the bottom of the plot below about 500 μm in diameter. These bubbles are too small to be considered as cavitation bubbles. The final case for the Monte Carlo simulation was a nuclei distribution similar to the one obtained in the experiment. This distribution was shown earlier in Fig. 7. The results for this simulation are shown in Fig. 11. These results were compared to the actual cavitation data shown in Fig. 8. One of the major differences between the actual data and the simulation was the large number of bubbles at S/R locations greater than about 1.5. In a sample calculation, bubbles ranging in size from 50 μm to 450 μm were allowed to travel along a 5.08 cm diameter body. The results are shown in Fig. 12. The calculation shows that bubbles observed on the videotape far downstream were not likely to have been cavitation bubbles-even from very large nuclei. The authors attribute these to three possibilities: 1) rebounded bubbles, which the Rayleigh-Plesset code does not account for due to computational time limits, 2) large bubbles

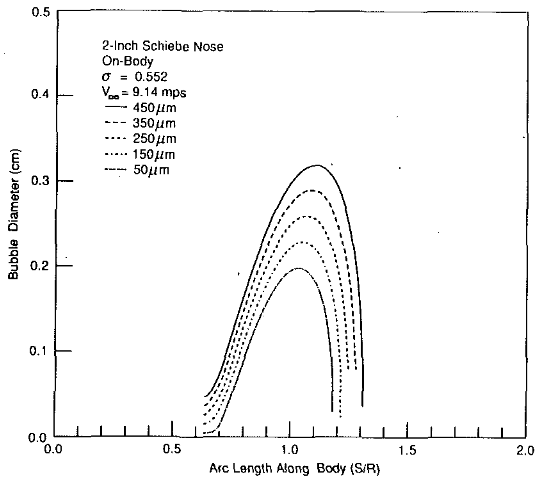

Fig. 12 Diameter of cavitation bubbles on a 5.08 cm Schiebe headform as a function of arc length for various initial sizes

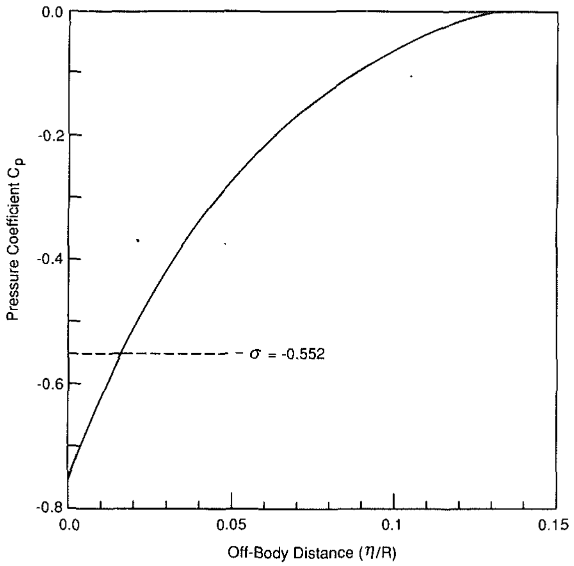

Fig. 13 Pressure coefficient as a function of Off-body distance for Schiebe half-body with minimum pressure coefficient of −0.75

Table 1 Tabulated summary of bubble size for simulations with same input conditions as experiment

Case	Percentage of Bubbles in Size Range		
	500-1500 μm	501-2500 μm	> 2500 μm
Actual Data	57	38	5
Simulation 1	63	42	1
Simulation 2	59	39	2
Simulation 3	55	42	3
Simulation 4	61	38	1

in the freestream mistaken for cavitation bubbles, and 3) highly distorted bubble shapes on the body surface which appear to be very large if assumed to be hemispherical. For purposes of comparing the experimental results to the Monte Carlo simulation, these questionable bubbles were ignored. The other difference in appearance between the experiment and the simulation was that the experimental data is banded into discrete bins, whereas the simulation results have not been banded. To compare the two, it is necessary to discretize the simulation results. The bubble sizes were grouped into size bins and the results are tabulated in Table. 1. The simulation was conducted four times with different random numbers each time and the results looked similar. This indicates that the ensemble was sufficiently large for repeatability. Bubbles below 500 μm were ignored as before. The remaining bubbles were divided into three bins: 0.51-1.52 mm, 1.52-2.54 mm, and greater than 2.54 mm. The numbers show good agreement in the two smaller bands. The largest band shows slightly more bubbles in the experimental data; however, these numbers in the largest band are all too low to be statistically significant. The ensemble size would have to increase by an order of magnitude which would have been prohibitive due to computer time restrictions. In addition, the initial microbubble distribution was determined from analysis of holographic data, and the number density accuracy for the largest size is low due to the comparably small water sample size. Overall, the numerical results match the experiment very well. One of the limitations in the study of cavitation has been the lack of a quantitative method to define inception. It is difficult to determine whether or not the Monte Carlo simulation results accurately model inception in an experimental situation because of the subjectiveness of the experiment.

Off-Body Effect on Critical Bubble Diameter. In the previous section, one of the random variables in the Monte Carlo process was offbody distance. It was found to be perhaps the single most important factor in determining whether or not a given bubble would cavitate. Shen and Dimotakis (1989) also showed that bubble growth was very sensitive to off-body position on a two-dimensional hydrofoil. The reason for this is the variation in the pressure field around the body. This particular body has a very low minimum pressure coefficient on the body; however, it relaxes very steeply as one moves away from the body. This was previously illustrated in Fig. 3, which shows constant C_p contours in the field around a Schiebe body with a minimum pressure coefficient of -0.8-nearly identical to the body used in this investigation. Schiebe's solution, as well as the body used in this investigation, relied on potential flow theory. As previously mentioned, it has been demonstrated by Gates et al. (1979) that no laminar separation occurs on the body. If pressure coefficient is plotted as a function of off-body distance-defined on a line normal to the body surface-as it is in Fig. 13, we see that at a distance of approximately 0.013 body radii, the C_p is equal to the negative of the cavitation number-implying $P_v = P_l$. For the given cavitation number, $\sigma = 0.552$, any bubble must travel closer to the body than 0.013 body radii in order to cavitate. Even when this condition is met, the bubble must still meet the critical bubble size criterion given by Eq. (2). In Fig. 14, the critical bubble diameter is plotted as a function of off-body distance at a value $\sigma = 0.552$. If we reason that there is an even probability of finding a given bubble anywhere in the flow, we find that there is very little chance of any given bubble traveling directly on the body. The traditional definition of critical bubble diameter is based on the minimum pressure coefficient of the body. The consequence of off-body effect is that there is virtually no chance of a bubble of the critical diameter cavitating. It is, therefore, necessary to define a critical bubble diameter based on something other $C_{p\min}$ for the purpose of seeding water tunnel flows to model cavitation inception. This new critical bubble diameter can be obtained from a statistical analysis of the initial bubble distribution and a definition of cavitation inception.

Effect of Model Size on Bubble Growth. Solutions were calculated for spherical bubbles traveling along a 5.08 cm diameter body for various initial sizes. The deviation of the bubbles from sphericity is ignored in this case although it has been clearly demonstrated that this case is unrealistic. Since this investigation is only a first-order approximation, some complicated effects are beyond its scope. The incipient cavitation number was fixed at a value determined in the experi-

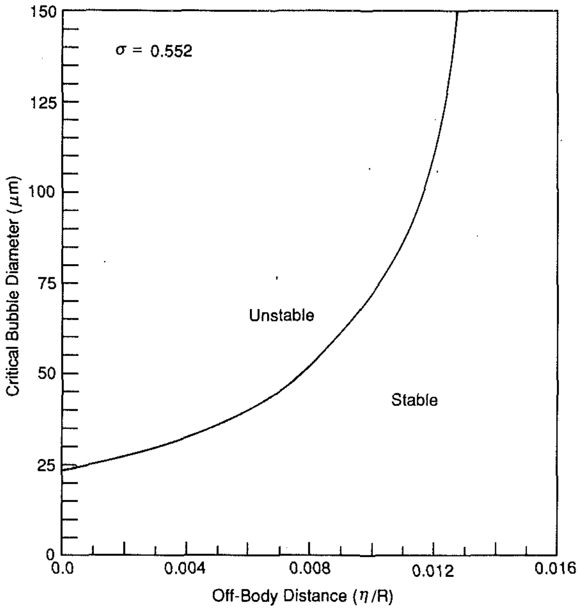

Fig. 14 Critical bubble diameter as a function of off-body distance for Schiebe half-body with minimum pressure coefficient of −0.75

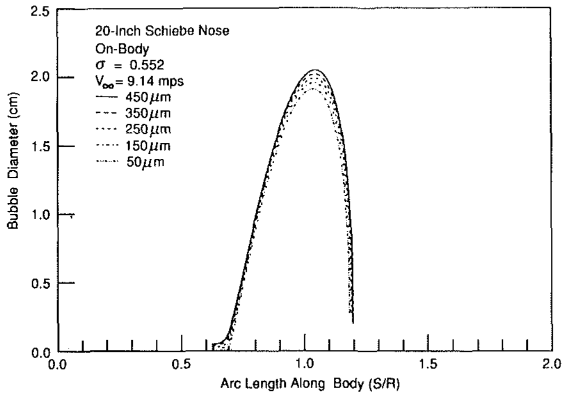

Fig. 15 Diameter of cavitating bubbles on a 50.8 cm Schiebe headform as a function of arc length for various initial sizes

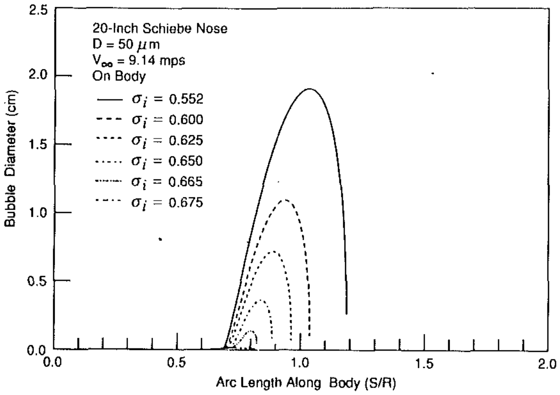

Fig. 16 Exploded view of maximum diameter of cavitating bubbles on a 50.8 cm Schiebe headform with various initial sizes

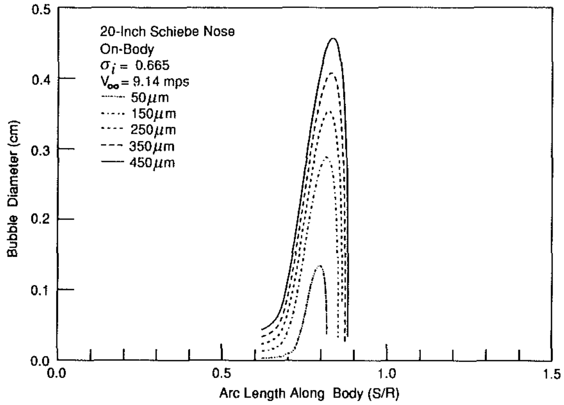

Fig. 17 Bubble diameter as a function of arc length at various cavitation numbers for a 50.8 cm Schiebe Nose and a 50 μm bubble

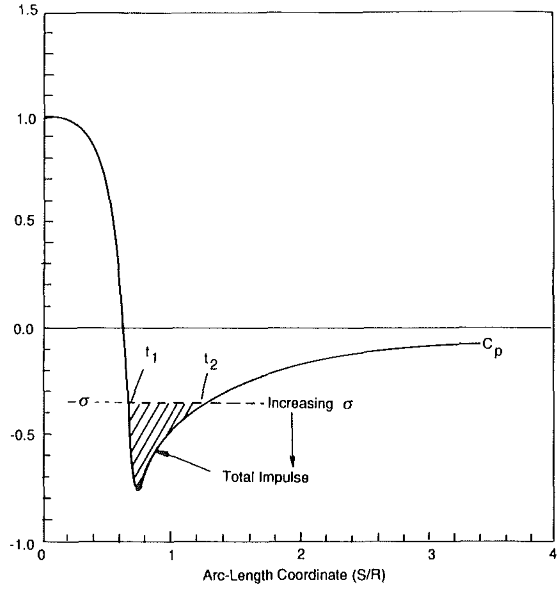

Fig. 18 Illustration of bubble impulse using the pressure distribution over a Schiebe headform

ment with the 5.08 cm nose. Bubbles ranging in size from 50 μm to 450 μm were allowed to travel along the body. For the 5.08 cm case, the results were shown previously in Fig. 12. In order to demonstrate the effect of scale, the analysis was repeated for a similar 50.8 cm Schiebe headform at the same flow conditions. Figure 15 shows these results. The bubbles grow to nearly 2.5 cm in diameter and the effect of nuclei size seems to be less pronounced for the larger diameter. Upon closer inspection, we see approximately the same absolute difference in maximum diameter as a function of initial diameter. However, it might be argued that this condition with the 50.8 cm nose is not representative of cavitation inception, and the cavitation number should be increased until the same size bubbles appear as in the 5.08 cm case. Applying this reasoning, the cavitation number was systematically increased and the bubble response was plotted in Fig. 16. The initial size was fixed at 50 μm because this was the minimum size that was studied in this investigation. A maximum diameter of 1270 μm was again chosen as the criterion for cavitation. In Fig. 16, it is shown that this condition is satisfied with a cavitation number of about 0.665. The analysis then repeated for the same range of bubble sizes as before with a cavitation number of 0.665 on the 50.8 cm body. These results were plotted in Fig. 17. In these results, we see the dependence on initial nuclei size, i.e., the larger nuclei still grow to a larger maximum diameter. This result indicates that initial size is still an important parameter even at large scales. A simple explanation of this can be noted by considering the bubble impulse function, defined by

$$I = \int_{t_1}^{t_2} (P_v - P_l)\, dt \tag{10}$$

where t_1 and t_2 bound the region where $P_v - P_l > 0$. This is illustrated in Fig. 18. The total amount of impulse is analogous to the hatched region. The maximum diameter of any cavitating bubble of a given initial size is approximately a function of the total impulse the bubble experiences. By increasing the size of the model, one is increasing the bubble impulse. This explains why the bubble grows so much larger by just increasing the model size. To get the same size cavitation bubble, as with a smaller body, the amount of impulse must be the same. Thus, the cavitation number must differ.

Conclusions

The following conclusions are to be made from this investigation: 1) Traveling bubble cavitation is very sensitive to nuclei size. 2) Critical bubble diameter based on the minimum pressure coefficient is not representative of the size of bubble necessary in modeling distributions and seeding water tunnels. Results show that much larger bubbles are necessary because of the off-body pressure gradients. 3) There is a need for a set of quantitative criteria in defining inception in order to correlate nuclei spectra to cavitation inception. 4) The bubble impulse function is useful in scaling cavitation number between model and prototype.

Acknowledgments

This investigation was supported by the E/F program of the Applied Research Laboratory of Penn State University.

References

Acosta, A. J. and Parkin, B. R., 1970, "Cavitation Inception-A Selective Review," *Proceedings of the 17th ATTC.*

Arakeri, V. J., and Acosta, A. J., 1973, "Viscous Effects in Inception of Cavitation on Axiymmetric Bodies," ASME JOURNAL OF FLUIDS ENGINEERING, Vol. 95, No. 4, pp. 519-527.

Basset, A. B., 1988, *Treatise on Hydrodynamics*, Deighton Bell, London, Vol. 2, Chapter 22, pp. 285-297.

Billet, M. L., and Holl, J. W., 1988, *Scale Effects on Various Types of Limited Cavitation*," ASME International Symposium on Cavitation Inception, pp. 11-24.

Billet, M. L., 1986, "The Importance and Measurement of Cavitation Nuclei," *Advancements in Aerodynamics, Fluid Mechanics, and Hydraulics*, American Society of Civil Engineers, pp. 967-988.

Brennen, C. E., and Ceccio, S. L., 1989, "Recent Observations on Cavitation and Cavitation Noise," *Proceedings of the Third Symposium on Cavitation Noise*, ASME Winter Annual Meeting, San Francisco, CA, pp. 67-78.

Chahine, G. L., Duraiswami, R., and Lakshminarasimha, A. N., 1991, "Dynamical Interactions in a Bubble Cloud," Proceedings of the 26th Cavitation and Multiphase Flow Forum, ASME-JSME Fluids Engineering Conference, Portland, Oregon, pp. 49-54.

Corrsin, S., and Lumley, J. L., "On the Equation of Motion for a Particle in a Turbulent Fluid," *Applications of Scientific Research*, Vol. A6, pp. 114-116.

Dergarabedian, P., 1953, "The Rate of Growth of Vapor Bubbles in Superheated Water," ASME *Journal of Applied Mechanics*, Vol. 20, No. 4, Dec., pp. 537-545.

Gates, E. M., Billet, M. L., Katz, J., Ooi, K. K., Holl, J. W., Acosta, A. J., 1979, "Cavitation Inception and Nuclei Distribution-Joint ARL/CIT Experiments," California Institute of Technology, Division of Engineering and Applied Science, Report No. E244.1.

Gates, E. M., and Billet, M. L., 1980, "Cavitation Nuclei and Inception," *Proceedings of the International Association for Hydraulic Research Symposium*, Vol. 1, Tokyo, Japan, pp. 3-26.

Gowing, S., and Shen, Y. T., 1987, "Cavitation Susceptibilities in Ocean Waters," David Taylor Research Center Report DTNSRDC-SHD-1241-01, Aug.

Hinze, J. O., 1975, *Turbulence*, McGraw-Hill, New York, pp. 463-464.

Hoffman, G. H., 1988, "The Trajectory of Gas Bubbles in an Axisymmetric Turbulent Boundary Layer," ARL Penn State Technical Memorandum, File No. TM88-136.

Holl, J. W., and Kornhauser, A. L., 1970 "Thermodynamic Effects on Desinent Cavitation on Hemispherical Nosed Bodies in Water at Temperatures from 80 deg F to 260 deg F," ASME *Journal of Basic Engineering*, Vol. 92D, No. 1, pp. 44-58.

Johnson, V. E., Hsieh, T., 1966, "The Influence of the Trajectories of Gas Nuclei on Cavitation Inception," *Sixth Naval Hydrodynamics Symposium*, pp. 163-182.

Johnsson, C. A., 1969, "Cavitation Inception on Headforms, Further Tests," 12th ITTC, Rome, Italy, pp. 381-392.

Kang, I. S., and Leal, L. G., 1988, "Small-Amplitude Perturbations of Shape for a Nearly Spherical Bubble in an Inviscid Straining Flow (Steady Shapes and Oscillatory Motion)," *Journal of Fluid Mechanics*, Vol. 187, pp. 231-266.

Katz, J., 1981, "Cavitation Inception in Separated Flow," California Institute of Technology, Report No. Eng. 183-5.

Kuiper, G., 1976, "Cavitation Inception on Ship Propeller Models," Ph.D. dissertation, Netherlands Ship Model Basin, Wageningen, The Netherlands.

Le Goff, J., and Lecoffre, Y., 1983, "Nuclei and Cavitation," *Fourteenth Symposium on Naval Hydrodynamics*, pp. 215-243.

Lindgren, H., and Johnsson, C. A., 1966, "Cavitation Inception on Headforms-ITTC Comparative Experiments," Publication of the Swedish State Shipbuilding Experimental Tank, No. 58.

Maxey, M. R., Riley, J. J., "Equation of Motion for a Small Rigid Sphere in a Nonuniform Flow," *Physics of Fluids*, Vol. 26, No. 4, pp. 883-889.

Meyer, R. S., 1989, "An Investigation of the Relation Between Free-Stream Nuclei and Traveling-Bubble Cavitation," M.S. thesis, The Pennsylvania State University.

O'Hern, T. J., Katz, J., and Acosta, A. J., 1985, "Holographic Measurements of Nuclei in the Sea," *Cavitation and Multiphase Flow Forum*, ASME, Albuquerque, NM, pp. 39-42.

Panton, R. L, 1984, *Incompressible Flow*, John Wiley, pp. 554-559.

Schiebe, F. R., 1972, "Measurement of the Cavitation Susceptibility of Water Using Standard Bodies," Report No. 118, St. Anthony Falls Hydraulic Laboratory, University of Minnesota.

Shen, Y. T., and Dimotakis, P. E., 1989, "Viscous and Nuclei Effects on Hydrodynamic Loadings and Cavitation of a NACA 66 (MOD) Foil Section," ASME *Journal of Fluids Engineering*, Vol. 111, No. 3, pp. 306-316.

Shen, Y. T., Gowing, S., and Eckstein, B., 1986, "Cavitation Susceptibility Measurements of Ocean, Lake, and Laboratory Waters, David Taylor Research Center Report No. 86/019.

Tchen, C. M., 1947, PhD. thesis, Delft Martinus Nijhoff, the Hague.

Van der Meulen, J. H. J., 1976, "A Holographic Study of Cavitation on Axisymmetric Bodies and the Influence of Polymer Additives," Publication No. 509, Netherlands Ship Model Basin, Wageningen, The Netherlands.

Georges L. Chahine[1]

Ramani Duraiswami

DYNAFLOW, Inc.,
Fulton, MD 20759

Dynamical Interactions in a Multi-Bubble Cloud

Results of studies on the dynamics of "clouds" of bubbles via both an analytical technique using asymptotic expansions, and via numerical simulation using a three-dimensional boundary element technique (BEM) are reported. The asymptotic method relies on the assumption that the characteristic bubble size is much smaller than the characteristic inter-bubble distance. Results obtained from the two methods are compared, and are found to agree in the domain of validity of the asymptotic technique, which is for very low void fractions. Next, results of several numerical experiments conducted using the BEM algorithm are reported. The results indicate the influence of the mutual interaction on the dynamics of multiple bubble clouds.

1 Introduction

Practical liquid flows contain many microscopic bubbles which respond dynamically to the flow. These bubbles can grow explosively and collapse, leading to cavitation and all its deleterious effects (Plesset and Prosperetti 1977, Blake and Gibson, 1987). These bubbles seldom occur singly, and their mutual interaction is likely to play an important part in the fluid dynamics. However, most previous studies consider only the problem of single bubbles (including only spherical or axisymmetric deformations in their models), or consider highly simplified models of multiple bubble interactions. To study cavitation in practical flows one needs to be able to properly model these interactions. Mathematically the problem is a difficult one, as it is intrinsically three-dimensional, and involves multiple free surfaces (with the associated nonlinearity). Purely analytical progress into the problem is clearly out of reach presently.

Van Wijngaarden (1968, 1972) proposed a set of heuristic effective equations for bubbly liquids. These equations are space averaged, and the system is closed by prescribing the dynamics of individual bubbles to be governed by the Rayleigh-Plesset equation. These equations were shown to hold rigorously for the propagation of acoustic waves in bubbly liquids, in the limit of dilute bubble volume fraction by Caflisch et al., (1985). Commander and Prosperetti (1989) and Lu et al., (1990) have exploited these equations to describe the acoustical properties of bubbly liquids and bubble clouds. Using a similar model but including the effects of slip and allowing for larger volume fractions, d'Agostino and Brennen (1988, 1989) studied the dynamics of a spherical bubble cloud. Omta (1988) also studied the spherical bubble cloud. All these studies were devoted to the solution of linearized versions of the equations.

Our studies into the subject of bubble clouds have proceeded along two different paths. In the first, (Chahine, 1982b, Chahine, 1983; Chahine, 1991) an asymptotic approach was employed, using the assumption that the characteristic inter-bubble distance was large compared to the characteristic bubble size. Solutions valid to the third order in this parameter were obtained. Our more recent efforts have been devoted to the development of a completely three-dimensional boundary element method capable of handling multiple free-surfaces, and rigid surfaces and particles. A computer program (3DynaFS) implementing the method has been developed. It has been applied to problems involving single bubbles in a variety of configurations, and more recently to problems involving several bubbles, or where the bubbles are in either a shear flow (Chahine, 1990b) or in the flow field of a Rankine vortex (Chahine, 1990a).

In this paper we present some preliminary results from numerical experiments with the code 3DynaFS. We study a number of flows involving a few bubbles, with particular emphasis on the effects of various parameters on bubble growth and collapse. Additionally the "exact" numerical solutions from the boundary element technique are used to obtain a domain of validity for the asymptotic studies.

2 Mathematical Formulation

Consider an incompressible liquid in an infinite domain (this restriction can be relaxed to allow rigid boundaries or other free surfaces within the domain). Distributed in this liquid are N bubbles, numbered $1, \ldots N$. Since we shall be concerned with cavitation bubbles where relatively large wall velocities are involved, viscosity has no appreciable effect on the dynamics of the bubble. Additionally, we restrict the case to flows where the Mach number is small enough so that the incompressibility assumption holds. (We are currently working to relax this assumption). These two assumptions are classical in cavitation bubble studies, and with suitable initial conditions the flow is irrotational. Following standard procedure we introduce a velocity potential ϕ, in terms of which the conservation laws in the liquid may be stated in the form

---

[1] Also Research Professor, Department of Mechanical Engineering, The Johns Hopkins University, Baltimore, MD 21218.

Contributed by the Fluids Engineering Division for publication in the JOURNAL OF FLUIDS ENGINEERING. Manuscript received by the Fluids Engineering Division April 9, 1991. Associate Technical Editor: F. T. Dodge.

$$\nabla^2\phi = 0 \tag{1}$$

and

$$P + \rho\left(\frac{\partial\phi}{\partial t} + \frac{1}{2}\,|\nabla\phi|^2\right) = \text{constant}, \tag{2}$$

where P is the pressure. Here (2) is the Bernoulli integral of the momentum equation at time t. We shall study the reaction of this system to a prescribed pressure field at infinity, $P_\infty(t)$. These equations are subject to initial conditions for the potential, and boundary conditions on the surfaces of the bubbles (and on any rigid surfaces in the domain). At all boundaries we impose the condition that the surface is a material surface and moves with the flow, so that

$$\mathbf{n}\cdot\nabla\phi = \mathbf{n}\cdot\mathbf{V}_s, \tag{3}$$

where $\mathbf{V}_s$ is the velocity of the surface, and $\mathbf{n}$ is the local unit vector normal to the surface. In addition on the surface of the bubble we must balance the normal stresses in the liquid and the gas. The bubble is assumed to contain both noncondensible gas and vapor. Within the bubble the pressure is assumed not to vary spatially, and to be given by the sum of the partial pressures of the noncondensible gas, P_g, and that of the vapor, P_v. Vaporization of the liquid is assumed to occur at a fast enough rate so that the vapor pressure can be assumed constant throughout the simulation and equal to the equilibrium vapor pressure at the liquid ambient temperature. Since time scales associated with gas diffusion are much larger than those of interest, the amount of noncondensible gas inside the bubbles is assumed to remain constant. This gas is assumed to satisfy the polytropic relation, $P\mathcal{V}^k = constant$, where $\mathcal{V}$ is the bubble volume, and k the polytropic index, with $k=1$ representing isothermal behavior and $k = C_p/C_v$ adiabatic behavior. With these assumptions the condition of normal stress balance, at any time t, on any point $\mathbf{x}_S$ on the surface, may be stated as

$$P_L(\mathbf{x}_S,\, t) = P_v + P_{g0}\left(\frac{\mathcal{V}_0}{\mathcal{V}(t)}\right)^k - \sigma\mathcal{C}(\mathbf{x}_S,\, t), \tag{4}$$

where P_L is the liquid pressure at the bubble wall, P_{g0} and $\mathcal{V}_0$ are the initial gas pressure and volume respectively, σ is the surface tension coefficient, $\mathcal{C}$ the local curvature of the bubble, and $\mathcal{V}$ the instantaneous value of the bubble volume. Here P_{g0} and $\mathcal{V}_0$ are known quantities at $t=0$. The curvature of the bubble can be computed using the relation $\mathcal{C} = \nabla\cdot\mathbf{n}$. The pressure at the bubble surfaces can be related to the potential using Bernoulli's equation, to give

$$\rho\left[\frac{\partial\phi}{\partial t} + \frac{1}{2}\,|\nabla\phi|^2\right]_S = P_\infty(t) - P_v - P_{g0}\left(\frac{\mathcal{V}_0}{\mathcal{V}}\right)^k + \sigma\nabla\cdot\mathbf{n}. \tag{5}$$

On any moving rigid surface, we need an equation similar to (5) relating the velocity of the surface to the pressure. Equations (1)-(5), along with prescribed initial conditions, form a complete system of equations for the variables ϕ, $\mathbf{x}_S$, P_L, and determine the location and geometry of the bubbles and the pressure and velocity in the domain. The two methods used to solve this nonlinear problem are described briefly in what follows. For more complete descriptions see Chahine (1983), Chahine and Perdue (1989) and Chahine et al., (1989).

Boundary Element Solution. The boundary element method (BEM) uses Green's identity to solve Laplace's equation. If the velocity potential, ϕ (or its normal derivative, $\partial\phi/\partial n$) is known on the boundaries of the domain, and ϕ satisfies the Laplace equation, then ϕ can be determined anywhere in the domain of the fluid using the identity:

$$\int_S\left[-\frac{\partial\phi(\mathbf{y})}{\partial n_y}\,\frac{1}{|\mathbf{x}-\mathbf{y}|} + \phi(\mathbf{y})\,\frac{\partial}{\partial n_y}\left(\frac{1}{|\mathbf{x}-\mathbf{y}|}\right)\right]dS_y = a\pi\phi(\mathbf{x}). \tag{6}$$

We first select $\mathbf{x}$ on the boundary to determine $\partial\phi/\partial n$ (or ϕ) on the boundary, and then using the known values on the boundary determine ϕ at the required point in the domain. Here $a\pi = \Omega$ is the solid angle under which the point $\mathbf{x}$ sees the fluid, with

$a=4$ if $\mathbf{x}$ is a point in the fluid
$a=2$ if $\mathbf{x}$ is a point on a smooth surface
$a<4$ if $\mathbf{x}$ is a point at a sharp corner on the boundary.

The advantage of this representation is that it reduces the dimension of the problem by one. If the point $\mathbf{x}$ is selected to be on the boundary of the fluid domain (a bubble surface or on any other boundary), then a closed system of equations can be obtained and used at each time step to solve for values of $\partial\phi/\partial n$ (or ϕ). The points on the moving boundaries (bubble surfaces) are advanced in a Lagrangian fashion using the calculated velocities, while the potential at the subsequent times is obtained by integrating (5).

To solve (6) numerically, we discretize the bubble surfaces as well as other boundaries into panels. A local linear basis for ϕ and $\partial\phi/\partial n$ is assumed over each panel. Integration in performed over each panel, and the results summed up to complete the integration over the complete boundary. The initially spherical bubble is discretized into a geodesic shape using flat, triangular panels. Equation (6) then becomes a set of M linear equations (M is the total number of discretization nodes) of index i of the type:

$$\sum_{j=1}^{M}\left(A_{ij}\cdot\frac{\partial\phi_j}{\partial n}\right) = \sum_{j=1}^{M}(B_{ij}\cdot\phi_j) - a\pi\phi_i, \tag{7}$$

where A_{ij} and B_{ij} are elements of matrices which are the discrete equivalent of the integral operators given in Eq. (6). Details of the calculation of these matrices, of the geometrical quantities needed (normal, curvature, volume), the other physical variables (tangential and normal velocities, pressure), and the time integration scheme can be found in Chahine and Perdue (1989) and Chahine et al., (1989). The time stepping is based on a simple explicit Euler time stepping scheme, with the time step δt at each step determined adaptively by the following prescription:

$$\delta t = a\frac{l_{\min}}{V_{\max}},$$

where $l_{\min}$ is the minimum length of a panel side and $V_{\max}$ the magnitude of the maximum node velocity at the current step, while a is a constant, in the range $0.001-0.05$, with the smaller numbers being used when the spatial discretization is more coarse. This choice of the time step has the great advantage of being simple, and adaptive. The time step is refined when the velocity gets higher (toward the end of the collapse) and increased during the period of slow bubble size variation. In our experience this choice also reduces potential problems of surface folding due to numerical instabilities during the latest stages of bubble collapse. During the phase where the bubble attains a maximum size and where velocities are very small, a limit on the maximum time step size is imposed. In the present computations this value was $T_{Rayleigh}/1000$, where $T_{Rayleigh}$ is the Rayleigh time scale. More complicated implicit schemes could perhaps be tried, but would have the disadvantage of requiring multiple iterative solutions of the linear system at each time step. Results of the validation of this code may be found in Chahine et al., (1989), Chahine (1990a), and Chahine (1990b).

If the potential at a point within the domain is needed, (6) (or its discrete equivalent (7)) can be used. the known values of ϕ and $\partial\phi/\partial n$ on the boundary are used to compute the integrals on the left-hand side. To calculate velocities at an interior point the potential in a neighborhood of the point is obtained and local finite-differencing used, while the pressure is obtained via the Bernoulli Eq. (2).

Asymptotic Solutions. We seek asymptotically valid solutions to Eq. (1)-(5), under the assumption that the characteristic size, r_{b0}, of the bubbles is small compared with a characteristic inter-bubble distance l_0. The small parameter used to linearize the system is the ratio between r_{b0} and l_0 denoted ϵ. The zero order approximation ($\epsilon = 0$) reduces to the case of a single bubble in an infinite medium. In the absence of relative motion with respect to the surrounding fluid, each of the bubbles reacts to the local pressure variations spherically, as if isolated.

At higher orders of approximation ($\epsilon \neq 0$), mutual bubble interactions and individual bubble motion and deformation come to play. These approximations are obtained by means of the method of matched asymptotic expansions. The "outer problem" is that obtained when the reference length is chosen to be l_0. This problem is associated with the macroscopic behavior of the cloud, and each bubble appear in it only as the summation of singularities of various orders. The "inner problem" is that obtained when the lengths are normalized by r_{b0}. The solution of this problem provides the microscopic details of the behavior of the cloud, i.e., in the vicinity of an individual bubble center (B_i). The presence of the other bubbles, all considered to be at infinity in the "inner problem," is sensed only by means of the matching condition with the "outer problem." The boundary conditions at infinity for the "inner problem" are obtained, at each order of approximation by the asymptotic behavior of the outer solution in the vicinity of B_i. Thus, if one knows the behavior of all bubbles except B_i, the motion, deformation and pressure field due to this cavity can be determined by solving linearized, nondimensional versions of Eq. (1)-(5). The nondimensionalization yields the following parameters ϵ, $\mathcal{P}$, $\mathcal{W}$, ν, N. These are defined by

$$\epsilon = \frac{r_{b0}}{l_0} \quad \mathcal{P} = \frac{P_\infty(0) - P_v}{\Delta P}$$

$$\mathcal{W} = \frac{r_{b0}\Delta P}{\sigma} \quad \nu = \omega r_{b0}\sqrt{\frac{\rho}{\Delta P}}. \tag{8}$$

Here ϵ is a measure of the void fraction in the bubble cloud, $\mathcal{P}$ is a "cavitation number," $\mathcal{W}$ is a Weber number, ν is the ratio of the forcing frequency ω and the natural frequency of a bubble with radius r_{b0}, while ΔP is the characteristic pressure variation associated with the forcing P_∞.

At the lowest order, $\epsilon = 0$, each bubble, B_i, behaves spherically as if in an infinite medium and the time dependence of its radius, $a_0^i(t)$, is given by the Rayleigh-Plesset equation (Plesset and Prosperetti, 1977). This first approximation of the whole flow field (a distribution of sources or sinks representing all bubble oscillations) sets the boundary conditions at infinity at the following order of approximation. The same process is then repeated for the successive orders. One can show, (Chahine, 1983; Chahine and Liu, 1985), that *up to the order* $O(\epsilon^3)$, the influence of the remaining bubbles on each bubble B_i, can be schematically replaced by the influence of a single equivalent bubble centered at G_i (see Fig. 1). The growth rate and position of this equivalent bubble are determined by the distribution and the growth rate of the other cavities. In general, this fictitious bubble is equivalent to the "rest-of-the-cloud," and the corresponding "cloud center" and "equivalent bubble intensity" are different for each bubble. If θ_{ig} is the angle between the direction of the center, B_iG_i, and the direction of a field point $\overline{B_iM}$, the equation of the surface of the axisymmetric bubble $\overline{B_i}$ can be written in the form:

$$R(\theta_{ij}, \varphi, t) = a_0^i(t) + \epsilon a_1^i(t) + \epsilon^2[a_2^i(t) + f_2^i(t)\cdot\cos\theta_{ij}] + \epsilon^3[a_3^i(t) + f_3^i(t)\cdot\cos\theta_{ij} + g_3^i(t)P_2(\cos\theta_{ij})] + o(\epsilon^3), \tag{9}$$

where P_2 is the Legendre polynomial of order 2, and argument $\cos\theta_{ij}$, while the φ dependence is not seen till the order of the included terms.

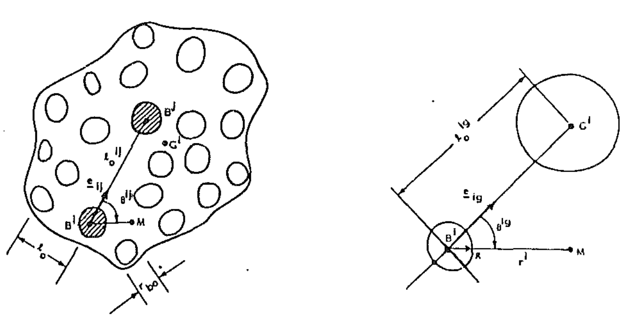

Fig. 1 Geometry of the bubble cloud. The influence of the bubble cloud (bubbles B^j) on a bubble B^i may be replaced by the action of a single bubble placed at G^i.

The first component, $a_0^i(t)$, is given by the Rayleigh-Plesset equation, while the other components, a_n^i, f_n^i and g_n^i, are given by similar second order differential equations which can be written in symbolic form as follows:

$$\mathfrak{D}_2(y_n^i) = \sum_j \left(\frac{l_0}{l_0^{ij}}\right)^m \mathfrak{F}_j^i(y_0^i, \ldots, y_{n-1}^i) P_m(\cos\theta^{ij}) \tag{10}$$

Here $\mathfrak{D}_2(y_n^i)$ represents a second order, nonlinear, differential operator in time, acting on the radius component y_n^i (one of a_n^i, f_n^i, g_n^i) of the bubble i; l_0^{ij} is the initial distance between the bubbles B_i and B_j; $\mathfrak{F}_j^i(y_0^i, \ldots, y_{n-1}^i)$ is known (it is a function of the terms (y_k^i), determined at the preceding orders); m indicates the order of the spherical harmonic; θ_{ij} is the angle between the direction $\overline{B_iB_j}$ connecting the bubble centers and the direction of motion of bubble i toward the cloud center, B_g; and n indicates the order of approximation. The detailed expressions can be found in Chahine (1983). The behavior of B_i can then be computed by integration of the obtained system of differential equations using a Runge-Kutta procedure. The behavior of the whole cloud is thus obtained.

Earlier studies (Chahine, 1982a, Chahine, 1983; Chahine and Liu, 1985) have shown that collective bubble behavior can have a dramatic effect on both bubble growth and implosion. Specifically, bubble growth is inhibited by bubble interactions, while bubble collapse is enhanced. This cumulative effect comes from the fact that the interaction reduces any driving pressure drop as a result of the other bubble growth, while it increases the collapse driving pressure as a result of the other bubble collapse. Due to the cumulative effects of the collapse of all the bubbles in the cloud, each bubble ends its collapse under the influence of a pressure which is orders of magnitude higher than that for an isolated bubble (see Figs. 6 and 7).

3 Numerical Experiments

Comparison of the Two Methods. While the BEM code represents a significant advance in that it allows us to simulate flows with very strong bubble interactions in a relatively accurate way, it is computationally intensive compared to the asymptotic code. While the latter requires $O(N)$ floating point operations per time step, where N is the number of bubbles, the BEM code requires $O(M^3)$ operations per time step where M is the total number of nodes in the discretization. It is thus a matter of some interest to determine the region in the parameter space (see (8)) for which the asymptotic analysis holds. A complete map of the parameter space is a matter of current study. Here a few preliminary results are presented.

In all cases presented for comparison here the ratio ϵ is the ratio of the *initial* radius of the bubble, and the minimum distance (at $t = 0$) between any two bubbles in the configuration. The study was restricted to one particular form of the driving pressure field-a drop in the pressure field at time $t = 0$. Thus the influence of the parameter ν is not studied. Two values of the initial pressure drop were chosen corresponding to values for $\mathcal{P}$ of 1.004 (a very large drop) and 2.508 (a

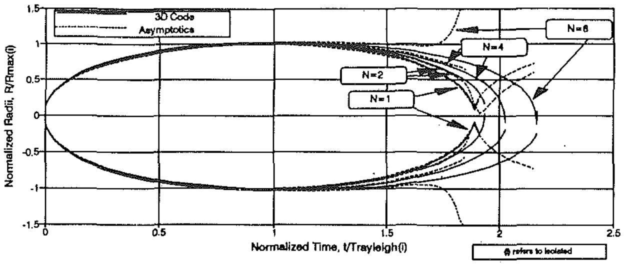

Fig. 2 Motion of the bubble points farthest and closest to the "cloud center" versus time for 1, 2, 4, and 8-bubble symmetric configurations. Comparison between 3DynaFS and the asymptotic code results. $\epsilon=0.0076$, $\mathcal{P}=1.0014$, $\mathcal{W}=2.4\times10^9$. Note $\epsilon=0.07$ if it were calculated at maximum bubble size.

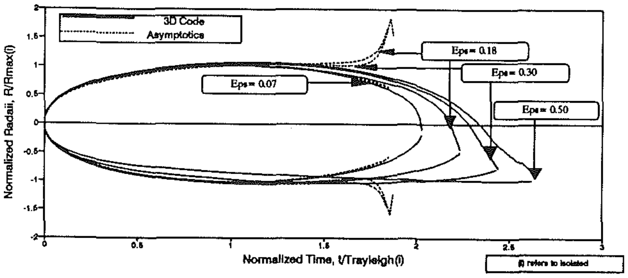

Fig. 3 Motion of the bubble points farthest from a closest to the "cloud center" versus time for a 4-bubble symmetric configuration. Comparison between 3DynaFS code results and the asymptotic code results. Influence of bubble priximity or $\epsilon=R_{\max}l_0$. $\mathcal{P}=1.0014$, $\mathcal{W}=2.4\times10^9$. The values of ϵ used in the asymptotic calculations is based on the initial radius, and are 0.076, 0.02, 0.0323, and 0.0543, respectively for the cases shown.

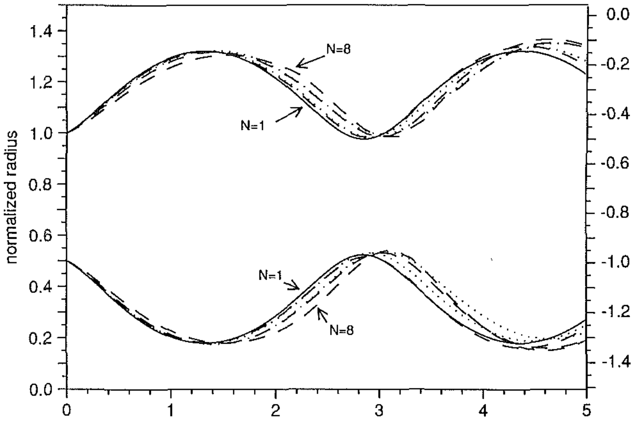

Fig. 4 The effect of changing the number of bubbles. $\epsilon=0.047$ $\mathcal{P}=2.508$, $\mathcal{W}=6.7\times10^5$. This case is one where the collapse is less violent. Note the substantial improvement in the agreement of the asymptotic analysis and the results from 3DynaFS. The solid line indicates the Rayleigh-Plesset solution, the dashes the BEM solution, while the dots indicate the asymptotic results.

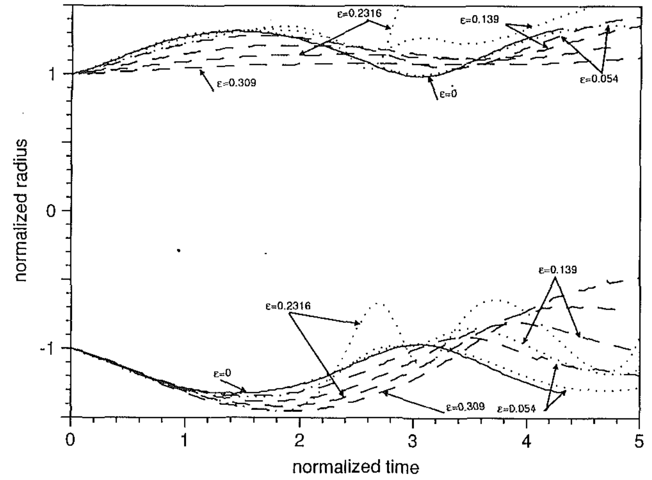

Fig. 5 The effect of changing ϵ. $N=4$, $\mathcal{P}=2.508$, $\mathcal{W}=6.7\times;10^5$. The asymptotic results are indicated with dots, and the BEM results with dashes. The solid line indicates the Rayleigh-Plesset solution. Asymptotic results for $\epsilon=0.309$ are not shown.

relatively milder drop). The number of bubbles varied from 2 to 8, while the value of epsilon was also varied. The studies were performed for large $\mathcal{W}$. Symmetric bubble configurations were chosen for ease of visualization, and efficiency in computation. The bubbles were arranged respectively at the edges of a line, a square, and a cube. In each case the bubble oscillations caused "collapse" of the bubble in the direction towards the center of the cloud. The data for the "radii" reported are for points on a bubble which are closest to the cloud center initially (the positive radii in Fig. 2) and that which are farthest from the cloud center (the negative radii).

As can be seen (Fig. 2) the BEM code shows that the time period of the oscillation of the bubbles increases with the number of interacting bubbles. The maximum bubble size along the jet axis is however modified very little. The jet advancement toward the cloud center increases with N. This is seen from the fact that the upper curves in the graph cross the $r=0$ axis earlier an N increases. This effect is more pronounced as ϵ is increased (Fig. 3). The asymptotic code predicts substantially the same curves for small N (Fig. 2) and low ϵ (Fig. 3), but begins to diverge at higher values. The method predicts either a much faster collapse for $N=2$, 4 or an unexpected early rebound for $N=8$ (Fig. 2).

In the cases addressed in Figs. 2 and 3 the collapse of the bubbles was relatively intense. This may be seen from the fact that the value of $\mathcal{P}=1.001$, corresponds to a pressure drop of 240 times the original. Thus it is unreasonable to expect good agreement from the asymptotic analysis. To check if the method fares better in case the pressure drop is milder, a case where P_∞ is reduced to approximately 40 percent of its original value was studied, corresponding to $\mathcal{P}=2.508$. Results from such a study are shown Figs. 4 and 5. The agreement between the asymptotic method and the BEM code is seen to be quite good at low ϵ. Figure 4 presents the influence of changing N while Fig. 5 presents results for a four bubble study where ϵ is varied from 0.05404 to 0.386. (Note that the bubbles would touch for $\epsilon=0.5$, as the scaling is based on the radius.)

The relative influence the dynamics of an individual bubble has on its neighbors may be best understood by examining the pressure at a point and compare it with its value in the absence of the bubbles. Figures 6 and 7 show the pressure at the center of the cloud, nondimensionalized with respect to the maximum pressure that would have been induced by a "Rayleigh-Plesset bubble" (i.e., an isolated bubble at a distance $l_0/2$ away). The pressure predicted by the asymptotic analysis is seen to be much higher during collapse. This high value is explained by the much higher values of the velocity during collapse predicted by the asymptotic analysis (see Figs. 2, 3, and 4) than by the BEM code. Again the influence of increasing N or increasing ϵ is to make the asymptotic analysis less accurate.

An explanation of why the predictions of the asymptotic method are in error during the collapse phase is provided by Fig. 8, which shows the collapse of a 4 bubble cloud. Here the value of $\epsilon=0.4$. Here two cross-sectional cuts of the cloud are shown, the first being a top-view, while the second is a view from the plane of the bubbles with the viewing angle perpendicular to an edge. The fact that the bubbles are distributed in a plane is clearly visible from the appearance of the jet,

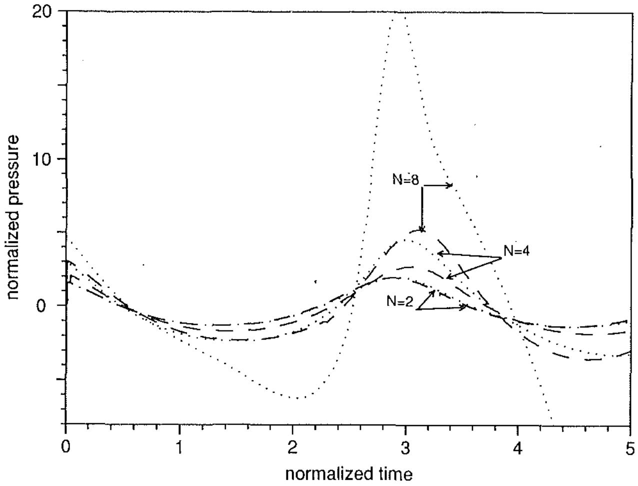

Fig. 6 Comparison of the pressure predicted by 3DynaFS and the asymptotic analysis at the center of the bubble cloud for Fig. 4. The pressure is nondimensionalized by the max. pressure that would be felt in the field of an isolated bubble at a distance $l_0/2$ from the center. This scaling was chosen to highlight any relationship between N and the increase in the pressure. The agreement for $N=2$ is good, but worsens for other cases for reasons cited in the text.

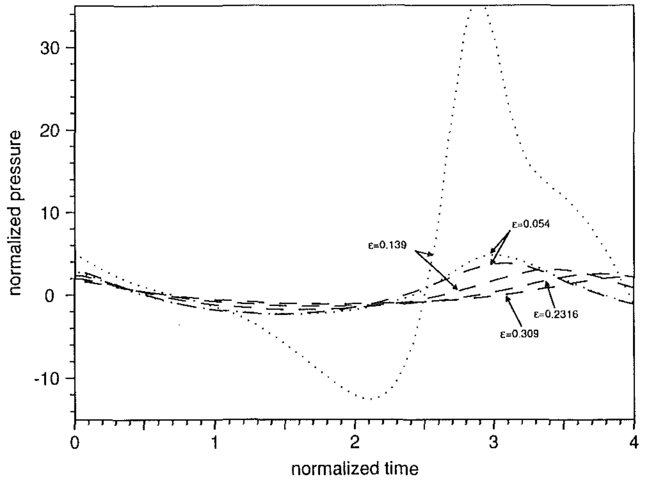

Fig. 7 Comparison of the pressure predicted by 3DynaFS and the asymptotic analysis for Fig. 5. The results from the asymptotic analysis are shown only for the $\epsilon=0.054$ and $\epsilon=0.139$ cases. The scaling is as in Fig. 6.

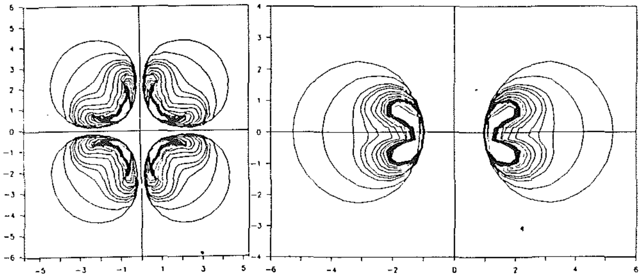

Fig. 8 Bubble contours during collapse of a 4-bubble configuration. (*a*) Cross sectional view in the plane $Z=0$. (*b*) Cross sectional view in the plane $Y=X$. $\epsilon=0.498$ based on the maximum radius. Note the nonaxisymmetric shape of the jet during collapse.

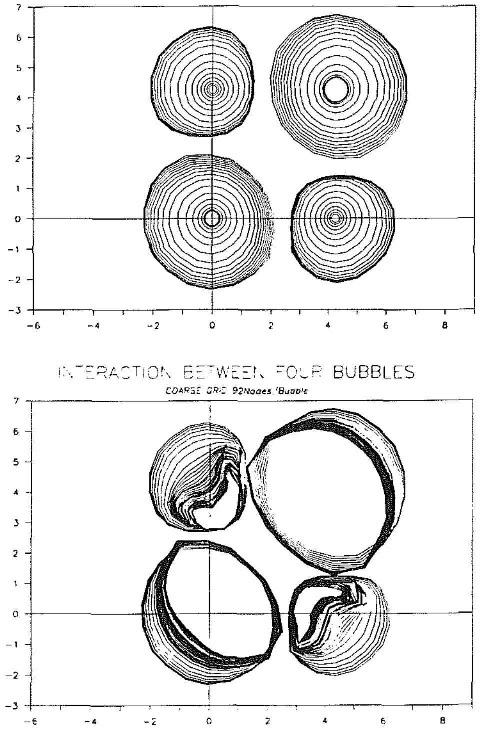

Fig. 9 Growth and collapse of 4 identical bubbles initially symmetrically distributed but with different initial radii (2, 1, 3, 1 clockwise starting from origin). The figure shows the influence of "phasing" (see discussion in §3) on the dynamics.

which is seen to have a two-dimensional flat appearance, rather than a conical axisymmetric shape. Since the asymptotic method, to the order we have solved for ($O(\epsilon^3)$), only allows for deformations expressible in terms of the first three Legendre modes, it becomes inaccurate during the final stages of the collapse. The error made in the pressure is much higher since it depends on the time derivative of the shape (the velocity).

From these numerical experiments we may conclude that, as expected, the asymptotic method is good for relatively large inter bubble separation, for a small number of bubbles, and when the bubble collapse is weak.

Other Numerical Experiments. Here we report the results of some numerical experiments performed with 3DynaFS on some asymmetric bubble configuration. The effects of phasing (i.e., the introduction of differences in the temporal response), and the screening effect of the outer bubbles in a cloud on their inner members are studied.

Figure 9 shows a four-bubble configuration where the bubbles are centered on the corners of a square. All bubbles were chosen so that they would behave identically if in an infinite medium. However, a time delay between the bubble oscillations was imposed. As a result, at $t=0$ the bubbles had relative initial sizes in the ratios 2, 1, 3, 1 counter-clockwise starting from the bubble centered at the origin. A dramatic modification in the behavior of the cloud is seen. The bubble periods appear to be increased for the larger bubbles at $t=0$. The "delayed" bubbles (the smaller ones at $t=0$) are prevented by the other bubbles from growing much, and collapse very early in their history. These bubbles, on the other hand, significantly influence the "earlier" ones by increasing at some point the pressure drop these bubbles sense and then by preventing them from collapsing later. Since the code presently breaks down during the last stages of a violent collapse, we can only speculate that a very strong collapse of the larger bubbles would ensue, because of the large pressure produced by the collapse of the smaller bubbles. This can be illustrated by observing the modification of the imposed pressure drop by the behavior of an individual bubble. As shown in Fig. 8, the bubble growth initially reduces the effective pressure drop that would be felt by a second bubble at the distance l_0, this trend is later reversed,

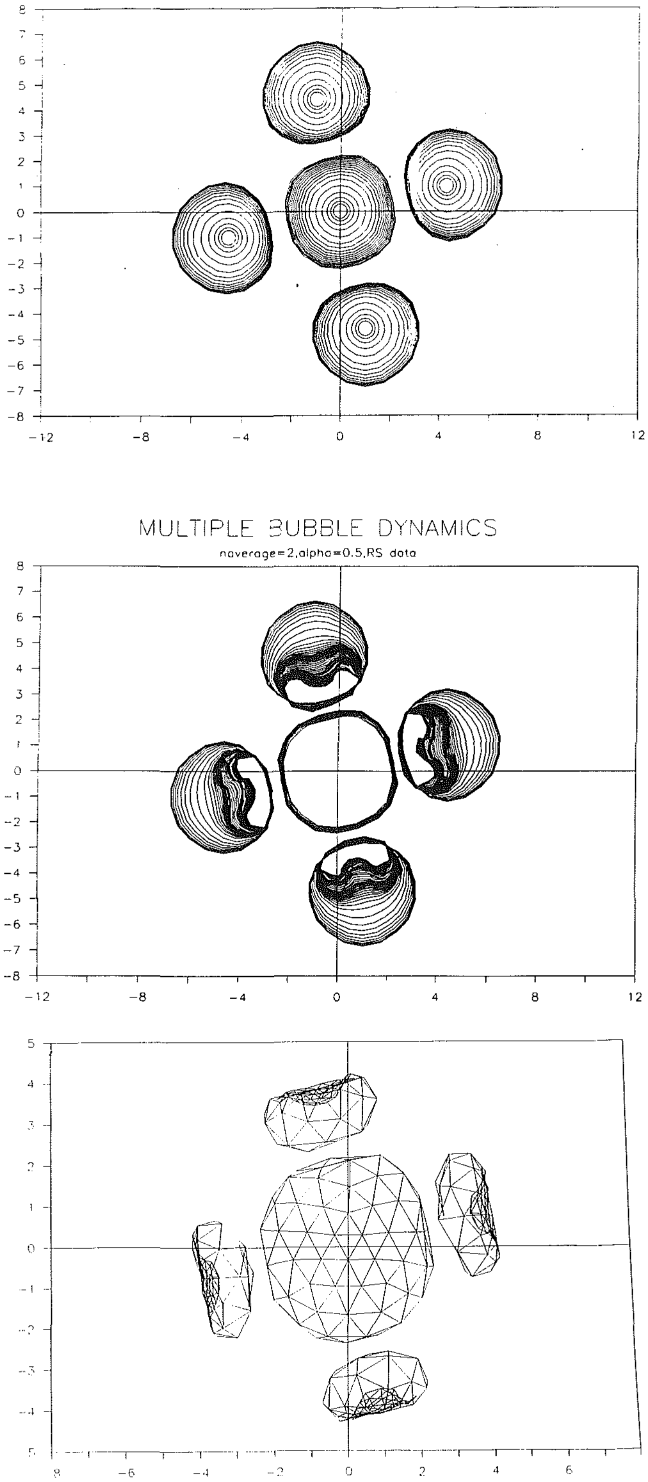

Fig. 10 Growth and collapse of 5 bubbles having the same initial size and internal pressure. Influence of the initial bubble geometry on dynamics. $\epsilon = 0.474$ based on the maximum radius. The center bubble is seen to have a remarkably different behavior.

and is followed by a significant pressure rise during the bubble collapse.

Figure 10 shows the case of an asymmetric five bubble configuration. All bubbles have the same initial radius and internal pressure, and are initially spherical and located in the same plane. The most visible effect is observed on the center bubble. Its growth is initially similar to that of the other bubbles, but later it is the least deformed. As the collapse phase advances with the development of a reentrant jet directed toward the central bubble, this bubble appears to be shielded by the rest of the cloud. Its period appears to be at least double that of the other bubbles. Unfortunately, the code cannot presently follow the dynamics beyond this point since it fails following the touchdown of the first reentrant jet on the opposite bubble side. Here, this occurs before much collapse of the central bubble is observed. The issue of continuing the computations beyond this point is clearly important and is presently the subject of an ongoing research program at DYNAFLOW. Figure 11 shows a similar computation for a 16 bubble cloud. Here due to memory limitations the discretization is coarser. However the same qualitative features as the 5 bubble cloud can be observed.

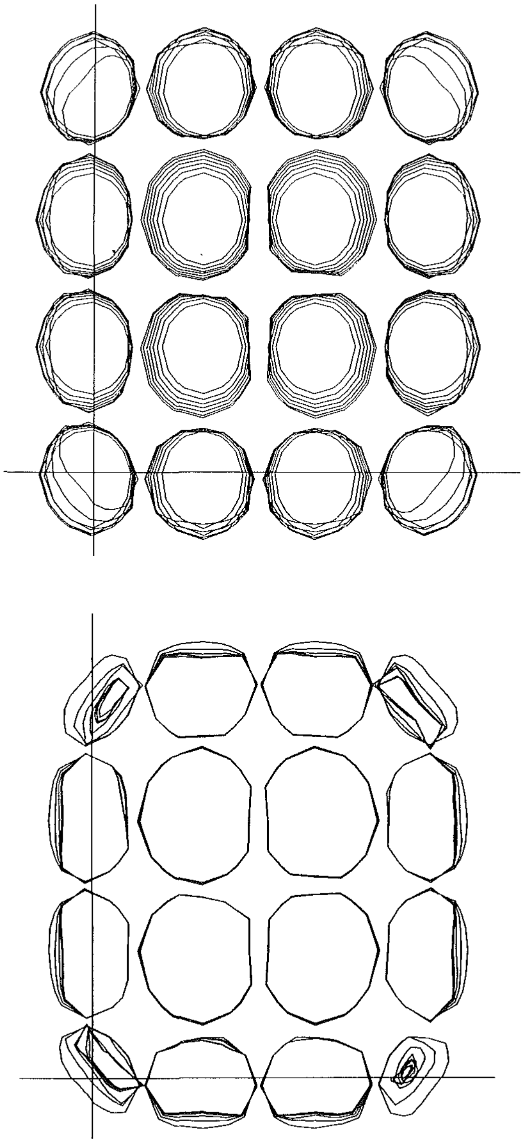

Fig. 11 Contours of the collapse of a sixteen bubble cloud. The bubbles are arranged initially on a regular grid in a plane. Again the central bubbles show different behavior than the outer bubbles. Contours from the end of the growth case and the collapse phase are shown.

4 Conclusion

The dynamics of a multi-bubble system was considered using an asymptotic method and a three-dimensional Boundary Element model. While the asymptotic method is simple and satisfactory for relatively weak interactions and nonviolent bubble oscillations, the 3-D numerical approach is more involved computationally, but allows one to study both very large deformations and very intense oscillations. For multibubble interaction the 3-D code shows significant modifications of the bubble dynamics and shape. For identical bubbles acting in concert, an increase in the bubble period is observed without significant modification of the bubble maximum size when the number of bubbles increase or when their separation distance decreases. For violent interaction the asymptotic approach allows one to follow the dynamics only partially during the collapse. The pressures that it predicts during the collapse increase tremendously at the "cloud center" with the number of bubbles. Comparisons with the BEM code results show that the asymptotic approach can significantly overpredict the velocities at the end of the collapse, which implies that the conclusions on the pressures drawn in earlier studies (Chahine, 1983), while still correct, need to be tempered. Similarly, other real fluid flow conditions, such as the presence in the cloud of various bubble sizes, the presence of a velocity or pressure gradient, etc., moderate the conclusions drawn from simplified symmetric models. These various effects can be considered and analyzed using the 3-D code.

The screening effect observed in the multiple bubble simulations shows that the dynamics of a cloud of bubbles is very different from that of a single bubble. The differences in the collapse periods for the outer and inner bubbles in a cloud (Fig. 10 and Fig. 11) with the inner bubble collapse period being larger, may perhaps be similar to those found in the prediction by d'Agostino and Brennen (1988, 1989) of the appearance of low frequency modes in the collective oscillation of bubbles in a spherical bubble cloud. Their work was based on the solution of a set of heuristic effective equations, with the system closed by requiring that the individual bubbles underwent spherical oscillations according to the Rayleigh-Plesset equation. Thus a direct comparison between the present results and those presented there is not possible.

The phasing study indicates that the influence of compressibility on the dynamics of multiple bubbles is likely to be significant. We are presently attempting to repeat our asymptotic analysis by including compressibility. The results from the phasing study indicate that the compressibility of the medium is likely to play an important role, as identical bubbles would receive pressure information at different times, and consequently could have very different behavior. The large reduction of the sound speed (from its value in pure water) in a bubbly medium makes it important that such an effect be included.

The BEM code 3DynaFS represents a significant advancement in our ability to computationally treat problems hitherto impossible in an efficient way. However, its application to more realistic problems requires much further work. In a current study at DYNAFLOW we are attempting to take advantage the inherent parallelizability of the BEM technique by implementing it on a Connection Machine.

Acknowledgments

This study was supported by the Office of Naval Research, Contract N00014-89-C-0025. The authors are grateful to colleagues at DYNAFLOW, especially to Dr. A. N. Lakshminarasimha for assistance with the BEM computations, Dr. Ken Kalumuck for his comments on an earlier draft of the paper, and Mr. S. Gupta for help with the figures.

References

Blake, J. R., and Gibson, D. C., 1987, "Cavitation Bubbles Near Boundaries," *Annual Review of Fluid Mechanics*, Vol. 19, pp. 99–123.

Caflisch, R. E., Miksis, M. J., Papanicolau, G. C., and Ting, L., 1985, "Effective Equations for Wave Propagation in Bubbly Liquids," *Journal of Fluid Mechanics*, Vol. 153, pp. 259–273.

Chahine, G. L., 1982a, "Pressure Field Generated by the Collective Collapse of Cavitation Bubbles," *Proceedings, IAHR Symposium on Operating Problems of Pump Stations and Power Plants*, Amsterdam, Holland, Vol. 2-1, pp. 1–12.

Chahine, G. L., 1982b, "Experimental and Asymptotic Study of Non-spherical Bubble Collapse," *Applied Scientific Research*, Vol. 38, pp. 187–197.

Chahine, G. L., 1983, "Cloud Cavitation: Theory," *14th Symposium on Naval Hydrodynamics*, Ann Arbor, Mich., National Academy Press, Washington, D.C., pp. 165–195.

Chahine, G. L., and Liu, H. L., 1985, "A Singular Perturbation Theory of the Growth of a Bubble Cluster in a Super-heated Liquid," *Journal of Fluid Mechanics*, Vol. 156, pp. 257–274.

Chahine, G. L., Perdue, T. O., and Tucker, C. B., 1989, "Interaction Between an Underwater Explosion Bubble and a Solid Submerged Body," Technical Report 89006-1, DYNAFLOW Inc., Fulton, MD.

Chahine, G. L., and Perdue, T. O., 1989, "Simulation of the Three-Dimensional Behavior of an Unsteady Large Bubble Near a Structure," *A.I.P. Conference Proceedings 197, Drops and Bubbles*, Third International Colloquium, ed., Wang, T. G., American Institute of Physics, New York, pp. 188–199.

Chahine, G. L., 1989, "A Numerical Model for Three-Dimensional Bubble Dynamics in Complex Geometries," 22nd American Towing Tank Conference, St. Johns, Newfoundland, Canada.

Chahine, G. L., 1990, "Nonspherical Bubble Dynamics in a Line Vortex" *ASME 1990 Cavitation and Multiphase Flow Forum*, Toronto, Canada.

Chahine, G. L., 1990, "Numerical Modelling of the Dynamic Behavior of Bubbles in Nonuniform Flow Fields" *ASME 1990 Symposium on Numerical Methods for Multiphase Flows*, Toronto, Canada.

Chahine, C. L., 1991, "Dynamics of the Interaction of Non-Spherical Cavities," *Mathematical Approaches in Hydrodynamics*, ed., T. Miloh, Society for Industrial Applications of Mathematics, Philadelphia, pp. 51–67.

Commander, K. W., and Prosperetti, A., 1989, "Linear Pressure Waves in bubbly Liquids: Comparison Between Theory and Experiments," *Journal of the Acoustical Society of America*, Vol. 85, pp. 732–746.

D'Agostino, L., and Brennen, C. E., 1988, "Acoustical Absorption and Scattering Cross Sections of Spherical Bubble Clouds," *Journal of the Acoustical Society of America*, Vol. 84, pp. 2126–2134.

D'Agostino, L., and Brennen, C. E., 1989, "Linearized Dynamics of Spherical Bubble Clouds," *Journal of Fluid Mechanics*, Vol. 199, pp. 155–176.

Lu, N. Q., Prosperetti, A., and Yoon, S. W., "Underwater Noise Emission from Bubble Clouds," *IEEE J. Oceanic Engineering*, Vol. 15, 275–281, (1990).

Omta, R., 1987, "Oscillations of a Cloud of Bubbles of Small and Not so Small Amplitude," *Journal of the Acoustical Society of America*, Vol. 82, pp. 1018–1033.

Plesset, M. S., and Prosperetti, A., 1977, "Bubble Dynamics and Cavitation," *Annual Review of Fluid Mechanics*, Vol. 9, pp. 145–185.

Van Wijngaarden, L., 1964, "On the Collective Collapse of a Large Number of Gas Bubbles in Water," *Proc. 11th International Congress* of Applied Mechanics, Springer, Berlin, pp. 854–865.

Van Wijngaarden, L., 1968, "On the Equations of Motion for Mixtures of Liquid and Gas Bubbles," Vol. 33, pp. 465–474.

Van Wijngaarden, L., 1972, "One-Dimensional Flow of Liquids Containing Small Gas Bubbles," *Annual Review of Fluid Mechanics*, Vol. 4, pp. 369–396.

Journal of Fluids Engineering
Technical Briefs

The Effect of Blade Manipulator in Fully Developed Pipe Flow

Y. A. Mah,[1] B. C. Khoo,[1] and Y. T. Chew[1]

Experiments were carried out in applying the concept of passive device called BLADEs (boundary-layer alteration devices) to fully developed pipe flow to assess its feasibility as a drag reduction device. The results of both the volumetric flow rate measurement and the pipe wall pressure distribution taken far downstream show that there is a net increase in drag with the device. With BLADES in tandem arrangement, there is a further net increase in drag which is contrary to its counterpart in boundary layer flow. Although the wall shear stress measurement following the device indicates some reduction in local drag, its magnitude of reduction is much smaller than that seen in the equivalent boundary flow. All these results suggest little possibility of any useful application of BLADEs to pipe flow.

1 Introduction

Ever since the successful attempt by Nagib and coworkers in reducing overall drag of up to 20 percent in boundary-layer flow with the use of passive device called BLADEs or commonly referred to as LEBUs (large eddy break-up devices), there has been a steady surge of interest to this promising new area. However, this initial euphoria is not matched by the consistency of results. Studies by other workers like Bertelrud et al. (1982), Nguyen et al. (1984), and Sahlin et al. (1986) among others, have obtained results with none or varying degree of net drag reduction. Part of the discrepancies probably can be attributed to the small overall drag reduction, if any, and is influenced by the respective measurement technique. Despite this, the more recent works of Savill and Mumford (1988) and Guezennec and Nagib (1990) clearly suggest that there is local drag reduction immediately downstream of the BLADE, and the consensus is that the overall drag reduction (inclusive of device drag) is positive, although it is not as high as that found by Corke et al. (1981, 1982).

While the controversies about the usefulness of BLADEs in shear flow seem to have abated, there is a conspicuous dearth of application to internal flow. This provides us with the motivation of introducing BLADEs in pipe flow, to assess its feasibility as a drag reduction device. Because the mechanism responsible for the beneficial effect of BLADEs in boundary layer flow is not clearly established, it is hence not possible to argue the likely effect of applying BLADEs to pipe flow. In addition, the results of the BLADEs in pipe flow may provide further insight into the physics of the flow in view that both the boundary layer and pipe flows share some common traits in the near wall region and differ only in the wake region.

The present paper focus on the volumetric flow rate and pressure distribution along the pipe wall for various configurations of BLADEs in single and tandem arrangements. Measurements of the local wall shear stress are also reported.

2 Experimental Setup and Conditions

The apparatus consisted of a perspex pipe of over 10 meters length with an internal diameter (D) of 92mm. At the exit of the pipe system was the axial fan, separated from the rest by a flexible tube and a flow straightener. The axial fan, driven by a 3 phase motor, was linked to a controller and can maintain a preset fan speed to within ±1 rpm. For all runs, the fan speed ranged from about 2000 rpm to 3000 rpm, corresponding to Reynolds number Re_D (based on mean flow velocity and pipe diameter) between 3×10^4 and 7×10^4. At the inlet end of the pipe was the conical inlet, made according to British Standard specifications (BS 848). The pressure drop across the conical inlet was used to compute the volumetric flow rate and the uncertainty was within 0.3 percent.

Pressure taps were made along the length of the pipe wall at 0.6m apart and at close interval near the BLADEs. At each location, four pressure taps distributed equally round the pipe circumference were connected to a pressure transducer (Setra-239) and data were acquired using the DAS-20 acquisition system. In the wall pressure measurement for every BLADEs configuration, the corresponding pressure without the device was also obtained.

The probe for the wall shear stress measurement consisted of 5μm-diameter gold-plated wire of sensing length 1.0mm mounted at 50μm above the surface of a 3mm diameter perspex plug. The plug was in turn mounted flush with the pipe wall. According to Ajagu and Libby (1982), this kind of arrangement ensured a faster response and was less sensitive to fluctuations in the wall temperature. Calibration was done insitu with the fully developed pipe flow and was carried out in every occasion prior to the measurement with the BLADE in placed.

The BLADEs were hollow cylinders with diameters (d) of 0.22D, 0.25D, 0.35D, 0.43D, 0.5D, and 0.65D. The length of each device was R (pipe radius) with a thickness of 0.3mm and tapering towards a sharp trailing edge. The BLADE was secured firmly to the pipe wall by means of two razor-blade legs soldered horizontally to the device, and extending through two tiny slots made on the pipe wall for attachment to the pipe.

---

[1] Department of Mechanical & Production Engineering, National University of Singapore, Kent Ridge, Singapore 0511. Dr. Y. T. Chew is a Mem. ASME.

Contributed by the Fluids Engineering Division of THE AMERICAN SOCIETY OF MECHANICAL ENGINEERS. Manuscript received by the Fluids Engineering Division October 2, 1991. Associate Technical Editor: T. T. Huang.

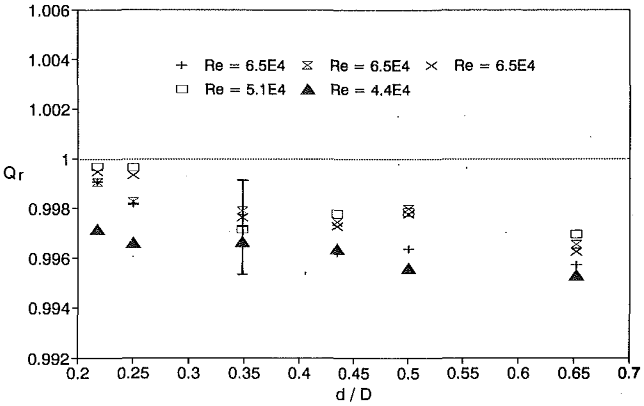

Fig. 1 Q_r **for different single-BLADE diameters at various** Re_D

3 Presentation of Results

3.1 Volumetric Flow Rate for Single BLADE. The ratio of the volumetric flow rate through the pipe with and without the device, Q_r, is shown in Fig. 1 for various BLADE diameters. Each data point was based on 4096 × 40 readings and for each case, the fan speed was kept constant at a preset value. Tests were carried out for different fan speeds and operating conditions equivalent to a range of Re_D for 4.4×10^4 to 6.5×10^4.

The plot generally shows that as the BLADE diameter increases, the volumetric flow rate through the pipe decreases monotonically. Although the error bars may appear large, the above trend is fairly consistent with the salient feature that none of the set-up with device can outperform the case without the device. For the present range of BLADE diameters tested, the 0.22D device registered the maximum volumetric flow rate.

3.2 Wall Pressure Distribution for Single BLADE. The flow rate experiments have shown that the presence of BLADE has resulted in an increase in drag. A check on the above conclusion can be made by comparing the wall pressure downstream of the device to the distribution without the device.

Plotted in Fig. 2 is the ratio of wall pressure coefficient, $(C_p)_r$ [$\equiv C_p/C_{po}$, C_p being defined as $(P_{\text{ref}} - P)/0.5\rho U^2$ where U is the measured mean velocity and subscript o refers to the case without device] versus streamwise distance downstream of the reference point, $(X_i - X_{\text{ref}})/R$, for BLADE diameters of 0.22D, 0.5D, and 0.65D. It can be seen that $(C_p)_r$ increases in the immediate vicinity following the device and subsequently decreases and asymptotes to a value greater than 1.0 much further downstream. This trend is the same for all the different devices. Since each graph asymptotes to a quantity greater than 1.0, it can be concluded that the pressure with the BLADE in placed is generally lower than its counterpart without the BLADE. Also, $(C_p)_r$ tends to be relatively smaller in magnitude for the smaller diameter device ($d/D = 0.22$) on comparing to the larger diameter device ($d/D = 0.5$ and 0.65). This is consistent with the volumetric flow experiments that the 0.22D device has better performance than the 0.5D or 0.65D device, although *none* of them is better than the no-device case.

3.3 Volumetric Flow Rate for Tandem BLADEs. In boundary-layer flow, the use of tandem BLADES leads to larger net drag reduction. This provides us with the motivation to test if tandem BLADES might produce a net drag reduction in pipe flow despite the failure to obtain any drag reduction with single BLADE.

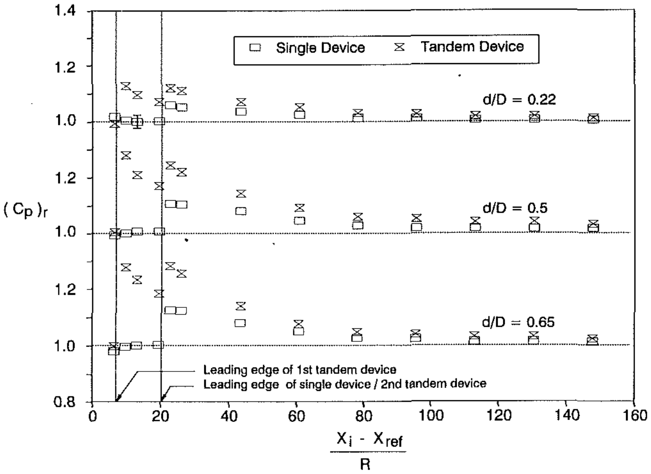

Fig. 2 Distribution of $(C_p)_r$ **for various diameter device(s) at** $Re_D = 65000$

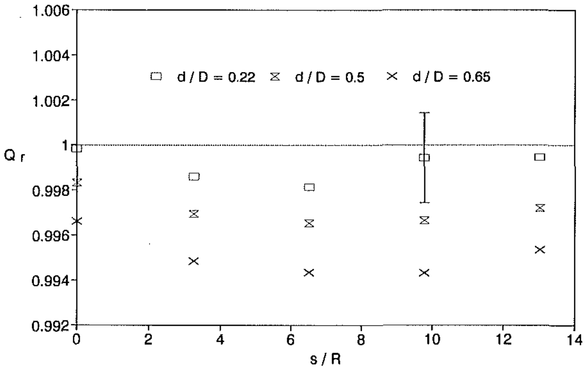

Fig. 3 Q_r **versus** s/R **for different BLADE diameters at** $Re_D = 65000$

Shown in Fig. 3 is Q_r (the ratio of volumetric flow rate with the tandem BLADES to the flow rate without any device) versus tandem separation, s, for different BLADE diameters of 0.22D, 0.5D and 0.65D (s is defined as the distance between leading edge of the devices). The plot shows that with tandem arrangement, the respective flow rates are lower than those of the corresponding configuration of a single BLADE. Apparently, the use of tandem BLADEs has led to further increase in drag. However, among the various tandem arrangement, the one with the separation distance of 13R seems to give the least increase in drag.

3.4 Wall Pressure Distribution for Tandem BLADEs. The wall pressure coefficient $(C_p)_r$ versus distance downstream, for the (best) tandem separation, $s = 13R$, is shown in Fig. 2, for various BLADE diameters. In each case, $(C_p)_r$ increases after the first device of the tandem arrangement. This behavior is similar to that of a single device except that the increment is larger for the former. However, as $(C_p)_r$ decreases from the peak with distance downstream, its trend is arrested by the presence of the second device which causes $(C_p)_r$ to increase in the immediate vicinity before decreasing monotonically downstream. At far downstream location, $(C_p)_r$ for the tandem BLADES asymptotes to a value greater than 1.0 and is larger in magnitude when compared with its counterpart of the single BLADE. This implies that the performance of tandem BLADES is clearly inferior to the single BLADE, which is consistent with the flow rate results of Fig. 3.

3.5 Wall Shear Stress Measurements. Since there is no net drag reduction in pipe flow for any of the BLADEs's configuration, it would be interesting to check if this is also the case for the local skin friction distribution. In boundary layer flow, the net drag reduction materializes largely as the result of contribution from local wall skin friction reduction over long distances behind the device, which more than offset the device's drag.

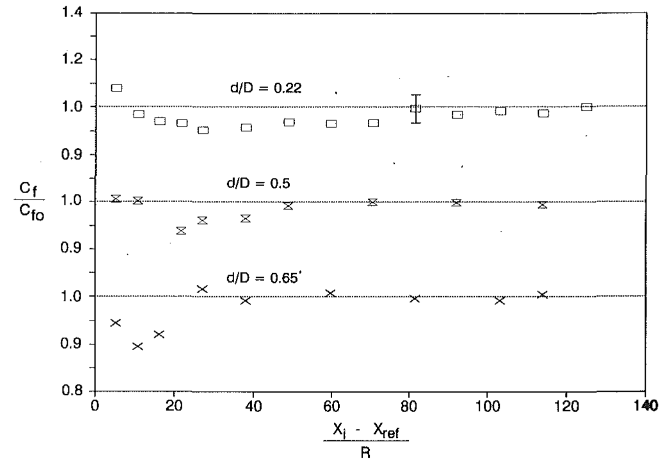

Fig. 4 Distribution of C_f/C_{fo} for various single BLADE diameters

Figure 4 shows the dimensionless skin friction coefficient ratio, C_f/C_{fo} (taken w.r.t. skin friction without the device), versus streamwise distance downstream for BLADE diameters of 0.22D, 0.5D, and 0.65D. Amidst some experimental uncertainty, generally a reduction of the local skin friction can be observed. The length in which the skin friction recovers back to the normal state is shortest for the 0.65D diameter device. It is at about 30R downstream, followed by the 0.5D device at 60R, and finally the 0.22D device at about 90R. The converse is the device with the shortest recovery length has the maximum local skin friction reduction: the 0.65D device has reduction of about ten percent at location 10R downstream, the 0.5D device has seven percent reduction in drag at 20R, and the 0.22D device achieves only a maximum local drag reduction of about five percent at close to 30R downstream. On associating R with δ (the boundary-layer thickness of external shear flow), a comparison can be made between the wall shear stress distribution for equivalent configuration of BLADE in pipe and external shear flows (Savill and Mumford, 1988). It is found that the reduction of wall shear stress following BLADE is generally lower for pipe flow, which probably accounts for the overall increase in drag with BLADE in the former.

4 BLADEs in Other Internal Flows

The use of BLADEs in internal flow was carried out by Prahbu et al. (1987) for the case of channel flow. In their experiments, Prahbu et al. could not find any net drag reduction, whether for single or tandem BLADEs. For their tandem BLADES, an even larger pressure drop was found. Despite the increase in overall drag, they found that there is a reduction of local wall skin friction following the device. Since channel flow shares common features with pipe flow, their finding is entirely consistent with ours.

Pollard et al. (1989) investigated the effect of BLADEs in developing pipe flow. They found no net drag reduction, and observed that the effect of BLADEs in the more developed region of the pipe flow was fairly independent of the device height. It should be noted, however, that their conclusion was based on only 3 devices with $d/D = 0.7$, 0.8 and 0.9. From our Fig. 1, the differences in the flow rates for the larger diameter devices are fairly small, which is consistent with their observation.

5 Concluding Remarks

The present results show that both the mass flow rate experiment and the pipe wall pressure distribution taken far downstream of the device do not indicate any overall drag reduction. Despite this, the wall shear stress measurement shows a reduction of local skin friction following the device, but the magnitude of reduction is much smaller than that found in boundary-layer flow.

References

Ajagu, C. O., and Libby, P. A., 1982, "Modified Gauge for Time-Related Skin-friction Measurements," *Rev. Sci. Instrum.*, Vol. 53, No. 12, pp. 1920–1926.

Bertelrud, A., Trủong, T. V., and Avellan, F., 1982, "Drag Reduction in Boundary Layers Using Ribbons," AIAA Paper 82-1370.

Corke, T. C., Guezennec, Y. G., and Nagib, H. M., 1981, "Modification in Drag of Turbulent Boundary Layers Resulting from Manipulation of Large Scale Structures," NASA CR-3444.

Corke, T. C., Nagib, H. M., and Guezennec, Y. G., 1982, "New View on Origin, Role and Manipulation of large Scales in Turbulent Boundary Layers," NASA CR-165861.

Guezennec, Y. G., and Nagib, H. M., 1990, "Mechanism Leading to Net Drag Reduction in Manipulated Boundary Layers," *AIAA J.*, Vol. 28, No. 2, pp. 245–252.

Nguyen, V. D., Dickinson, J., Jean, Y., Chalifour, Y., Anderson, J., Lemay, J., Haeberle, D., and Larose, G., 1984, "Some Experimental Observations of the Law of the Wall Behind Large-eddy Breakup Devices Using Servo-Controlled Skin Friction Balances," AIAA Paper 84-0346.

Pollard, A., Savill, A. M., and Thomann, H., 1989, "Turbulent Pipe Flow Manipulation: Some Experimental and Computational Results for Single Manipulator Rings," *J. Appl. Sci. Res.*, Vol. 46, No. 3, pp. 281–290.

Prabhu, A., Nath, P. K., Kulkarni, R. S., and Narasimha, R., 1987, "Blade Manipulators in Channel Flows," *Proc. IUTAM Symp. on Turb. Management and Relaminarisation*, Bangalore, Springer-Verlag, pp. 97–108.

Sahlin, A., Alfredsson, P. H., and Johansson, A. V., 1986, "Direct Drag Measurement for a Flat Plate with Passive Boundary Layer Manipulators," *Physics of Fluids*, Vol. 29, No. 3, pp. 696–700.

Savill, A. M., and Mumford, J. C., 1988, "Manipulation of Turbulent Boundary Layers by Outer-layer Devices: Skin Friction and Flow Visualisation Results," *Journal of Fluid Mechanics*, Vol. 191, pp. 389–418.

Reaction Forces During Two-Phase Discharges

J. C. Leung[1]

Nomenclature

A = flow area
C_{pf} = liquid specific heat at constant pressure
C_{pg} = gas specific heat at constant pressure
C_{vg} = gas specific heat at constant volume
D = pipe diameter
f = Fanning friction factor
Fi = flow inclination number (Leung, 1990a)
G = mass flux or velocity
G_0 = mass flux pertaining to nozzle case
G^* = normalized mass flux
h_{fg} = latent heat of vaporization
H = elevation rise
k = gas phase specific heat ratio
L = pipe equivalent length
P = pressure
T = temperature
T_R = thrust or reaction force
u = velocity
v = specific volume
v_{fg} = specific volume difference between vapor and liquid
W = mass flow rate
x = quality or vapor mass fraction

---

[1] Fauske & Associates, Inc., Burr Ridge, Ill. 60521.

Contributed by the Fluids Engineering Division of THE AMERICAN SOCIETY OF MECHANICAL ENGINEERS. Manuscript received by the Fluids Engineering Division December 28, 1991. Associate Technical Editor: E. E. Michaelides.

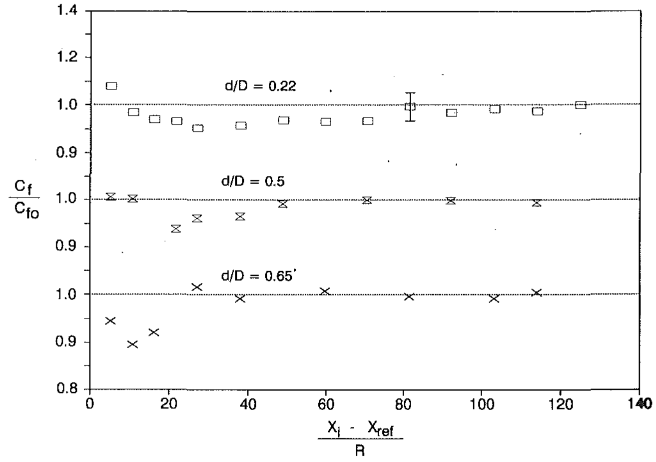

Fig. 4 Distribution of C_f/C_{fo} for various single BLADE diameters

Figure 4 shows the dimensionless skin friction coefficient ratio, C_f/C_{fo} (taken w.r.t. skin friction without the device), versus streamwise distance downstream for BLADE diameters of 0.22D, 0.5D, and 0.65D. Amidst some experimental uncertainty, generally a reduction of the local skin friction can be observed. The length in which the skin friction recovers back to the normal state is shortest for the 0.65D diameter device. It is at about 30R downstream, followed by the 0.5D device at 60R, and finally the 0.22D device at about 90R. The converse is the device with the shortest recovery length has the maximum local skin friction reduction: the 0.65D device has reduction of about ten percent at location 10R downstream, the 0.5D device has seven percent reduction in drag at 20R, and the 0.22D device achieves only a maximum local drag reduction of about five percent at close to 30R downstream. On associating R with δ (the boundary-layer thickness of external shear flow), a comparison can be made between the wall shear stress distribution for equivalent configuration of BLADE in pipe and external shear flows (Savill and Mumford, 1988). It is found that the reduction of wall shear stress following BLADE is generally lower for pipe flow, which probably accounts for the overall increase in drag with BLADE in the former.

4 BLADEs in Other Internal Flows

The use of BLADEs in internal flow was carried out by Prahbu et al. (1987) for the case of channel flow. In their experiments, Prahbu et al. could not find any net drag reduction, whether for single or tandem BLADEs. For their tandem BLADES, an even larger pressure drop was found. Despite the increase in overall drag, they found that there is a reduction of local wall skin friction following the device. Since channel flow shares common features with pipe flow, their finding is entirely consistent with ours.

Pollard et al. (1989) investigated the effect of BLADEs in developing pipe flow. They found no net drag reduction, and observed that the effect of BLADEs in the more developed region of the pipe flow was fairly independent of the device height. It should be noted, however, that their conclusion was based on only 3 devices with $d/D = 0.7$, 0.8 and 0.9. From our Fig. 1, the differences in the flow rates for the larger diameter devices are fairly small, which is consistent with their observation.

5 Concluding Remarks

The present results show that both the mass flow rate experiment and the pipe wall pressure distribution taken far downstream of the device do not indicate any overall drag reduction. Despite this, the wall shear stress measurement shows a reduction of local skin friction following the device, but the magnitude of reduction is much smaller than that found in boundary-layer flow.

References

Ajagu, C. O., and Libby, P. A., 1982, "Modified Gauge for Time-Related Skin-friction Measurements," *Rev. Sci. Instrum.*, Vol. 53, No. 12, pp. 1920–1926.

Bertelrud, A., Truong, T. V., and Avellan, F., 1982, "Drag Reduction in Boundary Layers Using Ribbons," AIAA Paper 82-1370.

Corke, T. C., Guezennec, Y. G., and Nagib, H. M., 1981, "Modification in Drag of Turbulent Boundary Layers Resulting from Manipulation of Large Scale Structures," NASA CR-3444.

Corke, T. C., Nagib, H. M., and Guezennec, Y. G., 1982, "New View on Origin, Role and Manipulation of large Scales in Turbulent Boundary Layers," NASA CR-165861.

Guezennec, Y. G., and Nagib, H. M., 1990, "Mechanism Leading to Net Drag Reduction in Manipulated Boundary Layers," *AIAA J.*, Vol. 28, No. 2, pp. 245–252.

Nguyen, V. D., Dickinson, J., Jean, Y., Chalifour, Y., Anderson, J., Lemay, J., Haeberle, D., and Larose, G., 1984, "Some Experimental Observations of the Law of the Wall Behind Large-eddy Breakup Devices Using Servo-Controlled Skin Friction Balances," AIAA Paper 84-0346.

Pollard, A., Savill, A. M., and Thomann, H., 1989, "Turbulent Pipe Flow Manipulation: Some Experimental and Computational Results for Single Manipulator Rings," *J. Appl. Sci. Res.*, Vol. 46, No. 3, pp. 281–290.

Prabhu, A., Nath, P. K., Kulkarni, R. S., and Narasimha, R., 1987, "Blade Manipulators in Channel Flows," *Proc. IUTAM Symp. on Turb. Management and Relaminarisation*, Bangalore, Springer-Verlag, pp. 97–108.

Sahlin, A., Alfredsson, P. H., and Johansson, A. V., 1986, "Direct Drag Measurement for a Flat Plate with Passive Boundary Layer Manipulators," *Physics of Fluids*, Vol. 29, No. 3, pp. 696–700.

Savill, A. M., and Mumford, J. C., 1988, "Manipulation of Turbulent Boundary Layers by Outer-layer Devices: Skin Friction and Flow Visualisation Results," *Journal of Fluid Mechanics*, Vol. 191, pp. 389–418.

Reaction Forces During Two-Phase Discharges

J. C. Leung[1]

Nomenclature

A = flow area
C_{pf} = liquid specific heat at constant pressure
C_{pg} = gas specific heat at constant pressure
C_{vg} = gas specific heat at constant volume
D = pipe diameter
f = Fanning friction factor
Fi = flow inclination number (Leung, 1990a)
G = mass flux or velocity
G_0 = mass flux pertaining to nozzle case
G^* = normalized mass flux
h_{fg} = latent heat of vaporization
H = elevation rise
k = gas phase specific heat ratio
L = pipe equivalent length
P = pressure
T = temperature
T_R = thrust or reaction force
u = velocity
v = specific volume
v_{fg} = specific volume difference between vapor and liquid
W = mass flow rate
x = quality or vapor mass fraction

---

[1] Fauske & Associates, Inc., Burr Ridge, Ill. 60521.

Contributed by the Fluids Engineering Division of The American Society of Mechanical Engineers. Manuscript received by the Fluids Engineering Division December 28, 1991. Associate Technical Editor: E. E. Michaelides.

α_0 = inlet void fraction
η = pressure ratio relative to P_0
ρ = density
ω = compressible flow parameter, Eq. (4)

Subscripts

a = ambient
c = critical or choked
e = exit
f = liquid
g = gas or vapor
0 = stagnation inlet condition

Introduction

Reaction (thrust) forces are produced from high pressure discharges as in the venting or blowdown of chemical reactors and nuclear reactors. The design of piping support, anchors, and containment vessels, therefore, must include consideration of these forces. Although the reaction forces due to compressible gas discharge and incompressible liquid discharge are well known (Shapiro, 1953; Churchill, 1980), such treatment for two-phase discharge has not established any simple design guide. In his pioneering work, Moody (1969) presented graphs on thrust forces for both steam and saturated water blowdown from an initial pressure typical of the boiling-water reactor. To this date no general correlation for two-phase discharge reaction forces exists.

Recent realization that two-phase discharges are quite frequent during chemical reactor emergency venting (Fisher, 1985; Huff, 1988) has led to a growing need for such a generalized treatment for industrial fluids. The purpose of this note is to present, for the first time, a design correlation for the reaction forces during two-phase discharges from piping. The proposed correlation is general enough for any fluid application and will be shown to be in reasonable agreement with experimental data, hence it is adequate for most engineering design. Both flashing and non-flashing two-phase flows (as in noncondensable gas liquid system) are covered in this treatment.

Referring to Fig. 1, the thrust developed from a nozzle or pipe discharge can be derived from momentum consideration (Shapiro, 1953),

$$T_R = Wu_e + A_e(P_e - P_a) \tag{1}$$

Here the thrust is composed of two components: the first term represents the fluid momentum expulsion rate and the second term represents the exit plane pressure (imbalance) force. For a perfect converging nozzle, the compressible (ideal) gas flow solution is given by (Shapiro, 1953)

$$\frac{T_R}{P_0A_e} = 2\left(\frac{2}{k+1}\right)^{\frac{1}{k-1}} - \frac{P_a}{P_0} \tag{2}$$

Here $k = C_{pg}/C_{vg}$ is the specific heat ratio for the ideal gas and T_R/P_0A_e is termed the normalized thrust. For convenience, we shall denote the quantity $[T_R/(P_0A_e) + P_a/P_0]$ as the "thrust coefficient" and according to Eq. (2) it has a numerical value of 1.21 for $k = 1.001$ (large molecular weight gas limit) and 1.27 for $k = 1.4$ (for diatomic gases such as nitrogen); thus it is nearly invariant with k. For the case of incompressible liquid nozzle discharge, it can be easily shown that (Moody, 1969)

$$\frac{T_R}{P_0A_e} = 2\left(1 - \frac{P_a}{P_0}\right) \tag{3}$$

or the thrust coefficient is simply $2.0 - P_a/P_0$. In arriving at the above result, the mass flow is given by the well-known Bernoulli equation $[W = A_e\sqrt{2\rho_f(P_0 - P_a)}]$ and the exit pressure is simply the downstream back pressure ($P_e = P_a$).

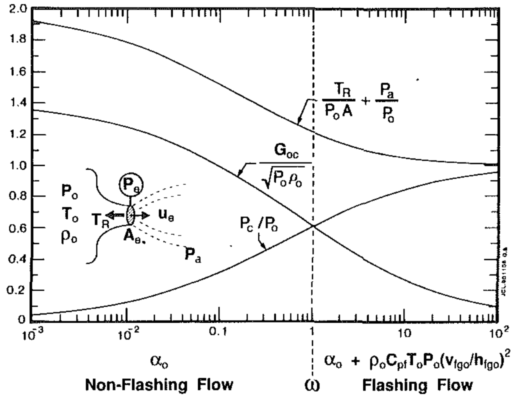

Fig. 1 Normalized critical mass flux, critical pressure ratio, and thrust coefficient in two-phase discharge from nozzle

Two-Phase Nozzle Discharges

The proposed correlation for the exit thrust from a two-phase nozzle discharge is based on the author's "ω" method (Leung, 1986 and Leung, 1990), which was developed for the choked flow discharge of a homogeneous (equal velocity in both phases) two-phase mixture. The "compressible flow parameter" ω was demonstrated to successfully correlate nozzle choked flow of widely different fluids and for quality x_0 ranging from 0 to 1.0 (Leung, 1986). It is made up of two parts, one reflecting the compressibility of the mixture due to the vapor/gas volume present and the other reflecting the compressibility due to phase change (or flashing), i.e.,

$$\omega = \alpha_0 + (1-\alpha_0)\rho_f C_{pf} T_0 P_0 \left(\frac{v_{fg0}}{h_{fg0}}\right)^2 \tag{4}$$

Here all properties are defined at the known inlet stagnation conditions. In the case of non-flashing two-phase flow, the flashing term disappears and ω reduces simply to the inlet void fraction α_0 (Leung, 1990). In such a treatment, the two-phase expansion law can be approximated by the following P-v relationship:

$$\frac{v}{v_0} = \omega\left(\frac{P_0}{P} - 1\right) + 1 \tag{5}$$

For $\omega = \alpha_0 = 1$, the above equation simply reduces to the gas flow case with $k = 1.0$, which has been used frequently for engineering design calculation (API, 1990). In this two-phase flow treatment, the critical pressure ratio (throat choked pressure/stagnation inlet pressure) $\eta_{0c} = P_c/P_0$ can be obtained from the following transcendental equation:

$$\eta_{0c}^2 + (\omega^2 - 2\omega)(1-\eta_{0c})^2 + 2\omega^2\ln\eta_{0c} + 2\omega^2(1-\eta_{0c}) = 0 \tag{6}$$

Substitution of η_{0c} into the following expression yields the exit choking mass flux G_{0c} pertaining to the nozzle,

$$G_{0c}^* = \frac{G_{0c}}{\sqrt{P_0\rho_0}} = \frac{\eta_{0c}}{\sqrt{\omega}} \tag{7}$$

where G_{0c}^* is the normalized critical mass flux. Alternatively one can substitute η_{0c} for η into a more general formula,

$$G_0^* = \frac{G_0}{\sqrt{P_0\rho_0}} = \frac{\{-2[\omega\ln\eta + (\omega-1)(1-\eta)]\}^{1/2}}{\omega\left(\frac{1}{\eta} - 1\right) + 1} \tag{8}$$

This expression is valid for both choked flow and unchoked (subcritical) flow. Such a unified treatment allows the critical flow parameters (G_{0c}^* and η_{0c}) to be uniquely determined as a function of ω as presented in Fig. 1. Here the flashing flow solution lies to the right side of $\omega = 1$ while the non-flashing two-phase flow solution lies to the left side of $\omega = 1$. The

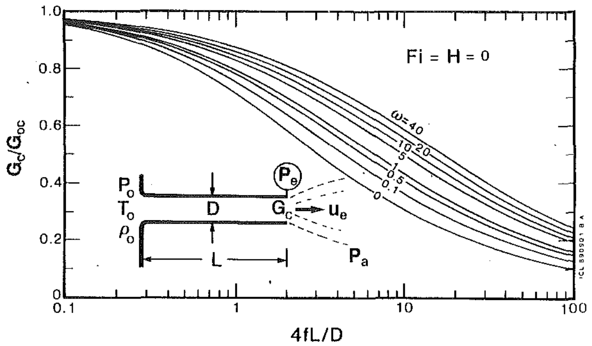

Fig. 2 Mass flux ratio for horizontal two-phase discharge from pipe

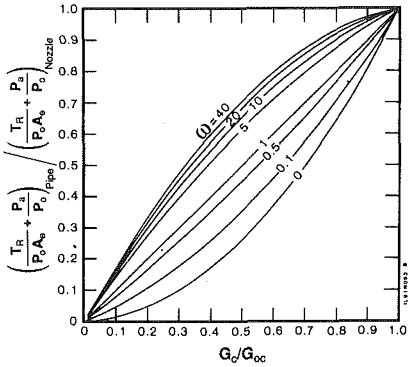

Fig. 3 Thrust coefficient ratio for two-phase pipe discharge

limiting gas flow result (with $k = 1.0$) forms the boundary between these two regimes. Note that at the limit of $\omega \rightarrow 0$ (i.e., $\alpha_0 \rightarrow 0$) in the nonflashing flow regime, the G^* solution in Fig. 1 shows an asymptotic approach to the incompressible Bernoulli's flow although this result is more readily obtained from Eq. (8).

To arrive at a generalized thrust expression, Eq. (1) can be rearranged to give the normalized thrust as,

$$\frac{T_R}{P_0A_e}=\frac{G^2}{P_0\rho_0}\left(\frac{v_e}{v_0}\right)+\left(\frac{P_e}{P_0}-\frac{P_a}{P_0}\right) \tag{9}$$

which is in terms of the exit mass flux and exit specific volume. For the case of critical flow nozzle, substitution of Eqs. (5) and (7) yields (while noting that $P_e = P_c$ and $P_c/P_0 = \eta_{0c}$),

$$\frac{T_R}{P_0A_e}=\eta_{0c}\left[2-\eta_{0c}\left(1-\frac{1}{\omega}\right)\right]-\frac{P_a}{P_0} \tag{10}$$

As already been shown, the critical pressure ratio η_{0c} for the nozzle case is only dependent on ω via Eq. (6), hence the thrust coefficient can be uniquely determined by the ω parameter as well as presented in Fig. 1. Here the thrust coefficient is bounded by a value of 2 at ω approaching 0 and a value of 1 at ω of about 100. Thus at the limit of nonflashing (incompressible) liquid discharge the thrust coefficient attains the maximum asymptotic value of 2 which is in agreement with the classical solution represented by Eq. (3). At the other limit with flashing liquid discharge ($\omega > 1$), a minimum value of 1.0 is approached for the thrust coefficient. While at $\omega = 1$ the thrust coefficient has a value of 1.21 which is in agreement with the classical solution (Eq. (2) with $k = 1.001$).

For the case of unchoked exit, the exit pressure imbalance term in Eq. (9) vanishes and the thrust is only dependent on the exit momentum rate. Making substitution of Eqs. (5) and (8) into Eq. (9) gives

$$\frac{T_R}{P_0A_e}=\frac{2[-\omega\ln\eta_a-(\omega-1)(1-\eta_a)]}{\omega\left(\frac{1}{\eta_a}-1\right)+1} \tag{11}$$

where $\eta_a = P_a/P_0$.

Two-Phase Pipe Discharges

The exit thrust for a pipe discharge situation can be given by Eq. (9) also. The exit choking pressure ratio in this case is governed by a similar expression as Eq. (7) and therefore is related to that for the nozzle discharge via,

$$\eta_c=\eta_{0c}(G_c/G_{0c}) \tag{12}$$

where η_{0c} and G_{0c} denote the critical pressure ratio and mass flux corresponding to a nozzle (pipe with zero length). The mass flux ratio G_c/G_{0c} has been correlated in terms of three dimensionless variables—ω, $4f\,L/D$ and a so-called flow inclination number $\mathrm{Fi} \equiv \rho_0 gH/P_0/(4f\,L/D)$ where H denotes the elevation rise of the pipe exit and is positive for upflow—in a design chart format (Leung and Grolmes, 1987; Leung and Epstein, 1990; Leung, 1990) for the two-phase discharge from pipes in any orientation. The case for horizontal discharge ($\mathrm{Fi} = H = 0$) is illustrated in Fig. 2 (refer to latter two references for $\mathrm{Fi} > 0$ solution charts). This mass flux ratio G_c/G_{0c} is hence equivalent to a discharge coefficient for pipe flow. Such graphical representation is most convenient for design calculation as is commonly employed in adiabatic gas pipe flow (Shapiro, 1953; Perry, 1984). According to Eqs. (10) and (12), a useful quantity for presentation of the thrust result is to evaluate the following thrust coefficient ratio:

$$\frac{\left[\frac{T_R}{P_0A_e}+\frac{P_a}{P_0}\right]_{\text{pipe}}}{\left[\frac{T_R}{P_0A_e}+\frac{P_a}{P_0}\right]_{\text{nozzle}}}=\frac{\left(\frac{G_c}{G_{0c}}\right)\left[2-\eta_{0c}\left(\frac{G_c}{G_{0c}}\right)\left(1-\frac{1}{\omega}\right)\right]}{2-\eta_{0c}\left(1-\frac{1}{\omega}\right)} \tag{13}$$

This result as shown in Fig. 3 covers both flashing flow and nonflashing flow regimes. So for a given pipe flow problem with ω, $4f\,L/D$ and Fi defined, the corresponding G_c/G_{0c} ratio is obtained from previous solution charts such as Fig. 2. Figure 3 then offers a most expedient way of estimating the resulting exit thrust. It is interesting to note that for the gas flow ($\omega = 1$) case, Eq. (13) yields a thrust coefficient ratio equal to G_c/G_{0c}, see also Fig. 3. The same result is obtained from a more rigorous adiabatic gas flow treatment but the derivation involves much more tedious manipulation.

Data Comparison

The first set of experimental data for comparison was taken at the Kraftwerk Union (KWU) facility (Kastner et al., 1978). It employed a tapered nozzle at the exit end together with a rapid-closing valve which upon opening would allow saturated water discharging from a high pressure vessel. The experimental thrust forces were measured by two methods—one from a strain gauge device and the other from the measured mass flow rate and the exit pressure. Typically a 10 percent discrepancy between these two measurements was observed with the former method yielding consistently lower value. Table 1 shows the comparison of the test results against the present predictions. Based on the reported piping resistance ($4f\,L/D$) of about 0.82, Fig. 2 was used to yield G_c/G_{0c} value and the thrust coefficient was then obtained from Figs. 1 and 3. The predicted thrust forces fall in between the two experimental measurements for the first test and are about 10–15 percent higher for the second and third tests. Considering that a sophisticated computer code could not produce closer agreement (Tomasko, 1980), the present predictions are regarded as satisfactory.

The second set of data was taken at the Japan Atomic Energy

Table 1 Thrust data comparison from high pressure saturated water discharge

Source	Test ID	Vessel pressure MPa	Exit area cm^2	Piping resistance $4fL/D$	ω parameter —	Thrust coefficient —	Thrust forces (kN)	
							Experimental	Predicted
KWU	NW50-6	9.62	19.6	0.81	4.1	0.98	15.4-19.7	18.3
KWU	NW65-3	9.87	33.2	0.82	4.0	0.98	26.0-28.2	30.9
KWU	NW65-4	5.31	33.2	0.82	5.2	0.98	14.5-16.1	17.0
JAERI	5509	11.3	47.3	~0	3.3	1.10	57.0	58.0
JAERI	5608	6.86	112.0	~0	4.6	1.08	80.0	81.9

Research Institute (JAERI) in a high-pressure water facility (Yano et al., 1982, 1983). It employed a rupture disk (at the pipe exit end) which was burst with an electric arc and the thrust force was measured with a load cell near the exit elbow. The reported exit area was taken to be the observed broken area of the rupture disk which in these tests was about 80 percent of the fully open area. Due to such a restriction at the rupture disk, the upstream piping resistance was ignored in the present analysis. Table 1 shows that the present predictions are higher by 1-2 percent.

Discussion

The relative insensitivity to inlet quality x_0 as reported by Isozaki et al. (1984) is confirmed by the present correlation where for x_0 varies from 0 to 0.01 corresponding to ω values of 4.6 and 4.0, respectively, pertaining to steam-water at 6.9 MPa, the resulting thrust according to Fig. 1 varies by less than 2 percent.

There seems to be contradiction in the literature as to whether the slip model would increase the thrust relative to the homogeneous model (Tomasko, 1980; Yano et al., 1982). But as demonstrated in these two articles, the effect of slip results in less than 5 percent variation from the homogeneous flow case. From an engineering design standpoint, the homogeneous flow model is justified.

The effect of thermal nonequilibrium in flashing flow can be easily assessed by the present correlation. For short pipe where this nonequilibrium (flashing) effect is most pronounced, the lack of flashing causes the discharge rate to greatly increase. Figure 1 can provide a quick estimate of such flow rate (i.e., nonflashing regime with $\omega = \alpha_0$) as well as the exit thrust. It is noted, however, that the maximum augmentation of the thrust relative to the flashing flow case ($\omega >> 1$) is only a factor of 2.0.

References

American Petroleum Institute, 1990, "Guide for Pressure-Relieving and Depressuring Systems," API RP-521, 3rd ed.

Churchill, S. W., 1980, *The Practical Use of Theory in Fluid Flow, Book I, Inertial Flows*, Chapter 4, Etaner Press, Thornton, Pa.

Fisher, H. G., 1985, "DIERS Research Program on Emergency Relief Systems," *Chemical Engineering Progress*, Vol. 81(8), pp. 33-36.

Huff, J. E., 1988, "Frontiers in Pressure-Relief System Design," *Chemical Engineering Progress*, Vol. 84(9), pp. 44-51.

Isozaki, T., Yano, T., Miyazaki, N., Kato, R., Kurihara, R., Ueda, S., and Miyazono, S., 1984, "Test Results of Jet Discharge from a 4-inch Pipe Under BWR LOCA Conditions," *Nuclear Engineering and Design*, Vol. 79, pp. 81-92.

Kastner, W., Eichler, R., and Riedle, K., 1978, "Experimental Studies on Forces of Critical Two-Phase Jets for Traverse and Longitudinal Cracks in Pipelines," NRC Translation 478, U.S. Nuclear Regulatory Commission, Sept.

Leung, J. C., 1986, "A Generalized Correlation for One-Component Homogeneous Equilibrium Flashing Choked Flow," *American Institute of Chemical Engineering Journal*, Vol. 32 (10), pp. 1743-1746.

Leung, J. C., and Grolmes, M. A., 1987, "The Discharge of Two-Phase Flashing Flow in a Horizontal Duct," *American Institute of Chemical Engineers Journal*, Vol. 33(3), p. 524 (1987); also errata, 34(6), p. 1030, (1988).

Leung, J. C., 1990, "Similarity Between Flashing and Non-Flashing Two-Phase Flows," *American Institute of Chemical Engineers Journal*, Vol. 36(5), pp. 797-800.

Leung, J. C., and Epstein, M., "The Discharge of Two-Phase Flashing Flow from an Inclined Duct," ASME *Trans. Journal of Heat Transfer*, Vol. 112(2), p. 524, May.

Moody, F. J., 1989, "Prediction of Blowdown Thrust and Jet Forces," Paper No. 69-HT-31 presented at ASME-AIChE Heat Transfer Conference, Minneapolis, Minn., August 3-6.

Perry, R. H., and Green, D., eds., 1984, *Perry's Chemical Engineer's Handbook*, 6th ed., McGraw-Hill, New York, pp. 5-28.

Shapiro, A. H., 1953, *The Dynamics and Thermodynamics of Compressible Fluid Flow*, Vol. I, The Ronald Press, New York.

Tomasko, D., 1980, "Two-Phase Jet Loads—Fiscal Year 1979 Annual Report," U.S. Nuclear Regulatory Commission Report, NUREG/CR-1292.

Yano, T., Miyazaki, N., and Isozaki, T., 1982, "Transient Analysis of Blowdown Thrust Force Under PWR LOCA," Nuclear Engineering & Design, Vol. 75, pp. 157-168.

Yano, T., Isozaki, T., Ueda, S., Miyazaki, N., Kurihara, R., Kato, R., and Miyazono, S., 1983, "An Experimental Study of Blowdown Thrust and Jet Forces by 6-inch Pipe Under BWR LOCA," Thermal-Hydraulics of Nuclear Reactors, Vol. II, pp. 761-768, published by American Nuclear Society.

Phase Discrimination in Gas-Particle Flows Using Thermal Anemometry

M. L. Ritsch[1] **and J. H. Davidson**[1]

A technique to measure gas-phase turbulence modification by micron-sized particles with thermal anemometry is presented. Bridge output is first digitized and then spikes produced by particle impingement on the hot-wire probe detected using a slope threshold method and replaced by holding the last digital value before each spike. This procedure has negligible effect on flow statistics if spike duration is short compared to the time between spikes.

Nomenclature

d = diameter, m
$E(n)$ = energy spectrum, $\mathrm{m}^2/\mathrm{s}^2/\mathrm{Hz}$
$f(t)$ = bridge output, V
$F(t)$ = corrected digital signal, V
$g(t)$ = spike substitution function, V
$I(t)$ = phase indicator function
L = length, m
n = frequency, Hz
N = number of data points
$R(s)$ = autocovariance, $\mathrm{m}^2/\mathrm{s}^2$
s = time interval, s
t = time, s
T = total sample time, s
u = velocity, m/s
$1/\alpha$ = time between particle impingement spikes, s
$1/\beta$ = duration of impingement spike, s
γ = specific weight

Superscripts

$\bar{\ }$ = mean quantity
$'$ = fluctuating quantity

---

[1] Civil Engineering Department, Colorado State University, Fort Collins, CO 80523.

Contributed by the Fluids Engineering Division of THE AMERICAN SOCIETY OF MECHANICAL ENGINEERS. Manuscript received by the Fluids Engineering Division July 17, 1992. Associate Technical Editor: E. E. Michaelides.

Table 1 Thrust data comparison from high pressure saturated water discharge

Source	Test ID	Vessel pressure MPa	Exit area cm^2	Piping resistance $4f L/D$	ω parameter —	Thrust coefficient —	Thrust forces (kN)	
							Experimental	Predicted
KWU	NW50-6	9.62	19.6	0.81	4.1	0.98	15.4-19.7	18.3
KWU	NW65-3	9.87	33.2	0.82	4.0	0.98	26.0-28.2	30.9
KWU	NW65-4	5.31	33.2	0.82	5.2	0.98	14.5-16.1	17.0
JAERI	5509	11.3	47.3	~0	3.3	1.10	57.0	58.0
JAERI	5608	6.86	112.0	~0	4.6	1.08	80.0	81.9

Research Institute (JAERI) in a high-pressure water facility (Yano et al., 1982, 1983). It employed a rupture disk (at the pipe exit end) which was burst with an electric arc and the thrust force was measured with a load cell near the exit elbow. The reported exit area was taken to be the observed broken area of the rupture disk which in these tests was about 80 percent of the fully open area. Due to such a restriction at the rupture disk, the upstream piping resistance was ignored in the present analysis. Table 1 shows that the present predictions are higher by 1-2 percent.

Discussion

The relative insensitivity to inlet quality x_0 as reported by Isozaki et al. (1984) is confirmed by the present correlation where for x_0 varies from 0 to 0.01 corresponding to ω values of 4.6 and 4.0, respectively, pertaining to steam-water at 6.9 MPa, the resulting thrust according to Fig. 1 varies by less than 2 percent.

There seems to be contradiction in the literature as to whether the slip model would increase the thrust relative to the homogeneous model (Tomasko, 1980; Yano et al., 1982). But as demonstrated in these two articles, the effect of slip results in less than 5 percent variation from the homogeneous flow case. From an engineering design standpoint, the homogeneous flow model is justified.

The effect of thermal nonequilibrium in flashing flow can be easily assessed by the present correlation. For short pipe where this nonequilibrium (flashing) effect is most pronounced, the lack of flashing causes the discharge rate to greatly increase. Figure 1 can provide a quick estimate of such flow rate (i.e., nonflashing regime with $\omega = \alpha_0$) as well as the exit thrust. It is noted, however, that the maximum augmentation of the thrust relative to the flashing flow case ($\omega >> 1$) is only a factor of 2.0.

References

American Petroleum Institute, 1990, "Guide for Pressure-Relieving and Depressuring Systems," API RP-521, 3rd ed.

Churchill, S. W., 1980, *The Practical Use of Theory in Fluid Flow, Book I, Inertial Flows*, Chapter 4, Etaner Press, Thornton, Pa.

Fisher, H. G., 1985, "DIERS Research Program on Emergency Relief Systems," *Chemical Engineering Progress*, Vol. 81(8), pp. 33-36.

Huff, J. E., 1988, "Frontiers in Pressure-Relief System Design," *Chemical Engineering Progress*, Vol. 84(9), pp. 44-51.

Isozaki, T., Yano, T., Miyazaki, N., Kato, R., Kurihara, R., Ueda, S., and Miyazono, S., 1984, "Test Results of Jet Discharge from a 4-inch Pipe Under BWR LOCA Conditions," *Nuclear Engineering and Design*, Vol. 79, pp. 81-92.

Kastner, W., Eichler, R., and Riedle, K., 1978, "Experimental Studies on Forces of Critical Two-Phase Jets for Traverse and Longitudinal Cracks in Pipelines," NRC Translation 478, U.S. Nuclear Regulatory Commission, Sept.

Leung, J. C., 1986, "A Generalized Correlation for One-Component Homogeneous Equilibrium Flashing Choked Flow," *American Institute of Chemical Engineering Journal*, Vol. 32 (10), pp. 1743-1746.

Leung, J. C., and Grolmes, M. A., 1987, "The Discharge of Two-Phase Flashing Flow in a Horizontal Duct," *American Institute of Chemical Engineers Journal*, Vol. 33(3), p. 524 (1987); also errata, 34(6), p. 1030, (1988).

Leung, J. C., 1990, "Similarity Between Flashing and Non-Flashing Two-Phase Flows," *American Institute of Chemical Engineers Journal*, Vol. 36(5), pp. 797-800.

Leung, J. C., and Epstein, M., "The Discharge of Two-Phase Flashing Flow from an Inclined Duct," ASME *Trans. Journal of Heat Transfer*, Vol. 112(2), p. 524, May.

Moody, F. J., 1989, "Prediction of Blowdown Thrust and Jet Forces," Paper No. 69-HT-31 presented at ASME-AIChE Heat Transfer Conference, Minneapolis, Minn., August 3-6.

Perry, R. H., and Green, D., eds., 1984, *Perry's Chemical Engineer's Handbook*, 6th ed., McGraw-Hill, New York, pp. 5-28.

Shapiro, A. H., 1953, *The Dynamics and Thermodynamics of Compressible Fluid Flow*, Vol. I, The Ronald Press, New York.

Tomasko, D., 1980, "Two-Phase Jet Loads—Fiscal Year 1979 Annual Report," U.S. Nuclear Regulatory Commission Report, NUREG/CR-1292.

Yano, T., Miyazaki, N., and Isozaki, T., 1982, "Transient Analysis of Blowdown Thrust Force Under PWR LOCA," Nuclear Engineering & Design, Vol. 75, pp. 157-168.

Yano, T., Isozaki, T., Ueda, S., Miyazaki, N., Kurihara, R., Kato, R., and Miyazono, S., 1983, "An Experimental Study of Blowdown Thrust and Jet Forces by 6-inch Pipe Under BWR LOCA," Thermal-Hydraulics of Nuclear Reactors, Vol. II, pp. 761-768, published by American Nuclear Society.

Phase Discrimination in Gas-Particle Flows Using Thermal Anemometry

M. L. Ritsch[1] and J. H. Davidson[1]

A technique to measure gas-phase turbulence modification by micron-sized particles with thermal anemometry is presented. Bridge output is first digitized and then spikes produced by particle impingement on the hot-wire probe detected using a slope threshold method and replaced by holding the last digital value before each spike. This procedure has negligible effect on flow statistics if spike duration is short compared to the time between spikes.

Nomenclature

d = diameter, m
$E(n)$ = energy spectrum, m^2/s^2/Hz
$f(t)$ = bridge output, V
$F(t)$ = corrected digital signal, V
$g(t)$ = spike substitution function, V
$I(t)$ = phase indicator function
L = length, m
n = frequency, Hz
N = number of data points
$R(s)$ = autocovariance, m^2/s^2
s = time interval, s
t = time, s
T = total sample time, s
u = velocity, m/s
$1/\alpha$ = time between particle impingement spikes, s
$1/\beta$ = duration of impingement spike, s
γ = specific weight

Superscripts

$\overline{}$ = mean quantity
$'$ = fluctuating quantity

---

[1] Civil Engineering Department, Colorado State University, Fort Collins, CO 80523.

Contributed by the Fluids Engineering Division of THE AMERICAN SOCIETY OF MECHANICAL ENGINEERS. Manuscript received by the Fluids Engineering Division July 17, 1992. Associate Technical Editor: E. E. Michaelides.

Subscripts

f = autocovariance with $f(t)$
g = autocovariance with $g(t)$
F = autocovariance with $F(t)$
I = autocovariance with $I(t)$
rms = root-mean-square

Introduction

Although numerous studies address modification of gas-phase turbulence by solid or liquid particles, no concrete consensus exists on the effects of fine particles on either the magnitude or structure of the carrier-phase turbulent flow field. This is partially due to the perception that particles with diameters less than 5 μm follow the flow, and, thus, do not affect turbulence, but also due to the difficulty of discriminating between particle and gas velocities. Laser Doppler anemometry (LDA) is restricted to flows where the particles of interest are substantially larger than the seeding particles. Thermal anemometry may be used to measure carrier-phase turbulence modification if a correction is made for voltage spikes caused by particles hitting the sensor.

Hetsroni and Sokolov (1971) used hot-wire anemometry to measure modification of an air jet by cotton-seed oil (d = 13 μm), but the "clipper circuit" used to reduce the amplitude of the spikes produced errors in flow statistics. Wang et al. (1989) used a better approach in bubbly flow. Anomalies produced as bubbles swept over the wire were replaced in the digitized signal by the mean voltage.

A modified technique for gas or liquid flows, with much smaller particles is presented. Effects on flow statistics are discussed in terms of a flow created by adding 5×10^{-8} g/cm^3 of atomized oleic acid particles (γ = 0.891, d = 2 μm) to a rectangular duct air flow with bulk velocity = 0.6 m/s and Reynolds number = 2000.

Particle Impingement

Figure 1 is a typical voltage spike caused by particle impingement on a platinum-coated hot-film probe (d = 51 μm, L = 1 mm). This spike lasts 2.4 ms with an initial rise time of 40 μs, and maximum amplitude 5 V above the true signal. Elimination of particle impingement using smaller hot-wires is unsuccessful. Nor is it possible to decrease residence time of the particle on the probe by increasing the over-heat ratio. Moreover, analog filtering is useless.

Digitization must be extremely fast to detect rapid phase changes as particles impact the probe and to prevent aliasing. In this study, the signal is amplified 30 dB and digitized at 20 kHz. Data is obtained over 26 seconds, in 32 contiguous, 16,384 point arrays. Spikes are detected with a slope threshold method. The average slope between successive data points is calculated. Then, if the slope between any two points is greater than 6 times the average, the points are considered part of a particle spike and deleted. With a particle mass loading of 4×10^{-5}, 30 spikes occur in one 26 second data set.

Spike Replacement and Statistics

The best value to replace the deleted signal is the one that adds the least spectral noise. Buchave et al. (1979) considered a similar problem with LDA trackers when the presence of multiple particles in the measuring volume causes signal "drop-out," and found that in situations, like this one, where the time between signal discontinuities is long compared to duration of the discontinuity, the erroneous signal should be replaced by the last digital value occurring before the discontinuity.

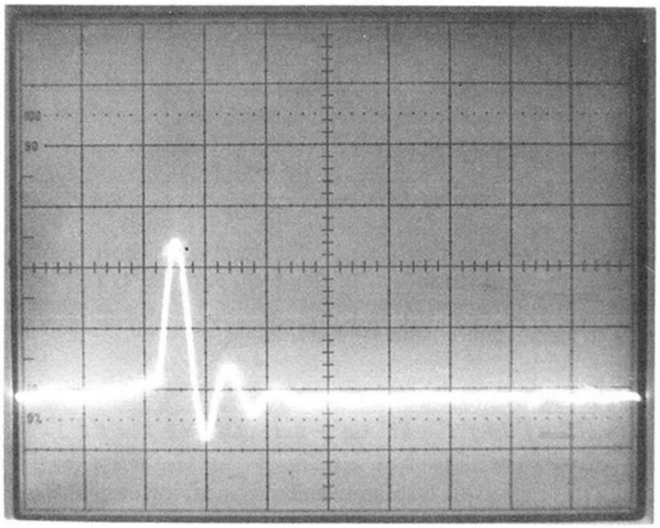

Fig. 1 Oscilloscope trace of particle induced voltage spike (0.2 ms/division, 2.0 V/division)

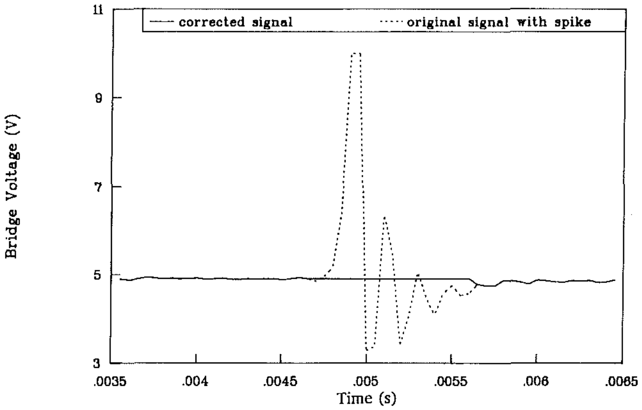

Fig. 2 Comparison of digital signal before and after spike removal and replacement

Figure 2 shows a digitized impingement spike and the adjusted signal in which the spike is replaced by holding the last digital value. The corrected bridge output digitized signal, $F(t)$, is,

$$F(t) = f(t)I(t) + g(t)[1 - I(t)] \qquad (1)$$

where $f(t)$ is the bridge output signal. The phase indicator function, $I(t)$, equals +1 when the signal is particle-free and 0 when a particle is detected. During particle impingement, $g(t)$ is held at the last digital value before the spike; otherwise, $g(t)$ equals $f(t)$.

Replacing the spikes with a constant value reduces the mean-square of the signal. Thus, the best method to evaluate mean and mean-square velocities is to first remove the particle spikes and then reduce the number of data points (N) to account for deleted data. This procedure may be unnecessary if spikes occupy a relatively small portion of the data.

To determine averaged quantities, each term in Eq. (1) is represented by the sum of a mean and fluctuating component and then the expression is Reynolds averaged yielding,

$$\overline{F} = \overline{f}\,\overline{I} + \overline{g} - \overline{g}\,\overline{I} + \overline{f'I'} + \overline{g'I'}. \qquad (2)$$

Because fluctuations in $f(t)$ and $g(t)$ are uncorrelated with those in $I(t)$, the last two terms in this expression may be neglected.

The expected time between spikes is $1/\alpha$ while the duration of a spike is $1/\beta$. Thus, the probability of being in a spike at any instant is $\alpha/(\alpha + \beta)$ and the probability of being in a particle-free signal is $\beta/(\alpha + \beta)$. Consequently, the mean of $I(t)$ is,

$$\overline{I(t)} = \frac{N\left[\dfrac{\beta}{(\alpha+\beta)}\right](1) + N\left[\dfrac{\alpha}{(\alpha+\beta)}\right](0)}{N} = \frac{\beta}{(\alpha+\beta)} \tag{3}$$

and the mean-square of $I(t)$ is,

$$\overline{(I')^2} = \frac{\alpha\beta}{(\alpha+\beta)^2}. \tag{4}$$

Except in dense-particle flows, spike duration is short relative to the time between spikes. In this case, $\alpha/\beta \ll 1$, $\overline{I(t)} \approx 1$ and $\overline{F(t)}$ approaches $\overline{f(t)}$.

The mean-square value of $F(t)$, is,

$$\overline{(F')^2} = \overline{[\bar{f}I' + f'\bar{I} + f'I' - \bar{g}I' + g' - g'\bar{I} - g'I' - \overline{g'I'} - \overline{f'I'}]^2}. \tag{5}$$

Once this expression is squared and averaged, it is easy to show that with $\bar{I} \approx 1$ and $\overline{I'^2} \approx 0$ for $\alpha/\beta \ll 1$, $\overline{F'^2}$ becomes,

$$\overline{(F')^2} = \overline{(f')^2} + \overline{(g')^2} - \overline{f'g'}. \tag{6}$$

But since $f(t) \approx g(t)$, and $\overline{f'g'} \approx \overline{g'^2}$, $\overline{F'^2}$ approaches $\overline{f'^2}$. For the mass loadings considered, using the corrected signal to compute u_{rms} results in an underestimate of 2 percent.

The autocovariance must be evaluated from the corrected signal since a continuous time series is required. The autocovariance of the corrected signal is,

$$R_F(s) = \lim_{T\to\infty} \frac{1}{T} \int_0^T F(t)F(t+s)ds. \tag{7}$$

To compute R_F, autocovariance tensors:

$$R_f = \overline{f'(0)f'(s)} \tag{8a}$$

$$R_I = \overline{I'(0)I'(s)} \tag{8b}$$

$$R_F = \overline{F'(0)F'(s)} \tag{8c}$$

$$R_{fg} = \overline{f'(0)g'(s)} \tag{8d}$$

$$R_g = \overline{g'(0)g'(s)} \tag{8e}$$

are introduced. Following the usual averaging procedures with the mean value removed, R_F is,

$$R_F = \overline{I^2}R_f + [R_f + R_g - 2R_{fg}]R_I + 2\bar{I}(1-\bar{I})R_{fg} + [1 - 2\bar{I} + \overline{I^2}]R_g. \tag{9}$$

Once again assuming that $\alpha/\beta \ll 1$, all but the first term, the desired autocovariance, can be neglected.

Since the energy spectrum, $E(n)$, is the Fourier transform of R_F, the last three terms in Eq. (9) add broad-band noise to the spectrum. Low energy noise is most likely to affect the shape of the spectrum at high frequencies. Noise in the spectrum is analyzed by comparing the energy spectrum from a particle-free signal to the spectrum of the same signal with the spike replacement procedure applied, where the number and location of spikes are matched to those in a data set with 5×10^{-8} g/cm^3 particles. Figure 3 shows that the two spectra are indistinguishable.

Summary

Hot-film anemometry can be used to discriminate gas-phase from fine-particle velocities if the signal is digitized at rates sufficiently high to identify particle impingement spikes and prevent aliasing. Voltage spikes can then be removed from the data using a slope threshold detection method and replaced with the last digital value before the spike. Errors in flow statistics are negligible if particle concentration is sufficiently low so that particle-induced voltage spikes make-up only a small portion of the total signal. Changes in probe calibration due to contamination can be handled by calibrating a clean probe at several over-heat ratios, and then using the calibration that most closely matches that of the dirty probe.

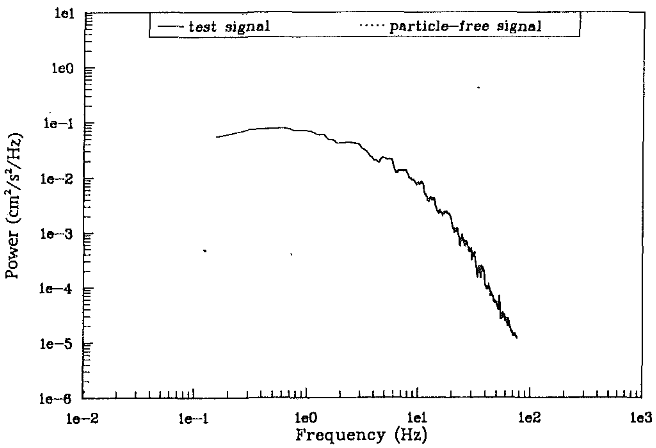

Fig. 3 Comparison of energy spectrum of particle-free signal to energy spectrum of a corrected signal with artificial spikes imposed

Acknowledgment

The financial support of the U.S. Environmental Protection Agency through grant number R-815298-01 is appreciated.

References

Buchave, P., George, W. K., and Lumley, J. L., 1979, "The Measurement of Turbulence with the Laser-Doppler Anemometer," *Annual Review of Fluid Mechanics*, Vol. 11, pp. 443-503.

Hetsroni, G., and Sokolov, M., 1971, "Distribution of Mass, Velocity, and Intensity of Turbulence in a Two-Phase Turbulent Jet," ASME *Journal of Applied Mechanics*, Vol. 12, pp. 315-327.

Wang, S. K., Lee, S. J., Jones, Jr., O. C., and Lahey, Jr., R. T., 1990, "Statistical Analysis of Turbulent Two-Phase Pipe Flow," ASME JOURNAL OF FLUIDS ENGINEERING, Vol. 112, pp. 89-95.

A Near-Wall Model for Separated Turbulent Flows

U. C. Goldberg[1]

A near-wall model for separated turbulent flows is presented and evaluated. The model is based on experimental observations, in particular, the wake-like behavior of turbulence away from walls, the influence of walls on this behavior, the diffusion/dissipation energy balance observed in the backflow portion of detached flow regions, and the near-wall behavior of eddy-viscosity. These lead to two analytically solvable ODE's for the normal-to-wall behavior of turbulence kinetic energy and eddy-viscosity. The model is applied in conjunction with an outer eddy-viscosity model (such as a $k - \epsilon$ model) to predict eddy-viscosity distribution in separated flow regions. Predictions of two flow cases, using this approach, are shown.

Introduction

Turbulent detached flow regions exhibit a strong wake-like behavior close to solid surfaces. This behavior precludes the

---

[1] Member Technical Staff, Rockwell International Science Center, Thousand Oaks, CA 91360.

Contributed by the Fluids Engineering Division of THE AMERICAN SOCIETY OF MECHANICAL ENGINEERS. Manuscript received by the Fluids Engineering Division January 30, 1992. Associate Technical Editor: D. M. Bushnell.

$$\overline{I(t)} = \frac{N\left[\frac{\beta}{(\alpha+\beta)}\right](1) + N\left[\frac{\alpha}{(\alpha+\beta)}\right](0)}{N} = \frac{\beta}{(\alpha+\beta)} \tag{3}$$

and the mean-square of $I(t)$ is,

$$\overline{(I')^2} = \frac{\alpha\beta}{(\alpha+\beta)^2}. \tag{4}$$

Except in dense-particle flows, spike duration is short relative to the time between spikes. In this case, $\alpha/\beta \ll 1$, $\overline{I(t)} \approx 1$ and $\overline{F(t)}$ approaches $\overline{f(t)}$.

The mean-square value of $F(t)$, is,

$$\overline{(F')^2} = \overline{[\bar{f} I' + f'\bar{I} + f'I' - \bar{g}I' + g' - g'\bar{I} - g'I' - \overline{g'I'} - \overline{f'I'}]^2}. \tag{5}$$

Once this expression is squared and averaged, it is easy to show that with $\bar{I} \approx 1$ and $\overline{I'^2} \approx 0$ for $\alpha/\beta \ll 1$, $\overline{F'^2}$ becomes,

$$\overline{(F')^2} = \overline{(f')^2} + \overline{(g')^2} - \overline{f'g'}. \tag{6}$$

But since $f(t) \approx g(t)$, and $\overline{f'g'} \approx \overline{g'^2}$, $\overline{F'^2}$ approaches $\overline{f'^2}$. For the mass loadings considered, using the corrected signal to compute u_{rms} results in an underestimate of 2 percent.

The autocovariance must be evaluated from the corrected signal since a continuous time series is required. The autocovariance of the corrected signal is,

$$R_F(s) = \lim_{T\to\infty} \frac{1}{T}\int_0^T F(t)F(t+s)ds. \tag{7}$$

To compute R_F, autocovariance tensors:

$$R_f = \overline{f'(0)f'(s)} \tag{8a}$$

$$R_I = \overline{I'(0)I'(s)} \tag{8b}$$

$$R_F = \overline{F'(0)F'(s)} \tag{8c}$$

$$R_{fg} = \overline{f'(0)g'(s)} \tag{8d}$$

$$R_g = \overline{g'(0)g'(s)} \tag{8e}$$

are introduced. Following the usual averaging procedures with the mean value removed, R_F is,

$$R_F = \overline{I^2}R_f + [R_f + R_g - 2R_{fg}]R_I + 2\bar{I}(1-\bar{I})R_{fg} + [1 - 2\bar{I} + \overline{I^2}]R_g. \tag{9}$$

Once again assuming that $\alpha/\beta \ll 1$, all but the first term, the desired autocovariance, can be neglected.

Since the energy spectrum, $E(n)$, is the Fourier transform of R_F, the last three terms in Eq. (9) add broad-band noise to the spectrum. Low energy noise is most likely to affect the shape of the spectrum at high frequencies. Noise in the spectrum is analyzed by comparing the energy spectrum from a particle-free signal to the spectrum of the same signal with the spike replacement procedure applied, where the number and location of spikes are matched to those in a data set with 5×10^{-8} g/cm^3 particles. Figure 3 shows that the two spectra are indistinguishable.

Summary

Hot-film anemometry can be used to discriminate gas-phase from fine-particle velocities if the signal is digitized at rates sufficiently high to identify particle impingement spikes and prevent aliasing. Voltage spikes can then be removed from the data using a slope threshold detection method and replaced with the last digital value before the spike. Errors in flow statistics are negligible if particle concentration is sufficiently low so that particle-induced voltage spikes make-up only a small portion of the total signal. Changes in probe calibration due to contamination can be handled by calibrating a clean probe at several over-heat ratios, and then using the calibration that most closely matches that of the dirty probe.

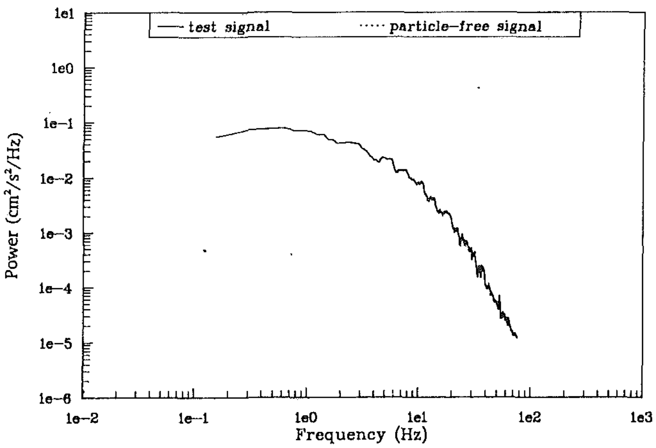

Fig. 3 Comparison of energy spectrum of particle-free signal to energy spectrum of a corrected signal with artificial spikes imposed

Acknowledgment

The financial support of the U.S. Environmental Protection Agency through grant number R-815298-01 is appreciated.

References

Buchave, P., George, W. K., and Lumley, J. L., 1979, "The Measurement of Turbulence with the Laser-Doppler Anemometer," *Annual Review of Fluid Mechanics*, Vol. 11, pp. 443-503.

Hetsroni, G., and Sokolov, M., 1971, "Distribution of Mass, Velocity, and Intensity of Turbulence in a Two-Phase Turbulent Jet," ASME *Journal of Applied Mechanics*, Vol. 12, pp. 315-327.

Wang, S. K., Lee, S. J., Jones, Jr., O. C., and Lahey, Jr., R. T., 1990, "Statistical Analysis of Turbulent Two-Phase Pipe Flow," ASME JOURNAL OF FLUIDS ENGINEERING, Vol. 112, pp. 89-95.

A Near-Wall Model for Separated Turbulent Flows

U. C. Goldberg[1]

A near-wall model for separated turbulent flows is presented and evaluated. The model is based on experimental observations, in particular, the wake-like behavior of turbulence away from walls, the influence of walls on this behavior, the diffusion/dissipation energy balance observed in the backflow portion of detached flow regions, and the near-wall behavior of eddy-viscosity. These lead to two analytically solvable ODE's for the normal-to-wall behavior of turbulence kinetic energy and eddy-viscosity. The model is applied in conjunction with an outer eddy-viscosity model (such as a $k - \epsilon$ model) to predict eddy-viscosity distribution in separated flow regions. Predictions of two flow cases, using this approach, are shown.

Introduction

Turbulent detached flow regions exhibit a strong wake-like behavior close to solid surfaces. This behavior precludes the

---

[1] Member Technical Staff, Rockwell International Science Center, Thousand Oaks, CA 91360.

Contributed by the Fluids Engineering Division of THE AMERICAN SOCIETY OF MECHANICAL ENGINEERS. Manuscript received by the Fluids Engineering Division January 30, 1992. Associate Technical Editor: D. M. Bushnell.

use of the Law of the Wall as a tool for analyzing such flow regions and necessitates development of specialized models for the treatment of these regions.

Experiments in turbulent flow recirculation zones by Simpson (1981) and Delery (1983) indicate that there is a wide class of such flows in which the backflow region is characterized by negligible turbulence production. In such cases the balance of turbulence energy is between energy diffusion from the outer (large-scale turbulence) flow into the reversed flow region and its dissipation within that region. This observation formed the basis for a previous model (Goldberg, 1992 and Goldberg et al., 1992) whose formulation, however, ignored the influence of solid surfaces on the behavior of the turbulence kinetic energy.

The current model, like the previous one, is based on solving an ordinary differential equation (ODE) in the normal-to-wall direction to establish a general behavior of eddy-viscosity as a function of wall distance; unlike the previous model, the current one features an additional ODE, this one for the turbulence kinetic energy itself, based on experimental observations of the near-wall behavior of eddy-viscosity in separated flow regions.

The performance of this model was evaluated through comparisons with experimental data from several flow cases, two of which are reported here.

Model Formulation

The standard turbulence kinetic energy equation (with gradient diffusion model and a dissipation rate model) is given by

$$\frac{\partial}{\partial t}(\rho k)+\frac{\partial}{\partial x_i}(\rho U_i k)=\frac{\partial}{\partial x_i}\left[(\mu+\mu_t/\sigma_k)\frac{\partial k}{\partial x_i}\right]-\rho\overline{u_i' u_j'}\frac{\partial U_i}{\partial x_j}-C_k\frac{(\rho k)^2}{\mu_t} \quad (1)$$

where k is the turbulence kinetic energy, ρ is the density, U_i and u_i' are the cartesian mean and fluctuating velocity components, respectively, μ and μ_t are the molecular and eddy-viscosities, respectively, x_i are the cartesian coordinates, and t is time. The modeling constants are $\sigma_k \cong 1.0$, $C_k \cong 0.08$.

This equation is simplified based on experimental observations of separated turbulent flows (e.g., Simpson, 1981 and Delery, 1983), suggesting that the kinetic energy of turbulence behaves in a wake-like manner between some near-wall location and the outer flow. This behavior is altered within the near-wall region due to the wall influence, as seen in Fig. 1. These observations further suggest that a class of separated flows contains a diffusion/dissipation energy balance in the backflow portion of the separation bubble, with production of turbulence being of secondary importance. In addition, Driver (1991) observed an approximately linear distribution of eddy-viscosity normal to walls in backflow regions.

For the purpose of modeling the turbulence within such regions, k is treated as a function of the normal-to-wall distance, y, with streamwise variations in k effected implicitly only. Using this concept in Eq. (1) and retaining only the diffusion and dissipation terms, results in the equation

$$\frac{d}{dy}\left[\left(\mu+\frac{\mu_t}{\sigma_k}\right)\frac{dk}{dy}\right]-C_k\frac{(\rho k)^2}{\mu_t}=0. \quad (2)$$

The effect of molecular diffusion in the near-wall zone is taken implicitly into account through the derived model for k (see below), and will not be retained explicitly, further reducing Eq. (2) to read

$$\frac{d\psi}{dy}-\left[\frac{C_k}{\sigma_k}(\rho k)^2\frac{dk}{dy}\right]\frac{1}{\psi}=0,\ \psi\equiv\frac{\mu_t}{\sigma_k}\frac{dk}{dy}. \quad (3)$$

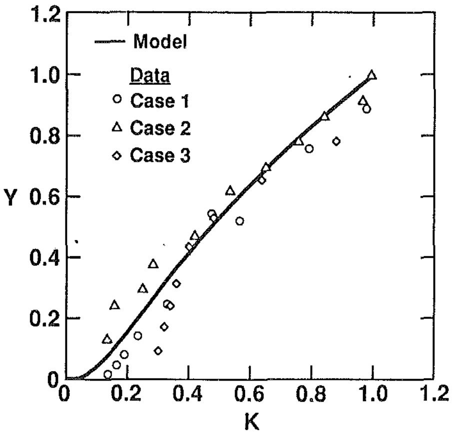

Fig. 1 Model and data comparison of kinetic energy versus wall distance

The general solution to Eq. (3), assuming no explicit dependence of density on distance from the wall, and with kinetic energy satisfying the boundary condition $k = 0$ at $y = 0$, is given by

$$\mu_{t_s}=y_m\frac{\sqrt{\frac{2}{3}\sigma_k C_k\rho(\rho k)_{\max}K^3}}{\frac{dK}{dY}},\ dK/dY\neq 0 \quad (4)$$

where

$$K\equiv\frac{(\rho k)_s}{(\rho k)_{\max}},\ Y\equiv y/y_m,\ y_m\equiv y_{(\rho k)_{\max}}$$

and subscript s denotes separated flow. Here $(\rho k)_{\max}$ is the local maximum density-weighted kinetic energy, supplied by the outer model. Equation (4) is applicable only in the range $Y \leq 1$ since turbulence production may be significant for $Y > 1$, rendering Eq. (2) invalid in that region.

To force a linear behavior on $\mu_{t_s}(Y)$ requires that

$$\frac{dK}{dY}-\frac{K^{3/2}}{\beta^2 Y}=0. \quad (5)$$

The solution to this ODE, subject to the boundary condition $K = 1$ at $Y = 1$, is

$$K=\left(\frac{-2\beta^2}{\ln Y-2\beta^2}\right)^2 \quad (6)$$

and the corresponding eddy-viscosity, combining Eqs. (4) and (5), is given by

$$\mu_{t_s}=\beta^2 y\sqrt{\frac{2}{3}\sigma_k C_k\rho(\rho k)_{\max}},\ y\leq y_m. \quad (7)$$

To determine β^2, Eq. (6) is compared with experimental data, and an optimum value is then chosen. Figure 1 compares Eq. (6) with typical data within separated flow regions. These data are taken from the following flow cases: (1) transonic flow over an axisymmetric bump of Bachalo and Johnson (1979); (2) transonic flow over a two-dimensional bump of Delery (1983); (3) low subsonic flow over a backward-facing step of Driver and Seegmiller (1985). The figure shows that the experimental kinetic energy profiles are of similar shape, in spite of the different flow cases and mechanisms by which the separated flow regions were induced (e.g. geometry-induced vs shock-induced). A good fit to the data is obtained with $\beta^2 \approx 0.5$. The modeled curve captures both the near-wall and the wake-like behavior of K versus Y.

The final eddy-viscosity distribution is produced in the form

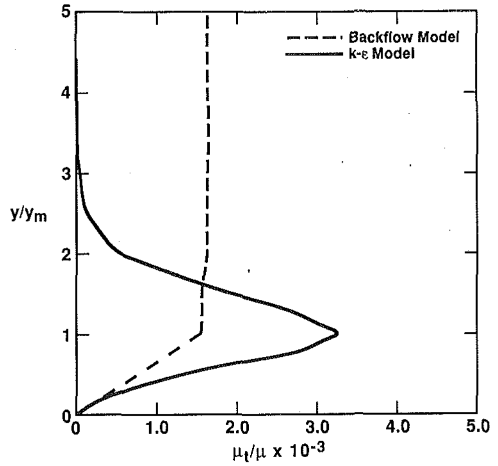

Fig. 2 Typical eddy-viscosity profiles produced by outer and backflow models separately

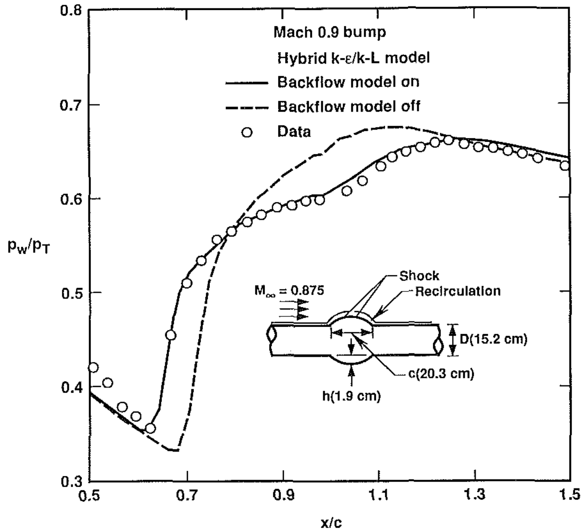

Fig. 3(*a*) Transonic bump flow: wall pressure distribution comparison

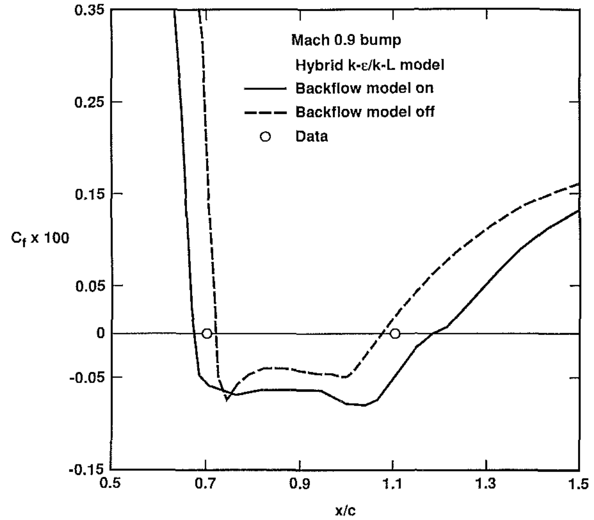

Fig. 3(*b*) Transonic bump flow: skin friction distribution comparison

$$\mu_t = \min\{\mu_{t_s}, \mu_{t_{\text{outer}}}\} \tag{8}$$

with μ_{t_s} kept at its $Y = 1$ level for $Y > 1$. Figure 2 shows a typical eddy-viscosity profile calculated with this model, and the corresponding profile predicted by a $k - \epsilon$ outer model. The present model's formulation, Eq. (7), remains unchanged in three-dimensional flow situations.

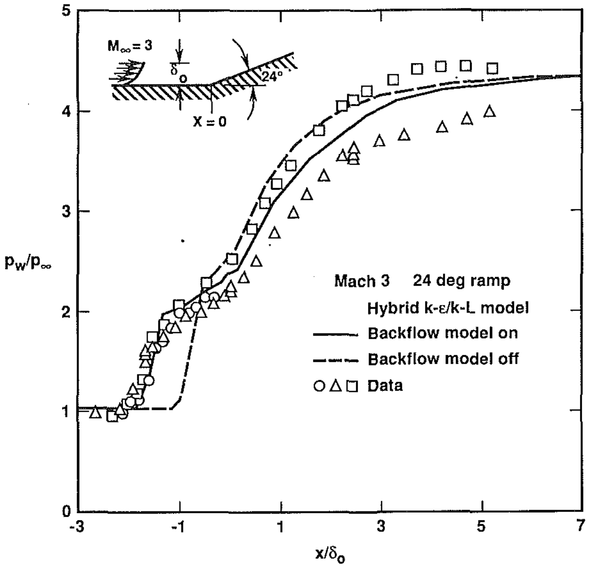

Fig. 4(*a*) Supersonic ramp flow: wall pressure distribution comparison

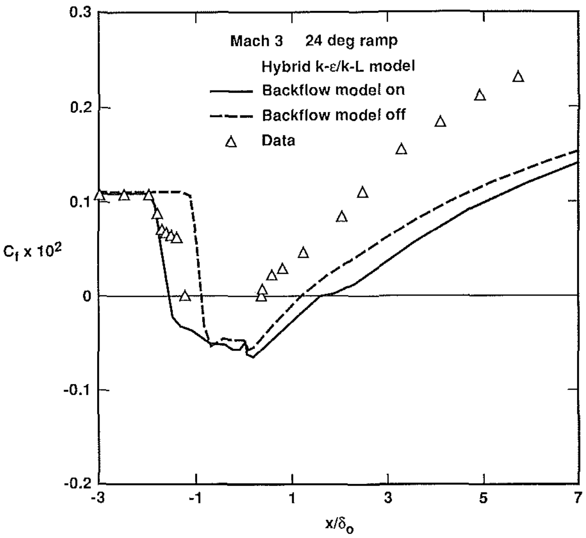

Fig. 4(*b*) Supersonic ramp flow: skin friction distribution comparison

Model Evaluation

The present model was included in the USA Reynolds-averaged Navier-Stokes flow solver (Chakravarthy et al., 1988). Several flow cases were successfully computed, two of which are reported here.

Case 1. This case is the transonic flow over an axisymmetric bump of Bachalo and Johnson (1979). Here a normal shock, impinging on the bump, induces a separated flow region. In Figs. 3(*a*) and (*b*) x is the axial coordinate, with origin at the bump leading edge; and y is the radial coordinate, with origin at the axis of symmetry. The figures present comparisons between predictions and data for surface pressure (p_w), and skin friction (C_f). The pressure is scaled by the upstream total pressure, p_T. The outer model was a hybrid 2-eq./1-eq. turbulence model (Goldberg and Ramakrishnan, 1992) which includes a near-wall treatment for attached flows. Results are shown with and without invoking the present model. A 101 × 50 grid size was used, with at least three cells inside the viscous sublayer ($y^+ \leq 11$). Grid refinement yielded no change in the flow predictions.

Case 2. This case is the supersonic two-dimensional flow over a 24 deg ramp of Settles et al. (1979), with additional data by Dolling and Murphy (1983), and by Selig et al. (1989). An oblique shock, impinging on the boundary layer ahead of the ramp corner, due to upstream influence, induces a separated flow region. Figures 4 show predictions and data comparisons for surface pressure and skin friction. Here, too, the hybrid turbulence model served as the outer model. Results are shown with and without the present model. A 125 × 50 grid size was employed, with at least four cells within the viscous sublayer.

Summary

A near-wall model for separated turbulent flows was introduced and tested. The model is based on experimental observations, in particular, the wake-like behavior of turbulence away from the vicinity of walls, the change in this behavior in near-wall regions due to the influence of solid surfaces, the behavior of eddy-viscosity in backflow regions, and the type of energy balance observed in such regions. These observations lead to two analytically solvable ODE's for eddy-viscosity and kinetic energy, the former resulting from a reduced form of the kinetic energy transport equation. These ODE's establish the velocity- and length-scales of the current model. The model is applied together with an outer turbulence model (such as a $k - \epsilon$ model) to predict eddy-viscosity distribution in separated flow regions, while the outer model alone predicts eddy-viscosity throughout the rest of the flow-field. This approach may be applicable to three-dimensional flows. Calculations of several cases involving separated flow regions, using this approach, are encouraging.

Since the model is based on observed physics it may prove a useful tool for engineering applications.

References

Bachalo, W. D., and Johnson, D. A., 1979, "An Investigation of Transonic Turbulent Boundary Layer Separation Generated on an Axisymmetric Flow Model," AIAA Paper 79-1479.

Chakravarthy, S. R., Szema, K.-Y., and Haney, J. W., 1988, "Unified 'Nose-to-Tail' Computational Method for Hypersonic Vehicle Applications," AIAA Paper 88-2564.

Delery, J. M., 1983, "Experimental Investigation of Turbulence Properties in Transonic Shock/Boundary-Layer Interactions," *AIAA Journal*, Vol. 21, No. 2, pp. 180–185.

Dolling, D. S., and Murphy, M. T., 1983, "Unsteadiness of the Separation Shock Wave Structure in a Supersonic Compression Ramp Flowfield," *AIAA Journal*, Vol. 21, No. 12, pp. 1628–1634.

Driver, D. M., and Seegmiller, H. L., 1985, "Features of a Reattaching Turbulent Shear Layer in Divergent Channel Flow," *AIAA Journal*, Vol. 23, No. 2, pp. 163–171.

Driver, D. M., 1991, "Reynolds Shear Stress Measurements in a Separated Boundary Layer Flow," AIAA Paper 91-1787.

Goldberg, U. C., Bihari, B. L., and Ramakrishnan, S. V., 1992, "Model for Turbulent Backflows," *AIAA Journal*, Vol. 30, No. 2, Feb. 1992, pp. 557–559.

Goldberg, U. C., 1992, "A Three-Layer Model for Separated Turbulent Flows," ASME JOURNAL OF FLUIDS ENGINEERING, Vol. 114, Sept., pp. 333–337.

Goldberg, U. C., and Ramakrishnan, S. V., 1992, "Flowfield Predictions with a Hybrid $k - \epsilon/k - L$ Turbulence Model," AIAA Paper 92-2645.

Selig, M. S., Andreopoulos, J., Muck, K. C., Dussauge, J. P., and Smits, A. J., 1989, "Turbulence Structure in a Shock Wave/Boundary Layer Interaction," *AIAA Journal*, Vol. 27, No. 7, pp. 862–869.

Settles, G. S., Fitzpatrick, T. J., and Bogdonoff, S. M., 1979, "Detailed Study of Attached and Separated Compression Corner Flowfields in High Reynolds Number Supersonic Flow," *AIAA Journal*, Vol. 17, No. 6, pp. 579–585.

Simpson, R. L., 1981, "A Review of Some Phenomena in Turbulent Flow Separation," ASME JOURNAL OF FLUIDS ENGINEERING, Vol. 103, pp. 520–533.